LA-14417-T
Thesis

A Hierarchical Framework for the Multiscale Modeling of Microstructure Evolution in Heterogeneous Materials

Los Alamos
NATIONAL LABORATORY
EST. 1943

This thesis was accepted by the George W. Woodruff School of Mechanical Engineering, Georgia Institute of Technology, in partial fulfillment of the requirements for the degree of Doctor of Philosophy. The text and illustrations are the independent work of the author, and only the front matter has been edited by the IRM-CAS Writing and Editing staff to conform with Department of Energy and Los Alamos National Laboratory publication policies.

Los Alamos National Laboratory, an Affirmative Action/ Equal Opportunity Employer, is operated by Los Alamos National Security, LLC, for the National Nuclear Security Administration of the U.S. Department of Energy under contract DE-AC52-06NA25396.

LA-14417-T
Thesis
Issued: April 2010

A Hierarchical Framework for the Multiscale Modeling of Microstructure Evolution in Heterogeneous Materials

Darby J. Luscher

Los Alamos
NATIONAL LABORATORY
EST. 1943

A HIERARCHICAL FRAMEWORK FOR THE MULTISCALE MODELING OF MICROSTRUCTURE EVOLUTION IN HETEROGENEOUS MATERIALS

A Dissertation
Presented to
The Academic Faculty

By

Darby J. Luscher

In Partial Fulfillment
of the Requirements for the Degree
Doctor of Philosophy in the
George W. Woodruff School of Mechanical Engineering

Georgia Institute of Technology

May 2010

GEORGIA INSTITUTE OF TECHNOLOGY
Office of Graduate Studies & Research

CERTIFICATE OF THESIS APPROVAL FOR DOCTORAL STUDENTS

GTID# 902013989

Name: Darby (First) Jon (Middle) Luscher (Last)

Thesis Title:

A Hierarchical Framework for the Multiscale Modeling of Microstructure Evolution in Heterogeneous Materials

We, the below signed, hereby state our full approval of the thesis submitted by the above student in partial fulfillment of the requirements for the degree of Doctor of Philosophy in the School/College of Mechanical Engineering.

Approved by:

Thesis Advisor	McDowell, ME Print last name & dept.	Member, Reading Committee	Garmestani, MSE Print last name & dept.
Member, Reading Committee	Qu, ME Print last name & dept.	Member, Reading Committee	Haj-Ali, CEE Print last name & dept.
Member, Reading Committee	Zhou, ME Print last name & dept.	Member, Reading Committee	Print last name & dept.

The above named student has completed all departmental requirements and oral presentation.

School Chair/Graduate Coordinator — 3/17/10 Date

* *

(GEORGIA TECH GRADUATE OFFICE USE ONLY)

The Georgia Tech Graduate Office has received the above dissertation and appropriate forms.

Signature — RECEIVED MAR 3 1 2010 Date

rev. 1/2002

A HIERARCHICAL FRAMEWORK FOR THE MULTISCALE MODELING OF MICROSTRUCTURE EVOLUTION IN HETEROGENEOUS MATERIALS

Approved by:

Dr. David McDowell, Advisor
George W. Woodruff School of
Mechanical Engineering
Georgia Institute of Technology

Dr. Hamid Garmestani
School of Material Science
and Engineering
Georgia Institute of Technology

Dr. Min Zhou
George W. Woodruff School of
Mechanical Engineering
Georgia Institute of Technology

Dr. Rami Haj-Ali
School of Civil and Environmental
Engineering
Georgia Institute of Technology

Dr. Jianmin Qu
George W. Woodruff School of
Mechanical Engineering
Georgia Institute of Technology

Date Approved: 03/16/2010

ACKNOWLEDGEMENTS

As far as I am concerned, there is no better way to celebrate a success than to share the credit with those that have contributed to the effort. Here I share credit with those people that have had tremendous impact to the successful completion of requirements for my PhD degree at Georgia Tech, including this dissertation.

Of primary importance in this acknowledgement is to convey how substantial I consider my wife's sacrifices over the last five years. With the sole exception of unmarried PhD candidates, I do not imagine that there exists a PhD thesis whose acknowledgement section does not make reference to the author's spouse. So I strive to make this acknowledgement of my wife's contributions to my success so compelling and unique that it escapes the status of 'formality'. To attempt this, I will provide a single anecdote selected from five years of worthy material.

Stephanie Luscher endured months alone keeping our house in Los Alamos while I was in Atlanta attending classes and fulfilling residency requirements. During that time, she continued working as an engineering design review coordinator at Los Alamos National Lab. While in Oregon to visit family during the winter of 2004-5, a water pipe inside our Los Alamos house froze and burst. Over the next week, 90,000 gallons of water flowed throughout our house ruining just about everything. We returned home and opened soggy Christmas presents from the relative comfort of our car parked in the driveway while contemplating our next course of action. Our house required extensive repairs including a new heating system, kitchen cabinets, flooring, and complete refinishing of the interior walls. We lived in a motor home, a rented house, and a hotel over the course of six months of these repairs. Within two weeks of this happening, I was back in Atlanta and Stephanie was left to manage the reconstruction effort by herself. Of course, this is a single example of how Stephanie has sacrificed, and tended to the many details of life, in order to allow me to focus attention on the work presented within this thesis. Stephanie, I thank

you for the support and sacrifice you have made to help me accomplish this goal. I'm glad you embraced "my goal" as "our goal."

Well in advance of thoughts regarding graduate school, my parents instilled a few helpful traits in me. As a young boy, during hot summers spent roofing with my Dad, Mark Luscher, I learned to work hard *and* to play hard. My Dad taught me that sometimes "getting the job done" is not elegant; it simply requires you to roll up your sleeves and get to work. As a complement to this, my Mom taught me the importance of precision and attention to detail. Together, my parents have taught me the importance of family, which supersedes all else.

My late grandfather, Benjamin Luscher, often said "I'm just a little boy who can barely cut a figure. If you'd like to hear a speech from me, you'll have to wait 'till I'm bigger." I never understood the origin of this phrase, but it conveyed the importance of humility to me. While I am confident in the pursuit of my goals, I recognize my limitations and general susceptibility to error.

I am grateful for the support of my advisor, Dr. Dave McDowell, during my career at Georgia Tech. He helped develop my vision of multiscale processes and encouraged the evolution of my research ideas. His knowledge, guidance, and encouragement have been invaluable. Our discussions generated many interesting ideas and have also provided directions to extend this work into future contributions.

I would also like to thank my dissertation reading committee, Drs. Jianmin Qu, Min Zhou, Hamid Garmestani, and Rami Haj-Ali for reviewing this thesis and participating in my proposal and defense presentations. I also want to thank Dr. Neu for mentoring me during the teaching practicum which I completed by assisting him with the fall 2005 undergraduate mechanics of materials course at Georgia Tech.

Successful completion of my PhD benefited from continued support of management at Los Alamos National Lab (LANL). As the division leader for then Engineering Sciences and Applications (ESA) division, Dr. Steve Girrens championed my return to academia and committed division level support to pursue this education. He was especially important in encouraging my growth during my early career at LANL. John Benner, the Weapon Systems

Engineering division leader (W-DO), gave me opportunities to excel within the weapons program. Ryan Maupin, group leader for Advanced Engineering Analysis (W-13) has enthusiastically supported and trusted me, both as my manager and friend, to pursue a course of research that will enhance my future contributions in our group. Dr. Curt Bronkhorst was unwavering in his commitment to fund my thesis research within the Advanced Simulation and Computing (ASC) program at LANL after I returned from completing coursework at Georgia Tech. He also provided significant technical and non-technical mentoring; anytime I felt disillusioned with the process he reminded me of the progress I had already made and encouraged me onward.

Dr. Chuck Farrar has been both mentor and friend through this process, helping me to think about the trajectory of my career and also giving me opportunities for teaching and collaborating within the LANL Engineering Institute and Structural Dynamics Summer School that he directs. A key point he continually emphasized is that the critical distinction between PhD theses is into one of two categories; those that are completed and those that aren't. Dr. Matt Bement has provided technical assistance with computational resources, code development, and has participated in many discussions on data modeling. He has also been a source of moral support and reviewed sections of the thesis to improve its accuracy and clarity. Dr. Don Hush met with me several times to discuss approaches to employ data modeling techniques and also reviewed the thesis providing helpful feedback. Drs. David Crane and Phil Schembri performed a thorough review of the developed theoretical framework and provided insightful discussions helping me to improve my own understanding of the larger context of this work. Along with Matt, David, and Phil, Dario Castano helped me prepare for the dissertation defense; their feedback caused a significant improvement in the clarity of presentation. Miles Buechler, Devin Shunk, Dr. Matt Lewis also devoted substantial time to reading the dissertation and making editorial and technical comments.

I appreciate the encouragement I received from friendships that developed during my time in Atlanta. I am grateful for the camaraderie with Jason Mayeur and Dr. Ambarish Kulkarni, which made our intense studying for the Ph.D. qualifying examination bearable. This work has benefited from many thought-provoking discussions with Jason Mayeur and Ryan Austin on applied and computational mechanics and crystal plasticity. I am also thankful to Ty Gailey for

sharing his house and time with me. The Friday nights spent sipping rum outside by the fire helped to pass my stay away from home.

Finally, I would like to attribute an incredible inspiration I've experienced to our son, Cole Benjamin Luscher, born June 29th, 2008.

TABLE OF CONTENTS

LIST OF TABLES

LIST OF FIGURES

SUMMARY

All materials are heterogeneous at various scales of observation. The influence of material heterogeneity on nonuniform response and microstructure evolution can have profound impact on continuum thermomechanical response at macroscopic “engineering” scales. In many cases, it is necessary to treat this behavior as a multiscale process thus integrating the physical understanding of material behavior at various physical (length and time) scales in order to more accurately predict the thermomechanical response of materials as their microstructure evolves. The intent of the dissertation is to provide a formal framework for multiscale hierarchical homogenization to be used in developing constitutive models.

This research developed a hierarchical multiscale approach for modeling microstructure evolution. A theoretical framework for the hierarchical homogenization of inelastic response of heterogeneous materials was developed with a special focus on scale invariance principles needed to assure physical consistency across scales. Within this multiscale framework, the second gradient is used as a nonlocal kinematic link between the response of a material point at the coarse scale and the response of a neighborhood of material points at the fine scale. Kinematic consistency between two scales results in specific requirements for constraints on the fluctuation field. A multiscale internal state variable (ISV) constitutive theory is developed that is couched in the coarse scale intermediate configuration and from which an important new concept in scale transitions emerges, namely scale invariance of dissipation.

At the fine scale, the material is treated using finite element models of statistical volume elements of microstructure. Fine scale boundary conditions are developed that satisfy kinematic consistency requirements and methods for numerical implementation of such boundary conditions are developed and evaluated in the context of fine scale response. The coarse scale is treated using a mixed-field finite element approach. The coarse scale constitutive equations are implemented in a finite deformation hyperelastic inelastic integration scheme developed for second gradient constitutive models. An example problem based on an idealized porous

microstructure is presented to illustrate the approach and highlight its predictive utility. This example and a few variations are explored to address the boundary-value-problem dependant nature of length scale parameters employed in nonlocal continuum theories.

Finally, strategies for developing meaningful kinematic ISVs, free energy functions, and the associated evolution kinetics are presented. These strategies are centered on the goal of accurately representing the energy stored and dissipated during irreversible processes.

CHAPTER I

INTRODUCTION

All materials are heterogeneous at various scales of observation. While material heterogeneities are interesting in and of themselves, it is ultimately through their influence on non-uniform response and microstructure evolution that they have profound impact on continuum thermomechanical response at macroscopic "engineering" scales. That many materials can be treated as homogeneous continua owes to the distinct separation of the scale of the problem under consideration and the scales at which actual heterogeneities affect physical processes. These physical processes include various sources of inelastic behavior such as plasticity, nucleation and growth of damage, and phase transformation, to name a few. Historical approaches to model such processes that reflect an intimate coupling of physical scales consist of phenomenological constitutive relations that are developed either empirically or by analytical micromechanics and subsequently fit to experiment. The primary shortcoming of such approaches are that the developed models do not necessarily accurately reflect the physical processes occurring at various scales and, in some aspects, can be characterized as highly nonlinear curve fits to limited sets of data. In order to more accurately predict the thermomechanical response of materials as their microstructure evolves, it is necessary to treat this behavior as a multiscale process thus integrating the physical understanding of material behavior at various physical (length and time) scales.

Explosive growth in computational power coupled with innovation in numerical modeling has enabled detailed modeling efforts to explore and quantify the thermomechanical response of materials across a multitude of physical scales for a variety of inelastic processes. Multiscale modeling has inspired a new vision of being able to develop constitutive models for use at physical scales common to engineering problems using detailed information developed from a

hierarchy of models at finer scales. Recent advances have been made in this area with emphasis on simultaneously linking numerical models of processes occurring at each scale. Such approaches offer advantages in avoiding constitutive complexity and reducing uncertainty at engineering scales at the cost of tremendous computational burden when compared to historical phenomenological engineering-scale models.

An alternative approach is to build constitutive models from successive homogenization of modeling conducted at other scales in a hierarchical fashion. This approach results in constitutive models at the largest scales that reflect the complexities of processes at finer scales in some homogenized sense without the need to conduct simulations at all scales simultaneously. However, in order to build the heterogeneous response of materials into computational models for use at engineering scales, for example in finite element simulations of system response, numerical modeling conducted at each scale must be arranged in a formal hierarchy such that fundamental quantities of the physical laws governing each scale are preserved across scale transitions. In fact, recent advances made both in concurrent scale linking and hierarchical transitions in scale are lacking in their formality and rigor when accounting for physical quantities that enter balance laws at separate scales. Additionally, heterogeneous response of materials is inherently nonlocal; this nonlocal nature of multiscale response should be reflected in such a hierarchical homogenization scheme.

These considerations suggest that a significant contribution towards multiscale modeling of heterogeneous materials can be made by developing a formal framework for the hierarchical homogenization of thermomechanical response. The objectives of this dissertation are to:

- Develop a theoretical framework for scale transitions that assures physical consistency across scales and reflects effects of gradients of deformation
- Implement the theoretical framework in numerical models at separate scales
- Apply the developed framework and numerical implementation to an example problem and demonstrate the intended approach highlighting important aspects of the theory and the associated improvements to predictive capabilities.

At the core of this framework is a set of principles that enforces kinematic consistency and scale invariance of mass, momentum, and energy. Thermodynamics of irreversible processes, in particular Internal State Variable (ISV) theory, is employed to ensure common representation of free energy and dissipation at all scales within a hierarchy. A second order Taylor series kinematic decomposition is employed at the coarse scale resulting in a nonlocal second gradient continuum description of the coarse scale material response. This aspect of the framework introduces an implicit material length scale associated with the dominant length scale of material response. The critical aspect of this framework is the selection of physically meaningful ISVs and the associated constitutive description of their irreversible evolution.

While the physical principles and quantitative approach are applicable to more general scale transitions, for example, atomistic to continuum, theoretical development and numerical implementation are focused on transitions between scales each amenable to a continuum description. It is intended that one of the two scales can describe in greater detail the heterogeneous characteristics of the material response; that scale is referred to as the fine scale. The example problems presented are limited to relatively simple problems in order to highlight the approach and conceptual features. Also, while the framework is motivated in the context of truly multiscale problems, concentration is focused on a single transition in scale. Additional scales would be introduced by successive nested application of the developed framework. Attention in the presented examples is typically restricted to two dimensional response, simple descriptions of heterogeneous features, and simple fine scale constitutive response.

Potential application areas of the developed framework and related computational codes include model development for the inelastic response of high explosives, development of multiscale ISV models for the prediction of dynamic fracture and fragmentation of polycrystalline metals, computational material design of nuclear fuels for optimal performance, and for modeling of energy dissipation to enhance control algorithms for structural and mechanical systems and machining processes. These specific application areas are current areas of interest in numerical modeling at the Los Alamos National Laboratory that pose significant challenges to the existing methods. They are not a central focus of this dissertation for two reasons. First, it is desired to develop a framework that provides sufficient generality to be applicable to a range of problems

rather than an *ad hoc* problem-specific scheme. Second, the future application areas require such broad modeling expertise and significant depth that they demand collaborative effort. It is envisioned that the developed framework is a roadmap for such collaborative multiscale constitutive model development.

The remainder of this dissertation is organized as follows. Chapter 2 provides a conceptual overview of the multiscale hierarchy, covers essential physical principles, and discusses recent and emerging approaches to multiscale modeling of heterogeneous materials from the technical literature. Using the physical principles established in Chapter 2, a theoretical framework for scale transitions is developed in Chapter 3. Chapter 4 addresses numerical modeling at the fine scale with discussion on techniques for constructing models of microstructure response, development and implementation of boundary conditions applicable to such models, and computation of important physical quantities of interest in these numerical simulations. The numerical implementation at the coarse scale is based on a finite element formulation for second gradient response that adheres to the constitutive requirements developed in Chapter 3. This implementation, numerical testing and code verification efforts are detailed in Chapter 5. An example is presented in Chapter 6 in which an extruded channel comprising an idealized porous microstructure is subjected to loading that emphasizes bands of shear localization. The example compares solutions using an explicit representation of the microstructure in the coarse scale problem with solutions obtained from an idealized phenomenological model and those obtained from the approach developed in this dissertation. Chapter 7 explores strategies to develop coarse scale internal state variable constitutive relations based on fine scale microstructure simulations. Finally, the unique contributions of this work are summarized and concluding comments are made in Chapter 8.

The unique contributions of this dissertation are summarized as follows. This dissertation uniquely

- develops a formal framework for scale transitions between continuum scales that ensures physical consistency across scales, including dissipation,

- employs this framework in the context of a complete second gradient kinematic description,
- develops new theoretical requirements for fine scale boundary conditions on microstructure simulations and approaches for numerical implementation, including effects of nonzero second gradient,
- examines the relative effects of various sets of fine-scale boundary conditions,
- establishes the precise nature of antisymmetry of coarse scale Cauchy stress in second-gradient continua,
- establishes the importance of body forces in computation of coarse scale stresses especially regarding internal fluctuation constraints,
- develops a fully finite deformation hyperelastic inelastic constitutive integration algorithm for second gradient inelastic response,
- demonstrates application of the framework and implementation to a multiscale problem which highlights
    - ISVs that capture effects of fine scale heterogeneous microstructure evolution
    - The effect of non-locality in coarse scale model on eliminating artificial mesh dependence of strain localization
    - The role of length scale parameters related to specific mechanisms of response
- proposes and demonstrates strategies for computing coarse scale internal state variables directly from fine scale simulations and constructing numerical models of their evolution kinetics.

CHAPTER II

OVERVIEW OF MULTISCALE MODELING CONCEPTS

The objective of this dissertation is to develop a formal framework to which multiscale material model research and development efforts can adhere in order to ensure physical consistency across broad ranges of computational and experimental methods. The role of this chapter is to convey a conceptual view of the hierarchical arrangement of physical scales, establish a prioritized list of criteria that defines "physical consistency", and compare the concepts of this framework to historical and emerging approaches. To achieve this goal, Chapter 2 comprises four sections; Section 2.1 illustrates the hierarchy of scales and modeling philosophy, Section 2.2 establishes and justifies the essential tenets of the multiscale framework, Section 2.3 compares this perspective to that of other emerging approaches, and summarizing comments are made in Section 2.4.

2.1 A Hierarchical Multiscale Modeling Philosophy

This section begins with a hypothetical example to introduce a general hierarchy of material scales. While this example is not the particular focus of the dissertation, it serves to illustrate the type of problems which the framework will address in future application. Figure 1 depicts the multiscale hierarchy which may be associated with a (a) fragmentation device composed of (b) composite high-explosive (HE) and a (c) polycrystalline metal. The hierarchy is arranged with finer scales to the left of coarser scales. Scale 0, at the far right side, is the scale of application or the coarsest scale at which modeling is conducted to address specific questions. For example, if the purpose of the modeling effort were to identify the potential fragment size and velocity distributions under an accident scenario where it is dropped during shipping, then the scale of application would be the continuum macroscale (a). If, instead, we are interested only in identifying local temperatures and strain rates which would initiate an HE burn, then the scale of

application would be a microstructural window of the composite explosive material (b). In either case, we assume there exists a specific purpose for the model under development and designate the scale at which the model will be directly applied as scale 0.

If understanding of explicit effects of material heterogeneity at a scale finer than scale 0 is necessary to satisfactorily model the response of the material at scale 0, then a multiscale approach is warranted and will consist of at least scale 1 and scale 0 responses, where scale 1 is the next finer scale. This philosophy lets the application drive the modeling effort and provides a natural means for establishing which physical scales of material response need to be considered. This top-down approach is distinct from a bottom-up approach, in which one would start at the finest scale under consideration and build upwards until reaching the desired end-point. Implementation details of these two approaches are not necessarily different; however, the top-down approach implies that a scale 0 model is continually being updated as additional information propagates upwards from finer scales as necessary. The bottom-up approach seems to rely on an arbitrary selection of the finest scale from which to start.

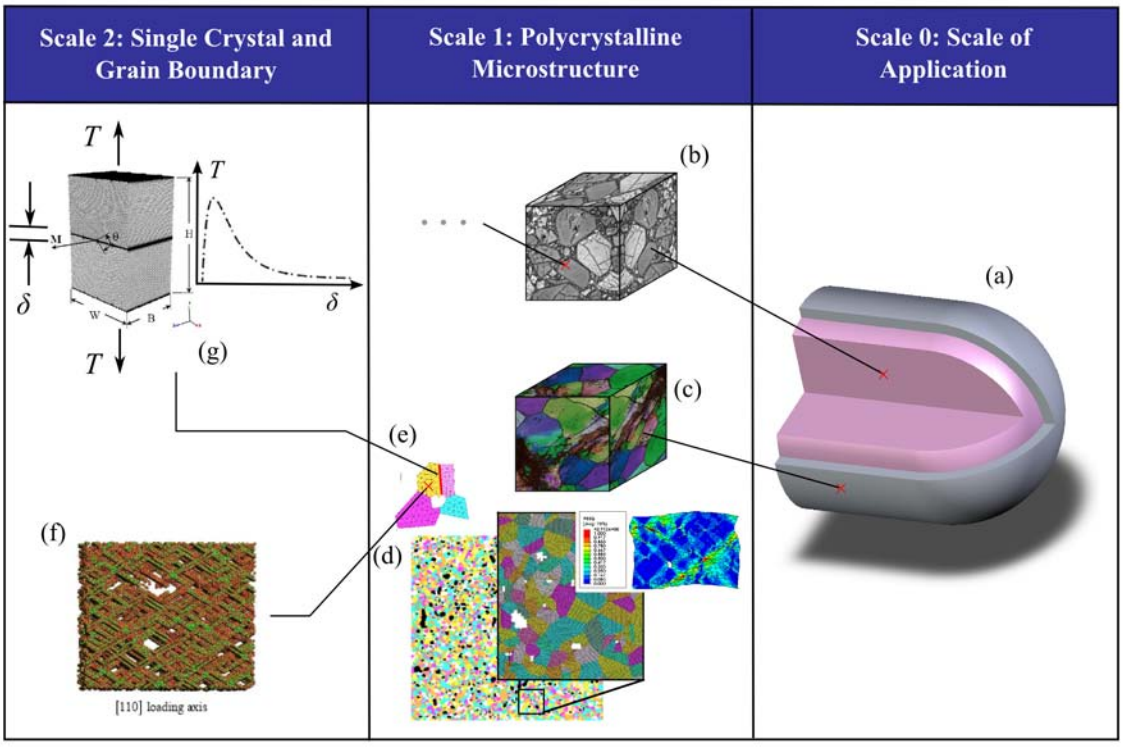

Figure 1. Example of a multiscale hierarchy.

In this example, modeling at scale 1 is necessary in order to identify the dependence of scale 0 deformation and stresses on the growth of intergranular cracks and porosity at scale 1. Additionally, fluctuations of homogenized parameters from scale 1 contribute to localization patterns at scale 0. In the polycrystalline metal alloy (c), referential statistical volume elements (rSVEs, to be defined later) of material are simulated using a finite element model of a synthesized geometric model of the microstructure. Using existing techniques, one could develop an rSVE model that possesses grain-size and orientation distributions, porosity distributions, and other geometric properties consistent with the actual microstructure as determined by micrographs and orientation imaging microscopy[1]. Each rSVE simulation might consist of a single crystal plasticity model for each grain (d) and a cohesive traction-separation behavior specified on grain boundaries (e). The single crystal plasticity models could be derived from and fit to (f) a suite of simulations at the atomistic scale (in this case Scale 2) in order to adequately capture the influence of dislocation structures on particular slip planes. Likewise, the grain-boundary traction separation potentials could be derived from (g) atomistic simulations of grain boundary interfaces. A similar sub-hierarchy exists within the rSVE of HE material (c).

The example hierarchy of Figure 1 is generalized into a hierarchy of N scales as depicted in Figure 2. Every material point, identified by the vector position $\mathbf{x}_o$, in the scale 0 continuum represents the behavior of a neighborhood of material response, ${}^{x}\Omega_o^1$, at scale 1 (finer than scale 0). This neighborhood of material points at scale 1 is defined by the referential statistical volume element (rSVE), which is not necessarily a referential *representative* volume element (rRVE) in the rigorous sense. It is understood that coarse scale behavior is reflected by the responses of a statistical population of rSVEs rather than a single rSVE. The term referential is used to denote an undeformed reference configuration. The local constitutive behavior of each material point, identified by the vector position $\mathbf{y}_o$ in the scale 1 coordinate system, within the rSVE domain, ${}^{x}\Omega_o^1$, at scale 1 is defined by a free energy function, mechanical strain, temperature, a set of

[1] In this dissertation a referential statistical volume element (rSVE) is not necessarily a representative volume element (RVE) which has specific connotations. This distinction is discussed further in Chapter III.

internal state variables that subsume effects of yet finer scale heterogeneity, and corresponding evolution equations that are derived as necessary from computational simulations of the rSVE at scale 2. In general, the transition to a coarser scale, *k*, is performed by solving the initial boundary value problem for an rSVE of material points at scale *k+1*, as shown in Figure 2. In this process, new internal state variables are introduced to represent the manifestation of kinematic degrees of freedom associated with evolving microstructure at scale *k+1*. Simultaneously, those internal state variables (ISVs) associated with the kinematic degrees of freedom at scale *k+2* are *released*. Therefore, ISVs from scale *k+2* and finer are only present at scales *k* and higher due to their implicit mapping into the newly introduced ISVs at scale *k*. In other words, as the scale of observation increases, the number of degrees of freedom used to quantify kinematics of the finest scales decreases. Conceptually, this suggests that one cannot fully ascertain all details of the fine scale response while observing from the coarse scale. The physical implication will be explained in Chapter 3 where it is shown that, through the hierarchy of scale transitions, dissipation and local stored energy are smeared from scale to scale. Practically, the result is that each significant process at each significant scale will require detailed study to develop appropriate scale-specific constitutive relations. It is inappropriate, in general, to simply use the volume average of finer scale constitutive relations to model the response of coarser scales if we insist on certain invariance requirements introduced subsequently, as will be shown. This assertion represents a distinction of the present work from much of the existing literature in homogenization of materials with evolving microstructure.

The framework developed in this dissertation is decidedly focused on transitions between scales of material response that are each amenable to a continuum description; however, the hierarchical concepts presented in this chapter and the physical principles applied in Chapter 3 could equally well be applied to linking continuum response at a course scale to atomistic simulations over a finer scale of observation (cf. Figure 1, Scale 2 and Zhou and McDowell (2002)). Moreover, we focus on a sequential hierarchical approach, but the same principles can hold value for concurrent approaches, in which the solutions of initial boundary value problems for all scales of interest are generated simultaneously.

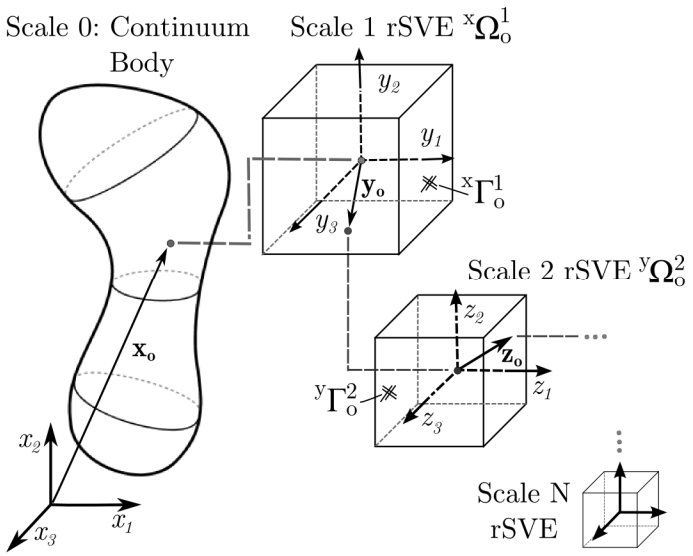

Figure 2. General N-scale hierarchy.

2.2 Essential Tenets of the Multiscale Approach

For each upward transition in scale (*k+1* to *k*) we demand that certain physical principles be adhered to for a fixed reference volume of observation, Ω_o. In addition to satisfaction of classical continuum balance laws at each scale, the issues central to this framework are maintaining kinematic consistency and invariance of mass, linear and angular momentum, and energy with respect to the scale at which a given set of mass particles are observed. Furthermore, we assert that in addition to scale invariance of the total energy, the partition of total energy into recoverable, stored, and dissipated parts shall also be invariant with respect to the scale at which a given set of mass particles are observed. Each of these elements of the framework is addressed at a conceptual level in the ensuing sections to establish their significance. Chapter 3 will use these principles to develop the theoretical framework for scale transitions.

2.2.1 Kinematic Consistency of Deformation

Deformation of the rSVE at two scales of observation must be kinematically consistent. Kinematic consistency is realized by requiring that the description of deformation be the same at each scale with the exception of a fine scale fluctuation field whose mean value vanishes over

certain coarse length scales. The general idea is that the smooth long wavelength deformation is the same at coarse and fine scales, while fine scale heterogeneity is accommodated by fluctuations over wavelengths that cannot be directly resolved at the coarse scale. This is, of course, a common tenet of homogenization theories. Fine scale fluctuations in deformation should have zero projection onto coarse scale kinematic variables; in other words, they should be orthogonal. Furthermore, the kinematic decomposition of the fine scale deformation must be uniquely associated with coarse scale kinematic variables. The most natural and direct way to accommodate this demand is to ensure orthogonality of independent contributions to the fine scale deformation.

2.2.2 Scale Invariance of Linear Momentum

It is a fundamental requirement of continuum theories at all scales that momentum must be balanced, giving rise to continuum equations of motion. At any particular scale, computational methods (e.g., finite element) are often employed to solve the initial boundary value problem in accordance with a weak form of linear momentum balance. Linear momentum is a fundamental quantity that should be invariant with respect to the scale of observation. In other words, the significance of linear momentum to the continuum response at every scale establishes that maintaining the same notion of momentum for a fixed set of mass particles between two scales of observation is crucial to physical consistency. In practice, this principle guides the derivation of coarse scale stress terms that are conjugate to the coarse scale manifestation of the fine scale deformation and are consistent with the distribution of fine scale stresses and inertia via the principle of virtual velocities (PVV).

2.2.3 Scale Invariance of Angular Momentum

In standard first order nonpolar continuum theories (at an arbitrary scale), balance of angular momentum imparts symmetry of the Cauchy stress tensor. In higher order theories, angular momentum is used to augment equations of motion with a balance involving polar stresses arising from resistance to material or substructure spin. Scale invariance of angular momentum in this multiscale framework establishes the lack of symmetry of the coarse scale Cauchy stress tensor

due to the distribution of finer scale tractions and long range gradients of deformation (cf. Chapter 3). Within the multiscale framework, there is further implication of anti-symmetry of the coarse scale Cauchy stress with regard to conservation of energy at the coarse scale.

2.2.4 Scale Invariance of Total Energy

The total energy within an rSVE of material should be invariant with respect to the scale of observation. In continuum thermomechanics, the two most common contributors to energy at any given scale are thermal and mechanical. Implementation of the developed framework to transitions between scales which are both represented by a continuum should assert that the total thermal and mechanical energy are equivalent at both scales of observation. However, it is possible that when transitioning to or from a scale that is treated in a discrete manner, for example molecular dynamics (MD) simulations, mechanical energy of finer scale fluctuations may translate into thermal energy at a continuum scale (Zhou, 2003). In continuum-to-continuum scale transitions, the total mechanical energy is consistent between both scales of observation if they exhibit scale invariance of momentum for all time. Thermal energy equivalence gives rise to a coarse scale definition of specific heat. Total energy invariance also dictates temperature changes due to dissipation associated with irreversible processes.

2.2.5 Scale Invariance of Dissipation

A change of total energy of an rSVE can be partitioned into a change of free energy and an amount that has been dissipated. The change in free energy can be further decomposed into elastically recoverable and stored free energy. The energy dissipated during an irreversible process should be invariant with respect to the scale of observation. This principle is difficult to precisely adhere to in practice and it is possible to predict stresses and deformations at a coarse scale in a manner consistent with the deformation and distribution of stresses at a finer scale and fully complicit with all governing laws at both scales (conservation of mass, momentum, and energy, and non-negative dissipation) *without* enforcing the same dissipation at both scales. In fact, this has been largely overlooked in prior literature regarding homogenization of materials with evolving microstructure. Specifically, the assertion that intrinsic (mechanical) dissipation

associated with evolving microstructure be scale invariant is rarely, if ever, considered. In a multiscale modeling strategy it is desirable to pursue scale invariance of the dissipation on physical grounds.

In addressing behavior of highly heterogeneous media, consideration of stored or dissipated energy requires that we have been diligent in carrying that dissipation up through finer scales properly. For example, shear band formation during high strain-rate response of metals is often accentuated by the rapid generation of heat due to energy dissipated by irreversible deformation processes. This resulting increase in temperature causes additional softening of the material, further accentuating the deformation rate in a feedback cycle that causes strong localization at the coarse scale. The actual rate of dissipation, and not simply the rate of plastic work, establishes the rate of heat generation. Typically, this effect is modeled by assuming adiabatic conditions and that the true dissipation is a constant factor multiplied by the plastic work. It has been explained analytically (Rosakis et al., 2000), shown by experiment (Hodowany et al., 2000), and demonstrated by direct simulation (Clayton, 2005) that the actual ratio of dissipation to plastic work is not constant during deformation, and depends on the evolution of finer scale processes that store energy at various scales of microstructure.

As another example, one might consider modeling of nucleation of damage at a particular scale as the inability of the material point to further store energy at finer scales, (cf. Lemaitre, 1998, p. 98). This concept can be illustrated by a series of cascading buckets of water; each bucket represents a particular scale of observation. As one bucket becomes full it spills over into the next causing a progression of nucleation and growth from the finest to the coarsest scales. This approach to modeling damage nucleation requires a precise representation of the energy stored and dissipated at each scale.

2.2.6 Summary of Scale Invariance Principles

We have presented certain scale invariance principles based on a conceptual hierarchy of material scales. Central to this theme is the physical argument that quantities which are governed by physical laws at each scale of observation be invariant with respect to scale of observation for a given set of mass particles. Some quantities may violate this principle (e.g., dissipation) without

a direct consequence on predicting stresses consistent with momentum balance. Nonetheless, there are physical grounds for the scale invariance principles. A theoretical framework that establishes quantitative relationships between two scales of material response based on these principles is presented in Chapter III. Current and emerging multiscale approaches found in literature are discussed in the next section.

2.3 Comparison with Other Emerging Approaches

The problem of modeling the thermomechanical response of materials undergoing microstructure evolution is inherently of multiscale nature. From a continuum mechanics perspective, multiscale modeling approaches fall under three categories: phenomenological continuum models, hierarchical scale linking, and concurrent scale linking. The most debilitating limitations of phenomenological models are their lack of direct physical representation of the underlying microstructure. They are based on insight and experimental observations and are limited in predictive character.

A majority of efforts in multiscale modeling of microstructure evolution attempt to relate either (a) a heterogeneous fine scale continuum rSVE to a coarse scale material point or (b) a discrete atomistic ensemble to a higher scale of continuum description. This research falls decidedly into category (a); however, the scale bridging methods being explored in category (b) reveal some general trends that can be applied to the former. Accordingly this section is organized into four subsections to discuss concurrent (Section 2.3.1) and hierarchical (Section 2.3.2) approaches for scale linking between continuum models, and concurrent (Section 2.3.3) and hierarchical (Section 2.3.4) approaches for scale linking between atomistic and continuum models.

2.3.1 Concurrent Continuum-to-Continuum Scale Linking Approaches

Concurrent methods achieve a two-way coupling between relevant scales by simultaneously solving the problem at each scale of resolution and passing information back and forth (cf. Ghosh et al., 2001; Kouznetsova et al., 2002; Kadowaki and Liu, 2004; Kouznetsova et al., 2004; Markovic et al., 2004; Rong et al., 2006; Ghosh et al., 2007). Generally, boundary conditions for a fine scale simulation are extracted from the deformation response of the next coarse scale, and

the stress-strain behavior of the coarse scale is determined from volume averages of the fine scale solution. The strengths of concurrent approaches are that they apply for any arbitrary deformation history, are useful in modeling localization processes, and do not demand complex coarse scale constitutive descriptions of finer scale processes. The inherent weakness of these approaches is the computational burden relative to the other methods, which is excessive even by standards of the foreseeable future. Moreover, the approach is only as accurate as the constitutive equations used for fine and coarse scale behaviors, as in a hierarchical approach. An additional limitation is that the concurrent coupled simulation strategy is not easily amenable to modern, commercially available continuum mechanics codes. A few examples highlighting strengths and weaknesses of these approaches are discussed in the following.

The "bridging multiscale method" has been applied to concurrently link fine and coarse continuum scales (Kadowaki and Liu, 2004). The total deformation field is decomposed into coarse and higher order fine scales and multiscale balance laws for higher order stresses are developed via the principle of virtual velocities, resulting in a multiscaled finite element solution. This work focuses primarily on the numerical implementation of multiscaled kinematics; however, the explicit nature of the heterogeneity of the underlying material (e.g., topology of phases, size and shape distributions) is not addressed, and therefore the approach may be of limited utility in representing real microstructures, for example.

Concurrent approaches that do incorporate material heterogeneities are built around the concept of a nested analysis of a heterogeneous rRVE acting as the constitutive model for a coarse scale material point. For example, Markovic et al. (2004) use a Lagrange multiplier-coupled two-scale finite element procedure to address the effects of mesoscale heterogeneity on macroscopic response. During solution of the global macroscale problem, each coarse scale finite element serves as the kinematic frame for an associated mesoscale rRVE solution. Information is only passed between a macroscale finite element and its associated microscale simulation leading to an efficient parallel implementation.

This nested finite element concept is also applied by Kouznetsova et al. (2002; 2004) who additionally introduce higher order kinematics through a Taylor series expansion of the fine scale

deformation field. Their approach results in a second order computational homogenization of the direct mesoscale rSVE simulation with the coarse scale gradient of the deformation gradient augmenting the kinematic description and its conjugate stress derived by equating the virtual internal stress power between the two scales. The work of Kouznetsoza et al. represents the first attempt to apply multiscale homogenization concepts to second gradient continua, a term given to continuum theories for which second order stress terms conjugate to the long range (coarse scale) gradient of the deformation gradient contribute to the balance of momentum.

Second gradient continuum theories have evolved as a special and restricted case of micromorphic theories (Toupin, 1963; Mindlin, 1964; Germain, 1973; Fleck and Hutchinson, 1993, 1997; Eringen, 1999; Chambon et al., 2001; Chambon et al., 2004) which were generalized from the couple stress theory of the Cosserats (Cosserat and Cosserat, 1909). A micromorphic theory permits additional kinematic degrees of freedom at a material point which represent the motion of material points over a shorter range than the usual deformation field itself. For example, micropolar theories permit the material to spin locally, independent of the long range deformation. On the other hand, micromorphic theories permit both short range spin and stretch. A second gradient continua is one for which the second order kinematic term is constrained to be the long range gradient of the deformation gradient and, as shown in Chapter III, arises as a result of an assumed second order Taylor series expansion of the deformation of a fine scale rSVE in the vicinity of a coarse scale material point. Fleck and Hutchinson (1993, 1997) have pioneered work in strain gradient plasticity that employs couple stresses as higher order stresses, a theory in which the “flow” (as opposed to “deformation”) based variation can be tied into the coarse scale constitutive portion of the framework presented in Chapter 3. Chambon et al. (2001; 2004) presented some theoretical concepts based on the notion of a second gradient continuum, but did not seek to establish the constitutive equations from finer scale response of an rSVE. Larrson and Diebels (2007) presented a homogenization procedure aligned with the task of identifying coarse scale response from fine scale computations; however their framework is based only on that component of the second gradient that contributes to micropolar (or curvature) deformation and their work does not yet address the construction of constitutive models from the homogenized rSVE response. Kaczmarczyk, et al. (2008) provided a similar scale transition framework

employed in the concurrent approach, however, on account of their solution scheme the framework is restricted to linear elastic problems. One advantage of a second gradient kinematic theory is that the link between the coarse and fine scale response is nonlocal. For both concurrent and hierarchical approaches, the incorporation of higher order deformation gradients into the coarse scale solution is known to provide a regularizing effect on the numerical solution, eliminating artificial mesh dependence, for example.

Recently, adaptive multiscale approaches have been used to introduce enhanced resolution in regions of strong damage localization, cf. (Ghosh et al., 2001; Rong et al., 2006; Ghosh et al., 2007). Rong et al. (2006) employed an adaptive mesh refinement technique to simulate the progressive localization of mesoscopic damage to catastrophic failure. Artificial heterogeneity is introduced to the mesoscale by assigning the local failure criteria parameters from a Weibull distribution. Because no spatial correlation is taken into consideration, the heterogeneity likely has an artificial length scale related to the initial mesh density. Their results demonstrate the importance of stress redistribution in the evolution and clustering of material damage, a deviation from mean-field theories. However, this implementation is not truly multiscale; a distinction between the scale of physics and size of element is important, yet often overlooked.

On the other hand, Ghosh et al., (2001; 2007) devised a multiscale adaptive approach that "zooms in" as necessary to resolve finer details of physics at lower scales. Specifically, this approach conducts simulations at the macroscale with each material point behaving in accordance with a continuum damage mechanics constitutive model. Higher order gradients are computed to identify regions of damage localization. Where the higher order gradient fields satisfy predefined criteria, the model zooms in by replacing the scale[2] 0 constitutive model with a direct scale 1 simulation of an assumed representative volume element (RVE). As the localization process continues, the assumption of periodicity breaks down and the affected scale 0 region is replaced by a direct scale 1 simulation of representative microstructure. This is perhaps the most complete and realistic treatment of continuum scale transitions in a concurrent fashion. However, the internal state variables of the continuum damage mechanics model at the coarse scale are

[2] The scale labels of Ghosh, et al. (2001, 2007) are replaced by ours for consistency.

discarded as the procedure zooms in. That is, the current ISV values at the coarse scale are not used to initialize the periodic cell nor representative microstructure fine scale solutions. Because there is no association of ISVs between scales, difficulties of linking the kinetics of microstructure evolution at the various scales are obviated. However, the reverse problem of zooming back out cannot be addressed without identifying a relationship between the coarse scale ISVs and the kinematics of the fine scale microstructure rearrangement process and formulating kinetic relations that govern their evolution. Accordingly, the influence of localization on structural scale behavior is not addressed.

A completely separate approach to concurrent multiscale modeling is the approach of embedding fine scale or short wavelength response functions within the coarse scale solution algorithm by separating the weak form of momentum balance into coarse scale and fine scale parts (Garikipati and Hughes, 2000). This approach offers an enriched kinematic description that is useful, for example, in capturing strain localization at the coarse scale, but does not address the complexities presented at various scales due to heterogeneous microstructure evolution. The variational multiscale method of Garikipati and Hughes (2000) has been extended by Hughes and Sangalli (2007) who employ Green's functions to enrich the kinematic description, however, this approach is more accurately described as a multi-resolution or embedded, enhanced resolution modeling approach rather than multiscale modeling as multiple scales of physical constitutive behavior is not considered.

2.3.2 Hierarchical Continuum-to-Continuum Scale Linking Approaches

Hierarchical approaches overcome the computational burden of concurrent methods by attempting to capture the effective details of the subscale processes via direct numerical simulation of a material RVE or embedding analytical idealizations into formal volume averages. The primary disadvantage is the difficulty of carrying out simulations beyond the point of strong fine scale localization within the RVE, because such processes invalidate the assumption that an RVE is *representative*. Traditional hierarchical homogenization conducts averaging over a representative neighborhood of material response at one scale to determine the constitutive behavior at a higher scale (Carrere et al., 2004; Hao et al., 2004; McVeigh et al., 2007). This is

typically achieved by conducting direct numerical simulation of a material RVE or by embedding analytical idealizations into formal volume averages. This approach is distinct from strictly phenomenological models in the order and formality of the averaging scheme. Furthermore, some representation of finer scale structure (e.g., microstructure, mesostructure) is directly incorporated, such that effects of variation in microstructure, whether over time or space, can be addressed. The most common weaknesses of these approaches are (1) the kinematic framework for the homogenization process is not rich enough, (2) the kinetic equations of defect evolution are not always defined in a manner that preserves scale invariance of the fundamental quantities of mass, momentum, energy, and dissipation, and (3) the homogenization process inadvertently removes long range fluctuations important in the coarse scale response of the problem, e.g., coarse scale variations in microstructural material properties.

For example, Carrere et al. (2004) used finite element analysis of a unit cell of metal matrix composite as the basis of a multiscaled investigation of the influence of matrix texture and matrix/fiber debonding on scale 0 stress-strain behavior. This is a fairly typical example. A single crystal plasticity model was used to represent the material response at a grain level. A modified version of Kroner's localization rule was used to "map" a given mesoscopic stress to the grain scale in order to account for peak local stresses. This polycrystal homogenization scheme results in a constitutive model employed in the mesoscale unit cell simulation. The macrostresses were computed from the unit cell simulation in terms of respective volume averages. While this approach certainly spans a few scales simultaneously without an unwieldy set of degrees of freedom, the transition to macroscale is incomplete. In order to predict macroscale behavior, a constitutive model with appropriate kinematical and kinetic descriptions of the underlying processes should be developed. On account of their homogenization process, Carrere et al. (2004) neglected many details of the heterogeneity that affect the consistency of energy dissipation between scales.

Decohesion of an otherwise homogeneous matrix from an embedded inclusion is often considered to be one mechanism for nucleation of porosity. Growth models have been developed and modified to provide a porosity dependent yield function. Void growth and eventual coalescence are typically modeled as a function of stress triaxiality. McVeigh et al. (2007) used direct

mesoscale simulations to identify competing mechanisms (i.e., void sheeting) and propose a phenomenological extension to Gurson's flow potential that enhances the coalescence behavior particularly under pure shear loading (does not result in additional porosity increase). Their hierarchical multiscale approach to simulate the effects of two distinct scales of inclusions consisted of: (1) assessing the kinetics of the underlying mechanisms from direct numerical simulation, (2) fitting the modified Gurson flow surface to the simulated response of a unit cell of small inclusions, and (3) using this fit to represent the matrix in another unit cell simulation conducted at a higher scale to address debonding of larger inclusions. In a similar manner, Hao et al. (2004) made the final transition to the macroscale by identifying key mechanisms and developing a plastic potential function used in the simulation of laboratory scale fracture test specimen. One weakness of this approach is that it does not insist on scale invariance of momentum, energy, and dissipation.

Motivated by the importance of distributions of damage at the mesoscale to the evolution of damage, Voyiadjis et al. (2001) have constructed a multiscaled constitutive framework that incorporates mesoscale and macroscale gradients of internal state variables. Macroscale gradients have been used with increasing frequency for non-local modeling of inelastic and damage response, especially to eliminate unrealistic mesh dependency during localization. Mesoscale gradients, on the other hand, are powerful in capturing the effects of specific distributions of damage and microstructure heterogeneities on the kinetics of damage evolution (Lacy et al., 1999). The constitutive development follows the theory of internal state variables by postulating the free energy potential as a function of a set of plastic and damage internal state variables, as well as their respective macro- and meso- gradients and these gradients' interactions. However, the sheer number of internal state variables that are retained to build the multiscale model results in a cumbersome framework. A possible simplification might be to use mesoscale gradients of damage ISVs and material heterogeneities and macro gradients of inelastic strain. The framework proposed by Voyiadjis et al. (2001) does not directly address scale invariance of momentum, energy storage and dissipation.

Rather than using higher-order homogenization to pass information up scales, Kwon (2004) passed information to lower scales to zoom in on fine details, for example at a crack tip. The

boundary conditions for each lower scale were derived from the next higher scale simulation. At each scale a stochastic analysis of the response was performed by randomly assigning local properties from distributions. An extension of this idea is to pass information between scales (in both directions) in a probabilistic manner.

McVeigh et al. (2006) used additional subvolume averages of the rate of deformation to develop an N-scale hierarchical constitutive model with the goal of maintaining the identity (and contribution) of all scales of interest at the highest scale. The relationship between the multiscaled stress and deformation terms were provided by a generalized constitutive law which utilizes the same set of ISVs and form of evolution equations at each scale. Parameters of the evolution equations at each scale were identified by a hierarchy of direct simulations of representative unit cells. One criticism of this approach is that it implicitly assumes the kinetics of microstructure evolution have the same form at each scale. This is not generally true. For example, the material behavior at one scale may be dominated by the nucleation and accumulation of dislocations within the lattice, at the next scale perhaps the grain boundary separation is highly dependent upon lattice misorientation, at the next scale distributions of porosity affect the local stress field and influence the grain boundary separation process, and at the highest scale nucleation and growth of macroscopic cracks and voids is dependent in a non-intuitive manner on each of the underlying scales. This behavior would not be amenable by recourse to the same definition of ISVs and form of evolution kinetics at each scale. Additionally, the generalized N-scale form of this framework seems to suffer from the potential of “double-dipping” when accounting for internal stress power and dissipation. This emphasizes the importance of building a multiscaled framework with a formal relation between the kinematics at all scales of interest and ensuring that the kinematic terms are independent with respect to dissipation. Recently, variations on this approach have been introduced by Liu and McVeigh {, 2008 #159} to apply it in a hierarchical fashion; however, details pertaining to the multiscale constitutive description have not been addressed and are in conflict with strong assertions made in this thesis in Chapter 3. In particular, their approach seems to reflect the idea that the same constitutive behavior governs the response at all scales.

2.3.3 Concurrent Atomistic-to-Continuum Scale Linking Approaches

In this and the next section, scale linking between atomistic and continuum models is only briefly touched on. These approaches are not central to the thrust of this dissertation and are included only to set this work in context with other multiscale modeling approaches and illustrate the general concept of atomistic to continuum model linking. Accordingly, these sections are not an intensive review, rather a narrow sampling, of recent work.

Liu et al. (2004) concluded that the computational demands of atomistic simulation render it incapable of independently treating many application problems even within the nanoscale, thus motivating multiscaled approaches. The general idea is to treat localized inhomogeneities that influence damage mechanisms with atomistic simulations (e.g., highly refined region near a crack tip) while transitioning to a continuum description for computation of long-range deformation behavior. For example, Wagner and Liu (2003) developed the bridging scale method to concurrently link finite element and atomistic simulations. In this approach, the deformation field is decomposed into orthogonal coarse and fine scale components. The coarse scale is ascribed to a finite element and applied over the entire problem domain, while the fine scale is associated with the molecular dynamics solution and is only used in locations where local features must be resolved. Using this technique, Park et al. (2004) computed the coarse-scale continuum temperature field from the energy associated with higher-order atomistic velocities. The MD-finite element bridging scale has also been applied to simulate the quasistatic buckling of nanotubes and dynamic fracture of a center cracked plate (Liu et al., 2006). While the concurrent bridging between atomistic and finite element simulations has restricted utility in addressing problems for which initialization and localization of damage is distributed throughout a large domain, this work reinforces the ideas of partitioning and augmenting the kinematical description of the problem. These ideas are reflected in Chapter 3.1.

2.3.4 Hierarchical Atomistic-to-Continuum Scale Linking Approaches

In contrast to the concurrent bridging scale technique, a hierarchical paradigm for bringing information from atomistic scales to bear on the problem at continuum scales is discussed at this point. The general idea is to use results from quantum mechanics or molecular dynamics

simulations to develop coarser scaled potentials from which constitutive relations are derived. For example, MD simulations of interfacial separation have been used to construct cohesive traction-separation laws for use at higher scales (Hao et al., 2004; Braides et al., 2006).

Molecular dynamics simulations of the deformation and eventual separation of an aluminum-silicon interface have been conducted by Gall et al. (2000b). A similar simulation of the interfacial separation of a copper grain boundary was conducted by Spearot et al. (2004) . Results from these works lead one to question the general applicability of postulated local action in modeling interfacial separation at such scales. Spearot et al. (2004) addressed this by introducing the idea of a general N-gradient internal state variable cohesive model, which would be derived and fit from a suite of MD simulations for the interface under consideration and then applied to modeling at the mesoscale. A common weakness of many atomistic approaches is that a representative set of higher scale defect features (e.g. dislocations, precipitates, nanoporosity) are typically not introduced. These features will heavily influence the nonlocality of the interfacial response (Braides et al., 2006). This importance of the nonlocal nature of heterogeneous material response conveys to continuum scales as well, motivating a nonlocal framework for the fine to coarse scale linking in this dissertation.

Hao et al. (2004) used a hierarchical approach to incorporate the influence of two distinct scales of inclusions on the macroscopic fracture behavior of a laboratory specimen. Quantum mechanical solutions were used to develop constitutive models for the iron matrix and cohesive debonding potentials between matrix and two distinct sizes of inclusions. The short-range decohesive forces across the interface in atomistic models were rescaled to be applicable to continuum models. The result was a cohesive potential function fit to quantum mechanics simulations. Their scaling parameter is likely related to the above mentioned nonlocal zone of influence for interfacial separation.

As stated, this dissertation focuses on the transition between material scales that are each amenable to a continuum description. However, the atomistic to continuum scale transitions illustrate some of the important features of scale transitions, in particular, the necessity of formally addressing the kinematic relationships between two scales and the importance of

nonlocality of microstructure evolution. The hierarchical development of interface cohesive potentials represents a particular area where continuum multiscaled approaches can reach down into finer scales for supplementary information, for example, cf. Figure 1.

2.4 Salient Points from Recent Literature

2.4.1 Summary

Concurrent multiscale modeling approaches often benefit from the simplicity of handling complex microstructure by virtue of direct mesoscale simulations. Many of these techniques are well suited for parallel computation; however, the computational burden can be excessive for problems where material heterogeneity is important over a large fraction of the macroscale domain. This technique is most efficient for simulations where the multiscaled nature of the problem is important in only a select area of the overall problem domain (e.g., a single crack tip). Clearly, a viable application for concurrent approches is the analysis of material failure at isolated "hot spots".

An advantage of hierarchical constitutive models is they can be directly incorporated at the material point level in a conventional finite element analysis code. Although perhaps less robust than concurrent approaches in their domain of applicability, hierarchical approaches render a framework readily amenable to solving engineering problems in commercial codes. Unique contributions made by this research to improve upon hierarchical modeling techniques are the development of:

(1) a formal framework based on principles discussed in Section 2.2,

(2) computational methods to compute coarse scale quantities identified in Section 2.2 from direct simulations of fine scale response,

(3) methods for identifying suitable non-local coarse scale constitutive relations from fine scale response, and

(4) methods for embedding fine scale heterogeneity into coarse scale response for evolution of microstructure.

2.4.2 Localization and Limitations on Hierarchical Frameworks

Hierarchical scale transition approaches are limited in representation of localization of inelastic deformation (e.g., plasticity, damage); they are more appropriate for incipient localization, rather than post-bifurcation behavior. This owes to two features. First, it is required that the fine scale fluctuations do not have a correlation length on the order of the size of the volume element for which they are subjected to coarse-graining. Second, higher order moments of fluctuation would be required to rectify the kinematic complexity of post-localization behavior. One strategy would be to conduct a fine scale-resolved high degree-of-freedom simulation in regions where localization is indicated by incipient localization criteria embedded within a domain treated using various scales of the hierarchical formulation (like an "onion" being peeled back in layers). This requires restart of the solution from zero time. Another approach is to employ a fully concurrent multiscale modeling strategy at all points in which localization could occur, but this is quite costly. Yet another approach is to use a concurrent multiscale modeling strategy in which regions undergoing localization are successively refined and subjected to fine scale simulations. It may be possible to conceive of a hybrid approach in which hierarchical models at various scales are employed selectively in a concurrent scheme similar to that of Ghosh et al. (2001; 2007) by imposing boundary conditions from a coarse scale solution subject to the requirement that the domain receiving enhanced resolution is large enough to ensure that stress and displacement redistribution due to localization has not yet substantially occurred.

Additionally, the hierarchical homogenization approach explicitly introduces length scales related to the adopted rSVE size as well as implicit length scales related to correlation lengths of dominant microstructure heterogeneity that are smaller than adopted finite rSVE domains. This emphasizes the importance of proper selection of the finite domain size to study at each scale transition. In some cases the finite domain size will be smaller than that necessary for a statistically representative volume element (rRVE) such that stochastic analysis methods must be used based on a family of rSVE simulations.

CHAPTER III

HIERARCHICAL MULTISCALE FRAMEWORK

In this chapter the essential components of the hierarchical approach are laid out. The hierarchy of scales is that presented in Chapter 2; however, here we focus on a single coarse to fine scale transition. Section 3.1 develops the kinematics required for transition from fine to coarse scale. The principle of virtual velocities is applied in Section 3.2 to derive proper coarse scale stresses and identify relationships required for satisfaction of scale invariance of momentum. In Section 3.3, governing thermodynamic principles are used to develop an internal state variable theory based on the kinematics of Section 3.1 and stresses of Section 3.2.

3.1 Multiscale Kinematics

Figure 3 depicts the relationship between a material point at scale k and its associated neighborhood of material points at scale $k+1$. The details of this transition can be replicated at any scale transition, so it is without a loss of generality that scale k and $k+1$ are hereafter referred to as coarse and fine scales, respectively. For $k = 0$, the coarse scale is the engineering scale (scale of application, cf. Section 2.1) and in these cases a particular point in the coarse scale corresponds to a material point in the continuum body rather than the coarse scale volume element. No distinction need be made regarding the nature of a referential volume element at this point. Therefore, the use of rSVE should be interpreted as a volume element of material in its reference configuration, i.e., prior to deformation, which in some cases may be demonstrated to serve as an rRVE or designed as a unit cell in cases of periodic microstructure. These distinctions are clarified in Chapter 4.

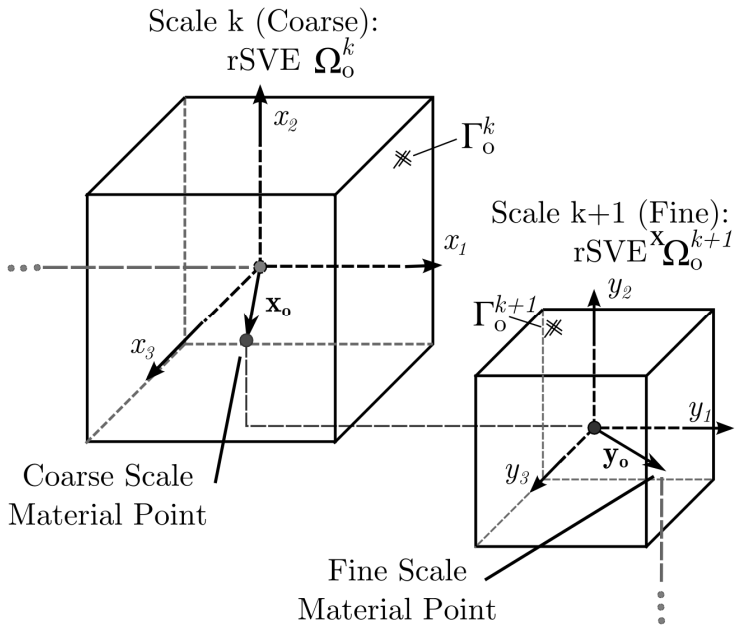

Figure 3. Illustration of a scale transition between fine and coarse scales.

At scale *k* each material point in the referential volume element, Ω_o^k, is labeled by its reference coordinates, $\mathbf{x}_o$. Associated with each material point, $\mathbf{x}_o$, is a referential volume element of material at the next finer scale (*k+1*). This volume element is labeled ${}^x\Omega_o^{k+1}$, identifying it as the fine scale volume of material in the original (o) undeformed configuration associated with the coarse scale material point $\mathbf{x}_o$. As the continuum body at scale 0 undergoes deformation, the rSVE of material at each finer scale will deform in a manner that is not generally kinematically compatible. That is, the volume elements at *k+1* cannot be stitched together to form a deformed volume element at scale *k*. This fact will prove consequential to momentum balance between two consecutive scales.

3.1.1 Taylor Series Decomposition

Within the current configuration of scale *k+1*, the deformed coordinates of each material point, $\mathbf{y}_o$ in the reference configuration, are given by the fine scale mapping $\mathbf{y}(\mathbf{x}_o, \mathbf{y}_o)$. A general polynomial equation expressing this fine scale deformation is

$$\mathbf{y}(\mathbf{x}_o, \mathbf{y}_o) = \mathbf{A}_0(\mathbf{x}_o) + \mathbf{A}_1(\mathbf{x}_o) \cdot \mathbf{y}_o + \mathbf{A}_2(\mathbf{x}_o) : \mathbf{y}_o \otimes \mathbf{y}_o + \cdots \tag{3.1}$$

where each coefficient in the polynominal $\mathbf{A}_i$ is an order *i+1* tensor that is assumed constant over an rSVE but allowed to vary with respect to coarse scale position $\mathbf{x}_o$. At the coarse scale, the deformed position of a material point, $\mathbf{x}_o$, is given by the mapping $\mathbf{x}(\mathbf{x}_o)$. Accordingly, the coarse scale deformation gradient is defined as $\mathbf{F}(\mathbf{x}_o) = \mathbf{x}\overset{\leftarrow}{\nabla}_o = \dfrac{\partial \mathbf{x}}{\partial \mathbf{x}_o}$. The gradient of the deformation gradient, i.e., second gradient, is defined as $\mathbf{G}(\mathbf{x}_o) = \mathbf{F}\overset{\leftarrow}{\nabla}_o = (\mathbf{x}\overset{\leftarrow}{\nabla}_o)\overset{\leftarrow}{\nabla}_o = \dfrac{\partial^2 \mathbf{x}}{\partial \mathbf{x}_o^2}$, a third-order tensor symmetric in the last two indices. Truncating Eq. (3.1) to quadratic terms and setting $\mathbf{A}_0 = \mathbf{0}$, $\mathbf{A}_1 = \mathbf{F}$, and $\mathbf{A}_2 = \frac{1}{2}\mathbf{G}$ and adding a truncation term $\mathbf{h}(\mathbf{y}_o)$ which includes all higher order fluctuations, results in a second order Taylor series expansion of the fine scale deformation field, i.e.,

$$\underbrace{\mathbf{y}(\mathbf{x}_o, \mathbf{y}_o)}_{\text{fine scale}} = \underbrace{\mathbf{F}(\mathbf{x}_o) \cdot \mathbf{y}_o + \tfrac{1}{2}\mathbf{G}(\mathbf{x}_o) : \mathbf{y}_o \otimes \mathbf{y}_o}_{\text{coarse scale expansion}} + \underbrace{\mathbf{h}(\mathbf{y}_o)}_{\substack{\text{fine scale} \\ \text{fluctuation}}} \tag{3.2}$$

The Taylor series expansion is taken about the origin of the fine scale rSVE ($\mathbf{y}_o = \mathbf{0}$), which is assumed to be located at the geometric center of the fine scale rSVE and coincident with the coarse scale material point, $\mathbf{x}_o$, for convenience. A second order Taylor series is employed here; however, in principle any order of Taylor series can be used to kinematically link the deformation between two scales. Inclusion of the second gradient gives rise to a second gradient continua and naturally accommodates a nonlocal coarse scale description of the irreversible fine scale deformation. Omitting the second gradient results in an otherwise local description of the coarse scale constitutive behavior within a classical Cauchy continuum framework. Higher order

theories can be developed by including additional terms in Eq. (3.1); however, it will prove difficult to adhere to the requirement of kinematic orthogonality for higher than quadratic polynomials. To capture higher-order effects it would be more fruitful to pursue other basis decompositions such as Fourier, wavelets, or empirical orthogonal functions derived by principal component analysis, for example. In either case, all of the fine scale fluctuations are included in $\mathbf{h}(\mathbf{y}_o)$.

The coarse scale kinematic description is essentially that of Germain's second gradient continua (Germain, 1973). The distinction between the more general case of micromorphic continua and second gradient continua is that, for the micromorphic case, coefficients in Eq. (3.1) are related but not identical to the coarse scale gradients of deformation. Note that in the second gradient approach to kinematics, micromorphic internal state variables can be introduced at a given scale to represent the many-body response of finer scales, if necessary.

We employ homogeneous coordinates between the reference configurations of both scales such that $\frac{\partial}{\partial \mathbf{x}_o} = \frac{\partial}{\partial \mathbf{y}_o}$. The fine scale deformation gradient and its gradient are defined by $\mathbf{f}(\mathbf{y}_o) = \mathbf{y}\overleftarrow{\nabla}_o = \frac{\partial \mathbf{y}}{\partial \mathbf{y}_o}$, and $\mathbf{f}\overleftarrow{\nabla}_o = (\mathbf{y}\overleftarrow{\nabla}_o)\overleftarrow{\nabla}_o = \frac{\partial^2 \mathbf{y}}{\partial \mathbf{y}_o^2}$, respectively, so that according to Eq. (3.2), we have

$$\mathbf{f}(\mathbf{x}_o, \mathbf{y}_o) = \mathbf{F}(\mathbf{x}_o) + \mathbf{G}(\mathbf{x}_o) \cdot \mathbf{y}_o + \mathbf{h}\overleftarrow{\nabla}_o \tag{3.3}$$

The three distinct terms on the right side of Eq. (3.3) are labeled $\mathbf{f}_1 = \mathbf{F}$, $\mathbf{f}_2 = \mathbf{G} \cdot \mathbf{y}_o$, and $\mathbf{f}_3 = \mathbf{h}\overleftarrow{\nabla}_o$.

3.1.2 Orthogonality of Kinematic Decomposition

Kinematic consistency is realized by requiring that the description of deformation be the same at each scale with the exception of a fluctuation field whose mean value vanishes over certain length scales. The general idea is that the smooth long wavelength deformation is the same at coarse and fine scales, while fine scale heterogeneity is accommodated by fluctuations over wavelengths

that cannot be directly resolved at the coarse scale. Fine scale fluctuations in deformation should have zero projection onto coarse scale kinematic variables. Furthermore, the kinematic decomposition of the fine scale deformation must be uniquely associated with coarse scale kinematic variables. The most direct way to accommodate this demand is to ensure orthogonality of independent contributions to the fine-scale deformation. Orthogonality of the separate contributions of each coarse scale field variable to fine scale deformation is enforced by requiring the integral of the scalar product of infinitesimal and differential vectors from two contributing fields vanish over the domain of the rSVE. To do this we start with an arbitrary infinitesimal differential vector in the reference configuration, i.e., $\mathbf{dy}_{\mathrm{o}}$. This vector is mapped into the current configuration by the compatible fine scale deformation gradient according to $\mathbf{dy} = \mathbf{f} \cdot \mathbf{dy}_{\mathrm{o}}$. The mapping is decomposed consistent with (3.3) such that

$$\mathbf{dy} = \mathbf{f}_1 \cdot \mathbf{dy}_{\mathrm{o}} + \mathbf{f}_2 \cdot \mathbf{dy}_{\mathrm{o}} + \mathbf{f}_3 \cdot \mathbf{dy}_{\mathrm{o}} \tag{3.4}$$

Finally, orthogonality is asserted between each of the vectors on the RHS of (3.4) according to $\int_{\Omega_{\mathrm{o}}^{\mathrm{x}}} \mathbf{dy}_i \cdot \mathbf{dy}_j \; d\Omega_{\mathrm{o}} = \mathbf{0}$ for $i \neq j$, which is equivalent to $\mathbf{dy}_{\mathrm{o}} \otimes \mathbf{dy}_{\mathrm{o}} : \int_{\Omega_{\mathrm{o}}^{\mathrm{x}}} \mathbf{f}_i^T \cdot \mathbf{f}_j \; d\Omega_{\mathrm{o}} = \mathbf{0}$ for $i \neq j$, and, due to the arbitrary selection of $\mathbf{dy}_{\mathrm{o}}$, results in

$$\int_{\Omega_{\mathrm{o}}^{\mathrm{x}}} \mathbf{f}_i^T \cdot \mathbf{f}_j d\Omega_{\mathrm{o}} = \mathbf{0} \text{ for } i \neq j \tag{3.5}$$

The coarse scale deformation gradient and the second gradient are constant within the fine scale rSVE such that $\mathbf{f}_1 \perp \mathbf{f}_2 \leftrightarrow \int_{\Omega_{\mathrm{o}}^{\mathrm{x}}} \mathbf{y}_{\mathrm{o}} d\Omega_{\mathrm{o}} = \mathbf{0}$, a condition satisfied by locating the origin of the fine scale at the geometric center of the rSVE *a priori* for convenience. Orthogonality between the coarse scale deformation gradient and the fluctuation field is not satisfied trivially, and requires that

$$\mathbf{f}_1 \perp \mathbf{f}_3 \leftrightarrow \int_{\Omega_{\mathrm{o}}^{\mathrm{x}}} \mathbf{h} \tilde{\nabla}_{\mathrm{o}} d\Omega_{\mathrm{o}} = \mathbf{0} \tag{3.6}$$

The volume average of the fine scale deformation gradient is obtained by integrating Eq. (3.3) over the referential volume element, i.e.,

$$\left\langle \mathbf{f}\left(\mathbf{x}_{\mathrm{o}},\mathbf{y}_{\mathrm{o}}\right)\right\rangle_{\mathrm{x}} = \mathbf{F}\left(\mathbf{x}_{\mathrm{o}}\right) + \frac{1}{\Omega_{\mathrm{o}}^{\mathrm{x}}}\int_{\Omega_{\mathrm{o}}^{\mathrm{x}}} \mathbf{h}\tilde{\nabla}_{\mathrm{o}} d\Omega_{\mathrm{o}} \tag{3.7}$$

Thus, satisfaction of Eq. (3.6) demands that the volume average of the fine scale deformation gradient be equivalent to the coarse scale deformation gradient. This relationship is a fundamental kinematic assertion of classical first order homogenization principles (cf. Hill, 1972) and has also been employed by Kouznetsova et al. (2002; 2004) for development of a concurrent second order homogenization. However, in the present multiscale framework it is not an *a priori* assertion, rather a byproduct of the requirement for kinematic consistency via orthogonal decomposition. Finally, requiring the contribution of the coarse scale second gradient to the fine scale deformation field be orthogonal to the fluctuation field, i.e.,

$$\mathbf{f}_2 \perp \mathbf{f}_3 \leftrightarrow \int_{\Omega_{\mathrm{o}}^{\mathrm{x}}} \mathbf{h}\tilde{\nabla}_{\mathrm{o}} \otimes \mathbf{y}_{\mathrm{o}}\, d\Omega_{\mathrm{o}} = \mathbf{0} \tag{3.8}$$

requires that the first spatial moment of the gradient of the fluctuation field be zero. Orthogonality conditions (3.6) and (3.8) form the minimal essential requirements of boundary conditions on fine scale rSVE simulations to ensure *kinematic* consistency with the coarse scale.

3.1.3 The Second Gradient

Kinematic significance of the second gradient is explored here before introducing the intermediate configuration and accompanying decompositions of relevant kinematic quantities. Indicial notation is used on occasion for clarity. The second gradient presented above, $G^{i}_{\cdot JK} = \dfrac{\partial F^{i}_{\cdot J}}{\partial x^{K}_{\mathrm{o}}} = \dfrac{\partial^2 x^{i}}{\partial x^{J}_{\mathrm{o}} \partial x^{K}_{\mathrm{o}}}$, is a mixed-variant third order tensor that is symmetric in *J* and *K* indices; this is the same kinematic tensor as that introduced by Mindlin (1964) and Germain (1973) in their second gradient theories, adopted by Fleck and Hutchinson (1993, 1997) for strain gradient plasticity, and used by Kouznetsova, et al. (2004), in a concurrent multiscale approach. Note that the notation employed here differs in the ordering of indices from some of these prior works.

The deformation modes of the material rSVE that correspond to particular components of the second gradient tensor, $\mathbf{G}$, are characterized in Table 1, with a few specific examples illustrated

in Figure 4. In these examples, we associate a cubic lattice of coarse scale material points in the reference configuration with a grid of the same material points in the current configuration after undergoing deformation defined purely by the coarse scale gradient of the deformation gradient. This grid is for illustration only and does not reflect underlying microstructural lattice curvature, nor does it reflect contributions from a fine scale fluctuation field. No summation is implied over repeated indices in Table 1 and unique indices are never equal. There are four distinct categories of deformation: extensional, trapezoidal, curvature, and twist, named according to their affect on an otherwise undeformed cubic rSVE. Both extensional and trapezoidal components contribute to dilatational gradients. In Figure 4, the coarse scale deformation gradient, $\mathbf{F}$, is equal to the identity tensor and all components of $\mathbf{G}$ are zero except the labeled nonzero component. Note that extensional and curvature modes are consistent with the displacement requirements of periodicity; however, the trapezoidal and twist modes exhibit aperiodic deformation.

Table 1. Characterization of deformation modes associated with the second gradient.

Mode of Deformation	**Nonzero Components of G**
Extensional	G_{iii}: G_{111} G_{222} G_{333}
Trapezoidal	$G_{i(ji)}$: $G_{121} = G_{112}$
Curvature	G_{ijj}: G_{122} G_{211} G_{322}
Twist/Torsion	G_{ijk}: $G_{123} = G_{132}$

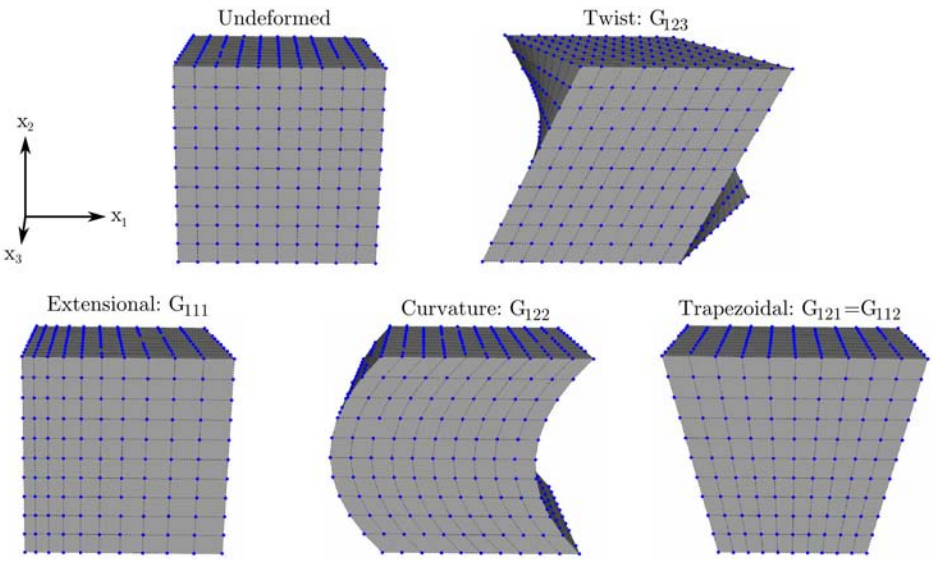

Figure 4. Examples of rSVE deformation associated with nonzero components of **G**.

Various kinematic measures commonly used in strain gradient plasticity are directly related to the second gradient. The fine scale displacement field is expressed as

$$\begin{aligned} \mathbf{u}\left(\mathbf{x}_{\mathrm{o}},\mathbf{y}_{\mathrm{o}}\right) = \mathbf{y}-\mathbf{y}_{\mathrm{o}} &= \underbrace{\left(\mathbf{F}-\mathbf{I}\right)\cdot\mathbf{y}_{\mathrm{o}}+\tfrac{1}{2}\mathbf{G}:\mathbf{y}_{\mathrm{o}}\otimes\mathbf{y}_{\mathrm{o}}} + \mathbf{h}\left(\mathbf{y}_{\mathrm{o}}\right) \\ &= \qquad\qquad \bar{\mathbf{u}}\left(\mathbf{x}_{\mathrm{o}},\mathbf{y}_{\mathrm{o}}\right) \qquad\quad + \mathbf{h}\left(\mathbf{y}_{\mathrm{o}}\right) \end{aligned} \tag{3.9}$$

where $\bar{\mathbf{u}}$ represents the coarse scale displacement field , $\mathbf{h}$ is the fluctuation field, and $\mathbf{I}$ is the second order identity tensor. The second gradient of the deformation field is clearly equivalent to the second gradient of the coarse scale displacement field, i.e., $G^{i}_{\cdot JK} = \dfrac{\partial^2 \overline{u}^{i}}{\partial x^{J}_{\mathrm{o}}\partial x^{K}_{\mathrm{o}}}$, thus providing a bridge to the kinematic quantities defined in strain gradient plasticity. For example, the coarse scale "small" strain field is computed from the coarse scale displacement field as $\varepsilon_{ij} = \frac{1}{2}\left(\overline{u}_{i,j}+\overline{u}_{j,i}\right)$ and the gradient of "small" strain is the left symmetrized part of the second-gradient, $\dfrac{\partial \varepsilon_{ij}}{\partial x^{\mathrm{o}}_{k}} = \frac{1}{2}\left(\overline{u}_{i,jk}+\overline{u}_{j,ik}\right) = \frac{1}{2}\left(G_{ijk}+G_{jik}\right)$, which is no longer symmetric in the last two indices, in general. Consistent with conventional continuum descriptions, we can define the linearized coarse scale material rotation vector as $\theta_i = \frac{1}{2}e_{imk}\overline{u}_{k,m}$. The spatial gradient of this

vector is the material curvature tensor, $\chi_{ij} \equiv \dfrac{\partial \theta_i}{\partial x_j}$, directly related to the second-gradient by $\chi_{ij} = \frac{1}{2} e_{imk} G_{kmj}$, where e_{imk} is the third order permutation tensor. This curvature tensor can be phenomenologically related to the population of geometrically necessary dislocations (GND) (Fleck and Hutchinson, 1997). In Fleck and Hutchinson's deformation version of couple stress theory, the overall effective strain is defined as $\hat{\varepsilon} = \sqrt{\varepsilon_e^2 + l^2 \chi_e^2}$, where the effective small strain is $\varepsilon_e = \sqrt{\frac{2}{3} \varepsilon_{ij} \varepsilon_{ij}}$, the effective curvature is $\chi_e = \sqrt{\frac{2}{3} \chi_{ij} \chi_{ij}}$, and l is a material length scale.

In the multiscale framework presented here, the phenomena that accommodate geometric curvature *must* depend on the particular scale of reference and physical mechanisms for microstructure evolution, and therefore may or may not involve GNDs. For example, GNDs may account for geometric curvature of the lattice at, say, scale *four*, but the presence of curvature at scale *two* might be predominantly accommodated by non-uniform redistribution of porosity and microcracks. At scale *zero*, curvature is generally associated with macroscopic bending and is accommodated by non-uniform axial inelastic strain, generally implying scale zero gradients in the evolution of kinematic variables at all lower scales.

There is further connection with gradients of finite strain and rotation that requires mapping the second gradient by the deformation gradient in a manner that is reminiscent of computing the Cauchy right deformation tensor from the deformation gradient itself, i.e. $C_{IJ} = F^k_{.I} g_{km} F^m_{.J}$, where g_{km} are the coefficients of the metric tensor in the current configuration. A covariant coefficient reference configuration measure of second order strain is

$$\Gamma^*_{IJK} = F^m_{.I} g_{mn} G^n_{.JK} = \tfrac{1}{2}\left(C_{JK,I} + C_{IK,J} - C_{IJ,K} \right), \tag{3.10}$$

such that the gradient of the coarse scale finite Green-Lagrange strain tensor, $E_{IJ} = \frac{1}{2}(C_{IJ} - \delta_{IJ})$ is expressed in manner analogous to that of small strain, that is, $\dfrac{\partial E_{IJ}}{\partial x^K_{\mathrm{o}}} = \dfrac{1}{2}\left(F^m_{.J} g_{mn} G^n_{.IK} + F^m_{.I} g_{mn} G^n_{.JK} \right) = \frac{1}{2}\left(\Gamma^*_{IJK} + \Gamma^*_{JIK} \right)$, the left-symmetrized part of Γ^*.

Note that Γ^* is *not* a proper pull back of the second gradient into the reference configuration; however, through this transformation Γ^* resides entirely within the reference configuration. A proper pull-back of the second-gradient into the reference configuration yields the mixed-variant wryness tensor of Eringen (1999) which has been used in the second gradient context by Chambon et al. (2001; 2004), i.e., $\Gamma^I_{\cdot JK} = \overset{-1}{F}{}^I_{\cdot m} G^m_{\cdot JK}$. Eringen also defines an alternative second order wryness tensor that would be expressed in the context of second gradient continua as $\Upsilon_{IJ} \equiv \frac{1}{2} e_{IMN} F^q_{\cdot N} g_{qs} G^s_{\cdot MJ} = \frac{1}{2} e_{IMN} \Gamma^*_{NMJ}$. Finally, the curvature tensor of finite deformation, $\mathbf{X}$, is computed via polar decomposition of the deformation gradient (Larsson and Diebels, 2007), i.e., $\mathbf{F} = \mathbf{R} \cdot \mathbf{U}$ and $\mathbf{X} = -\frac{1}{2}\mathbf{e} : \mathbf{R}^T \cdot \frac{\partial \mathbf{R}}{\partial \mathbf{x}_o}$. Note that material curvature discussed in this section is not the same as lattice curvature, in general, as the latter is typically associated with curvature of the inelastic portion of the deformation occurring at finer scales.

Smyshlyaev and Fleck (1996) decomposed the second gradient into four parts in a manner analogous to the dilatational-deviatoric split of first order stress and strain tensors, i.e.,

$$
\begin{aligned}
G_{ijk} &= G^H_{ijk} + G^{D1}_{ijk} + G^{D2}_{ijk} + G^{D3}_{ijk} \\
G^H_{ijk} &= \tfrac{1}{5}\big(G_{ppi}\delta_{jk} + G_{ppj}\delta_{ki} + G_{ppk}\delta_{ij} \big) \\
G'_{ijk} &= G_{ijk} - G^H_{ijk} \\
G^S_{ijk} &= \tfrac{1}{3}\big(G'_{ijk} + G'_{jki} + G'_{kij} \big) \\
G^{D1}_{ijk} &= G^S_{ijk} - \tfrac{1}{5}\big(G^S_{ppi}\delta_{jk} + G^S_{ppj}\delta_{ki} + G^S_{ppk}\delta_{ij} \big) \\
G^{D2}_{ijk} &= \tfrac{1}{6}\big(-e_{ijp}e_{kmn}G'_{nmp} - e_{ikp}e_{jmn}G'_{nmp} + 2G'_{ijk} - G'_{jik} - G'_{kji} \big) \\
G^{D3}_{ijk} &= G'_{ijk} - G^{D1}_{ijk} - G^{D2}_{ijk} \\
&= \tfrac{1}{6}\big(e_{ijp}e_{kmn}G'_{nmp} + e_{ikp}e_{jmn}G'_{nmp} + 2G'_{ijk} - G'_{jik} - G'_{kji} \big) \\
&\quad + \tfrac{1}{5}\big(G'_{ppi}\delta_{jk} + G'_{ppj}\delta_{ki} + G'_{ppk}\delta_{ij} \big)
\end{aligned}
\tag{3.11}
$$

where a proper accounting of the variance of indices has been omitted here for simplicity of notation. The resulting four third-order tensors, G^H_{ijk}, G^{D1}_{ijk}, G^{D2}_{ijk}, and G^{D3}_{ijk} represent the gradient of dilatational deformation, gradient of symmetric deviatoric deformation, symmetric curvature, and anti-symmetric curvature, respectively.

Within this multiscale framework, the second gradient is used as a nonlocal kinematic link between the response of a material point at the coarse scale and the response of a neighborhood of material points at the fine scale. The second gradient discussed here is the same kinematic tensor as that introduced by Mindlin (1964) and Germain (1973) in the second gradient theory, adapted by Fleck and Hutchinson (1997) for strain-gradient plasticity, and used by Kouznetsova, et al. (2002; 2004), for a concurrent multiscale approach. This section illustrates the nature of the second gradient and draws relevant ties to other kinematic quantities.

3.1.4 Compatibility

Generally, the deformed fine scale rSVEs associated with two adjacent coarse scale material points are incompatible (cf. Sections 3.1.3 and 3.1.5). On the other hand, the deformation within a single fine scale rSVE is compatible under the condition that the fourth order Riemannian curvature tensor vanishes for all possible deformation fields (Blume, 1989), i.e.,

$$R_{ijkl} = \Gamma_{ijl,k} - \Gamma_{ijk,l} + C^{-1}_{pq}\left(\Gamma_{pjk}\Gamma_{ilq} - \Gamma_{pjl}\Gamma_{qik}\right) = 0 \tag{3.12}$$

where the second order strain, Γ, introduced in the previous section, is defined subsequently by Eq. (3.33). From (3.12), one can recognize the role of the second order strain as Christoffel symbols of the first kind on the current configuration, much like the right Cauchy deformation tensor acts as a metric on that configuration. The only requirement resulting from Eq. (3.12) is that the second-order strain, and consequently, the second gradient, must be symmetric in the last two indices, i.e.,

$$\Gamma_{ijk} = \Gamma_{ikj} \Rightarrow G_{ijk} = G_{ikj} \tag{3.13}$$

Intuitively, this condition arises from the lack of uniqueness associated with a fine scale deformation field if the coarse scale second gradient were not symmetric.

3.1.5 Boundary Conditions

Upon specification of **F**, and **G** for the rSVE, the coarse scale or homogenized displacement field is entirely known. Therefore, specification of fine scale displacement boundary conditions is accomplished by specification of constraints on the fluctuation field, **h**. Numerical

implementation and consequences of each of these sets of boundary conditions are discussed in Chapter 4; here attention is focused on developing fluctuation constraints that ensure kinematic consistency between scales. Specifically, in what follows, constraints on the fine scale fluctuations are obtained through a detailed examination of the zero and first order moments of the gradient of the fluctuation field given in Eqs. (3.6) and (3.8).

Expressions for fluctuation constraints are enhanced by introducing tangential surface (surfacial) coordinates and assuming a right prismatic rSVE, for example, the cube shown in Figure 5. On the rSVE boundary, i.e. $\forall\, \mathbf{y}_o \in \Gamma_o^x$, the tangential surface coordinates, $\boldsymbol{\eta}_o$, are obtained by removal of the normal component of the position coordinate, i.e., $\boldsymbol{\eta}_o = \mathbf{y}_o \cdot (\mathbf{I} - \mathbf{n}_o \otimes \mathbf{n}_o)$, where $\mathbf{n}_o$ is the unit outward normal vector.

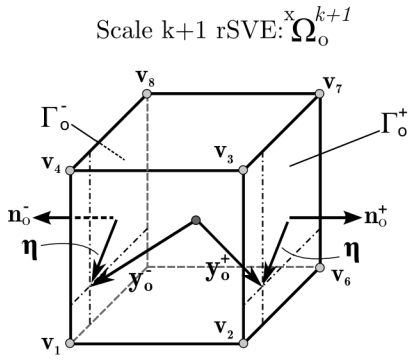

Figure 5. Diagram of surfacial coordinates on opposing rSVE boundary surfaces.

Following Kouznetsova et al. (2004), we apply the generalized divergence theorem to the left hand side of Eq (3.6) to develop boundary constraints, i.e.,

$$\int_{\Omega_o^x} \mathbf{h}\bar{\nabla}_o d\Omega_o = \int_{\Gamma_o^x} \mathbf{h} \otimes \mathbf{n}_o \, d\Gamma_o = 0 \tag{3.14}$$

Unlike in their homogenization scheme, however, we include the requirement from Eq. (3.8). Application of the chain rule and generalized divergence theorem to Eq. (3.8) equates the requirement for vanishing first spatial moment of the fluctuation gradient to Eq. (3.15) which requires the boundary integral of the spatial moment be balanced by the mean of the fluctuation field over the rSVE , i.e.,

$$\int_{\Gamma_o^x} \mathbf{h} \otimes \mathbf{n}_o \otimes \mathbf{y}_o \, d\Gamma_o = \mathbf{I} \otimes \int_{\Omega_o^x} \mathbf{h} \, d\Omega_o \tag{3.15}$$

The rSVE unit outward normal vector $\mathbf{n}_o$ in the integrand effectively decomposes Eq. (3.15) into constraints on opposite pairs of boundary faces, i.e., (Γ_o^+, Γ_o^-). Substitution of surfacial coordinates allows further decomposition into normal and tangential constraint equations, i.e.,

$$\frac{L_{rSVE}}{2}\left(\int_{\Gamma_o^{x,(+)}} \mathbf{h} \, d\Gamma_o + \int_{\Gamma_o^{x,(-)}} \mathbf{h} \, d\Gamma_o \right) = \int_{\Omega_o^x} \mathbf{h} \, d\Omega_o \tag{3.16}$$

$$\int_{\Gamma_o^{x,(+)}} \mathbf{h} \otimes \boldsymbol{\eta}_o \, d\Gamma_o = \int_{\Gamma_o^{x,(-)}} \mathbf{h} \otimes \boldsymbol{\eta}_o \, d\Gamma_o \tag{3.17}$$

where L_{rSVE} is the length of the rSVE sides for a cube. We impose that both sides of Eq. (3.16) independently vanish as a stronger requirement in order to restrain rigid body deformation. It is convenient at this point to separately impose that each term on the left hand side of Equation (3.16) vanish and that both sides of Equation (3.17) be set to zero, although strictly speaking this requirement arises due to scale invariance of momentum, and is explained further in Section 3.2.

$$\int_{\Omega_o^x} \mathbf{h} \, d\Omega_o = \mathbf{0} \tag{3.18}$$

$$\int_{\Gamma_o^{x,(+,-)}} \mathbf{h} \, d\Gamma_o = 0 \tag{3.19}$$

Finally, requirements imposed upon fine scale rSVE boundary conditions consist of Eqs. (3.14), (3.17), (3.18), and (3.19). Specific sets of boundary conditions that satisfy these requirements are now discussed.

The most direct, albeit trivial, case satisfying Eqs. (3.14), and (3.17)-(3.19) is a constraint on the kinematic motion of every fine scale material point, i.e.,

$$\mathbf{h}\left(\mathbf{y}_o\right) = \mathbf{0} \;\forall\, \mathbf{y}_o \in \Omega_o^x \tag{3.20}$$

thus removing the fluctuation field entirely, so that the coarse and fine scale descriptions of the kinematic response are identical. Note that implementation of such a constraint would require application of body forces throughout the fine scale rSVE. While such a constraint is unnecessarily restrictive to satisfy Eqs. (3.14), and (3.17)-(3.19), it introduces the notion of

internal fluctuation constraints. An alternative case is obtained by specifying that the fluctuation field must disappear on the boundaries, Γ_o^x , of the rSVE, resulting in a second-order generalization of the uniform Dirichlet boundary conditions often assumed for solution of first-order micromechanical homogenization problems, and given as

$$\mathbf{h}\left(\mathbf{y}_o\right) = \mathbf{0} \;\forall\, \mathbf{y}_o \in \Gamma_o^x \tag{3.21}$$

For the second-gradient multiscale framework, Eq. (3.21) does not satisfy Eq. (3.18) which must be independently imposed as an additional internal fluctuation constraint for non-zero components of **G**. Constraint equation (3.18) also implies the presence of body forces applied to the interior of the rSVE; however, it is a weaker condition than constraining the fluctuation at every material point. Eqs. (3.21) and (3.18) form a complete set of fluctuation constraints for kinematic consistency between the coarse and fine scales referred to here as *second gradient direct boundary conditions*.

A further, less restrictive set of boundary conditions satisfying this relationship is facilitated by introducing a particular rSVE for analysis, cf. Figure 5. For every pair of opposing boundary surfaces (Γ_o^+, Γ_o^-) with collinear unit outward surface normals ($\mathbf{n}_o^+ = -\mathbf{n}_o^-$), *generalized periodic boundary conditions* are prescribed by

$$\mathbf{h}^+\left(\boldsymbol{\eta}\right) = \mathbf{h}^-\left(\boldsymbol{\eta}\right) \tag{3.22}$$

Upon integration of Eq. (3.22) in Eq. (3.14) it is directly verified that these generalized periodic boundary conditions satisfy the latter. For $\mathbf{G} = \mathbf{0}$, Eq. (3.22) are the classical periodic boundary conditions, cf. van der Sluis et al. (2000), Kouznetsova et al. (2004), and the top case of Figure 6. Also note that Eq. (3.22) directly satisfies the requirement of Eq. (3.17). For non-zero components of the second gradient, Eq. (3.22) will not generally maintain periodic compatibility of the deformed rSVE, for example, cf. bottom of Figure 6. Furthermore, boundary conditions of Eq. (3.22) are not sufficient to satisfy Eqs. (3.18)-(3.19). Therefore, Eqs. (3.18), (3.19) and (3.22) form the necessary constraint equations for generalized periodic boundary conditions in the case of nonzero second gradient.

Mesarovich and Padbidri (2005) proposed a set of minimal boundary conditions for a fine scale rSVE in the sense that they provided the least possible constraint on the system in order to achieve a desired coarse scale homogenized strain. In this spirit, constraint Eqs. (3.14), and (3.17)-(3.19) are grouped together to form the *minimal boundary conditions* for a second gradient continua. In the absence of a second gradient, only Eq. (3.14) is required and it can be shown that this is equivalent to the boundary conditions presented by Mesarovic and Padbidri under conditions of small coarse scale deformation.

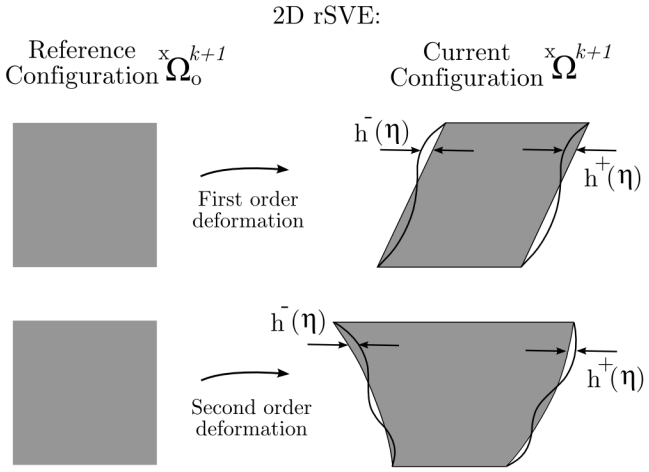

Figure 6. Illustration of fine scale generalized periodic boundary conditions under first order (top) and second order (bottom) coarse scale modes of deformation.

Requirements of Eqs. (3.14), and (3.17)-(3.19) ensure orthogonality of the kinematic terms that define the fine scale deformation gradient. Some of the results from these requirements have been introduced for other purposes in recent second gradient computational work (Kouznetsova et al., 2002; Kouznetsova et al., 2004; Larsson and Diebels, 2007) and are consistent with the numerical procedures outlined in Chapter 4. For example, Kouznetsova et al. (2002) require that the mean fluctuation vanish along each surface of the rSVE (cf. Eq. (3.19)) because, otherwise, their generalized periodic boundary conditions would only directly involve two distinct

components of a 2D second gradient. However, the present work is the first time the complete set of requirements for boundary conditions has been developed from certain kinematic principles. Here these conditions are developed in order to ensure kinematic orthogonality, which is important to scale invariance of momentum via the principle of virtual velocities in the next section.

3.1.6 Intermediate Configuration

This section describes the kinematic terms employed in scale transitions within the multiscale hierarchical approach. It is therefore preferable to restrict attention to the kinematics of multiscaled deformation and postpone particular details of requisite forces that cause deformation until Section 3.2. However, it is necessary that a vague notion of such stresses be introduced for the purpose of enabling further decomposition of kinematic terms. At the very minimum it is required to acknowledge that internal and external forces give rise to material stresses which *lead to* the deformation at the coarse scale, $\mathbf{x}(\mathbf{x}_o)$, and the fine scale, $\mathbf{y}(\mathbf{y}_o)$.

Initially (prior to application of any external loads), the spatial location of every material point in the rSVE is coincident with its material coordinates, $\mathbf{y}(\mathbf{y}_o) = \mathbf{y}_o$. Generally, and especially under external forces, the current spatial position of material points within the deformed rSVE, $\mathbf{y}(\mathbf{y}_o)$, will differ from that in the reference state, $\mathbf{y}_o$, and this deformed configuration is labeled the *current* configuration. If at some particular time after any *irreversible* deformation has occurred all forces external to the rSVE are removed, the rSVE would be in a different configuration than either the reference configuration or that current configuration which preceded the removal of external forces. Thus, for each current configuration there exists an accompanying *intermediate* configuration associated with removal of external forces. The intermediate configuration is often referred to as stress-free configuration; this description is consistent with that adopted here based on the definitions of coarse scale stress in the next section. It must be noted, however, that there are nonzero 'residual' fine scale stress fields associated with a stress free coarse scale after irreversible microstructure evolution (cf. Clayton and McDowell, 2003).

A variety of inconsistencies confer the intermediate configuration the status of being fictitious. First, there is a time scale issue associated with the removal of tractions. Clearly, for rate-dependent processes within the rSVE, the rate at which tractions are removed is critical. One can assert that tractions are removed instantaneously, in which case the next issue is for how long the tractions are removed before the intermediate configuration had been reached. If it is asserted that the intermediate configuration is that reached in the steady state, then there can be no intermediate configuration if the inelastic deformation processes do not consider such a steady state (consider the Maxwell viscoelastic model for example). On the other hand, if the intermediate configuration is taken as that configuration resulting immediately after instantaneous removal of the boundary traction, then strictly speaking, due to inertia one would find the intermediate configuration is always coincident with the current configuration. As a compromise, we define the intermediate configuration to be that configuration resulting from the instantaneous removal of boundary tractions after the rSVE has inertially self-equilibrated in the absence of any additional rate-dependent microstructural evolution; we are at liberty to make this assertion. This description will be made more precise in the next two sections. For now we proceed by postulating the existence of an intermediate configuration.

The intermediate configuration is of high utility as it represents the kinematical consequences of microstructure evolution most directly. The free energy function introduced subsequently is most aptly written in this configuration because irreversible evolution is present, while conveniently, long range reversible deformation has been recovered. Moreover, for certain processes involving underlying material substructure, it has a strong physical basis (e.g., crystal plasticity.) In order to realize such conveniences, the kinematic terms must be mapped into the intermediate configuration correctly. In order to develop the required push-forward and pull-back operations in the proper context of differential geometry, equations in this section will often be presented in indicial notation with capital indices indicating the reference configuration, lower case indices representing the current configuration, and lower case indices with an over-tilde representing the intermediate configuration. Also, raised indices are used for contravariant components while lowered indices are used for covariant components.

The spatial locations of fine scale material points in the intermediate configuration are denoted $\tilde{\mathbf{y}}$. The kinematic deformation field of the intermediate configuration is decomposed within an rSVE consistent with Eq. (3.2), i.e.,

$$\tilde{\mathbf{y}} = \mathbf{F}^{in} \cdot \mathbf{y}_{\mathrm{o}} + \tfrac{1}{2}\mathbf{G}^{in} : \mathbf{y}_{\mathrm{o}} \otimes \mathbf{y}_{\mathrm{o}} + \tilde{\mathbf{h}}\left(\mathbf{y}_{\mathrm{o}}\right) \tag{3.23}$$

where the subscript *in* is used to indicate inelastic components and a tilde appears above **y** and **h** because the single covariant component for these vectors resides entirely within the intermediate configuration. In contrast, $\mathbf{F}^{in}$ and $\mathbf{G}^{in}$ do not receive this special demarcation, as their contravariant component lies in the intermediate configuration whilst their covariant components are in the reference configuration.

The total coarse scale deformation gradient is then multiplicatively decomposed according to

$$\begin{aligned} \mathbf{F} &= \mathbf{F}^{e} \cdot \mathbf{F}^{in} \\ F^{i}_{\ .J} &= {}^{e}F^{i}_{\ .\tilde{k}}\ {}^{in}F^{\tilde{k}}_{\ .J} \end{aligned} \tag{3.24}$$

Note that the superscripts *e* and *in* for elastic and inelastic components, respectively, are moved to the left side of the main tensoral symbol as necessary to make room for indices on the right side. This notation convention is used for clarity where appropriate. The multiplicative decomposition of (3.24) is illustrated by Figure 7. For the purposes of discussion, a multiplicative decomposition of the fine scale deformation gradient is also introduced (as in Clayton and McDowell, 2003), i.e.,

$$\mathbf{f} = \mathbf{f}^{e} \cdot \mathbf{f}^{in} \tag{3.25}$$

We note in passing that more complex multiplicative decompositions could be introduced at this point to represent the accommodational contributions of damage, thermal expansion, phase transformation and other phenomena, as necessary. Equation (3.25) is not expressed in indicial notation because the inner most indices would reside in none of the configurations presented thus far, but rather in a fine scale intermediate configuration. This motivates an important discussion. From Eq. (3.7) and constraints on the rSVE in Eq. (3.14) it is possible to write

$$\mathbf{F} = \mathbf{F}^{e} \cdot \mathbf{F}^{in} = \tfrac{1}{\Omega^{\mathrm{x}}_{\mathrm{o}}} \int_{\Omega^{\mathrm{s}}_{\mathrm{o}}} \mathbf{f}^{e} \cdot \mathbf{f}^{in} d\Omega \tag{3.26}$$

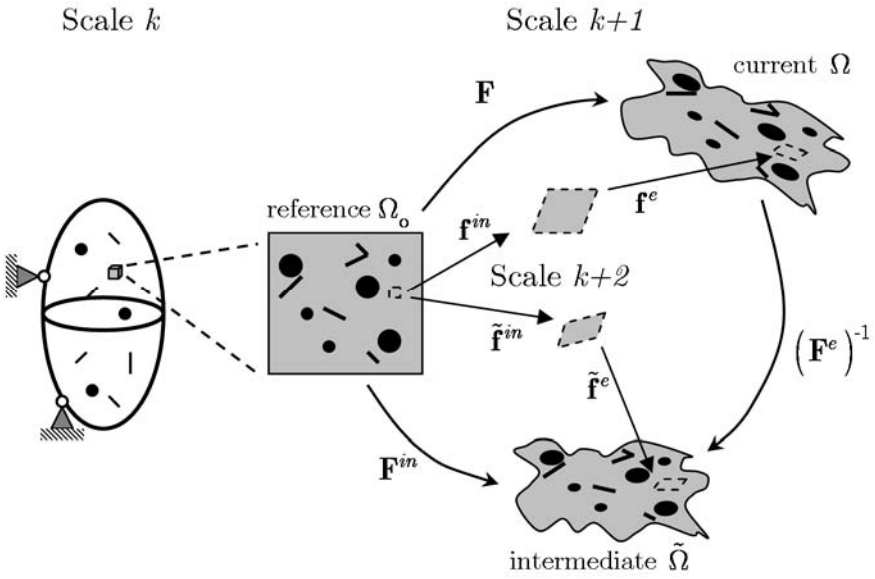

Figure 7. Configurations associated with multiplicative decomposition of deformation gradient.

However, because the fine and coarse scale intermediate configurations differ, the fine scale inelastic deformation gradient generally cannot be integrated to obtain the coarse scale inelastic deformation gradient and likewise for the elastic component of deformation, since the resulting incompatibility of each is not rectified on the coarse scale, i.e.,

$$\begin{aligned} \mathbf{F}^{in} &\neq \tfrac{1}{\Omega_o^x}\int_{\Omega_o^x} \mathbf{f}^{in}\, d\Omega \\ \mathbf{F}^{e} &\neq \tfrac{1}{\Omega_o^x}\int_{\Omega_o^x} \mathbf{f}^{e}\, d\Omega \end{aligned} \tag{3.27}$$

One can, however, relate the inelastic coarse scale deformation gradient to the volume average of the fine scale (total) deformation gradient, $\tilde{\mathbf{f}} = \frac{\partial \tilde{\mathbf{y}}}{\partial \mathbf{y}_o}$, in the intermediate configuration, i.e.,

$$\mathbf{F}^{in} = \tfrac{1}{\Omega_o^x}\int_{\Omega_o^x} \tilde{\mathbf{f}}\, d\Omega \tag{3.28}$$

This assumes that the intermediate configuration is a compatible configuration (cf. Clayton and McDowell, 2003), a condition that is locally obeyed, i.e., within the domain of the rSVE.

Further recognize that the fine scale deformation gradient in the intermediate configuration can also be multiplicatively decomposed, i.e., $\tilde{\mathbf{f}} = \tilde{\mathbf{f}}^{e} \cdot \tilde{\mathbf{f}}^{in}$, where the tilde configuration is that corresponding to $\mathbf{F}^{in}$ in Figure 7; it is these components of deformation that motivate the incorporation of additional internal kinematic variables and serve as the discriminating factor for the partitioning of inelastic work of coarse scale deformation into dissipation and elastic energy stored within the fine scale field.

The Green-Lagrange strain, $\mathbf{E}$, is defined from the right Cauchy deformation tensor, $\mathbf{C}$, as

$$\begin{aligned} C_{IJ} &= F^{k}_{.I} g_{km} F^{m}_{.J} \\ E_{IJ} &= \tfrac{1}{2}(C_{IJ} - \delta_{IJ}) \end{aligned} \tag{3.29}$$

where the metric tensor, g_{km}, has been included to keep indices proper; because Cartesian coordinates are used exclusively in this work, it is simply equal to the identity tensor. It is clear from the indices of (3.29), that the Green-Lagrange strain completely resides within the reference configuration. Almansi's strain results from the push-forward of Green-Lagrange strain into the current configuration, $\mathbf{e} = \phi_{*}(\mathbf{E}) = \frac{1}{2}(\mathbf{I} - \mathbf{b}^{-1})$, where $\mathbf{b} = \mathbf{F} \cdot \mathbf{F}^{T}$ is the finger tensor. The Green-Lagrange strain referred to the intermediate configuration is obtained by the inelastic push-forward of the Green-Lagrange strain, $\tilde{\mathbf{E}} = \phi^{in}_{*}(\mathbf{E})$ or the elastic pull-back of Almansi's strain into the intermediate configuration, $\tilde{\mathbf{E}} = \phi^{*}_{e}(\mathbf{e})$. By the former method

$$\tilde{\mathbf{E}} = \mathbf{F}^{-T}_{in} \cdot \mathbf{E} \cdot \mathbf{F}^{-1}_{in} \tag{3.30}$$

which is decomposed into elastic and inelastic parts by substitution of (3.24) and then (3.29), i.e.,

$$\begin{aligned} \tilde{\mathbf{E}} &= \mathbf{F}^{-T}_{in} \cdot (\mathbf{F}^{T} \cdot \mathbf{F} - \mathbf{I}) \cdot \mathbf{F}^{-1}_{in} \\ &= \tfrac{1}{2}(\mathbf{F}^{T}_{e} \mathbf{F}_{e} - \mathbf{I}) + \tfrac{1}{2}(\mathbf{I} - \mathbf{F}^{-T}_{in} \mathbf{F}^{-1}_{in}) \\ &= \quad \tilde{\mathbf{E}}_{e} \quad + \quad \tilde{\mathbf{E}}_{in} \end{aligned} \tag{3.31}$$

The total coarse scale second gradient is expanded using the chain rule and the multiplicative decomposition of the total coarse scale deformation gradient in Eq. (3.24), i.e.,

$$
\begin{aligned}
G^{i}_{\cdot JK} &= \frac{\partial F^{i}_{\cdot J}}{\partial x^{K}_{\mathrm{o}}} = \frac{\partial \left({}^{e}F^{i}_{\cdot \tilde{m}}\, {}^{in}F^{\tilde{m}}_{\cdot J} \right)}{\partial x^{K}_{\mathrm{o}}} \\
&= \frac{\partial\, {}^{e}F^{i}_{\cdot \tilde{m}}}{\partial x^{K}_{\mathrm{o}}}\, {}^{in}F^{\tilde{m}}_{\cdot J} + {}^{e}F^{i}_{\cdot \tilde{m}}\, \frac{\partial\, {}^{in}F^{\tilde{m}}_{\cdot J}}{\partial x^{K}_{\mathrm{o}}}
\end{aligned}
\tag{3.32}
$$

This is pulled back to the reference configuration according to

$$
\Gamma^{I}_{\cdot JK} = F^{-1}_{\cdot i}{}^{I}\, \frac{\partial\, {}^{e}F^{i}_{\cdot \tilde{m}}}{\partial x^{K}_{\mathrm{o}}}\, {}^{in}F^{\tilde{m}}_{\cdot J} + {}^{in}F^{-1}_{\cdot \tilde{m}}{}^{I}\, \frac{\partial\, {}^{in}F^{\tilde{m}}_{\cdot J}}{\partial x^{K}_{\mathrm{o}}}
\tag{3.33}
$$

and finally pushed forward into the intermediate configuration, resulting in an additive decomposition into elastic and inelastic parts yielding a mixed-variant second-order strain referred to the intermediate configuration, i.e.,

$$
\begin{aligned}
\tilde{\Gamma}^{\tilde{i}}_{\cdot \tilde{j}\tilde{k}} &= {}^{e}F^{-1}_{\tilde{i}\cdot m}\, \frac{\partial\, {}^{e}F^{m}_{\cdot \tilde{j}}}{\partial x^{N}_{\mathrm{o}}}\, {}^{in}F^{-1}_{\cdot \tilde{k}}{}^{N} + {}^{in}F^{-1}_{\cdot \tilde{j}}{}^{M}\, \frac{\partial\, {}^{in}F^{\tilde{i}}_{\cdot M}}{\partial x^{N}_{\mathrm{o}}}\, {}^{in}F^{-1}_{\cdot \tilde{k}}{}^{N} \\
&= \quad {}^{e}\tilde{\Gamma}^{\tilde{i}}_{\cdot \tilde{j}\tilde{k}} \quad + \quad {}^{in}\tilde{\Gamma}^{\tilde{i}}_{\cdot \tilde{j}\tilde{k}}
\end{aligned}
\tag{3.34}
$$

The latter term in Eq. (3.34) is recognized as the inelastic push-forward of the inelastic second-gradient introduced in Eq. (3.23), i.e. $\tilde{\Gamma}^{in} = \phi^{in}_{*}(\mathbf{G}^{in})$. Note the distinction between the total second gradient within the intermediate configuration and the inelastic portion of the second gradient. Our definition of a mixed variant intermediate configuration second-order strain presents a particular convenience in its additive decomposition into elastic and entirely inelastic parts.

The covariant second-order strain, $\mathbf{\Gamma}^{*}$, is decomposed into elastic and inelastic parts by substitution of the decomposition of the second gradient Eq. (3.32), and the multiplicative decomposition of the deformation gradient into the definition of second order strain Eq. (3.10), i.e.,

$$
\begin{aligned}
\Gamma^{*}_{IJK} &= F^{q}_{\cdot I} g_{qr}\, \frac{\partial\, {}^{e}F^{r}_{\cdot \tilde{m}}}{\partial x^{K}_{\mathrm{o}}}\, {}^{in}F^{\tilde{m}}_{\cdot J} + {}^{e}F^{r}_{\cdot \tilde{m}} g_{qr}\, {}^{e}F^{q}_{\cdot \tilde{k}}\, {}^{in}F^{\tilde{k}}_{\cdot I}\, \frac{\partial\, {}^{in}F^{\tilde{m}}_{\cdot J}}{\partial x^{K}_{\mathrm{o}}} \\
&= F^{q}_{\cdot I} g_{qr}\, \frac{\partial\, {}^{e}F^{r}_{\cdot \tilde{m}}}{\partial x^{K}_{\mathrm{o}}}\, {}^{in}F^{\tilde{m}}_{\cdot J} + C^{e}_{\tilde{m}\tilde{k}}\, {}^{in}F^{\tilde{k}}_{\cdot I}\, \frac{\partial\, {}^{in}F^{\tilde{m}}_{\cdot J}}{\partial x^{K}_{\mathrm{o}}} \\
&= \quad \hat{\Gamma}^{*}_{IJK} \quad + \quad \widehat{\Gamma}^{*}_{IJK}
\end{aligned}
\tag{3.35}
$$

where $C^e_{\tilde{i}\tilde{j}} = {}^eF^k_{.\tilde{i}}\, g_{km}\, {}^eF^m_{.\tilde{j}}$ is the elastic Cauchy deformation tensor acting as the metric on the intermediate configuration, that is the elastic pull-back of the metric on the current configuration. Finally, $\mathbf{\Gamma}^*$ is pushed forward into the intermediate configuration as

$$\begin{aligned}
\tilde{\Gamma}^*_{\tilde{i}\tilde{j}\tilde{k}} &= {}^eF^q_{.\tilde{i}}\, g_{qr}\, \frac{\partial\, {}^eF^r_{.\tilde{j}}}{\partial x^L_{\mathrm{o}}}\, {}^{in}F^{-1}{}^L_{.\tilde{k}} + C^e_{\tilde{m}\tilde{i}}\, \frac{\partial\, {}^{in}F^{\tilde{m}}_{.P}}{\partial x^L_{\mathrm{o}}}\, {}^{in}F^{-1}{}^P_{.\tilde{j}}\, {}^{in}F^{-1}{}^L_{.\tilde{k}} \\
&= \hat{\tilde{\Gamma}}^*_{\tilde{i}\tilde{j}\tilde{k}} + \widehat{\tilde{\Gamma}}^*_{\tilde{i}\tilde{j}\tilde{k}} \\
&= C^e_{\tilde{m}\tilde{i}}\, {}^e\tilde{\Gamma}^{\tilde{m}}_{.\tilde{j}\tilde{k}} + C^e_{\tilde{m}\tilde{i}}\, {}^{in}\tilde{\Gamma}^{\tilde{m}}_{.\tilde{j}\tilde{k}}
\end{aligned} \tag{3.36}$$

One is free to assign the labels elastic and inelastic (or plastic) to the separate terms in the additive decompositions of (3.35) and (3.36), for example, $\mathbf{\Gamma}^{*e} = \hat{\mathbf{\Gamma}}^*$ and $\mathbf{\Gamma}^{*in} = \widehat{\mathbf{\Gamma}}^*$; however, the role of the elastic Cauchy deformation tensor as a metric in each of these terms implies that a purely elastic change in deformation will result in a change in the so-called inelastic portion of the decomposition. In Section 3.3 the utility of (3.34) will be demonstrated as it enables the separation of purely non-dissipative processes from generally irreversible processes, i.e., there are no terms associated with a purely reversible deformation contributing to $\tilde{\Gamma}^{in}$. The complete push forward of $\mathbf{\Gamma}$ to the current configuration results in a similar coupling of elastic and inelastic measures of deformation. This issue reinforces the special advantages afforded by adopting an intermediate configuration, e.g., the free-energy function (introduced in Section 3.3.3) is most aptly written in this configuration.

3.1.7 Time Rates of Kinematic Variables

The principle of virtual velocities and thermodynamic principles of the subsequent sections require time derivatives of kinematic quantities. The proper time derivative of a quantity that is defined with respect to an evolving (e.g. intermediate) configuration is the Lie derivative. The Lie derivative is the push forward of the material time derivative of the pull-back of the particular tensor into a fixed reference configuration, i.e., $L_v(\mathbf{T}) = \phi_*\left(\frac{D}{Dt}\phi^*(\mathbf{T})\right)$.

For the Green-Lagrange strain referred to the intermediate configuration, the Lie derivative is simply the inelastic push forward of the rate of Green-Lagrange strain in the reference configuration, i.e.,

$$\begin{aligned} L_v(\tilde{\mathbf{E}}) &= \phi_*^{in}(\dot{\mathbf{E}}) = \tilde{\mathbf{D}} \\ &= \tfrac{1}{2}\Big(\mathbf{F}^{in,-T}\cdot\dot{\mathbf{F}}^{T}\cdot\mathbf{F}\cdot\mathbf{F}^{in,-1} + \mathbf{F}^{in,-T}\cdot\mathbf{F}^{T}\cdot\dot{\mathbf{F}}\cdot\mathbf{F}^{in,-1}\Big) \end{aligned} \tag{3.37}$$

Substitution of the multiplicative decomposition of $\mathbf{F}$ Eq. (3.24) into the above gives

$$\tilde{\mathbf{D}} = \tfrac{1}{2}\Big(\dot{\mathbf{F}}^{e,T}\cdot\mathbf{F}^{e} + \mathbf{F}^{e,T}\cdot\dot{\mathbf{F}}^{e} + \mathbf{F}^{in,-T}\cdot\dot{\mathbf{F}}^{in}\cdot\mathbf{F}^{e,T}\cdot\mathbf{F}^{e} + \mathbf{F}^{e,T}\cdot\mathbf{F}^{e}\cdot\dot{\mathbf{F}}^{in}\cdot\mathbf{F}^{in,-1}\Big) \tag{3.38}$$

The inelastic push forward of the time derivative of the deformation gradient gives the velocity gradient referred to the intermediate configuration, i.e.,

$$\begin{aligned} \tilde{\mathbf{L}} = \phi_*^{in}(\dot{\mathbf{F}}) &= \mathbf{F}^{e,-1}\cdot\dot{\mathbf{F}}^{e} + \dot{\mathbf{F}}^{in}\cdot\mathbf{F}^{in,-1} \\ &= \quad \tilde{\mathbf{L}}^{e} \quad + \quad \tilde{\mathbf{L}}^{in} \end{aligned} \tag{3.39}$$

From Eqs. (3.38) and (3.39) one finds that

$$\begin{aligned} \tilde{\mathbf{D}} &= \underbrace{\tfrac{1}{2}\Big(\mathbf{C}^{e}\cdot\tilde{\mathbf{L}}^{e} + \tilde{\mathbf{L}}^{e,T}\cdot\mathbf{C}^{e}\Big)}_{} + \underbrace{\tfrac{1}{2}\Big(\mathbf{C}^{e}\cdot\tilde{\mathbf{L}}^{in} + \tilde{\mathbf{L}}^{in,T}\cdot\mathbf{C}^{e}\Big)}_{} \\ &= \qquad \tilde{\mathbf{D}}^{e} \qquad + \qquad \tilde{\mathbf{D}}^{in} \end{aligned} \tag{3.40}$$

so that $\tilde{\mathbf{D}}$ (and its elastic and inelastic parts) are obtained from the symmetric part of $\tilde{\mathbf{L}}$ (and its elastic and inelastic parts) where the symmetrization is assisted by the elastic Cauchy right deformation tensor, $\mathbf{C}^{e}$, acting as a metric on the intermediate configuration. Application of the chain rule to the elastic part of Eq. (3.31) reveals that $\tilde{\mathbf{D}}^{e} = \dot{\tilde{\mathbf{E}}}^{e}$; however, $\tilde{\mathbf{D}}^{in} \neq \dot{\tilde{\mathbf{E}}}^{in}$.

The Lie derivative of the second-order strain, $\tilde{\boldsymbol{\Gamma}}$, can be decomposed into elastic and inelastic parts as

$$\begin{aligned} L_v\left(\tilde{\boldsymbol{\Gamma}}\right) &= L_v\left(\tilde{\boldsymbol{\Gamma}}^{e}\right) + L_v\left(\tilde{\boldsymbol{\Gamma}}^{in}\right) \\ &= \phi_*^{in}\left(\dot{\boldsymbol{\Gamma}}^{e}\right) \; + \; \phi_*^{in}\left(\dot{\boldsymbol{\Gamma}}^{in}\right) \end{aligned} \tag{3.41}$$

where the inelastic rates, $\dot{\boldsymbol{\Gamma}}^{in}$ and $L_v\left(\tilde{\boldsymbol{\Gamma}}^{in}\right)$ are zero for any purely elastic deformation. The Lie derivative of $\boldsymbol{\Gamma}^{*}$ (defined in the reference configuration) is simply its time rate, which is also additively decomposed as

$$L_v\left(\boldsymbol{\Gamma}^{*}\right) = \dot{\boldsymbol{\Gamma}}^{*} = \dot{\hat{\boldsymbol{\Gamma}}}^{*} + \dot{\tilde{\boldsymbol{\Gamma}}}^{*} \tag{3.42}$$

but $\dot{\tilde{\boldsymbol{\Gamma}}}^{*}$ is nonzero, in general, under arbitrary elastic deformation processes.

3.1.8 Summary of Section

The kinematic relationships developed in this section will be used in the following two sections to develop the required scale invariance principles of momentum, energy, and dissipation. These quantities are directly computed from finite simulations of rSVEs in Chapter 4 and used to develop the constitutive framework in Chapter 5. In summary, this section has laid out the kinematics involved with each scale transition. Cases where the second-gradient is absent from the coarse scale expansion, $\mathbf{G} = \mathbf{G}_{in} = \mathbf{0}$, result in a first-order homogenization with the addition of the fluctuation field. For cases where a higher order Taylor series is pursued, considerable additional work will be needed to develop the third gradient and associated terms. It is expected that efforts to this end would be better directed at using other kinematic enrichment schemes, e.g., mesoscale gradients or wavelets.

3.2 Principle of Virtual Velocities

In this section the principle of virtual velocities (PVV) is used to preserve linear and angular momentum in the transition between fine and coarse scales.

3.2.1 Linear Momentum

At the fine scale of observation, for a classical Cauchy continuum, the strong form of the linear balance of momentum expressed with respect to the reference configuration is

$$\vec{\nabla}_{\mathrm{o}} \cdot \mathbf{p} + \rho_{\mathrm{o}} \mathbf{b} = \rho_{\mathrm{o}} \frac{d\mathbf{v}}{dt} \tag{3.43}$$

Where $\mathbf{p}$ is the fine-scale nominal stress (transpose of the first Piola-Kirchhoff stress), $\mathbf{b}$ is a fine-scale body force, $\mathbf{v}$ is the fine scale velocity, and ρ_{o} is the mass per unit volume in the reference configuration. Note that due to conservation of mass, $\rho d\Omega = \rho_{\mathrm{o}} d\Omega_{\mathrm{o}}$, the relationship between body forces $\rho \mathbf{b} d\Omega = \rho_{\mathrm{o}} \mathbf{b}_{\mathrm{o}} d\Omega_{\mathrm{o}} \Rightarrow \mathbf{b} = \mathbf{b}_{\mathrm{o}}$. Consider cases where (3.43) is true for each location within the fine scale rSVE, i.e. the fine scale can be described as a classical continuum. To develop the weak-form of momentum balance, a weighting function ($\delta\mathbf{v}$) is multiplied by (3.43) and integrated over an arbitrary domain in the reference configuration, i.e.,

$$\int_{\Omega_o} \delta\mathbf{v} \cdot \left(\vec{\nabla}_o \cdot \mathbf{p} + \rho_o \mathbf{b} - \rho_o \frac{d\mathbf{v}}{dt} \right) d\Omega_o = 0 \tag{3.44}$$

Owing to the product rule of differentiation,

$$\vec{\nabla}_o \cdot \left(\delta\mathbf{v} \cdot \mathbf{p}^T \right) = \mathbf{p} : \left(\delta\mathbf{v} \vec{\nabla}_o \right)^T + \delta\mathbf{v} \cdot \left(\vec{\nabla}_o \cdot \mathbf{p} \right) \tag{3.45}$$

which upon substitution into (3.44) gives

$$\int_{\Omega_o} \vec{\nabla}_o \cdot \left(\delta\mathbf{v} \cdot \mathbf{p}^T \right) - \mathbf{p} : \left(\delta\mathbf{v} \vec{\nabla}_o \right)^T d\Omega_o = \int_{\Omega_o} \rho_o \delta\mathbf{v} \cdot \frac{d\mathbf{v}}{dt} d\Omega_o - \int_{\Omega_o} \rho_o \delta\mathbf{v} \cdot \mathbf{b}_o \, d\Omega_o \tag{3.46}$$

Employing the divergence theorem to convert the first term in the LHS of (3.46) to an integral over the bounding surface, Γ_o, with outward surface unit normal vector $\mathbf{n}_o$ gives

$$\int_{\Omega_o} \vec{\nabla}_o \cdot \left(\delta\mathbf{v} \cdot \mathbf{p}^T \right) d\Omega_o = \int_{\Gamma_o} \left(\mathbf{p}^T \cdot \mathbf{n}_o \right) \cdot \delta\mathbf{v} \, d\Gamma_o = \int_{\Gamma_o} \mathbf{t}_o \cdot \delta\mathbf{v} \, d\Gamma_o \tag{3.47}$$

where $\mathbf{t}_o$ is a surface traction defined in the reference configuration and according to Cauchy's law $\mathbf{t}_o = \mathbf{n}_o \cdot \mathbf{p}$. Finally, the weakened form of (3.43) is obtained by substitution of (3.47) into (3.46):

$$\int_{\Gamma_o} \mathbf{t}_o \cdot \delta\mathbf{v} \, d\Gamma_o + \int_{\Omega_o} \rho_o \mathbf{b} \cdot \delta\mathbf{v} \, d\Omega_o = \int_{\Omega_o} \mathbf{p} : \left(\delta\mathbf{v} \vec{\nabla}_o \right)^T d\Omega_o + \int_{\Omega_o} \rho_o \delta\mathbf{v} \cdot \frac{d\mathbf{v}}{dt} d\Omega_o \tag{3.48}$$

If $\delta\mathbf{v}$ is prescribed as any kinematically admissible velocity field, equation (3.48) is the Principle of Virtual Velocities (PVV) applicable at any scale for a Cauchy continuum over any arbitrary domain Ω_o in the reference configuration bounded by the surface Γ_o.

Application of (3.48) to the rSVE provides a relationship between the local balance of momentum at the coarse scale and weak momentum balance at the fine scale, i.e.,

$$\delta P_{int}(\mathbf{x}_o) + \delta P_{kin}(\mathbf{x}_o) = \delta P_{ext}^t(\mathbf{x}_o) + \delta P_{ext}^b(\mathbf{x}_o) \tag{3.49}$$

where terms comprising coarse scale internal, kinetic, and external virtual power, respectively, are defined as

$$\delta P_{int}(\mathbf{x}_o) = \frac{1}{\Omega_o^x} \int_{\Omega_o^x} \mathbf{p} : \delta\dot{\mathbf{f}}^T d\Omega_o \tag{3.50}$$

$$\delta P_{kin}(\mathbf{x}_{\mathrm{o}}) = \frac{1}{\Omega_{\mathrm{o}}^{\mathrm{x}}} \int_{\Omega_{\mathrm{o}}^{\mathrm{x}}} \rho_{\mathrm{o}} \delta \mathbf{v} \cdot \frac{d\mathbf{v}}{dt} d\Omega_{\mathrm{o}} \tag{3.51}$$

$$\delta P_{ext}(\mathbf{x}_{\mathrm{o}}) = \frac{1}{\Omega_{\mathrm{o}}^{\mathrm{x}}} \int_{\Gamma_{\mathrm{o}}^{\mathrm{x}}} \mathbf{t}_{\mathrm{o}} \cdot \delta \mathbf{v} \, d\Gamma_{\mathrm{o}} + \frac{1}{\Omega_{\mathrm{o}}^{\mathrm{x}}} \int_{\Omega_{\mathrm{o}}^{\mathrm{x}}} \rho_{\mathrm{o}} \mathbf{b} \cdot \delta \mathbf{v} \, d\Omega_{\mathrm{o}} \tag{3.52}$$

The connection between coarse and fine scales is completed by substitution of any kinematically admissible fine scale velocity field into Eqs. (3.50)-(3.52). The set of kinematically admissible fine scale velocity fields consistent with rSVE boundary conditions is

$$\begin{aligned} \delta \mathbf{v} &= \delta \dot{\mathbf{F}} \cdot \mathbf{y}_{\mathrm{o}} + \tfrac{1}{2} \delta \dot{\mathbf{G}} : \mathbf{y}_{\mathrm{o}} \otimes \mathbf{y}_{\mathrm{o}} + \delta \dot{\mathbf{h}} \\ \delta \dot{\mathbf{f}} &= \delta \dot{\mathbf{F}} + \delta \dot{\mathbf{G}} \cdot \mathbf{y}_{\mathrm{o}} + \delta \dot{\mathbf{h}} \bar{\nabla}_{\mathrm{o}} \end{aligned} \tag{3.53}$$

subject to requirements in Eqs. (3.14), and (3.17)-(3.19).

After substitution of (3.53) into virtual power terms, the internal stress power within the rSVE associated with the material point $\mathbf{x}_{\mathrm{o}}$ is

$$\begin{aligned} \delta P_{int}(\mathbf{x}_{\mathrm{o}}) = \frac{1}{\Omega_{\mathrm{o}}^{\mathrm{x}}} \int_{\Omega_{\mathrm{o}}^{\mathrm{x}}} \mathbf{p} \, d\Omega_{\mathrm{o}} : \delta \dot{\mathbf{F}}^{T} + \frac{1}{\Omega_{\mathrm{o}}^{\mathrm{x}}} \int_{\Omega_{\mathrm{o}}^{\mathrm{x}}} \mathbf{p}^{T} \otimes \mathbf{y}_{\mathrm{o}} d\Omega_{\mathrm{o}} \vdots \delta \dot{\mathbf{G}} \\ + \frac{1}{\Omega_{\mathrm{o}}^{\mathrm{x}}} \int_{\Omega_{\mathrm{o}}^{\mathrm{x}}} \mathbf{p} : \delta (\dot{\mathbf{h}} \bar{\nabla}_{\mathrm{o}})^{T} \, d\Omega_{\mathrm{o}} \end{aligned} , \tag{3.54}$$

the external power due to tractions is

$$\begin{aligned} \delta P_{ext}^{t}(\mathbf{x}_{\mathrm{o}}) = \frac{1}{\Omega_{\mathrm{o}}^{\mathrm{x}}} \int_{\Gamma_{\mathrm{o}}^{\mathrm{x}}} \mathbf{t}_{\mathrm{o}} \otimes \mathbf{y}_{\mathrm{o}} \, d\Gamma_{\mathrm{o}} : \delta \dot{\mathbf{F}} + \frac{1}{2\Omega_{\mathrm{o}}^{\mathrm{x}}} \int_{\Gamma_{\mathrm{o}}^{\mathrm{x}}} \mathbf{t}_{\mathrm{o}} \otimes \mathbf{y}_{\mathrm{o}} \otimes \mathbf{y}_{\mathrm{o}} \, d\Gamma_{\mathrm{o}} \vdots \delta \dot{\mathbf{G}} \\ + \frac{1}{\Omega_{\mathrm{o}}^{\mathrm{x}}} \int_{\Gamma_{\mathrm{o}}^{\mathrm{x}}} \mathbf{t}_{\mathrm{o}} \cdot \delta \dot{\mathbf{h}} \, d\Gamma_{\mathrm{o}} \end{aligned} , \tag{3.55}$$

the external power attributed to the distribution of fine scale body forces

$$\begin{aligned} \delta P_{ext}^{b}(\mathbf{x}_{\mathrm{o}}) = \frac{1}{\Omega_{\mathrm{o}}^{\mathrm{x}}} \int_{\Omega_{\mathrm{o}}^{\mathrm{x}}} \rho_{\mathrm{o}} \mathbf{b} \otimes \mathbf{y}_{\mathrm{o}} \, d\Omega_{\mathrm{o}} : \delta \dot{\mathbf{F}} + \frac{1}{2\Omega_{\mathrm{o}}^{\mathrm{x}}} \int_{\Omega_{\mathrm{o}}^{\mathrm{x}}} \rho_{\mathrm{o}} \mathbf{b} \otimes \mathbf{y}_{\mathrm{o}} \otimes \mathbf{y}_{\mathrm{o}} \, d\Omega_{\mathrm{o}} \vdots \delta \dot{\mathbf{G}} \\ + \frac{1}{\Omega_{\mathrm{o}}^{\mathrm{x}}} \int_{\Omega_{\mathrm{o}}^{\mathrm{x}}} \rho_{\mathrm{o}} \mathbf{b} \cdot \delta \dot{\mathbf{h}} \, d\Omega_{\mathrm{o}} \end{aligned} \tag{3.56}$$

and finally the internal power due to distributions of microinertia

$$\begin{aligned}\delta P_{kin}(\mathbf{x}_{\mathrm{o}}) = \frac{1}{\Omega_{\mathrm{o}}^{\mathrm{x}}}\int_{\Omega_{\mathrm{o}}^{\mathrm{x}}} \rho_{\mathrm{o}}\mathbf{a}\otimes\mathbf{y}_{\mathrm{o}} d\Omega_{\mathrm{o}} : \delta\dot{\mathbf{F}} \\ + \frac{1}{2\Omega_{\mathrm{o}}^{\mathrm{x}}}\int_{\Omega_{\mathrm{o}}^{\mathrm{x}}} \rho_{\mathrm{o}}\mathbf{a}\otimes\mathbf{y}_{\mathrm{o}}\otimes\mathbf{y}_{\mathrm{o}} d\Omega_{\mathrm{o}} \vdots \delta\dot{\mathbf{G}} + \frac{1}{\Omega_{\mathrm{o}}^{\mathrm{x}}}\int_{\Omega_{\mathrm{o}}^{\mathrm{x}}} \rho_{\mathrm{o}}\mathbf{a}\cdot\delta\dot{\mathbf{h}} d\Omega_{\mathrm{o}}\end{aligned} \tag{3.57}$$

where $\mathbf{a} = \dfrac{d\mathbf{v}}{dt}$ is the actual fine scale acceleration field. For independent and arbitrary virtual quantities $\delta\dot{\mathbf{F}}$, $\delta\dot{\mathbf{G}}$, and $\delta\dot{\mathbf{h}}$, the combination of (3.54)-(3.57) and (3.49) provide the relationships

$$\begin{aligned}\frac{1}{\Omega_{\mathrm{o}}^{\mathrm{x}}}\int_{\Gamma_{\mathrm{o}}^{\mathrm{x}}} \mathbf{t}_{\mathrm{o}}\otimes\mathbf{y}_{\mathrm{o}}\, d\Gamma_{\mathrm{o}} + \frac{1}{\Omega_{\mathrm{o}}^{\mathrm{x}}}\int_{\Omega_{\mathrm{o}}^{\mathrm{x}}} \rho_{\mathrm{o}}\mathbf{b}\otimes\mathbf{y}_{\mathrm{o}}\, d\Omega_{\mathrm{o}} \\ = \frac{1}{\Omega_{\mathrm{o}}^{\mathrm{x}}}\int_{\Omega_{\mathrm{o}}^{\mathrm{x}}} \mathbf{p}^{T}\, d\Omega_{\mathrm{o}} + \frac{1}{\Omega_{\mathrm{o}}^{\mathrm{x}}}\int_{\Omega_{\mathrm{o}}^{\mathrm{x}}} \rho_{\mathrm{o}}\mathbf{a}\otimes\mathbf{y}_{\mathrm{o}} d\Omega_{\mathrm{o}}\end{aligned} \tag{3.58}$$

$$\begin{aligned}\frac{1}{2\Omega_{\mathrm{o}}^{\mathrm{x}}}\int_{\Gamma_{\mathrm{o}}^{\mathrm{x}}} \mathbf{t}_{\mathrm{o}}\otimes\mathbf{y}_{\mathrm{o}}\otimes\mathbf{y}_{\mathrm{o}}\, d\Gamma + \frac{1}{2\Omega_{\mathrm{o}}^{\mathrm{x}}}\int_{\Omega_{\mathrm{o}}^{\mathrm{x}}} \rho_{\mathrm{o}}\mathbf{b}\otimes\mathbf{y}_{\mathrm{o}}\otimes\mathbf{y}_{\mathrm{o}}\, d\Omega_{\mathrm{o}} \\ = \frac{1}{\Omega_{\mathrm{o}}^{\mathrm{x}}}\int_{\Omega_{\mathrm{o}}^{\mathrm{x}}} \mathbf{p}^{T}\otimes\mathbf{y}_{\mathrm{o}} d\Omega + \frac{1}{2\Omega_{\mathrm{o}}^{\mathrm{x}}}\int_{\Omega_{\mathrm{o}}^{\mathrm{x}}} \rho_{\mathrm{o}}\mathbf{a}\otimes\mathbf{y}_{\mathrm{o}}\otimes\mathbf{y}_{\mathrm{o}} d\Omega_{\mathrm{o}}\end{aligned} \tag{3.59}$$

$$\begin{aligned}\frac{1}{\Omega_{\mathrm{o}}^{\mathrm{x}}}\int_{\Gamma_{\mathrm{o}}^{\mathrm{x}}} \mathbf{t}_{\mathrm{o}}\cdot\delta\dot{\mathbf{h}}\, d\Gamma_{\mathrm{o}} + \frac{1}{\Omega_{\mathrm{o}}^{\mathrm{x}}}\int_{\Omega_{\mathrm{o}}^{\mathrm{x}}} \rho_{\mathrm{o}}\mathbf{b}\cdot\delta\dot{\mathbf{h}}\, d\Omega_{\mathrm{o}} \\ = \frac{1}{\Omega_{\mathrm{o}}^{\mathrm{x}}}\int_{\Omega_{\mathrm{o}}^{\mathrm{x}}} \mathbf{p} : \delta(\dot{\mathbf{h}}\bar{\nabla}_{\mathrm{o}})^{T} d\Omega_{\mathrm{o}} + \frac{1}{\Omega_{\mathrm{o}}^{\mathrm{x}}}\int_{\Omega_{\mathrm{o}}^{\mathrm{x}}} \rho_{\mathrm{o}}\mathbf{a}\cdot\delta\dot{\mathbf{h}} d\Omega_{\mathrm{o}}\end{aligned} \tag{3.60}$$

Under equilibrium, $\mathbf{a} = \mathbf{0}$, and in the absence of body forces, $\mathbf{b} = \mathbf{0}$, a second gradient extension of the Hill-Mandel condition is (cf. Fleck and Hutchinson, 1997; Kouznetsova et al., 2002; Larsson and Diebels, 2007)

$$\delta P_{int}(\mathbf{x}_{\mathrm{o}}) = \mathbf{P} : \delta\dot{\mathbf{F}}^{T} + \mathbf{Q}\vdots\delta\dot{\mathbf{G}} \tag{3.61}$$

which states that for any kinematically admissible set of virtual velocities consistent with prescribed boundary conditions, the actual coarse scale stresses are work conjugates to the corresponding virtual velocities that give an equivalent virtual power at coarse and fine scales of representation. Thus, from equation (3.61), (3.54), and (3.58)-(3.59), in the absence of fine scale inertia and body forces, one can readily identify the proper definition of coarse scale stresses, i.e.,

$$\begin{aligned}\mathbf{P} &= \frac{1}{\Omega_{\mathrm{o}}^{\mathrm{x}}}\int_{\Gamma_{\mathrm{o}}^{\mathrm{x}}} \mathbf{y}_{\mathrm{o}}\otimes\mathbf{t}_{\mathrm{o}}\, d\Gamma_{\mathrm{o}} &&= \frac{1}{\Omega_{\mathrm{o}}^{\mathrm{x}}}\int_{\Omega_{\mathrm{o}}^{\mathrm{x}}} \mathbf{p}\, d\Omega_{\mathrm{o}} \\ \mathbf{Q} &= \frac{1}{2\Omega_{\mathrm{o}}^{\mathrm{x}}}\int_{\Gamma_{\mathrm{o}}^{\mathrm{x}}} \mathbf{t}_{\mathrm{o}}\otimes\mathbf{y}_{\mathrm{o}}\otimes\mathbf{y}_{\mathrm{o}}\, d\Gamma_{\mathrm{o}} &&= \frac{1}{\Omega_{\mathrm{o}}^{\mathrm{x}}}\mathrm{symR}\left(\int_{\Omega_{\mathrm{o}}^{\mathrm{x}}} \mathbf{p}^{T}\otimes\mathbf{y}_{\mathrm{o}} d\Omega_{\mathrm{o}}\right)\end{aligned} \tag{3.62}$$

Note that the top equation in (3.62) provides a relationship between surface tractions on the boundary of an rSVE (or any body) and the volume-averaged nominal stress as developed by Hill (1972) under equilibrium conditions *and* in the absence of external body forces. The bottom equation in (3.62) is a direct analog for second order stresses. Because the second gradient is symmetric in the last two indices, it is only that part of the volume integral in the right side of the bottom equation in (3.62) symmetric in the second and third indices that contributes to the second order stress. Note, that (3.60) and (3.61) *require* that

$$\frac{1}{\Omega_{\mathrm{o}}^{\mathrm{x}}}\int_{\Gamma_{\mathrm{o}}^{\mathrm{x}}} \mathbf{t}_{\mathrm{o}} \cdot \delta\dot{\mathbf{h}}\, d\Gamma_{\mathrm{o}} = \frac{1}{\Omega_{\mathrm{o}}^{\mathrm{x}}}\int_{\Omega_{\mathrm{o}}^{\mathrm{x}}} \mathbf{p} : \delta(\dot{\mathbf{h}}\tilde{\nabla}_{\mathrm{o}})^{T}\, d\Omega_{\mathrm{o}} = 0 \tag{3.63}$$

Condition (3.63) is a manifestation of the Hill-Mandel condition, namely, that no work is done by tractions external to the rSVE on the fluctuation field. Conceptual implications of this requirement are noteworthy. It is a consequence of balance of momentum *within* the fine scale rSVE that the boundary integral of work done by tractions on velocity fluctuations is equal to the volume integral of work done by local stresses on the fluctuation gradients. The internal fluctuation power requirement arises due to balance of momentum *between* scales, i.e., scale invariance of momentum, because the transition from fine to coarse scale relinquishes the precise identification of the fine scale degrees of freedom. Conceptually, this requirement asserts that a particular fine scale rSVE associated with a coarse scale material point may exchange momentum with another fine scale rSVE associated with a neighboring coarse scale material point, *only* through the coarse scale kinematic variables, $\mathbf{V}$, $\dot{\mathbf{F}}$,and $\dot{\mathbf{G}}$. This conceptual perspective of the momentum balance within and in between scales is an important aspect of this section. This condition can be proven to be satisfied by the direct, periodic, and minimal boundary conditions introduced in Section 3.1.5.

For dynamic cases and in the presence of externally applied body forces (such as those implied by constraint (3.16)) the definition of coarse scale stresses must be extended. The central issue is whether to maintain that the coarse scale nominal stress is the volume average of the fine scale nominal stress, i.e., $\mathbf{P}' = \frac{1}{\Omega_{\mathrm{o}}^{\mathrm{x}}}\int_{\Omega_{\mathrm{o}}^{\mathrm{x}}} \mathbf{p}\, d\Omega_{\mathrm{o}} = \frac{1}{\Omega_{\mathrm{o}}^{\mathrm{x}}}\int_{\Gamma_{\mathrm{o}}^{\mathrm{x}}} \mathbf{y}_{\mathrm{o}} \otimes \mathbf{t}_{\mathrm{o}}\, d\Gamma - \frac{1}{\Omega_{\mathrm{o}}^{\mathrm{x}}}\int_{\Omega_{\mathrm{o}}^{\mathrm{x}}} \rho_{\mathrm{o}}\mathbf{y}_{\mathrm{o}} \otimes \mathbf{a}\, d\Omega_{\mathrm{o}}$, or to enforce that the coarse scale nominal stress must be conjugate to the time rate of deformation gradient

consistent with (3.61). The former method, $\mathbf{P}'$ implies that any net microinertia is interpreted as an external body force augmenting the local coarse scale momentum equation. This perspective is physically inconsistent for two reasons. First, in laboratory experiments (as discussed in Hill, 1972) one cannot directly measure either the volume average stress or the net microinertia. Thus, if the coarse scale stress is defined as the nominal stress, then the constitutive relations so developed could not be fit to or meaningfully compared against experimental data. The second reason to avoid the former definition of stress is that the resulting 'augmenting body force' cannot be arbitrarily applied (as typically expected for external loads). Rather it will depend upon the coarse scale material response coupled with the fine scale microstructural features which give rise to the heterogeneous inertia distribution. Wang and Sun (2002) used this approach to study the effect of net microinertia on the growth of a single isolated void embedded in a plastic matrix. In their case the 'augmenting body force' could be directly identified by means of micromechanical analysis, however, this approach is not advocated here due to its lack of generality. The basis of the Cauchy definition of stress is a traction vector acting over a (real or fictitious) surface with a particular orientation. This basis reinforces the idea of using tractions applied on the external boundary of the rSVE to define the coarse scale nominal stress. More importantly, the only definition of nominal stress, **P**, and second order stress, **Q**, consistent with the balance of momentum at the fine scale and across scales as expressed by (3.49), (3.54)-(3.57) are

$$\begin{aligned}\mathbf{P} &= \frac{1}{\Omega_{\mathrm{o}}^{\mathrm{x}}}\int_{\Gamma_{\mathrm{o}}^{\mathrm{x}}} \mathbf{y}_{\mathrm{o}} \otimes \mathbf{t}_{\mathrm{o}}\, d\Gamma_{\mathrm{o}} + \frac{1}{\Omega_{\mathrm{o}}^{\mathrm{x}}}\int_{\Omega_{\mathrm{o}}^{\mathrm{x}}} \rho_{\mathrm{o}}\mathbf{y}_{\mathrm{o}} \otimes \mathbf{b}_{\mathrm{o}} d\Omega_{\mathrm{o}} \\ &= \frac{1}{\Omega_{\mathrm{o}}^{\mathrm{x}}}\int_{\Omega_{\mathrm{o}}^{\mathrm{x}}} \mathbf{p}\, d\Omega + \frac{1}{\Omega_{\mathrm{o}}^{\mathrm{x}}}\int_{\Omega_{\mathrm{o}}^{\mathrm{x}}} \rho_{\mathrm{o}}\mathbf{y}_{\mathrm{o}} \otimes \mathbf{a} d\Omega_{\mathrm{o}}\end{aligned} \tag{3.64}$$

and

$$\begin{aligned}\mathbf{Q} &= \frac{1}{2\Omega_{\mathrm{o}}^{\mathrm{x}}}\int_{\Gamma_{\mathrm{o}}^{\mathrm{x}}} \mathbf{t}_{\mathrm{o}} \otimes \mathbf{y}_{\mathrm{o}} \otimes \mathbf{y}_{\mathrm{o}}\, d\Gamma_{\mathrm{o}} + \frac{1}{2\Omega_{\mathrm{o}}^{\mathrm{x}}}\int_{\Omega_{\mathrm{o}}^{\mathrm{x}}} \rho_{\mathrm{o}}\mathbf{b}_{\mathrm{o}} \otimes \mathbf{y}_{\mathrm{o}} \otimes \mathbf{y}_{\mathrm{o}} d\Omega_{\mathrm{o}} \\ &= \frac{1}{\Omega_{\mathrm{o}}^{\mathrm{x}}}\mathrm{sym}_{23}\left(\int_{\Omega_{\mathrm{o}}^{\mathrm{x}}} \mathbf{p}^{T} \otimes \mathbf{y}_{\mathrm{o}} d\Omega_{\mathrm{o}}\right) + \frac{1}{2\Omega_{\mathrm{o}}^{\mathrm{x}}}\int_{\Omega_{\mathrm{o}}^{\mathrm{x}}} \rho_{\mathrm{o}}\mathbf{a} \otimes \mathbf{y}_{\mathrm{o}} \otimes \mathbf{y}_{\mathrm{o}} d\Omega_{\mathrm{o}}\end{aligned} \tag{3.65}$$

respectively. The dynamic Hill-Mandel condition extends to

$$\frac{1}{\Omega_{\mathrm{o}}^{\mathrm{x}}}\int_{\Gamma_{\mathrm{o}}^{\mathrm{x}}}\mathbf{t}_{\mathrm{o}}\cdot\delta\dot{\mathbf{h}}\,d\Gamma_{\mathrm{o}}+\frac{1}{\Omega_{\mathrm{o}}^{\mathrm{x}}}\int_{\Omega_{\mathrm{o}}^{\mathrm{x}}}\rho_{\mathrm{o}}\mathbf{b}\cdot\delta\dot{\mathbf{h}}\,d\Omega_{\mathrm{o}}=$$
$$\frac{1}{\Omega_{\mathrm{o}}^{\mathrm{x}}}\int_{\Omega_{\mathrm{o}}^{\mathrm{x}}}\mathbf{p}:\delta(\dot{\mathbf{h}}\tilde{\nabla})^{T}\,d\Omega_{\mathrm{o}}+\frac{1}{\Omega_{\mathrm{o}}^{\mathrm{x}}}\int_{\Omega_{\mathrm{o}}^{\mathrm{x}}}\rho_{\mathrm{o}}\mathbf{a}\cdot\delta\dot{\mathbf{h}}\,d\Omega_{\mathrm{o}}=0 \tag{3.66}$$

which permits a net internal fluctuation power that is exactly balanced by an opposing net inertial fluctuation. In this dynamic case one can further offer the interpretation that this restriction implies that microfluctuation waves cannot propagate throughout the coarse scale field independent of the coarse scale variables, i.e., the fluctuation field cannot transport momentum out of the rSVE. It can be shown that (3.66) is satisfied under the same conditions as (3.63).

First we consider the body forces introduced by a constraint equation that would be used to enforce Eq. (3.18). As will be shown in Chapter 4, such a constraint equation will be developed by recourse to gauss quadrature to integrate over the domain of the rSVE according to

$$\sum_{el=1}^{N_{el}}\sum_{ip=1}^{N_{ip}} w_{ip}\,N_I\big|_{ip}\,\hat{h}_{Ij}=0 \tag{3.67}$$

where *el* is the element, N_{el} is the total number of elements comprising the rSVE, *ip* is the Gauss quadrature (integration) point, N_{ip} is the number of integration points in element *el*, w_{ip} is the Gauss weight for the *ip* integration point, N_I is the shape function corresponding to node *I* evaluated at the integration point, $\hat{h}_{Ij}$ is the j^{th} component of the nodal fluctuation at *I*. and summation over all nodes associated with element *el* is implied. Since all terms in Eq. (3.67) can be computed prior to conducting fine scale simulations, it can be rewritten as

$$A_I\hat{h}_{Ij}=0 \tag{3.68}$$

where A_I are a set of nodal coefficients reflecting node *I*'s contribution to Gauss integration of a constant over the entire rSVE domain and summation over all nodes in the domain is implied. Such a constraint equation introduces an internal force to the solution of the form

$$f_{Ij}=\frac{A_I}{A_0}f_{0j} \tag{3.69}$$

where A_0 is the coefficient corresponding to the nodal DOF removed from the solution and f_{0j} is the j^{th} component of the force introduced to eliminate that DOF. From Eq. (3.69) it is clear that

the force introduced at each nodal DOF in the constraint Eq. (3.68) is in direct proportion to that nodes coefficient. Since the nodal coefficient reflects the integration of a constant over the associated elements, the internal forces generated by constraint Eq. (3.18) reflect a constant body force field so that we may write

$$\frac{1}{\Omega_{\mathrm{o}}^{\mathrm{x}}}\int_{\Omega_{\mathrm{o}}^{\mathrm{x}}}\rho_{\mathrm{o}}\mathbf{b}\cdot\delta\dot{\mathbf{h}}\,d\Omega_{\mathrm{o}} = \rho_{\mathrm{o}}\mathbf{b}\cdot\frac{1}{\Omega_{\mathrm{o}}^{\mathrm{x}}}\int_{\Omega_{\mathrm{o}}^{\mathrm{x}}}\delta\dot{\mathbf{h}}\,d\Omega_{\mathrm{o}} = 0 \tag{3.70}$$

where the middle part of the equation is obtained because the body force field is constant and the RHS (zero) is due to the constraint Eq. (3.18).

Tractions can be handled in a similar manner. First consider the direct boundary conditions. In this case the fluctuation field must vanish everywhere on the boundary, so $\int_{\Gamma_{\mathrm{o}}^{\mathrm{x}}}\mathbf{t}_{\mathrm{o}}\cdot\delta\dot{\mathbf{h}}\,d\Gamma_{\mathrm{o}} = \mathbf{0}$ trivially, regardless of the distribution of surface tractions. For the periodic and minimal boundary conditions we decompose the surface tractions according to

$$\mathbf{t}_{\mathrm{o}} = {}^{0}\mathbf{t}_{\mathrm{o}} + {}^{1}\mathbf{t}_{\mathrm{o}} + {}^{2}\mathbf{t}_{\mathrm{o}} + \cdots + {}^{N_{ce}}\mathbf{t}_{\mathrm{o}} \tag{3.71}$$

where N_{ce} is the number of constraint equations (in addition to the 0$^{\text{th}}$ constraint equation discussed subsequently) introduced to satisfy fluctuation constraints on the boundary. Of course, the mere definition of the fluctuation field implies a constraint equation to enforce

$$\mathbf{h} = \mathbf{u} - \left(\mathbf{F}-\mathbf{I}\right)\cdot\mathbf{y}_{\mathrm{o}} - \mathbf{G}:\left(\mathbf{y}_{\mathrm{o}}\otimes\mathbf{y}_{\mathrm{o}}\right) \tag{3.72}$$

However, Eq. (3.72) merely redefines a single new fluctuation DOF by eliminating the single corresponding displacement DOF. There is not a force introduced to the rSVE directly on account of Eq. (3.72) so ${}^{0}\mathbf{t}_{\mathrm{o}} = \mathbf{0}$. Note that this result was implicitly used in the body force discussion above. Periodicity constraints involving nodes on opposing boundaries where the boundary with a *positive* unit surface normal is labeled (+) and the boundary with a *negative* unit surface normal is labeled (-) can be written

$$\hat{h}_j^{(+)} - \hat{h}_j^{(-)} = 0 \tag{3.73}$$

Using the same arguments as in (3.69), Eq. (3.73) introduces equal and opposite constraint forces implying a contribution to surface tractions of

$$ {}^{1}\mathbf{t}_{\mathrm{o}}^{(+)}\left(\boldsymbol{\eta}_{\mathrm{o}}\right) = -{}^{1}\mathbf{t}_{\mathrm{o}}^{(-)}\left(\boldsymbol{\eta}_{\mathrm{o}}\right) \tag{3.74} $$

where superscript '1' is in reference to the periodicity constraint. Eq. (3.19) will be implemented via separate constraint equations for each boundary. By the same arguments used in developing Eqs. (3.67)-(3.69) and the ensuing conclusion it is straightforward to recognize that Eq. (3.19) will introduce boundary tractions constant along each boundary, i.e.,

$$ \begin{aligned} {}^{2}\mathbf{t}_{\mathrm{o}}\left(\mathbf{y}_{\mathrm{o}}\right) &= \begin{cases} {}^{2}\overline{\mathbf{t}}_{\mathrm{o}}, \text{ constant } \forall\, \mathbf{y}_{\mathrm{o}} \in \Gamma_{\mathrm{o}}^{A} \\ \mathbf{0} \;\forall\, \mathbf{y}_{\mathrm{o}} \notin \Gamma_{\mathrm{o}}^{A} \end{cases} \\ {}^{3}\mathbf{t}_{\mathrm{o}}\left(\mathbf{y}_{\mathrm{o}}\right) &= \begin{cases} {}^{3}\overline{\mathbf{t}}_{\mathrm{o}}, \text{ constant } \forall\, \mathbf{y}_{\mathrm{o}} \in \Gamma_{\mathrm{o}}^{B} \\ \mathbf{0} \;\forall\, \mathbf{y}_{\mathrm{o}} \notin \Gamma_{\mathrm{o}}^{B} \end{cases} \\ {}^{4}\mathbf{t}_{\mathrm{o}}\left(\mathbf{y}_{\mathrm{o}}\right) &= \begin{cases} {}^{4}\overline{\mathbf{t}}_{\mathrm{o}}, \text{ constant } \forall\, \mathbf{y}_{\mathrm{o}} \in \Gamma_{\mathrm{o}}^{C} \\ \mathbf{0} \;\forall\, \mathbf{y}_{\mathrm{o}} \notin \Gamma_{\mathrm{o}}^{C} \end{cases} \\ {}^{5}\mathbf{t}_{\mathrm{o}}\left(\mathbf{y}_{\mathrm{o}}\right) &= \begin{cases} {}^{5}\overline{\mathbf{t}}_{\mathrm{o}}, \text{ constant } \forall\, \mathbf{y}_{\mathrm{o}} \in \Gamma_{\mathrm{o}}^{D} \\ \mathbf{0} \;\forall\, \mathbf{y}_{\mathrm{o}} \notin \Gamma_{\mathrm{o}}^{D} \end{cases} \end{aligned} \tag{3.75} $$

for a 2D rSVE (cf. Figure 29 in Chapter 4) and the results can be easily extended to 3D. Now, $\int_{\Gamma_{\mathrm{o}}^{\mathrm{x}}} \mathbf{t}_{\mathrm{o}} \cdot \delta\dot{\mathbf{h}}\, d\Gamma_{\mathrm{o}}$ can be written as

$$ \begin{aligned} &\int_{\Gamma_{\mathrm{o}}^{\mathrm{x}}} {}^{1}\mathbf{t}_{\mathrm{o}} \cdot \delta\dot{\mathbf{h}}\, d\Gamma_{\mathrm{o}} + \\ &\int_{\Gamma_{\mathrm{o}}^{A}} {}^{2}\overline{\mathbf{t}}_{\mathrm{o}} \cdot \delta\dot{\mathbf{h}}\, d\Gamma_{\mathrm{o}} + \int_{\Gamma_{\mathrm{o}}^{B}} {}^{3}\overline{\mathbf{t}}_{\mathrm{o}} \cdot \delta\dot{\mathbf{h}}\, d\Gamma_{\mathrm{o}} + \\ &\int_{\Gamma_{\mathrm{o}}^{C}} {}^{4}\overline{\mathbf{t}}_{\mathrm{o}} \cdot \delta\dot{\mathbf{h}}\, d\Gamma_{\mathrm{o}} + \int_{\Gamma_{\mathrm{o}}^{D}} {}^{5}\overline{\mathbf{t}}_{\mathrm{o}} \cdot \delta\dot{\mathbf{h}}\, d\Gamma_{\mathrm{o}} = \\ &\int_{\Gamma_{\mathrm{o}}^{\mathrm{x}}} {}^{1}\mathbf{t}_{\mathrm{o}} \cdot \delta\dot{\mathbf{h}}\, d\Gamma_{\mathrm{o}} + \\ &{}^{2}\overline{\mathbf{t}}_{\mathrm{o}} \int_{\Gamma_{\mathrm{o}}^{A}} \delta\dot{\mathbf{h}}\, d\Gamma_{\mathrm{o}} + {}^{3}\overline{\mathbf{t}}_{\mathrm{o}} \int_{\Gamma_{\mathrm{o}}^{B}} \delta\dot{\mathbf{h}}\, d\Gamma_{\mathrm{o}} + \\ &{}^{4}\overline{\mathbf{t}}_{\mathrm{o}} \int_{\Gamma_{\mathrm{o}}^{C}} \delta\dot{\mathbf{h}}\, d\Gamma_{\mathrm{o}} + {}^{5}\overline{\mathbf{t}}_{\mathrm{o}} \int_{\Gamma_{\mathrm{o}}^{D}} \delta\dot{\mathbf{h}}\, d\Gamma_{\mathrm{o}} = \int_{\Gamma_{\mathrm{o}}^{\mathrm{x}}} {}^{1}\mathbf{t}_{\mathrm{o}} \cdot \delta\dot{\mathbf{h}}\, d\Gamma_{\mathrm{o}} \end{aligned} \tag{3.76} $$

where advantage was taken of the constant components of traction (2-5) by moving them outside their respective integrals. Finally, Eqs. (3.73) and (3.74) permit

$$\begin{aligned}\int_{\Gamma_o^x} {}^1\mathbf{t}_o \cdot \delta\dot{\mathbf{h}}\, d\Gamma_o &= \int_{\Gamma_o^{(+)}} {}^1\mathbf{t}_o^{(+)} \cdot \delta\dot{\mathbf{h}}^{(+)}\, d\Gamma_o + \int_{\Gamma_o^{(-)}} {}^1\mathbf{t}_o^{(-)} \cdot \delta\dot{\mathbf{h}}^{(-)}\, d\Gamma_o \\ &= \int_{\Gamma_o^{(+)}} \left({}^1\mathbf{t}_o^{(+)} + {}^1\mathbf{t}_o^{(-)} \right) \cdot \delta\dot{\mathbf{h}}^{(+)}\, d\Gamma_o \\ &= \int_{\Gamma_o^{(+)}} \left({}^1\mathbf{t}_o^{(+)} - {}^1\mathbf{t}_o^{(+)} \right) \cdot \delta\dot{\mathbf{h}}^{(+)}\, d\Gamma_o = 0\end{aligned} \tag{3.77}$$

so that, collectively, Eqs. (3.76) and (3.77) establish that $\int_{\Gamma_o^x} \mathbf{t}_o \cdot \delta\dot{\mathbf{h}}\, d\Gamma_o = 0$. Eq. (3.75) pertains to the minimal constraints also. In the case of minimal constraints, the periodic constraints are omitted, however a new set of constraints will be employed to enforce the independent vanishing moment of fluctuation along each boundary. The arguments made in developing Eqs. (3.67)-(3.69) are extended to the implementation of constraint Eq. (3.17). By inspection (and previous arguments) this case will result in a linearly varying traction introduced along each boundary. The tractions due to constraint Eq. (3.17) along a single boundary (labeled 'A') of the rSVE can be written as

$${}^{1,A}\mathbf{t}_o = {}^{1,A}\overline{\mathbf{t}}_o + {}^{1,A}\overline{\overline{\mathbf{t}}}_o \cdot \boldsymbol{\eta} \tag{3.78}$$

Along this boundary,

$$\begin{aligned}\int_{\Gamma_o^A} {}^1\mathbf{t}_o \cdot \delta\dot{\mathbf{h}}\, d\Gamma_o &= \int_{\Gamma_o^A} {}^{1,A}\mathbf{t}_o \cdot \delta\dot{\mathbf{h}}\, d\Gamma_o \\ &= {}^{1,A}\overline{\mathbf{t}}_o \cdot \int_{\Gamma_o^A} \delta\dot{\mathbf{h}}\, d\Gamma_o + {}^{1,A}\overline{\overline{\mathbf{t}}}_o \int_{\Gamma_o^A} \delta\dot{\mathbf{h}} \otimes \boldsymbol{\eta}\, d\Gamma_o\end{aligned} \tag{3.79}$$

According to Eq. (3.19), $\int_{\Gamma_o^A} \delta\dot{\mathbf{h}}\, d\Gamma_o = \mathbf{0}$. If we also *require* that $\int_{\Gamma_o^A} \delta\dot{\mathbf{h}} \otimes \boldsymbol{\eta}\, d\Gamma_o = \mathbf{0}$ independently for *each* boundary (this is stronger than Eq. (3.17) demands) then Eq. (3.79) becomes

$$\int_{\Gamma_o^A} {}^1\mathbf{t}_o \cdot \delta\dot{\mathbf{h}}\, d\Gamma_o = 0 \tag{3.80}$$

Repeating these steps for each boundary we find that $\int_{\Gamma_o^x} \mathbf{t}_o \cdot \delta\dot{\mathbf{h}}\, d\Gamma_o = 0$ is true for minimal conditions if $\int_{\Gamma_o^i} \delta\dot{\mathbf{h}} \otimes \boldsymbol{\eta}\, d\Gamma_o = \mathbf{0}$ is enforced for each boundary independently.

Attention is now returned to the presence of body forces in the coarse scale stress expression. For comparison to the aforementioned work of Wang and Sun (2002) see Molinari and Mercier

(2001) who use a Cauchy stress implementation of Eq. (3.64) in the *absence* of body forces to assess the constraining effect of microinertia on dynamic void growth in plastic matrix material. Neither of these two approaches is in total agreement with what is presented here, for reasons discussed below.

Clayton and McDowell (2004) show that under cases of equilibrium the nominal stress defined from boundary tractions as in the left equality of the top equation in (3.62) accurately captures the effect of external tractions acting on internal surfaces, for example cohesive tractions acting on newly opened cracks, while a direct volume average of stress does not. Clayton (2005) extends this concept to dynamic cases for analysis of polycrystalline tungsten rSVEs in a manner that is precisely consistent with (3.64) in the *absence* of body forces. Specifically, he shows

$$\begin{aligned}\mathbf{P} = \frac{1}{\Omega_{\mathrm{o}}^{\mathrm{x}}}\int_{\Gamma_{\mathrm{o}}^{\mathrm{x}}} \mathbf{y}_{\mathrm{o}} \otimes \mathbf{t}_{\mathrm{o}}\, d\Gamma_{\mathrm{o}} &= \frac{1}{\Omega_{\mathrm{o}}^{\mathrm{x}}}\int_{\Omega_{\mathrm{o}}^{\mathrm{x}}} \mathbf{p}\, d\Omega_{\mathrm{o}} + \frac{1}{\Omega_{\mathrm{o}}^{\mathrm{x}}}\sum_{k}\int_{\Gamma_{\mathrm{o}}^{(k)}} \mathbf{y}_{\mathrm{o}}^{(k)} \otimes \mathbf{t}_{\mathrm{o}}{}^{(k)}\, d\Gamma_{\mathrm{o}} \\ &+ \frac{1}{\Omega_{\mathrm{o}}^{\mathrm{x}}}\int_{\Omega_{\mathrm{o}}^{\mathrm{x}}} \rho_{\mathrm{o}}\mathbf{y}_{\mathrm{o}} \otimes \mathbf{a}\, d\Omega_{\mathrm{o}}\end{aligned} \tag{3.81}$$

where the summation is over all newly opening crack surfaces $\Gamma_{\mathrm{o}}^{(k)}$ within the rSVE, and it is implied that the tractions are internal in the sense that they arise due to the local response of the material rather than by some external means, e.g., fluid pressure. As will be explained subsequently, the approach specified in Clayton (2005, 2006) is *not* consistent with that developed in this section in the *presence* of externally applied body forces (cf. Clayton, 2006, Eq. 10). The distinction bears no consequence on that particular work, as body forces were not introduced during those computations; however, body forces are *implied* by the kinematic constraints (3.18) introduced in this work and must be addressed. Unfortunately, inclusion of fine scale body forces "muddies the water" to some extent and requires careful analysis to maintain physical consistency. What follows is conceptually consistent with the recognition that the body forces are applied externally, as are external tractions, and are not a microstructure response, such as local stress and inertia. Accordingly, the only means of incorporating body forces in a manner consistent with the balance of momentum at the fine scale that respects scale invariance of momentum is as written in Eqs. (3.64) and (3.65).

A pedagogical example is presented to reinforce the treatment of body forces in Eqs. (3.64) and (3.65). Consider a thin disc of homogeneous material, free of any external tractions and at rest in equilibrium with radial body forces as indicated in Figure 8. For example, this scenario might be realized under a magnetic field. In a polar coordinate system the applicable part of fine scale momentum balance equation (3.43) is $\frac{\partial \sigma_r}{\partial r} + \frac{\sigma_r - \sigma_\theta}{r} + B_o r = 0$. The non-zero components of strain are $\varepsilon_r = \frac{\partial u_r}{\partial r}$, $\varepsilon_\theta = \frac{u}{r}$, and $\varepsilon_z = \frac{\partial u_z}{\partial z}$. Small strain, plane stress, and isotropic linear elastic response are assumed; thus, the local constitutive equations are $\sigma_r = \left(\frac{E}{1-\nu^2}\right)\left(\varepsilon_r + \nu\varepsilon_\theta\right)$, $\sigma_\theta = \left(\frac{E}{1-\nu^2}\right)\left(\varepsilon_\theta + \nu\varepsilon_r\right)$, and $\sigma_z = 0$.

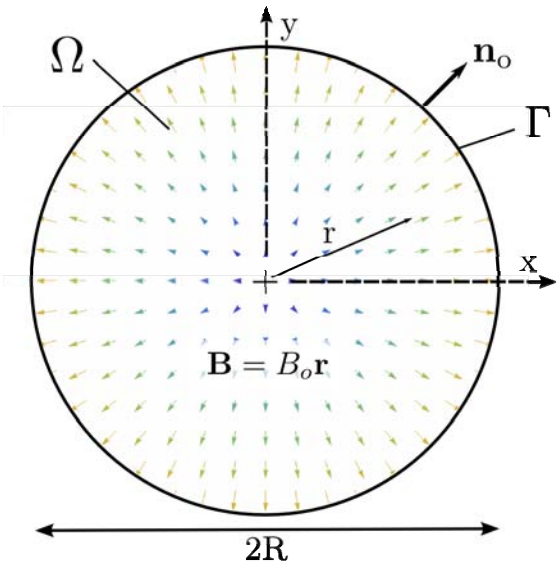

Figure 8. Thin disc exposed to a radial body force field.

Expressed in polar coordinates, the solutions for radial displacement and normal stresses are

$$\begin{aligned} u_r(r) &= \frac{B_o}{8}\left(\frac{1-\nu^2}{E}\right)\left(\left(\frac{3+\nu}{1+\nu}\right)R^2 r - r^3\right) \\ \sigma_r(r) &= \frac{B_o}{8}(3+\nu)(R^2 - r^2) \\ \sigma_\theta(r) &= \frac{B_o}{8}\Big(R^2(3+\nu) - r^2(1+3\nu)\Big) \end{aligned} \tag{3.82}$$

which can be compared to solutions for the classic spinning disc problem. In order to demonstrate that the macroscale stress should be computed from the distribution of body forces as expressed in the middle equation of (3.64), the proposed homogenization procedures are now applied to this disc specimen resulting in the expected macroscopic stress versus macroscopic strain relationship. Because the material is homogenous within the disc and the macroscopic response is purely dilatational, we expect to recover a volumetric stress strain relationship that preserves the fine scale elastic constants, i.e., $K_{coarse} = K_{fine} = \dfrac{E}{3(1-2\nu)}$.

The displacement solution is expressed in Cartesian coordinates,

$$\begin{aligned} u_x &= \left(\frac{1-\nu^2}{E}\right)\frac{B_o}{8}\left(\left(\frac{3+\nu}{1+\nu}\right)R^2 - x^3 - xy^2\right) \\ u_y &= \left(\frac{1-\nu^2}{E}\right)\frac{B_o}{8}\left(\left(\frac{3+\nu}{1+\nu}\right)R^2 - y^3 - x^2 y\right) \end{aligned} \tag{3.83}$$

from which the small strains are computed in Cartesian coordinates

$$\begin{aligned} \varepsilon_{11} &= \left(\frac{1-\nu^2}{E}\right)\frac{B_o}{8}\left(\left(\frac{3+\nu}{1+\nu}\right)R^2 - 3x^2 - y^2\right) \\ \varepsilon_{22} &= \left(\frac{1-\nu^2}{E}\right)\frac{B_o}{8}\left(\left(\frac{3+\nu}{1+\nu}\right)R^2 - 3y^2 - x^2\right) \\ \varepsilon_{12} &= -\left(\frac{1-\nu^2}{E}\right)\frac{B_o}{4}xy \end{aligned} \tag{3.84}$$

The coarse scale or macroscopic deformation can be obtained by finding the volume average of local strain (3.84) or by computing the deformation gradient from the values of displacement on the boundary, i.e. $F_{ij} = \frac{1}{\Omega_o}\int_{\Gamma_o}(x_i + u_i)n_j^o \, d\Gamma_o$. In both cases, the non-zero components of effective coarse scale small strain are found to be

$$\left\langle \varepsilon_{11} \right\rangle = \left\langle \varepsilon_{22} \right\rangle = \frac{B_o R^2}{4}\frac{(1-\nu)}{E}$$
$$\left\langle \varepsilon_{33} \right\rangle = -\frac{B_o R^2}{2}\frac{\nu}{E} \tag{3.85}$$

From the middle equation in (3.64) the non-zero components of coarse scale nominal stress (equivalent to Cauchy stress for infinitesimal strain) are computed as

$$P_{11} = P_{22} = \frac{B_o R^2}{4} \tag{3.86}$$

Finally the "homogenized" coarse scale bulk modulus is determined by dividing the coarse scale pressure by the coarse scale volumetric strain,

$$K_{coarse} = \frac{\frac{1}{3}(P_{11} + P_{22})}{\left\langle \varepsilon_{11} \right\rangle + \left\langle \varepsilon_{22} \right\rangle + \left\langle \varepsilon_{33} \right\rangle} = \frac{E}{3(1-2\nu)} = K_{fine} \tag{3.87}$$

which is precisely equivalent to the fine scale bulk modulus as expected. This simple example illustrates how the fine scale distribution of externally applied body forces contribute to the coarse scale stress which is work conjugate to the coarse scale deformation. If the distribution of body forces were moved to the RHS of equations (3.64) such that the coarse scale stress were computed solely from external tractions, then the coarse scale stress in this case would be zero and would not accurately reflect the work done on the disc. Note also that in this example the volume average of the body force is zero. Applying body forces to a lab specimen is typically not an efficient means to ascertain stress-strain relationships; however, it will be shown in Chapter 4 that such body forces arise due to internal constraints on the fluctuation field and are implicit in the rSVE solution for nonzero second gradient, **G**. In these cases the applied body forces must be accounted for properly when computing the coarse scale stress in order to ensure scale invariance of momentum.

3.2.2 Role of Body Force Field in Establishing Uniform Fine Scale Second Gradient

In this subsection it is demonstrated that an external body force field is required to develop a uniform second gradient within a rSVE of homogenous material. This is important because it implies that a fine scale simulation of an rSVE with second gradient boundary conditions that

omit the internal fluctuation constraint of Eq. (3.18) will cause unrealistic local distributions of gradients unless body forces are applied to support the deformation. The concept generalizes equally to the heterogeneous response of a fine scale rSVE. Physically, this requirement manifests itself as a strong and localized "tweaking" of corners and "sagging" of boundaries of the rSVE for the generalized periodic boundary conditions in the absence of a augmenting body force field.

In what follows the term "rSVE" is applied to a pure homogenous material in order to make a conceptual connection even though the example would not necessitate an rSVE nor multiscale approach. Consider an rSVE of homogenous material comprising a square in 2D with sides of length L. Here it is assumed that the displacements are infinitesimal such that there is no difference between reference and current configurations. The material obeys isotropic linear elasticity everywhere within the rSVE, i.e. $\sigma_{ij} = \lambda\,\varepsilon_{kk}\delta_{ij} + 2\mu\,\varepsilon_{ij}$, where $\lambda = \frac{\nu E}{(1-2\nu)(1+\nu)}$ is Lame's elastic constant and μ is the elastic shear modulus. The strong form of momentum balance within the rSVE is satisfied if, under equilibrium, $\vec{\nabla}\cdot\boldsymbol{\sigma} + \rho\mathbf{b} = 0$. Substitution of the local fine scale constitutive law into momentum balance equation yields $\frac{\partial\sigma_{ij}}{\partial y_i} = \lambda\frac{\partial\varepsilon_{kk}}{\partial y_j} + 2\mu\frac{\partial\varepsilon_{ij}}{\partial y_i} = -\rho b_j$. A uniform second gradient deformation field is obtained if the gradients of strain are constant within the rSVE, in particular recall from section 3.1 $\frac{\partial\varepsilon_{ij}}{\partial y_k} = \frac{1}{2}(G_{ijk} + G_{jik})$. Solving for the required external augmenting body force,

$$-\rho b_j = \lambda G_{kkj} + \mu(G_{iji} + G_{jii}) \tag{3.88}$$

Recognize that the total body force is assumed to be the combination of any external body force and the additional augmenting body force of Eq. (3.88). In practice, only the augmenting body force is used for a fine scale rSVE simulation. That is, external body forces other than the augmenting body force of Eq. (3.88) are not typically considered in this multiscale framework. Also, Eq. (3.88) has no further utility at higher scales in that the augmenting body force contributes to coarse scale stresses and, therefore, does not need to be explicitly introduced to coarse scale simulations. It is instructive to identify those conditions for which a uniform second

gradient will exist in the absence of any external body force. Setting the left side of (3.88) to zero, requiring planar deformation ($G_{ij3} = G_{i3k} = G_{3jk} = 0$), and recognizing the symmetry of the second gradient results in the following independent hypersurfaces in two separate subspaces of the second gradient components

$$\begin{aligned} \lambda(G_{111} + G_{221}) + \mu(2G_{111} + G_{221} + G_{122}) = 0 \\ \lambda(G_{121} + G_{222}) + \mu(2G_{222} + G_{121} + G_{211}) = 0 \end{aligned} \tag{3.89}$$

There are only two independent modes of deformation for a homogenous 2D rSVE consistent with a uniform second gradient. Each of these hypersurfaces spans a particular subspace of second-gradient components associated with a generalized bending along a particular axis. If we substitute a constant material curvature, $\chi_{ij} = \frac{1}{2} e_{imn} G_{mnj}$ into (3.89), we find

$$\begin{aligned} (\lambda + 2\mu)(G_{111} + G_{221}) + 2\mu\,\chi_{32} = 0 \\ (\lambda + 2\mu)(G_{121} + G_{222}) + 2\mu\,\chi_{31} = 0 \end{aligned} \tag{3.90}$$

which is a constraint that the gradient of dilatational strain normal to each primary direction of curvature be related to that curvature by, e.g. $\left(G_{111} + G_{221}\right) = -\frac{2\mu}{\lambda+2\mu}\chi_{32} = -\frac{2\nu-1}{\nu-1}\chi_{32}$. Here the primary direction of curvature is the axis along which material 'curves' away from rather than the axis of rotation. This relationship implies that dilatational gradients should arise solely due to the Poisson effects of curvature, i.e., as material fibers oriented along a particular direction stretch (or compress) due to curvature they induce a dilatational gradient normal to that axis of corresponding sign and magnitude depending on Poisson ratio.

In Chapter 4 body forces such as (3.88) arise from internal constraints on the fluctuation field. The consequence of not addressing this issue is observed at the rSVE corners, (for example, Kouznetsova et al., 2002, Figure 7) and will be discussed in Chapter 4.

3.2.3 Cauchy Stress

The definition of Cauchy stress in terms of variables in the current configuration is pertinent to conservation of angular momentum, which is most readily addressed in that configuration. Based on the definition of nominal stress resulting from PVV applied to the rSVE (3.64), one might

expect that the (true) Cauchy stress for an rSVE be computed by $\Sigma_{ij} = \frac{1}{\Omega^{\mathrm{x}}}\int_{\Gamma^{\mathrm{x}}} y_i t_j \, d\Gamma + \frac{1}{\Omega^{\mathrm{x}}}\int_{\Gamma^{\mathrm{x}}} \rho y_i b_j \, d\Omega$. In the following we will show that this is not generally true, but is valid for a range of conditions common in rSVE simulations. First, we require that

$$\tfrac{1}{\rho}\boldsymbol{\Sigma}\colon\delta\mathbf{L}^T = \tfrac{1}{\rho_{\mathrm{o}}}\mathbf{P}\colon\delta\dot{\mathbf{F}}^T \tag{3.91}$$

where the set of kinematically admissible virtual velocity gradients $\delta\mathbf{L}$ is determined by the actual push-forward of the virtual rate of the deformation gradient, i.e., $\delta\mathbf{L} = \delta\dot{\mathbf{F}}\cdot\mathbf{F}^{-1}$ so that (3.91) becomes

$$\left(\mathbf{F}^{-1}\cdot\boldsymbol{\Sigma} - \frac{\rho}{\rho_{\mathrm{o}}}\mathbf{P}\right)\colon\delta\dot{\mathbf{F}}^T = 0 \tag{3.92}$$

from which it is clear that,

$$\boldsymbol{\Sigma} = \frac{\mathbf{F}\cdot\mathbf{P}}{\det(\mathbf{F})} \tag{3.93}$$

Note that the Cauchy stress is conjugated against the transpose of the velocity gradient, rather than the rate-of-deformation tensor, since the Cauchy stress is not symmetric, in general. Next we substitute the left-hand side of the definition of nominal stress (3.64) into (3.93), resulting in

$$\boldsymbol{\Sigma} = \frac{1}{\Omega^{\mathrm{x}}}\int_{\Gamma_{\mathrm{o}}^{\mathrm{x}}}\left(\mathbf{F}\cdot\mathbf{y}_{\mathrm{o}}\right)\otimes\mathbf{t}_{\mathrm{o}}\,d\Gamma_{\mathrm{o}} + \frac{1}{\Omega^{\mathrm{x}}}\int_{\Omega_{\mathrm{o}}^{\mathrm{x}}}\left(\mathbf{F}\cdot\mathbf{y}_{\mathrm{o}}\right)\otimes\rho_{\mathrm{o}}\mathbf{b}_{\mathrm{o}}\,d\Omega_{\mathrm{o}} \tag{3.94}$$

Recognizing that the following are true within and along the boundary of the rSVE,

$$\begin{aligned}\mathbf{t}_{\mathrm{o}}d\Gamma_{\mathrm{o}} &= \mathbf{t}\,d\Gamma\\ \rho_{\mathrm{o}}d\Omega_{\mathrm{o}} &= \rho d\Omega\\ \mathbf{F}\cdot\mathbf{y}_{\mathrm{o}} &= \mathbf{y} - \left(\tfrac{1}{2}\mathbf{G}:(\mathbf{y}_{\mathrm{o}}\otimes\mathbf{y}_{\mathrm{o}}) + \mathbf{h}\right)\end{aligned}\quad, \tag{3.95}$$

the Cauchy stress can be expressed as

$$\begin{aligned}\boldsymbol{\Sigma} = \frac{1}{\Omega^{\mathrm{x}}}\int_{\Gamma^{\mathrm{x}}}\mathbf{y}\otimes\mathbf{t}\,d\Gamma + \frac{1}{\Omega^{\mathrm{x}}}\int_{\Omega^{\mathrm{x}}}\mathbf{y}\otimes\rho\mathbf{b}\,d\Omega - \tfrac{1}{2}\mathbf{G}:\mathbf{Q}\\ -\frac{1}{\Omega^{\mathrm{x}}}\int_{\Gamma_{\mathrm{o}}^{\mathrm{x}}}\mathbf{h}\otimes\mathbf{t}_{\mathrm{o}}\,d\Gamma_{\mathrm{o}} - \frac{1}{\Omega^{\mathrm{x}}}\int_{\Omega_{\mathrm{o}}^{\mathrm{x}}}\mathbf{h}\otimes\rho_{\mathrm{o}}\mathbf{b}_{\mathrm{o}}\,d\Omega_{\mathrm{o}}\end{aligned} \tag{3.96}$$

The last two terms of (3.96) disappear according to the extended Hill-Mandel condition. The third term in (3.96) is zero for first-order homogenization problems or anytime **G** = **0**. In such cases

the Cauchy stress is determined in an analogous fashion to nominal stress without approximation and in the absence of inertia is precisely the volume-average of the fine scale Cauchy stress. Consider those cases where the last three terms of (3.96) disappear. Then by applying the divergence theorem, Nanson's relation, $\mathbf{n} \cdot \boldsymbol{\sigma} = \mathbf{t}$, and the strong form of the fine scale momentum balance in the current configuration, $\vec{\nabla} \cdot \boldsymbol{\sigma} + \rho \mathbf{b} = \rho \mathbf{a}$, and the manipulations in (3.97), the relationship between coarse and fine scale Cauchy stress becomes apparent:

$$\begin{aligned} \boldsymbol{\Sigma} &= \frac{1}{\Omega^{\mathrm{x}}} \int_{\Gamma^{\mathrm{x}}} \mathbf{y} \otimes \mathbf{t} \, d\Gamma + \frac{1}{\Omega^{\mathrm{x}}} \int_{\Omega^{\mathrm{x}}} \mathbf{y} \otimes \rho \mathbf{b} \, d\Omega \\ &= \frac{1}{\Omega^{\mathrm{x}}} \int_{\Omega^{\mathrm{x}}} \boldsymbol{\sigma} \; d\Omega + \frac{1}{\Omega^{\mathrm{x}}} \int_{\Omega^{\mathrm{x}}} \mathbf{y} \otimes \rho \mathbf{a} \; d\Omega \end{aligned} \tag{3.97}$$

Note however, the coarse scale Cauchy stress (3.93) is generally not the volume-average of its fine scale counterpart due to both inertia as well as the third term in (3.96), which is generally nonzero in the presence of a second-gradient.

3.2.4 Balance of Angular Momentum

Balance of angular momentum requires that the time rate of change of the angular momentum of a body with respect to any arbitrary, yet fixed, point in space equal the resulting moment of forces acting on the body with respect to the same point in space. For a Cauchy continua (zero second-gradient) this principle, which is independent of the balance of linear momentum, leads to the classical result that the Cauchy stress must be symmetric. It will now be shown that this result is not true for second gradient continua.

Conservation of angular momentum within the rSVE is readily analyzed in the current configuration. This analysis will proceed with the supposition that within the rSVE the material possesses no internal angular momentum or spin and there are no volumetric body couples (e.g., due to electromagnetic interaction). These assumptions are not fundamental limitations of this framework; it can easily be extended to deal with such occurrences. Rather, they are introduced to highlight the influence of material curvature on developing macroscale polar stresses for a material that would be considered 'classical' in the sense that its microstructural constituents behave coaxially and do not give rise to local polar stress fields. The angular momentum of each rSVE about the origin of the rSVE coordinates (fixed in space) is

$$\mathbf{M} = \int_{\Omega^x} \mathbf{y} \times \rho \mathbf{v} \, d\Omega \tag{3.98}$$

The net moment of forces acting on the rSVE about the origin is

$$\mathbf{T} = \int_{\Gamma^x} \mathbf{y} \times \mathbf{t} \, d\Gamma + \int_{\Omega^x} \mathbf{y} \times \rho \mathbf{b} \, d\Omega \tag{3.99}$$

The expression of balance of angular momentum for the rSVE becomes

$$\int_{\Gamma^x} \mathbf{y} \times \mathbf{t} \, d\Gamma + \int_{\Omega^x} \mathbf{y} \times \rho \mathbf{b} \, d\Omega = \frac{d}{dt} \int_{\Omega^x} \mathbf{y} \times \rho \mathbf{v} \, d\Omega \tag{3.100}$$

The time derivative on the right hand side of (3.100) is moved inside the integral (both operations are linear) and expanded by chain rule

$$\int_{\Gamma^x} \mathbf{y} \times \mathbf{t} \, d\Gamma + \int_{\Omega^x} \mathbf{y} \times \rho \mathbf{b} \, d\Omega = \int_{\Omega^x} \mathbf{v} \times \rho \mathbf{v} + \mathbf{y} \times \frac{d\rho \mathbf{v}}{dt} \, d\Omega \tag{3.101}$$

The first term on the right hand side of (3.101) must vanish (from the definition of cross product) and the latter term is reduced by recourse to Reynold's transport theorem, i.e.,

$$\int_{\Gamma^x} \mathbf{y} \times \mathbf{t} \, d\Gamma + \int_{\Omega^x} \mathbf{y} \times \rho \mathbf{b} \, d\Omega = \int_{\Omega^x} \mathbf{y} \times \rho \mathbf{a} d\Omega \tag{3.102}$$

The cross product of two vectors, $\mathbf{v}^3 = \mathbf{v}^1 \times \mathbf{v}^2$, can be expressed as the double contraction of the last two components of the third order permutation tensor, $\boldsymbol{\varepsilon}$, by the dyadic product of the two vectors, i.e. $\mathbf{v}^3 = \boldsymbol{\varepsilon} : \left(\mathbf{v}^1 \otimes \mathbf{v}^2 \right)$ or in indicial notation $v_i^3 = \varepsilon_{ijk} v_j^1 v_k^2$. Performing this change in notation, moving the permutation tensor out of each integral (the permutation tensor is constant), and collecting

$$\boldsymbol{\varepsilon} : \left(\int_{\Gamma^x} \mathbf{y} \otimes \mathbf{t} \, d\Gamma + \int_{\Omega^x} \mathbf{y} \otimes \rho \mathbf{b} \, d\Omega \right) = \boldsymbol{\varepsilon} : \int_{\Omega^x} \mathbf{y} \otimes \rho \mathbf{a} d\Omega \tag{3.103}$$

There are a number of conclusions that can be drawn from (3.103) and the results from the previous subsection. In the absence of microinertia, coarse scale second-gradient, and body forces, and subject to requirements on boundary conditions established in Section 3.1.5, the coarse scale Cauchy stress is $\boldsymbol{\Sigma} = \int_{\Gamma^x} \mathbf{y} \otimes \mathbf{t} \, d\Gamma$ and (3.103) reduces to $\boldsymbol{\varepsilon} : \boldsymbol{\Sigma} = \mathbf{0}$, i.e. the coarse scale Cauchy stress is symmetric. For nonzero microinertia in the absence of a second gradient, the symmetry of the Cauchy stress depends upon the symmetry of the net microinertia. For

nonzero second gradient, the Cauchy stress is not generally symmetric, regardless of microinertia. To continue the analysis (3.96) is substituted into (3.103) to yield

$$\boldsymbol{\varepsilon} : \left(\boldsymbol{\Sigma} + \mathbf{A}_1 + \mathbf{A}_2 \right) = \boldsymbol{\varepsilon} : \tfrac{1}{\Omega^{\mathrm{x}}} \int_{\Omega^{\mathrm{x}}} \mathbf{y} \otimes \rho \mathbf{a} \, d\Omega \tag{3.104}$$

where

$$\begin{aligned} \mathbf{A}_1 &= \mathbf{G} : \frac{1}{2\Omega^{\mathrm{x}}} \left(\int_{\Gamma_{\mathrm{o}}^{\mathrm{x}}} \mathbf{y}_{\mathrm{o}} \otimes \mathbf{y}_{\mathrm{o}} \otimes \mathbf{t}_{\mathrm{o}} \, d\Gamma_{\mathrm{o}} + \int_{\Omega_{\mathrm{o}}^{\mathrm{x}}} \mathbf{y}_{\mathrm{o}} \otimes \mathbf{y}_{\mathrm{o}} \otimes \rho_{\mathrm{o}} \mathbf{b}_{\mathrm{o}} \, d\Omega_{\mathrm{o}} \right) \\ \mathbf{A}_2 &= \frac{1}{\Omega^{\mathrm{x}}} \int_{\Gamma_{\mathrm{o}}^{\mathrm{x}}} \mathbf{h} \otimes \mathbf{t}_{\mathrm{o}} \, d\Gamma_{\mathrm{o}} + \frac{1}{\Omega^{\mathrm{x}}} \int_{\Omega_{\mathrm{o}}^{\mathrm{x}}} \mathbf{h} \otimes \rho_{\mathrm{o}} \mathbf{b}_{\mathrm{o}} \, d\Omega_{\mathrm{o}} \end{aligned} \tag{3.105}$$

$\mathbf{A}_2$ disappears under those boundary and body conditions for the rSVE that satisfy the internal power fluctuation requirement of Eq. (3.66) From the definition of the higher-order stress $\mathbf{Q}$ in (3.64) we see that

$$\mathbf{A}_1 = \frac{1}{\det(\mathbf{F})} \mathbf{G} : \mathbf{Q}^T \tag{3.106}$$

Hence, we may rewrite (3.104) as

$$\boldsymbol{\varepsilon} : \left(\boldsymbol{\Sigma} + \tfrac{1}{\det(\mathbf{F})} \mathbf{G} : \mathbf{Q}^T \right) = \boldsymbol{\varepsilon} : \tfrac{1}{\Omega^{\mathrm{x}}} \int_{\Omega^{\mathrm{x}}} \mathbf{y} \otimes \rho \mathbf{a} \, d\Omega \tag{3.107}$$

Equivalently,

$$\boldsymbol{\varepsilon} : \left(\mathbf{F} \cdot \mathbf{P} + \mathbf{G} : \mathbf{Q}^T \right) = \det(\mathbf{F}) \boldsymbol{\varepsilon} : \int_{\Omega^{\mathrm{x}}} \mathbf{y} \otimes \rho \mathbf{a} \, d\Omega \tag{3.108}$$

There are a number of conclusions that can be drawn from (3.107) and the results from the previous subsection. In the absence of microinertia and coarse scale second gradient the coarse scale Cauchy stress is symmetric. For nonzero microinertia in the absence of a second-gradient, the symmetry of the Cauchy stress depends upon the symmetry of the net microinertia. For nonzero second gradient, even in the absence of net microinertia, the coarse scale Cauchy stress is not generally symmetric due to couple stresses resulting from interactions of curvature and the higher order stresses.

3.2.5 Strong Form of Coarse Scale Momentum Balance

The principle of virtual velocities is now applied directly to the coarse scale to ensure that momentum is conserved within the coarse scale in a manner consistent with the fine scale. The following derivation essentially follows that of Germain (1973) for the second gradient continuum used recently by Kouznetsova et al. (2002; 2004) in concurrent multiscale modeling with an extension to macroscopically dynamic cases. Integrating the specific internal power over an arbitrary volume at the coarse scale gives

$$\int_{\Omega_o} \delta \mathrm{P}_{int}(\mathbf{x}_o)\, d\Omega_o = \int_{\Omega_o} \mathbf{P} : \delta\dot{\mathbf{F}}^T + \mathbf{Q}\vdots\delta\dot{\mathbf{G}}\, d\Omega_o \tag{3.109}$$

where $\delta\dot{\mathbf{F}}^T = \bar{\nabla}\delta\mathbf{V}$ and $\delta\dot{\mathbf{G}}^T = (\delta\mathbf{V})\bar{\nabla}\bar{\nabla}$. From the chain rule of differentiation,

$$\mathbf{P} : (\bar{\nabla}\delta\mathbf{V}) = \bar{\nabla}\cdot(\mathbf{P}\cdot\delta\mathbf{V}) - (\bar{\nabla}\cdot\mathbf{P})\cdot\delta\mathbf{V} \tag{3.110}$$

$$\mathbf{Q}\vdots(\delta\mathbf{V})\bar{\nabla}\bar{\nabla} = \big((\delta\mathbf{V}\bar{\nabla}) : \mathbf{Q}\big)\cdot\bar{\nabla} - \big(\delta\mathbf{V}\cdot(\mathbf{Q}\cdot\bar{\nabla})\big)\cdot\bar{\nabla} + \delta\mathbf{V}\cdot\big((\mathbf{Q}\cdot\bar{\nabla})\cdot\bar{\nabla}\big) \tag{3.111}$$

After substituting (3.110) and (3.111) into (3.109) , applying the divergence theorem,

$$\begin{aligned}\delta \mathrm{P}_{int} = &-\int_{\Omega_o}(\bar{\nabla}\cdot\mathbf{P})\cdot\delta\mathbf{V}\, d\Omega_o + \int_{\Omega_o}\delta\mathbf{V}\cdot\big((\mathbf{Q}\cdot\bar{\nabla})\cdot\bar{\nabla}\big)\, d\Omega_o \\ &+\int_{\Gamma_o}\mathbf{N}\cdot(\mathbf{P}\cdot\delta\mathbf{V})\, d\Gamma_o - \int_{\Gamma_o}\big(\delta\mathbf{V}\cdot(\mathbf{Q}\cdot\bar{\nabla})\big)\cdot\mathbf{N}_o\, d\Gamma_o \\ &+\int_{\Gamma_o}\big((\delta\mathbf{V}\bar{\nabla}) : \mathbf{Q}\big)\cdot\mathbf{N}\, d\Gamma_o\end{aligned} \tag{3.112}$$

Collecting terms in (3.112) gives

$$\begin{aligned}\delta \mathrm{P}_{int} = &\int_{\Omega}\bar{\nabla}\cdot((\mathbf{Q}\cdot\bar{\nabla})^T - \mathbf{P})\cdot\delta\mathbf{V}\, d\Omega_o \\ &+\int_{\Gamma}\delta\mathbf{V}\cdot(\mathbf{P}^T - (\mathbf{Q}\cdot\bar{\nabla}))\cdot\mathbf{N}\, d\Gamma_o \\ &+\int_{\Gamma_o}\delta\mathbf{V}\bar{\nabla} : \mathbf{Q}\cdot\mathbf{N}\, d\Gamma_o\end{aligned} \tag{3.113}$$

The last term in (3.113) contains the work done by second order stresses on the deformation gradient along the boundary. However, components of the rate of the deformation gradient which lie within the surface tangent plane are redundant with the surface velocities, motivating the following decomposition into tangential and normal components (cf. Fleck and Hutchinson, 1997).

$$\begin{aligned}\vec{\nabla}\delta\mathbf{V} &= (\mathbf{I}-\mathbf{N}\otimes\mathbf{N})\cdot\vec{\nabla}\delta\mathbf{V} + (\mathbf{N}\otimes\mathbf{N})\cdot\vec{\nabla}\delta\mathbf{V} \\ &= \quad \vec{\nabla}_t\delta\mathbf{V} \quad + \quad \vec{\nabla}_n\delta\mathbf{V}\end{aligned} \tag{3.114}$$

The following holds true by chain rule

$$\vec{\nabla}_t\cdot(\delta\mathbf{V}\cdot\mathbf{Q}\cdot\mathbf{N}) = \delta\mathbf{V}\cdot(\mathbf{Q}\cdot\mathbf{N})\cdot\vec{\nabla}_t + \delta\mathbf{V}\vec{\nabla}_t : (\mathbf{Q}\cdot\mathbf{N}) \tag{3.115}$$

and when combined with (3.114) results in

$$\delta\mathbf{V}\vec{\nabla} : (\mathbf{Q}\cdot\mathbf{N}) = \vec{\nabla}_t\cdot(\delta\mathbf{V}\cdot\mathbf{Q}\cdot\mathbf{N}) - \delta\mathbf{V}\cdot(\mathbf{Q}\cdot\mathbf{N})\cdot\vec{\nabla}_t + \delta\mathbf{V}\vec{\nabla}_n : (\mathbf{Q}\cdot\mathbf{N}) \tag{3.116}$$

From the surface divergence theorem (cf. Appendix 3.1)

$$\begin{aligned}&\int_{\Gamma_o}\vec{\nabla}_t\cdot(\delta\mathbf{V}\cdot\mathbf{Q}\cdot\mathbf{N})\,d\Gamma_o = \\ &\qquad \int_{\Gamma_o}\delta\mathbf{V}\cdot(\mathbf{N}\cdot\mathbf{Q}\cdot\mathbf{N})(\vec{\nabla}_t\cdot\mathbf{N})\,d\Gamma_o + \oint_c(\delta\mathbf{V}\cdot\mathbf{Q}\cdot\mathbf{N})\cdot\mathbf{M}\,dl_o\end{aligned} \tag{3.117}$$

where $\vec{\nabla}_t\cdot\mathbf{N}$ is twice the mean surface curvature and $\mathbf{M}=\mathbf{T}\times\mathbf{N}$ is the vector tangent to surface Γ and perpendicular to the curve c bounding Γ. If Γ has a continuous outward surface normal (i.e. Γ is everywhere smooth) then the last term in (3.117) vanishes. Otherwise, if the surface is continuously connected in a piecewise fashion such that there are k curves bounding k connected and smooth surfaces which make up Γ, then the last term in (3.117) becomes $\sum_k\oint_{c^{(k)}}\delta\mathbf{V}\cdot\left[\!\left[(\mathbf{Q}\cdot\mathbf{N}_o^{(k)})\cdot\mathbf{M}^{(k)}\right]\!\right]dl_o^{(k)}$, where $[\![\bullet]\!]$ is used to denote a (Hadamard) jump in the argument across the k[th] bounding curve. Substituting this result into (3.117) and combining with (3.116), (3.113) becomes

$$\begin{aligned}\delta\mathrm{P}_{int} = &\int_\Omega\vec{\nabla}\cdot((\mathbf{Q}\cdot\vec{\nabla})^T - \mathbf{P})\cdot\delta\mathbf{V}\,d\Omega + \int_\Gamma\delta\mathbf{V}\cdot(\mathbf{P}^T - (\mathbf{Q}\cdot\vec{\nabla}))\cdot\mathbf{N}\,d\Gamma \\ &+\int_\Gamma\delta\mathbf{V}\cdot(\mathbf{Q}:\mathbf{N}\otimes\mathbf{N})(\vec{\nabla}_t\cdot\mathbf{N})d\Gamma - \int_\Gamma\delta\mathbf{V}\cdot\left(\mathbf{Q}\cdot\mathbf{N}\right)\cdot\vec{\nabla}_t\,d\Gamma \\ &+\int_\Gamma(\mathbf{N}\cdot\vec{\nabla}\delta\mathbf{V})\cdot(\mathbf{Q}:\mathbf{N}\otimes\mathbf{N})\,d\Gamma \\ &+\sum_k\oint_{c^{(k)}}\delta\mathbf{V}\cdot\left[\!\left[\mathbf{Q}:\mathbf{M}^{(k)}\otimes\mathbf{N}^{(k)}\right]\!\right]dl^{(k)}\end{aligned} \tag{3.118}$$

Considering (3.118), it is concluded that the external virtual power must consist of coarse scale tractions $\mathbf{T}$ conjugate with velocity, double-stress tractions $\mathbf{T}'$ conjugate to the normal component of the gradient of velocity and a set of line forces $\mathbf{Z}$ conjugate to velocities along lines that stitch together smooth sections of the surface. The external virtual power will also consist of

conventional body forces conjugate to velocity in the body $\mathbf{B}$ and body double forces $\mathbf{B}'$ conjugate to the deformation gradient within the body. Accordingly the external virtual power is written

$$\begin{aligned}\delta \mathrm{P}_{ext} &= \int_{\Omega} \mathbf{B} \cdot \delta \mathbf{V} \; d\Omega_{\mathrm{o}} + \int_{\Omega} \mathbf{B}' : \delta \mathbf{V} \overleftarrow{\nabla} \; d\Omega_{\mathrm{o}} \\ &+ \int_{\Gamma} \mathbf{T} \cdot \delta \mathbf{V} \; d\Gamma_{\mathrm{o}} + \int_{\Gamma} \mathbf{T}' \cdot (\mathbf{N}_{\mathrm{o}} \cdot \vec{\nabla} \delta \mathbf{V}) \, d\Gamma_{\mathrm{o}} + \sum_{k} \oint_{c^{(k)}} \mathbf{Z} \cdot \delta \mathbf{V} \, dl_{\mathrm{o}}^{(k)}\end{aligned} \tag{3.119}$$

Because the deformation gradient and second-gradient are completely defined by a given coarse scale displacement field, the coarse scale inertial resistance to motion is the coarse scale mass density and no higher order ordered microinertia tensors are introduced. Recall, the fine-scale micro-inertial resistance manifests within the coarse scale nominal stress in this framework. Accordingly we define the coarse scale kinematic power as

$$\delta \mathrm{P}_{kin} = \int_{\Omega_{\mathrm{o}}} \overline{\rho} \dot{\mathbf{V}} \cdot \delta \mathbf{V} \; d\Omega_{\mathrm{o}} \tag{3.120}$$

Note that this is different from micromorphic theories in which higher ordered inertial tensors are introduced because the fine scale deformation gradients are not directly related to their coarse scale counterparts (cf. Toupin, 1963; Mindlin, 1964; Germain, 1973; Eringen, 1999). In these theories, the acceleration of microstructure spin is resisted by microinertia. The precise physical interpretation of this fine scale relationship is elusive. On the other hand, in the framework presented here any microinertial effects will enter into constitutive relations and the fine scale (microstructure) cannot spin independent of the coarse scale, such that (3.120) is adequate. Recent work of Vernerey et al. (2008) includes several inertial tensors as their material is an Nth ordered micromorphic continua, thus implying several scales of microstructure which spin completely independent of each other. As discussed in Chapter 2, this idea of introducing all finer scales to the single coarsest scale of application concurrently, while interesting and potentially quite useful, has several unresolved conceptual issues. For example, how these microinertial tensors are to be computed (or even interpreted) for actual materials such that contributions to total virtual inertial power from each scale are unique is unclear. More aligned with the approach favored here, Chambon et al. (2004) omit contributions from underlying

microinertial tensors in their coarse scale formulation; however, they do not incorporate this resistance in constitutive relations either.

The coarse scale balance of momentum is satisfied if the power of actual external forces acting on virtual velocities is equal to the power of actual stresses acting on internal virtual velocities plus the virtual inertial power due to the actual acceleration field for any set of kinematically admissible coarse scale velocities. Accordingly, after collecting body, surface, and line integrals, we may write

$$\int_{\Omega_{\mathrm{o}}} \left(\bar{\nabla} \cdot (\mathbf{P} - (\mathbf{Q} \cdot \bar{\nabla})^T) + \mathbf{B} + \mathbf{B}' \cdot \bar{\nabla} \right) \cdot \delta \mathbf{V} \, d\Omega_{\mathrm{o}} = \int_{\Omega} \bar{\rho} \dot{\mathbf{V}} \cdot \delta \mathbf{V} \, d\Omega_{\mathrm{o}} \tag{3.121}$$

$$\begin{gathered} \int_{\Gamma} \delta \mathbf{V} \cdot \left(\mathbf{T} + \mathbf{N}_{\mathrm{o}} \cdot \mathbf{B}'^T \right) \cdot d\Gamma_{\mathrm{o}} + \int_{\Gamma} \mathbf{T}' \cdot (\mathbf{N}_{\mathrm{o}} \cdot \bar{\nabla} \delta \mathbf{V}) \, d\Gamma_{\mathrm{o}} = \\ \int_{\Gamma_{\mathrm{o}}} \delta \mathbf{V} \cdot (\mathbf{P}^T - (\mathbf{Q} \cdot \bar{\nabla})) \cdot \mathbf{N}_{\mathrm{o}} + (\mathbf{Q} : \mathbf{N}_{\mathrm{o}} \otimes \mathbf{N}_{\mathrm{o}})(\bar{\nabla}_t \cdot \mathbf{N}_{\mathrm{o}}) - \left(\mathbf{Q} \cdot \mathbf{N}_{\mathrm{o}} \right) \cdot \bar{\nabla}_t \, d\Gamma_{\mathrm{o}} \\ + \int_{\Gamma_{\mathrm{o}}} (\mathbf{N}_{\mathrm{o}} \cdot \bar{\nabla} \delta \mathbf{V}) \cdot (\mathbf{Q} : \mathbf{N}_{\mathrm{o}} \otimes \mathbf{N}_{\mathrm{o}}) \, d\Gamma_{\mathrm{o}} \end{gathered} \tag{3.122}$$

$$\sum_k \oint_{c^{(k)}} \mathbf{Z}^{(k)} \cdot \delta \mathbf{V} \, dl_{\mathrm{o}}{}^{(k)} = \sum_k \oint_{c^{(k)}} \delta \mathbf{V} \cdot \left[\!\!\left[\mathbf{Q} : \mathbf{M}^{(k)} \otimes \mathbf{N}_{\mathrm{o}}^{(k)} \right]\!\!\right] dl_{\mathrm{o}}{}^{(k)} \tag{3.123}$$

where (3.121) and (3.122) must hold for arbitrary volume and any kinematically admissible velocity field implying the strong form of coarse scale momentum balance:

$$\bar{\nabla} \cdot (\mathbf{P} - (\mathbf{Q} \cdot \bar{\nabla})^T) + \left(\mathbf{B} + \mathbf{B}' \cdot \bar{\nabla} \right) = \bar{\rho} \dot{\mathbf{V}} \tag{3.124}$$

$$\begin{gathered} \mathbf{T} + \mathbf{N}_{\mathrm{o}} \cdot \mathbf{B}'^T = \\ (\mathbf{P}^T - (\mathbf{Q} \cdot \bar{\nabla})) \cdot \mathbf{N}_{\mathrm{o}} + (\mathbf{Q} : \mathbf{N}_{\mathrm{o}} \otimes \mathbf{N}_{\mathrm{o}})(\bar{\nabla}_t \cdot \mathbf{N}_{\mathrm{o}}) - \left(\mathbf{Q} \cdot \mathbf{N}_{\mathrm{o}} \right) \cdot \bar{\nabla}_t \\ \mathbf{T}' = \mathbf{Q} : \mathbf{N}_{\mathrm{o}} \otimes \mathbf{N}_{\mathrm{o}} \end{gathered} \tag{3.125}$$

Moreover, the line load acting on curves connecting separately smooth surfaces is

$$\mathbf{Z}^{(k)} = \left[\!\!\left[\mathbf{Q} : \mathbf{M}^{(k)} \otimes \mathbf{N}^{(k)} \right]\!\!\right] \tag{3.126}$$

3.2.6 Weak Form of Coarse Scale Momentum Balance

The components of the weak form of coarse scale momentum balance have been developed in the previous subsection. Assembled here in accordance with PVV, the weak form of momentum balance (3.127) implies the strong form (3.124) coupled with the natural traction boundary conditions (3.125) and line loading condition (3.126).

$$\int_{\Omega_o} \mathbf{P} : \delta\dot{\mathbf{F}}^T + \mathbf{Q} \vdots \delta\dot{\mathbf{G}}\, d\Omega_o + \int_{\Omega_o} \overline{\rho}\dot{\mathbf{V}} \cdot \delta\mathbf{V}\, d\Omega_o = \int_{\Omega_o} \mathbf{B} \cdot \delta\mathbf{V}\, d\Omega_o + \int_{\Omega_o} \mathbf{B}' : \delta\mathbf{V}\bar{\nabla}\, d\Omega_o + \int_{\Gamma_o} \mathbf{T} \cdot \delta\mathbf{V}\, d\Gamma_o + \int_{\Gamma_o} \mathbf{T}' \cdot (\mathbf{N}_o \cdot \bar{\nabla}\delta\mathbf{V})\, d\Gamma_o + \sum_k \oint_{c^{(k)}} \mathbf{Z} \cdot \delta\mathbf{V}\, dl_o^{(k)} \tag{3.127}$$

This weak form will serve as the foundation for a discretized computation of coarse scale response consistent with the fine scale in terms of kinematics and momentum balance as discussed in Chapter 5.

Attention is now turned to thermodynamics of internal state variable theory and the applicable thermodynamic balance principles pertinent to the scale transition, which together build the constitutive requirements of this framework.

3.3 Thermodynamics of Irreversible Processes

In "The Thermomechanics of Nonlinear Irreversible Behaviors: An Introduction", Maugin warns in jest:

> *"…the wise man's attitude towards thermodynamics should be to have nothing to do with it. To deal with thermodynamics is to look for trouble… Why do we need to get involved in a field of knowledge which, within the last hundred years, has exhibited the largest number of schizophrenics and megalomaniacs, imbalanced scientists, paranoiacs, egocentrists, and probably insomniacs and sleepwalkers?"*

In the context of the introductory chapter of his monograph, this message is clearly in jest. Regardless, it does seem that there is no other area within modern mechanics that causes such misunderstanding, sharply critical debate, and general confusion regarding the applicability of competing accepted approaches as thermodynamics. Nevertheless, thermodynamic principles are fundamental to processes where energy is transferred by various mechanisms and must be treated.

In this multiscale framework, thermodynamics is addressed both at each particular scale and between two adjacent scales. At any particular scale of observation the fundamental laws of thermodynamics must be satisfied. The first law of thermodynamics enforces that the total energy of a system consisting of a given set of mass particles is conserved for any admissible

reversible or irreversible process. The second law of thermodynamics provides a restriction on the path of irreversible processes and, when combined with the first law, specifies when dissipated energy is stored or dissipated as heat. Classical thermodynamics deals with transitions between equilibrium states of a system. The thermodynamics of irreversible processes extends the classic concepts to non-equilibrium states so long as those states are "near enough" to equilibrium. For example, the temperature of a system is well-defined only if the system is at thermal equilibrium. However, even for small deviations from thermal equilibrium the overall temperature at which heat is rejected to the surroundings provides a meaningful concept of temperature and entropy. These concepts are discussed in the context of the multiscale framework below.

3.3.1 Conservation of Energy

For a given system of mass particles, the total change of energy must equal the total work done on the system plus any heat added to the system. At any particular time the relationship

$$\tfrac{d}{dt} E_{total} = P_{input} + Q_{input} \tag{3.128}$$

must hold, where the power input to the system through external boundaries is that developed in the previous section with virtual velocities replaced by their actual values. At the fine scale of observation for any closed volume, the total energy (internal plus kinetic), power input to system, and total heat added to system are given by (3.129)-(3.131), respectively, i.e.,

$$E_{total} = \int_{\Omega_o} \rho_o u \, d\Omega_o + \tfrac{1}{2} \int_{\Omega_o} \rho_o \mathbf{v} \cdot \mathbf{v} \, d\Omega_o \tag{3.129}$$

$$\begin{aligned} P_{input} &= \int_{\Gamma_o} \mathbf{t}_o \cdot \mathbf{v} \, d\Gamma_o + \int_{\Omega_o} \rho_o \mathbf{b}_o \cdot \mathbf{v}_o \, d\Omega_o \\ &= \int_{\Omega_o} \rho_o \tfrac{d\mathbf{v}}{dt} \cdot \mathbf{v} \, d\Omega_o + \int_{\Omega_o} \mathbf{p} : \dot{\mathbf{f}}^T \, d\Omega_o \end{aligned} \tag{3.130}$$

$$\begin{aligned} Q_{input} &= \int_{\Omega_o} r_o \, d\Omega_o - \int_{\Gamma_o} \mathbf{q}_o \cdot \mathbf{n}_o \, d\Gamma_o \\ &= \int_{\Omega_o} r_o \, d\Omega_o - \int_{\Omega_o} \vec{\nabla}_o \cdot \mathbf{q}_o \, d\Omega_o \end{aligned} \tag{3.131}$$

The power input to the system is that due to external tractions and body forces. The top equation in (3.130) is modified by using the definition of surface tractions, divergence theorem, and strong

form of the balance of momentum at the fine scale to get the bottom equation. Likewise, the heat added to the system is specified in terms of the heat generated locally, r, and the heat flux through the boundary, $\mathbf{q}$, defined with positive values indicating heat flow out of the system. Taking the time derivative of (3.129), making use of the transport theorem, and substituting along with (3.130) and (3.131) into (3.128) gives

$$\begin{aligned}\int_{\Omega_o} \rho_o \dot{u}\, d\Omega_o + \int_{\Omega_o} \rho_o \tfrac{d\mathbf{v}}{dt} \cdot \mathbf{v}\, d\Omega = \\ \int_{\Omega_o} \rho_o \tfrac{d\mathbf{v}}{dt} \cdot \mathbf{v}\, d\Omega_o + \int_{\Omega_o} \mathbf{p} : \dot{\mathbf{f}}^T\, d\Omega_o + \int_{\Omega_o} r_o\, d\Omega_o - \int_{\Omega_o} \vec{\nabla}_o \cdot \mathbf{q}_o\, d\Omega_o\end{aligned} \tag{3.132}$$

Because this is true for any arbitrary volume, the equivalent strong form is (expressed in terms of Lagrangian variables with respect to the reference configuration)

$$\rho_o \dot{u} = \mathbf{p} : \dot{\mathbf{f}}^T + r_o - \vec{\nabla}_o \cdot \mathbf{q}_o \tag{3.133}$$

From a coarse scale of observation the total power input to the system is expressed as

$$P_{input} = \left(\mathbf{P} : \dot{\mathbf{F}}^T + \mathbf{Q} \vdots \dot{\mathbf{G}}\right)\Omega_o \tag{3.134}$$

The time derivative of the total energy in the system is expanded into coarse scale kinematic variables based on the kinematic decomposition, i.e.,

$$\begin{aligned}\tfrac{d}{dt} E_{total} &= \int_{\Omega_o} \rho_o \dot{u}\, d\Omega_o + \int_{\Omega_o} \rho_o \tfrac{d\mathbf{v}}{dt} \cdot \mathbf{v}\, d\Omega_o \\ &= \int_{\Omega_o} \rho_o \dot{u}\, d\Omega_o + \int_{\Omega_o} \rho_o \tfrac{d\mathbf{v}}{dt} \otimes \mathbf{y}_o d\Omega_o : \dot{\mathbf{F}} + \int_{\Omega_o} \rho_o \tfrac{d\mathbf{v}}{dt} \otimes \mathbf{y}_o \otimes \mathbf{y}_o d\Omega_o \vdots \dot{\mathbf{G}}\end{aligned} \tag{3.135}$$

where again, it is emphasized that $\dot{\mathbf{F}}$ and $\dot{\mathbf{G}}$ are constant over the rSVE *by definition*. We define two new coarse scale variables, the coarse scale heat generation per unit volume, $\bar{r}_o = \frac{1}{\Omega_o}\int_{\Omega_o} r_o\, d\Omega_o$, and the coarse scale heat flux, which is related to the fine scale only by the constraint that the net heat loss from the rSVE be the same for coarse and fine scales, i.e., $\vec{\nabla}_o \cdot \bar{\mathbf{q}}_o = \frac{1}{\Omega_o}\int_{\Omega_o} \vec{\nabla}_o \cdot \mathbf{q}_o\, d\Omega_o$. The expression for heat input is modified accordingly, i.e.,

$$\begin{aligned}Q_{input} &= \int_{\Omega_o} r_o\, d\Omega_o - \int_{\Omega_o} \vec{\nabla}_o \cdot \mathbf{q}_o\, d\Omega_o \\ &= \Omega_o\left(\bar{r}_o - \vec{\nabla}_o \cdot \bar{\mathbf{q}}_o\right)\end{aligned} \tag{3.136}$$

Combining (3.134)-(3.136) within the first law as expressed in (3.128) gives the local strong form of conservation of energy at the coarse scale in terms of Lagrangian variables, i.e.,

$$\overline{\rho}_o \dot{\overline{u}} = \mathbf{P} : \dot{\mathbf{F}}^T + \mathbf{Q} \vdots \dot{\mathbf{G}} + \overline{r}_{\mathrm{o}} - \vec{\nabla}_{\mathrm{o}} \cdot \overline{\mathbf{q}}_{\mathrm{o}} \tag{3.137}$$

so that scale invariance of total internal energy implies that

$$\begin{aligned} \overline{\rho}_{\mathrm{o}} \dot{\overline{u}} = & \tfrac{1}{\Omega_{\mathrm{o}}} \int_{\Omega_{\mathrm{o}}} \rho_{\mathrm{o}} \dot{u} \, d\Omega_{\mathrm{o}} + \tfrac{1}{\Omega_{\mathrm{o}}} \int_{\Omega_{\mathrm{o}}} \rho_{\mathrm{o}} \tfrac{d\mathbf{v}}{dt} \otimes \mathbf{y}_{\mathrm{o}} d\Omega_{\mathrm{o}} : \dot{\mathbf{F}} \\ & + \tfrac{1}{\Omega_{\mathrm{o}}} \int_{\Omega_{\mathrm{o}}} \rho_{\mathrm{o}} \tfrac{d\mathbf{v}}{dt} \otimes \mathbf{y}_{\mathrm{o}} \otimes \mathbf{y}_{\mathrm{o}} d\Omega_{\mathrm{o}} \vdots \dot{\mathbf{G}} \end{aligned} \tag{3.138}$$

where the time rate of change of the coarse scale specific internal energy has a contribution from both the fine scale internal energy and the net microinertial power. Therefore the total coarse scale internal energy is equal to the volume average of the fine scale internal energy only if there is no net microinertia at the fine scale. As adjacent material points exchange momentum with a particular coarse scale material point, any net microinertia is part of the coarse scale internal energy. Over time, it will self-equilibrate by increasing the local fine scale internal energy and the local fine scale stresses; thus, (3.137) accurately reflects the balance of energy between scales and is consistent with the momentum concepts laid out previously.

Recall that the coarse scale Cauchy stress is not generally symmetric (3.107). It may seem concerning that the internal energy depends upon anti-symmetry of the Cauchy stress, which would ordinarily imply that the material constitutive relations are somehow dependent upon rigid rotations of the material. However, for second gradient continua it will be shown that the anti-symmetry of the Cauchy stress, being induced by the curvature associated with the second gradient, does not make a net contribution to internal energy.

The internal specific power per unit mass is written in indicial notation as

$$P_{int} = \tfrac{1}{\rho_{\mathrm{o}}} \Big(P^{Ij} \, g_{jk} \dot{F}^k_{\ .I} + Q^{jNO} g_{jk} \dot{G}^k_{\ .NO} \Big) \tag{3.139}$$

The Lie derivative of the second order strain is

$$\begin{aligned} L_v \big(\tilde{\mathbf{\Gamma}} \big)^{\tilde{q}}_{.\tilde{r}\tilde{s}} &= \phi^{in}_* \Big(\dot{\mathbf{\Gamma}}^I_{\ .JK} \Big) \\ &= {}^{in}F^{\tilde{q}}_{\ .M} \dot{F}^{-1M}_{\ \ .j} G^j_{\ .NO} \, {}^{in}F^{-1N}_{\ \ .\tilde{r}} \, {}^{in}F^{-1O}_{\ \ .\tilde{s}} + {}^{e}F^{-1\tilde{q}}_{\ \ .j} \dot{G}^j_{\ .NO} \, {}^{in}F^{-1N}_{\ \ .\tilde{r}} \, {}^{in}F^{-1O}_{\ \ .\tilde{s}} \end{aligned} \tag{3.140}$$

such that $\dot{G}^{k}_{.NO} = {}^{e}F^{k}_{.\tilde{q}} L_v \left(\tilde{\mathbf{G}}\right)^{\tilde{q}}_{.\tilde{r}\tilde{s}} {}^{in}F^{\tilde{r}}_{.N} {}^{in}F^{\tilde{s}}_{.O} - F^{k}_{.M} \dot{F}^{-1M}_{\quad .i} G^{i}_{.NO}$, which is substituted into (3.139) to get

$$P_{int} = \frac{1}{\rho_o} P^{Ij} g_{jk} \dot{F}^{k}_{.I} + \frac{1}{\rho_o}\left(Q^{jNO} g_{jk} {}^{e}F^{k}_{.\tilde{q}} {}^{in}F^{\tilde{r}}_{.N} {}^{in}F^{\tilde{s}}_{.O} \right) L_v \left(\tilde{\mathbf{G}}\right)^{\tilde{q}}_{.\tilde{r}\tilde{s}} - Q^{jNO} g_{jk} F^{k}_{.M} \dot{F}^{-1M}_{\quad .i} G^{i}_{.NO} \quad (3.141)$$

Making use of $\dot{\mathbf{F}}^{-1} = -\left(\mathbf{F}^{-1} \cdot \dot{\mathbf{F}} \cdot \mathbf{F}^{-1}\right)$, $\mathbf{L} = \dot{\mathbf{F}} \cdot \mathbf{F}^{-1}$, and (3.91), equation (3.141) becomes,

$$P_{int} = \frac{1}{\rho}\left(\Sigma^{ij} + \frac{\rho}{\rho_o} G^{i}_{.NO} Q^{jNO} \right) g_{jk} L^{k}_{.i} + \frac{1}{\rho_o}\left(Q^{jNO} g_{jk} {}^{e}F^{k}_{.\tilde{q}} {}^{in}F^{\tilde{r}}_{.N} {}^{in}F^{\tilde{s}}_{.O} \right) L_v \left(\tilde{\mathbf{G}}\right)^{\tilde{q}}_{.\tilde{r}\tilde{s}} \quad (3.142)$$

Substitution of the decomposition of the velocity gradient into symmetric and anti-symmetric parts, $\mathbf{D} = \frac{1}{2}\left(\mathbf{L} + \mathbf{L}^T\right)$ and $\mathbf{W} = \frac{1}{2}\left(\mathbf{L} - \mathbf{L}^T\right)$, respectively, yields

$$\begin{aligned} P_{int} = {} & \frac{1}{\rho}\left(\Sigma^{(ij)} + \frac{\rho}{\rho_o} G^{(i}_{.NO} Q^{j)NO} \right) D_{ij} + \frac{1}{\rho_o}\left(Q^{jNO} g_{jk} {}^{e}F^{k}_{.\tilde{q}} {}^{in}F^{\tilde{r}}_{.N} {}^{in}F^{\tilde{s}}_{.O} \right) L_v \left(\tilde{\mathbf{G}}\right)^{\tilde{q}}_{.\tilde{r}\tilde{s}} \\ & + \frac{1}{\rho}\left(\Sigma^{[ij]} + \frac{\rho}{\rho_o} G^{[i}_{.NO} Q^{j]NO} \right) W_{ji} \end{aligned} \quad (3.143)$$

Recall from (3.107), in the absence of a net inertial spin and under particular rSVE constraints at the fine scale, the anti-symmetric part of the coarse scale Cauchy stress is $\Sigma^{[ij]} = -\frac{1}{\det(\mathbf{F})} G^{[i}_{.MN} Q^{j]}_{.MN}$. Making the substitution into (3.143), we are left with

$$P_{int} = \frac{1}{\rho}\left(\Sigma^{(ij)} - \Sigma^{*(ij)} \right) D_{ij} + \frac{1}{\tilde{\rho}} \tilde{Q}^{\tilde{q}}_{.\tilde{r}\tilde{s}} L_v \left(\tilde{\mathbf{\Gamma}}\right)^{\tilde{q}}_{.\tilde{r}\tilde{s}} \quad (3.144)$$

where the projected stress, $\mathbf{\Sigma}^{*}$, is defined as

$$\Sigma^{*ij} = -\frac{1}{\det(\mathbf{F})} G^{(i}_{.MN} Q^{j)}_{.MN} \quad (3.145)$$

and the intermediate configuration second-order stress, $\tilde{\mathbf{Q}}$, is

$$\tilde{Q}^{\tilde{q}}_{.\tilde{r}\tilde{s}} = \frac{1}{\det(\mathbf{F}_m)} Q^{jNO} g_{jk} {}^{e}F^{k}_{.\tilde{q}} {}^{in}F^{\tilde{r}}_{.N} {}^{in}F^{\tilde{s}}_{.O} \quad (3.146)$$

The first term on the right side of (3.144) is pulled back into the intermediate configuration to give a fully consistent expression, i.e.,

$$P_{int} = \frac{1}{\tilde{\rho}}(\tilde{S}^{(\tilde{i}\tilde{j})} - \tilde{S}^{*(\tilde{i}\tilde{j})}) \tilde{D}_{\tilde{i}\tilde{j}} + \frac{1}{\tilde{\rho}} \tilde{Q}^{\tilde{q}}_{.\tilde{r}\tilde{s}} L_v \left(\tilde{\mathbf{\Gamma}}\right)^{\tilde{q}}_{.\tilde{r}\tilde{s}} \quad (3.147)$$

where the mass per unit volume in the intermediate configuration, $\tilde{\rho}$, has been introduced and satisfies $\tilde{\rho} = \rho \det\left(\mathbf{F}^e\right)$. Equation (3.147) has a similar structure to that of Chambon et al. (2004), however, they are not the same because their expression develops from anticipation of a constitutive coupling between second gradient response and the first order stress-strain response. On the other hand, relation (3.147) comes from a strict accounting of the balance of angular momentum which quantified the anti-symmetric part of the Cauchy stress coupled with a precise enforcement of the balance of linear momentum between scales. A final point of distinction is that in this work the constitutive laws will provide a relationship between $\tilde{\mathbf{S}}$ and $\tilde{\mathbf{E}}$, and $\tilde{\boldsymbol{Q}}$ and $\tilde{\boldsymbol{\Gamma}}$; $\tilde{\mathbf{S}}^*$, meanwhile, is determined entirely from the projection of $\boldsymbol{Q}$ by $\mathbf{G}$ onto that part of the deformation measured by $\tilde{\mathbf{E}}$. It is therefore superfluous to develop another set of constitutive couplings relating $\tilde{\mathbf{S}}^*$ to $\tilde{\boldsymbol{\Gamma}}$ to represent *this* behavior, although it is entirely possible (and readily handled in this framework) that an independent physical coupling may exist between $\tilde{\mathbf{S}}$ and $\tilde{\boldsymbol{\Gamma}}$, and, $\tilde{\boldsymbol{Q}}$ and $\tilde{\mathbf{E}}$.

The second Piola-Kirchhoff stress in the intermediate configuration (both direct and projected portions) is obtained by either the inelastic push forward from the reference configuration, or equivalently, an elastic pull back of the Cauchy stress from the current configuration, i.e.,

$$\tilde{\mathbf{S}} = \frac{\mathbf{F}_{in} \cdot \mathbf{S} \cdot \mathbf{F}_{in}^T}{\det(\mathbf{F}_{in})} = \det(\mathbf{F}_e)\left(\mathbf{F}_e^{-1} \cdot \boldsymbol{\Sigma} \cdot \mathbf{F}_e^{-T}\right) \tag{3.148}$$

In modern computational mechanics codes heat transfer is more readily addressed in the current configuration. Modifying the heat flux and generation terms accordingly to pull back into the intermediate configuration and substituting the results of (3.147) into the energy equation (3.137) gives

$$\tilde{\rho}\dot{\tilde{u}} = (\tilde{S}^{(\tilde{i}\tilde{j})} - \tilde{S}^{*(\tilde{i}\tilde{j})})\tilde{D}_{\tilde{i}\tilde{j}} + \tilde{Q}^{\tilde{q}}_{.\tilde{r}\tilde{s}}\, L_v\left(\tilde{\boldsymbol{\Gamma}}\right)^{\tilde{q}}_{.\tilde{r}\tilde{s}} + \left(\overline{r} - \vec{\nabla} \cdot \overline{\mathbf{q}}\right)\det(\mathbf{F}_e) \tag{3.149}$$

Equation (3.149) represents the conservation of energy at the coarse scale in the intermediate configuration.

3.3.2 Second Law of Thermodynamics

Thermodynamics of irreversible processes (TIP) places a central focus on the concept of entropy as a state function and manner in which entropy may be generated. It is convenient to decompose the rate of change in entropy into a part associated with reversible equilibrium processes and a part due to irreversible processes

$$\dot{S} = \dot{S}^e + \dot{S}^i \tag{3.150}$$

where $\dot{S}^e$ is the rate that entropy that is provided to the system externally, and $\dot{S}^i$ is the rate at which entropy is generated within the system. The second law of thermodynamics dictates that the total change in entropy be greater than or equal to the entropy supplied externally to the system, i.e.

$$\dot{S}^i \geq 0 \tag{3.151}$$

where the equality must hold for purely reversible processes and the rate of internal entropy generation is nonnegative for any irreversible process. The rate at which entropy is added to a system that cannot exchange mass with its surroundings is given by

$$\dot{S}^e = \frac{Q_{input}}{T} \tag{3.152}$$

where Q_{input} is the rate at which heat is added to the system and T is the absolute system temperature at which heat is received. The total rate of change of entropy in the system is taken to be the volume integral of the product of mass density and specific entropy per unit mass, s, within the system, i.e.,

$$S = \int_\Omega \rho s \, d\Omega \tag{3.153}$$

which implies the existence of a continuously defined local specific entropy that is postulated to be a state function for the material. Applying the transport theorem to the time rate of change of (3.153), combining (3.152) and the expression for heat input to the system (cf. (3.136)), gives

$$\int_\Omega \rho \dot{s} \, d\Omega \geq \int_\Omega \frac{r}{T} d\Omega - \int_\Gamma \frac{\mathbf{q} \cdot \mathbf{n}}{T} d\Gamma \tag{3.154}$$

The system temperature, previously assumed uniform for the entire system, has been moved into the integral, implying that we will accommodate local temperature fluctuations so long as they do not present a perturbation "too far" from equilibrium. The surface integral on the right side of (3.154) is converted to a volume integral by the divergence theorem and expanded by chain rule, after which the strong form of the second law of thermodynamics is recovered (recognizing the weak form applies to arbitrary volumes), i.e.,

$$\rho\dot{s} \geq \frac{r}{T} - \frac{\vec{\nabla}\cdot\mathbf{q}}{T} + \mathbf{q}\cdot\frac{\vec{\nabla}T}{T^2} \tag{3.155}$$

The Helmholtz free energy per unit mass is defined as that portion of internal energy available to do work at constant temperature, i.e.,

$$\psi = u - Ts \tag{3.156}$$

After substitution of the fine scale internal energy of Eq. (3.133) converted to its current configuration form, the time derivative of free energy is

$$\dot{\psi} = \frac{1}{\rho}\left(\boldsymbol{\sigma} : \mathbf{d} + r - \vec{\nabla}\cdot\mathbf{q}\right) - \dot{T}s - T\dot{s} \tag{3.157}$$

where $\boldsymbol{\sigma}$ and $\mathbf{d}$ are the fine scale Cauchy stress and symmetric rate of deformation tensor, respectively. Equation (3.157) is substituted into (3.155) yielding the following form of the Clausius-Duhem inequality, valid for first order continua, i.e., absent second gradient (**G** = **0**)

$$\boldsymbol{\sigma} : \mathbf{d} - \left(\rho\dot{\psi} + \rho\dot{T}s\right) - \mathbf{q}\cdot\frac{\vec{\nabla}T}{T} \geq 0 \tag{3.158}$$

3.3.3 Discussion of Internal State Variable Theory

Internal State Variable (ISV) theory borrows from statistical mechanics (both equilibrium and non-equilibrium). In these areas, the essential thermodynamic state of a high degree-of-freedom, many body dynamical system is captured by a few state variables that are representative of the ensemble. Loosely, an ensemble is essentially an infinite collection of dynamical states that each have the same thermodynamic state. The kinematic coordinates of each particle in the many-bodied system, their rates, and the associated momenta are replaced by classic state variables (e.g., temperature, specific volume, etc.). Accordingly, the precise dynamical state remains

undefined even for an exact specification of the thermodynamic state (Hill, 1987). This relationship is developed at equilibrium for reversible processes for which the internal energy and state variables sufficiently characterize the state. It is generally agreed that these state variables can be directly influenced or controlled by external stimuli (Bridgman, 1941; Germain et al., 1983; Kestin, 1992).

Thermodynamics of irreversible processes (TIP) extends the notion that a state function represents the ensemble behavior to non-equilibrium processes by the introduction of additional internal state variables that characterize the irreversible rearrangement of the ensemble (Rice, 1971; Germain et al., 1983). In contrast to the classical state variables, the internal variables cannot be directly controlled and therefore cannot directly contribute to external mechanical work. Under specific conditions, a generally non-equilibrium irreversible process can be treated as a sequence of constrained equilibrium states. This argument is apparently subject to debate in the irreversible thermodynamics community; however, it has proven to be a useful foundation for modern constitutive theories (Rice, 1971; Kestin, 1992, 1993). The concept of constrained equilibrium can be imagined by virtually "freezing" the internal variables to take a "snapshot" of the state of a material at a particular time. The thermodynamic forces conjugate to the internal variables can be viewed as the constraints required to "lock in" the material at this constrained equilibrium state. One might now argue that a thermodynamic force is performing mechanical work to evolve the corresponding internal variable. As will be shown subsequently, this work is merely a partition of the macroscopic mechanical work that is irrecoverable. Thus, the total mechanical work is quantified by the classical state variables with the internal variables removing some of the energy available to do work. These details are important to the proposed development.

The sequence of constrained equilibrium states is referred to as the local accompanying process to the generally non-equilibrium irreversible process. Inherent in this approach is the assumption, or perhaps restriction, that the relaxation times characteristic of the evolution of internal state from one "snapshot" to the next are negligible when compared to the rate of change in the thermodynamic force. Kestin (1992) discusses this restriction of the formalism in that it results in infinite velocities of propagation of small disturbances. As suggested previously, for cases where

the rate of change of the external forces approaches that of the relaxation times for the internal state variables the "viscosity" of the non-linear thermodynamic process becomes non-trivial and the constrained equilibrium approach will break down. Extended irreversible thermodynamics approaches that incorporate additional fluxes of internal variables have been proposed to address such cases (Jou et al., 1988; Lebon et al., 1993; Serdyukov, 2004; Xia and Hanagud, 2007).

The postulation of a state function implies the existence of a representative volume that constitutes a thermodynamic system. The existence of an rRVE of material is often implicitly assumed in both experimental and computational research without due consideration. Stroeven et al. (2004) review several definitions of the minimum size of an rRVE. Among them, Ostoja-Starzewski (1998) requires that the considered volume is either a unit cell in a periodic material or contains a mathematically infinite set of microscale elements. More recently, the relationship between ergodicity, stationarity, and boundary conditions as they concern the attainment of rRVE for specific classes of boundary value problems has been thoroughly investigated (Ostoja-Starzewski, 2006). Pragmatically, Ostoja-Starzewski provides a means to estimate a reasonable size for the rRVE based on the convergence trend of the apparent stiffness behavior bounded by an upper estimate from a Dirichlet problem (essential boundary conditions) and lower estimate from the Neumann (natural boundary conditions) problem. Of course, the rRVE considered must be representative for all responses of interest, not only effective elastic stiffness. For example, the minimum rRVE size for capturing the homogenized damage-dependent elastic response is smaller than that required for representing the evolution of damage within the rRVE (Lacy et al., 1999). Alternatively, one can consider a statistical volume element (rSVE) and construct an ensemble average for the concerned behavior by repeatedly collecting observations (from simulation or experiment) over some number of realizations. McDowell (1997, 2005) has considered various cases involving evolution of microstructure and their implications for the size of the rRVE for each considered response function, clearly distinguishing the rRVE size between stationary (e.g., elastic stiffness of microstructure ensemble) and evolving cases (plastic deformation and damage).

3.3.4 Internal State Variable Theory for the Fine Scale

A conventional internal state variable theory is adopted for the constitutive response of evolving constituents at the fine scale, representative of even finer scale evolutionary processes (sub-fine scale). A typical development is presented here for the fine scale which comprises a classical first order Cauchy continuum. The formulation is presented in terms of the fine scale infinitesimal strain tensor decomposed into elastic and inelastic parts, $\varepsilon = \varepsilon^e + \varepsilon^{in}$, for clarity; however, the results are readily generalized to finite deformation occurring at the fine scale. In the subsequent subsection, the coarse scale version of ISV theory is developed under general finite deformations. Conventional ISV theory begins with the postulation that the Helmholtz free energy is a state function of the continuum state variables in addition to a set of *k* augmenting internal state variables (ISVs) of generalized displacement type, $\boldsymbol{\xi}^{(k)}$, i.e.,

$$\psi = \hat{\psi}(\boldsymbol{\varepsilon}^e, T, \boldsymbol{\xi}^{(k)}) = \hat{\psi}(\boldsymbol{\varepsilon}, \boldsymbol{\varepsilon}^{in}, T, \boldsymbol{\xi}^{(k)}) \tag{3.159}$$

None of the *k* ISVs should duplicate the inelastic strain, as this would present the potential for double counting of dissipation. Houlsby and Puzrin (cf. , 2006) formulate the theory with a set of completely general ISVs and only during implementation do they partition parts of the total strain. Their presentation of the theory is well aligned with that of Ziegler (1977), somewhat different from that presented here, which more closely follows that of Lemaitre and Chaboche (1990). All of these approaches result in the same fundamental theory; their differences elucidate the significance of ISV selection.

The total time rate of change in free energy is computed by the chain rule, i.e.,

$$\dot{\psi} = \frac{\partial \psi}{\partial \boldsymbol{\varepsilon}} : \dot{\boldsymbol{\varepsilon}} + \frac{\partial \psi}{\partial T}\dot{T} + \sum_{j=1}^{k} \frac{\partial \psi}{\partial \boldsymbol{\xi}^{(j)}} * \dot{\boldsymbol{\xi}}^{(j)} \tag{3.160}$$

where the * operator is used to denote the proper scalar product depending upon the tensoral character of each particular internal state variable. Upon substitution of Eqs. (3.159) and (3.160) into the second law Clausius-Duhem (CD) inequality and accounting for the additive decomposition of the small strain rate into elastic and plastic parts, the CD inequality is rewritten as

$$\boldsymbol{\sigma} : \dot{\boldsymbol{\varepsilon}}^{in} + \left(\boldsymbol{\sigma} - \rho \frac{\partial \psi}{\partial \boldsymbol{\varepsilon}^e} \right) : \dot{\boldsymbol{\varepsilon}}^e - \rho \left(s + \frac{\partial \psi}{\partial T} \right) \dot{T} - \left(\rho \frac{\partial \psi}{\partial \boldsymbol{\xi}^{(j)}} * \dot{\boldsymbol{\xi}}^{(j)} \right) - \mathbf{q} \cdot \frac{\vec{\nabla} T}{T} \geq 0 \qquad (3.161)$$

The summation over *j=1,2,…, k* internal state variables is implied. Under a reversible process the equality in Eq. (3.161) must hold. Considering the case of purely elastic and isothermal deformation under uniform temperature, it is clear that the local Cauchy stress must be determined by

$$\boldsymbol{\sigma} = \rho \frac{\partial \psi}{\partial \boldsymbol{\varepsilon}^e} \qquad (3.162)$$

Alternately, considering a uniform change in uniform temperature during which no mechanical (reversible or irreversible) deformation takes place,

$$s = -\frac{\partial \psi}{\partial T} \qquad (3.163)$$

which provides a continuum definition for specific entropy (per unit mass), namely, the negative rate of change in free energy with respect to temperature. The generalized thermodynamic forces, $\boldsymbol{\beta}$, conjugate to the internal state variables, are defined by logical extension of (3.162) and (3.163), i.e.

$$\boldsymbol{\beta}^{(j)} = \rho \frac{\partial \psi}{\partial \boldsymbol{\xi}^{(j)}} \qquad (3.164)$$

Some authors include a negative sign on the definition of $\boldsymbol{\beta}$ which bears no real consequence so long as the definition is consistently applied. However, the presence or absence of this negative sign does imply a particular point of view of the role of the conjugate pair in the rearrangement process. In the case adopted here, a positive force works against a positive evolution of an internal state variable to store elastic free energy within the microstructure. Equivalently, a negative force could be interpreted to resist further evolution of the ISV consistent with the idea of pinning the microstructure in a frozen equilibrium state. The former case helps to identify that energy stored locally rather than dissipated during inelastic evolution, whereas the latter is perhaps more consistent with the originating concept of constrained equilibrium.

These alternate views are in total physical and quantitative agreement, so long as the dissipation rate is expressed consistently. Substitution of (3.162) and (3.163) into the CD inequality (3.161) give

$$\boldsymbol{\sigma} : \dot{\boldsymbol{\varepsilon}}^{in} - \rho \frac{\partial \psi}{\partial \boldsymbol{\xi}^{(k)}} * \dot{\boldsymbol{\xi}}^{(k)} - \mathbf{q} \cdot \frac{\vec{\nabla} T}{T} \geq 0 \tag{3.165}$$

A stronger form of (3.165) is typically assumed,

$$\begin{aligned} \Phi_{mec} &= \boldsymbol{\sigma} : \dot{\boldsymbol{\varepsilon}}^{in} - \rho \frac{\partial \psi}{\partial \boldsymbol{\xi}^{(k)}} * \dot{\boldsymbol{\xi}}^{(k)} \geq 0 \\ \Phi_{thm} &= -\mathbf{q} \cdot \frac{\vec{\nabla} T}{T} \geq 0 \end{aligned} \tag{3.166}$$

This assertion regarding the separation of intrinsic (mechanical), Φ_{mec}, and thermal, Φ_{thm}, dissipation reflects the hypothesis that the dissipative mechanical response cannot cause heat to flow from cold regions to hot regions and that the *dissipation* of heat flow cannot reverse mechanical dissipative processes, e.g. *cause* mechanical healing. The first equation in (3.166) defines the rate of mechanical dissipation and demands that it be non-negative. The intrinsic mechanical dissipation, Φ_{mec}, is a quantity central to the multiscale ideas presented subsequently.

In addition to the Helmholtz free energy state function and associated ISVs, equations that define the kinetics of ISV evolution under irreversible processes are needed, i.e., $\dot{\boldsymbol{\xi}}^{(j)} = \mathbf{K}^{(j)}\left(\boldsymbol{\sigma}, T, \boldsymbol{\xi}^{(i)}\right)$. These relations can be postulated in any of a number of ways so long as they obey the governing equations outlined previously and are consistent with observed behavior. For a certain class of material behavior it can be asserted that evolution of each ISV depends only on its own conjugate force (Rice, 1971; Yang et al., 2006). A classic example is that the rate of slip on a particular slip plane depends only upon the resolved shear stress on that plane. This assertion gives rise to a normality structure of the evolution equations, such that they can be derived directly from a potential function. A *flow* potential in the form $\varphi = \hat{\varphi}\left(\boldsymbol{\sigma}, T, \boldsymbol{\xi}^{(k)}\right)$ governs the evolution rates via the relation $\dot{\xi}^{(j)} = \dfrac{\partial \varphi}{\partial \boldsymbol{\beta}^{(j)}}$. Each mechanism contributes independently to the flow potential such

that it can be constructed according to $\varphi = \sum_k \hat{\varphi}^{(k)}, \;\; \hat{\varphi}^{(k)} = \int_0^{\boldsymbol{\beta}^{(k)}} \dot{\xi}^{(k)} \, d\boldsymbol{\beta}^{(k)}$ (Yang et al., 2006). This is referred to as generalized normality and is consistent with the heuristic principle of maximal dissipation. A yield or flow surface (generally distinct from the potential) can be used to set a threshold below which inelastic kinematic evolutions do not occur. If the flow surface and the flow potential are one and the same then the evolution equations are considered associated; otherwise, they are considered non-associated (Abu Al-Rub and Voyiadjis, 2003). The framework of a flow potential (or combination of pseudo-potentials for various mechanisms) is a convenient, although inessential, format for the constitutive behavior. Alternatively, the kinetic equations for evolution of the internal state variables can be formed explicitly with (or without) coupling to the extent desired. The inconsistent terminology and application of flow potentials in the literature motivates a discussion on the relationships between microstructure evolution (e.g. dissipation, threshold surfaces) and force and flow potentials in Section 3.3.6.

Next we turn attention to an ISV theory suitable for the second gradient coarse scale description and implications of the scale invariance of dissipation.

3.3.5 Coarse Scale ISV Theory and Implications for Dissipation

The thermodynamic ingredients comprising ISV theory presented in the preceding two subsections are now addressed in the context of a scale transition. A primary assertion of this dissertation is that a multiscale approach must respect invariance of fundamental quantities related to the exchange of mass, momentum, and energy to the scale of observation of a given process. Regardless of whether a particular scale is useful for capturing precisely the kinematic details of a process, the partitions of energy into elastically recoverable, stored, and dissipated "bins" must match up across all scales for a particular physical region or system. The theory developed here arrives in a somewhat expected form, albeit slightly more cumbersome on account of the second gradient framework.

The coarse scale temperature is developed by adopting a simple volume averaging homogenization scheme; accordingly, $\overline{T} = \dfrac{1}{\Omega_{\mathrm{o}}^{x}} \int_{\Omega_{\mathrm{o}}^{x}} T \, d\Omega_{\mathrm{o}}^{x}$ and the coarse scale specific entropy is

defined likewise, i.e., $\overline{s} = \dfrac{1}{\overline{\rho}\Omega_{\mathrm{o}}^{x}}\int_{\Omega_{\mathrm{o}}^{x}} \rho s \, d\Omega_{\mathrm{o}}^{x}$, which results in the same total entropy at both the coarse and fine scales of representation over a particular rSVE. The coarse scale Helmholtz free energy is defined as

$$\overline{\psi} = \overline{u} - \overline{s}\overline{T} \tag{3.167}$$

The rate of change of free energy is obtained by differentiation with respect to time, i.e.,

$$\dot{\overline{\psi}} = \dot{\overline{u}} - \dot{\overline{s}}\overline{T} - \overline{s}\dot{\overline{T}} \tag{3.168}$$

We postulate that at the coarse scale, Helmholtz free energy is a function of the finite elastic strain, elastic part of second gradient strain, coarse scale temperature, and a set of coarse scale internal state variables and is cast in the coarse scale intermediate configuration as

$$\overline{\psi} = \overline{\psi}(\tilde{\mathbf{E}}^{e}, \tilde{\mathbf{\Gamma}}^{e}, \overline{T}, \overline{\xi}^{(j)}) \tag{3.169}$$

As will be discussed in detail subsequently, the set of coarse scale internal state variables is necessarily distinct from those introduced to represent material points at the fine scale. The rate of change of free energy is then expressed in terms of partial derivatives as

$$\dot{\overline{\psi}} = \frac{\partial \overline{\psi}}{\partial \tilde{\mathbf{E}}^{e}} : \tilde{\mathbf{D}}^{e} + \frac{\partial \overline{\psi}}{\partial \tilde{\mathbf{\Gamma}}^{e}} L_{v}(\tilde{\mathbf{\Gamma}}^{e}) + \frac{\partial \overline{\psi}}{\partial \overline{T}}\dot{\overline{T}} + \frac{\partial \overline{\psi}}{\partial \overline{\xi}^{(j)}} * L_{v}(\overline{\xi}^{(j)}) \tag{3.170}$$

This is substituted along with the coarse scale energy Eq. (3.149) into Eq. (3.168), which is rearranged to obtain

$$\begin{aligned}\tilde{\rho}\dot{\overline{s}}\overline{T} = {} & (\tilde{\mathbf{S}} - \tilde{\mathbf{S}}^{*}) : \tilde{\mathbf{D}} + \tilde{\mathbf{Q}} \vdots L_{v}(\tilde{\mathbf{\Gamma}}) + \left(\overline{r} - \vec{\nabla}\cdot\overline{\mathbf{q}}\right)\det(\mathbf{F}_{e}) \\ & - \left(\frac{\partial \overline{\psi}}{\partial \tilde{\mathbf{E}}^{e}} : \tilde{\mathbf{D}}^{e} + \frac{\partial \overline{\psi}}{\partial \tilde{\mathbf{\Gamma}}^{e}} L_{v}(\tilde{\mathbf{\Gamma}}^{e}) + \frac{\partial \overline{\psi}}{\partial \overline{T}}\dot{\overline{T}} + \frac{\partial \overline{\psi}}{\partial \overline{\xi}^{(j)}} * L_{v}(\overline{\xi}^{(j)}) \right) - \tilde{\rho}\dot{\overline{s}}\overline{T}\end{aligned} \tag{3.171}$$

Additive decompositions of $\tilde{\mathbf{D}}$ and the Lie derivative of the second order strain enable the rearrangement

$$\begin{aligned}\tilde{\rho}\dot{\overline{s}}\overline{T} = {} & (\tilde{\mathbf{S}} - \tilde{\mathbf{S}}^{*}) : \tilde{\mathbf{D}}^{in} + \tilde{\mathbf{Q}} \vdots L_{v}(\tilde{\mathbf{\Gamma}}^{in}) - \tilde{\rho}\frac{\partial \overline{\psi}}{\partial \overline{\xi}^{(j)}} * L_{v}(\overline{\xi}^{(j)}) \\ & + \left(\tilde{\mathbf{S}} - \tilde{\mathbf{S}}^{*} - \tilde{\rho}\frac{\partial \overline{\psi}}{\partial \tilde{\mathbf{E}}^{e}} \right) : \tilde{\mathbf{D}}^{e} + \left(\tilde{\mathbf{Q}} - \tilde{\rho}\frac{\partial \overline{\psi}}{\partial \tilde{\mathbf{\Gamma}}^{e}} \right) \vdots L_{v}(\tilde{\mathbf{\Gamma}}^{e}) - \left(\tilde{\rho}\overline{s} + \frac{\partial \overline{\psi}}{\partial \overline{T}} \right)\dot{\overline{T}} \\ & + \left(\overline{r} - \vec{\nabla}\cdot\overline{\mathbf{q}}\right)\det(\mathbf{F}^{e})\end{aligned} \tag{3.172}$$

Substitution of Eq. (3.172) into the second law of thermodynamics written at the coarse scale yields the following strong form of the coarse scale Clausius-Duhem inequality

$$\begin{aligned}&\left((\tilde{\mathbf{S}}-\tilde{\mathbf{S}}^{*})-\tilde{\rho}\frac{\partial\overline{\psi}}{\partial\tilde{\mathbf{E}}_{e}}\right):\tilde{\mathbf{D}}^{e}+\left(\tilde{\mathbf{Q}}-\tilde{\rho}\frac{\partial\overline{\psi}}{\partial\tilde{\mathbf{\Gamma}}^{e}}\right)\vdots L_{v}(\tilde{\mathbf{\Gamma}}^{e})-\left(\tilde{\rho}\overline{s}+\tilde{\rho}\frac{\partial\overline{\psi}}{\partial\overline{T}}\right)\dot{\overline{T}}\\&+(\tilde{\mathbf{S}}-\tilde{\mathbf{S}}^{*}):\tilde{\mathbf{D}}^{in}+\tilde{\mathbf{Q}}\vdots\mathbf{L}_{v}(\tilde{\mathbf{\Gamma}}^{in})-\tilde{\rho}\frac{\partial\overline{\psi}}{\partial\overline{\xi}^{(j)}}*L_{v}(\overline{\xi}^{(j)})\\&-\det(\mathbf{F}^{e})\left(\overline{\mathbf{q}}\cdot\frac{\vec{\nabla}\overline{T}}{\overline{T}}\right)\geq 0\end{aligned}\tag{3.173}$$

Under reversible isentropic processes the equality in Eq. (3.173) holds true, and therefore

$$\tilde{\mathbf{S}}=\tilde{\rho}\frac{\partial\overline{\psi}}{\partial\tilde{\mathbf{E}}^{e}}+\tilde{\mathbf{S}}^{*},\ \tilde{\mathbf{Q}}=\tilde{\rho}\frac{\partial\overline{\psi}}{\partial\tilde{\mathbf{\Gamma}}^{e}},\ \overline{s}=-\frac{\partial\overline{\psi}}{\partial\overline{T}}\tag{3.174}$$

After substitution back into Eq. (3.173) and separating mechanical and thermal dissipation, we arrive at

$$\begin{aligned}\overline{\Pi}_{mec}&=(\tilde{\mathbf{S}}-\tilde{\mathbf{S}}^{*}):\tilde{\mathbf{D}}^{in}+\tilde{\mathbf{Q}}\vdots L_{v}(\tilde{\mathbf{\Gamma}}^{in})-\tilde{\rho}\frac{\partial\overline{\psi}}{\partial\overline{\xi}^{(j)}}*L_{v}(\overline{\xi}^{(j)})\geq 0\\\overline{\Pi}_{thm}&=-\det(\mathbf{F}^{e})\left(\overline{\mathbf{q}}\cdot\frac{\vec{\nabla}\overline{T}}{\overline{T}}\right)\geq 0\end{aligned}\tag{3.175}$$

Substitution of Eqs. (3.168), (3.170), and (3.174) into the coarse scale first law Eq. (3.149) gives

$$(\tilde{\mathbf{S}}-\tilde{\mathbf{S}}^{*}):\tilde{\mathbf{D}}^{in}+\tilde{\mathbf{Q}}\vdots L_{v}(\tilde{\mathbf{\Gamma}}^{in})-\tilde{\rho}\frac{\partial\overline{\psi}}{\partial\overline{\xi}^{(j)}}*L_{v}(\overline{\xi}^{(j)})+\left(\overline{r}-\vec{\nabla}\cdot\overline{\mathbf{q}}\right)\det(\mathbf{F}^{e})-\tilde{\rho}\dot{\overline{s}}\overline{T}=0\tag{3.176}$$

The rate of change in coarse scale entropy is

$$\begin{aligned}\dot{\overline{s}}&=-\frac{d}{dt}\left(\frac{\partial\overline{\psi}}{\partial\overline{T}}\right)=-\frac{\partial^{2}\overline{\psi}}{\partial\overline{T}\partial\tilde{\mathbf{E}}^{e}}:\tilde{\mathbf{D}}^{e}-\frac{\partial^{2}\overline{\psi}}{\partial\overline{T}\partial\tilde{\mathbf{\Gamma}}^{e}}\vdots L_{v}(\tilde{\mathbf{\Gamma}}^{e})-\frac{\partial^{2}\overline{\psi}}{\partial\overline{T}^{2}}\dot{\overline{T}}-\frac{\partial^{2}\overline{\psi}}{\partial\overline{T}\partial\overline{\xi}^{(j)}}*L_{v}(\overline{\xi}^{(j)})\\&=-\frac{\partial\left(\tilde{\mathbf{S}}-\tilde{\mathbf{S}}^{*}\right)/\tilde{\rho}}{\partial\overline{T}}:\tilde{\mathbf{D}}^{e}-\frac{\partial\left(\tilde{\mathbf{Q}}/\tilde{\rho}\right)}{\partial\overline{T}}\vdots L_{v}(\tilde{\mathbf{\Gamma}}^{e})+\frac{\partial\overline{s}}{\partial\overline{T}}\dot{\overline{T}}-\frac{\partial\left(\overline{\beta}^{(j)}/\tilde{\rho}\right)}{\partial\overline{T}}*L_{v}(\overline{\xi}^{(j)})\end{aligned}\tag{3.177}$$

Substitution of the entropy rate into Eq. (3.176) and rearranging gives an expression that defines the rate at which the coarse scale temperature changes, i.e.,

$$\begin{aligned}\tilde{\rho}\overline{c}_v\dot{\overline{T}} = (\tilde{\mathbf{S}}-\tilde{\mathbf{S}}^*):\tilde{\mathbf{D}}^{in} + \tilde{\mathbf{Q}}\vdots L_v(\tilde{\mathbf{\Gamma}}^{in}) - \tilde{\rho}\frac{\partial\overline{\psi}}{\partial\overline{\xi}^{(j)}} * L_v(\overline{\xi}^{(j)}) \\ +\tilde{\rho}\overline{T}\left(\frac{\partial\left(\tilde{\mathbf{S}}-\tilde{\mathbf{S}}^*\right)\big/_{\tilde{\rho}}}{\partial\overline{T}}:\tilde{\mathbf{D}}^e + \frac{\partial\left(\tilde{\mathbf{Q}}\big/_{\tilde{\rho}}\right)}{\partial\overline{T}}\vdots L_v(\tilde{\mathbf{\Gamma}}^e) + \frac{\partial\left(\overline{\beta}^{(j)}\big/_{\tilde{\rho}}\right)}{\partial\overline{T}} * L_v(\overline{\xi}^{(j)})\right) \\ +\left(\overline{r}-\vec{\nabla}\cdot\overline{\mathbf{q}}\right)\det(\mathbf{F}^e)\end{aligned} \tag{3.178}$$

where the course scale specific heat $\overline{c}_v = \overline{T}\dfrac{\partial\overline{s}}{\partial\overline{T}}$ has been introduced. For comparison to Eq. (3.178) for classical Cauchy continuum, cf. Clayton (2005, Eq. 19). The first three terms represent the coarse scale dissipation, the next term contains the thermoelastic coupling and the final term gives the change in temperature due to heat transferred and generated within the rSVE.

A new principle of scale invariance of dissipation is introduced, i.e.,

$$\overline{\Pi}_{mec} = \frac{1}{\Omega^x_{\mathrm{o}}}\int_{\Omega^x_{\mathrm{o}}}\Phi_{mec}\,d\Omega^x_{\mathrm{o}} \tag{3.179}$$

which asserts that the total energy dissipated (as heat in accordance with Eq. (3.178)) for a fixed set of mass particles is invariant with respect to scale of observation. Note that thermal dissipation equivalence between scales, that is $\overline{\Pi}_{thm} = \dfrac{1}{\Omega^x_{\mathrm{o}}}\int_{\Omega^x_{\mathrm{o}}}\Phi_{thm}\,d\Omega^x_{\mathrm{o}}$, is handled naturally by homogenization of finer scale heat transfer processes. Upon substitution of the coarse scale dissipation rate Eq. (3.175) and fine scale dissipation rate Eq. (3.166) we obtain a fundamental assertion of this multiscale framework, namely

$$\begin{aligned}(\tilde{\mathbf{S}}-\tilde{\mathbf{S}}^*):\tilde{\mathbf{D}}^{in} + \tilde{\mathbf{Q}}\vdots L_v(\tilde{\mathbf{\Gamma}}^{in}) - \overline{\beta}^{(j)} * L_v(\overline{\xi}^{(j)}) \\ = \frac{1}{\Omega^x_{\mathrm{o}}}\int_{\Omega^x_{\mathrm{o}}}\boldsymbol{\sigma}:\mathbf{d}^{in}d\Omega^x_{\mathrm{o}} - \frac{1}{\Omega^x_{\mathrm{o}}}\int_{\Omega^x_{\mathrm{o}}}\beta^{(k)} * \dot{\xi}^{(k)}d\Omega^x_{\mathrm{o}}\end{aligned} \tag{3.180}$$

Rearranged,

$$\underbrace{\overline{\beta}^{(j)} * L_v(\overline{\xi}^{(j)})}_{\substack{\text{rate energy stored}\\ \text{at coarse scale}\\ \text{to evolve microstructure}}} = \underbrace{\left\langle\beta^{(k)} * \dot{\xi}^{(k)}\right\rangle}_{\substack{\text{rate energy stored in}\\ \text{sub fine-scale processes}}} + \underbrace{(\tilde{\mathbf{S}}-\tilde{\mathbf{S}}^*):\tilde{\mathbf{D}}^{in} + \tilde{\mathbf{Q}}\vdots L_v(\tilde{\mathbf{\Gamma}}^{in}) - \left\langle\boldsymbol{\sigma}:\mathbf{d}^{in}\right\rangle}_{\substack{\text{energy stored due to inelastic}\\ \text{incompatibility at fine scale}}} \tag{3.181}$$

Eq. (3.181), a completely new concept in material scale transitions, states that the rate energy is stored at the coarse scale is equal to the rate energy is stored below the fine scale averaged across

the rSVE plus additional energy stored due to inelastic incompatibilities registered by a difference in coarse scale and fine scale inelastic power.

Equipresence of ISVs at differing scales is invalid for two reasons. For one, the second term on the RHS of Eq. (3.181) introduces energy storage mechanisms that are only implicitly dependent on the evolution of ISVs that represent sub-fine scale processes. At a minimum, new ISVs must be introduced to capture the related fine scale processes at the coarse scale due to the latter three terms on the RHS of Eq. (3.181). Additionally, the first term on the RHS of Eq. (3.181) averages (or conceptually speaking, smears) the spatially variable storage of energy due to sub-fine scale processes. Carrying the full rSVE field of ISVs to represent sub-fine scale evolutionary processes to higher scales would be unnecessary and computationally unwieldy, since only the rSVE field average of the energy storage is important from a thermodynamic standpoint.

The nature of the selected ISVs and the form of the evolution kinetics may be similar at each scale; however, if the set of coarse scale ISVs are merely the volume average of finer scale ISVs, then we should question the importance of the particular scale transition within the overall hierarchy. That is, if there is no imbalance of inelastic work between the two scales, then there is insignificant heterogeneity occurring at the particular scale (last three terms) and one could make a larger transition in scales. In other words, heterogeneity engenders a statistical field of microstructure evolution and this character is particularly influenced by the last three terms on the RHS of Eq. (3.181). This hierarchical framework requires one to repeat the process of identifying kinematic variables and associated evolution kinetics at each scale transition. However, we now have principles to govern the relation of these fields.

3.3.6 Dissipation rate, force potential, and flow potentials

The notion of a *dissipation* potential is often confused with that of the flow potential. The concepts are summarized here and then illustrated in two simple examples which highlight the limitations of dissipation and flow potentials and the more broad role of dissipation in a multiscale approach. The purpose of this subsection is to demonstrate (1) the relationship of dissipation rate, force potential, and flow potentials, (2) the connection between threshold or yield functions and rate–independent evolution kinetics, (3) the breakdown of a connection between

dissipation and flow potentials for nonlinear hardening models. To this end, there is no significant departure from the work of Houlsby and Puzrin (2006); however, the concepts of deriving evolution kinetics from potential functions and the associated limitations are requisite for subsequent chapters.

First we define an intrinsic dissipation function of the inelastic strain rate and rates of state variables, which is equal to the actual mechanical dissipation of (3.166) for all time, i.e.,

$$\Phi \equiv \hat{\Phi}(\varepsilon, T, \dot{\varepsilon}^p, \dot{\xi}^{(k)}) = \Pi_{mec} \tag{3.182}$$

Note the distinction between the actual dissipation rate of (3.166) versus the dissipation function (3.182) which is a model hypersurface in the space of generalized internal state variable rates and which may have additional parameters, e.g., temperature. Only under certain circumstances can this hypersurface be used as a flow potential from which the conjugate generalized stress can be derived. First we define the "dissipative" generalized stresses as

$$\beta_d^{(k)} = -\frac{\partial \hat{\Phi}}{\partial \dot{\xi}^{(k)}}, \boldsymbol{\sigma}_d = \frac{\partial \hat{\Phi}}{\partial \dot{\boldsymbol{\varepsilon}}^{in}} \tag{3.183}$$

If the dissipation function is a homogeneous function of first order (in its arguments, i.e. rates), then by Euler's theorem,

$$\hat{\Phi} = \frac{\partial \hat{\Phi}}{\partial \dot{\boldsymbol{\varepsilon}}^{in}} * \dot{\boldsymbol{\varepsilon}}^{in} + \frac{\partial \hat{\Phi}}{\partial \dot{\xi}^{(k)}} * \dot{\xi}^{(k)} \tag{3.184}$$

and, in conjunction with (3.166) and (3.183), we conclude that

$$\begin{gathered} \boldsymbol{\sigma}_d : \dot{\boldsymbol{\varepsilon}}^{in} - \beta_d^{(k)} * \dot{\xi}^{(k)} = \boldsymbol{\sigma} : \dot{\boldsymbol{\varepsilon}}^{in} - \beta^{(k)} * \dot{\xi}^{(k)} \\ \left(\boldsymbol{\sigma}_d - \boldsymbol{\sigma}\right) : \dot{\boldsymbol{\varepsilon}}^{in} - \left(\beta_d^{(k)} - \beta^{(k)}\right) : \dot{\xi}^{(k)} = 0 \end{gathered} \tag{3.185}$$

Equation (3.185) is the basis of Ziegler's so called "orthogonality principle" (Ziegler, 1977), which gives rise to a principle of maximal dissipation under conditions of associated flow. However, the assertions

$$\begin{aligned} \boldsymbol{\sigma} = \boldsymbol{\sigma}_d &= \frac{\partial \hat{\Phi}}{\partial \dot{\boldsymbol{\varepsilon}}^{in}} \\ \beta^{(k)} = \beta_d^{(k)} &= -\frac{\partial \hat{\Phi}}{\partial \dot{\xi}^{(k)}} \end{aligned} \tag{3.186}$$

are in fact a stronger assumption than is strictly justified by (3.185), which would merely require that the difference between the true generalized stresses and the "dissipative" stresses derived from the dissipation function as a force potential is orthogonal to the rates of evolution of internal state variables. That is, any difference between the stress and dissipative stress does not participate in dissipation, thus justifying the common acceptance of (3.186). More importantly, in this case the dissipation function can serve as a force potential because it is first order homogeneous in the rates of inelastic strain and ISVs.

Inspection of the true dissipation (3.166) shows that the generalized stresses must be independent of the rates of evolution for the dissipation function to be first order homogeneous. In other words, the dissipative process must be rate independent to be described by a first order homogeneous dissipation function. Under generally rate dependent cases a variety of possibilities exist. If the dissipation function is homogeneous of order *n* then the dissipation function is a pseudo-potential that can be converted to a force potential. If the dissipation function is quasi-homogeneous, i.e., it consists of terms which are each homogeneous of a different order, then the conversion to a force potential is conducted in a straight forward manner term by term. However, if the function is non-homogenous then it may or may not be amenable to conversion to a force potential.

Derivation of the generalized stresses is not the chief benefit of obtaining a force potential from the dissipation function. The compelling motivation is that a true force potential can be transformed to a flow potential by Legendre-Fenchel transform, i.e.,

$$F(\sigma,\beta^{(k)}) = \sup_{\dot{\xi}^{(k)},\dot{\varepsilon}^{in}} \left\{ \sigma : \dot{\varepsilon}^{in} - \beta^{(k)} * \dot{\xi}^{(k)} - \hat{\Phi}(\dot{\varepsilon}^{in},\dot{\xi}^{(k)} \right\} \tag{3.187}$$

$$\dot{\varepsilon}^{in} = \frac{\partial F}{\partial \sigma},\ \dot{\xi}^{(k)} = \frac{\partial F}{\partial \beta^{(k)}} \tag{3.188}$$

where temperature dependence has been omitted for simplicity.

Therefore, under particular circumstances, an analysis of the dissipation of an irreversible process can directly provide the evolution equations of the internal state variables. However, in practice it seems as though the requirements under which the dissipation will adhere to such mathematical

analysis restrict the nature of the physical phenomena that can be included. Houlsby and Puzrin have put together a suite of models based on this "hyperplasticity" framework that cover a broad range of material behaviors. For our purposes a quick exploration of two simple examples will shed light on the limitations and at the same time reinforce the significance of dissipation, force and flow potentials in the context of irreversible behavior. In many cases evolution equations are derived from a pseudo flow potential, which is not a true flow potential if it is not the Fenchel dual of the force potential.

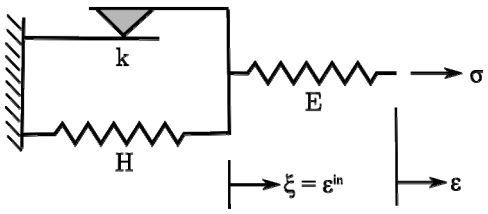

Figure 9. Schematic of a linear kinematic hardening mechanism.

Consider the following example taken directly from Houlsby and Puzrin (2006) and based on the mechanism shown in Figure 9. The mechanism consists of a single internal state variable, inelastic strain ε^{in}. Although in general we do not advocate use of inelastic strain as a state variable, it is appropriate for this particular rheological model because it describes the deformation of the spring at left in the mechanism of Figure 9. The Helmholtz free energy function for this system is

$$\psi = \frac{1}{2}E(\varepsilon - \xi)^2 + \frac{1}{2}H\xi^2 \quad , \quad \xi = \varepsilon^{in} \tag{3.189}$$

We define the backstress, $\chi = H\xi$. The generalized stresses are derived from the free energy function

$$\begin{aligned} \sigma &= \frac{\partial \psi}{\partial \varepsilon} = E(\varepsilon - \xi) \\ \beta &= \frac{\partial \psi}{\partial \xi} = -(\sigma - \chi) \end{aligned} \tag{3.190}$$

The mechanical dissipation rate is

$$\Pi_{mec} = (\sigma - \chi)\dot{\xi} \tag{3.191}$$

and is expressed in terms of system parameters by the dissipation function

$$\hat{\Phi}(\dot{\xi}) = k\left|\dot{\xi}\right| \; \forall \, \dot{\xi} \neq 0 \tag{3.192}$$

The dissipation function is first order homogeneous in $\dot{\xi}$ and therefore acts as a potential for the dissipative generalized stress, i.e.,

$$\beta^d = -\frac{\partial \hat{\Phi}}{\partial \dot{\xi}} = -k\,\mathrm{sgn}(\dot{\xi}) \tag{3.193}$$

The rate of mechanical dissipation (3.191) must be equivalent to the dissipation function (3.192) for all non-zero values of the ISV rate, i.e.,

$$\Pi = \frac{\partial \hat{\Phi}}{\partial \dot{\xi}}\dot{\xi} = -\beta^d \dot{\xi} = (\sigma - \chi)\dot{\xi} \tag{3.194}$$

Equations (3.193) and (3.194) provide the following relationships:

$$\begin{aligned} \beta^d &= -(\sigma - \chi) \\ k &= \left|\sigma - \chi\right| \forall \, \dot{\xi} \neq 0 \end{aligned} \tag{3.195}$$

Note that, in this case, the backstress, χ, introduced as a phenomenologically motivated modeling convenience, is not a thermodynamic generalized stress. Rather, the difference between the stress and the backstress (overstress) is the generalized stress conjugate to the ISV. Again, in this case the single ISV is coincident with the inelastic portion of strain; however, in general one should avoid reintroducing the inelastic portion of strain as an additional ISV because it is kinematically redundant.

In terms of convex analysis, the dissipation function which acts as a force potential is the support function dual to the indicator function of the elastic or reversible region in the space of

generalized stresses. The indicator function takes on a value of zero within the space of reversible deformation, expressed as the set R in (3.196), and infinity outside this region.

$$\begin{aligned} R &= \left\{ -\beta^d \mid \left\langle -\beta^d, \dot{\xi} \right\rangle \leq k \left| \dot{\xi} \right|, \forall\, \dot{\xi} \right\} \\ &= \left\{ (\sigma - \chi) \mid (\sigma - \chi)\, \dot{\xi} \leq k \left| \dot{\xi} \right|, \forall\, \dot{\xi} \right\} \end{aligned} \tag{3.196}$$

The gauge function of the reversible region is the smallest positive factor by which the set of reversible stresses can be scaled such that the set still contains β^d; it defines the distance from a point in stress space to the threshold of reversible behavior, i.e.,

$$\begin{aligned} \gamma_{R}(\beta^d) &= \sup_{\dot{\xi} \neq 0} \frac{\left\langle -\beta^d, \dot{\xi} \right\rangle}{\hat{\Phi}(\dot{\xi})} \\ &= \frac{\left| \sigma - \chi \right|}{k} \end{aligned} \tag{3.197}$$

Intuitively, the gauge function is related to the yield function; accordingly, Houlsby and Puzrin define a canonical yield function as

$$\begin{aligned} \overline{f}(\beta^d) &\equiv \gamma(\beta^d) - 1 \\ &= \frac{\left| \sigma - \chi \right|}{k} - 1 \end{aligned} \tag{3.198}$$

The yield function is set equal to zero to define the yield surface and finally, the flow potential is obtained as the indicator function of the region of reversible behavior, which is computed here by converting the canonical yield function to a proper indicator function

$$I_{R}(\beta^d) = \begin{Bmatrix} 0, \beta^d \in R \\ \infty, \beta^d \notin R \end{Bmatrix} \tag{3.199}$$

and

$$F\left(\beta^d\right) = I_{R}(\beta^d) = I_{[-\infty,0]}\, \overline{f}(\beta^d) \tag{3.200}$$

From which the evolution equations are derived as the normal cone on the threshold surface, i.e.,

$$\begin{aligned} \dot{\xi} &= \partial F = N_{R}(\beta^d) = \lambda \partial \overline{f}(\beta^d) \\ &= \frac{\lambda}{k} \operatorname{sgn}(\sigma - \chi) \end{aligned} \tag{3.201}$$

From the Kuhn-Tucker consistency condition which assures that the behavior remains on or within the threshold surface in the case of rate-independent inelastic response, we write

$$\frac{\partial \bar{f}}{\partial \beta^d}\dot{\beta}^d = 0 = \frac{\mathrm{sgn}(\sigma - \chi)}{k}(\dot{\sigma} - \dot{\chi}) \tag{3.202}$$

Substitution of the stress and backstress from (3.190) and solving for λ gives

$$\lambda = \dot{\varepsilon}\frac{kE}{E+H}\mathrm{sgn}(\sigma - \chi) \tag{3.203}$$

Finally the constitutive relations are

$$\begin{aligned} \sigma &= E(\varepsilon - \xi) \\ \chi &= H\xi \\ \beta &= -(\sigma - \chi) \\ \dot{\xi} &= \dot{\varepsilon}\left(\frac{E}{E+H}\right)\mathrm{sgn}(\sigma - \chi) \end{aligned} \tag{3.204}$$

Through this example we have explored the significance and relationship between the dissipation rate, and force and flow potentials. In this case, focus was placed on a conventional simple linear kinematic hardening model.

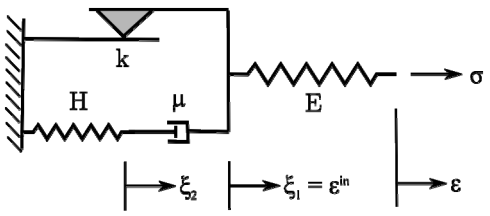

Figure 10. Schematic of a mechanism for rate-dependent kinematic hardening.

Now consider a model for rate dependent kinematic hardening based on the mechanical system shown in Figure 10. In this case there are two internal state variables, namely, the inelastic

component of strain and an additional independent displacement-type internal variable. The Helmholtz free energy is expressed as

$$\psi(\varepsilon,\xi_1,\xi_2) = \frac{1}{2}E(\varepsilon-\xi_1)^2 + \frac{1}{2}H\xi_2^2 \tag{3.205}$$

and the generalized stresses are computed as

$$\begin{aligned} \sigma &= \frac{\partial\psi}{\partial\varepsilon} = E(\varepsilon-\xi_1) \\ \beta_1 &= \frac{\partial\psi}{\partial\xi_1} = -\sigma \\ \beta_2 &= \frac{\partial\psi}{\partial\xi_2} = H\xi_2 \end{aligned} \tag{3.206}$$

The dissipation rate can be expressed as $\Pi_{mec} = -\beta_1\dot{\xi}_1 - \beta_2\dot{\xi}_2$, or equivalently,

$$\Pi_{mec} = \sigma\dot{\varepsilon}^{in} - \beta_2\dot{\xi}_2 \tag{3.207}$$

Whether or not we recognize the inelastic portion of total strain as one of the internal variables at the outset, the results are identical so long as we treat the ISV appropriately. The dissipation function,

$$\hat{\Phi} = k\left|\dot{\xi}_1\right| + \mu(\dot{\xi}_1 - \dot{\xi}_2)^2 \tag{3.208}$$

contains two terms, the first is homogeneous of order one in the rates and the second is homogeneous of order two in rates. In this case the dissipation function is not a true potential, but rather a pseudo potential. The form of the dissipation function implies two things: (1) a yield or threshold surface exists for at least one of the internal state variables, (2) the irreversible behavior is rate dependent. Reconciliation of these two points will require a “non-associated” flow rule, i.e., the flow potential will differ from the yield function by an additional term.

In this case, $\hat{\Phi}$, is pseudo-homogeneous. A true force potential can be computed from a pseudo homogeneous function by

$$\tilde{\Phi} = \sum_{k=1}^{N}\frac{1}{n_k}\hat{\Phi}_k \tag{3.209}$$

where N is the number of terms in the dissipation function, $\hat{\Phi}_k$ is the k[th] term in the dissipation function, and n_k is the order of homogeneity of the k[th] term, or for a generally non-homogeneous dissipation function,i.e.,

$$\tilde{\Phi} = \int_{-\infty}^{0} \hat{\Phi}\left(e^{x}\dot{\xi}_j\right)dx \tag{3.210}$$

For the rate-dependent kinematic hardening model,

$$\tilde{\Phi} = k\left|\dot{\xi}_1\right| + \frac{\mu}{2}(\dot{\xi}_1 - \dot{\xi}_2)^2 \tag{3.211}$$

The dissipative generalized stresses are derived from the flow potential (3.211),

$$\begin{aligned} \beta_1^d &= -\frac{\partial\Phi}{\partial\dot{\xi}_1} = -k\,\mathrm{sgn}(\dot{\xi}_1) - \mu(\dot{\xi}_1 - \dot{\xi}_2) \\ \beta_2^d &= -\frac{\partial\Phi}{\partial\dot{\xi}_2} = \mu(\dot{\xi}_1 - \dot{\xi}_2) \end{aligned} \tag{3.212}$$

Ziegler's orthogonality condition implies,

$$\begin{aligned} -\beta_1 &= \sigma = k\,\mathrm{sgn}(\dot{\xi}_1) + \mu(\dot{\xi}_1 - \dot{\xi}_2) \\ \beta_2 &= H\xi_2 = \mu(\dot{\xi}_1 - \dot{\xi}_2) = \sigma - k\,\mathrm{sgn}(\dot{\xi}_1) \end{aligned} \tag{3.213}$$

Which is easily confirmed by inspection of Figure 10. Following the previous example, the flow potential is computed by Legendre-Fenchel transform

$$\begin{aligned} F(\beta_1,\beta_2) &= \sup_{\dot{\xi}_1,\dot{\xi}_2}\{-\beta_1\dot{\xi}_1 - \beta_2\dot{\xi}_2 - \tilde{\Phi}(\dot{\xi}_1,\dot{\xi}_2)\} = \\ F(\sigma,\beta_2) &= \sup_{\dot{\varepsilon}^{in},\dot{\xi}_2}\{\sigma\dot{\varepsilon}^{in} - \beta_2\dot{\xi}_2 - k\left|\dot{\xi}_1\right| - \frac{\mu}{2}(\dot{\xi}_1 - \dot{\xi}_2)^2\} \end{aligned} \tag{3.214}$$

Noting that $\frac{\beta_2}{2}(\dot{\xi}_1 - \dot{\xi}_2) = \frac{\beta_2^2}{2\mu}$ and therefore $\frac{\mu}{2}(\dot{\xi}_1 - \dot{\xi}_2)^2 = \beta_2\dot{\xi}_1 - \beta_2\dot{\xi}_2 - \frac{\beta_2^2}{2\mu}$, (3.214) becomes

$$\begin{aligned} F(\sigma,\beta_2) &= \sup_{\dot{\varepsilon}^{in},\dot{\xi}_2}\{\left(\sigma - \beta_2 - k\,\mathrm{sgn}(\dot{\xi}_1)\right)\dot{\xi}_1 + \frac{\beta_2^2}{2\mu}\} \\ &= \left(\left|\sigma - \beta_2\right| - k\right)\lambda + \frac{\beta_2^2}{2\mu} \end{aligned} \tag{3.215}$$

The evolution equations are derived as

$$\begin{aligned}\dot{\xi}_1 &= \frac{\partial F}{\partial \sigma} = \operatorname{sgn}(\sigma - \beta_2)\lambda \Rightarrow \lambda = \left|\dot{\xi}_1\right| \\ \dot{\xi}_2 &= -\frac{\partial F}{\partial \beta_2} = \operatorname{sgn}(\sigma - \beta_2)\lambda - \frac{\beta_2}{\mu} = \dot{\xi}_1 - \frac{\sigma - k\operatorname{sgn}(\dot{\xi}_1)}{\mu}\end{aligned} \tag{3.216}$$

Equations (3.206) and (3.216) define the constitutive response for the rate dependent linear kinematic hardening case. Finally, we eliminate the rate dependence of the previous model by normalizing the viscosity by the magnitude of the inelastic strain rate,

$$\mu = \frac{H}{\gamma\lambda} \tag{3.217}$$

After substitution of this "pseudo-viscosity" relationship the rate independent constitutive equations are:

$$\begin{aligned}\sigma &= E(\varepsilon - \xi_1) \\ \chi &= \beta_2 = H\xi_2 \\ \dot{\xi}_1 &= \lambda\operatorname{sgn}(\sigma - \chi) \\ \dot{\xi}_2 &= \dot{\xi}_1 - \tfrac{\gamma}{H}\chi\left|\dot{\xi}_1\right|\end{aligned} \tag{3.218}$$

After some simple substitutions we determine that the backstress, χ, evolves according to

$$\dot{\chi} = H\dot{\xi}_1 - \gamma\,\chi\left|\dot{\xi}_1\right| \tag{3.219}$$

which compares directly to fading memory nonlinear kinematic hardening models (Lemaitre and Chaboche, 1990). Notice that the second term in the evolution equation for backstress represents the so-called fading memory effect. From a hyperplasticity framework the equations for a rate dependent kinematic hardening model were derived and then transformed to nonlinear rate independent kinematic hardening. However, one could not derive (3.219) from the dissipation function (3.208) if the substitution (3.217) were performed prior to converting the force potential to a flow potential. The now rate-independent dissipation function becomes

$$k\left|\dot{\xi}_1\right| + \frac{H(\dot{\xi}_1 - \dot{\xi}_2)^2}{\gamma\dot{\xi}_1^2} \tag{3.220}$$

which is not suitable as a force potential or pseudo-potential and therefore cannot be converted into a flow potential by Legendre-Fenchel transform. We can go from an *ad hoc* flow pseudo-potential to a dissipation function, but the interconvertability is not present with this type of

behavior. Models such as the fading memory nonlinear kinematic hardening model are relatively simple and powerful; however, they are not easily treated by strict adherence to the concept of flow and force potentials. In moving forward we focus on the analysis of dissipation across scales but, recognizing certain limitations, do not necessarily adhere to a framework of strict potentials. This does not imply a restriction to associated or non-associated evolution equations which, as stated, may be derived from assumed pseudo-potentials or simply defined as desired.

3.4 Summary of Chapter

A theoretical framework for the hierarchical multiscale modeling of inelastic response of heterogeneous materials has been presented in this chapter. The second gradient is used as a nonlocal kinematic link between the response of a material point at the coarse scale and the response of a neighborhood of material points at the fine scale. Establishing kinematic consistency between these scales results in new constraints that must be imposed upon the fine scale solution. In particular internal constraints are required to ensure the mean fluctuation field vanishes. Body forces implied by such internal constraints are addressed in the definition of coarse scale stresses developed in Section 3.2. The numerical implementation of internal constraints on the fluctuation field and the consequences of not including them appropriately are addressed in Chapter 4.

A new principle of scale invariance of dissipation has been introduced in order to assure that the thermodynamic framework adopted at the coarse scale is physically consistent with the evolutionary processes observed at finer scales. An ISV theory for modeling irreversible microstructure evolution is employed at the fine scale and extended to accommodate higher order kinematics at the coarse scale. Specific details of the evolution kinetics for this constitutive framework are necessarily application specific and, accordingly, are not stipulated within this Chapter. Such details are discussed in Chapters 5-7.

It is intended that the presented framework be used to develop second gradient constitutive models which reflect the nature of the underlying heterogeneous evolutionary processes in a hierarchically homogenized manner. To this end, Chapter 4 provides details on conducting

simulations of microstructural rSVEs at the fine scale, while Chapter 5 presents the implementation of the second gradient continuum and constitutive relations at the coarse scale.

CHAPTER IV

DIRECT SIMULATION OF FINE SCALE RESPONSE

Direct simulation of microstructure response has become commonplace following the rise of computational power. Microstructure simulations are becoming viable tools for providing quantitative insight to behavior previously only addressed through experiment. While physical experiments remain the vital link to reality, increase in fidelity of microstructure models allows the experimental burden to be shifted to testing of new theory and validation of computational models. Microstructure models facilitate direct assessments of the sensitivity of response to specific microstructure parameters (e.g. morphology), enable rapid development of new theories regarding, for example, competing evolutionary mechanisms, and offer more quantitative information than an experiment. Perhaps lagging the growth in the capability of microstructure models, is their realized utility in multiscale modeling due in part because they have not been properly coupled through scale transitioning physical principles such as the framework presented in Chapter 3.

This chapter is an overview of direct numerical simulation of fine scale response by finite element analysis of referential volume elements of material microstructure. The first section reviews various methods for constructing a rSVE suitable for finite element simulation. An efficient method for numerical implementation of the fine scale boundary conditions presented in Chapter 3 is detailed in Section 4.2. Certain aspects of these boundary conditions reflect a new contribution to microstructure scale simulations. The multiscale framework presented in Chapter 3 depends upon the notion of an intermediate configuration. Direct computation of an intermediate configuration and subsequent post-processing to calculate coarse scale variables from the fine scale simulation results are presented in Sections 4.4 and 4.4.1, respectively. Several examples are given in Section 4.5 accompanied by a discussion about observed microstructural evolution in the context of the multiscale framework. Section 4.6 addresses the

influence of rSVE construction technique, rSVE size, and boundary conditions on the coarse scale response in a statistical sense.

4.1 Techniques for construction of a rSVE

Several techniques for construction of an rSVE of material microstructure have been developed. This section gives a non comprehensive overview intended to show the range in both the methods and fidelity of microstructure model. While diagrams and examples are given in two dimensions, all of these approaches are amenable to fully three dimensional implementation.

4.1.1 Image Preprocessing and Analysis

Examples for many of the techniques described in this section will be based on a micrograph of uranium-oxide (UO_2) from Une et al. (2001). From this micrograph, shown in Figure 11, significant porosity is evident. The volume fraction of porosity for UO_2 in the state captured by the micrograph is reported to be 17.5%. This porosity is partly attributed to the material processing of UO_2 for nuclear fuel pellets and partly to the nucleation and growth of gas bubbles as a byproduct of the nuclear fission reaction for irradiated (used) nuclear fuels. Prior to applying various fine scale modeling techniques discussed in this section, a series of image analysis steps were applied to the original micrograph in order to emphasize the porosity and render a single black and white image to serve as a common starting point for the rSVE construction techniques discussed subsequently. The purpose of this section is to document the image analysis steps used in establishing the final example image.

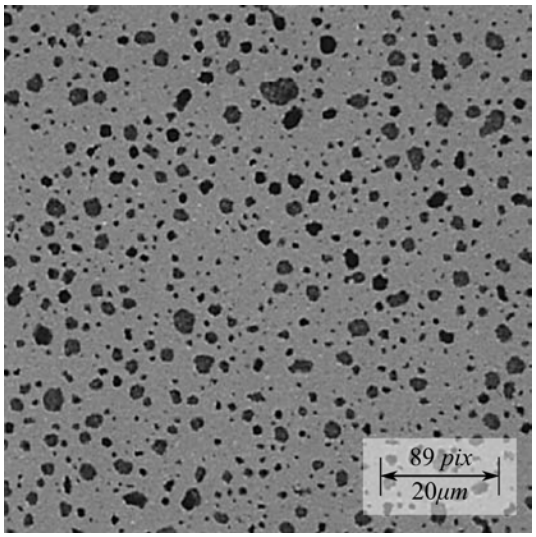

Figure 11. Micrograph of UO_2 from Une et al., 2001. Dark regions indicate porosity.

All image manipulation was done in python using the Python Imaging Library (PIL) (Lundh, 2005), Numpy modules, and additional custom modules as necessary. The image size of the micrograph in Figure 11is 401 x 401 pixels. Based on a length scale reported in Une et al. (2001) this corresponds to a physical size of 90μm x 90μm. However, for convenience the pixel size is asserted to be 1μm x 1μm so that the effective physical size of this micrograph is 401μm x 401μm in the examples of subsequent subsections. In the original truecolor image, each pixel is associated with a point in a red (r), green (g), and blue (b) color space with the coordinates (r,g,b) taking on integer values on the interval [0,255]. Accordingly, there are over 16 million possible unique colors. The original pixel values were converted to luminance (grayscale) values according to the ITU-R 601-2 luma transform $Lum = (^{299}/_{1000})\,r + (^{587}/_{1000})\,g + (^{184}/_{1000})\,b$, compressing the total color space to 256. This grayscale image was then normalized by computing the histogram of pixel luminance values removing 5% of the lightest and darkest values from the histogram and mapping the original values such that the lightest and darkest remaining pixels correspond to luminance values of 255 and 0, respectively. The resulting image is shown in Figure 13A.

Next, the image is filtered by assigning the value of each pixel to be the median value of the pixels in a 5 x 5 pixel grid centered on the pixel in question in order to achieve a smoother image as shown in Figure 13B. Then, the pixel luminance values were converted to binary by assigning all pixels with a luminance below a cutoff threshold to be 0 and those above to be 1. This threshold value was selected from analysis of the histogram of pixel luminance values. The histogram at the top of Figure 12 exhibits superposition of three distributions: (left) a normal distribution centered on mean pore pixel values, (right) a normal distribution centered on the mean solid pixel values and (center) uniform random noise. There are three common methods for selecting a threshold value to discriminate features of an image, viz. (1) adjusting by trial and error until the original grayscale image seems similar in features to the black and white image, (2) finding the location of a minimum between feature modes in the pixel luminance histogram, and (3) using the Otsu method which maximizes the interclass variance ratio of pixel luminance values (Otsu, 1979; Wojnar et al., 2004). Method (1) is a 'supervised' method, thus subjected to operator bias and is not reliably repeatable even for the same operator. Method (2) is sensitive to error (i.e. local minima and non-uniqueness) for images with uniformly distributed noise between feature peaks in the histogram. The Otsu method is a quantitative, unsupervised, and repeatable method that will uniquely define a threshold luminance level for discrimination of features exhibiting peaks in the histogram. The pixel luminance histogram and ratio of pore pixel variance to total image variance are shown in the top and bottom, respectively, of Figure 12. The Otsu method selects a threshold luminance value (131) that maximizes this interclass variance and is indicated in Figure 12 as a triangle.

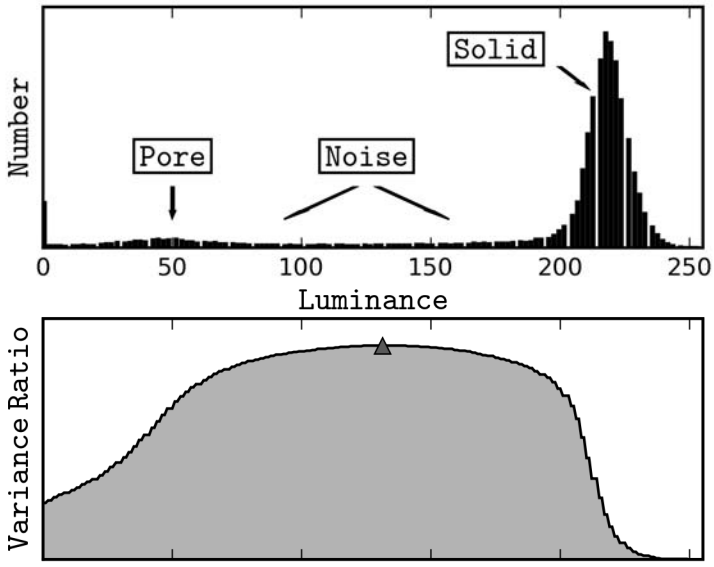

Figure 12. Luminance histogram and interclass variance ratio for image "B".

This threshold operation could be generalized to identify N distinct phases for micrographs where phases are distinguishable by color values. In theory N must be less than 256 for a grayscale image; however, in practice the limit will be dictated by the relative magnitude of noise in the image when compared to contrast between luma associated with a particular phase. Figure 13C shows the resulting black and white image where pores are identified by black pixels and solid material by white pixels.

There are a number of small features (pores) that would cause excessively small finite element size during subsequent mesh generation, so, for convenience, all pores smaller than a particular size ($20\mu m^2$) were identified and removed. This operation involved identifying connected clusters of pixels that have values corresponding to porosity (black) using the Hoshen-Kopelman algorithm. The Hoshen-Kopelman algorithm essentially scans the image assigning potentially non-unique labels to pixels that comprise contiguous regions and then applies a label conflict-resolution logic to assign unique labels to connected clusters (Hoshen and Kopelman, 1976; Babalievski, 1998; Hoshen, 1999). The image resulting from removing small features is referred to subsequently as the "processed image" and is shown in Figure 13D.

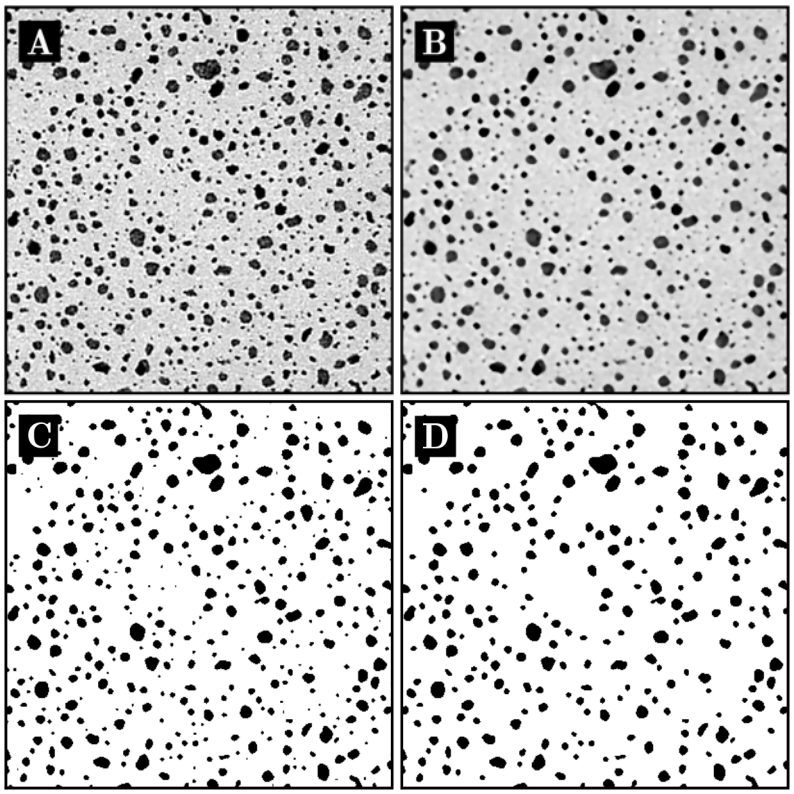

Figure 13. A comparison of example micrograph at various stages of image processing.

At this point, we can compare the results of image analysis to those reported by Une, et al. (2001) for UO_2 and discuss various sources of error. First, the area fraction of voids in image C is 13.1% and in image D is 12.0%, as compared with 17.5% reported by Une, et al. It is known that for randomly distributed features, the feature volume fraction is expected to be equal to the area fraction on a random plane intersecting that volume. In this case the values are representative of detectable porosity. The value reported by Une, et al. is based on image analysis of the original micrograph; however, the techniques employed are not discussed. The differences between the two porosities are presumably largely due to differences in the two techniques and it is not clear which is more accurate. However, both values omit pores that are smaller than the resolution of

the image. That is, based on measured and theoretical mass densities, Une et al. report a total porosity near 21%.

Une et al. also report a number density of pores by size classification per *area* of microstructure. By approximating the pores as circles in the micrograph, a similar distribution was constructed for the processed image (Figure 13D) and plotted against that of Une, et al. for comparison in Figure 14. Note that within this plot, the length scale used is consistent with that reported in Une, et al., rather than the one adopted elsewhere in this section. From this plot it is evident that the pore size distribution is similar for pore sizes beyond the threshold size removed in this work (which would have an effective size of 1.13). It is not imperative to subsequent sections that the image be a *precise* representation of UO_2. Subsequent simulations are not directly representative of uranium-oxide, rather a fictitious porous material with local properties that have been selected to highlight aspects of the multiscale framework. The comparison is made here only to demonstrate that the resulting image is a *reasonable* representation of porosity in two dimensions. In an actual multiscale study of this particular material, the differences between experimentally determined porosity and pore size distributions would lead to the introduction of a finer scale, i.e. scale 2. At this finer scale the influence of porosity finer than the selected cutoff size would be addressed.

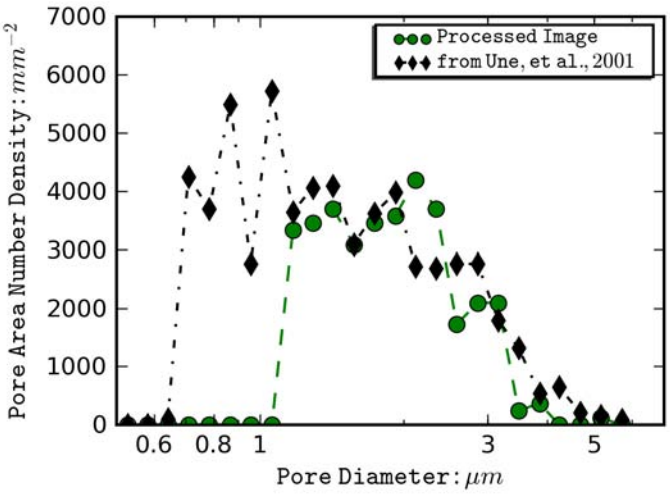

Figure 14. Comparison of pore size distribution to Une et al. (2001). Pore size distribution of processed image (green circles) reflects the removal of features smaller than the cutoff size.

In general, three-dimensional information on the distributions of heterogeneity in microstructure cannot be precisely indentified from a single two dimensional image. There are methods for converting two-dimensional distributions to pseudo three-dimensional distributions based on assumptions of the form of the feature distribution. For example, the Scheil-Saltykov method (Exner, 2004; Gegner, 2006) can be used to convert the feature (e.g., pore or inclusion) size distribution obtained in two-dimensions to what would be expected in three-dimensions assuming a lognormal distribution of spherical features. It is noted that, in general, the geometry, and consequently, response of real three-dimensional microstructure cannot be directly obtained from a single two-dimensional image. For the purposes of this section, it is not imperative to precisely represent the three-dimensional microstructure; it is sufficient to demonstrate the techniques in two dimensions recognizing that the approaches can be extended to three dimensions.

4.1.2 Unit Cell of Idealized Morphology

The simplest method for constructing a rSVE of microstructure is to idealize the microstructure morphology into a unit cell that consists of one or more simple geometric entities. The concept is straightforward such that an example is better than a detailed explanation. Assume that one wants to identify constants of Gurson's model from an analysis of porous microstructure. An idealized unit cell model could be constructed such that a unit cell consisting of a single pore is used to represent the entire microstructure as shown in Figure 15. In this manner, the unit cell implies an array of identical heterogeneous features whose statistical description of real materials is poor, as every particle possesses the same nearest neighbor distance (r_n) and particle size ($2a, 2b$). The unit cell can be constructed from statistical information obtained by microscopy or other methods, but is limited to reflecting distribution averages. For example, the void size and nearest neighbor spacing can be selected to obtain the mean area (or volume) fraction of porosity identified by microscopy. The geometry is readily discretized into a computational mesh suitable for finite element simulation.

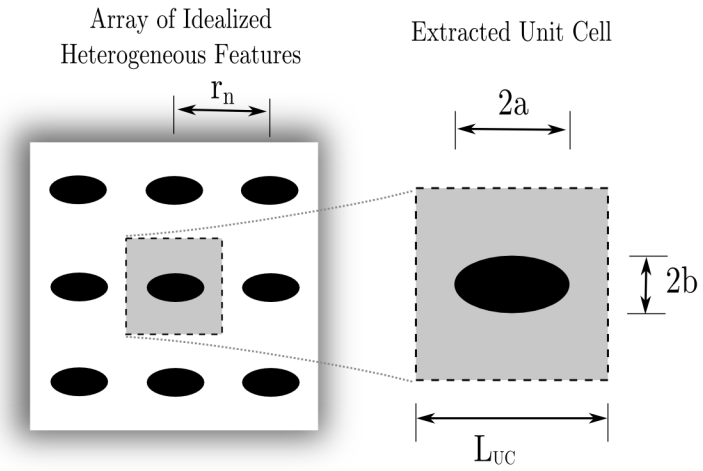

Figure 15. Example of a unit cell: ellipsoidal void in homogeneous matrix.

Several recent works have used variations of this idealized approach to study, for example, the effect of different shapes of inclusions and voids on the driving force of fatigue crack growth (Gall et al., 2000a; Gall et al., 2001), three dimensional deformation of inclusions and crack generation (Yu et al., 2008), and void growth and coalescence in porous ductile metals (Siad et al., 2008). This approach is particularly useful for illustrating theoretical models without the distraction of more complex behavior and interaction. Likewise, the unit cell is valuable in establishing connections or improving upon models developed from analytical micromechanics concepts which typically employ the same level of idealization (Gurson, 1977). Note that the fine and coarse scale behavior of a unit cell with doubly periodic boundary conditions is identical to the response of a periodic array of multiple unit cells (such as shown on the left side of Figure 15) under first-order boundary conditions, i.e., no coarse scale second gradient. For cases where boundary conditions are prescribed to induce a coarse scale second gradient, deformation of the unit cell will not maintain periodicity (even under generalized periodic boundary conditions) and therefore is not identical to the response of the larger periodic array of multiple unit cells.

4.1.3 rSVE of idealized particle system

The next level of complexity in rSVE simulations is to employ an idealized particle system which serves as the geometric representation of heterogeneous features of the microstructure. Examples of microstructure simulation based on this approach are (Austin et al., 2006; Clements et al., 2006; Ionita et al., 2006; Ionita and Weitsman, 2006; Mas et al., 2006; Reusch et al., 2008). Extensive discussions of methods for generating such particle representations are provided in (Torquato, 2001). The idea is to replace each feature, e.g. pore, in an actual microstructure image with a geometrically idealized particle (e.g., circle) in the rSVE. The particle geometries and locations could be (a) based on a direct idealization of micrograph or (b) fit to various size and location distribution functions derived from actual microstructure. Method (a) gives a more faithful representation of a specific micrograph, whereas method (b) permits more detailed statistical analyses over perturbations of distribution parameters. Method (b) can also more readily accommodate arbitrary rSVE sizes larger than the original.

For example, we return to the porous microstructure image from Section 4.1.1 as shown on the left of Figure 16. The obvious pore structure is amenable to treatment as a system of particles whereby each pore is represented by a circle with an equivalent area. The Hoshen-Kopelman algorithm (Hoshen and Kopelman, 1976) was used to identify connected clusters of black (pore) pixels which represent distinct voids. In turn, each pore was analyzed to identify its area and the coordinates of its centroid. The direct idealization of this microstructure morphology was constructed by locating, for each identified void, a circle whose area and centroid coincide with that of the void. The resulting geometry is depicted on the right side of Figure 16.

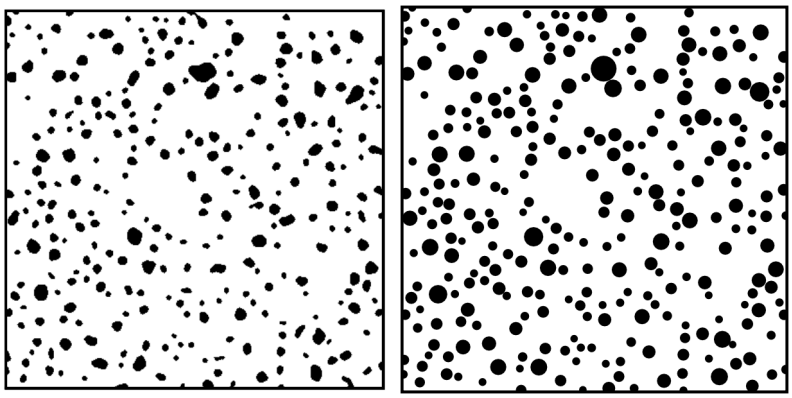

Figure 16. Comparison of (left) two-phase image and (right) direct idealization of that image. Connected clusters of black pixels in the image at left have been replaced by circles of equivalent area on the right.

Information on the distribution of pore size and location is used for synthesis of idealized rSVEs. A shifted lognormal probability distribution fit to the normalized (probability density) histogram of void area is shown in Figure 17. Additionally, the nearest neighbor distance (that distance between the centroid of a particle and the next closest particle centroid) was computed from the processed image. A lognormal distribution fit to this data is plotted against the corresponding normalized histogram in Figure 18.

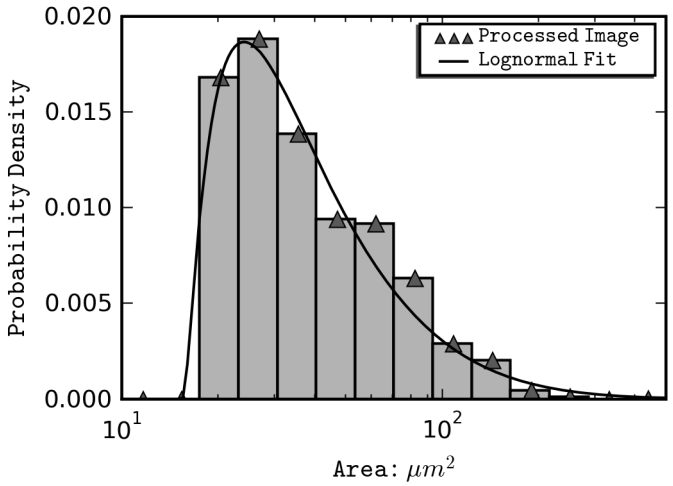

Figure 17. Distribution of pore area size from image analysis.

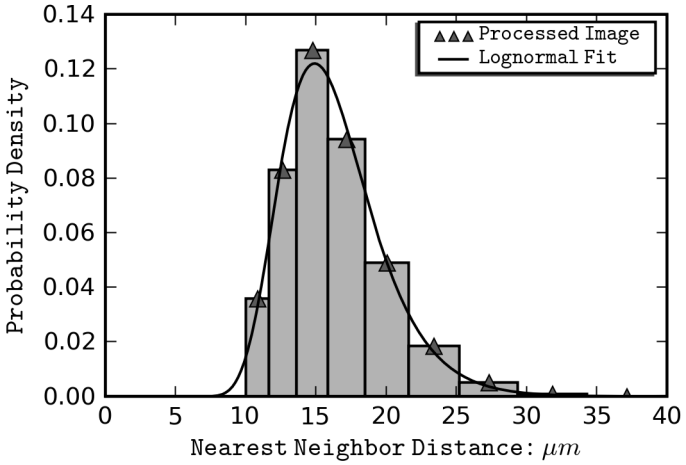

Figure 18. Distribution of nearest neighbor distance from image analysis.

The synthesis of idealized microstructure morphology proceeds as follows. The target area fraction of pores is assigned to be that observed from the processed image, A_f, yielding a target net pore area of $A_{\text{net}} = A_f L_{rVE}^2$. A random sample of void sizes from the target void area distribution (Figure 17) is collected until the net pore area is greater than or equal to the target net pore area. The last void added is reduced in size so that the target net area is exactly matched.

A circle representing each void area is located randomly within the rSVE under constraints that no void may be located within a specified distance of the corner or any other void. The specified distance is selected for mesh considerations and the requirement to stay out of the rSVE corner facilitates implementation of boundary conditions discussed in a subsequent section. The positioning of the voids is done largest first in descending order of size to reduce potential interference. Additionally, in order to ensure periodicity of the synthesized microstructure, for every particle which overlaps the rSVE boundary an identical particle is placed on the opposite boundary, i.e. $\tilde{x} = x \pm L_{rSVE}$ and $\tilde{y} = y \pm L_{rSVE}$ as appropriate where $\left(x, y\right)$ are the coordinates

of the original particle and $(\tilde{x},\tilde{y})$ are the points of the accompanying periodic particle. These duplicate particles are considered in the constraints mentioned above.

Figure 19 shows (left) the idealized morphology resulting from this random sampling and placement approach with the computed histograms for (center) void area and (right) nearest neighbor distribution plotted against the corresponding target probability density functions fit to actual morphology. Clearly, the resulting nearest neighbor distribution is not in agreement with the target distribution after the pore placement procedure.

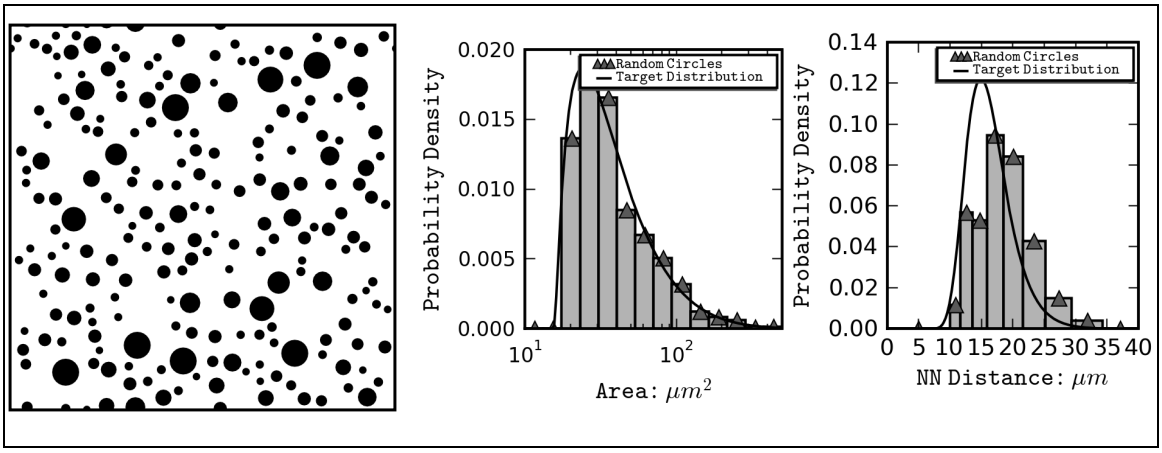

Figure 19. Synthesized idealization of pores prior to optimization of nearest neighbor distance (NND) distribution. Arrangement of circles is shown at left, while the area distribution and NND distribution are shown center and right, respectively.

The next step in the synthesis is to optimize the pore locations such that error between the resulting nearest-neighbor distribution and the target distribution is minimized. A simulated-annealing algorithm (SA) was employed to achieve this. The notion of simulated annealing comes from physical annealing during solidification where a metal is cooled from a liquid to a solid. In this solidification process the temperature of the metal affects the likelihood for atomic rearrangement. At high temperatures, the atoms can rearrange easily into higher and lower energy configurations; whereas, at lower temperatures the movement of atoms is inhibited (solidified). If the material is cooled sufficiently slowly then enough random motion of the atoms can occur to result in a near minimum energy state. However, if the material is cooled rapidly

(i.e. quenched) it can be trapped in a non-minimum energy state. The algorithm is discussed briefly here.

A popular stochastic approach to global optimization is the Monte-Carlo technique. Other stochastic methods exist, e.g. genetic algorithms; however, the advantage of the Monte-Carlo technique is that it requires relatively few parameters, is straightforward to implement, and typically requires fewer function evaluations than comparable genetic algorithms. The general idea is to randomly perturb the state and see if an objective function, usually the sum-of-squares error between the target and realized distributions, decreases. If the objective function decreases for a change in state then that state is accepted, if not, there are various heuristic rules for accepting updated states, i.e. probability of transition. The Metropolis Algorithm is obtained when the probability of transition is a function of the change in error and resembles the underlying distribution. For an assumed Boltzmann distribution, the Simulated Annealing method is recovered. Other probability of transitions exist, for example, the great deluge (GD) accepts all changes of state that result in an error increase that is below some threshold, while a greedy algorithm only accepts decreases in error unless it becomes stuck.

In this application of simulated annealing, the specific set of locations of all pores represents a state, *s*. At each iteration small random perturbations distributed uniformly on the interval $\left[-\frac{r}{2},\frac{r}{2}\right]$, where r is the radius of the pore were applied to the coordinates of a subset (5%) of the pores. If the change results in a decrease in the sum-of-squares error the new state is accepted, if not, the probability of acceptance is given by a Boltzmann distribution, i.e. $P(s) = \exp\left(\frac{-\Delta \mathrm{E}(s)}{T}\right)$, where *s* denotes the state and *T* is a variable "temperature" control parameter. The initial value of *T* is selected to yield approximately 50% likelihood of accepting a change which initially increases sum-of-squares error. The subsequent schedule for reduction of *T* (annealing schedule) is an exponential decay with parameters selected to optimize the optimization process. The morphology resulting from minimization of the error between target and realized nearest neighbor distributions using simulated annealing is shown in Figure 20 (left) along with the area and nearest neighbor distribution (center, right, respectively).

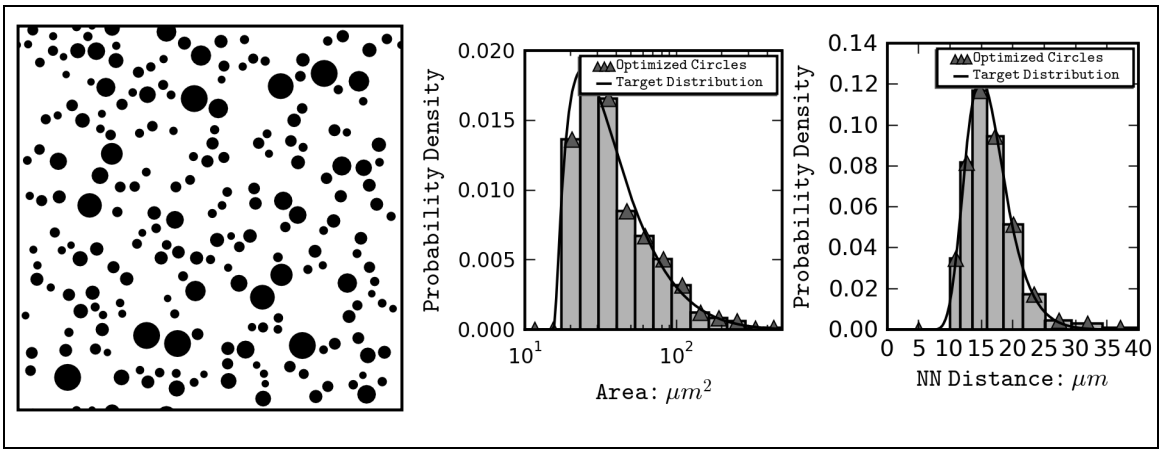

Figure 20. Synthesized idealization of pores after optimization of NND. Arrangement of circles is shown at left, while the area distribution and NND distribution are shown center and right, respectively.

Further improvements to this synthesis could be made by quantizing the pore areas into four (or N) bins representing the quartiles (or 1/N percentiles) of the area distribution. These N bins of pore sizes could be treated as separate phases or particle types and the nearest neighbor distributions computed between each of the N particle types. This enhancement would reflect more detail of the spatial distribution of pore sizes. Furthermore to this end, the second, third, etc. nearest neighbor distributions could be estimated from the micrograph and used to optimize pore placement. Another improvement would be to consider elliptical voids and identify distributions of minor and major axes, and orientation angle. Such extensions are beyond the scope of this section.

The advantage of the particle idealization approaches are that they capture more details of the spatial distribution of heterogeneous features without cumbersome complexity of direct pixel methods discussed subsequently. One disadvantage is that their synthesis requires more computation than idealized unit cell models possibly at the cost of clarity for understanding simple phenomena. Furthermore, if the actual heterogeneous features cannot be idealized by simple geometric shapes treated as particles, then this method is inappropriate. This approach is readily generalized to three-dimensions and would be equally effective for square, rectangular, or needle inclusions. For example, Zhai et al. (2004) use windows of idealized elliptical TiB_2 particles within Al_2O_3 matrix to simulate the dynamic fracture of ceramic composite center

cracked plates. In their simulations, cohesive finite elements are embedded between each adjacent pair of continuum finite-elements to provide arbitrary path for crack propagation. In another example, Kumar et al. (2006) model low-cycle fatigue behavior of nickel-base superalloys using an idealization of gamma precipitates as square particles located randomly within statistical volume elements.

4.1.4 Direct Image Conversion

There are a variety of methods by which an rSVE geometry can be developed directly from a microscopic image. In fact, the direct idealization discussed previously could be considered a form of direct image conversion. Another technique is pixel-by-pixel mapping from the image to a finite element mesh. In this approach each pixel in the micrograph becomes an element in the rSVE simulation whose phase is associated with a grayscale luminance value. The corresponding elements properties are determined by such pixel information.

Unstructured meshes of varying element shape and size can utilize a similar method by interpolating material phase information from the image, for example, by using the mode of pixel values in a region of pixels spanned by a finite element. Other methods include using mesh generation software that discretizes geometric features identified using image analysis techniques. The software package, OOF (Object-Oriented Finite Element Analysis), has been developed by NIST (2008) to simplify this process. For example, Clayton (2005) used OOF to generate a finite element mesh of polycrystalline tungsten heavy alloy directly from micrograph for subsequent simulation of dynamic damage evolution. Shan and Gokhale (2004) generate finite element meshes directly from micrographs of A356 to simulate the multiscale response. They employ windows of varying resolution to independently resolve porosity and Si particles which are present at distinct physical sizes. Chawla et al. (Chawla et al., 2004) apply this approach in three-dimensions to model the mechanical behavior of SiC reinforced aluminum composites.

4.1.5 Reconstruction from Spatial Correlation Functions

It is generally accepted that morphology of microstructure can be exactly represented by an infinite set of n-point correlation functions (Torquato and Stell, 1982; Hill, 1987; Coker and

Torquato, 1995). In many cases, relatively small sets of these probability distributions can be used to quantify and predict the response of materials in a meaningful manner. For example, the volume fraction of a particular phase (e.g. porosity) is a one-point correlation function and can be defined as the probability that any randomly selected point within the microstructure lies in the particular phase. Low-order statistical descriptors such as this are often, although not always, effective in predicting mean-field type phenomena (e.g. elastic response, thermal conductivity). However, it is widely known that localized phenomena such as material failure are sensitive to extreme values of microstructure characteristics that lie in the tails of distributions. The two-point correlation function is defined as the probability that each end of an oriented vector randomly "tossed" into the microstructure will have each end lie in the particular phase (Torquato and Stell, 1982). As its length approaches zero, the oriented vector collapses to a point and consequently the full two-point correlation function also contains the 1-pt correlation function. Likewise, the *n*-point correlation function is the probability that *n* points correlated by a set of oriented vectors all lie in the particular phase.

A detailed discussion of the subject can be found in the text by Torquato (2001). Mathematical development of this class of correlation function begins by construction of an indicator function that evaluates to unity at any point (i.e. pixel) which resides in phase *i*, and zero elsewhere, i.e.,

$$I_i(\mathbf{x}) = \begin{cases} 1, & \text{if } \mathbf{x} \text{ in phase } i \\ 0, & \text{otherwise} \end{cases} \tag{4.1}$$

The general *n*-point correlation functions are defined mathematically as: $S^n_{ij\cdots k}(\mathbf{r}_1,\cdots,\mathbf{r}_{n-1}) = \left\langle I_i(\mathbf{x}) I_j(\mathbf{x}+\mathbf{r}_1)\cdots I_k(\mathbf{x}+\mathbf{r}_{n-1})\right\rangle$, where here <*> represents the ensemble average of * and the microstructure is assumed ergodic, i.e., the ensemble average may be obtained from the volume average. Additionally, the spatial dependence of the correlation function disappears under an implicit assumption of statistical homogeneity, which in turn relates directly to the concept of an RVE.

Because they are probability functions, there is a set of rules that place constraints on physically realizable two-point correlation functions, thus comprising the *microstructure hull* (Gokhale et al., 2005; Jefferson et al., 2005) , viz.,

$$\begin{aligned} \sum_{j=1}^{N} S_{ij}^{2}\left(\underset{\sim}{r}\right) &= \phi_i \\ \sum_{i=1}^{N}\sum_{j=1}^{N} S_{ij}^{2}\left(\underset{\sim}{r}\right) &= \sum_{i=1}^{N} \phi_i = 1 \\ S_{ij}^{2}\left(\underset{\sim}{r}\right) &= S_{ji}^{2}\left(\underset{\sim}{r}\right) \end{aligned} \tag{4.2}$$

where here N is the number of distinct phases under consideration and ϕ_i is the area fraction in 2D or volume fraction in 3D of the i^{th} phase. The set of constraints provided by the microstructure hull implies that for a two phase material, the entire set of one and two point correlation functions are contained within the autocorrelation of a single phase, i.e.,

$$\begin{aligned} S_2\left(\mathbf{r}\right) &\equiv S_{11}^{2}\left(\mathbf{r}\right) \\ \phi_1 &= S_2\left(\mathbf{0}\right) \\ \phi_2 &= 1 - S_2\left(\mathbf{0}\right) \\ S_{12}^{2} &= S_{21}^{2} = S_2\left(\mathbf{0}\right) - S_2\left(\mathbf{r}\right) \\ S_{22} &= 1 - 2S_2\left(\mathbf{0}\right) + S_2\left(\mathbf{r}\right) \end{aligned} \tag{4.3}$$

Accordingly, we have introduced the notation $S_2\left(\mathbf{r}\right)$ for the autocorrelation of pixels that lie in the phase of a particular feature (e.g., porosity) and ϕ is the corresponding area fraction. For random microstructures, i.e., those lacking long-range periodic correlation,

$$\lim_{r\to\infty} S_2\left(\mathbf{r}\right) = \phi^2 \tag{4.4}$$

which expresses that the probability of two points lying in a specific phase approaches the probability of two independent events as the distance between the points grows. Furthermore, the slope of the autocorrelation function at the origin is related to the specific interfacial surface area per unit volume, s_v, by the following relation for isotropic media where $r = \left|\mathbf{r}\right|$,

$$\lim_{r\to 0} \frac{S_2(r)}{r} = \frac{\partial S_2(r)}{\partial r} = -\frac{s_v}{4} \tag{4.5}$$

For anisotropic media, the correlation function is averaged over the half space of orientation angles to compute (4.5).

Spatial correlation functions can be estimated from digitized micrographs by a variety of image analysis techniques (Corson, 1974a; Berryman, 1985; Garmestani et al., 2001). Perhaps the most

intuitive method is to systematically scan a digital image, essentially performing a direct summation, i.e.,

$$S^n_{ij\cdots k}(\mathbf{r}_1,\cdots,\mathbf{r}_{n-1}) = \frac{1}{N_{pix}}\sum_{\mathbf{x}\in\Omega} I_i(\mathbf{x})I_j(\mathbf{x}+\mathbf{r}_1)\cdots I_k(\mathbf{x}+\mathbf{r}_{n-1}) \tag{4.6}$$

A more efficient technique is to use Fourier transform. The inverse Fourier transform of power spectral density returns the correlation function. For example, the 2-pt autocorrelation function can be computed by

$$\begin{aligned} \hat{I}_i(\boldsymbol{\omega}) &= FFT[I_i(\mathbf{x})] \\ S_2(\mathbf{r}) &= IFFT2\left[\left|\hat{I}_i(\boldsymbol{\omega})\right|^2\right] \end{aligned} \tag{4.7}$$

This procedure requires on the order of $\left(N_{pix}\ln N_{pix} + N_{pix}\right)$ operations compared to roughly N^2_{pix} operations for computing the 2-pt correlation function by systematic scanning.

Empirical forms of two-point distribution functions have been developed for various microstructures (Corson, 1974b; Cule and Torquato, 1999). For example, the general form of Corson's relationship is $S_2\left(r\right) = \alpha + \beta\exp\left(-c\,r^n\right)$. Constraints imposed by the microstructure hull reduce this general form; Gokhale et al. (2005) proved that n=1, Jefferson et al. (2005) showed that $c = 1/r_0$ and that the relationship between slope and specific surface area imply $r_0 = \dfrac{2\phi\left(1-\phi\right)}{s_v}$. Saheli et al., (2004) modified Corson's relationship to account for anisotropy. The result of these modifications and simplifications is

$$\begin{aligned} S_2\left(\mathbf{r}\right) &= \phi^2 + \phi\left(1-\phi\right)\exp\left(-r\frac{s_v\left(\theta,\varphi\right)}{2\phi\left(1-\phi\right)}\right) \\ s_v\left(\theta,\varphi\right) &= s_v^0\left(\kappa + \left(1-\kappa\right)\sin\left(\theta-\theta_0\right)\right) \end{aligned} \tag{4.8}$$

This is one example of an empirical correlation function. There are many other empirical and analytical correlation functions in the literature (cf. Cule and Torquato, 1999; Rozman and Utz, 2001; Torquato, 2001). Using empirical correlation functions such as (4.8), one can develop a parameterized model of microstructure morphology. The parameters of such representations

would become the key morphological descriptors and could be used to construct the geometry of rSVEs as discussed next.

In order to demonstrate the amount of information contained in various correlation functions and to simulate realizable microstructures, the inverse problem of microstructure reconstruction from correlation functions has been addressed (Yeong and Torquato, 1998; Rozman and Utz, 2001; Sheehan and Torquato, 2001; Xu and Graham-Brady, 2005; Graham-Brady and Xu, 2008). The most common approach is to use some form of Monte Carlo optimization to reduce the error between correlation functions of the reconstructed image and a target correlation function. Cule and Torquato (1999) introduce an empirical 2-pt correlation function which exhibits considerable short-range order with two dominant length scales and employ simulated annealing to reconstruct realizations of morphology that best approximate the target correlation function. They additionally employed Monte Carlo optimization using a great deluge (GD) acceptance algorithm and demonstrated that this approach is an order of magnitude faster in convergence than SA. Yeong and Torquato (1998) follow a similar approach except that they add the lineal path function to the set of target distributions. In these two works, pixels of opposite phase were selected at random and their phases swapped to generate a trial state. The trial correlation function was computed by the fast Fourier transform method discussed previously. If the sum-of-squares error between target and trial correlation functions was reduced then the trial state was accepted. If not, the trial state was accepted according to the particular acceptance rule adopted, (e.g., Boltzman distribution with systematically reduced "temperature" → simulated annealing). The method of pixel swapping ensures that the total area fraction of each phase remain as initialized and is initialized to be the value of the target autocorreltion function at the origin.

Rozman and Utz (2001) recognized that the bottleneck in stochastic reconstruction is computing the correlation function for each trial (iteration). The two-point correlation function is predominantly unchanged for a trial state that is identical to the previous state except for two pixels that have been swapped. Rather than compute the entire correlation function, they update the previous correlation function by identifying discrete locations where the trial correlation function is affected by the pixel swap. Thus, the computational cost of each iteration is reduced

in order from $\left(N_{pix} \ln N_{pix} + N_{pix}\right)$ to N_{pix}. Furthermore, they only select pixels that lie on a phase interface to swap values. This improves the convergence rate by avoiding transitions that add spurious noise within distinct pixel clusters.

Image synthesis is not unique to modeling microstructure morphology. The task of synthesizing texture that is similar in visual appearance to an existing image sample is germane to animation. Copeland et al. (2001) apply stochastic techniques to reconstruct grayscale (multiphase) images with a variety of target textures. They refer to the pixel swapping technique as the spin-exchange algorithm and, in contrast, explore a spin-flip algorithm, where a randomly selected pixel is flipped to a new grayscale level without regard to any other pixel to generate a trial state. They demonstrate that spin-flip is generally more efficient than spin-exchange; however the final area fraction of each grey level (phase) is unconstrained. Additionally, they employ a greedy acceptance criterion, where the probability of accepting a transition state is zero for any state which increases sum-of-squares error.

Graham-Brady and Xu (2008) introduce the notion of short-range correlation (SRC) models, where the target and trial correlation functions are ignored outside a predetermined window. This increases computational efficiency and also serves to focus the optimization on short-range correlation thereby reducing visual "noise" in the reconstructed image. The disadvantage of this approach is that the appropriate size of the SRC window can only be determined through trial and error. They also adopt the spin-flip algorithm and, therefore, add the area fraction of the targeted phase to the target distribution function. Of course, this is somewhat redundant because the two-point correlation function contains the one-point correlation information at a vector length of zero (origin). Therefore, explicitly adding the volume fraction to the target distribution function represents a weighting on the zero-length correlation function term in the sum-of-squares error. They also perform reconstructions to reach targeted three-point correlation functions. The three-point correlation functions return better reconstructions of the original, but at a significantly higher computational cost.

An example of morphology synthesis by image reconstruction to minimize the sum-of-squares error between target and synthesized correlation functions is given here. First the two-point

correlation function is computed from the processed image (Figure 13D) using the fast Fourier transform. The two-point correlation function for the pore phase is plotted against normalized radial distance for four orientation angles in Figure 21. Notice that the value at the origin is 0.12 as expected and the correlation function asymptotically approaches 0.0144 plus a fluctuation indicating some long range order.

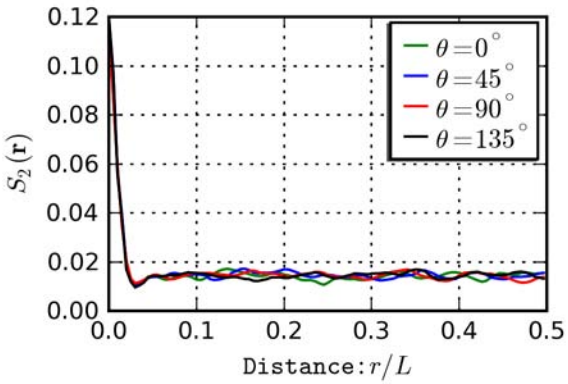

Figure 21. Two point correlation function for porosity in processed image.

Monte Carlo stochastic optimization with a greedy acceptance criteria was used in the present work to optimize the pixel arrangement minimizing error between the target and synthesized two-point correlation function. The reconstruction algorithm employed here is:

1) Randomly initialize the appropriate area fraction of image pixels to be exactly consistent with target correlation function, $\tilde{S}_2(\mathbf{r})$,i.e.,

$$\begin{aligned} N_1 &= \tilde{S}_2(\mathbf{r})\big|_{\mathbf{r}=\mathbf{0}} \times L_{rve}^2 \\ N_0 &= L_{rve}^2 - N_1 \end{aligned} \tag{4.9}$$

2) Compute the initial correlation function using fast Fourier transform,

$$\begin{aligned} \hat{I}(\boldsymbol{\omega}) &= FFT[I(\mathbf{x})] \\ S_2(\mathbf{r}) &= IFFT2\left[\left|\hat{I}(\boldsymbol{\omega})\right|^2\right] \end{aligned} \tag{4.10}$$

3) Identify pixels which lie on phase interface by computing the first-order finite divided difference of pixel values for the image. Note that this is a standard edge-detection technique in image analysis.

$$I_{edge}(\mathbf{x}) = \max\left(1,\ \begin{Bmatrix} \left|I(x_2, x_1 + \Delta x_1) - I(x_2, x_1)\right| + \\ \left|I(x_2, x_1 - \Delta x_1) - I(x_2, x_1)\right| + \\ \left|I(x_2 + \Delta x_2, x_1) - I(x_2, x_1)\right| + \\ \left|I(x_2 - \Delta x_2, x_1) - I(x_2, x_1)\right| \end{Bmatrix}\right)$$
$$\mathbf{x}_{edge} = \left\{\ \mathbf{x} : I_{edge}(\mathbf{x}) = 1\right\} \tag{4.11}$$

4) Randomly select without replacement two pixels of differing phase from the interface set, i.e.,

$$\mathbf{x}_a,\ \mathbf{x}_b \in \mathbf{x}_{edge} : I(\mathbf{x}_a) \neq I(\mathbf{x}_b) \tag{4.12}$$

5) Compute the trial correlation function by updating the current correlation function according to

$$\begin{aligned} S_2^*(\mathbf{r}) = S_2(\mathbf{r}) - I\left(\mathbf{x}_a - \mathbf{r}\right) + I_i\left(\mathbf{x}_b - \mathbf{r}\right) - I_i\left(\mathbf{x}_a + \mathbf{r}\right) + I_i\left(\mathbf{x}_b + \mathbf{r}\right) \\ -\delta\left(\mathbf{x}_a - \mathbf{x}_b + \mathbf{r}\right) - \delta\left(\mathbf{x}_a - \mathbf{x}_b + \mathbf{r}\right) + 2\delta\left(\mathbf{r}\right) \end{aligned} \tag{4.13}$$
$$\text{where, } \delta(\mathbf{x}) = \begin{cases} 1, & \mathbf{x} = \mathbf{0} \\ 0, & \text{otherwise} \end{cases}$$

6) Compute the sum of squares error between trial and target correlation functions, i.e.,

$$E^* = \sum_{\mathbf{r} \in R_{SRC}} \left(S_2^*(\mathbf{r}) - \tilde{S}_2^*(\mathbf{r})\right)^2 \tag{4.14}$$

7) If error reduced update:

$$\begin{aligned} &\text{if } E^* - E < 0 : \\ &\quad E^* \rightarrow E \\ &\quad I(\mathbf{x}_a) \leftrightarrow I(\mathbf{x}_b) \end{aligned} \tag{4.15}$$

8) Return to Step 4 unless:

   a. some fraction of interface pixel set exhausted (e.g. 0.75) in which case return to Step 3, or

   b. the maximum allowable number of iterations has been reached in which case stop.

Figure 22 shows the evolution of the reconstructed image along with a plot of the convergence in normalized error. The final image has features of random porosity similar to the target image, but obviously lacks some detail of the local pore shapes and does not capture the breadth of the pore size distribution. This is somewhat to be expected, as the two-point correlation function represents volume averaged correlation behavior. One could extend this approach by adding other correlation functions, such as the cluster and blocking functions or lineal-path function which preserve more information regarding the spatial correlation of connectivity. Alternatively, three, four, or N point correlation functions could be used as the target function for optimization. These approaches come at significant computational cost and, thus, there is interest in determining whether or not morphology synthesized from two-point correlation function yields representative thermomechanical (both elastic and irreversible) response as other techniques.

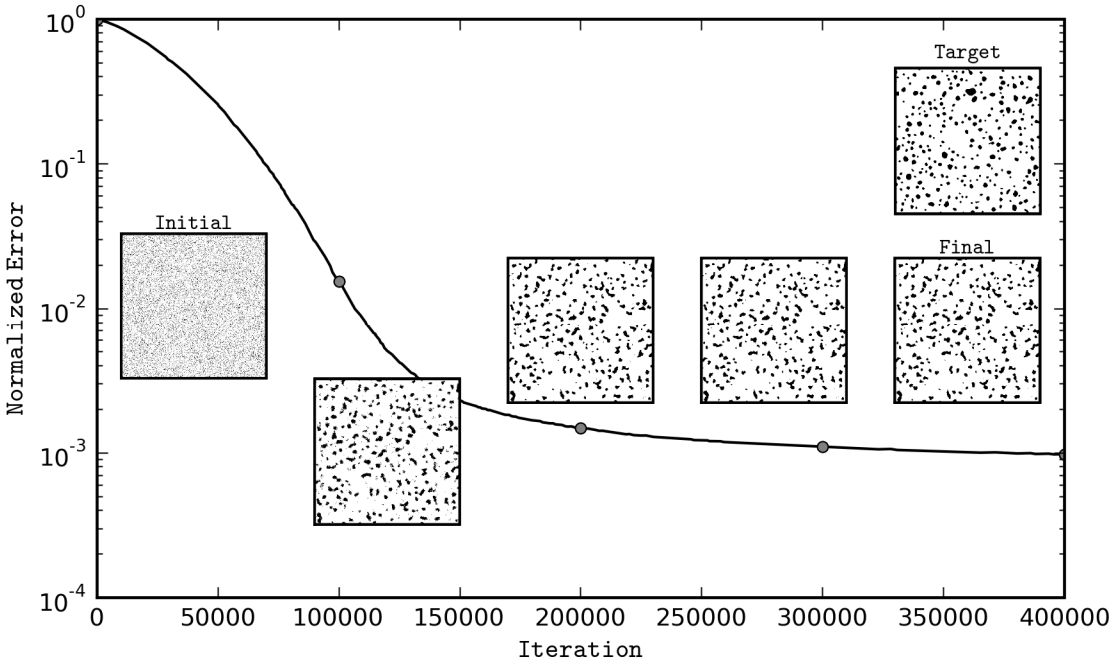

Figure 22. Progression of image reconstruction by optimization of S_2.

The images generated in this fashion can be converted to a suitable finite element mesh by any of the methods discussed in Section 4.1.4.

4.1.6 Grain Morphology from Voronoi Tessellation

The examples of rSVE morphology construction given up to this point are primarily applicable to heterogeneous features such as inclusions, porosity, discrete phases, etc. For modeling of polycrystalline or granular materials there is a more efficient technique for creating the geometric description. These cases are briefly addressed here for completeness, although specific examples will not be pursued in this dissertation.

A tessellation is a tiling of a space which fills that space without overlaps or gaps. A Voronoi tessellation is one in which a region of space is divided into N discrete polygonal cells such that every point within a cell is closer to the seed of that cell than any of the other N-1 seeds. A seed can be thought of as representing the initial location of nucleation of solid phase in a liquid upon cooling. Following this analogy, the Voronoi cell represents a grain. A line segment between two adjacent grains is the locus of points equidistant between the seeds of these two grains and represents the grain boundary. For example, if seeds are uniformly positioned within a region of a plane such that the seeds form equilateral triangles with their nearest neighbors the Voronoi tessellation is a tiling of hexagons as shown on the left of Figure 23. If the seeds are located randomly in the plane the resulting tessellation appears similar to that shown on the right of Figure 23. In this figure, the seeds are black dots and the Voronoi cells are filled with a randomly selected color. Boundaries between adjacent cells are black lines. Voronoi tessellations of a region result in cell boundaries that extend infinitely from the outer edges of that region. Typically, this is mitigated by seeding a region that is larger than the rSVE itself and cropping the resulting cells to lie solely within the region. In order to ensure periodicity of the microstructure, this is often achieved by creating a 3 x 3 tiling of the original seeds and performing the Voronoi tessellation on the tiled version (as illustrated in Figure 24). Only the cells, and portions thereof, within the rSVE region are retained subsequently.

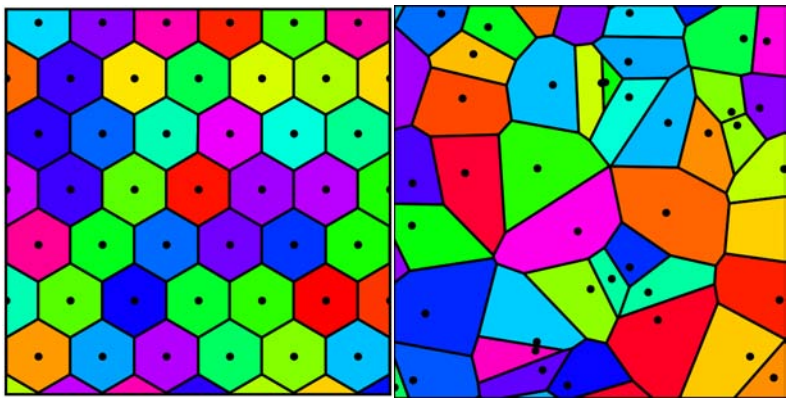

Figure 23. Examples of Voronoi tessellation in a plane: (left) hexagonal (right) random.

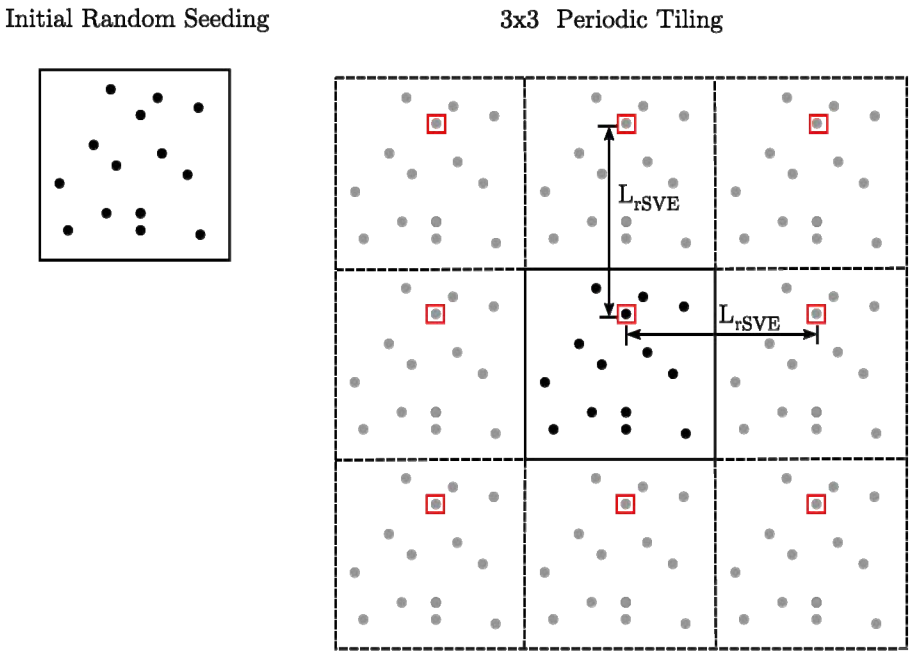

Figure 24. Tiling of Voronoi seeds to ensure periodicity.

In consideration of mesh generation requirements, it is advantageous to merge cell vertices located so close together that they have a significant impact on the smallest element size for a finite element mesh. For a randomly seeded Voronoi tessellation the grain size will approach a lognormal distribution as the number of grains in the rSVE increases. For example a tessellation with 100 grains and the corresponding grain area distribution are shown in Figure 25. Because the rSVE represents a finite sample of the entire population, its distribution of grain size may or may not adequately reflect the underlying distribution. If not, a stochastic optimization can be performed on the initial seed locations, for example, using the simulated annealing technique described in Section 4.1.3, previously. If the actual microstructure does not exhibit such a lognormal distribution of grain sizes, then again, stochastic optimization should be used. An example of such a procedure and various implications are discussed in (Gross and Mo, 2002). The optimization process will benefit from having a reasonable set of initial conditions (seed locations). In some cases this may be achieved by using specific patterns for initial seed locations, e.g. consistent with hexagonal tiling.

In some cases, it may be desirable to model a finite thickness grain boundary region between each grain. In such cases, each cell may be scaled such that it shrinks inwards toward the seed. While this operation can be applied uniformly to each cell, it also motivates further cell transformations such as shearing or rotating cells that can be performed on an individual and random basis. For example, consider the variation shown at left in Figure 26 in which each grain is surrounded by a finite thickness grain boundary region. Properties specific to grain boundary behavior could be assigned in this region based on the mis-orientation angle of the two adjacent grains. The example on the right of Figure 26 could be appropriate for granular materials (e.g., the particle composite high-explosives PBX-9501 and PBX-9502) with particles bonded by some other material.

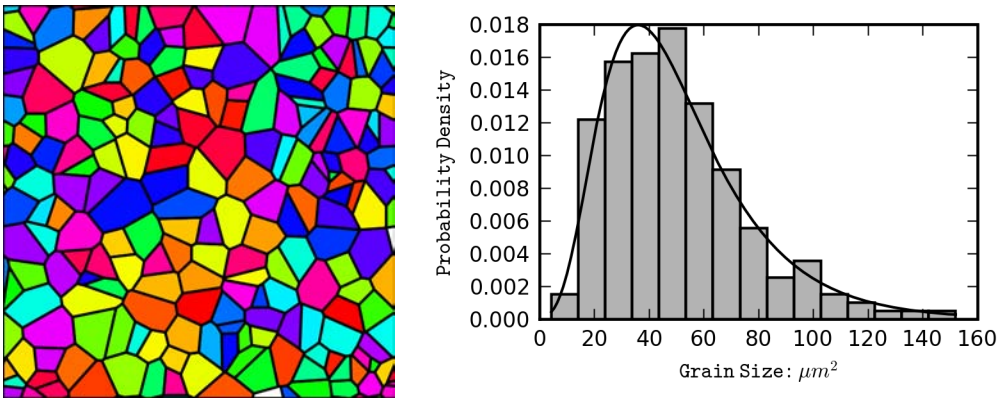

Figure 25. Random periodic grain morphology and resulting grain size distribution.

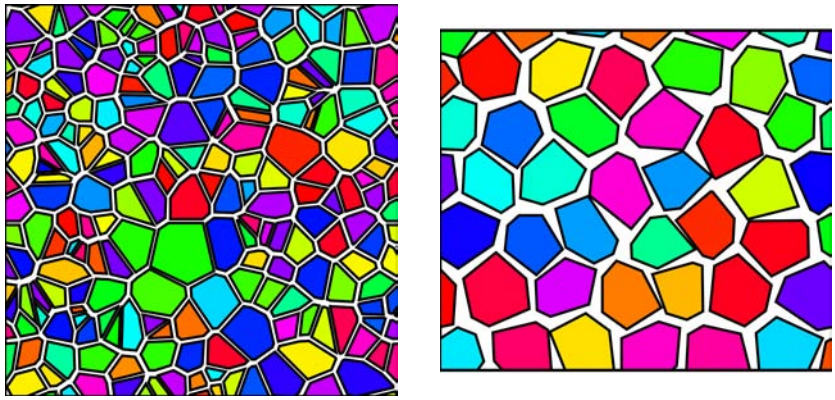

Figure 26. Variations on Voronoi tessellation morphology: (left) finite thickness grain boundaries, (right) shrink and random rotation.

Figure 27 illustrates another variation of this approach in combination with 'nearest-neighbor' interpolation method of 4.1.4 for direct representation of porosity (black in left pane of Figure 27) from micrograph. In this example, the Voronoi seeding was manipulated such that pores were generally located at triple points of grain boundaries. Additionally, contact surfaces (red in middle pane of Figure 27) were specified on the interior of pores and cohesive elements were introduced between adjacent grains to simulate the damage nucleation and growth process under large deformation compression.

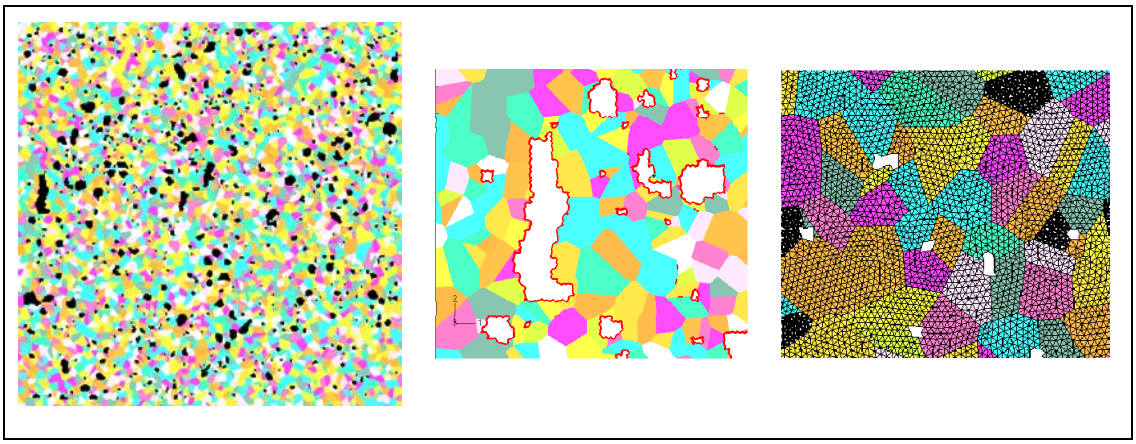

Figure 27. Example illustration of superposition of porosity from micrograph and grain morphology by Voronoi tessellation.

Applications employing the Voronoi approach are prevalent. For example, Zavattieri and Espinosa (2001) use the Voronoi tessellation to construct synthetic grain morphologies for a stochastic analysis of intergranular crack initiation and growth in brittle materials. Grain boundaries are modeled as cohesive elements between adjacent grains, thus providing a crack propagation path through the polycrystal region. Bronkhorst et al. (2007) use Voronoi tessellation to generate polycrystalline morphology in a two-scale simulation of adiabatic shear localization in hat-shaped specimen of tantalum.

4.1.7 Discretization of Geometry into Finite Element Mesh

For the simulations discussed subsequently, finite-element meshes were constructed from idealized and Voronoi geometries using the geometry and mesh generation toolkit developed at Sandia National Laboratories, (Cubit, 2008). Discretization of real and synthesized images were developed using a regular structured grid of elements whose material phase was dictated by the mode of pixel values for a region of pixels bounded by the finite element area, as discussed in Section 4.1.4.

In the ensuing examples, four-node quadrilateral and three-node triangular generalized plane-strain finite elements are used. These elements employ full integration and linear interpolation of nodal values. While the methods discussed subsequently are applicable to any Lagrangian finite

element code, the implementation examples were developed using Abaqus Standard version 6.7 (Abaqus, 2007). Generalized plane strain elements (GPE3, GPE4 in Abaqus) are particularly well suited to two-dimensional rSVE simulations as they allow arbitrary volume-averaged coarse-scale strain in the out-of-plane direction. This is important, since purely plane-strain elements that enforce no out-of-plane strain everywhere within the rSVE do not allow simulation of rSVE states with zero out-of-plane stress. Furthermore, plane-stress elements result in aphysical local out-of-plane deformation response. In the generalized plane strain theory used by Abaqus, every 2D element in the rSVE is assumed to have a finite thickness contained between two bounding planes (Abaqus, 2007). These bounding planes are allowed to deform relative to each other as rigid bodies with three global degrees of freedom, i.e., translation in the thickness direction and rotation about two in-plane axes, such that the out-of-plane thickness at any pointing the rSVE is described by:

$$h\left(x_1, x_2\right) = h_{\text{o}} + \Delta u_3 + \Delta\phi_1(y - y^*) - \Delta\phi_2(x - x^*) \tag{4.16}$$

where the quantities are as indicated in Figure 28.

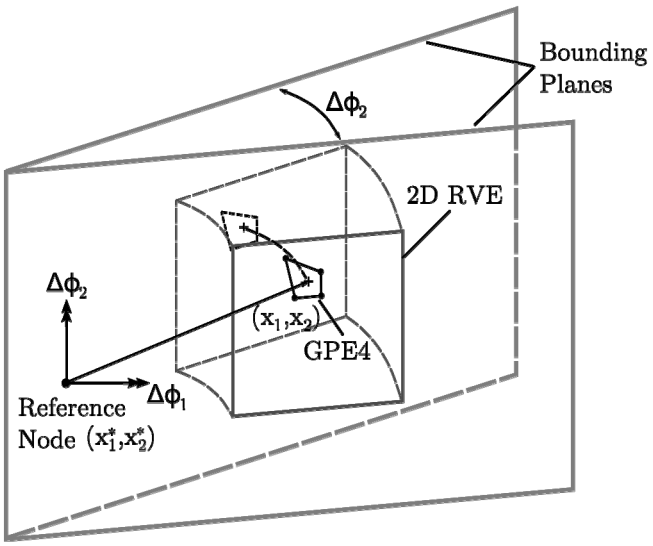

Figure 28. Diagram of out-of-plane behavior for generalized plane strain element in rSVE simulations.

4.2 Numerical Implementation of Boundary Conditions on rSVE

Boundary conditions are imposed to the rSVE through enforcement of a number of kinematic constraints and specification of either coarse-scale kinematic or stress terms. This section reviews the nature of the kinematic constraints, formulation into linear constraint equations, and their numerical implementation in the finite element code Abaqus (Abaqus, 2007). Specification of coarse-scale stress terms, rather than kinematic quantities is discussed in Section 4.4.

Recall from Section 3.1 the kinematic coupling between coarse and fine scales is achieved through

$$\mathbf{y}\left(\mathbf{x}_{\mathrm{o}},\mathbf{y}_{\mathrm{o}}\right)=\mathbf{C}\left(\mathbf{x}_{\mathrm{o}}\right)+\mathbf{F}\left(\mathbf{x}_{\mathrm{o}}\right)\cdot\mathbf{y}_{\mathrm{o}}+\tfrac{1}{2}\mathbf{G}\left(\mathbf{x}_{\mathrm{o}}\right):\mathbf{y}_{\mathrm{o}}\otimes\mathbf{y}_{\mathrm{o}}+\mathbf{h}\left(\mathbf{y}_{\mathrm{o}}\right) \tag{4.17}$$

For a fixed rSVE,

$$\mathbf{y}\left(\mathbf{y}_{\mathrm{o}}\right)=\mathbf{F}\cdot\mathbf{y}_{\mathrm{o}}+\tfrac{1}{2}\mathbf{G}:\mathbf{y}_{\mathrm{o}}\otimes\mathbf{y}_{\mathrm{o}}+\mathbf{h}\left(\mathbf{y}_{\mathrm{o}}\right) \tag{4.18}$$

where the rSVE constant term has been assumed zero without loss of generality. The fine-scale displacement field is

$$\mathbf{d}=\mathbf{y}-\mathbf{y}_{\mathrm{o}}=\left(\mathbf{F}-\mathbf{I}\right)\cdot\mathbf{y}_{\mathrm{o}}+\tfrac{1}{2}\mathbf{G}:\mathbf{y}_{\mathrm{o}}\otimes\mathbf{y}_{\mathrm{o}}+\mathbf{h}\left(\mathbf{y}_{\mathrm{o}}\right) \tag{4.19}$$

As simple rearrangement of (4.19) yields an expression for the fluctuation field in terms of coarse scale kinematic quantities and the fine scale displacement field, i.e.,

$$\mathbf{h}\left(\mathbf{y}_{\mathrm{o}}\right)=\mathbf{d}\left(\mathbf{y}_{\mathrm{o}}\right)-\left(\mathbf{F}-\mathbf{I}\right)\cdot\mathbf{y}_{\mathrm{o}}-\tfrac{1}{2}\mathbf{G}:\mathbf{y}_{\mathrm{o}}\otimes\mathbf{y}_{\mathrm{o}} \tag{4.20}$$

Also recall from Section 3.1.3, requirements for guaranteeing that the decomposition of (4.19) be orthogonal are

$$\int_{\Omega_{\mathrm{o}}^{\mathrm{x}}}\frac{\partial h_i}{\partial y_j^{\mathrm{o}}}\,d\Omega=0 \tag{4.21}$$

$$\int_{\Omega_{\mathrm{o}}^{\mathrm{x}}}\frac{\partial h_i}{\partial y_j^{\mathrm{o}}}\,y_k^{\mathrm{o}}\,d\Omega=0 \tag{4.22}$$

Here we adopt the two-dimensional square rSVE shown in Figure 29 to develop these requirements into kinematic constraints for the fine-scale rSVE; the obvious generalization to a

three-dimensional cube rSVE and further generalization to arbitrary cuboidal shapes follows the same procedure. Using the divergence theorem (4.21) is transformed to

$$\int_{\Gamma_{rVE}} h_i n_j^{\mathrm{o}}\, d\Gamma_{\mathrm{o}} = 0 \tag{4.23}$$

which is evaluated in accordance with Figure 29 to get

$$\begin{aligned} \int_{\Gamma_A} h_i\, d\Gamma_{\mathrm{o}} - \int_{\Gamma_C} h_i\, d\Gamma_{\mathrm{o}} = 0 \\ \int_{\Gamma_B} h_i\, d\Gamma_{\mathrm{o}} - \int_{\Gamma_D} h_i\, d\Gamma_{\mathrm{o}} = 0 \end{aligned} \tag{4.24}$$

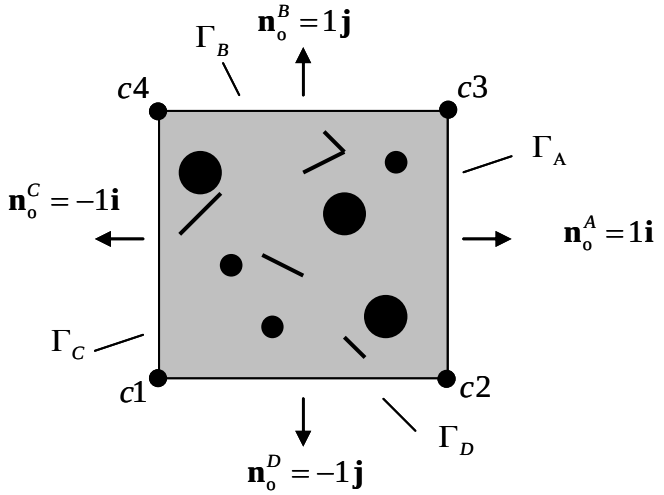

Figure 29. Square rSVE used for developing 2D kinematic constraints.

Before moving on we note that (4.24) not only ensures orthogonality of the fine scale deformation associated with the coarse-scale deformation gradient and the fluctuation field, but also guarantees that the coarse-scale deformation gradient is the volume average of the fine-scale deformation gradient. Intuitively, these two issues are not separate, but two perspectives of the same matter.

Equation (4.22) is modified by application of the chain rule and divergence theorem to obtain

$$\int_{\Gamma_{rVE}} h_i n_j^{\mathrm{o}} y_k^{\mathrm{o}}\, d\Gamma_{\mathrm{o}} = \delta_{jk} \int_{\Omega_{\mathrm{o}}^{\mathrm{x}}} h_i\, d\Omega \tag{4.25}$$

The unit normal vector effectively decomposes (4.25) into constraints on opposite pairs of boundary faces. Considering the pair A-C first, i.e. $j = 1$, there are two cases. For the case where $k = 1$,

$$\tfrac{1}{2} L \int_{\Gamma_A} h_i \, d\Gamma_o + \tfrac{1}{2} L \int_{\Gamma_C} h_i \, d\Gamma_o = \int_{\Omega_{rVE}} h_i \, d\Omega \tag{4.26}$$

and for $k = 2$,

$$\int_{\Gamma_A} h_i y_2^o \, d\Gamma_o - \int_{\Gamma_C} h_i y_2^o \, d\Gamma_o = 0 \tag{4.27}$$

Likewise for pair B-D,

$$\tfrac{1}{2} L \int_{\Gamma_B} h_i \, d\Gamma_o + \tfrac{1}{2} L \int_{\Gamma_D} h_i \, d\Gamma_o = \int_{\Omega_{rVE}} h_i \, d\Omega \tag{4.28}$$

$$\int_{\Gamma_B} h_i y_1^o \, d\Gamma_o - \int_{\Gamma_D} h_i y_1^o \, d\Gamma_o = 0 \tag{4.29}$$

Together, equations (4.20), (4.24), and (4.26)-(4.29) provide constraints on the fluctuation field (and, therefore, implicitly on the displacement field) such that it is totally in agreement with the kinematic framework of Section 3.1. The latter four are necessary only for fine scale simulations of a nonzero coarse scale second gradient, which we will refer to as second order simulations. For those cases where the coarse scale second gradient is zero, hereafter referred to as first order simulations, equations (4.20) and (4.24) are fully sufficient. Recognize that second order simulations involve a constraint not only on the fluctuations along external boundaries, but also within the interior of the rSVE. This is a new development in second order direct microstructural simulations.

We now proceed by detailing the numerical implementation of alternative sets of boundary conditions in order of decreasing constraint on the response of the rSVE. As will be seen, the boundary conditions of highest constraint are the most direct to implement, while those presenting a minimal constraint on the deformation of the rSVE are the most complex to implement.

4.2.1 Fundamental Decomposition

Common to all of the following first- and second-order boundary conditions is the fundamental kinematic relationship from Section 3.1, as re-expressed in (4.20). First, we introduce reference nodes to the fine-scale simulation whose global degrees-of-freedom represent specific components of the deformation gradient and second gradient. For example,

$$\begin{aligned} \hat{d}_i^{\mathrm{REF1}} &= F_{i1} - \delta_{i1} \\ \hat{d}_i^{\mathrm{REF2}} &= F_{i2} - \delta_{i1} \\ \hat{d}_i^{\mathrm{REF3}} &= G_{i11} \\ \hat{d}_i^{\mathrm{REF4}} &= G_{i12} \\ \hat{d}_i^{\mathrm{REF5}} &= G_{i22} \end{aligned} \tag{4.30}$$

This specific mapping is not unique and more efficient use of reference nodes could be accomplished by utilizing all of the available six DOFs at each reference node rather than two as indicated here. Nevertheless, the mapping of (4.30) was used to simplify bookkeeping and code debugging and verification processes. Now, we write the discretized version of (4.20), i.e.,

$$\begin{aligned} h_i\left(y_{\mathrm{o}}^1, y_{\mathrm{o}}^2\right) = \hat{d}_{iJ} N_J(\mathbf{y}_{\mathrm{o}}) - \hat{d}_i^{\mathrm{REF1}} y_{\mathrm{o}}^1 - \hat{d}_i^{\mathrm{REF2}} y_{\mathrm{o}}^2 \\ -\tfrac{1}{2}\hat{d}_i^{\mathrm{REF3}} y_{\mathrm{o}}^1 y_{\mathrm{o}}^1 - \hat{d}_i^{\mathrm{REF4}} y_{\mathrm{o}}^1 y_{\mathrm{o}}^2 - \tfrac{1}{2}\hat{d}_i^{\mathrm{REF5}} y_{\mathrm{o}}^2 y_{\mathrm{o}}^2 \end{aligned} \tag{4.31}$$

where the finite element shape function, $N_I(\mathbf{y}_{\mathrm{o}})$, has been introduced. The shape function is a set of Lagrange interpolating polynomials, one for each node, with the property that they evaluate to one at their associated node, zero at all other nodes, and are only defined within the domain of a specific element. Typically, the shape functions are expressed in terms of a set of natural coordinates, i.e., $N_I(\boldsymbol{\xi})$, and an isoparametric transformation between physical and natural coordinates $\left(\boldsymbol{\xi} \leftrightarrow \mathbf{y}_{\mathrm{o}}\right)$ is used to perform computations involving a particular element.

Equation (4.31) now contains a discretized portion (whose accuracy is determined by the order of shape functions; they are linear in this work but not necessarily so) and a continuous portion that is quadratic. There are two ways to proceed, viz., we can discretize the continuous portion of (4.31), thereby creating a new nodal response variable, or continue with the equation as is. The difference lies in the integration of the fluctuation field. We can exactly integrate the continuous

portion as is; however if we discretized it the accuracy of integration depends on the order of the shape function. The approach pursued here is to discretize the fluctuation field according to

$$\begin{aligned} h_{iJ} &= \hat{d}_{iJ} - \hat{d}_i^{\mathrm{REF1}} y_{\mathrm{o}J}^1 - \hat{d}_i^{\mathrm{REF2}} y_{\mathrm{o}J}^2 \\ &\quad -\tfrac{1}{2}\hat{d}_i^{\mathrm{REF3}} y_{\mathrm{o}J}^1 y_{\mathrm{o}J}^1 - \hat{d}_i^{\mathrm{REF4}} y_{\mathrm{o}J}^1 y_{\mathrm{o}J}^2 - \tfrac{1}{2}\hat{d}_i^{\mathrm{REF5}} y_{\mathrm{o}J}^2 y_{\mathrm{o}J}^2 \end{aligned} \tag{4.32}$$

where there is to be no summation over the *J* nodes. Accordingly, equation (4.31) is approximated using the element shape functions, i.e.,

$$h_i\left(y_{\mathrm{o}}^1, y_{\mathrm{o}}^2\right) \cong h_{iJ} N_J \tag{4.33}$$

where summation over *J* is implied. Clearly, (4.33) is exact for shape functions that are quadratic in order or higher; however, for the linear shape functions used this is a projection of the implied coarse scale displacement field onto the finite-element mesh. The implications of this approach are not considered further. As a final note, it is pointed out that fictitious or 'dummy' nodes can be introduced to explicitly represent the nodal values of the fluctuation field. This is a convenience for some of the boundary conditions discussed below.

4.2.2 Direct Boundary Conditions

The simplest boundary conditions to implement are those where the fluctuation vanishes everywhere on the boundary, i.e.,

$$\mathbf{h}\left(\mathbf{y}_{\mathrm{o}}\right) = \mathbf{0} \;\forall\, \mathbf{y}_{\mathrm{o}} \in \Gamma_{rSVE} \tag{4.34}$$

For every node on the boundary of the rSVE, the fluctuation is set to zero such that

$$\begin{aligned} 0 &= \hat{d}_{iJ} - \hat{d}_i^{\mathrm{REF1}} y_{\mathrm{o}J}^1 - \hat{d}_i^{\mathrm{REF2}} y_{\mathrm{o}J}^2 \\ &\quad -\tfrac{1}{2}\hat{d}_i^{\mathrm{REF3}} y_{\mathrm{o}J}^1 y_{\mathrm{o}J}^1 - \hat{d}_i^{\mathrm{REF4}} y_{\mathrm{o}J}^1 y_{\mathrm{o}J}^2 - \tfrac{1}{2}\hat{d}_i^{\mathrm{REF5}} y_{\mathrm{o}J}^2 y_{\mathrm{o}J}^2 \end{aligned} \tag{4.35}$$

thereby providing a set of N linear constraint equations, where N is the number of nodes on the boundary of the rSVE. Linear constraint equations of this type can be specified in Abaqus according to

$$A_1 d_{iP} + A_2 d_{jQ} + \cdots + A_N d_{kR} = 0 \tag{4.36}$$

where d_{iP} is DOF *i* at node *P* and A_n are the coefficients obtained from (4.35) (Abaqus, 2007). Every constraint equation eliminates one DOF from the model, so it is imperative to order the terms in each constraint equation such that the fine-scale DOF is eliminated while coarse-scale DOFs are preserved.

For first order simulations, specification of zero fluctuation for all nodes on the boundary according to (4.35) is all that is required to satisfy (4.24), which can be verified directly from that equation. The resulting boundary conditions are precisely the Dirichlet conditions. Second order simulations additionally require that the volume integral of the fluctuation field vanish in order to satisfy (4.26) and (4.28). Such integral constraints are developed using Gauss quadrature of a finite element. The nodal values of the fluctuation field are interpolated to the Gauss quadrature points using the element's shape functions. For two dimensional elements,

$$\begin{aligned} I_{el} &= \sum_{q1=1}^{N_{q1}} \sum_{q2=1}^{N_{q2}} \omega_{q1}\omega_{q2} h_{iJ} N_J\left(\xi_{q1},\eta_{q2}\right) \det\left[\mathbf{J}\left(\xi_{q1},\eta_{q2}\right)\right] \\ &= h_{iJ} \sum_{q1=1}^{N_{q1}} \sum_{q2=1}^{N_{q2}} \omega_{q1}\omega_{q2} N_J\left(\xi_{q1},\eta_{q2}\right) \det\left[\mathbf{J}\left(\xi_{q1},\eta_{q2}\right)\right] \end{aligned} \tag{4.37}$$

with the exception of triangular elements which can be expressed as

$$I_{el} = h_{iJ} \sum_{q1=1}^{N_{q2}} \omega_{q1} N_J\left(\xi_{q1},\eta_{q2}\right) \det\left[\mathbf{J}\left(\xi_{q1},\eta_{q2}\right)\right] \tag{4.38}$$

The isoparametric coordinates $\left(\xi,\eta\right)$ and weights ω_q for the gauss points, shape functions $N_J\left(\xi,\eta\right)$ and coordinate Jacobian matrix, $\mathbf{J}\left(\xi_{q1},\eta_{q2}\right)$,are defined for elements used here in the Abaqus theory manual (Abaqus, 2007).

The integration over the entire volume of the rSVE is the summation over all elements in the model, i.e.,

$$\int_{\Omega_{rVE}} h_i \, d\Omega \cong \sum_{el} I_{el} \Rightarrow \sum_{I=1} \hat{h}_{iJ} A_J \tag{4.39}$$

Because the integration takes place in the reference configuration (i.e. undeformed geometry), it can be expressed as a linear constraint equation of the form (4.36) involving pre-computed nodal

weighting coefficients, A_I. Nodal weighting coefficients are obtained by first initializing to zero, $A_I = 0$, and then looping over each element, *el*, in the rSVE. For each node, *J*, comprising element, *el*:

$$A_J = A_J + \sum_{q1=1}^{N_{q1}} \sum_{q2=1}^{N_{q2}} \omega_{q1}\omega_{q2} N_J\left(\xi_{q1}, \eta_{q2}\right) \det\left[J\left(\xi_{q1}, \eta_{q2}\right)\right] \tag{4.40}$$

The volume integral constraint is then enforced by the linear constraint equation

$$\sum_{J\in\Omega} A_J \hat{h}_{iJ} = 0 \tag{4.41}$$

4.2.3 Generalized Periodic Boundary Conditions

For first-order simulations, periodic boundary conditions reduce the constraint on rSVE deformation modes, while still satisfying kinematic compatibility requirements so that the response of an rSVE may be "tiled" in space. In fact, they have been shown to provide better approximation to the actual behavior than either uniform Dirichlet or Neumann conditions (Hazanov and Amieur, 1995; Terada et al., 2000; van der Sluis et al., 2000; Amanatidou and Aravas, 2002).

First-order periodic boundary conditions are defined in this multiscale framework by defining for each set of parallel rSVE faces, a dependent and independent face. We adopt the rule that the independent face is that face where the dot product of its surface normal and the global Cartesian coordinate basis is positive (i.e. "positive face") and the dependent face is the "negative face". For each node on the independent face we identify the node on the corresponding dependent face that shares identical surface coordinates (cf. Figure 5 in Section 3.1.5). Then, the requirement

$$\hat{\mathbf{h}}^{(-)}\left(\boldsymbol{\eta}\right) = \hat{\mathbf{h}}^{(+)}\left(\boldsymbol{\eta}\right) \tag{4.42}$$

is enforced by adding constraint equations (4.43) for each pair of opposite boundary nodes, with the exception of the corner nodes for a 2D rSVE and nodes on edges of boundary intersection for 3D rSVE. At such locations there are more than one independent node for each dependent node. The chain of dependence will establish the fluctuation DOF of all corner nodes should be equal to

the fluctuation DOF of a single independent node. In our implementation the unique independent corner node is the node located at vertex V3 in Figure 5 in Section 3.1.5.

$$\begin{aligned}(1)\hat{h}_1^D + (-1)\hat{h}_1^I &= 0\\ (1)\hat{h}_2^D + (-1)\hat{h}_2^I &= 0\end{aligned} \tag{4.43}$$

In addition to establishing the constraint equations for periodic boundary fluctuations, it is also necessary to provide a rigid body constraint on the fluctuation field, which can be accomplished for the first-order simulations by simply constraining the fluctuation at the independent corner node equal to zero,

$$h_1^{c3} = h_2^{c3} = 0 \tag{4.44}$$

Additional constraints provided for second-order simulations will obviate this corner boundary condition by removing rigid-body fluctuations in a weaker volume-averaged fashion. The first-order periodic boundary conditions comprising (4.32), (4.43), and (4.44) are sufficient to satisfy the requirement (4.24).

Second-order simulations must satisfy the requirements (4.26)-(4.29) in addition to (4.24). Enforcement of periodic fluctuations by (4.32), (4.43), and (4.44) will satisfy requirements (4.27) and (4.29) directly. On the other hand, requirements (4.26) and (4.28) involve further consideration. Equations (4.26) and (4.28) can be converted directly into constraint equations by adding to the nodal weighting coefficients computed by (4.40) for establishing the volume integral of nodal fluctuations over the rSVE, additional contributions corresponding to the integral over the boundary of the rSVE.

The boundary integral coefficients are computed by assuming linear interpolation of values between nodes on the boundary. Note that this assumption is precisely consistent with the use of linear finite elements. The boundary integral coefficients, B_J, are computed by updating for each element with an edge forming part of the rSVE boundary, the contribution to node, *J*, lying on the boundary according to

$$B_J = B_J + \tfrac{1}{2}\Delta L_{el} \tag{4.45}$$

where ΔL_{el} is the spacing between two nodes of element, *el*, lying on the boundary. It is only necessary to compute these coefficients for the independent boundaries, as the dependent boundary DOFs are eliminated by (4.43). To directly convert requirement into constraint equations we define

$$C_J^n = A_J - B_J^n L_{rVE}^n \tag{4.46}$$

and specify the constraint equation for each independent boundary, *n*,

$$\sum_{J\in\Omega} C_J^n \hat{h}_{iJ} = 0 \tag{4.47}$$

Results from preliminary second-order simulations demonstrated that removing rigid body fluctuations from the rSVE using (4.44) presented to strong of a constraint at corners of the rSVE for nonzero second gradient components. To reduce the nature of this constraint, the volume integral of fluctuation rather than the value at any particular node, is set to zero. Accordingly, equation (4.47) is modified to

$$\sum_{J\in\Omega} A_J \hat{h}_{iJ} = 0 \tag{4.48}$$

$$\sum_{J\in\Gamma^n} B_J^n \hat{h}_{iJ} = 0 \tag{4.49}$$

4.2.4 Minimal Boundary Conditions

For a first order simulation, the absolute minimal constraint on the boundary is provided by Equations (4.20) and (4.24). Here, rigid body fluctuation modes are removed by setting the integral of the fluctuation field over each side of the rSVE equal to zero. The resulting four linear constraint equations are the same as (4.49) with coefficients given by (4.45), with the exception that, by omitting periodicity condition, each of four sides must be included in one constraint equation.

Restraint of rigid body deformation under minimal boundary conditions for second-order simulations requires both the volume integral of the fluctuation field to vanish, enforced through constraint equation (4.41), as well as boundary integral of fluctuation over each side, using (4.49).

In order to satisfy requirements (4.27) and (4.29), an additional set of constraint equations is introduced, one for each pair of boundary edges with opposite outward surface normal, i.e.,

$$\sum_{J\in\left(\Gamma^{+},\Gamma^{-}\right)^{n}} D_J^n \hat{h}_{iJ} = 0 \tag{4.50}$$

The coefficients, D_J, are computed assuming linear interpolation between nodal values on the boundary and updating for each element with an edge forming part of the rSVE boundary, the contribution to node, *J*, lying on the boundary according to

$$D_J = D_J + \tfrac{1}{2}\eta_J \Delta L_{el} \tag{4.51}$$

where η is the appropriate component of the surface coordinates. The constraint equations of (4.50) involve the same DOFs as (4.49). Each constraint equation eliminates one DOF from the simulation and, moreover, the finite element code Abaqus will not permit subsequent constraint equations to be defined using eliminated DOFs as the dependent DOF. In order to remove eliminated DOFs from constraint equations we re-express (4.49) as

$$\sum_{J\in\Gamma^{n}} E_J^n \hat{h}_{iJ} = 0 \tag{4.52}$$

with the coefficients

$$E_J = B_J - \frac{B_0}{D_0} D_J \tag{4.53}$$

where B_0 is the coefficient corresponding to the leading DOF in constraint equations (4.49), D_0 is the coefficient corresponding to that same DOF in constraint equations (4.50). The eliminated DOF is not written into the constraint equations (coefficient of zero). Additionally note that only two of the four sides concerned in (4.49) need be treated in this manner, and that for the two sides that are treated in this manner, all the DOFs of the corresponding equation from (4.50) must be included, not simply those from equation (4.49).

4.2.5 Verification of Numerical Implementation of Boundary Conditions

This verification of implemented fine scale boundary conditions is not an exhaustive code verification study, but rather focuses on a few salient issues of the implementations relevant to subsequent simulations. First and foremost in this regard, we present a new principle for the appropriateness of boundary conditions, namely,

> *Boundary conditions applied to a homogeneous rSVE exhibiting infinitesimal elastic deformation should result in homogeneous response such that the fluctuation field vanishes everywhere within the rSVE.*

The proposed requirement pertains to infinitesimal elastic deformation, i.e., equilibrium is enforced in the reference, rather than current, configuration and the local constitutive response is reversible. Irreversible local constitutive behavior would not make a suitable test case because a homogeneous deformation field associated with a nonzero second gradient produces strain gradients such that irreversible mechanisms would be initiated in a non-homogeneous manner. Finite deformation theory (i.e., equilibrium is enforced in the current rather than reference configuration) is used for simulations in this dissertation and is essential for accurately computing the nonsymmetrical coarse scale Cauchy stress. However, when applied to a homogeneous rSVE under a second gradient deformation field, elastic finite deformation causes a bifurcation in the fluctuation field giving rise to a multitude of attainable fine-scale deformation fields for a given set of coarse scale boundary conditions. This phenomena has been studied in some detail and is presumed to be due to internal fluctuation bifurcation mechanisms which do not affect the global stability until fairly large deformations are encountered. Conceptually, kinematic constraints prevent the rSVE response from reaching the minimal total potential energy state attainable in the absence of fine-scale constraints, cf. Figure 30. The constrained minimal total potential energy is apparently non-unique so that when equilibrium is enforced in the deformed configuration, there are multiple configurations which satisfy the constrained equilibrium. Not only is the solution non-unique, it contains significant fluctuations that grow in magnitude much faster than the coarse scale DOFs until the point at which a global instability is reached. It will be demonstrated subsequently, that this issue is irrelevant to the response of a heterogeneous rSVE.

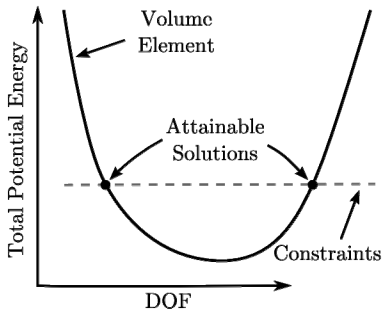

Figure 30. Conceptual illustration of bifurcation for one DOF.

The approach for verification of the 'appropriateness' of the proposed boundary conditions is to first evaluate satisfaction of the homogeneity principle for infinitesimal deformation, and then compare the response of heterogeneous rSVE under infinitesimal and finite deformation. Verification of the numerical implementation is conducted by assuring the deformation field satisfies requirements imposed on the fluctuation field (cf. Chapter 3) by numerical integration and inspecting deformation results, e.g., for periodicity. A square rSVE with sides 10 μm in length and a structured uniform finite element mesh whose elements' sides are 1 μm in length having a linear elastic constitutive relationship with Young's modulus of 175 GPa and Poisson ratio of 0.3 was used for this study. In turn, each component of coarse scale kinematic DOFs was independently perturbed by a small value holding all others fixed at zero. This process was repeated for each set of proposed boundary conditions, viz.: direct, periodic, and minimal. The perturbation value was selected to achieve a strain of approximately 0.1% for the coarse scale deformation gradient modes of response, e.g. F_{11}, F_{12}, F_{22} and to achieve a similar peak displacement for the coarse scale second gradient modes of response, e.g. $G_{111}, G_{121}, G_{122}$. Representative contours of the resulting fluctuation field are superposed on plots of the magnified (400x) deformed geometry in Figure 31. Direct and periodic boundary conditions exhibit negligible fluctuations for all sets of boundary conditions. The minimal boundary conditions appear acceptable for first order response, but cause excessive fluctuation at rSVE corners for second order simulations. Presumably, this could be alleviated by enforcing that the volume-

averaged fine scale gradient of the deformation gradient be equivalent to the coarse scale second-gradient. As discussed in Chapter 3, such a requirement would result in gradient boundary conditions on the boundaries and is not pursued here.

A dimensionless 'error' norm was introduced to quantify departure from homogeneous response, i.e.,

$$\text{Error} = \frac{\int_{\Omega_{rVE}} |\mathbf{h}| \, d\Omega}{\int_{\Omega_{rVE}} |\mathbf{d}| \, d\Omega} \tag{4.54}$$

Values of this norm computed for each of the coarse-scale modes of deformation and set of boundary conditions are presented in Table 2. These results confirm that the direct and periodic boundary conditions provide homogenous response for a homogeneous rSVE, while the minimal conditions do not for second gradient deformation modes. In addition, the volume and boundary integrals of the fluctuation field were confirmed to be negligible (essentially zero) for all cases, as appropriate.

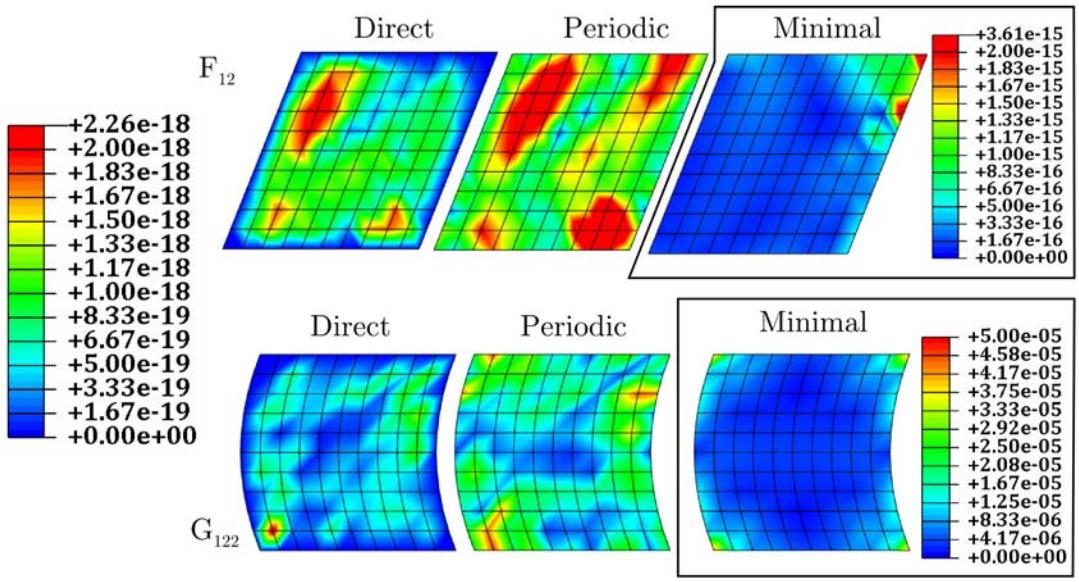

Figure 31. Contour plots of fluctuation (**h**) magnitude superposed for homogeneous rSVE. Scale at left pertains to the direct and periodic conditions. Scales for minimal conditions shown in boxed region with corresponding contour plot.

Table 2. Fluctuation (error) norm for deformation of homogeneous rSVE**.**

Nonzero Coarse Scale Component	Direct Boundary Conditions	Periodic Boundary Conditions	Minimal Boundary Conditions
F_{11}	2.0739e-016	3.4497e-016	3.5734e-013
F_{12}	3.2864e-016	5.3005e-016	9.9293e-014
F_{22}	2.5307e-016	3.5788e-016	1.5289e-013
G_{111}	6.9076e-016	1.2141e-015	8.6773e-003
G_{121}	4.3141e-016	1.0172e-015	1.5189e-002
G_{122}	6.2937e-016	1.1715e-015	5.7830e-003
G_{211}	4.5622e-016	7.7120e-016	5.7830e-003
G_{221}	3.9288e-016	6.8088e-016	1.5189e-002
G_{222}	5.1836e-016	1.1272e-015	8.6773e-003

Thus far the focus has been verification of the numerical boundary conditions under assumed infinitesimal deformation (i.e., equilibrium is enforced in undeformed configuration) and linear elasticity. As discussed previously, this assumption will not generally be useful in the multiscale framework. It is merely used as a stepping stone for verification given the bifurcation issue associated with finite deformation solutions of a homogeneous rSVE. As evidence that the proposed boundary conditions are suitable for modeling generally finite deformation response, the fluctuation fields of solutions obtained using both finite and infinitesimal deformation are compared for cases of small (order of 0.1%) and finite (order of 10%) strain. Both cases utilize linear elasticity. The extension to finite deformation is made by enforcing equilibrium in the deformed configuration, i.e., accounting for geometric stiffness in the fine scale finite element solution. Results are presented in Figure 32 for a particular mode of deformation, i.e., $G_{122} \neq 0$, in which contours of fluctuation fields and their differences are plotted on top of the deformed geometry whose displacements are magnified four and 400 times for the large and small

deformation cases, respectively. Results from this mode of deformation are representative of those from all modes. The top pane of Figure 32 compares the fluctuation fields for the small strain case. These results demonstrate similar fluctuation field solutions with peak local differences two orders of magnitude smaller than the peak local fluctuations. There is no bifurcation in the solution using finite deformation theory and the agreement of the results adds merit to the argument that these conditions are appropriate. The bottom pane illustrates significant differences in the local fluctuation field for a large strain case; however, the magnitudes and global distribution of the fluctuation field are similar and the finite strain solution does not present any concerns. Differences in the local spatial distribution of the fluctuation field around the pore are not alarming and in this context reaffirm the inappropriateness of infinitesimal strain theory for generally finite deformations. Again, this comparison is presented merely as evidence in support of the proposed numerical implementation of boundary conditions.

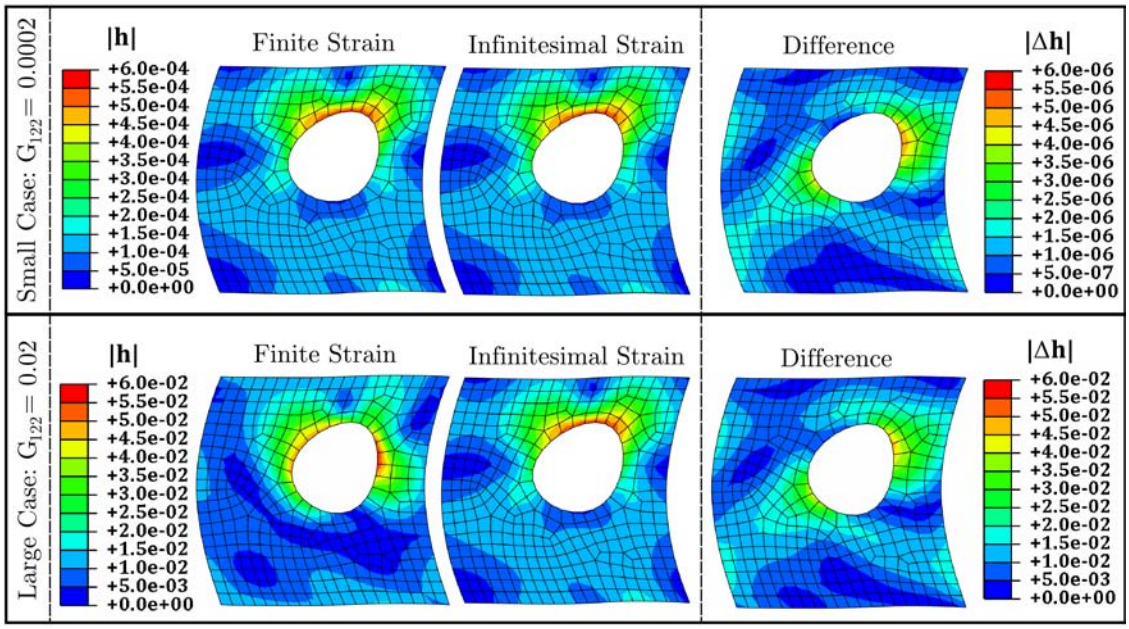

Figure 32. Fluctuation fields and their difference for elastic finite and infinitesimal deformation solutions.

4.2.6 Discussion

Direct boundary conditions are simple to implement and can easily accommodate arbitrary rSVE geometry and mesh, i.e., neither the geometry nor the mesh need be periodic. However, direct boundary conditions are widely known to impede the localization process and provide an upper, or overly stiff, bound on the stress-strain response.

Periodic boundary conditions, on the other hand, reduce the stiffness of constraint, thereby enabling physical localization modes. In fact, periodic boundary conditions have been shown to provide better approximation to the actual behavior than either direct Dirichlet or Neumann conditions (Amieur et al., 1993 ; Hazanov and Amieur, 1995; Terada et al., 2000; van der Sluis et al., 2000) for first order simulations; however, this has not been quantitatively studied for second order simulations. The disadvantage of such boundary conditions is that they require, at least conceptually, a periodic rSVE geometry. This requirement is absolute for modeling of porosity. The most direct implementations of periodic boundary conditions also require a periodic mesh, i.e., each node on a dependent boundary has a "master" node at the same surface coordinate on the opposing independent boundary. This requirement could be obviated by using the element shape function to interpolate the proper weighting coefficients defining the response of a dependent node on one or more independent nodes on the opposite boundary. However, this approach would not generally provide fluctuation continuity across adjacent periodic boundaries as a strictly periodic mesh does. The imposition of kinematically periodic constraint equations eliminates all fluctuation DOF at a particular dependent node. Consequently, an implicit reaction force exists at that node and is equal and opposite to the reaction force at the corresponding independent node. This, in turn, implies continuity of the stress field across adjacent periodic boundaries and that surface tractions *are* equal and opposite yielding truly periodic behavior. The boundary conditions presented here reduce to the classic periodic boundary conditions for purely first order deformation.

The generalized periodic boundary conditions presented differ from those proposed by Kouznetsova et al. (2002; 2004) in two respects. First, and most directly, Kouznetsova et al. do not include the requirement that the volume integral of the fluctuation field vanish. Second, their

vanishing boundary integral of fluctuation appears as the end result of a substantial modification of the definition of the second-gradient from that used in their original decomposition. Because they use two different definitions at various points in the development of their homogenization scheme, it is not consistent, and moreover, the derived stresses are not generally conjugate to the coarse scale kinematic terms.

A comparison of the fine scale response under the generalized periodic boundary conditions developed here to those of Kouznetsova et al. (2002; 2004) are presented in Figure 33 and Figure 34 for second-gradient deformation with the nonzero component of $G_{122} = 0.02$ and $G_{222} = 0.02$, respectively. In these figures the generalized periodic conditions presented here are labeled "Periodic (Luscher)", while those of Kouznetsova et al., are labeled "periodic (Kouznetsova)". A further distinction is made between the conditions specified by Kouznetosva et al. in which the fluctuation at the four corner nodes is fixed to zero, versus conditions where that constraint is not enforced at the corners, i.e., "Kouznetsova-Free". The local strain response is similar for all of these cases under the curvature mode of second gradient deformation. However, under an imposed gradient of axial strain the differences are substantial. First, the Kouznetsova conditions cause dramatic localization at the corners of the rSVE. This is due to (1) the lack of a volume integral constraint on fluctuation field, (2) constraining the fluctuation at the corner nodes to be zero, and (3) the need for body forces in establishing quasi-uniform gradients of strain in an rSVE (cf. Chapter 3 Section 3.2.2). The reaction force associated with the volume integral constraint equation is, precisely, the magnitude of the body force per unit undeformed volume needed to provide such a quasi-uniform gradient field. Releasing the corner constraints eliminates the problem of localization; however, the fluctuation field is no longer unique such that the rSVE can freely translate under a rigid mode of deformation. In either case the fluctuation field is not a fluctuation about the mean field displacement. Its gradient still has meaning, but the fluctuation field itself is of no descriptive significance. This discussion highlights the conceptual and physical differences between the boundary conditions of Kouznetsova and those presented here. We have focused on drawing a comparison with their work in particular because it is the most significant and well-established amongst the narrow field of direct second-gradient fine scale simulations and homogenization.

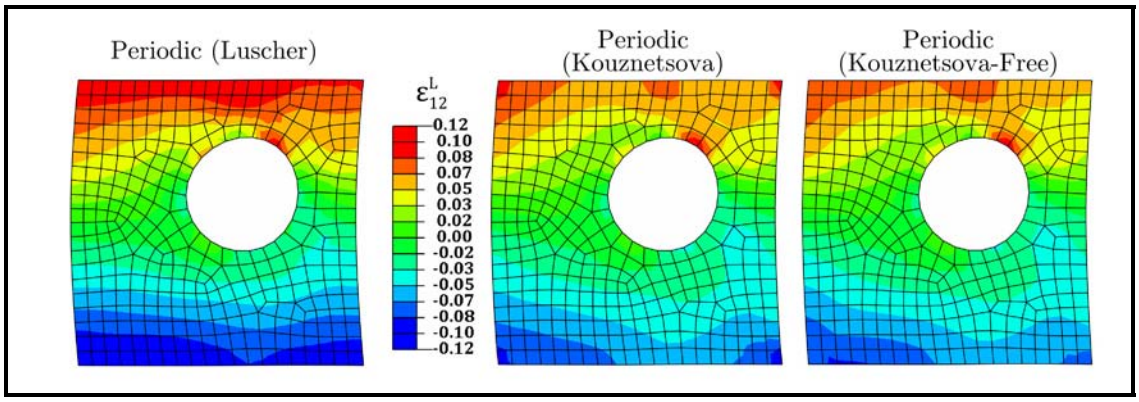

Figure 33. Comparison of local logarithmic shear strain for $G_{122} = 0.02\mu m^{-1}$ (curvature mode).

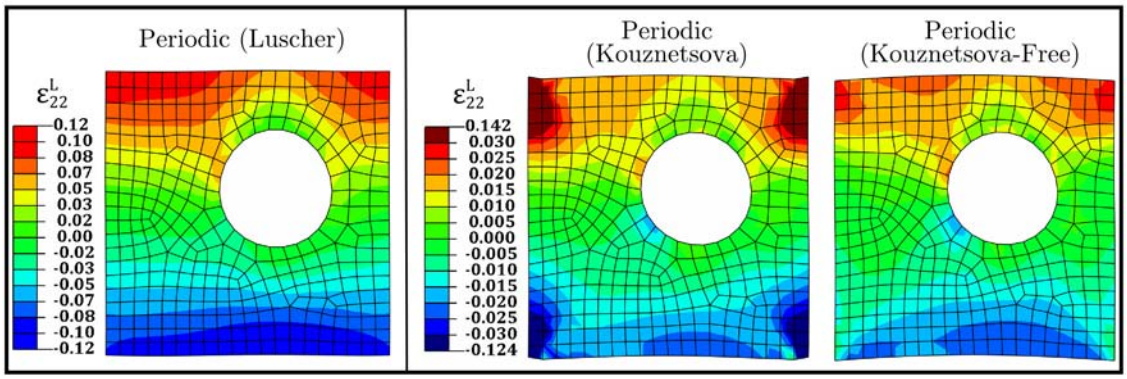

Figure 34. Comparison of local logarithmic axial strain for $G_{222} = 0.02\mu m^{-1}$ (extensional mode).

Both the direct and periodic boundary conditions present unnecessary constraint on the deformation of the rSVE in achieving a fine-scale response kinematically consistent with the coarse scale state of deformation. As noted by Mesarovic and Padbidri (2005), such unnecessary constraints cause boundary effects, overly stiff response, artificial spatial correlation of deformation response, and to various extents impede localization. To circumvent these deficiencies, Mesarovich and Padbidri (2005) defined minimal boundary conditions as those in

which only the "desired overall strain is imposed on the (rSVE)." Their proposed boundary conditions are only applicable to first order simulations and their implementation is specific to linear elastic response. The original concept of Mesarovich and Padbidri is expanded here significantly to the definition of minimal boundary conditions as those in which only the desired coarse scale description of deformation is imposed upon the fine scale deformation in a manner fully preserving kinematic consistency between the two scales of observation. The more general development here approaches theirs in the limit of infinitesimal deformation for purely first order response. The disadvantage of these boundary conditions are that they are untested and do not satisfy the homogeneity of response principle for second order response, as demonstrated previously. It should be noted that this principle is heuristic and, therefore, is not necessarily grounds for dismissal of such boundary conditions. While they represent the least possible constraint on the deformation of an rSVE to satisfy multiscale kinematic consistency, they may or may not yield simulations closer to the true physical response. This is a potentially valuable area of future research.

Contours of the local magnitude of fluctuation are plotted on deformed geometry (with displacements magnified 4x) for representative first order (Figure 35) and second order (Figure 36) modes of deformation. These plots are a good characterization of the two-dimensional boundary conditions and deformation modes. While the minimal boundary conditions did not adequately demonstrate the homogeneity principle, the deformed response under these boundary conditions is qualitatively reasonable when compare to that for the direct and periodic boundary conditions. Again, the homogeneity principle has been postulated here as a heuristic and no evidence has yet been presented to elevate it to a strict rule.

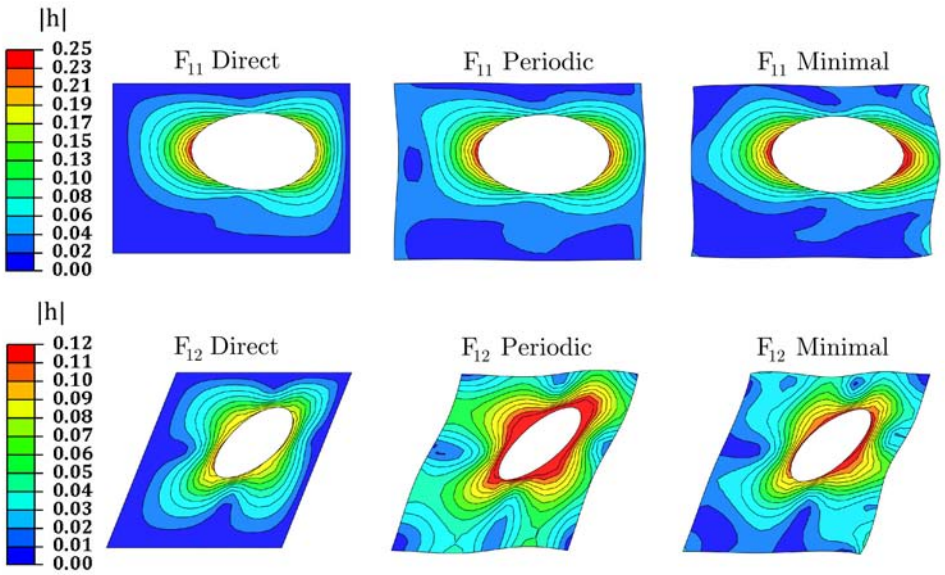

Figure 35. Comparison of local fluctuation field under direct, periodic, and minimal boundary conditions for first order extensional (top) and shear (bottom) deformation.

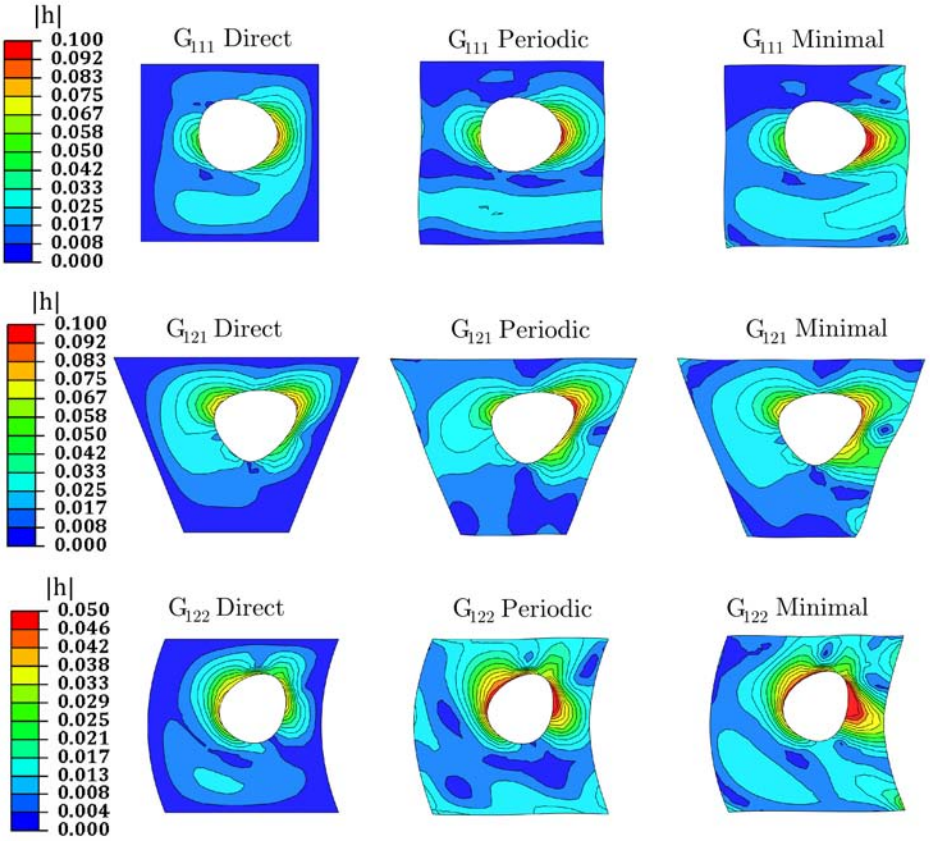

Figure 36. Local fluctuation fields under direct, periodic, and minimal boundary conditions for second order extensional (top), trapezoidal (middle), and curvature (bottom) deformation.

4.3 Computation of Coarse Scale Nominal Stresses

The computation of first and second order coarse scale nominal stresses benefits significantly from the principle of virtual velocities (PVV). Recall from Chapter 3 the coarse scale stresses are defined in accordance with multiscale PVV as,

$$\begin{aligned}
\mathbf{P} &= \frac{1}{\Omega_{\mathrm{o}}^{\mathrm{x}}}\int_{\Gamma_{\mathrm{o}}^{\mathrm{x}}} \mathbf{y}_{\mathrm{o}} \otimes \mathbf{t}_{\mathrm{o}}\, d\Gamma_{\mathrm{o}} + \frac{1}{\Omega_{\mathrm{o}}^{\mathrm{x}}}\int_{\Omega_{\mathrm{o}}^{\mathrm{x}}} \rho_{\mathrm{o}}\mathbf{y}_{\mathrm{o}} \otimes \mathbf{b}_{\mathrm{o}} d\Omega_{\mathrm{o}} &&= \frac{1}{\Omega_{\mathrm{o}}^{\mathrm{x}}}\int_{\Omega_{\mathrm{o}}^{\mathrm{x}}} \mathbf{p}\, d\Omega + \frac{1}{\Omega_{\mathrm{o}}^{\mathrm{x}}}\int_{\Omega_{\mathrm{o}}^{\mathrm{x}}} \rho_{\mathrm{o}}\mathbf{y}_{\mathrm{o}} \otimes \mathbf{a} d\Omega_{\mathrm{o}} \\
\mathbf{Q} &= \frac{1}{2\Omega_{\mathrm{o}}^{\mathrm{x}}}\int_{\Gamma_{\mathrm{o}}^{\mathrm{x}}} \mathbf{t}_{\mathrm{o}} \otimes \mathbf{y}_{\mathrm{o}} \otimes \mathbf{y}_{\mathrm{o}}\, d\Gamma_{\mathrm{o}} + \frac{1}{2\Omega_{\mathrm{o}}^{\mathrm{x}}}\int_{\Omega_{\mathrm{o}}^{\mathrm{x}}} \rho_{\mathrm{o}}\mathbf{b}_{\mathrm{o}} \otimes \mathbf{y}_{\mathrm{o}} \otimes \mathbf{y}_{\mathrm{o}} d\Omega_{\mathrm{o}} &&= \frac{1}{\Omega_{\mathrm{o}}^{\mathrm{x}}}\mathrm{symR}\left(\int_{\Omega_{\mathrm{o}}^{\mathrm{x}}} \mathbf{p}^{T} \otimes \mathbf{y}_{\mathrm{o}} d\Omega_{\mathrm{o}}\right) + \frac{1}{2\Omega_{\mathrm{o}}^{\mathrm{x}}}\int_{\Omega_{\mathrm{o}}^{\mathrm{x}}} \rho_{\mathrm{o}}\mathbf{a} \otimes \mathbf{y}_{\mathrm{o}} \otimes \mathbf{y}_{\mathrm{o}} d\Omega_{\mathrm{o}}
\end{aligned} \tag{4.55}$$

and can be computed from fine scale rSVE response by numerically integrating terms from either external forces or internal response. A computationally more efficient method is presented here along with numerical justification. The virtual power per specific volume resulting from the set of coarse scale virtual velocities is

$$\delta \mathrm{P}_{\mathrm{coarse}} = \mathbf{P} : \delta\dot{\mathbf{F}}^{T} + \mathbf{Q}\vdots\delta\dot{\mathbf{G}} \tag{4.56}$$

The virtual power per specific volume of the discrete fine scale rSVE simulation is

$$\delta \mathrm{P}_{\mathrm{rSVE}} = \frac{1}{\Omega_{\mathrm{o}}}\sum_{J=1}^{N\mathrm{ref}} RF_i \delta\hat{d}_i^{\mathrm{Ref}J} \tag{4.57}$$

where $RF_i^{\mathrm{Ref}J}$ is the i^{th} component of the J^{th} reference node used in (4.30). Enforcing that for any set of kinematically admissible virtual velocities,

$$\delta \mathrm{P}_{\mathrm{coarse}} = \delta \mathrm{P}_{\mathrm{rSVE}} \tag{4.58}$$

and using the relationship between the velocities of the reference node DOFs and coarse scale kinematic DOFs (4.30), the coarse scale nominal stresses are solved, i.e.,

$$\mathbf{P} = \frac{1}{\Omega_{\mathrm{o}}}\begin{bmatrix} RF_1^{\mathrm{Ref1}} & RF_2^{\mathrm{Ref1}} & 0 \\ RF_1^{\mathrm{Ref2}} & RF_2^{\mathrm{Ref2}} & 0 \\ 0 & 0 & RF_3^{\mathrm{Ref6}} \end{bmatrix} \tag{4.59}$$

and

$$\mathbf{Q} = \frac{1}{\Omega_o}\begin{bmatrix} \begin{bmatrix} RF_1^{\text{Ref3}} & \frac{1}{2}RF_1^{\text{Ref4}} & 0 \\ \frac{1}{2}RF_1^{\text{Ref4}} & RF_1^{\text{Ref5}} & 0 \\ 0 & 0 & 0 \end{bmatrix} \\ \begin{bmatrix} RF_2^{\text{Ref3}} & \frac{1}{2}RF_2^{\text{Ref4}} & 0 \\ \frac{1}{2}RF_2^{\text{Ref4}} & RF_2^{\text{Ref5}} & 0 \\ 0 & 0 & 0 \end{bmatrix} \\ \begin{bmatrix} 0 & 0 & -\frac{1}{2}RF_5^{\text{Ref6}} \\ 0 & 0 & \frac{1}{2}RF_4^{\text{Ref6}} \\ -\frac{1}{2}RF_5^{\text{Ref6}} & \frac{1}{2}RF_4^{\text{Ref6}} & 0 \end{bmatrix} \end{bmatrix} \tag{4.60}$$

To numerically verify that (4.59) and (4.60) are valid and that the implementation is correct, nominal stresses were computed by both full integration over the rSVE and using reaction forces and then compared for a set of sample calculations. This set of sample calculations consisted of exercising the rSVE over the mode of deformation attributed to each component of coarse scale kinematic response (e.g. G_{211}) , in turn, while all other coarse scale terms remained fixed at zero. This sequence of simulations was repeated for each set of boundary conditions. For each finite element discretization, quantified by characteristic element size, and set of boundary conditions, two error norms were computed. The first order error norm, $E_{\mathbf{P}}$, reflects the mean square root of sum of squares difference between the nominal stress components as computed by volume integral and reaction force. As shown in equation (4.61), this norm is computed only from the N_1 cases for which the first order deformation is induced. The second order error norm, $E_{\mathbf{Q}}$, is likewise computed for the N_2 second-order deformation cases, cf. (4.62).

$$E_{\mathbf{P}} = \frac{1}{N_1}\sum_{C=1}^{N_1}\left(\sqrt{\frac{\left(P_{ij}^{\int} - P_{ij}^{RF}\right)\left(P_{ij}^{\int} - P_{ij}^{RF}\right)}{P_{ij}^{\int}P_{ij}^{\int}}}\right)_C \tag{4.61}$$

$$E_{\mathbf{Q}} = \frac{1}{N_2}\sum_{C=1}^{N_2}\left(\sqrt{\frac{\left(Q_{ijk}^{\int} - Q_{ijk}^{RF}\right)\left(Q_{ijk}^{\int} - Q_{ijk}^{RF}\right)}{Q_{ijk}^{\int}Q_{ijk}^{\int}}}\right)_C \tag{4.62}$$

Error norm results are plotted against characteristic element size in Figure 37. The magnitude of error is reassuringly low for all cases, and converges towards zero error between the two methods

of computation as the mesh is refined. These results confirm the proposed method for computing coarse scale nominal stresses directly from rSVE reaction forces and, additionally, serve to verify the numerical implementation.

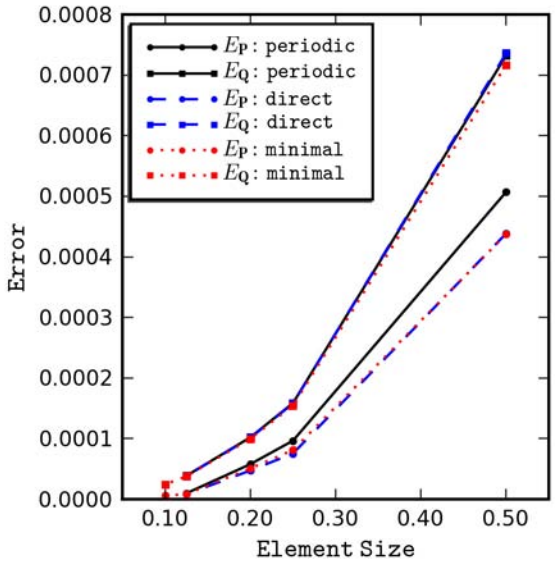

Figure 37. Convergence of error for coarse scale nominal stress computation.

4.4 Simulation of Coarse Scale Intermediate Configuration

Methods for defining the reference configuration and applying boundary conditions to ensure deformation consistent with coarse scale kinematics have been detailed up to this point. Modeling irreversible processes that involve microstructure evolution benefit from an intermediate configuration as defined in Chapter 3. The intermediate configuration is a coarse scale stress-free configuration of the rSVE that accompanies the current configuration through time. It is directly simulated by freeing the coarse scale kinematic DOFs (4.30) such that the associated reaction forces, and consequently coarse scale stresses, are zero. This unloading process is conducted for each increment, i.e., current configuration state, in a generally nonlinear and irreversible deformation history of the rSVE. As discussed in Chapter 3, this process requires

assumptions regarding the rate of unloading. In particular, if the fine scale material response is rate dependent the characteristic time for unloading should be sufficiently slow to allow the rSVE to attain equilibrium, while not so slow as to enable activation of new evolution mechanisms (e.g creep). The goal is to remove the elastically recoverable free energy from the system.

4.4.1 Computation of Coarse Scale Kinematic Variables

After unloading has been accomplished, the values of the coarse scale DOFs define the inelastic coarse scale kinematic quantities. Recall from Chapter 3, the deformed coordinates of a material point in the intermediate configuration are given by

$$\tilde{\mathbf{y}} = \mathbf{F}_{in} \cdot \mathbf{y}_{\mathrm{o}} + \tfrac{1}{2}\mathbf{G}_{in} : \mathbf{y}_{\mathrm{o}} \otimes \mathbf{y}_{\mathrm{o}} + \tilde{\mathbf{h}}\left(\mathbf{y}_{\mathrm{o}}\right) \tag{4.63}$$

All other kinematic constraints remain in effect so that $\mathbf{F}_{in}$ and $\mathbf{G}_{in}$ are constructed from the coarse scale DOFs by (4.30) for the intermediate configuration solution.

The elastic part of the deformation gradient is computed by $\mathbf{F}_e = \mathbf{F} \cdot \mathbf{F}_{in}^{-1}$ enabling calculation of the elastic right Cauchy deformation tensor, $\tilde{\mathbf{C}}_e = \mathbf{F}_e^T \cdot \mathbf{F}_e$. The elastic and inelastic strains in the intermediate configuration are computed as $\tilde{\mathbf{E}}_e = \frac{1}{2}\left(\tilde{\mathbf{C}}_e - \mathbf{I}\right)$ and $\tilde{\mathbf{E}}_{in} = \frac{1}{2}\left(\mathbf{I} - \mathbf{F}_{in}^{-T} \cdot \mathbf{F}_{in}^{-1}\right)$, respectively. Note that the total Green-Lagrange strain, $\mathbf{E} = \frac{1}{2}\left(\mathbf{F}^T \cdot \mathbf{F} - \mathbf{I}\right)$, pushed into the intermediate configuration, is equal to the sum of elastic and inelastic strains, i.e.,

$$\tilde{\mathbf{E}} = \mathbf{F}_{in}^{-T} \cdot \mathbf{E} \cdot \mathbf{F}_{in}^{-1} = \tilde{\mathbf{E}}_e + \tilde{\mathbf{E}}_{in} \tag{4.64}$$

Computation of second order strains proceeds according to the following notation. Indicial notation is used to avoid notational complexity related to definition of multiple transpositions of a third-order tensor. All indices are expressed as lower case Latin subscripts regardless of the configuration (i.e., reference, intermediate, current) or variance. For clarification on variance and configuration see Section 3.1.

Given the inelastic deformation gradient, $\mathbf{F}_{in}$, and inelastic second gradient, $\mathbf{G}_{in}$, computation of the inelastic second order strain in the intermediate configuration is accomplished by completing the inelastic-push forward, i.e.,

$$ {}^{in}\tilde{\Gamma}_{ijk} = {}^{in}G_{imn}\,{}^{in}F^{-1}_{mj}\,{}^{in}F^{-1}_{nk} \tag{4.65} $$

The total second order strain in the intermediate configuration is computed by the push-pull of all indices of the total second gradient into the intermediate configuration, i.e.,

$$ \tilde{\Gamma}_{ijk} = {}^{e}F^{-1}_{im}G_{mno}\,{}^{in}F_{jn}\,{}^{in}F_{ko} \tag{4.66} $$

Then the elastic part of the second order strain with referred to the intermediate configuration is computed by subtracting the inelastic part form the total second order strain, i.e.,

$$ {}^{e}\tilde{\Gamma}_{ijk} = \tilde{\Gamma}_{ijk} - {}^{in}\tilde{\Gamma}_{ijk} \tag{4.67} $$

4.4.2 Computation of Coarse Scale Stresses

The nominal stresses, **P**, and **Q** are assembled from the simulation constraint reaction forces a la Eqs. (4.59) and (4.60). The second Piola-Kirchhoff stress is computed by completing the pull-back of nominal stress to the reference configuration, i.e.,

$$ \mathbf{S} = \mathbf{P} \cdot \mathbf{F}^{-T} \tag{4.68} $$

The second Piola-Kirchhoff stress referred to the intermediate configuration is computed by the inelastic push forward of Eq. (4.68) and dividing by the determinant of the inelastic deformation gradient to account for mass density and equivalent stress power, i.e.,

$$ \tilde{\mathbf{S}} = \frac{\mathbf{F}_{in} \cdot \mathbf{S} \cdot \mathbf{F}^{T}_{in}}{\det\left(\mathbf{F}_{in}\right)} \tag{4.69} $$

Likewise, the reference nominal second order stress is computed by pull back of the second order stress, i.e.,

$$ \mathbf{Q}_{\mathrm{o}} = \mathbf{F}^{-1} \cdot \mathbf{Q} \tag{4.70} $$

The second order stress referred to the intermediate configuration is computed by the inelastic push forward of the reference nominal second order stress, i.e.,

$$ \tilde{Q}_{ijk} = \frac{{}^{in}F_{im}\,{}^{in}F_{jn}\,{}^{in}F_{kr}\,{}^{e}Q^{\mathrm{o}}_{mnr}}{\det(\mathbf{F}_{in})} \tag{4.71} $$

The projected coarse scale Cauchy stress is computed according to

$$\Sigma_{ij}^{*} = \frac{1}{2\det(\mathbf{F})}\left(G_{imn}Q_{jmn} + G_{jmn}Q_{imn} \right) \tag{4.72}$$

and then pulled into the intermediate configuration using an elastic pull-back, i.e.,

$$\tilde{\mathbf{S}}^{*} = \det\left(\mathbf{F}_{e}\right)\mathbf{F}_{e}^{-1} \cdot \boldsymbol{\Sigma}^{*} \cdot \mathbf{F}_{e}^{-T} \tag{4.73}$$

4.4.3 Computation of Kinematic Rates

Kinematic rates are computed in post-processing by using first order finite divided differences. The time step size from increment *k* to *k+1* is

$$\Delta t_{k+\frac{1}{2}} = t_{k+1} - t_{k} \tag{4.74}$$

The time rate of the deformation gradient at the midpoint of the increment is computed as

$$\dot{\mathbf{F}}_{k+\frac{1}{2}} \cong \frac{1}{\Delta t_{k+\frac{1}{2}}}\left(\mathbf{F}_{k+1} - \mathbf{F}_{k} \right) \tag{4.75}$$

Likewise for the elastic and inelastic components, i.e.,

$$\dot{\mathbf{F}}_{k+\frac{1}{2}}^{e} \cong \frac{1}{\Delta t_{k+\frac{1}{2}}}\left(\mathbf{F}_{k+1}^{e} - \mathbf{F}_{k}^{e} \right) \tag{4.76}$$

$$\dot{\mathbf{F}}_{k+\frac{1}{2}}^{in} \cong \frac{1}{\Delta t_{k+\frac{1}{2}}}\left(\mathbf{F}_{k+1}^{in} - \mathbf{F}_{k}^{in} \right) \tag{4.77}$$

The elastic part of the velocity gradient referred to the intermediate configuration is computed by performing the elastic pull-back of (4.76) using the elastic part of the deformation gradient estimated at the increment midpoint, i.e.,

$$\tilde{\mathbf{L}}_{k+\frac{1}{2}}^{e} = \mathbf{F}_{k+\frac{1}{2}}^{e-1} \cdot \dot{\mathbf{F}}_{k+\frac{1}{2}}^{e} \tag{4.78}$$

Similarly for the inelastic part of the velocity gradient at the increment midpoint, i.e.,

$$\tilde{\mathbf{L}}_{k+\frac{1}{2}}^{in} = \dot{\mathbf{F}}_{k+\frac{1}{2}}^{in} \cdot \mathbf{F}_{k+\frac{1}{2}}^{in-1} \tag{4.79}$$

The elastic and inelastic rate of deformation tensors are computed by performing the symmetrization of the elastic and inelastic velocity gradients, respectively, using a midpoint estimate of the elastic right Cauchy deformation tensor, i.e.,

$$\tilde{\mathbf{D}}^{e}_{k+\frac{1}{2}} = \frac{1}{2}\left(\tilde{\mathbf{C}}^{e}_{k+\frac{1}{2}} \cdot \tilde{\mathbf{L}}^{e}_{k+\frac{1}{2}} + \tilde{\mathbf{L}}^{eT}_{k+\frac{1}{2}} \cdot \tilde{\mathbf{C}}^{e}_{k+\frac{1}{2}} \right) \tag{4.80}$$

and

$$\tilde{\mathbf{D}}^{in}_{k+\frac{1}{2}} = \frac{1}{2}\left(\tilde{\mathbf{C}}^{e}_{k+\frac{1}{2}} \cdot \tilde{\mathbf{L}}^{in}_{k+\frac{1}{2}} + \tilde{\mathbf{L}}^{inT}_{k+\frac{1}{2}} \cdot \tilde{\mathbf{C}}^{e}_{k+\frac{1}{2}} \right) \tag{4.81}$$

Rates of the elastic and inelastic parts of the second order strain in the reference configuration are computed using the first order finite divided difference, i.e.,

$$\dot{\mathbf{\Gamma}}^{e}_{k+\frac{1}{2}} \cong \frac{1}{\Delta t_{k+\frac{1}{2}}}\left(\mathbf{\Gamma}^{e}_{k+1} - \mathbf{\Gamma}^{e}_{k} \right) \tag{4.82}$$

and

$$\dot{\mathbf{\Gamma}}^{in}_{k+\frac{1}{2}} \cong \frac{1}{\Delta t_{k+\frac{1}{2}}}\left(\mathbf{\Gamma}^{in}_{k+1} - \mathbf{\Gamma}^{in}_{k} \right) \tag{4.83}$$

Lie derivatives of the second order strain are computed by inelastic pushforward of the time rates from Eqs. (4.82) and (4.83), respectively, i.e.,

$$L_v\left(\tilde{\Gamma}^{e}_{ijk} \right) = F^{in-1}_{mi} F^{in-1}_{nj} F^{in-1}_{ok} \dot{\Gamma}^{e}_{mno} \tag{4.84}$$

and

$$L_v\left(\tilde{\Gamma}^{in}_{ijk} \right) = F^{in-1}_{mi} F^{in-1}_{nj} F^{in-1}_{ok} \dot{\Gamma}^{in}_{mno} \tag{4.85}$$

4.4.4 Computation of Energetic Terms

The elastically recoverable free energy per unit mass is computed as

$$\overline{\psi}^{e}_{k} = \frac{1}{\overline{\rho}_{\mathrm{o}} \Omega_{\mathrm{o}}}\left(ALLWK^{\Omega}_{k} - ALLWK^{\tilde{\Omega}}_{k} \right) \tag{4.86}$$

where $\overline{\rho}_{\mathrm{o}}$ is the rSVE averaged mass density and ALLWK is a variable stored by Abaqus reflecting the total external work applied to get to the current state. This calculation reflects the work recovered during elastic unloading from the current configuration to the intermediate configuration, i.e., elastically recovered free energy. Similarly, the stored energy is computed as

$$\overline{\psi}_k^s = \frac{1}{\overline{\rho}_{\mathrm{o}}\Omega_{\mathrm{o}}}\left(ALLSE_k^{\tilde{\Omega}} + \int_{\Omega_{\mathrm{o}}} \rho_{\mathrm{o}}\psi_k^s(\mathbf{y}_{\mathrm{o}})\, d\Omega_{\mathrm{o}} \right) \tag{4.87}$$

Note that the integral in the second term on RHS of Eq. (4.87) is zero for perfect plasticity at the fine scale.

4.4.5 Computation of Energetic Rates

The energetic rates, or specific power, are computed using first order finite divided differences of energy terms available from Abaqus, i.e.,

$$\mathbb{P}^{\mathrm{ext}}_{k+\frac{1}{2}} = \frac{\left(ALLWK_{k+1} - ALLWK_k \right)}{\Omega_{\mathrm{o}}\Delta t_{k+\frac{1}{2}}} \tag{4.88}$$

$$\mathbb{P}^{in-fine}_{k+\frac{1}{2}} = \frac{\left(ALLPD_{k+1} - ALLPD_k \right)}{\Omega_{\mathrm{o}}\Delta t_{k+\frac{1}{2}}} \tag{4.89}$$

by conjugating proper stress and deformation rate terms, i.e.,

$$\mathbb{P}^{in-coarse}_{k+\frac{1}{2}} = \det(\mathbf{F}^{in}_{k+\frac{1}{2}})(\tilde{\mathbf{S}}_{k+\frac{1}{2}} - \tilde{\mathbf{S}}^*_{k+\frac{1}{2}}) : \tilde{\mathbf{D}}^{in}_{k+\frac{1}{2}} + \tilde{\mathbf{Q}}_{k+\frac{1}{2}} \vdots L_v(\tilde{\mathbf{\Gamma}}_{in})_{k+\frac{1}{2}} \tag{4.90}$$

or using finite divided differences of previously computed energy densities, i.e.,

$$\dot{\overline{\psi}}^s_{k+\frac{1}{2}} = \frac{\overline{\psi}^s_{k+1} - \overline{\psi}^s_k}{\Delta t_{k+\frac{1}{2}}} \tag{4.91}$$

4.5 Example rSVE Simulations of Porous Microstructure

Examples of fine scale simulations are given in this section in order to illustrate the intended fine scale approach within this multiscale framework. The simulations discussed here are based on the geometric descriptions of porosity discussed for the sample microstructure of Figure 13D. For each of the following simulations, the matrix was modeled as elastic perfectly-plastic with

Young modulus, E = 175 GPa, Poisson ratio, ν = 0.3, and Mises yield stress, 1000 MPa. The finite element simulations were conducted using linear quadrilateral (four node) generalized plane strain (CPEG4) elements in Abaqus standard v. 6.7-1 (Abaqus, 2007). Boundary conditions were specified in accordance with the procedures outlined in Section 4.2 and coarse scale variables were computed from solution results in accordance with Sections 4.3 and 4.4.

4.5.1 Unit Cell Simulations

The unit cell geometry consisted of a single centrally located void modeled as a circle of missing material embedded within an otherwise homogeneous matrix. A finite element mesh of the unit cell geometry was developed using Cubit (Cubit, 2008) Various cases of coarse scale deformation gradient and second gradient were applied to the unit cell to evaluate the fine scale response. Selected results are presented here. For example, in Figure 38 are contour plots of fine scale effective plastic strain (PEEQ, at left) and the axial component of fine scale Cauchy stress (S11, right) superposed on the deformed finite element mesh for an applied coarse scale deformation of $F_{11} = 1.02$. The coarse scale stress versus strain history for this sample calculation is shown in Figure 39. The unit cell initially yields at a coarse scale stress near 680 MPa and then exhibits nonlinear hardening to about 760 MPa. The initial yield reflects the fine scale stress concentrations in the vicinity of the pore. The hardening is a manifestation of evolving heterogeneous residual elastic strains in the intermediate configuration and, as will be shown subsequently, is of kinematic nature. The elastic recoverable free energy, $\overline{\psi}_e$, is plotted versus the relevant component of the coarse scale elastic Green-Lagrange strain referred to the intermediate configuration (hereafter, elastic strain) in Figure 40. Note the apparent quadratic relationship between elastic free energy and elastic strain.

Figure 41 presents time histories of various computed energy and power densities, as well as the storage power ratio. The top of Figure 41 shows the recoverable (elastic, $\overline{\psi}_e$), stored ($\overline{\psi}_s$), and total ($\overline{\psi} = \overline{\psi}_e + \overline{\psi}_s$) free energy time histories. Prior to solution time of approximately 0.25s the elastic and total free energy appear to lie on top of each other, although it is clear from the plot of inelastic power (coarse and fine scale) in the middle of Figure 41 that irreversible deformation

has occurred prior to solution time of 0.2s. The ratio of the rate at which energy is stored in fine scale fluctuations (storage power) to the coarse scale inelastic power is plotted at the bottom of Figure 41. From this plot it is clear that significant energy storage is occurring during the initial microstructural rearrangement accommodating irreversible deformation. This ratio levels off and gradually declines over the late time deformation indicating that the heterogeneous residual elastic strain field in the intermediate configuration is becoming saturated. Note that subtracting this ratio from one (1.0) yields the so-called inelastic heat fraction employed in some finite element codes to reflect that amount of plastic work which causes generation of heat.

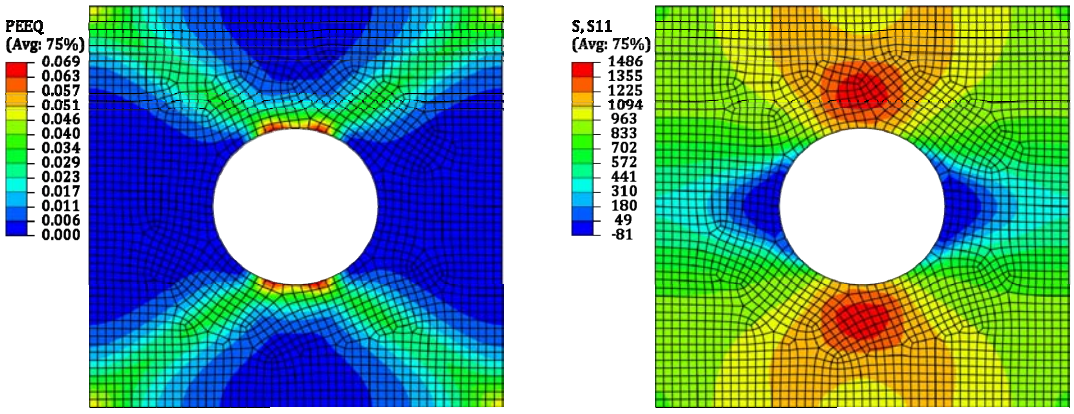

Figure 38. Contour plots of fine scale field response for coarse scale deformation F_{11}=1.02. Plastic effective strain (PEEQ) is shown at left and the axial component of Cauchy stress (S11) is shown at right.

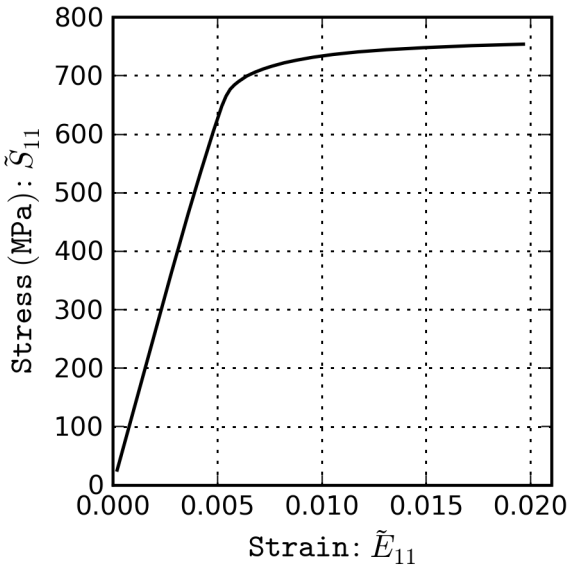

Figure 39. Coarse scale stress versus strain computed from unit cell response for first order deformation.

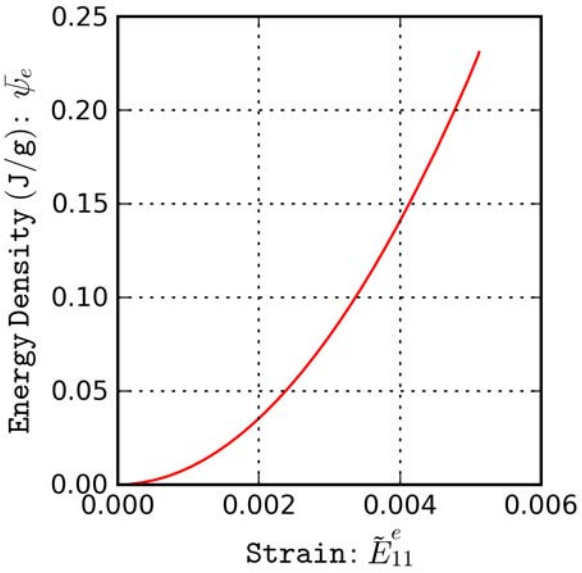

Figure 40. Coarse scale recoverable free energy versus elastic strain for first order case.

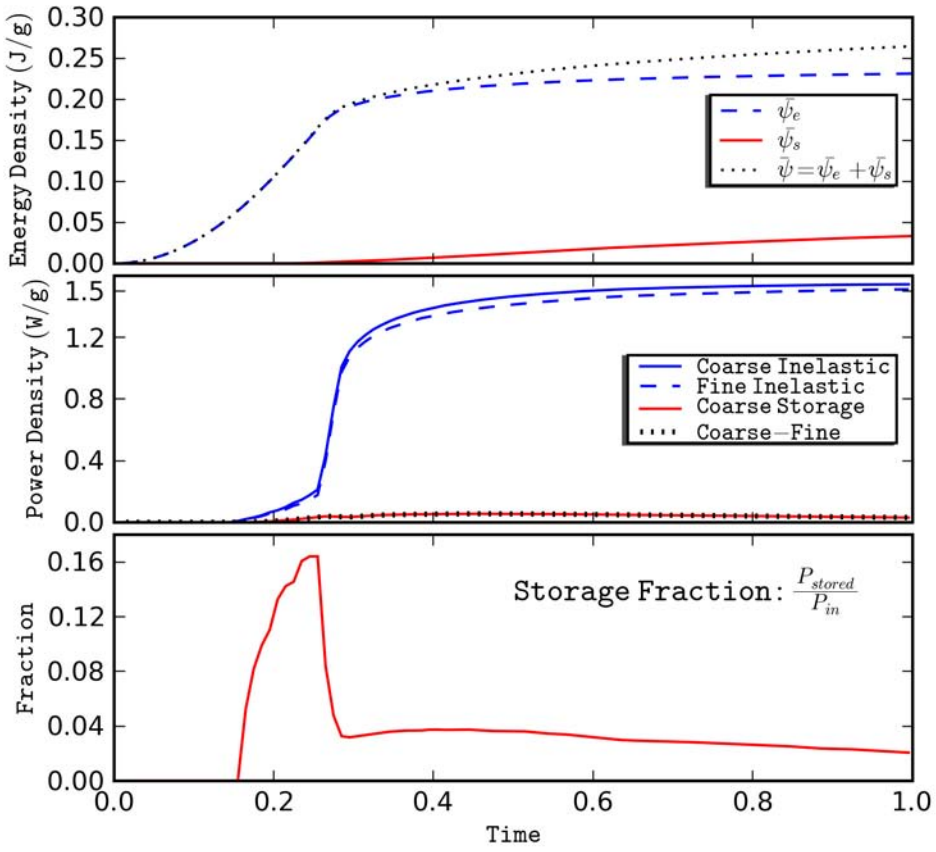

Figure 41. Energy (top) and power (middle) densities and storage power ratio (bottom) computed from first order deformation case.

As an example of a second gradient deformation case, results for unit cell simulation with G_{112} = 0.002 (=G_{121}) specified are included in Figure 42-Figure 44. For example, in Figure 42 are contour plots of fine scale effective plastic strain (PEEQ, at left) and the axial component of fine scale Cauchy stress (S11, right) superposed on the deformed finite element mesh. The coarse scale second order stress versus second order strain history for this sample calculation is shown in Figure 43, which exhibits a similar nonlinear hardening behavior as in the first order case (cf. Figure 39). The energy and power densities and storage power ratios are plotted as before in Figure 44.

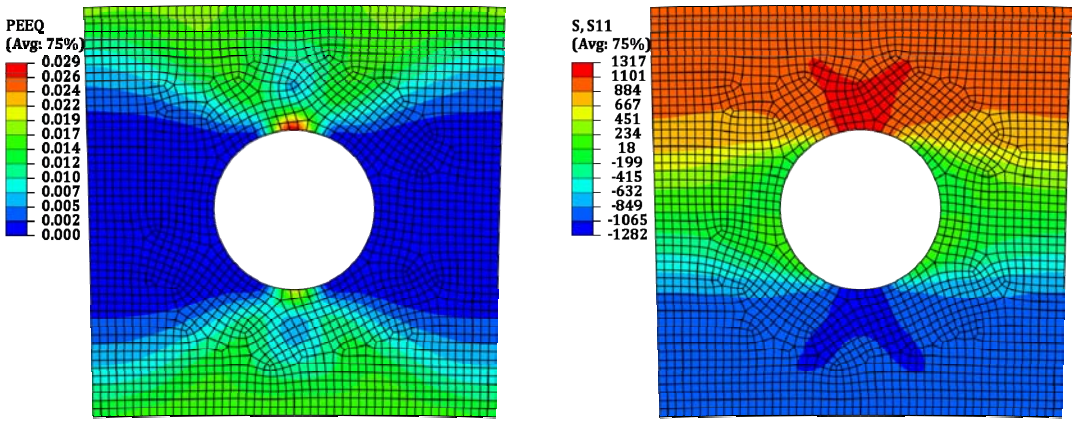

Figure 42. Contour plots of fine scale field response for coarse scale deformation G_{112} = .002. Plastic effective strain (PEEQ) is shown at left and the axial component of Cauchy stress (S11) is shown at right.

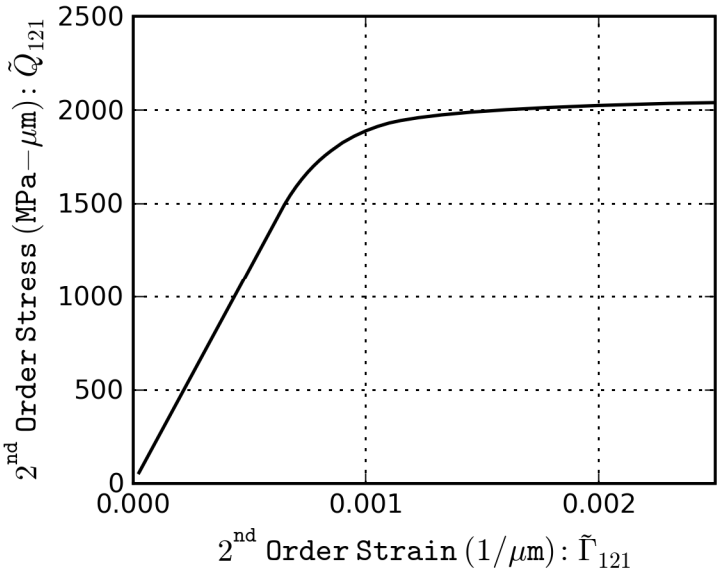

Figure 43. Coarse scale second order stress versus second order strain computed from unit cell response for second gradient deformation.

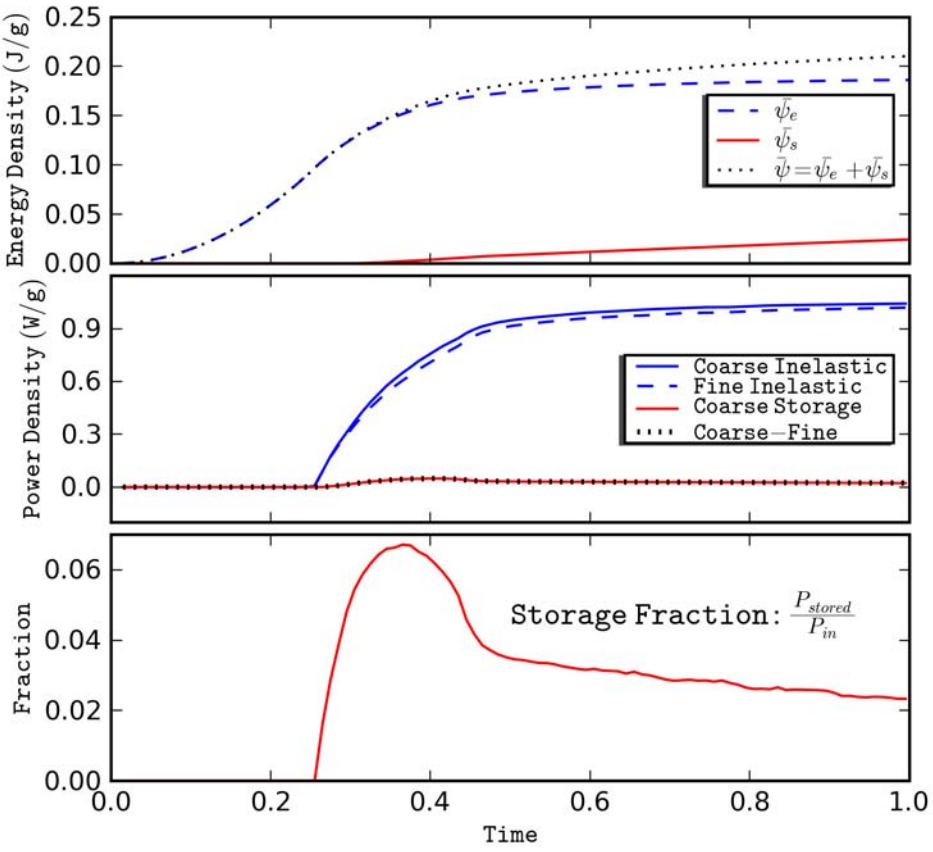

Figure 44. Energy (top) and power (middle) densities and storage power ratio (bottom) computed from first order deformation case.

4.5.2 rSVEs by Random Sequential Addition of Impenetrable (RSA-I) Circles

Using the process outlined in Section 4.1.3 an rSVE was constructed in order to conduct simulations to initially assess the influence of fine scale rSVE boundary conditions on the coarse scale stress strain response and to estimate the numerical accuracy associated with finite element mesh density used in subsequent sections. This geometric construction technique is referred to in subsequent sections as the random sequential addition of impenetrable circles (RSA-I). Recall from Section 4.1.3, this process involves sampling circle radii from a pore area distribution reflective of the microstructure image (micrograph in Figure 13D). A circle of each sampled radius is randomly located within the domain of the rSVE (a square with sides L_{rSVE} x L_{rSVE})

subjected to the constraint that a circle may not penetrate any other circle. Periodicity is enforced upon construction so that any circle crossing an rSVE border has a periodic 'partner' circle located appropriately in the vicinity of the opposite boundary. Also, for convenience (and numerical feasibility) circles are prohibited from occupying the corners of the rSVE. In this subsection a single geometry constructed using this technique was meshed using various finite element mesh densities, i.e., having various characteristic element sizes, and subjected to various sets of fine scale boundary conditions to assess the influence of element size and mesh density on stress-strain response and numerical accuracy.

Contour plots of fine scale effective plastic strain (PEEQ) are shown in Figure 45 for direct (left), periodic (middle), and minimal (right) boundary conditions superposed on the deformed rSVE geometry at the end of the deformation time history, i.e., F_{11}=1.03. The direct boundary conditions result in a relatively more uniform distribution of (PEEQ) response near the boundaries and relatively subdued hotspots on the interior. On the other hand, periodic and minimal boundary conditions result in marked plastic deformation bands connecting planes of high pore density preferentially oriented with respect to the direction of loading. While qualitatively similar, close inspection of the plastic band patterning for periodic and minimal boundary conditions reveals different locations of hot spots (for example, compare bottom left region of these two cases). Moreover, note the strong tweaking in the vicinity of the pore located on the left edge of the rSVE for the minimal boundary conditions. This effect is attributed the integration algorithm employed in developing constraint equations for the minimal boundary conditions in the presence of boundary spanning pores. It results in numerical difficulties for several simulations employing minimal boundary conditions in subsequent sections. The computed coarse scale stress versus strain history is shown in Figure 46 for each of the boundary condition sets. As should be expected, directed and minimal boundary conditions present the stiffest and most compliant response, respectively. Accordingly, periodic boundary conditions result in a coarse scale stress versus strain response between that of the direct and minimal cases.

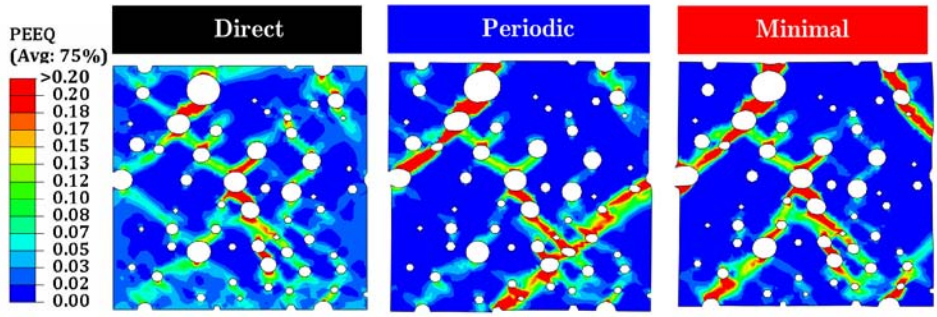

Figure 45. Contour plots of fine scale effective plastic strain (PEEQ) superposed on deformed geometries for an RSA-I rSVE under direct (left), periodic (center), and minimal (right) fine scale boundary conditions for coarse scale deformatioin gradient F_{11}=0.03.

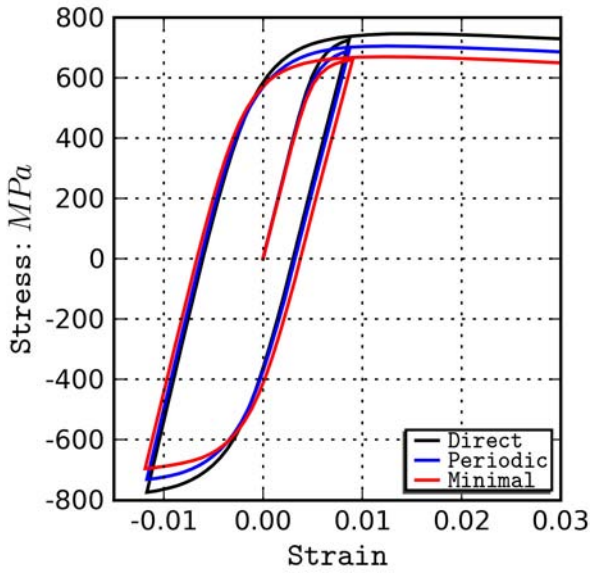

Figure 46. First order coarse scale stress versus strain illustrating influence of fine scale boundary conditions.

Six separate finite element meshes, each with a different characteristic element size, of the rSVE geometry were constructed. Coarse scale stress versus strain histories were computed using each mesh and are shown in Figure 47 for the case of periodic boundary conditions. Clearly, there is a pronounced difference in the results obtained using successively refined meshes. This has

implication to accuracy of the computed stress-strain solutions. Such considerations are conspicuously absent from discussion of finite element simulations of microstructure in the literature. Note that there is relatively larger discrepancy in the inelastic (yielding) portion of these curves compared to the elastic portion. Qualitatively, a mesh with a given characteristic element size is more accurate in regards to elastic response than inelastic response. Estimates of the error characteristic of the predicted coarse scale stress for each mesh, set of boundary conditions, and two deformation modes (shear and uniaxial) are presented in Table 3. These error estimates were computed using Richardson extrapolation for a particular convergent error ansatz by a method described in detail in Chapters 5 and 6. The finest (characteristic element size of 2μm) mesh is shown in Figure 48 for reference. It should be noted that a particular mesh size introduces a systemic numerical bias towards stiffer response. That is, convergence under kinematic fine scale displacement boundary conditions is from stiff towards more compliant behavior and it should be expected that an (notional) error free solution would be more compliant than that actual numerical simulations.

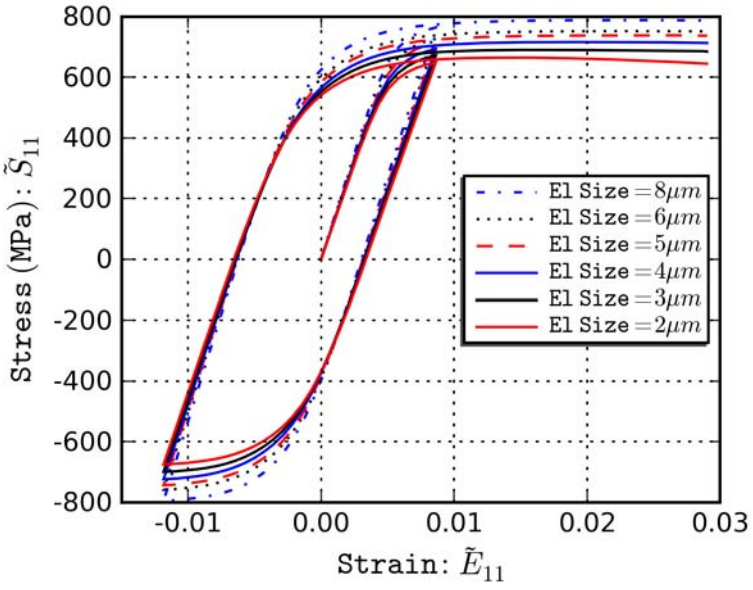

Figure 47. First order coarse scale stress versus strain for various characteristic element sizes illustrating influence of finite element mesh density.

Table 3. Estimated characteristic error in coarse scale stress for various boundary conditions and element sizes.

Element Size	Percent (%) Error - Shear			Percent (%) Error - Uniaxial		
	Direct	Periodic	Minimal	Direct	Periodic	Minimal
8 μm	17.4	19.3	18.8	19.8	26.2	---
6 μm	12.8	14.2	14.0	15.3	20.2	---
5 μm	9.5	11.1	10.4	13.4	17.9	---
4 μm	6.7	8.2	7.6	10.9	14.6	---
3 μm	4.3	5.7	5.1	7.9	10.7	---
2 μm	2.2	3.2	2.6	4.9	6.4	---

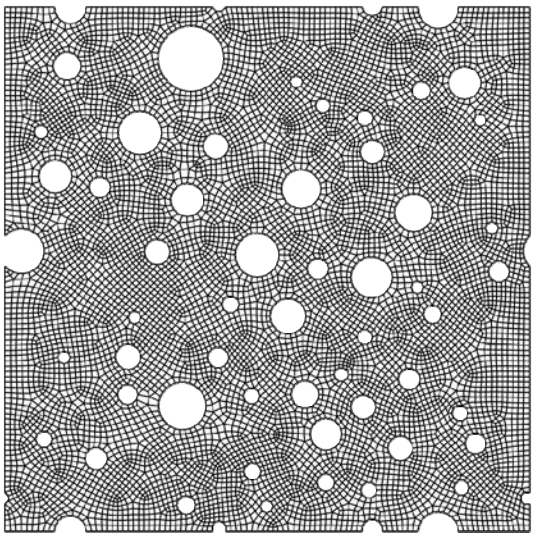

Figure 48. Finite element mesh with characteristic element size of 2μm and L_{rSVE}=200μm.

4.6 Statistics of rSVE Response for Selected Examples

In this section the responses of families of rSVEs are compared in a statistical sense to assess the influence of rSVE construction method, fine scale boundary conditions, and rSVE size on rSVEs response and variability. The terminology, boundary condition sets, and details of the rSVE

simulations are the same as in Section 4.5. In particular, we focus on a first order axial deformation mode in this section, although the principles apply to all deformation modes.

4.6.1 Comparison of Image Based and Idealization Based rSVE Response

Twenty rSVE samples with L_{rSVE}=200μm were generated from the microstructure image (400μm x 400μm) in Figure 13D. These samples were obtained by extracting a 200μm x 200μm window located randomly within the larger image. The original image was reflected across each boundary to permit samples spanning the border of the original image. A finite element mesh of the sampled image was constructed via a pixel-by-pixel process where each pixel representing solid phase is replaced by a quadrilateral (square) element in the mesh. An idealization employing circles as voids was created for each image-based rSVE according to the procedure detailed in Section 4.1.3. In particular, connected clusters of porosity were identified and located within the image sample using the Hoshen-Kopelman algorithm. For each cluster of porosity, a circle of the same area as that cluster was inserted into the Idealized rSVE at the location corresponding to the geometric centroid of the cluster in the original image. These rSVE construction techniques are referred to as 'Image' (for those directly converted from image samples) and 'Idealized' (for those created by idealization of the corresponding image-based rSVE).

A comparison of the responses for the Image and Idealized rSVEs are shown in Figure 49 for a selected case. The stress-strain curves are shown by black curves. The fine scale effective plastic strain field is shown at particular points in the deformation history for the Image rSVE (green alphabetic labels) and the corresponding Idealized rSVE (indicated by red numeric labels.) The fine scale patterning is similar between the two rSVE types although the Image rSVE appears to be more compliant (less stiff) than the corresponding Idealized rSVE. This difference can be partially attributed to the accuracy of the two distinct FE meshes. The Idealized case employs a mesh similar to that shown in Figure 48 with a characteristic element size of 2μm. On the other hand, the Image based approach results in a mesh with each element exactly 1μm by 1μm corresponding to the pixel size.

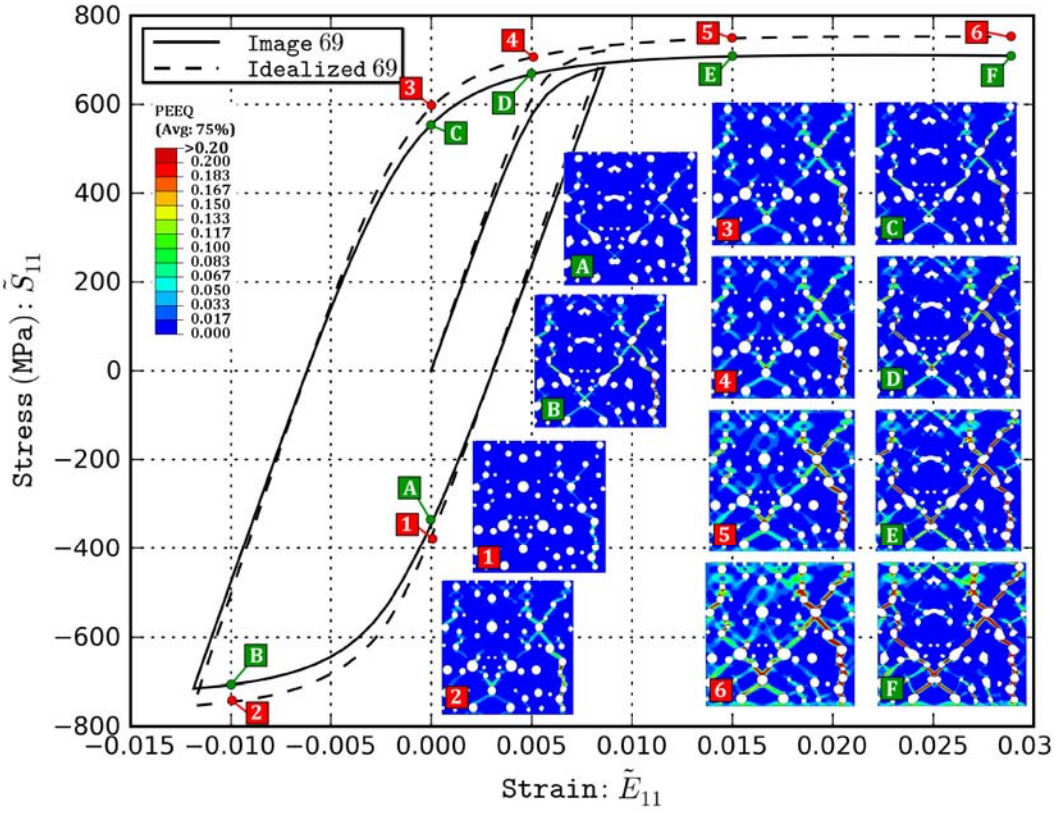

Figure 49. Comparison of response for rSVE constructed directly from image (Image 69) versus that for rSVE constructed by idealization of that image into circle voids (Idealized 69) for a selected case.

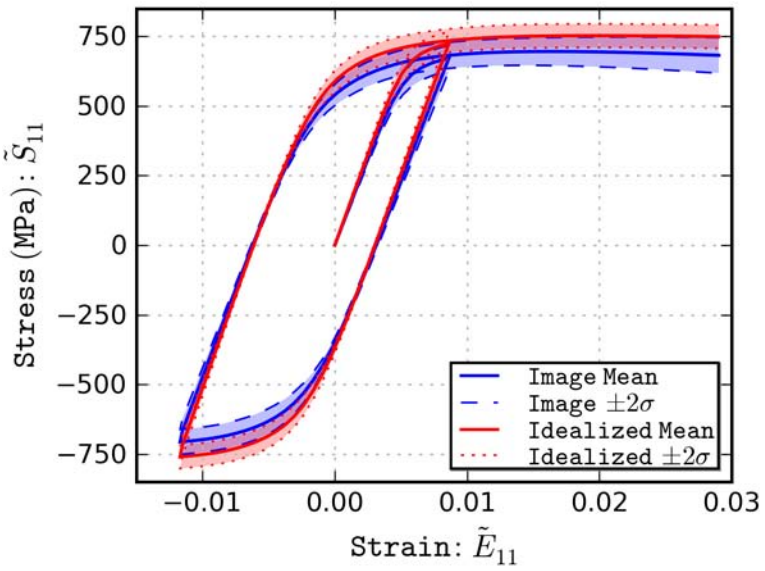

Figure 50. Comparison of stress versus strain statistics for 20 rSVEs sampled directly from image and 20 rSVEs constructed by idealization of those images.

A statistical comparison between these two families of rSVEs is made in Figure 50 where the mean stress strain curve is plotted by a solid line. The dashed lines correspond to the mean stress plus and minus two standard deviations for the particular family. The shaded area between the upper and lower dashed lines reflects the region that would contain roughly 95% of the individual stress-strain curves obtained from a population of the concerned rSVE construction. Note that there is a difference in the family mean response consistent with the difference observed in Figure 49. Additionally, the image-based family of response exhibits larger variability than the Idealized family.

4.6.2 Influence of Boundary Conditions and rSVE Size on rSVE Responses

The responses of the twenty image based rSVEs from the previous section were compared for direct and periodic fine scale boundary conditions. Minimal boundary conditions were omitted from the assessment, because an insufficient quantity of simulations was successfully completed on account of the numerical difficulties discussed in Section 4.5.2. The stress-strain statistics for this comparison of rSVE families are shown in Figure 51. Consistent with the conclusions from Section 4.5.2, periodic boundary conditions result in a more compliant response. From Figure 51 it is also clear that periodic boundary conditions produce larger variability in the rSVEs response.

In a similar manner, the responses for image based rSVEs with an rSVE size (L_{rSVE}) of 100μm and 200μm, respective, are compared in Figure 52. From this comparison one sees that the larger rSVEs are less stiff, i.e., lower coarse scale stresses, and exhibit less variability than the smaller rSVEs.

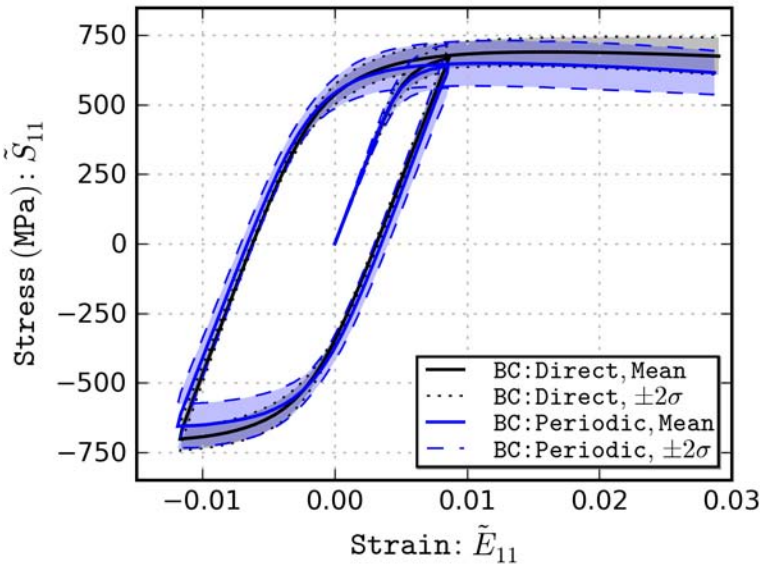

Figure 51. Comparison of stress versus strain statistics for 20 rSVEs sampled directly from image under direct and periodic fine scale boundary conditions.

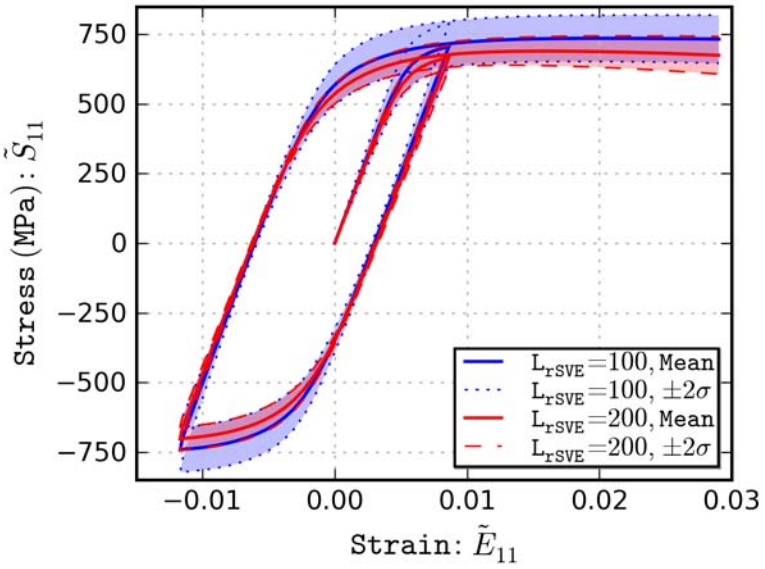

Figure 52. Comparison of stress versus strain statistics for sample of 20 rSVEs sampled directly from image with L_{rSVE}=100μm and 200μm, respectively.

4.6.3 Influence of Construction Method on Response of rSVEs

Here a comparison is made in the same fashion as the previous section for the responses of families of rSVEs constructed using the Image and RSA-I techniques. For each considered rSVE size, twenty rSVEs were constructed using the RSA-I technique. These rSVEs are created completely independent from the twenty Image based rSVE of corresponding size. That is, in contrast to the Idealized case discussed in Section 4.6.1, the RSA-I process employs randomly located circles. Figure 53 and Figure 54 present comparisons of coarse scale stress-strain statistics between the Image and RSA-I families for direct and periodic fine scale boundary conditions, respectively. In both cases, the Image based family of rSVEs exhibits more compliant response with a larger variability than that for RSA-I. Also, by comparing Figure 53 with Figure 54, we again see that the periodic boundary conditions are associated with larger variability in stress-strain response for a particular family of rSVEs.

Consider the standard deviation of all coarse scale stresses, $\tilde{S}_{11}$, from an rSVE family at a particular time, *t*, in the response history and label this quantity $X_{S_{11}}(t)$. We define the *integrated standard deviation* as $\int_0^{t_{\max}} X_{S_{11}}(t)\,dt$ and note that it is directly related to the shaded area of figures such as Figure 53 for one particular family of rSVE simulations comprising an rSVE size, construction method, and set of fine scale boundary conditions. Figure 55 compares the integrated standard deviation versus rSVE size (L_{rSVE}) for Image and RSA-I construction techniques and direct and periodic boundary conditions. Image based rSVEs generally exhibit larger variance in stress-strain response than the corresponding RSA-I rSVEs; however, the image based rSVEs converge in a steadier fashion towards zero variance. Additionally, periodic fine scale boundary conditions generally result in larger variance in stress-strain response than direct fine scale boundary conditions for the same rSVE family. In principle zero variance is required from a family of rSVE simulations to declare that each rSVE in the family is actually an rRVE. Clearly, even for coarse scale stress-strain response an exceptionally large rSVE size

would be needed in order to ensure *representative* behavior. This reinforces the importance of considering a family of rSVE responses in a multiscale framework.

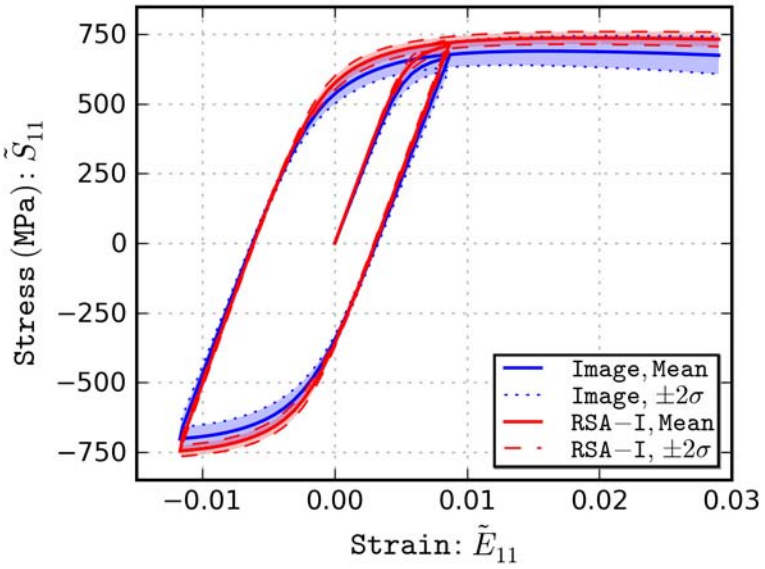

Figure 53. Comparison of stress versus strain statistics for 20 rSVEs sampled directly from image with that for 20 rSVEs constructed by RSA-I. L_{rSVE}= 200μm and direct fine scale boundary conditions are used for both cases.

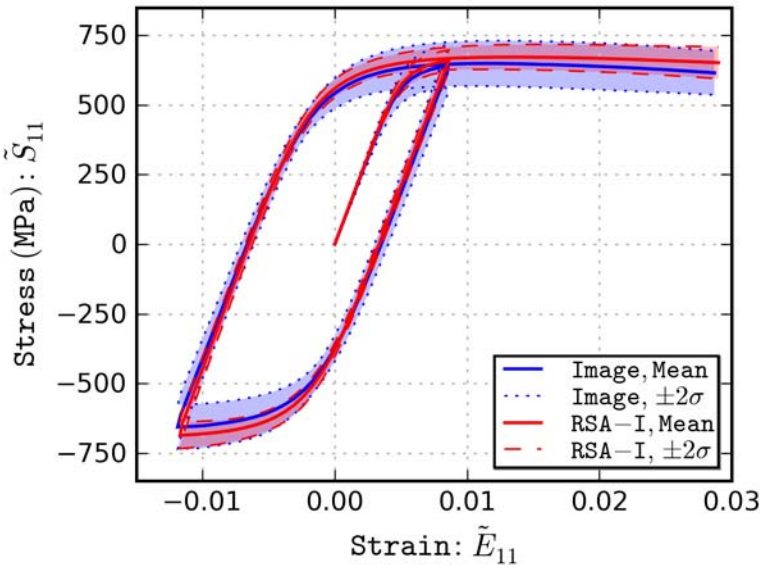

Figure 54. Comparison of stress versus strain statistics for sample of 20 rSVEs sampled directly from image with that for 20 rSVEs constructed by RSA-I. L_{rSVE}= 200μm and periodic fine scale boundary conditions are used for both cases.

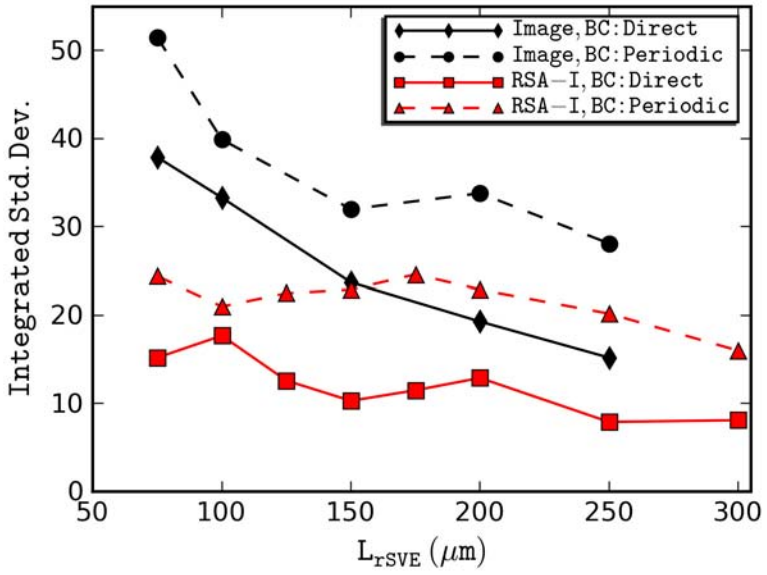

Figure 55. Influence of rSVE construction method and fine scale boundary conditions on convergence of total integrated standard deviation (root of variance) with increasing rSVE size.

4.7 Summary

This chapter is an overview of direct numerical simulation of fine scale response by finite element analysis of referential volume elements of material microstructure. Various methods for constructing a rSVE suitable for finite element simulation are reviewed. New and essential aspects of fine scale boundary conditions and an efficient method for their numerical implementation are presented. Simulation and post-processing algorithms to compute the coarse scale response variables are developed and implemented. Results from several example simulations are presented in order to discuss the effects of various sets of fine scale boundary conditions, size of rSVE, and construction techniques, for example, on the coarse scale response. Collectively, the sections of this chapter are intended to provide a clear perspective of the context of fine scale simulations and their associated homogenization within this multiscale framework.

CHAPTER V

NUMERICAL IMPLEMENTATION OF SECOND GRADIENT CONTINUUM FOR COARSE SCALE

This chapter details the numerical implementation of a second gradient continuum representation of the coarse scale. The coarse scale second gradient momentum equations presented in Chapter 3 are discretized using a mixed field finite element approach similar to those developed and employed recently by several authors for addressing strain- and second-gradient problems (cf. Shu and Fleck, 1998; Shu et al., 1999; Amanatidou and Aravas, 2002; Kouznetsova et al., 2002; Matsushima et al., 2002). The finite element equations and system Jacobian are developed in Section 5.1. Section 5.2 details the numerical implementation of constitutive equations in a manner consistent with the coarse scale ISV constitutive framework presented in Chapter 3. For the purposes of demonstrating an actual implementation, specific assumptions have been made regarding coarse scale constitutive laws that may or may not be appropriate for other cases. In such cases, the general approach presented in Section 5.2 will still be applicable, but the computational details must be adjusted accordingly. Code verification and numerical testing of the finite element discretization, as well as the constitutive implementation are presented in Section 5.3.

5.1 Finite Element Discretization of Coarse Scale Momentum Balance

The second gradient continuum is implemented at the coarse scale via the finite element method. In particular, a user-defined subroutine which specifies the behavior of a finite element has been developed for use in Abaqus (2007).

Recall, from Chapter 3, the weak form of conservation of at the coarse scale is expressed as

$$\begin{aligned}\int_{\Omega_o} \mathbf{P} : \delta\dot{\mathbf{F}}^T + \mathbf{Q}\vdots\delta\dot{\mathbf{G}}\, d\Omega_o + \int_{\Omega_o} \overline{\rho}\dot{\mathbf{V}}\cdot\delta\mathbf{V}\; d\Omega_o = \\ \int_{\Omega_o} \mathbf{B}\cdot\delta\mathbf{V}\; d\Omega_o + \int_{\Omega_o} \mathbf{B}' : \delta\mathbf{V}\bar{\nabla}\; d\Omega_o \\ + \int_{\Gamma_o} \mathbf{T}\cdot\delta\mathbf{V}\; d\Gamma_o + \int_{\Gamma_o} \mathbf{T}'\cdot(\mathbf{N}_o\cdot\bar{\nabla}\delta\mathbf{V})\, d\Gamma_o + \sum_k \oint_{c^{(k)}} \mathbf{Z}\cdot\delta\mathbf{V}\, dl_o^{(k)}\end{aligned} \tag{5.1}$$

where $\mathbf{P}$ is the nominal stress (transpose of the first Piola-Kirchhoff stress) conjugated with the transpose of the deformation gradient, i.e., $\mathbf{F}^T$, $\mathbf{Q}$ is the nominal second-order stress conjugated with the second gradient, $\mathbf{G}$, $\mathbf{V}$ is the velocity of a coarse scale material point, $\overline{\rho}$ is the coarse scale mass per unit volume, $\mathbf{B}$, $\mathbf{B}'$, $\mathbf{T}$, $\mathbf{T}'$ are the coarse scale body force, body couple, surface traction, and surface couple, respectively. Also, $\mathbf{Z}$ is an external force per unit length applied along lines of discontinuity in the bounding surface of a coarse scale continuum body. See Chapter 3 and, in particular, Section 3.2 for more details on the nature of these coarse scale field variables.

Equation (5.1) is rewritten as

$$\delta P_{tot} = \delta P_{int} - \delta P_{ext} + \delta P_{kin} = 0 \tag{5.2}$$

where δP_{tot} is the total virtual power, δP_{int} is the virtual power due to internal stresses working against generalized virtual velocities, δP_{ext} is the virtual power associated with external forces doing work on virtual velocities, and δP_{kin} is the kinetic virtual power associated with inertial forces, the latter three defined respectively as

$$\delta P_{int} = \int_{\Omega_o} \mathbf{P} : \delta\dot{\mathbf{F}}^T + \mathbf{Q}\vdots\delta\dot{\mathbf{G}}\, d\Omega_o \tag{5.3}$$

$$\begin{aligned}\delta P_{ext} = \int_{\Omega_o} \mathbf{B}\cdot\delta\mathbf{V}\; d\Omega_o + \int_{\Omega_o} \mathbf{B}' : \delta\mathbf{V}\bar{\nabla}\; d\Omega_o \\ + \int_{\Gamma_o} \mathbf{T}\cdot\delta\mathbf{V}\; d\Gamma_o + \int_{\Gamma_o} \mathbf{T}'\cdot(\mathbf{N}_o\cdot\bar{\nabla}\delta\mathbf{V})\, d\Gamma_o + \sum_k \oint_{c^{(k)}} \mathbf{Z}\cdot\delta\mathbf{V}\, dl_o^{(k)}\end{aligned} \tag{5.4}$$

and

$$\delta P_{kin} = \int_{\Omega_o} \overline{\rho}\dot{\mathbf{V}}\cdot\delta\mathbf{V}\; d\Omega_o \tag{5.5}$$

The remainder of this section is organized as follows. Section 5.1.1 discusses the mixed field approach used to solve Eq. (5.2) and Section 5.1.2 develops the discrete system of equations

using the finite element method. Linearization of the system of equations is used to develop Jacobian tangent matrices in section 5.1.3. A specific element, its nodal DOFs, and shape functions are introduced in Section 5.1.4 to finalize the implementation of coarse scale momentum conservation in Abaqus.

5.1.1 Mixed Field Approach

The presence of the second gradient in equation (5.2) requires finite elements whose interpolation functions possess C^1 continuity for a direct discretization using the displacement field as a primary field variable. Previous works by Xia and Hutchinson (1996), and Zervos et al. (2001) have demonstrated that C^1 continuous elements are either numerically unstable or require unacceptable limitations on element shape. An alternative approach is to introduce an additional field variable, $\hat{\mathbf{F}}$, referred to as the relaxed deformation gradient, which is kinematically related to the deformation gradient through Lagrange constraints. This mixed field approach has been used by Shu et al. (1999) who developed and compared several different finite elements employing C^0 continuous interpolation functions. Additional elements have been introduced by Matsushima et al. (2002) and Amantidou and Aravas (2002) which were all critically investigated in a head-to-head comparison by Kouznetsova et al. (2004). Their results were used to select the particular element type employed in this work and discussed in Section 5.1.2.

Solutions to the nonlinear optimization problem, $\delta P_{tot} = 0$, which satisfy the constraint $g = c$, can be obtained by introducing a Lagrange multiplier, λ, such that $\hat{P}_{tot} = P_{tot} + \lambda\left(g - c\right)$ and the constrained solution is obtained from the modified variation equation, $\delta \hat{P}_{tot} = 0$. In order to obviate the need for C^1 continuous interpolation functions, a new field variable, $\hat{\mathbf{F}}$ is introduced to the weak form along with the constraint $\dot{\hat{\mathbf{F}}} = \dfrac{\partial \mathbf{V}}{\partial \mathbf{x}_o}$. Because the weak form involves the velocity gradient both inside the body and on the surface, the mixed-field approach requires two constraints for $\hat{\mathbf{F}}$, namely an interior constraint

$$\dot{\hat{\mathbf{F}}} = \frac{\partial \mathbf{V}}{\partial \mathbf{x}_o} \forall\, \mathbf{x}_o \in \Omega_o \tag{5.6}$$

and a constraint on the surfacial component of deformation gradient (and its rate) on external surfaces, i.e.,

$$\dot{\bar{\mathbf{F}}} - \dot{\bar{\mathbf{F}}} \cdot \mathbf{N} \otimes \mathbf{N} = \mathbf{V}\bar{\nabla}^{s}_{\mathrm{o}} \;\; \forall \, \mathbf{x}_{\mathrm{o}} \in \Gamma_{\mathrm{o}} \tag{5.7}$$

The weak form from Eq. (5.1) is then modified to

$$\begin{gathered} \int_{\Omega_{\mathrm{o}}} \left(\mathbf{P} : \delta\vec{\nabla}\mathbf{V} + \mathbf{Q}\vdots\delta\dot{\bar{\mathbf{F}}}\bar{\nabla} \right) d\Omega_{\mathrm{o}} + \\ \int_{\Omega_{\mathrm{o}}} \delta\Big(\boldsymbol{\lambda} : (\dot{\bar{\mathbf{F}}} - \mathbf{V}\bar{\nabla}) \Big) d\Omega_{\mathrm{o}} + \int_{\Gamma_{\mathrm{o}}} \delta\Big(\boldsymbol{\lambda}^{s} : (\dot{\bar{\mathbf{F}}} - \dot{\bar{\mathbf{F}}} \cdot \mathbf{N} \otimes \mathbf{N} - \mathbf{V}\bar{\nabla}^{s}_{\mathrm{o}}) \Big) d\Gamma_{\mathrm{o}} \\ + \int_{\Omega_{\mathrm{o}}} \overline{\rho}\dot{\mathbf{V}} \cdot \delta\mathbf{V} \; d\Omega_{\mathrm{o}} = \\ \int_{\Omega_{\mathrm{o}}} \mathbf{B} \cdot \delta\mathbf{V} \; d\Omega_{\mathrm{o}} + \int_{\Omega_{\mathrm{o}}} \mathbf{B}' : \delta\dot{\bar{\mathbf{F}}} \; d\Omega_{\mathrm{o}} \\ + \int_{\Gamma_{\mathrm{o}}} \mathbf{T} \cdot \delta\mathbf{V} \; d\Gamma_{\mathrm{o}} + \int_{\Gamma_{\mathrm{o}}} \mathbf{T}' \cdot (\mathbf{N}_{\mathrm{o}} \cdot \delta\dot{\bar{\mathbf{F}}}^{T}) \, d\Gamma_{\mathrm{o}} + \sum_{k} \oint_{c^{(k)}} \mathbf{Z} \cdot \delta\mathbf{V} \, dl_{\mathrm{o}}^{(k)} \end{gathered} \tag{5.8}$$

It has been demonstrated by various authors that error introduced to the solution by omission of the surfacial constraint on the relaxed deformation gradient is negligible as the mesh size becomes sufficiently small, (cf. Shu and Fleck, 1998; Shu et al., 1999; Shu and Barlow, 2000; Kouznetsova et al., 2004). Furthermore, Shu and Fleck (1998) justify this omission for cases where the coarse scale boundary conditions are prescribed such that equation (5.7) is satisfied exactly. Shu and Barlow (2000) included the term for their crystal plasticity second gradient formulation, as did Amanatidou and Aravas (2002). However, based on convenience and following Shu et al. (1999), Matsushima et al. (2002), and Kouznetsova et al. (2004) the surface constraint is omitted in this work. Equation (5.8) is reduced accordingly and split into portions contributing to internal, external, and inertial virtual power, i.e.,

$$\delta\hat{P}_{\mathrm{int}} - \delta\hat{P}_{ext} + \delta\hat{P}_{kin} = 0 \tag{5.9}$$

where

$$\delta\hat{P}_{\mathrm{int}} = \int_{\Omega_{\mathrm{o}}} \mathbf{P} : \delta\vec{\nabla}\mathbf{V} + \mathbf{Q}\vdots\delta\dot{\bar{\mathbf{F}}}\bar{\nabla} + \delta\Big(\boldsymbol{\lambda} : (\dot{\bar{\mathbf{F}}} - \mathbf{V}\bar{\nabla}) \Big) \, d\Omega_{\mathrm{o}} \tag{5.10}$$

$$\begin{aligned} \delta\hat{P}_{ext} = & \int_{\Omega_{\mathrm{o}}} \mathbf{B} \cdot \delta\mathbf{V} \; d\Omega_{\mathrm{o}} + \int_{\Omega_{\mathrm{o}}} \mathbf{B}' : \delta\dot{\bar{\mathbf{F}}} \; d\Omega_{\mathrm{o}} \\ & + \int_{\Gamma_{\mathrm{o}}} \mathbf{T} \cdot \delta\mathbf{V} \; d\Gamma_{\mathrm{o}} + \int_{\Gamma_{\mathrm{o}}} \mathbf{T}' \cdot (\mathbf{N}_{\mathrm{o}} \cdot \delta\dot{\bar{\mathbf{F}}}^{T}) \, d\Gamma_{\mathrm{o}} + \sum_{k} \oint_{c^{(k)}} \mathbf{Z} \cdot \delta\mathbf{V} \, dl_{\mathrm{o}}^{(k)} \end{aligned} \tag{5.11}$$

$$\delta\hat{P}_{kin} = \int_{\Omega_{\mathrm{o}}} \overline{\rho}\dot{\mathbf{V}} \cdot \delta\mathbf{V} \; d\Omega_{\mathrm{o}} \tag{5.12}$$

For the following development of discrete numerical form of the weak form, a modified indicial notation is used in which lower case Latin subscripts indicate the directional component referred to a Cartesian basis and upper case Latin subscripts refer to contributions of a particular node. The internal virtual power is written in this indicial notation as,

$$\delta\hat{P}_{\text{int}} = \int_{\Omega_o} P_{ij}\,\delta\frac{\partial Vj}{\partial x_i^o} + Q_{ijk}\,\delta\frac{\partial}{\partial x_k^o}\dot{\hat{F}}_{ij} + \delta\left(\lambda_{ij}(\dot{\hat{F}}_{ij} - \frac{\partial V_i}{\partial x_j^o})\right) d\Omega_o \tag{5.13}$$

5.1.2 Finite Element Discretization of Mixed Field Weak Form

Discrete forms of the field variables are introduced by interpolation of nodal values within the domain of an element using that element's shape functions to be defined later, i.e.,

$$\begin{aligned} V_j\left(\mathbf{x}_o\right) &= {}^{u}N_A\left(\mathbf{x}_o\right)V_{Aj} \\ \hat{F}_{ij}\left(\mathbf{x}_o\right) &= {}^{F}N_A\left(\mathbf{x}_o\right)\hat{F}_{Aij} \\ \lambda_{ij}\left(\mathbf{x}_o\right) &= {}^{\lambda}N_A\left(\mathbf{x}_o\right)\lambda_{Aij} \end{aligned} \tag{5.14}$$

where ${}^{u}N_A\left(\mathbf{x}_o\right)$, ${}^{F}N_A\left(\mathbf{x}_o\right)$, and ${}^{\lambda}N_A\left(\mathbf{x}_o\right)$ are the interpolation functions used to interpolate nodal displacements, $\bar{\mathbf{u}}$, relaxed deformation gradient, $\hat{\mathbf{F}}$, and the Lagrange multiplier, $\boldsymbol{\lambda}$, respectively. The spatial dependence of the field variables and interpolation functions is dropped henceforth for convenience of notation. Spatial gradients of velocity and relaxed deformation gradient field are obtained by using shape function derivatives, i.e.,

$$\begin{aligned} \frac{\partial V_j}{\partial x_i^o} &= {}^{u}\beta_{iA}V_{Aj} \\ \frac{\partial \dot{\hat{F}}_{ij}}{\partial x_k^o} &= {}^{F}\beta_{iA}\dot{\hat{F}}_{Aij} \end{aligned} \tag{5.15}$$

where the shape function derivatives are defined as

$$\begin{aligned} {}^{u}\beta_{iA} &= \frac{\partial\,{}^{u}N_A}{\partial x_i^o} \\ {}^{F}\beta_{iA} &= \frac{\partial\,{}^{F}N_A}{\partial x_i^o} \end{aligned} \tag{5.16}$$

Note that there are separate interpolation functions for each field variable permitting mixed-interpolation of field variables over the element domain, i.e., ${}^{u}N_A \neq {}^{F}N_A$, for example. Upon substitution of the discrete form of field variables into (5.13) and expansion of the variation of the Lagrange constraint by chain rule,

$$\begin{aligned}\delta\hat{P}_{\text{int}} = \sum_{\forall El}\int_{\Omega_o} & P_{ji}\ {}^{u}\beta_{jA}\,\delta V_{Ai} + Q_{ijk}\ {}^{F}\beta_{iA}\delta\dot{\hat{F}}_{Aij} \\ & +{}^{\lambda}N_A\delta\lambda_{Aji}({}^{F}N_B\dot{\hat{F}}_{Bij} - {}^{u}\beta_{jB}\,V_{Bi}) \\ & +{}^{\lambda}N_A\lambda_{Aji}({}^{F}N_B\delta\dot{\hat{F}}_{Bij} - {}^{u}\beta_{jB}\,\delta V_{Bi})\,d\Omega_o^{El}\end{aligned} \tag{5.17}$$

Collection of virtual velocities, i.e.,

$$\begin{aligned}\delta\hat{P}_{\text{int}}^{El} = & \int_{\Omega_o}\left(P_{ji}\ {}^{u}\beta_{jA} - {}^{\lambda}N_B\lambda_{Bji}\ {}^{u}\beta_{jA}\right)d\Omega_o^{El} \quad \delta V_{Ai} \\ & +\int_{\Omega_o}\left(Q_{ijk}\ {}^{F}\beta_{iA} + {}^{\lambda}N_B\lambda_{Bji}\ {}^{F}N_A\ \right)d\Omega_o^{El}\ \delta\dot{\hat{F}}_{Aij} \\ & +\int_{\Omega_o}{}^{\lambda}N_A({}^{F}N_B\dot{\hat{F}}_{Bij} - {}^{u}\beta_{jB}\,V_{Bi})\,d\Omega_o^{El} \quad \delta\lambda_{Aji}\end{aligned} \tag{5.18}$$

gives rise to the following conjugate internal forces

$$\begin{aligned}{}^{u}f_{Ai}^{int} &= {}^{u}\beta_{jA}\int_{\Omega_o}\left(P_{ji} - {}^{\lambda}N_B\lambda_{Bji}\right)d\Omega_o \\ {}^{\hat{F}}f_{Aij}^{int} &= \int_{\Omega_o}\left(Q_{ijk}\ {}^{F}\beta_{iA} + {}^{\lambda}N_B\lambda_{Bji}\ {}^{F}N_A\ \right)d\Omega_o \\ {}^{\lambda}f_{Aij}^{int} &= \int_{\Omega_o}{}^{\lambda}N_A({}^{F}N_B\dot{\hat{F}}_{Bij} - {}^{u}\beta_{jB}\,V_{Bi})\,d\Omega_o\end{aligned} \tag{5.19}$$

For quasi-static simulations of coarse scale response, the discretized nodal forces associated with the Lagrange constraint, ${}^{\lambda}f_{Aij}$, can be equivalently computed according to

$${}^{\lambda}f_{Aij}^{int} = \int_{\Omega_o}{}^{\lambda}N_A({}^{F}N_B\hat{F}_{Bij} - {}^{u}\beta_{jB}\,X_{Bi})\,d\Omega_o^{El} \tag{5.20}$$

where, X_{Bi} are the coordinates of node B in the current configuration. A perturbed Lagrangian form of the internal power is obtained by adding a weighted sum of the squares of the Lagrange multiplier, i.e., $\frac{1}{2\alpha}\boldsymbol{\lambda}^T : \boldsymbol{\lambda}$, to the variational potential, thus penalizing the Lagrange multiplier. This modification affects only the internal forces associated with the Lagrange multiplier, which is updated accordingly, to

$$ {}^{\lambda}f_{Aij}^{int,per} = \int_{\Omega_o} {}^{\lambda}N_A({}^{F}N_B\hat{F}_{Bij} - {}^{u}\beta_{jB}\,X_{Bi} - \frac{1}{\alpha}\,{}^{\lambda}N_B\lambda_{Bji})\,d\Omega_o \tag{5.21} $$

The perturbed Lagrangian form is equivalent to a penalty method, where as α grows infinite the discrete form approaches a pure Lagrange constraint. The perturbed Lagrange approach was pursued as an extension of the pure Lagrange constraint due to numerical issues of implementing the latter within an Abaqus user-defined element (UEL) subroutine.

Discretization of the external virtual power begins by separating the external virtual power (5.11) according to contributions from coarse scale body, surface, and line forces as,

$$ \begin{aligned} \delta\hat{P}_{ext,\Omega_o} &= \int_{\Omega_o} \mathbf{B}\cdot\delta\mathbf{V}\; d\Omega_o + \int_{\Omega_o} \mathbf{B}' : \delta\dot{\hat{\mathbf{F}}}\; d\Omega_o \\ \delta\hat{P}_{ext,\Gamma_o} &= \int_{\Gamma_o} \mathbf{T}\cdot\delta\mathbf{V}\; d\Gamma_o + \int_{\Gamma_o} \mathbf{T}'\cdot(\mathbf{N}_o\cdot\delta\dot{\hat{\mathbf{F}}}^T)\,d\Gamma_o \\ \delta\hat{P}_{ext,l_o} &= \sum_k \oint_{c^{(k)}} \mathbf{Z}\cdot\delta\mathbf{V}\, dl_o^{(k)} \end{aligned} \tag{5.22} $$

The virtual power due to applied body forces is discretized using nodal virtual velocities and element shape functions,

$$ \delta\hat{P}_{ext,\Omega_o} = \int_{\Omega_o} {}^{u}N_A B_i\, d\Omega_o\, \delta V_{Ai} + \int_{\Omega_o} {}^{F}N_A B'_{ij} d\Omega_o\, \delta\dot{\hat{F}}_{Aij} \tag{5.23} $$

thereby giving rise to the definition of external nodal body forces, i.e.,

$$ \begin{aligned} {}^{u}f_{Ai}^{ext,\Omega_o} &= \int_{\Omega_o} {}^{u}N_A B_i\, d\Omega_o \\ {}^{F}f_{Aij}^{ext,\Omega_o} &= \int_{\Omega_o} {}^{F}N_A B'_{ij} d\Omega_o \end{aligned} \tag{5.24} $$

Contributions to the external nodal forces from surface tractions and double tractions, i.e.,

$$ \begin{aligned} {}^{u}f_{Ai}^{ext,\Gamma_o} &= \int_{\Gamma_o} {}^{u}N_A T_i\, d\Gamma_o \\ {}^{F}f_{Aij}^{ext,\Gamma_o} &= \int_{\Gamma_o} {}^{F}N_A T'_i n_j^o\, d\Gamma_o \end{aligned} \tag{5.25} $$

and line discontinuities, i.e.,

$$ f_{Ai}^{ext,l_o} = \sum_k \oint_{c^{(k)}} {}^{u}N_A Z_i\, dl_o^{(k)} \tag{5.26} $$

are developed in a likewise manner. The inertial virtual power is also discretized into the product of a nodal force and virtual velocity vector as

$$\begin{aligned} \delta \hat{P}_{kin} &= {}^{u}f_{Ai}^{kin}\delta V_{Ai} \\ {}^{u}f_{Ai}^{kin} &= \int_{\Omega_o} \overline{\rho}\, {}^{u}N_A \dot{V}_i \, d\Omega_o = \int_{\Omega_o} \overline{\rho}\, {}^{u}N_A \, {}^{u}N_B \, d\Omega_o \, \dot{V}_{Bi} \end{aligned} \tag{5.27}$$

Note that the accelerations in (5.27) are the actual, not virtual, quantities. The acceleration (second time rate) of the nodal deformation gradient, $\ddot{\hat{F}}_{Aij}$, does not appear in (5.27) as according to the arguments provided in Chapter 3. The discrete approximation of the weak form of coarse scale momentum balance is now written as

$$\delta V_{Ai}\left({}^{u}f_{Ai}^{\text{int}} - {}^{u}f_{Ai}^{ext} - {}^{u}f_{Ai}^{kin} \right) + \delta \dot{\hat{F}}_{Aij}\left({}^{F}f_{Ai}^{\text{int}} - {}^{F}f_{Ai}^{ext} \right) + \delta \lambda_{Aji}\left({}^{\lambda}f_{Ai}^{\text{int}} \right) = 0 \tag{5.28}$$

Equation (5.28) must hold true for any kinematically admissible coarse scale virtual velocity field consistent with external boundary conditions, so that the system of equations written in vector form becomes

$$\mathbf{r} = \mathbf{f}^{\text{int}} - \mathbf{f}^{ext} - \mathbf{f}^{kin} = \mathbf{0} \tag{5.29}$$

Here, $\mathbf{r}$ is a residual force vector associated with the nonlinear mixed-field system of equations.

5.1.3 Linearization and System Jacobian

In this dissertation, the commercial finite element package, Abaqus (2007) is used to solve the nonlinear system of equations (5.29). Explicit integration in time using a diagonalized mass matrix within Abaqus requires only the element-by-element contributions to the nodal global residual force vector as defined by Eqs. (5.19), (5.24)-(5.27) need to be computed within the user-defined subroutine. On the other hand, implicit integration in time and quasi-static solutions in Abaqus employ a Newton-Raphson based iterative solution procedure demanding computation of a system Jacobian. For each iteration of the nonlinear solution, the correction to the coarse scale field variables $\mathbf{c}$ is obtained by solving the linear system of equations,

$$\left[\mathbf{K}\right]\left\{\mathbf{c}\right\} = \left\{\mathbf{r}\right\} \tag{5.30}$$

where $\mathbf{K} = \dfrac{\partial \mathbf{r}}{\partial \mathbf{u}}$ is the solution Jacobian matrix and $\mathbf{u}$ is the *generalized* coarse scale displacement vector containing mixed-field nodal solution variables, i.e., $\bar{\mathbf{u}}$, $\hat{\mathbf{F}}$, and $\boldsymbol{\lambda}$. Accordingly, for

quasi-static or implicit dynamic solutions, Abaqus requires each element's contribution to the residual force vector *and* the solution Jacobian matrix.

The solution Jacobian is obtained by linearization of the system of equations (5.29) about the current solution. To do this, each term comprising the total residual force is linearized in turn. To begin with, consider the internal nodal forces associated with coarse scale displacement DOFs, i.e., top of Eq. (5.19). Linearization proceeds by computing an infinitesimal variation in these nodal forces, i.e.,

$$d\,{}^{u}f_{Ai}^{int} = {}^{u}\beta_{jA}\int_{\Omega_o}\left(dP_{ji} - {}^{\lambda}N_B d\lambda_{Bji}\right)d\Omega_o \tag{5.31}$$

The coarse scale nominal stress is equal to the partial push-forward of the second piola kirchoff stress, i.e., $\mathbf{P} = \mathbf{S}\cdot\mathbf{F}^T$. According to the product rule, the variation in nominal stress can be expressed as

$$dP_{ji} = dS_{jk}F_{ik} + S_{jk}dF_{ik} \tag{5.32}$$

The continuum tangent stiffness, C_{ijkl}^{SE}, is defined such that

$$dS_{ij} = C_{ijkl}^{SE}dE_{kl} \tag{5.33}$$

where the variation in Green-Lagrange strain is computed using its definition (cf. Chapter 3) and the product rule as

$$dE_{kl} = \frac{1}{2}\left(dF_{nk}F_{nl} + F_{nk}dF_{nl}\right) \tag{5.34}$$

Variation in the deformation gradient is equal to the variation in gradient of displacement computed within the domain of a finite element using the displacement shape function derivative and nodal displacement values, i.e., $dF_{ik} = {}^{u}\beta_{kB}du_{Bi}$. Appropriate substitution of this relationship into (5.34) yields

$$\begin{aligned} dE_{lm} &= \frac{1}{2}\left({}^{u}\beta_{lB}F_{nm} + F_{nl}\,{}^{u}\beta_{mB}\right)du_{Bn} \\ &= \mathbb{B}_{lmBn}du_{Bn} \end{aligned} \tag{5.35}$$

where the strain displacement relationship, $\mathbb{B}_{lmBn} = \frac{1}{2}\left({}^{u}\beta_{lB} F_{nm} + F_{nl} {}^{u}\beta_{mB} \right)$, has been introduced. Substitution of (5.35), (5.33), and (5.32) into (5.31) gives

$$\begin{aligned} d\,{}^{u}f_{Ai}^{int} &= \int_{\Omega_o} {}^{u}\beta_{jA} F_{ik} C_{jklm}^{SE} \mathbb{B}_{lmBn}\, du_{Bn}\, d\Omega_o + \int_{\Omega_o} {}^{u}\beta_{jA} S_{jk} {}^{u}\beta_{kB} du_{Bi}\, d\Omega_o \\ &\quad - \int_{\Omega_o} {}^{u}\beta_{jA} {}^{\lambda}N_B d\lambda_{Bji}\, d\Omega_o \end{aligned} \tag{5.36}$$

On account of the symmetry in the local tangent stiffness tensor, $C_{jklm}^{SE} = C_{kjlm}^{SE}$, the integrand of the first term in (5.36) can be equivalently written as $\mathbb{B}_{jkAi} C_{jklm}^{SE} \mathbb{B}_{lmBn}$. Finally, the variation in internal nodal forces associated with displacement DOFs is written

$$d\,{}^{u}f_{Ai}^{int} = \left(K_{AiBn}^{uu,mat} + K_{AiBn}^{uu,geo} \right) du_{Bn} + K_{AiBnm}^{u\lambda} d\lambda_{Bnm} \tag{5.37}$$

where the material, geometric, and Lagrange multiplier stiffness for displacement degrees of freedom are computed as

$$\begin{aligned} K_{AiBn}^{uu,mat} &= \int_{\Omega_o} \mathbb{B}_{jkAi} C_{jklm}^{SE} \mathbb{B}_{lmBn}\, d\Omega_o \\ K_{AiBn}^{uu,geo} &= \int_{\Omega_o} {}^{u}\beta_{jA} S_{jk} {}^{u}\beta_{kB}\, d\Omega_o\, \delta_{ni} \\ K_{AiBnm}^{u\lambda} &= -\int_{\Omega_o} {}^{u}\beta_{jA} {}^{\lambda}N_B\, d\Omega_o \delta_{jn} \delta_{mi} \end{aligned} \tag{5.38}$$

Linearization of the internal nodal forces conjugate to nodal deformation gradient components follows a similar procedure. An infinitesimal change (differential) in the internal nodal forces associated with deformation gradient DOFs are computed from (5.19) as

$$d\,{}^{\hat{F}}f_{Aij}^{int} = \int_{\Omega_o} \left(dQ_{ijk} {}^{F}\beta_{iA} + {}^{\lambda}N_B d\lambda_{Bji} {}^{F}N_A \right) d\Omega_o \tag{5.39}$$

and

$$\begin{aligned} dQ_{ijk} &= C_{ijklmn}^{QG} dG_{nml} \\ &= C_{ijklmn}^{QG} {}^{F}\beta_{lB} d\hat{F}_{Bnm} \end{aligned} \tag{5.40}$$

so that

$$\begin{aligned} d\,{}^{\hat{F}}f_{Aij}^{int} &= \int_{\Omega_o} {}^{F}\beta_{iA} C_{ijklmn}^{QG} {}^{F}\beta_{lB}\, d\Omega_o\, d\hat{F}_{Bnm} + \int_{\Omega_o} {}^{\lambda}N_B {}^{F}N_A\, d\Omega_o \delta_{jn} \delta_{im}\, d\lambda_{Bnm} \\ &= K_{AijBnm}^{\hat{F}\hat{F}} d\hat{F}_{Bnm} + K_{AijBnm}^{\hat{F}\lambda} d\lambda_{Bnm} \end{aligned} \tag{5.41}$$

where

$$
\begin{aligned}
K^{\hat{F}\hat{F}}_{AijBnm} &= \int_{\Omega_o} {}^{F}\beta_{iA} C^{QG}_{ijklmn} {}^{F}\beta_{lB}\, d\Omega_o \\
K^{\hat{F}\lambda}_{AijBnm} &= \int_{\Omega_o} {}^{\lambda}N_B {}^{F}N_A\, d\Omega_o\, \delta_{jn}\delta_{im}
\end{aligned}
\tag{5.42}
$$

In order to uncover the source of numerical difficulty for the standard Lagrange constraint approach, a linearization of the internal nodal forces associated with the Lagrange multiplier in equation (5.20) is investigated prior to developing the full stiffness matrix required for the augmented Lagrangian (penalty) case, i.e.,

$$
\begin{aligned}
d^{\lambda}f^{int}_{Aij} &= -\int_{\Omega_o} {}^{\lambda}N_A {}^{u}\beta_{jB}\, d\Omega_o\, du_{Bi} + \int_{\Omega_o} {}^{\lambda}N_A {}^{F}N_B\, d\Omega_o d\hat{F}_{Bij} \\
&= K^{\lambda u}_{AijBn} du_{Bn} + K^{\lambda\hat{F}}_{AijBnm} d\hat{F}_{Bnm}
\end{aligned}
\tag{5.43}
$$

where the stiffness terms contributing to global system Jacobian are

$$
\begin{aligned}
K^{\lambda u}_{AijBn} &= -\int_{\Omega_o} {}^{\lambda}N_A {}^{u}\beta_{jB}\, d\Omega_o \delta_{ni} \\
K^{\lambda\hat{F}}_{AijBnm} &= \int_{\Omega_o} {}^{\lambda}N_A {}^{F}N_B\, d\Omega_o \delta_{ni}\delta_{jm}
\end{aligned}
\tag{5.44}
$$

Conspicuously absent is any contribution to stiffness relating the internal nodal forces conjugate with the Lagrange multiplier to its variations. Consequently, the system Jacobian matrix would have zero coefficients on the diagonal for Lagrange multiplier DOFs leading to a non-positive definite system Jacobian. Solution techniques exist for such cases; however, Abaqus' nonlinear solver does not incorporate such techniques. To alleviate this problem, the perturbed Lagrangian approach is used, and consequently, terms are added to the system Jacobian reflecting the penalty stiffness in Lagrange multipliers, i.e.,

$$
K^{\lambda\lambda}_{AijBnm} = -\frac{1}{\alpha}\delta_{jn}\delta_{im}\int_{\Omega_o} {}^{\lambda}N_A {}^{\lambda}N_B\, d\Omega_o \tag{5.45}
$$

and the differential in internal nodal forces is

$$
d^{\lambda}f^{int}_{Aij} = K^{\lambda u}_{AijBn} du_{Bn} + K^{\lambda\hat{F}}_{AijBnm} d\hat{F}_{Bnm} + K^{\lambda\lambda}_{AijBnm} d\lambda_{Bnm} \tag{5.46}
$$

It may be computationally advantageous to develop the constitutive tangent stiffness in terms of the nominal stress, $\mathbf{P}$, and the deformation gradient, **F**, rather than second Piola-Kirchhoff stress and Green-Lagrange strain. Furthermore, coupling between the second-order stress, **Q**, and deformation gradient, **F**, may produce additional terms in the system Jacobian. For these reasons,

an alternative linearization is developed and a few comments regarding the numerical implementation will follow. Consider a variation in nominal stress expanded in terms of the deformation gradient and second gradient according to the chain rule, i.e.,

$$dP_{ji} = \frac{\partial P_{ji}}{\partial F_{kl}} dF_{kl} + \frac{\partial P_{ji}}{\partial G_{klm}} dG_{klm} \tag{5.47}$$

Substitution of Eq. (5.47) into Eq. (5.31) results in an alternate form for the variation in internal nodal forces associated with the displacement DOFs, i.e.,

$$\begin{aligned} d\,{}^{u}f_{Ai}^{int} = & \int_{\Omega_o} {}^{u}\beta_{jA} \frac{\partial P_{ji}}{\partial F_{kl}} {}^{u}\beta_{lB}\, d\Omega_o du_{Bk} + \int_{\Omega_o} {}^{u}\beta_{jA} \frac{\partial P_{ji}}{\partial G_{klm}} {}^{F}\beta_{mB}\, d\Omega_o\, d\hat{F}_{Bkl} \\ & - \int_{\Omega_o} {}^{u}\beta_{jA}\, {}^{\lambda}N_B\, d\Omega_o\, d\lambda_{Bji} \end{aligned} \tag{5.48}$$

or

$$d\,{}^{u}f_{Ai}^{int} = K_{AiBn}^{uu}\, du_{Bn} + K_{AiBnm}^{u\hat{F}} d\hat{F}_{Bnm} + K_{AiBnm}^{u\lambda} d\lambda_{Bnm} \tag{5.49}$$

where

$$\begin{aligned} K_{AiBk}^{uu} &= \int_{\Omega_o} {}^{u}\beta_{jA} C_{jikl}^{PF}\, {}^{u}\beta_{lB}\, d\Omega_o \\ K_{AiBkl}^{u\hat{F}} &= \int_{\Omega_o} {}^{u}\beta_{jA} C_{jiklm}^{PG}\, {}^{F}\beta_{mB}\, d\Omega_o \\ K_{AiBnm}^{u\lambda} &= -\int_{\Omega_o} {}^{u}\beta_{jA}\, {}^{\lambda}N_B\, d\Omega_o \delta_{jn}\delta_{mi} \end{aligned} \tag{5.50}$$

and the constitutive tangent stiffness tensors are defined as

$$C_{jikl}^{PF} = \frac{\partial P_{ji}}{\partial F_{kl}},\; C_{jiklm}^{PG} = \frac{\partial P_{ji}}{\partial G_{klm}} \tag{5.51}$$

Repeating the same procedure for the variation in second order stress, i.e.,

$$dQ_{ijk} = \frac{\partial Q_{ijk}}{\partial F_{nm}} dF_{nm} + \frac{\partial Q_{ijk}}{\partial G_{nml}} dG_{nml} \tag{5.52}$$

followed by substitution of Eq. (5.52) into Eq. (5.39) results in the alternate linearization of deformation gradient internal nodal force vector, i.e.,

$$d\,{}^{\hat{F}}f_{Aij}^{int} = K_{AijBn}^{\hat{F}u}\, du_{Bn} + K_{AijBnm}^{\hat{F}\hat{F}}\, d\hat{F}_{Bnm} + K_{AijBnm}^{\hat{F}\lambda}\, d\lambda_{Bnm} \tag{5.53}$$

and Jacobian stiffness term computed as

$$K^{\hat{F}u}_{AijBn} = \int_{\Omega_o} {}^{F}\beta_{iA} C^{QF}_{ijknm} {}^{u}\beta_{mB},\; C^{QF}_{ijknm} = \frac{\partial Q_{ijk}}{\partial F_{nm}} \tag{5.54}$$

Note that the only change to the system Jacobian is the addition of possibly non-zero coefficients for $\mathbf{K}^{\hat{F}u}$ and $\mathbf{K}^{u\hat{F}}$. The alternative form for $\mathbf{K}^{uu}$ is merely a matter of convenience, i.e., the numerical values shall be the same if computed properly according to either (5.50) or (5.38).

Linearization of external forces adds additional terms to the system Jacobian stiffness if geometry dependent (*follower*) loads, e.g. pressure normal to deforming external surface, are employed. For implicit dynamic analysis, a conventional mass matrix is defined as from Eq. (5.27), i.e.,

$$M_{AB} = \int_{\Omega_o} \overline{\rho}\, {}^{u}N_A\, {}^{u}N_B\, d\Omega_o \tag{5.55}$$

The usual trade-offs concerning consistent or lumped mass matrices apply for this traditional mass matrix (cf. Belytschko et al., 2000).

The research comprising this dissertation focused on the numerical implementation of a constitutive framework consistent with the theory presented in Chapter 3. As such, details of external loading and dynamic response were omitted in favor of pursuing and extending numerical techniques for solution of quasi-static finite-deformation second gradient problems. Accordingly, the stiffness manifested by inertial effects, i.e., mass, and follower forces is not considered. This is a fruitful area for future research, as not much has been done in the literature to address such issues for second gradient continua.

5.1.4 Implementation in Abaqus

The nonlinear solution to the system of equations (5.29) is carried out using Abaqus' built in nonlinear solver via a user-defined element subroutine (UEL). Essentially, the UEL subroutine is called by Abaqus for each finite element in the problem domain to compute that element's contribution to the nodal residual force vector and system Jacobian. Abaqus performs the assembly operation, assembling the element level contributions into a full system of equations, and solves for the corrections to the solution variables at each nonlinear iteration. A description of the implemented UEL is given here.

Finite element formulations for second gradient continua have been developed by, for example, Shu and Fleck (1998), Shu et al. (1999), Amanatidou and Aravas (2002), Matsushima et al., (2002). The performance of various mixed-field second-gradient finite-element formulations has been investigated by Kouznetsova (2002) to identify the most viable ones. The element user-subroutine implemented in this dissertation employs a two-dimensional nine-node plane-deformation quadrilateral element developed by Matsushima et al. (2002). A diagram of this element in isoparametric space is shown in Figure 56. The particular element has displacement degrees of freedom at eight nodes, such that the displacement field is consistent with a conventional serendipity quadratic element. Deformation gradient degrees of freedom exist at the four corner nodes with linear interpolation and Lagrange multiplier degrees of freedom exist at a single central node. There are a total of 36 DOFs associated with an element. This element was selected based on results of a patch test (cf. 5.3.1), combined with its relatively fewer total DOFs, and its demonstrated convergence in accuracy with relatively fewer integration points when compared to other formulations (Kouznetsova, 2002).

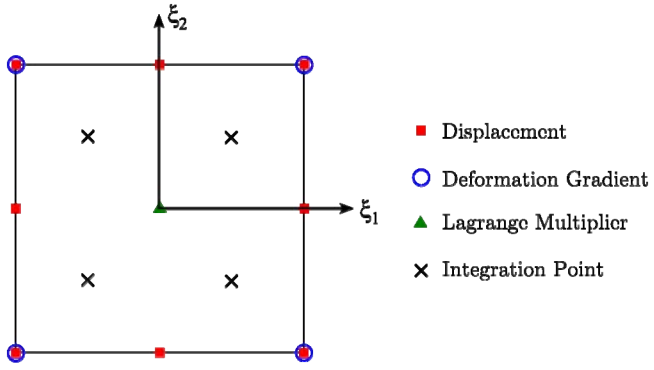

Figure 56. Diagram of mixed-field finite element in isoparametric space.

For the pure Lagrange constraint case, the Lagrange multiplier node could be removed as a global DOF and instead assigned as an internal solution field variable. Such an approach would remove issues of global numerical instability associated with the lack of stiffness for these DOFs, potentially obviating the necessity of using a perturbed Lagrangian constraint in the Abaqus UEL.

This numerical aspect was not pursued. Also note that the presence of plane-deformation implies out-of-plane stresses. For the second-gradient case, an often overlooked aspect of out-of-plane stresses is that a fully three dimensional coupling between second gradient and second order stress give rise to non-zero components of out of plane second-order stress, e.g. $Q_{123} \neq 0$ in general. The implication is that, while in theory, such components of stress are significant to inelastic constitutive response and in particular to evolution of an inelastic second-order strain, the details of this constitutive response cannot be identified from purely 2D fine-scale rSVE simulations. Accordingly, it is recognized here that an "effective" 2D second-order stress behavior will be adopted and this is merely an engineering approximation to the true response. This issue resolves itself for fully three dimensional implementations at the fine scale.

The element shape functions and derivatives for this element are tabulated in Appendix B. The elemental contributions to system nodal residual vector and Jacobian were computed using gauss quadrature to integrate over the domain of each element. Four integration points, shown as black x's in Figure 56, were used, resulting in reduced integration of the displacement interpolation functions, full integration of the deformation gradient interpolation functions, and beyond full integration for the constant Lagrange multiplier DOFs.

5.2 Implementation of Second Gradient Finite Deformation Hyperelastic Inelastic Constitutive Relations

Constitutive relations determine the coarse scale nominal stress, **P**, and second-order stress, **Q**, based on the current values of the deformation gradient, **F**, and second gradient, **G**, as well as the deformation history via internal state variables. In view of history dependence, the constitutive model is also responsible for updating the state of the material, a step which involves computing the evolution of the inelastic components of first order strain and second order strain and internal state variables. This section details the numerical implementation of constitutive models based on the ISV framework developed in Chapter 3 derived and/or fit to fine scale simulations described in Chapter 4.

The constitutive update is based on a finite deformation hyperelastic inelastic integration scheme. In particular we adapt the exponential mapping algorithm of Eidel and Gruttmann (2003) by extending to the second gradient continuum. Recall from Chapter 3,

$$\dot{\mathbf{F}}^{in} = \tilde{\mathbf{L}}^{in} \cdot \mathbf{F}^{in} \tag{5.56}$$

Assume, without loss of generality, that the evolution of inelastic strain can be defined by a direction normal to a flow (or pseudo-flow) potential, i.e.,

$$L_v\left(\tilde{\mathbf{E}}^{in}\right) = \tilde{\mathbf{D}}^{in} = \dot{\lambda}\frac{\partial F}{\partial \tilde{\mathbf{S}}_{\text{sym}}} \tag{5.57}$$

where $\dot{\lambda}$ is a multiplier, distinct from the mixed field Lagrange multiplier $\boldsymbol{\lambda}$ above, which reflects the non-uniqueness of the flow potential, in general. Only the symmetric part of the second Piola-Kirchhoff stress referred to the intermediate configuration, i.e., $\tilde{\mathbf{S}}_{\text{sym}}$, is used to determine the inelastic rate of deformation tensor, which is defined as a symmetric tensor. The assumption of Eq. (5.57) does not require purely associated flow as the flow potential need not be identical with an elastic threshold surface. Modifications must be made to the following procedure for cases where a flow potential is not available. However, such modifications are problem specific and cannot be anticipated for all cases.

The definition of a relaxed intermediate configuration (cf. Chapter 3) is unique up to, but excluding, a rigid rotation. The specification of this rotation is arbitrary and, while having implications to the implementation, need not restrict the theoretical consideration in any way. The central issue is the orientation of anisotropic structure within the material. Much confusion exists in the literature regarding plastic spin, continuum or plastic material spin, and substructure spin or the rate of change in sets of unit director vectors embedded in the material structure (Dafalias, 1998). The term ‘plastic spin’ is reserved to reflect the difference between the spin of the continuum, i.e., the anti-symmetric part of the velocity gradient, and the substructure spin (Aravas, 1994). For the i^{th} embedded anisotropic structure one can write,

$$skew\left(\tilde{\mathbf{L}}^{in}\right) = \boldsymbol{\omega}_i + \mathbf{W}_i^p \tag{5.58}$$

which specifies that the material spin, $skew\left(\tilde{\mathbf{L}}^{in}\right)$, is equal to the sum of the substructure spin, $\boldsymbol{\omega}_i$, and the plastic constitutive spin, $\mathbf{W}_i^p$. Eq. (5.58) holds true for each state variable which reflects an orientation dependence. The set of director vectors, $\mathbf{m}_i$, then evolve with respect to the (generally) rotating intermediate configuration according to $\dot{\mathbf{m}}_i = -\boldsymbol{\omega}_i \cdot \mathbf{m}_i$. Note that $skew\left(\tilde{\mathbf{L}}^{in}\right)$ is the spin of the intermediate configuration. The 'isoclinic' configuration is defined such that the material unit director vectors remain unchanged (of the same inclination) within the intermediate configuration. For this choice of intermediate configuration, i.e., $\dot{\mathbf{m}}_i = \mathbf{0} \rightarrow \boldsymbol{\omega}_i = \mathbf{0}$ one would have, $skew\left(\tilde{\mathbf{L}}^{in}\right) = \mathbf{W}_i^p$, which relates the continuum spin to the skew-symmetric part of evolution equations. Note that, while one could anticipate several separate orientation dependent mechanisms, the orientation dependence of each would necessarily be identical using an isoclinic intermediate configuration. This assumption is particularly useful for crystal plasticity models, for example, because the orientation dependence is only through lattice orientation and can be described by a single set of director vectors. On the other hand, Dafalias (1998) discusses the utility of a 'spinless' intermediate configuration, i.e., $skew\left(\tilde{\mathbf{L}}^{in}\right) = \mathbf{0}$. In this case, the underlying microstructure unit director vectors evolve with the substructure spin expressed as $\boldsymbol{\omega}_i = -\mathbf{W}_i^p$, i.e., $\dot{\mathbf{m}}_i = \mathbf{W}_i^p$. Following Gurtin and Anand (2005), Eidel and Gruttman (2003), Dafalias (1998), a 'spinless' intermediate configuration is adopted here. Note that this particular choice offers conveniences to the constitutive implementation without placing restriction or limitations on the theory developed in Chapter 3. Evolution of substructure orientation is still permitted via constitutive equations which would specify $\mathbf{W}_i^p$.

The additive decomposition of the inelastic part of the velocity gradient referred to the intermediate configuration is written as

$$\tilde{\mathbf{L}}^{in} = \mathbf{C}^{e,-1} \cdot \left(\tilde{\mathbf{D}}^{in} + skew\left(\tilde{\mathbf{L}}^{in}\right)\right) \tag{5.59}$$

Eq. (5.59) reflects the role of $\mathbf{C}^e$ acting as a metric on the intermediate configuration to raise and lower indices as necessary in computing symmetric and anti-symmetric parts of the mixed-variant

velocity gradient, . Recall from Chapter 3, the inelastic rate-of-deformation tensor referred to the intermediate configuration is computed as

$$\tilde{\mathbf{D}}^{in} = sym\Big(\tilde{\mathbf{L}}^{in}\Big) = \frac{1}{2}\Big(\mathbf{C}^{e}\cdot\tilde{\mathbf{L}}^{in} + \tilde{\mathbf{L}}^{in,T}\cdot\mathbf{C}^{e}\Big) = \phi_{e}^{*}\Big(\mathbf{D}^{in}\Big) \tag{5.60}$$

and likewise, the anti-symmetric part of the plastic velocity gradient is computed as (cf. Belytschko et al., 2000)

$$skew\Big(\tilde{\mathbf{L}}^{in}\Big) = \frac{1}{2}\Big(\mathbf{C}^{e}\cdot\tilde{\mathbf{L}}^{in} - \tilde{\mathbf{L}}^{in,T}\cdot\mathbf{C}^{e}\Big) = \phi_{e}^{*}\Big(\mathbf{W}^{in}\Big) \tag{5.61}$$

Having adopted a spinless intermediate configuration Eq. (5.59) can now be written

$$\tilde{\mathbf{L}}^{in} = \mathbf{C}^{e,-1}\cdot\tilde{\mathbf{D}}^{in} \tag{5.62}$$

Again, this does not imply that microstructural orientation is unchanged during irreversible processes, because such changes can be accommodated by evolving orientation or director vectors. Substitution of Eqs. (5.57) and (5.62) into Eq. (5.56) gives

$$\dot{\mathbf{F}}^{in} = \dot{\lambda}\mathbf{C}^{e}\cdot\frac{\partial F}{\partial\tilde{\mathbf{S}}_{\text{sym}}}\cdot\mathbf{F}^{in} \tag{5.63}$$

Equation (5.63) is distinct from Eidel and Gruttman (2003) because they make an incorrect assertion, namely, $\tilde{\mathbf{L}}^{in} = \tilde{\mathbf{D}}^{in}$, which cannot be true because the symmetrization of $\tilde{\mathbf{L}}^{in}$ to form $\tilde{\mathbf{D}}^{in}$ requires the use of $\mathbf{C}^{e}$ as metric on the intermediate configuration, cf. Chapter 3 and recall $\tilde{\mathbf{D}}^{in} = \frac{1}{2}\Big(\mathbf{C}^{e}\cdot\tilde{\mathbf{L}}^{in} + \tilde{\mathbf{L}}^{in,T}\cdot\mathbf{C}^{e}\Big)$. This distinction can be interpreted as a difference in the evolution equations rather than an error in their fundamental kinematics. Their error vanishes in the limit of infinitesimal elastic strain. Solution to the differential equation (5.63) over a time increment, $\Delta t = t_{k+1} - t_{k}$, proceeds by separation of variables and integration, i.e.,

$$\begin{aligned}
\int_{k}^{k+1}\mathbf{F}^{in,-1}\cdot d\mathbf{F}^{in} &= \int_{k}^{k+1}\dot{\lambda}\mathbf{A}\,dt \\
\ln\Big(\mathbf{F}_{k+1}^{in}\Big) - \ln\Big(\mathbf{F}_{k}^{in}\Big) &= \mathbf{A}\,\dot{\lambda}\Delta t \\
\mathbf{F}_{k+1}^{in}\cdot\mathbf{F}_{k}^{in,-1} &= \exp\Big(\gamma\mathbf{A}\Big) \\
\mathbf{F}_{k+1}^{in} &= \exp\Big(\gamma\mathbf{A}\Big)\cdot\mathbf{F}_{k}^{in}
\end{aligned} \tag{5.64}$$

where the plasticity parameter, $\gamma = \dot{\lambda}\Delta t$, has been introduced. This solution for the inelastic part of the deformation gradient at the *k+1* increment is exact if the terms in **A** are constant over the increment. Such is not the case for Eq. (5.63), so that we make the explicit (forward) approximation,

$$\mathbf{A} = \mathbf{C}_k^{e,-1} \cdot \left(\frac{\partial F}{\partial \tilde{\mathbf{S}}_{\text{sym}}} \right)_k \tag{5.65}$$

The exponential map is then stated as

$$\mathbf{F}_{k+1}^{in} = \exp\left[\gamma\, \mathbf{C}_k^{e,-1} \cdot \left(\frac{\partial F}{\partial \tilde{\mathbf{S}}_{\text{sym}}} \right)_k \right] \cdot \mathbf{F}_k^{in} \tag{5.66}$$

The Lie derivative of the inelastic second order strain in the intermediate configuration is assumed to evolve normal to a flow (or pseudo-flow) potential according to

$$L_v \left(\tilde{\mathbf{\Gamma}}^{in} \right)_{\cdot\tilde{j}\tilde{k}}^{\tilde{i}} = {}^{in}F_{\cdot M}^{\tilde{i}}\, {}^{in}\dot{\Gamma}_{\cdot NO}^{M}\, {}^{in}F_{\cdot\tilde{j}}^{\bar{N}^{-1}}\, {}^{in}F_{\cdot\tilde{k}}^{\bar{O}^{-1}} = -\dot{\lambda} \frac{\partial F}{\partial \tilde{Q}_{\tilde{i}}^{\cdot\tilde{j}\tilde{k}}} \tag{5.67}$$

Equation (5.67) is solved for the time derivative of the second order strain in the reference configuration, i.e.,

$${}^{in}\dot{\Gamma}_{\cdot NO}^{M} = -\dot{\lambda} \frac{\partial F}{\partial \tilde{Q}_{\tilde{i}}^{\cdot\tilde{j}\tilde{k}}}\, {}^{in}F_{\cdot\tilde{i}}^{\bar{M}^{-1}}\, {}^{in}F_{\cdot N}^{\tilde{j}}\, {}^{in}F_{\cdot O}^{\tilde{k}} = \dot{\lambda}\mathbf{H}_{\Gamma} \tag{5.68}$$

Explicit integration of (5.68), yields

$$\mathbf{\Gamma}_{k+1}^{in} = \mathbf{\Gamma}_k^{in} + \gamma \mathbf{H}_k^{\Gamma} \tag{5.69}$$

The update of the inelastic part of the second order strain with respect to the intermediate configuration is then finalized by performing the inelastic push forward of the inelastic second order strain in the reference configuration at the end of the increment, i.e.,

$$\left({}^{in}\tilde{\Gamma}_{\cdot\tilde{j}\tilde{k}}^{\tilde{i}} \right)_{n+1} = \left({}^{in}F_{\cdot M}^{\tilde{i}}\, {}^{in}\Gamma_{\cdot NO}^{M}\, {}^{in}F_{\cdot\tilde{j}}^{\bar{N}^{-1}}\, {}^{in}F_{\cdot\tilde{k}}^{\bar{O}^{-1}} \right)_{n+1} \tag{5.70}$$

The integration algorithm begins by computing a trial elastic state, i.e.,

$$
\begin{aligned}
\mathbf{F}_{k+1}^{e,trial} &= \mathbf{F}_{k+1}^{\text{-}1} \cdot \mathbf{F}_{k}^{in} \\
\tilde{\mathbf{E}}_{k+1}^{e,trial} &= \frac{1}{2}\left[\left(\mathbf{F}_{k+1}^{e,trial}\right)^{T} \cdot \mathbf{F}_{k+1}^{e,trial} - \mathbf{I}\right] \\
\tilde{\mathbf{\Gamma}}_{k+1}^{e,trial} &= \left({}^{e}\mathbf{F}_{k+1}^{\text{-}1}, {}^{in}\mathbf{F}_{k+1}^{\text{-}1}, {}^{in}\mathbf{F}_{k+1}^{\text{-}1}\right)^{trial} \cdot \mathbf{G}_{k+1} - \tilde{\mathbf{\Gamma}}_{k}^{in} \\
\boldsymbol{\xi}_{k+1}^{trial} &= \boldsymbol{\xi}_{k}
\end{aligned}
\tag{5.71}
$$

and

$$
\tilde{\mathbf{S}}_{k+1}^{trial} = \frac{\partial \overline{\psi}}{\partial \tilde{\mathbf{E}}_{k+1}^{e,tr}}, \;\; \tilde{\mathbf{Q}}_{k+1}^{trial} = \tilde{\rho}\frac{\partial \overline{\psi}}{\partial \tilde{\mathbf{\Gamma}}_{k+1}^{e,tr}}, \;\; \overline{\boldsymbol{\beta}}_{k+1}^{trial} = \tilde{\rho}\frac{\partial \overline{\psi}}{\partial \overline{\boldsymbol{\xi}}_{k+1}^{tr}} \tag{5.72}
$$

Next the yield condition is evaluated for this trial state. If the trial state lies within the bounding elastic threshold surface then the trial state is the final state for increment *k+1*, i.e.,

$$
\begin{aligned}
&\text{IF:} \\
&\quad f\left(\tilde{\mathbf{S}}_{k+1}^{trial}, \;\; \tilde{\mathbf{Q}}_{k+1}^{trial}, \;\; \overline{\boldsymbol{\beta}}_{k+1}^{trial}\right) \leq 0 \\
&\text{THEN:} \\
&\quad \tilde{\mathbf{S}}_{k+1} = \tilde{\mathbf{S}}_{k+1}^{trial}, \tilde{\mathbf{Q}}_{k+1} = \tilde{\mathbf{Q}}_{k+1}^{trial}, \\
&\quad \mathbf{F}_{k+1}^{in} = \mathbf{F}_{k}^{in}, \; \tilde{\mathbf{\Gamma}}_{k+1}^{in} = \tilde{\mathbf{\Gamma}}_{k}^{in}, \; \boldsymbol{\xi}_{k+1} = \boldsymbol{\xi}_{k}
\end{aligned}
\tag{5.73}
$$

Otherwise an iterative solver is used to solve the nonlinear equation (5.74), which demands that the current state lie on the yield surface at the end of the increment.

$$
f\left(\tilde{\mathbf{S}}_{k+1}, \;\; \tilde{\mathbf{Q}}_{k+1}, \;\; \overline{\boldsymbol{\beta}}_{k+1}\right) = 0 \tag{5.74}
$$

To develop the iterative solution technique we first invert relationship (5.66), i.e.,

$$
{}^{in}\mathbf{F}_{n+1,k}^{\text{-}1} = {}^{in}\mathbf{F}_{n}^{\text{-}1} \cdot \mathbf{exp}\left[-\gamma_{k}\, \mathbf{A}_{n}\, \right] \tag{5.75}
$$

and multiply by the deformation gradient to compute the elastic part of the deformation gradient for a particular iteration. This is written as

$$
\begin{aligned}
{}^{e}\mathbf{F}_{n+1,k} &= \mathbf{F}_{n+1} \cdot {}^{in}\mathbf{F}_{n}^{\text{-}1} \cdot \mathbf{exp}\left[-\gamma_{k}\, \mathbf{A}_{n}\, \right] \\
&= {}^{e}\mathbf{F}_{n+1}^{trial} \cdot \mathbf{exp}\left[-\gamma_{k}\, \mathbf{A}_{n}\, \right]
\end{aligned}
\tag{5.76}
$$

Likewise, the inverse of (5.76) provides

$$
{}^{e}\mathbf{F}_{n+1,k}^{\text{-}1} = \mathbf{exp}\left[\gamma_{k}\, \mathbf{A}_{n}\, \right] \cdot {}^{e}\mathbf{F}_{n+1}^{\text{-}1,trial} \tag{5.77}
$$

The current value of elastic strain for the k^{th} iteration is computed directly from (5.76), i.e., ${}^{e}\tilde{\mathbf{E}}_{n+1,k} = \frac{1}{2}\left({}^{e}\mathbf{F}^{T}_{n+1,k} \cdot {}^{e}\mathbf{F}_{n+1,k} - \mathbf{I} \right)$. An algorithm for computation of the current value of the elastic second order strain in the intermediate configuration is developed by pulling $\tilde{\mathbf{\Gamma}}^{in}_{k}$ into the reference configuration, i.e.,

$$\left({}^{in}\Gamma^{M}_{.NO} \right)_{n} = \left({}^{in}F^{-1}{}^{M}_{.\tilde{i}}\ {}^{in}F^{\tilde{j}}_{.N}\ {}^{in}F^{\tilde{k}}_{.O} \right)_{n} \left({}^{in}\tilde{\Gamma}^{\tilde{i}}_{.\tilde{j}\tilde{k}} \right)_{n} \tag{5.78}$$

integrating ${}^{in}\dot{\mathbf{\Gamma}}$ within the reference configuration using an explicit integration of equation (5.68) above,

$$\left({}^{in}\Gamma^{M}_{.NO} \right)_{n+1,k} = \left({}^{in}F^{-1}{}^{M}_{.\tilde{i}}\ {}^{in}F^{\tilde{j}}_{.N}\ {}^{in}F^{\tilde{k}}_{.O} \right)_{n} \left({}^{in}\tilde{\Gamma}^{\tilde{i}}_{.\tilde{j}\tilde{k}} \right)_{n} - \gamma_{k} \left({}^{in}F^{-1}_{.\tilde{i}}\ {}^{in}F^{\tilde{j}}_{.N}\ {}^{in}F^{\tilde{k}}_{.O} \right)_{n} \left(\frac{\partial F}{\partial \tilde{Q}^{.\tilde{j}\tilde{k}}_{\tilde{i}}} \right)_{n} \tag{5.79}$$

and pushing forward into the intermediate configuration, i.e.,

$$\left({}^{in}\tilde{\Gamma}^{\tilde{q}}_{.\tilde{r}\tilde{s}} \right)_{n+1,k} = \left({}^{in}F^{\tilde{q}}_{.M}\ {}^{in}F^{-1}{}^{N}_{.\tilde{r}}\ {}^{in}F^{-1}{}^{O}_{.\tilde{s}} \right)_{n+1,k} \left({}^{in}\Gamma^{M}_{.NO} \right)_{n+1,k} \tag{5.80}$$

Substitution of (5.66) and (5.75) into (5.80),

$$\begin{aligned} \left({}^{in}\tilde{\Gamma}^{\tilde{q}}_{.\tilde{r}\tilde{s}} \right)_{n+1,k} = {} & \exp\left[\gamma_{k}\, \mathbf{A}_{n} \right]^{\tilde{q}}_{.\tilde{v}} \exp\left[-\gamma_{k}\, \mathbf{A}_{n} \right]^{\tilde{t}}_{.\tilde{r}} \exp\left[-\gamma_{k}\, \mathbf{A}_{n} \right]^{\tilde{u}}_{.\tilde{s}} \\ & \left({}^{in}F^{\tilde{v}}_{.M},\ {}^{in}F^{-1}{}^{N}_{.\tilde{t}},\ {}^{in}F^{-1}{}^{O}_{.\tilde{u}} \right)_{n} \left({}^{in}\Gamma^{M}_{.NO} \right)_{n+1,k} \end{aligned} \tag{5.81}$$

which, when combined with (5.79), gives

$$\left({}^{in}\tilde{\Gamma}^{\tilde{q}}_{.\tilde{r}\tilde{s}} \right)_{n+1,k} = \exp\left[\gamma_{k}\, \mathbf{A}_{n} \right]^{\tilde{q}}_{.\tilde{i}} \exp\left[-\gamma_{k}\, \mathbf{A}_{n} \right]^{\tilde{j}}_{.\tilde{r}} \exp\left[-\gamma_{k}\, \mathbf{A}_{n} \right]^{\tilde{k}}_{.\tilde{s}} \left[\left({}^{in}\tilde{\Gamma}^{\tilde{i}}_{.\tilde{j}\tilde{k}} \right)_{n} - \gamma_{k} \left(\frac{\partial F}{\partial \tilde{Q}^{.\tilde{j}\tilde{k}}_{\tilde{i}}} \right)_{n} \right] \tag{5.82}$$

Likewise, the total second order strain referred to the intermediate configuration is updated for the k^{th} iteration by

$$\begin{aligned} \left(\tilde{\Gamma}^{\tilde{q}}_{.\tilde{r}\tilde{s}} \right)_{n+1,k} &= \left({}^{e}F^{-1}{}^{\tilde{q}}_{.m}\ {}^{in}F^{-1}{}^{N}_{.\tilde{r}}\ {}^{in}F^{-1}{}^{O}_{.\tilde{s}} \right)_{n+1,k} \left(G^{i}_{.JK} \right)_{n+1} \\ &= \exp\left[\gamma_{k}\, \mathbf{A}_{n} \right]^{\tilde{q}}_{.\tilde{i}}\ \exp\left[-\gamma_{k}\, \mathbf{A}_{n} \right]^{\tilde{j}}_{.\tilde{r}} \exp\left[-\gamma_{k}\, \mathbf{A}_{n} \right]^{\tilde{k}}_{.\tilde{s}}\ {}^{e,tr}F^{-1}{}^{\tilde{i}}_{.m} \left({}^{in}F^{-1}{}^{N}_{.\tilde{j}},\ {}^{in}F^{-1}{}^{O}_{.\tilde{k}} \right)_{n} \left(G^{m}_{.NO} \right)_{n+1} \\ &= \exp\left[\gamma_{k}\, \mathbf{A}_{n} \right]^{\tilde{q}}_{.\tilde{i}}\ \exp\left[-\gamma_{k}\, \mathbf{A}_{n} \right]^{\tilde{j}}_{.\tilde{r}} \exp\left[-\gamma_{k}\, \mathbf{A}_{n} \right]^{\tilde{k}}_{.\tilde{s}}\ \left(\tilde{\Gamma}^{\tilde{i}}_{.\tilde{j}\tilde{k}} \right)_{trial} \end{aligned} \tag{5.83}$$

such that the elastic part of the second order strain referred to the intermediate configuration is computed as

$$\begin{aligned}\left({}^{e}\tilde{\Gamma}^{\tilde{q}}_{\cdot\tilde{r}\tilde{s}}\right)_{n+1,k} &= \left(\tilde{\Gamma}^{\tilde{q}}_{\cdot\tilde{r}\tilde{s}}\right)_{n+1,k} - \left({}^{in}\tilde{\Gamma}^{\tilde{q}}_{\cdot\tilde{r}\tilde{s}}\right)_{n+1,k} \\ &= \exp\left[\gamma_k \mathbf{A}_n\right]^{\tilde{q}}_{\cdot\tilde{i}} \exp\left[-\gamma_k \mathbf{A}_n\right]^{\tilde{j}}_{\cdot\tilde{r}} \exp\left[-\gamma_k \mathbf{A}_n\right]^{\tilde{k}}_{\cdot\tilde{s}} \left[\left(\tilde{\Gamma}^{\tilde{i}}_{\cdot\tilde{j}\tilde{k}}\right)_{trial} - \left({}^{in}\tilde{\Gamma}^{\tilde{i}}_{\cdot\tilde{j}\tilde{k}}\right)_n + \gamma_k \left(\frac{\partial F}{\partial \tilde{Q}^{\cdot\tilde{j}\tilde{k}}_{\tilde{i}}}\right)_n\right] \\ &= M(\gamma_k)^{\tilde{q}\ldots\tilde{j}\tilde{k}}_{\cdot\tilde{r}\tilde{s}\tilde{i}} \left[\left({}^{e}\tilde{\Gamma}^{\tilde{i}}_{\cdot\tilde{j}\tilde{k}}\right)_{trial} + \gamma_k \left(\frac{\partial F}{\partial \tilde{Q}^{\cdot\tilde{j}\tilde{k}}_{\tilde{i}}}\right)_n\right]\end{aligned} \tag{5.84}$$

After computing ${}^{e}\tilde{\mathbf{E}}_{n+1,k}$, ${}^{e}\tilde{\mathbf{\Gamma}}_{n+1,k}$, and $\overline{\boldsymbol{\xi}}_{n+1,k}$ the associated thermodynamic stresses are computed according to

$$\tilde{\mathbf{S}}_{n+1,k} = \tilde{\rho}\frac{\partial\overline{\psi}}{\partial\,{}^{e}\tilde{\mathbf{E}}_{n+1,k}},\ \ \tilde{\mathbf{Q}}_{n+1,k} = \tilde{\rho}\frac{\partial\overline{\psi}}{\partial\,{}^{e}\tilde{\mathbf{\Gamma}}_{n+1,k}},\ \ \overline{\boldsymbol{\beta}}_{n+1,k} = \tilde{\rho}\frac{\partial\overline{\psi}}{\partial\overline{\boldsymbol{\xi}}_{n+1,k}} \tag{5.85}$$

and the yield function is evaluated, i.e.,

$$f(\gamma_k) = f\left(\tilde{\mathbf{S}}_{n+1,k},\ \ \tilde{\mathbf{Q}}_{n+1,k}, \overline{\boldsymbol{\beta}}_{n+1,k}\right) \tag{5.86}$$

These same steps are repeated in order to compute $f(\gamma_k + d\gamma)$ where $d\gamma$ is a small perturbation to the plasticity parameter introduced to numerically approximate the derivative of the yield function with respect to the plasticity parameter, i.e.,

$$f' \cong \frac{f\left(\gamma_k + d\gamma\right) - f\left(\gamma_k\right)}{d\gamma} \tag{5.87}$$

The plasticity parameter is then updated for the next iteration by the Newton-Raphson technique, i.e.,

$$\gamma_{k+1} = \gamma_k - \frac{f\left(\gamma_k\right)}{f'\left(\gamma_k\right)} \tag{5.88}$$

If $\left|f\left(\gamma_k\right)\right| < tol$, then the nonlinear iterations have converged and the constitutive update is completed by updating the internal state variables and inelastic components of deformation according to

$$ {}^{in}\mathbf{F}^{-1}_{n+1} = {}^{in}\mathbf{F}^{-1}_{n} \cdot \mathbf{exp}\left[-\gamma_k \, \mathbf{A}_n \right] \tag{5.89} $$

$$ \left({}^{in}\tilde{\Gamma}^{\tilde{q}}_{.\tilde{r}\tilde{s}} \right)_{n+1} = M(\gamma_k)^{\tilde{q}\ldots\tilde{j}\tilde{k}}_{.\tilde{r}\tilde{s}\tilde{i}} \left(\tilde{\Gamma}^{\tilde{i}}_{.\tilde{j}\tilde{k}} \right)_{trial} - \left({}^{e}\tilde{\Gamma}^{\tilde{q}}_{.\tilde{r}\tilde{s}} \right)_{n+1,k} \tag{5.90} $$

and, finally, pulling the necessary stress terms into the reference configuration, i.e.,

$$ \mathbf{P}_{n+1} = {}^{in}\mathbf{F}^{-1}_{n+1} \cdot \tilde{\mathbf{S}} \cdot {}^{e}\mathbf{F}^{T}_{n+1} \det({}^{in}\mathbf{F}_{n+1}) \tag{5.91} $$

$$ Q^{iJK}_{n+1} = g^{i}_{m} \left({}^{e}F^{-1}{}^{\tilde{q}}_{.m} \; {}^{in}F^{-1}{}^{J}_{.\tilde{r}} \; {}^{in}F^{-1}{}^{K}_{.\tilde{s}} \right)_{n+1} \left(\tilde{Q}^{\tilde{r}\tilde{s}}_{\tilde{q}} \right)_{n+1} \det({}^{in}\mathbf{F}_{n+1}) \tag{5.92} $$

The total specific energy per unit volume in the reference configuration is updated according to

$$ E^{total}_{n+1} = E^{total}_{n} + \mathbf{P}_{n+\frac{1}{2}} : \Delta\mathbf{F} + \mathbf{Q}_{n+\frac{1}{2}} \vdots \Delta\mathbf{G} \tag{5.93} $$

and the elastic strain energy density is computed as

$$ \rho_{\mathrm{o}} \overline{\psi}^{e}_{n+1} = \det(\mathbf{F}^{in}) \, \tilde{\rho} \, \overline{\psi}^{e} \left({}^{e}\tilde{\mathbf{E}}_{n+1}, {}^{e}\tilde{\mathbf{\Gamma}}_{n+1}, \overline{\boldsymbol{\xi}}^{j}_{n+1} \right) \tag{5.94} $$

Additionally, the specific dissipated energy per unit volume in the reference configuration is updated according to

$$ \begin{aligned} \rho_{\mathrm{o}}\Pi_{n+1} &= \rho_{\mathrm{o}}\Pi_{n} + \int_{t_n}^{t_{n+1}} \frac{\rho_{\mathrm{o}}}{\tilde{\rho}} \, \tilde{\rho} \, \dot{\Pi} \, dt \\ &= \rho_{\mathrm{o}}\Pi_{n} + \int_{t_n}^{t_{n+1}} \det(\mathbf{F}^{in}) \left[(\tilde{\mathbf{S}} - \tilde{\mathbf{S}}^{*}) : \tilde{\mathbf{D}}_{in} + \tilde{\mathbf{Q}} \vdots L_v(\tilde{\mathbf{\Gamma}}_{in}) - \overline{\boldsymbol{\beta}}^{j} * L_v(\overline{\boldsymbol{\xi}}^{j}) \right] dt \\ &\simeq \rho_{\mathrm{o}}\Pi_{n} + \det(\mathbf{F}^{in})_{n+\frac{1}{2}} \left[(\tilde{\mathbf{S}} - \tilde{\mathbf{S}}^{*})_{n+\frac{1}{2}} : \Delta\tilde{\mathbf{E}}^{in} + \tilde{\mathbf{Q}}_{n+\frac{1}{2}} \vdots \Delta\tilde{\mathbf{\Gamma}}^{in} - \sum_{j} \overline{\boldsymbol{\beta}}^{j}_{n+\frac{1}{2}} * \Delta\overline{\boldsymbol{\xi}}^{j} \right] \end{aligned} \tag{5.95} $$

A constitutive integration algorithm has been developed, implemented, and is presented in this section. The key features of this integration algorithm are that it is provides a hyperelastic definition of stresses, accommodates finite deformation without restrictions to small rotations or small elastic strains, permits anisotropy (as will be discussed in Chapter 6), and is conceptually and numerically consistent with the theoretical framework presented in Chapter 3.

5.3 Code Verification and Numerical Testing

The developed user-element and associated numerical algorithms were subjected to numerical tests and code verification prior to application to an example problem discussed in Chapter 6. A patch test was performed for initial confirmation of the implementation. Results of the patch test are presented in 5.3.1. Rigorous code verification tests were performed for a purely elastic case and are discussed in Section 5.3.2. For the inelastic case, numerical unit testing of sections of code and simulations of inelastic test cases exhibiting large deformation were employed to demonstrate (1) reasonable confidence in the code, (2) constitutive convergence and (3) physically reasonable output. Section 5.3.3 extends the numerical solutions for the problem used in Section 5.3.2 to cases exhibiting small inelastic deviations from the predominantly elastic response. Finally, the behavior of the code under large inelastic deformation leading to localization is examined in Section 5.3.4.

5.3.1 Patch Test

From a finite element formulation standpoint, the patch test is often used to demonstrate the validity of particular element formulation. In particular, the patch test has historically been used to ensure convergence of non conforming elements, although apparently there is some debate as to whether the patch test is even necessary or sufficient to establish such performance (cf. Stummel, 1980; Zienkiewicz and Taylor, 1997). The idea is that if a patch of elements are constructed such that at least one node lies on the interior of the problem and boundary conditions consistent with a uniform state of strain and stress are specified everywhere on the boundary, then the interior results should exactly satisfy the imposed solution, i.e. a uniform state of deformation and strain. A patch test was performed in this work to verify the numerical implementation rather than to demonstrate a valid element formulation as the latter has been demonstrated by Matsushima et al. (2002).

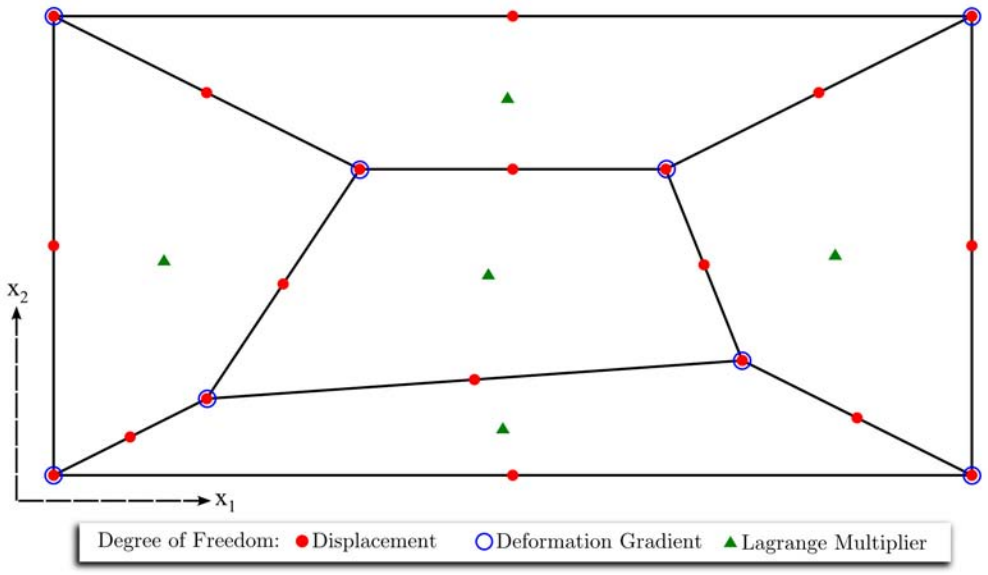

Figure 57. Finite element mesh used for patch test.

The finite element mesh used for this patch test is shown in Figure 57. The displacement solution imposed on the external boundary nodes is

$$\begin{aligned} u_1 &= u_0\left(x_1 + \tfrac{1}{2}x_2\right) \\ u_2 &= u_0\left(x_2 + \tfrac{1}{2}x_1\right) \end{aligned}, \tag{5.96}$$

corresponding to a uniform deformation gradient of

$$\mathbf{F} = \begin{bmatrix} 1+u_0 & \frac{1}{2}u_0 & 0 \\ \frac{1}{2}u_0 & 1+u_0 & 0 \\ 0 & 0 & F_{33} \end{bmatrix} \tag{5.97}$$

which was specified at the appropriate external nodes, i.e., those nodes on the external boundary for which relaxed deformation gradient DOFs exist. Two cases were considered, viz. case 1 corresponds to infinitesimal deformation and case 2 is finite deformation. In both cases the constitutive behavior is purely hyperelastic Kirchhoff model with elastic constants, $E = 10^6$ and $\nu = 0.25$. Numerical results for the exact solution of various components of strain and stress are reported in Table 4. For both cases the patch test results were in agreement with tabulated results.

Table 4. Exact solutions for patch test problem.

	Case 1	Case 2
u_0	1.e-3	1.e-1
E_{11}, E_{22}	0.0010	0.1063
E_{12}	0.0005	0.1100
S_{11}, S_{22}	1600.	170,000.
S_{12}	400.	44,000.

5.3.2 Convergence to Analytical Solution for Elastic Case

In order to further build confidence in the numerical implementation of the code, a mesh convergence study was performed on solutions to a boundary shear layer problem borrowed from Kouznetsova (2002). The advantage of this particular problem is that is has a closed form analytical solution so that pointwise error can be evaluated (rather than estimated) and the proper order of convergence demonstrated. Figure 58 depicts the boundary shear problem to be solved. A chunk of media infinitely long in the vertical direction and spanning a 'thickness' L in the x_1 dimension is restrained against all deformation on the left side. The right side is subjected to a vertical displacement of U_0 while other components of deformation are restrained.

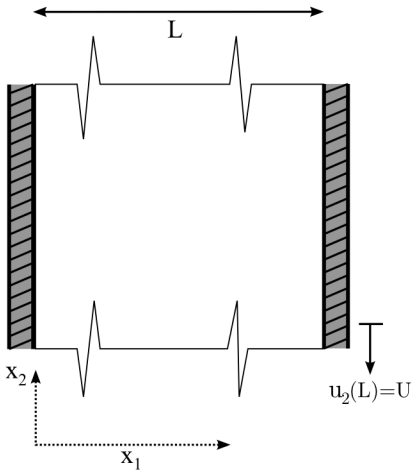

Figure 58. Diagram of thin boundary layer shear problem.

The problem has infinite symmetry in the vertical (x_2) direction, so it can be idealized as a one-dimensional problem, i.e. the solution varies only with x_1. The boundary conditions are

$$\begin{array}{ll} u_1(0) = 0 & u_1(L) = 0 \\ u_2(0) = 0 & u_2(L) = U_0 \\ \mathbf{F}(0) = \mathbf{I} & \mathbf{F}(L) = \mathbf{I} \end{array} \tag{5.98}$$

Strong form of equilibrium requires $\vec{\nabla}_{\mathrm{o}} \cdot \left(\mathbf{P} - \left(\vec{\nabla}_{\mathrm{o}} \cdot \mathbf{Q} \right)^T \right) = \mathbf{0}$, which after accounting for the one-dimensional nature of the problem yields two differential equations, i.e.,

$$\begin{aligned} \frac{\partial P_{11}}{\partial x_1} - \frac{\partial^2 Q_{111}}{\partial x_1^2} = 0 \\ \frac{\partial P_{12}}{\partial x_1} - \frac{\partial^2 Q_{211}}{\partial x_1^2} = 0 \end{aligned} \tag{5.99}$$

The relevant components of the deformation gradient and second gradient are

$$\begin{array}{ll} F_{11}(x_1) = 1 + \dfrac{\partial u_1(x_1)}{\partial x_1} & G_{111}\left(x_1\right) = \dfrac{\partial^2 u_1(x_1)}{\partial x_1^2} \\ F_{21}(x_1) = \dfrac{\partial u_2(x_1)}{\partial x_1} & G_{211}\left(x_1\right) = \dfrac{\partial^2 u_2(x_1)}{\partial x_1^2} \end{array} \tag{5.100}$$

Nonzero components of finite Green-Lagrange strain are expressed as

$$\begin{aligned} E_{11} &= \frac{1}{2}\left[\left(1 + \frac{\partial}{\partial x_1} u_1(x_1) \right)^2 + \left(\frac{\partial}{\partial x_1} u_2(x_1) \right)^2 - 1 \right] \\ E_{12} &= \frac{1}{2} \frac{\partial}{\partial x_1} u_2(x_1) \end{aligned} \tag{5.101}$$

Again we employ an elastic potential which results in a Kirchhoff hyperelastic model for the first-order constitutive response supplemented by Mindlin's second gradient elasticity (Mindlin, 1964), i.e.,

$$\begin{aligned} \overline{\psi}^e &= \tfrac{1}{2}\lambda E^e_{jj} E^e_{ii} + \mu E^e_{ij} E^e_{ij} \\ &\quad + a_1 G_{jij} G_{kik} + a_2 G_{kii} G_{jkj} + a_3 G_{kii} G_{kjj} + a_4 G_{kij} G_{kij} + a_5 G_{kij} G_{ijk} \end{aligned} \tag{5.102}$$

The relevant components of the stress field are then computed to be

$$
\begin{aligned}
P_{11} &= \frac{1}{2}\big(\lambda+2\mu\big)\left[\left(1+\frac{\partial}{\partial x_1}u_1(x_1)\right)^2+\left(\frac{\partial}{\partial x_1}u_2(x_1)\right)^2-1\right]\left(1+\frac{\partial}{\partial x_1}u_1(x_1)\right)\\
P_{12} &= \frac{1}{2}\big(\lambda+2\mu\big)\left[\left(1+\frac{\partial}{\partial x_1}u_1(x_1)\right)^2+\left(\frac{\partial}{\partial x_1}u_2(x_1)\right)^2-1\right]\left(\frac{\partial}{\partial x_1}u_2(x_1)\right)+\mu\frac{\partial}{\partial x_1}u_2(x_1)\\
Q_{111} &= 2\big(a_1+a_2+a_3+a_4+a_5\big)\frac{\partial^2}{\partial x_1^2}u_1(x_1)\\
Q_{211} &= 2\big(a_3+a_4\big)\frac{\partial^2}{\partial x_1^2}u_2(x_1)
\end{aligned}
\tag{5.103}
$$

Substitution of (5.103) into (5.99) gives a system of two coupled differential equations in two variables, u_1 and u_2, i.e.,

$$
\begin{aligned}
0 = &\big(\lambda+2\mu\big)\left(\left(1+\frac{\partial u_1}{\partial x_1}\right)\left(\frac{\partial^2 u_1}{\partial x_1^2}\right)+\left(\frac{\partial u_2}{\partial x_1}\right)\left(\frac{\partial^2 u_2}{\partial x_1^2}\right)\right)\left(1+\frac{\partial u_1}{\partial x_1}\right)\\
&+\big(\lambda+2\mu\big)\left(\frac{1}{2}\left(1+\frac{\partial u_1}{\partial x_1}\right)^2+\frac{1}{2}\left(1+\frac{\partial u_2}{\partial x_1}\right)^2-\frac{1}{2}\right)\left(\frac{\partial^2 u_1}{\partial x_1^2}\right)\\
&-2\big(a_1+a_2+a_3+a_4+a_5\big)\left(\frac{\partial^4 u_1}{\partial x_1^4}\right)
\end{aligned}
\tag{5.104}
$$

$$
\begin{aligned}
0 = &\big(\lambda+2\mu\big)\left(\left(1+\frac{\partial u_1}{\partial x_1}\right)\left(\frac{\partial^2 u_1}{\partial x_1^2}\right)+\left(\frac{\partial u_2}{\partial x_1}\right)\left(\frac{\partial^2 u_2}{\partial x_1^2}\right)\right)\left(\frac{\partial u_2}{\partial x_1}\right)\\
&+\big(\lambda+2\mu\big)\left(\frac{1}{2}\left(1+\frac{\partial u_1}{\partial x_1}\right)^2+\frac{1}{2}\left(1+\frac{\partial u_2}{\partial x_1}\right)^2-\frac{1}{2}\right)\left(\frac{\partial^2 u_2}{\partial x_1^2}\right)\\
&+\mu\left(\frac{\partial^2 u_2}{\partial x_1^2}\right)-2\big(a_3+a_4\big)\left(\frac{\partial^4 u_2}{\partial x_1^4}\right)
\end{aligned}
\tag{5.105}
$$

Assuming infinitesimal deformation allows simplification of the problem to a single differential equation in one variable, i.e.,

$$
\begin{aligned}
&\left(\frac{1}{l^*}\right)^2\frac{\partial^2 u_2}{\partial x_1^2}-\frac{\partial^4 u_2}{\partial x_1^4}=0\\
&l^*=\sqrt{\frac{2(a_3+a_4)}{\mu}}
\end{aligned}
\tag{5.106}
$$

the solution of which is obtained as

$$u_2\left(x_1\right) = U_0 \frac{\cosh\left(\frac{L}{l^*}\right) + \cosh(\frac{x_1}{l^*}) - \cosh(\frac{(x_1 - L)}{l^*}) - \frac{x_1}{l^*}\sinh\left(\frac{L}{l^*}\right) - 1}{2\left(\cosh\left(\frac{L}{l^*}\right) - 1\right) - \frac{L}{l^*}\sinh\left(\frac{L}{l^*}\right)}$$

$$F_{21}(x_1) = U_0 \frac{\sinh\left(\frac{L}{l^*}\right) - \sinh\left(\frac{x_1}{l^*}\right) + \sinh\left(\frac{x_1 - L}{l^*}\right)}{L\sinh\left(\frac{L}{l^*}\right) + 2l^*\left(1 - \cosh\left(\frac{L}{l^*}\right)\right)} \tag{5.107}$$

Isotropic first order elastic constants representative of steel were used for the numerical simulations, i.e., $E = 200\,GPa$ and $\nu = 0.3$, which corresponds to Lame parameters of $\lambda = 115.38\,GPa$ and $\mu = 76.92\,GPa$. The material specimen thickness, *L*, of 1 *mm* was used throughout this section. In order to assess the influence of competing length scales on the solution six separate cases, labeled A through F, were assessed. For each case the second order stiffness parameters, a_1 through a_5, were set equal to a single constant a_0 selected to give specific desired values of $\frac{l^*}{L}$ and are reported in Table 5.

Table 5. Second gradient elastic constants used for verification tests by case.

Case	$l^* \,/\, L$	$a_0\left(GPa - \mu m^2\right)$
A	0.01	1.923E3
B	0.10	1.923E5
C	0.25	1.202E6
D	0.50	4.808E6
E	1.00	1.923E7
F	2.00	7.692E7

For each case, solutions were obtained for eight different finite element discretizations. In the following discussion each particular discretization is referred to by a mesh label, e.g. Mesh 09 which has nine finite elements along the x_1 axis of the problem domain with a uniform element length of $h = L \,/\, 9$. Each of these discretizations consist of a single element in the x_2 direction

and periodic boundary conditions were applied at corresponding nodes on these two opposite boundaries to reflect the infinite symmetry in the x_2 direction.

Analytical solutions for each case along with the corresponding numerical solution from the finest discretization (Mesh 24) are shown in Figure 59. Inspection of these results shows that as $\frac{l^*}{L} \to \infty$ the solution converges to a single response. That is, as the microstructural length scale grows larger than the dominant geometric length scale the increase in influence of the second-gradient effect diminishes. At the other end of the spectrum, as the microstructural length scale tends to zero, the response becomes increasingly that of a conventional Cauchy continuum pure shear solution, such that $\frac{L}{U_0} F_{21}$ approaches unity everywhere in the problem domain. However, in the limit of $l^* = 0$ the second-gradient boundary conditions, $\mathbf{F}(0) = \mathbf{I}$ and $\mathbf{F}(L) = \mathbf{I}$, are inconsistent with a state of uniform pure shear; this conflict introduces spurious oscillations similar in nature to the so-called Gibbs' phenomenon. For small, yet nonzero, values of l^* such oscillations appear in the finite-element solution. The definition of small would seem to be related to the relationship between $\frac{l^*}{L}$ and $\frac{h}{L}$.

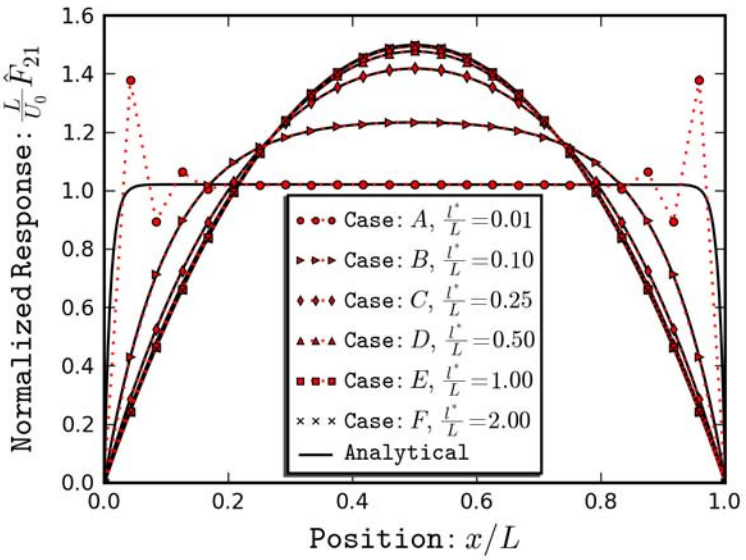

Figure 59. Comparison of analytical solution with FE solution from finest discretization.

Figure 60 shows a comparison between the analytical solution and finite-element solutions for several discretizations from two cases. Results from Case A (having a relatively small microstructural length scale), shown on the left, highlight the importance of competing length scales on the convergent behavior of the finite element solution under mesh refinement. Results from Case D shown on the right of Figure 60 are representative of other cases and demonstrate smooth convergence of the finite element solution to the analytical solution.

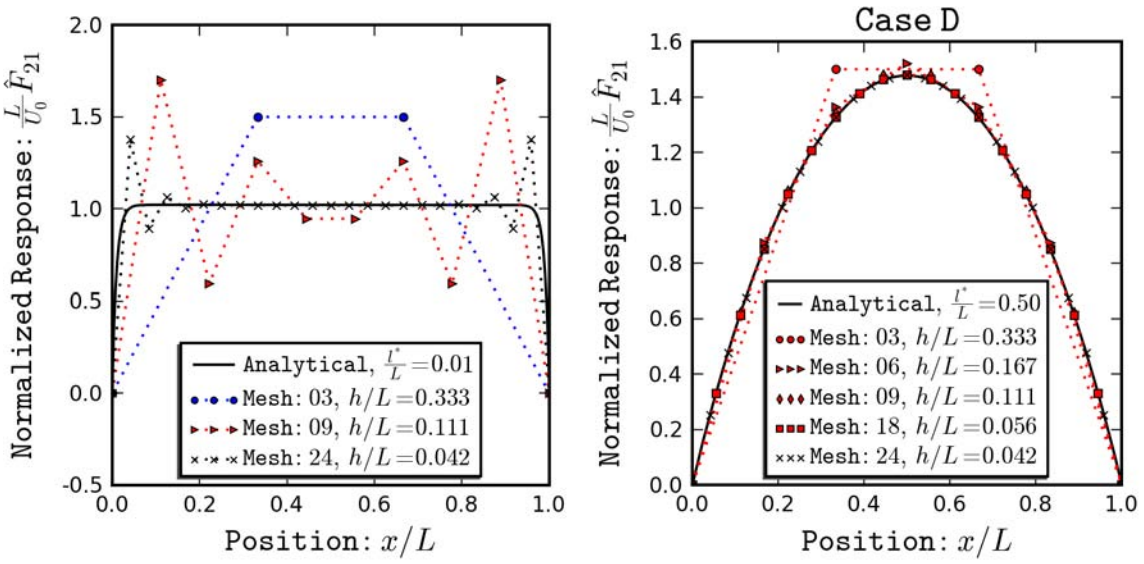

Figure 60. Comparison of analytical solution with FE solution from various discretizations for Case A (left) and Case D (right).

It is assumed that any discrepancy between the finite element and analytical solutions reflects error in the former. This assumption is important and is not strictly accurate because, (1) there are approximations made in the development of the analytical solution and (2) presumably the numerical evaluation of the analytical solution introduces error associated with, for example, machine precision and round off. Because the finite element solution is based on a discretization of the weak, i.e. global, form of conservation of momentum, strictly speaking convergence to the

exact solution is guaranteed only for a global error metric. In order to quantify the error associated with finite element solution of a particular discretization the following three error norms of Equation (5.108) are used, where *w* is the field response variable of interest, e.g., u_2, F_{21}:

$$\begin{aligned} L^1(w) &= \tfrac{1}{L}\int_L \left|\hat{w} - w\right| dx_1 \\ L^2(w) &= \tfrac{1}{L}\left[\int_L \left(\hat{w} - w\right)^2 dx_1\right]^{\frac{1}{2}} \\ L^\infty(w) &= \max\left(\left|\hat{w} - w\right|\right) \end{aligned} \tag{5.108}$$

As a matter of convenience, integration over the problem domain in Equation (5.108) is performed using Simpson's one third rule rather than Gauss quadrature of the underlying element shape functions. Of course, this introduces an integration error to the estimate of solution error; however, this discrepancy is assumed small and will converge to zero as finite element discretization becomes infinitesimally fine.

Plots of each of these error norms are plotted against relative element size are shown in Figure 61 for Case A and Case D on the left and right, respectively. Case A exhibits a region of non-monotone convergence for a relative element size greater than approximately 0.1. This behavior is especially prevalent for displacement response (u_2). Additionally the infinity error norm exhibits a stagnating convergence rate even for the finest discretizations. Case D, on the other hand, is representative of the other cases and demonstrates a clear convergence towards zero error in all norms for both the displacement and deformation gradient fields. The relationship between the ratios l^* / L and h / L bear consequence on the nature of mesh convergence and, furthermore, seem to define a cutoff for monotone versus non-monotone convergence.

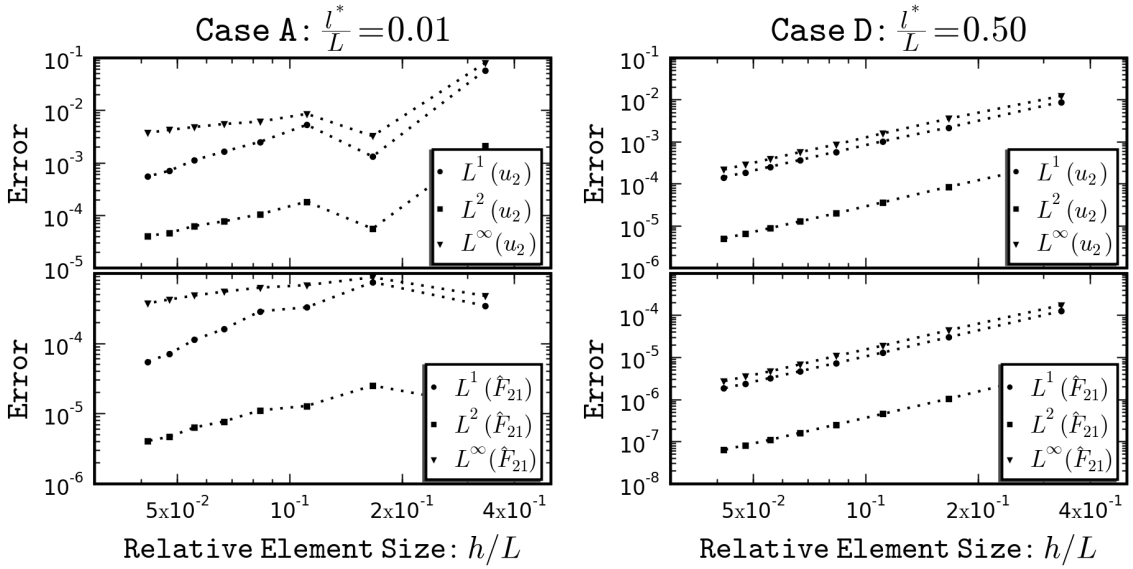

Figure 61. Plots of various error norms for Case A (left) and Case D (right) of mesh refinement study.

In order to determine the demonstrated order of convergence of the finite element code a particular error ansatz is adopted, i.e.,

$$Error = E_0 + E_1\left(\frac{h}{L}\right)^p \tag{5.109}$$

Equation (5.109) describes a power-law relationship of asymptotic convergence; as the computational mesh is refined, i.e., as $h \to 0$, the error approaches an asymptote of E_0. Nonzero values of the error asymptote, E_0, are attributed to either error in the analytical solution, discrepancies in the assumptions (e.g. boundary conditions) present in analytical and finite element solutions, or, in the worst case, non-conformity of the finite element discretization to the underlying physics, i.e., the developed FE method is not applicable to the particular problem. The most important parameter of Equation (5.109) is the order of convergence, *p*. For a finite element discretization deemed accurate to order *n*, *p* should be equal to *n*, otherwise some code or algorithmic error in the implementation is corrupting the solution scheme. Recognize that numerical implementations of additional physics, e.g., enforcing contact conditions, can

compromise the order of convergence below theoretical expectations based solely on the element discretization. This motivates the importance of focusing independently on specific aspects of the physics for verification of the computational code.

Non-monotone convergence is problematic in that it violates the fundamental ansatz adopted to establish the rate of convergence. Thus, discretizations associated with non-monotone convergence are deemed out of the asymptotic convergence range and are omitted from subsequent analysis. For each of the error norms and both displacement and deformation gradient response the error ansatz was fit to computed error values using a least-squares regression on the ansatz parameters, E_0, E_1, and p. Example fits are shown in Figure 62 for the L^2 error norm of the deformation gradient, F_{21}, for Case A (left) and Case D (right). The error data points from the coarsest three meshes in Case A are omitted because they lie outside of the asymptotic range.

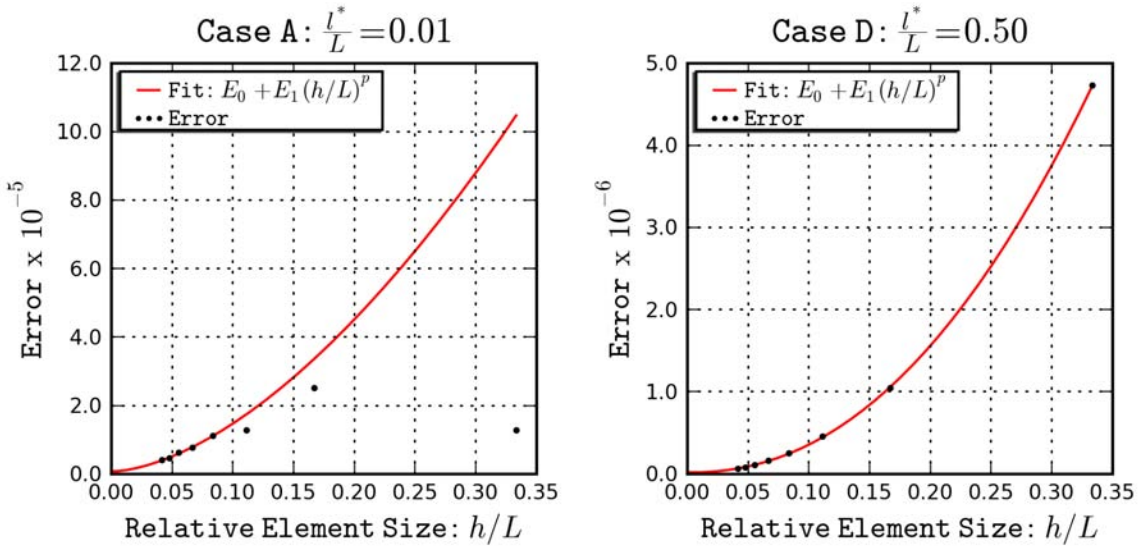

Figure 62. Computed L2 error norm and associated fit of error ansatz for Case A (left) and Case D (right).

The order of convergence for all fits are tabulated in Table 6. In all cases the residual error, E_0, was negligible. Owing to the discretization of the weak form of momentum balance, convergence is guaranteed only in a global sense. For example, total strain energy is expected to converge; however, a specific component of displacement at a specific location may not. Because the infinity error norm is extremely sensitive to local errors, we do not expect convergence at the theoretical rate in the L^{inf} norm. However, good convergence behavior of the L^1 and L^2 norm is expected. Recall the elements' shape functions are quadratic in displacement and linear in relaxed deformation gradient. Accordingly, the code should demonstrate an order of convergence of two for the displacement solution. Based on the linear nature of interpolation, one would be inclined to assume an order of convergence of one for the relaxed deformation gradient; however it proves to converge at a higher rate presumably because of the Lagrange constraint between these fields. The displacement solutions converged to the analytical solution with a demonstrated order of convergence that approached two with increasing l^* / L. The deformation gradient solutions demonstrate orders of convergence slightly better than two.

Table 6. Observed orders of convergence, *p*, for all error norms and test cases in verification study.

		Displacement: u_2			Deformation Gradient: F_{21}		
Case	l^*/L	L^1	L^2	L^{inf}	L^1	L^2	L^{inf}
A	0.01	1.55	1.16	----	2.61	1.66	----
B	0.10	1.94	2.09	----	1.92	2.08	2.36
C	0.25	2.07	2.00	1.80	2.02	2.17	2.16
D	0.50	2.01	1.95	1.78	2.07	2.18	1.99
E	1.00	2.01	1.95	1.78	2.08	2.18	1.96
F	2.00	2.01	1.96	1.79	2.08	2.18	1.96

5.3.3 Extension to Inelastic Case

Strictly speaking, rigorous code verification requires that the entire code be numerically evaluated to demonstrate convergence to an exact solution. For cases where a convenient problem with a closed-form analytical solution does not exist, the method of manufactured solutions can be used to mathematically construct an exact solution without regard to the physical problem the solution pertains to (Roache, 1998). The solution is then fed through the governing differential equations to determine consistent boundary conditions. Such an approach is well beyond the scope of this dissertation. In lieu of formal code verification for the inelastic case, we focus attention on code "confirmation" a less formal process of presenting a body of numerical evidence that supports the claim that the code is performing as intended. This body of evidence involves three distinct pieces: (1) Smooth convergence to solutions that are qualitatively consistent with the known elastic solution for small deviations from elastic response, (2) Smooth convergence and physically expected response under finite deformation, and (3) unit testing of blocks of code to ensure internal accuracy and consistency.

To develop a set of inelastic test problems, the effective stress, $\bar{\tau} = \left(\frac{1}{2}\, \tilde{\mathbf{S}}' : \tilde{\mathbf{S}}' + \frac{1}{2} \frac{\tilde{\mathbf{Q}} \vdots \tilde{\mathbf{Q}}}{(l^{in})^2} \right)^{\frac{1}{2}}$, was computed from the elastic analytical solution for fixed values of $l^{in} = l^{*}$ and is shown at left in Figure 63. For small values of the microstructural length scales, l^{*} and l^{in}, the solution exhibits a moderately uniform effective stress that is dominated by the first order Mises stress, cf. Case A. As the internal length scale is increased, the second order stresses become more significant and make a larger contribution to the effective stress near the constrained boundaries of the problem, i.e. $x_1 = 0$ and $x_1 = L$. Case C (highlighted in red in Figure 63) was selected for further investigation because both the first and second order stresses make a significant contribution to the effective stress resulting in an interesting distribution of effective stress across the problem domain. In order to assess the affect of the inelastic length scale on effective stress (independent of the elastic microstructural length scale, l^{*}) the ratio of $l^{in} \,/\, l^{*}$ was varied from *0.25* to *2.0* for Case C. The elastic effective stress computed from the analytical solution is shown on the right side of Figure 63. For fixed, l^{*}, the actual stresses **S** and **Q** are fixed such that changing the

inelastic length scale has the effect of scaling the contribution of **Q** to the effective stress, $\bar{\tau}$. Length scale ratios of *0.5*, 1.0, and 1.5 were selected for further investigation because they create effective stress profiles that will cause inelastic yielding to initiate at differing locations at nearly similar magnitudes of response.

With Case C serving as the elastic baseline solution, nine simulations were conducted under identical boundary conditions and material properties as that in Case C with the exception that the inelastic threshold function

$$f(\tilde{\mathbf{S}}, \tilde{\mathbf{Q}}) = \bar{\tau} - \tau_0 \tag{5.110}$$

was used in conjunction with associated flow according to the integration algorithm presented in Section 5.2. Three differing effective yield stresses, (τ_0 = *215*, *175*, and *125 MPa*) and the aforementioned three differing inelastic length scales were selected to cause slight deviations from the elastic solution. Solutions were obtained using each of eight FE discretizations (from Section 5.3.2) for each combination of τ_0 and l^{in} (excepting a single trivial case discussed subsequently), giving a combined total of 64 sets of results.

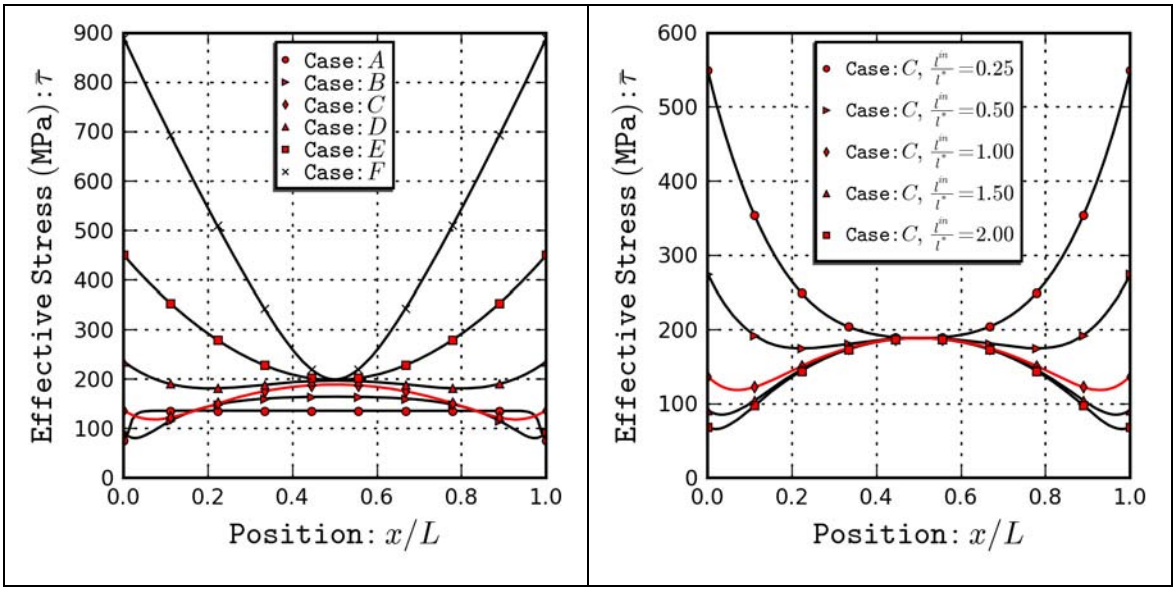

Figure 63. Effective stress computed from analytical elastic solution. All cases shown on left for length scale ration of one. Case C shown at right for various length scale ratios.

Nodal results obtained using each of the eight FE discretizations for each combination of τ_0 and l^{in} were fit to the assumed convergence ansatz, $N(h) = N_0 + Ah^p$. An example of one such fit is shown in Figure 64 with the corresponding extrapolated estimate of the converged solution, i.e., N_0 highlighted by a red pentagon. Approximating the extrapolation as a converged (accurate) solution, local error for the finest discretization was estimated at nodal locations. A cubic spline was then fit to interpolate this error at intermediate locations so that an estimate for the converged solution could be obtained at arbitrary locations within the problem domain. That is, the extrapolated solution serves as an approximation to a zero-error solution for the following discussion. Note that this approximation is only used for comparative discussion and is not being presented as an analytical solution.

For each case, the estimated converged inelastic solution is plotted using a red dashed line against the analytical elastic solution plotted in black in Figure 65. The combination of the largest yield stress and largest inelastic length scale are omitted because this combination would produce a purely elastic solution; a replicate of the case in the center of the top row of Figure 65.

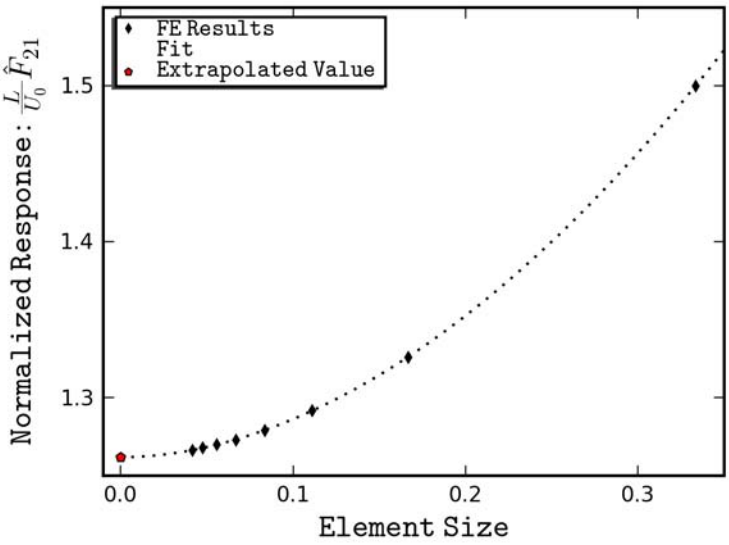

Figure 64. Example of Richardson extrapolation used to estimate converged local solution.

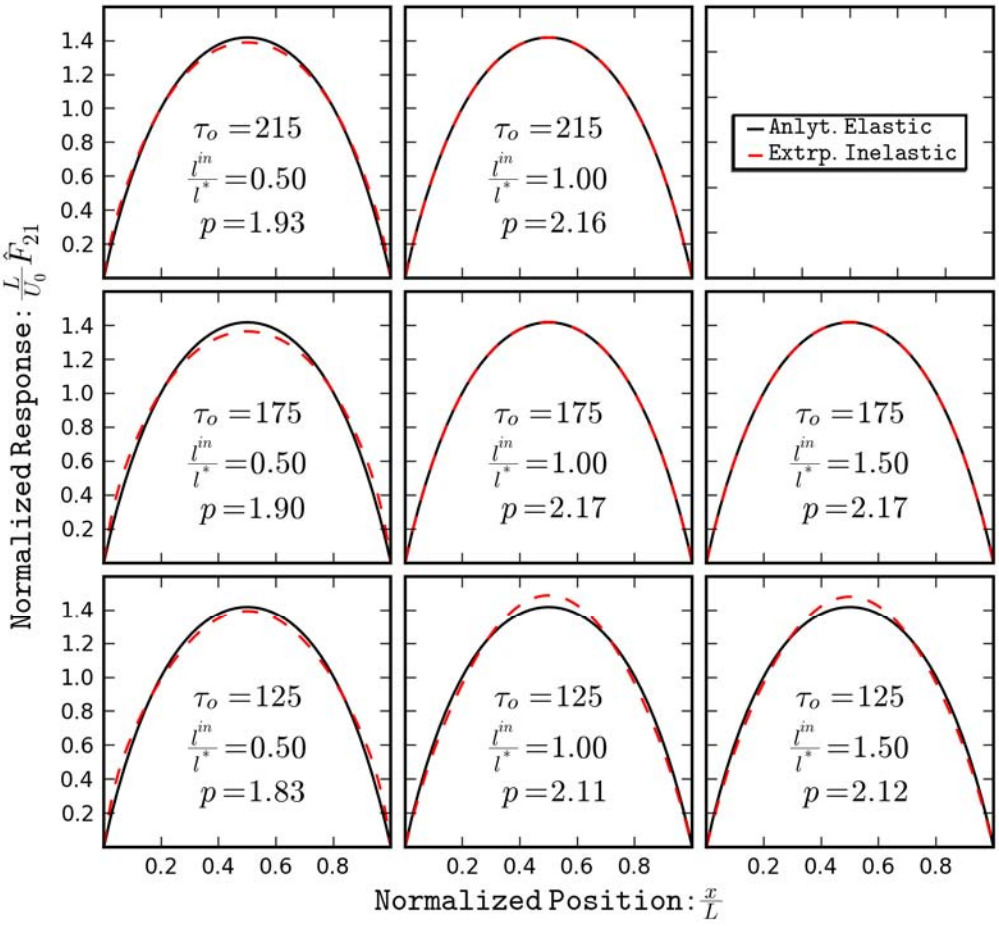

Figure 65. Converged solutions to various inelastic cases plotted with analytical solution to baseline elastic case.

The leftmost column of plots in Figure 65 are of results for the case where the inelastic length scale is half of the elastic length scale. For each of these cases, yielding initiated at the boundaries. This yielding was accompanied by an increase in the gradient of the deformation gradient, in turn, decreasing the shear deformation at the mid-thickness point of the solution. By contrast the results plotted in the center and right columns of the bottom row of Figure 65 are for cases where the yield stress was low enough and inelastic length scale large enough that the first-order stresses dominated the effective stress and yielding initiated at the mid-thickness position of the problem. In these cases, the yielding allows an increase in the deformation gradient at mid-

thickness giving a response that is opposite from the baseline elastic response when contrasted to those in the left column of Figure 65. The case shown in the center of the top row resulted in purely elastic response. The cases shown in the center and right columns of the middle row are not purely elastic, however they are nearly so.

Using the converged solution as an estimate of the exact solution, convergence rates of the L^2 error norm were computed for each case and are listed in Figure 65. For cases that exhibited purely or nearly elastic response the observed orders of convergence in L^2 error norm are identical to that reported in Table 6 (above), cf. Case C, F_{21}. Under cases where inelastic response is non-negligible, the observed order of convergence decreases from that observed for the elastic or nearly elastic cases. The numerical method used to perform the inelastic part of the constitutive update is first-order accurate, i.e., Euler integration. On the other hand, the FE integration of stresses into nodal residual forces is second order accurate as was demonstrated in Section 5.3.1.

The smoothly convergent behavior of the numerical solutions for inelastic cases, associated estimated orders of convergence, and qualitatively appropriate behavior consistent with a known and nearby elastic solution are used not to prove verification, but rather to assemble evidence that the code is behaving acceptably.

5.3.4 Convergent Behavior of Localization Under Inelastic Finite Deformation

As further demonstration of acceptable behavior of the code, a two dimensional plane deformation problem which exhibits localization was simulated using the developed finite element user-subroutine. The problem illustrated in Figure 66 consists of a uniform rectangle of homogeneous material (blue region) with the exception of a square region (orange) in the lower left corner which has an effective yield stress, τ_0, equal to 80% of that for the blue region. Yielding initializes in the orange region and causes the formation of a localization band and softening in the global force versus displacement curve. The nonlocal nature of the coarse scale constitutive response should provide a natural length scale to the problem such that artificial mesh dependency of localization is obviated. The geometry was discretized into four relatively

uniform meshes with characteristic element sizes of *300*, *200*, *100*, and *75* μm, respectively. Nodal boundary conditions were applied to the top and bottom edges consistent with that shown in Figure 66. Specifically, nodal displacements along the bottom edge were held fixed, i.e., $\overline{u}_2 = 0$. Likewise for the corresponding component of relaxed deformation gradient, i.e., $\hat{F}_{21} = 0$. Nodal displacements on the top edge were constrained to be equal to a specified value, $\overline{u}_2 = \delta$, and appropriate component of relaxed deformation gradient was held fixed, i.e., $\hat{F}_{21} = 0$. Rigid body translation in the horizontal direction was restrained by specifying zero horizontal displacement to the left uppermost node in the model.

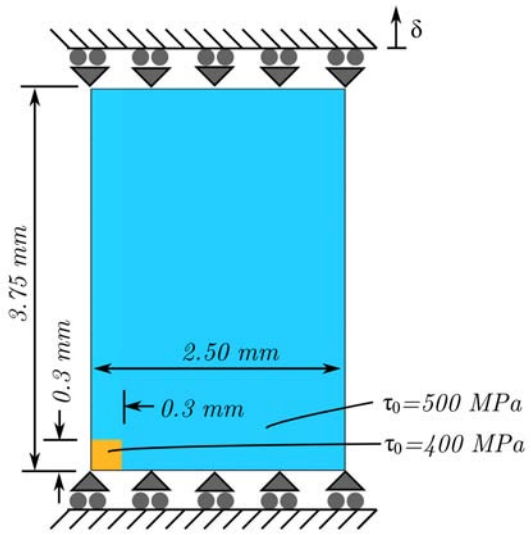

Figure 66. Diagram of geometry for non-trivial inelastic code test problem.

Figure 67 shows contour plots of the effective plastic strain at a top platen displacement of *300*μm for each of the four discretizations. The size of the localization band is geometrically consistent and does not exhibit artificial mesh dependence. The net resultant force versus applied platen displacement is plotted in Figure 68. After an initial elastic loading there is a small

inelastic hardening portion of the curve before a final softening region in which the spatial localization band develops. The force-displacement curves from each discretization lie essentially on top of each other and converge quickly with decrease in element size. From a qualitative perspective the finite-element solution to this non-trivial problem builds confidence in the developed code and is presented as part of a collective body of evidence that the numerical implementation of the user-element is adequate.

To further address confidence in the code, numerical unit testing was performed on discrete blocks of code. As a matter of distinction from code verification, we refer to this as code confirmation. For example, computation of the matrix exponential of a matrix argument is required for the inelastic constitutive update. This particular block of code was externally tested under a large range of matrix arguments to demonstrate acceptable levels of accuracy within the domain of typical input arguments.

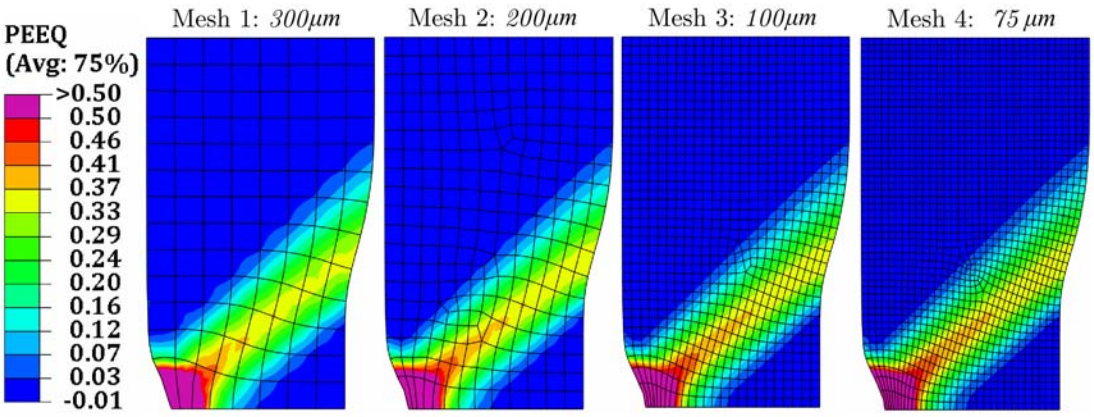

Figure 67. Contour plots of effective plastic strain (PEEQ) for non-trivial inelastic code test problem.

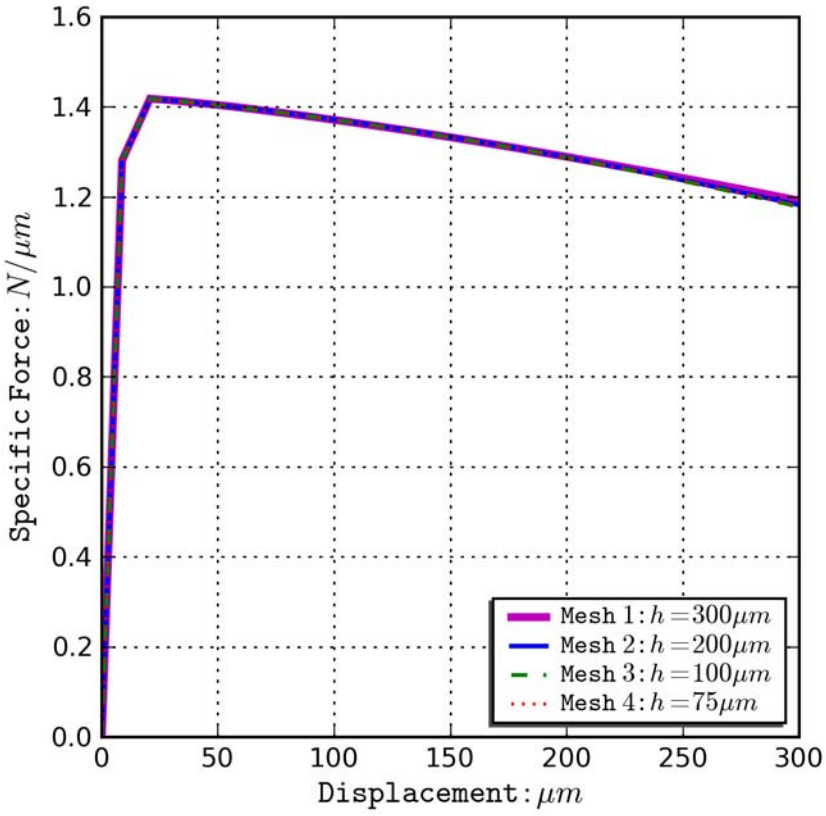

Figure 68. Global force versus displacement curves for non-trivial inelastic code test problem.

5.4 Summary

This chapter documents the implementation of the coarse scale conservation of momentum and constitutive equations in a finite element method via the user-subroutine interface of Abaqus. The mixed field finite element discretization of the weak form of conservation of momentum at the coarse scale gives rise to a nonlinear system of equations. An algorithm suitable for updating the stress and second order stress based on constitutive relations that adhere to the framework in Chapter 3 has been developed. This algorithm uses an exponential map over an increment to advance the inelastic part of the deformation gradient. The constitutive integration algorithm permits finite deformations in a hyperelastic-inelastic scheme that is conceptually well aligned with the ISV framework developed in Chapter 3. The implemented user-subroutine consisting of finite element equations and constitutive update algorithm was subjected to numerical testing and code verification to demonstrate overall acceptability of the user-subroutine as written. These efforts are documented and provide confidence in the code used in the example problem in Chapter 6.

CHAPTER VI

APPLICATION TO COARSE SCALE LOCALIZATION OF IDEALIZED POROUS MICROSTRUCTURE

In this chapter, the theoretical framework presented in Chapter 3 is used with the numerical methods discussed in Chapter 4 and the coarse scale second gradient finite element user subroutine discussed in Chapter 5 to conduct a multiscale simulation of deformation and shear band development for an example problem. The example problem is introduced in Section 6.1 along with a baseline solution comprising an explicit modeling of the microstructure (fine scale) within the coarse scale simulation. The process of identifying the proper form of the elastic (reversible) portion of the free energy function and computing parameters associated with a specific rSVE realization of the fine scale material description are presented in Section 6.2. Section 6.3 details a particular stored portion of free energy and kinetic description of irreversible deformation for the rSVE. This particular case is not general within the context of the multiscale framework; therefore advanced strategies for this aspect of the multiscale framework are discussed in more detail in Chapter 7. The developed constitutive model is implemented in the second gradient user-element and applied to the solution of the example problem and compared to the baseline response.

6.1 Description of Example Problem

The example problem is based on an idealized porous microstructure selected for its relative conceptual simplicity. This enables a clear demonstration of the framework without the unnecessary complexities that will arise with more realistic microstructures. While the applicability of the resulting constitutive equation may be limited, the framework that it highlights is general.

The coarse scale (Scale 0) of this problem is motivated by the combined experimental and numerical investigation of shear bands developed in tantalum under high-rate compression testing of top-hat shaped specimen (Bronkhorst et al., 2006; 2007). For the purposes of this chapter, the coarse scale specimen is an extruded channel of cross-section shown on the right side of Figure 69, which is consistent with the plane deformation implementation of the finite element subroutine developed in Chapter 5. The dimensions of the geometry shown in Figure 69 are presented in Table 7. Boundary conditions along the bottom edge of the coarse scale specimen consist of fixed (zero) vertical displacements. Symmetry of the model about the central vertical axis is used and symmetry conditions apply. Along the top surface of the hat the boundary conditions are prescribed vertical displacements equal to δ.

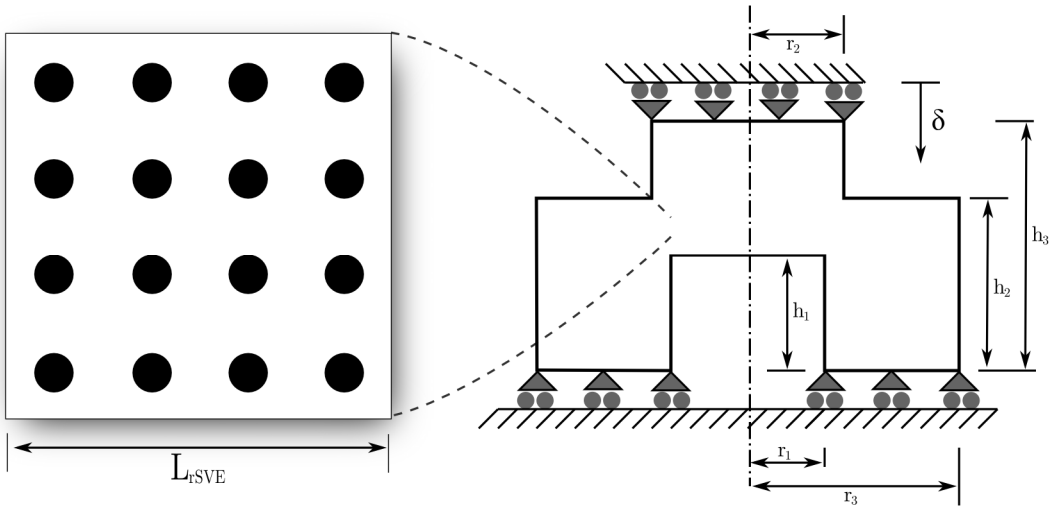

Figure 69. Illustration of geometry used for multiscale example problem.

Table 7. Dimensions for coarse scale geometry.

h_1 = 2.60 mm	r_1 = 2.09 mm
h_2 = 3.47 mm	r_2 = 2.28 mm
h_3 = 5.11 mm	r_3 = 4.30 mm

The fine scale is an idealized porous microstructure consisting of a uniform periodic array of circular voids embedded in an elastic perfectly plastic matrix material as shown on the left of Figure 69. Each rSVE of microstructure is composed of an *N* x *N* tiling of the unit cell shown in Figure 70. The unit cell is a square region of matrix material, whose sides have length r_n, and contains a single central void of radius r_v. The size of the rSVE is given by $L_{rSVE} = N \times r_n$. There are two physical length scales associated with this idealized microstructure morphology: the void nearest-neighbor distance, i.e., r_n, and r_v, which is the mean void radius. In addition, L_{rSVE} represents a non-physical (superficial) length scale introduced to the simulations. Any dependence of material response on L_{rSVE} is either an indication of a non-representative volume of material (rRVE) or, for second gradient modes of deformation, due to the proportionality between L_{rSVE} and fine scale stress and strain for a fixed value of second gradient. It will be shown that this effect introduces a dependence that increases second order elastic stiffness in proportion to L_{rSVE}^2.

The area fraction of closed porosity, A_f, is related to the square of a length scale ratio,

$$A_f = \pi \left(\frac{r_v}{r_n} \right)^2 \tag{6.1}$$

The volume fraction of porosity can be directly related to the area fraction depending on assumptions regarding the 3D nature of the microstructure, e.g. cylindrical voids, randomly distributed spherical voids. The area fraction is used here as the microstructure parameter representing the degree of porosity.

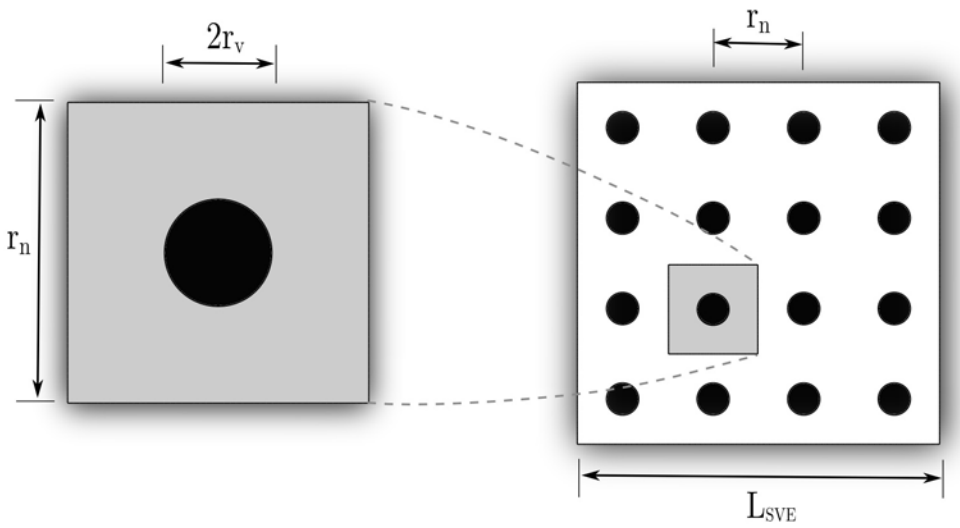

Figure 70. Relationship between Unit Cell (UC) and rSVE.

6.2 Baseline Simulation with Explicit Representation of Microstructure

The baseline solution to this problem is conducted for a nearest neighbor spacing of 18 μm and void radius of 3.52 μm, implying a pore area fraction of 12%. These parameters are consistent with the values obtained from image analysis discussed in Chapter 4. The fine scale constitutive description is isotropic elastic, perfectly-plastic with Young modulus, $E = 175\,GPa$, Poisson ratio, $\nu = 0.3$, and Mises effective yield stress of $\sigma_y = 1000\,MPa$. These parameters are roughly consistent with that of uranium-oxide at a temperature around 1700°C, however they were selected to emphasize the multiscale response of the example problem rather than accuracy in modeling a specific material. Furthermore, while the real material exhibits hardening which decreases appreciably with increase in temperature, perfect plasticity was assumed for the matrix material in this example to highlight the kinematic hardening introduced due to inelastic incompatibilities (i.e., eigenstrain fields) induced by heterogeneous response at the fine scale.

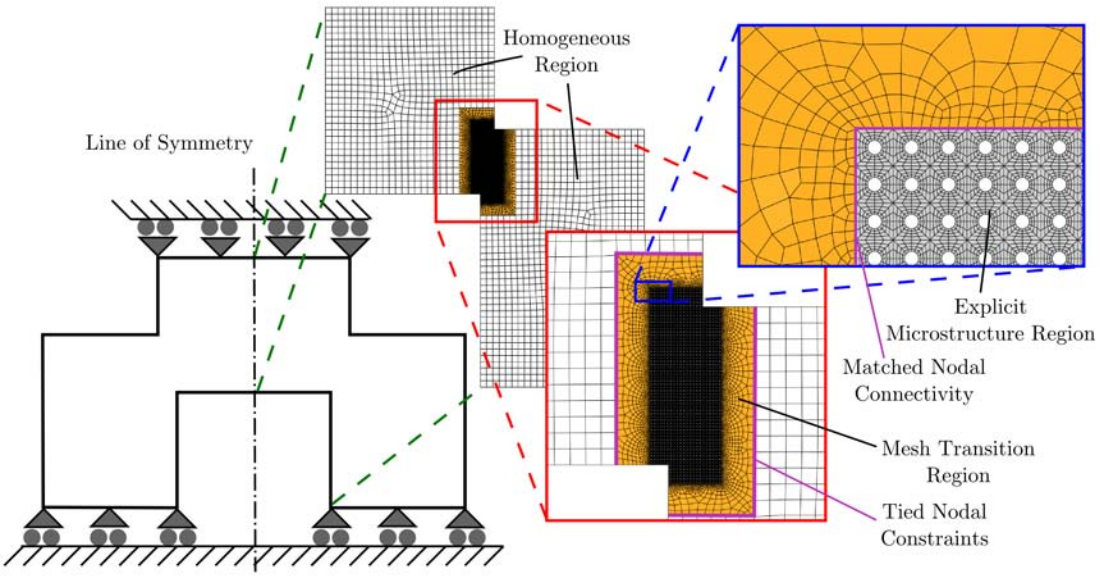

Figure 71. Finite element mesh used for baseline simulations with explicit modeling of fine and coarse scales.

The finite element mesh used for baseline simulations with explicit inclusion of the microstructure is shown in Figure 71. In order to mitigate the computational burden of simulations, the discrete microstructure is only included in a region where inelastic response is expected. Accordingly, the finite element mesh consists of three distinct regions, i.e. homogeneous, explicit microstructure, and a transition region between these two. Within the homogeneous region, orthotropic elastic properties for a classical first order Cauchy continuum govern the material response and the characteristic element size is approximately 85μm. The elastic properties used for the homogenized region were obtained from the results of Section 6.4.3. In the explicit microstructure region, the solid 'matrix' is modeled as an elastic perfectly plastic material with properties identical to those used in the unit cell calculations of Section 6.5.3. The characteristic element size for the mesh in the explicit microstructural region is 2μm. The transition region utilizes the same material constitutive description as the homogeneous region, but the element size is graded to achieve a smooth variation between the other regions. The interface between the explicit microstructure and transition region us achieved by shared

nodal connectivity, while the interface between transition and homogeneous regions consists of linear nodal constraint equations that tie the nodes on the boundary of the transition region to the adjacent surface of the homogeneous region. The element type is Abaqus' CPE4, a two dimensional continuum element comprising four nodes, linear interpolation, and full integration (Abaqus, 2007). Half symmetry is utilized such that only the domain to the right of the line of symmetry is discretized and displacements in the x_1 direction along this line are constrained to be zero. Displacements in the x_2 direction are constrained along the bottom edge, while constraint equations are used to enforce that u_2 is equal to δ everywhere along the top edge. There are approximately 84,000 elements and 93,000 nodes in the model. Note that this discretization is significantly coarser than the unit cell discretization employed in the fine scale simulations in the vicinity of pores (cf. Figure 71 and Figure 78). The baseline solution was obtained using Abaqus Standard version 6.7 by uniformly ramping δ from zero to 50 μm over fifty increments of a nonlinear step.

Contour plots of the plastic equivalent strain (PEEQ) are shown in Figure 72. There is a region of intense local (fine scale) plastic strain at the sharp corners between the top and bottom portions of the specimen. The localization band is of finite width when compared to the characteristic element size and the width of this band appears to be dictated by the interaction between orientations of maximal Mises stress, distance between the upper and lower sharp corners, and the microstructural length scales. The localization band does not taper in size to an infinitesimal length at the top nor bottom corners, rather maintains a finite width. The resulting net force versus top platen displacement is plotted in Figure 73. There is a considerable range of elastic response up to a non distinct yield point after which there is appreciable and nonlinear hardening.

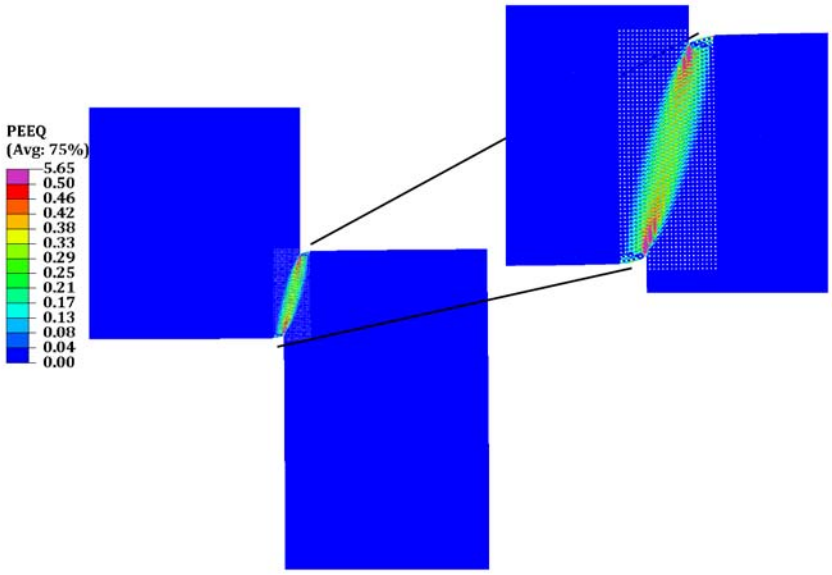

Figure 72. Contour plot of effective plastic strain (PEEQ) for baseline simulation with explicit treatment of microstructure.

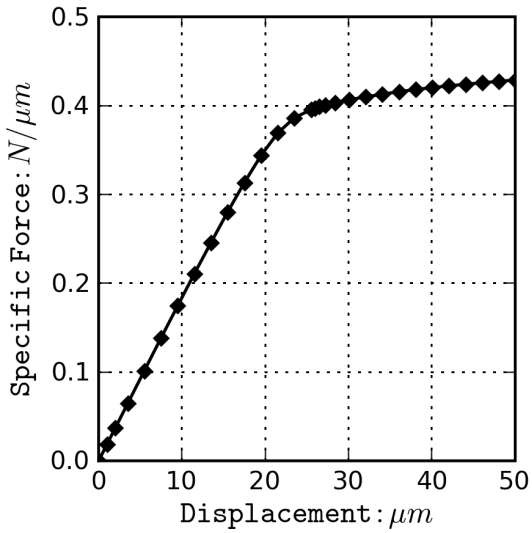

Figure 73. Applied force versus displacement for baseline simulation with explicit treatment of microstructure.

6.3 First Order Homogenization Based on Gurson's Yield Function

For purposes of comparison to the coarse scale simulation developed subsequently, simulations utilizing four distinct discretizations with characteristic element sizes of 20, 50, 80, and 110 μm using conventional plane strain finite elements (CPE4) were conducted. In these simulations, Gurson's local model for porosity dependent yield surface was used, i.e.,

$$f\left(\tau,\bar{\xi}_1\right)=\frac{\tau^2}{\left(\tau_0\right)^2}+2\bar{\xi}_1 q_1\cosh\left(q_2\frac{3}{2}\frac{\tau_m}{\tau_0}\right)-1-q_3\bar{\xi}_1^{\,2} \tag{6.2}$$

where the Mises effective stress is defined as $\tau^2=\frac{3}{2}\boldsymbol{\sigma}':\boldsymbol{\sigma}'$, $\bar{\xi}_1$ is the coarse scale porosity and with the standard Gurson parameters of $q_1=q_2=q_3=1.0$. These parameters correspond to Gurson's original development applicable under the conditions that pertain to this example problem, i.e., two dimensional cylindrical voids in perfectly plastic matrix undergoing planar deformation (Gurson, 1977). Gurson's model and relevant extensions are discussed in more detail in Section 6.5.1. The purpose of this set of simulations is to provide a basis of comparison with classical first order Cauchy modeling techniques that do not employ a formal hierarchical framework as presented in this dissertation. Of course, one could conduct the steps within this framework to determine parameters for the constitutive model that would yield better agreement with the force displacement relationship. The net force versus platen displacement results for each of the four discretizations is shown in Figure 74 along with the baseline direct simulation. The elastic portion of the curve matches well (recall that the orthotropic elastic parameters are actually those determined using the multiscale homogenization discussed in Section 6.4.3, below). The initial point of yield and subsequent post-yield deformation do not match the direct baseline simulation well; however it is noted that they are slowly converging towards the baseline simulation. Notice also that the hardening rate of the Gurson' based model saturates to a smaller slope than exhibited by the explicit microstructure simulation. Artificial mesh dependency is exhibited in the contour plots of effective plastic strain in the localization region as shown in Figure 75. While the midpoint thickness of the localization band seems to converge reliably, the region of localization at the top and bottom corners becomes infinitesimally narrow as the mesh is

refined. The localization region at the corner is accommodated by one or two elements, so that a characteristic length scale at this region is not recovered from first order simulations.

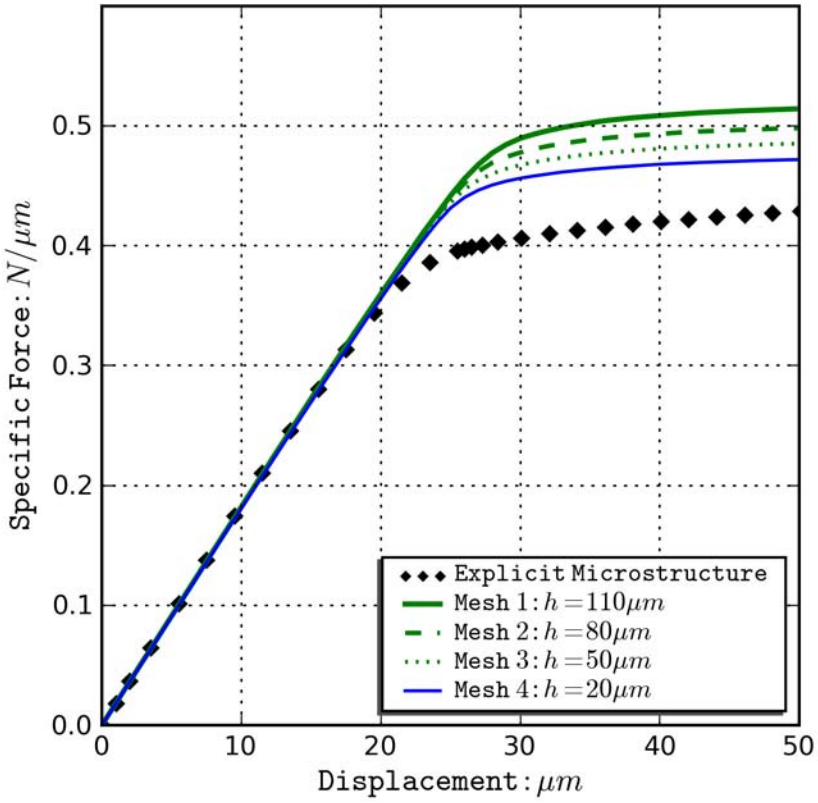

Figure 74. Force versus displacement results for standard local Gurson model for porosity dependent yield function.

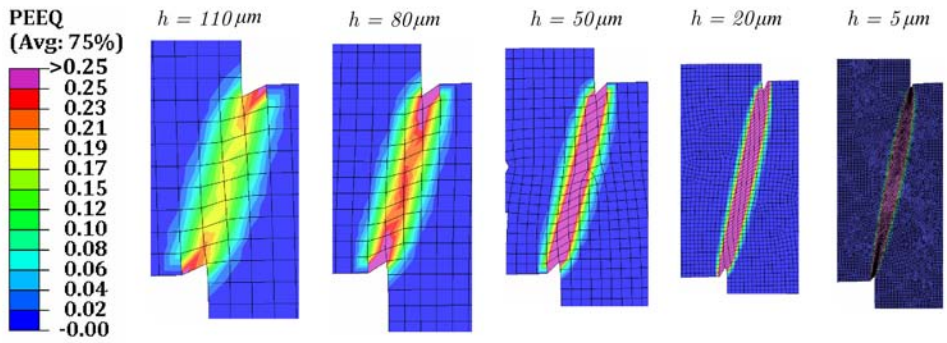

Figure 75. Effective plastic strain (PEEQ) for various mesh densities with standard local Gurson model of porosity dependent yield function.

6.4 Identification and Fitting of Free Energy Function

In this section a coarse scale free energy potential is developed to capture the elastically recoverable and stored elastic energy during the generally inelastic loading of the microstructure. The coarse scale Helmholtz free energy function is decomposed into components for elastic and stored energy as

$$\bar{\psi} = \bar{\psi}_e + \bar{\psi}_s \tag{6.3}$$

6.4.1 Elastic Free Energy Potential

The elastic free energy is expressed as a quadratic function of the elastic components of deformation, i.e.,

$$\psi^e = \frac{1}{2}\left(\tilde{\mathbf{E}}^e : \mathbf{C}^{SE} : \tilde{\mathbf{E}}^e + \tilde{\boldsymbol{\Gamma}}^e : \mathbf{C}^{Q\Gamma} : \tilde{\boldsymbol{\Gamma}}^e\right) \tag{6.4}$$

where, $\tilde{\mathbf{E}}^e$ is the elastic Green-Lagrange strain tensor in the intermediate configuration, $\tilde{\boldsymbol{\Gamma}}^e$ is the elastic portion of the second order strain in the intermediate configuration, $\mathbf{C}^{SE}$ is the fourth order elasticity tensor, and $\mathbf{C}^{QG}$ is a sixth-order elastic tensor relating the higher order stress, $\mathbf{Q}$, to the second gradient, $\mathbf{G}^e$. Refer to Chapters 3 and 4 for elaboration on these definitions. That Eq.

(6.4) is a sufficient description of the elastic free energy is confirmed by results of the direct numerical simulations presented in this section.

A single fine scale simulation consisting of several elastic loading steps was conducted in order to confirm the legitimacy of Eq. (6.4) and to establish the proper form of the constitutive tensors, $\mathbf{C}^{SE}$ and $\mathbf{C}^{QG}$. The morphological parameters selected for this particular simulation are listed in Table 8. These parameters differ from the stated example problem because they were chosen as matter of convenience prior to image analysis of Chapter 4 revealed a more appropriate set of parameters. There is no consequence of this apparent inconsistency as these parameters are used merely to establish qualitative elastic relationships and demonstrate the numerical accuracy associated with subsequently determined elastic parameters. The final elastic constitutive parameters used in Equation are computed for a range of fine scale microstructure parameters.

Table 8. Parameters for baseline elastic fine scale simulations.

Parameter	**Value**
N	1
r_n	$10\,\mu m$
r_v	$2\,\mu m$
A_f	0.126
L_{SVE}	$10\,\mu m$

Based on the uniformly periodic idealized morphology and the generalized plane strain analysis, the macroscopic first-order elastic response was expected to exhibit orthotropic behavior out of plane in conjunction with in-plane cubic symmetry.

Accordingly, the following compliance matrix is used to represent the first-order elastic response:

$$\left[\mathbf{S}^{ES}\right] = \begin{bmatrix} \frac{1}{E} & -\frac{\nu}{E} & -\frac{\nu_{zx}}{E_z} & 0 \\ -\frac{\nu}{E} & \frac{1}{E} & -\frac{\nu_{zx}}{E_z} & 0 \\ -\frac{\nu_{xz}}{E} & -\frac{\nu_{xz}}{E} & \frac{1}{E_z} & 0 \\ 0 & 0 & 0 & \frac{1}{\mu} \end{bmatrix} \tag{6.5}$$

The stiffness matrix is computed as the inverse of the compliance matrix, i.e., $\left[\mathbf{C}^{SE}\right] = \left[\mathbf{S}^{ES}\right]^{-1}$. In plane cubic material symmetry results in three independent in-plane properties, E, μ, and ν, i.e., $\mu \neq \frac{E}{2(1+\nu)}$. Furthermore, symmetry of the compliance matrix requires $\frac{\nu_{xz}}{E} = \frac{\nu_{zx}}{E_z}$, thus reducing the out-of-plane independent properties to E_z and $\nu_{zx} \rightarrow \nu_z$. In total, the first-order elastic response of the material can be described by five independent elastic constants.

According to Eq. (6.4), the elastic strain energy due to the gradient of the deformation gradient is also a quadratic function whose constants are provided by a second-gradient stiffness tensor . Various forms of this tensor have been proposed, for example, cf. Chapter 5.

Rather than assuming such elastic behavior, the second order elastic behavior was developed by seeking insight from the compliance of the material in a fashion analogous to the generalized Hooke's law. For example, consider a uniaxial stress-strain test. Under an axial applied normal stress with all other surfaces traction free, the normal strain is related to the normal stress in accordance with Hooke's law, i.e. $E\varepsilon_{axial} = \sigma_{axial}$, and the lateral strains are, of course, related to the axial strain through Poisson's ratio by $\varepsilon_{lat} = \nu\varepsilon_{axial}$. This relationship is recognized directly in the elastic compliance matrix of Eq. (6.5). The idea of a kinematic coupling in the compliance matrix motivates a similar form for the second gradient compliance. In order to identify which terms of $\left[\mathbf{S}^{GQ}\right]$ are non-zero, a simulation was conducted that consisted of an independent loading and unloading step for each of the six unique components of the second-gradient tensor. In each of these steps, the specified component of **G** was given a small non-zero value, while the remainder of the components remained unconstrained. Thus, each step results in one non-zero

component of the second-order stress, **Q**, and demonstrates the extent of kinematic coupling in the compliance tensor. Results from these six simulation steps are shown in Figure 76. Mises effective stress is plotted as color contour in units of MPa. Particular modes of deformation described in Chapter 3 can be visually identified in each of these plots. These results motivate relationship (6.6) between the second gradient, **G**, and the second-order stress, **Q**.

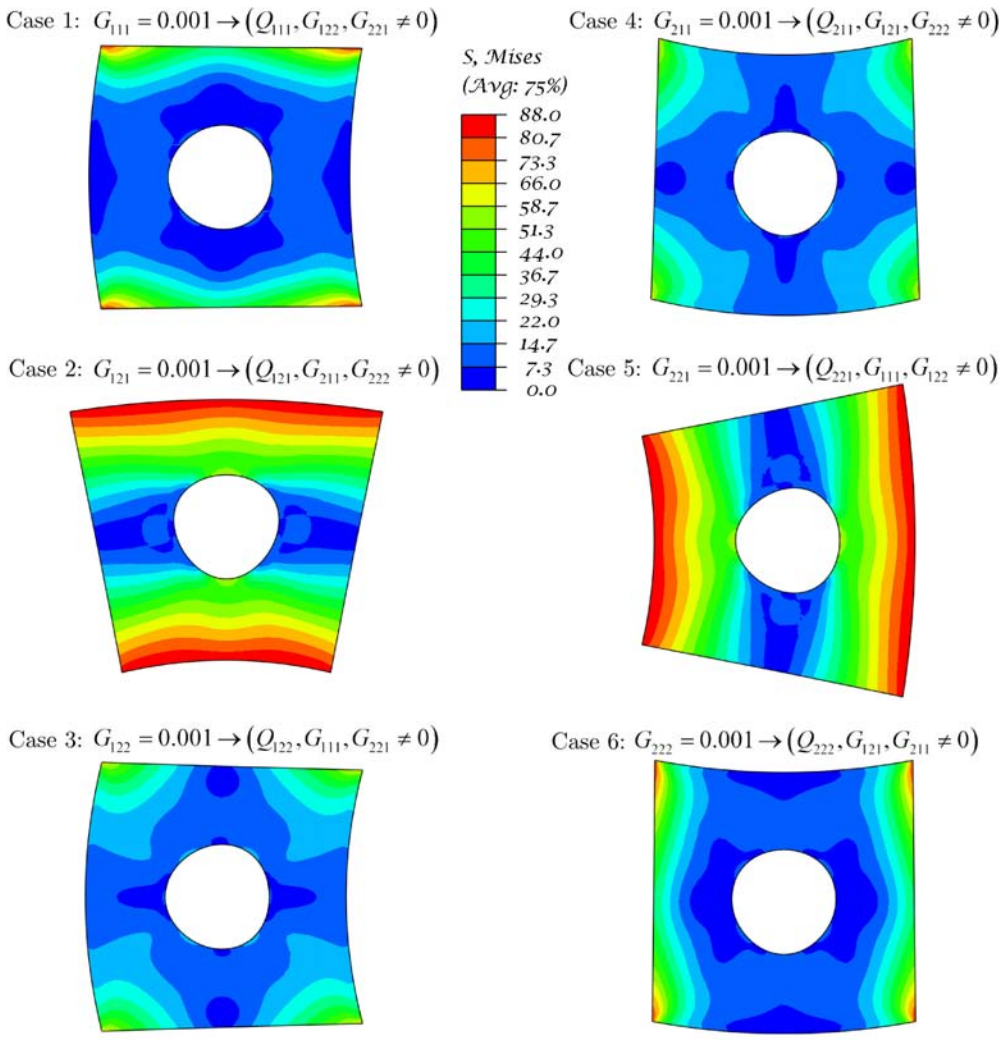

Figure 76. Contour plots of fine scale Mises stress for various second order deformation modes. Kinematic coupling is exhibited between unique components of **G**.

$$\begin{Bmatrix} G_{111} \\ G_{121} \\ G_{122} \\ G_{211} \\ G_{221} \\ G_{222} \end{Bmatrix} = \begin{bmatrix} \frac{1}{C_1} & 0 & \frac{\alpha_5}{C_3} & 0 & -\frac{\alpha_9}{C_5} & 0 \\ 0 & \frac{1}{C_2} & 0 & -\frac{\alpha_7}{C_4} & 0 & -\frac{\alpha_{11}}{C_6} \\ \frac{\alpha_1}{C_1} & 0 & \frac{1}{C_3} & 0 & -\frac{\alpha_{10}}{C_5} & 0 \\ 0 & -\frac{\alpha_3}{C_2} & 0 & \frac{1}{C_4} & 0 & \frac{\alpha_{12}}{C_6} \\ -\frac{\alpha_2}{C_1} & 0 & -\frac{\alpha_6}{C_3} & 0 & \frac{1}{C_5} & 0 \\ 0 & -\frac{\alpha_4}{C_2} & 0 & \frac{\alpha_8}{C_4} & 0 & \frac{1}{C_6} \end{bmatrix} \begin{Bmatrix} Q_{111} \\ Q_{121} \\ Q_{122} \\ Q_{211} \\ Q_{221} \\ Q_{222} \end{Bmatrix} \tag{6.6}$$

The constants in the compliance matrix of (6.6) were numerically determined by, for example, $C_1 = Q_{111} \,/\, G_{111}$, $\alpha_1 = G_{121} \,/\, G_{111}$, and $\alpha_2 = -G_{221} \,/\, G_{111}$, for case one, where G_{111} was the only *specified* component of **G** (top left hand of Figure 76). Likewise, for each case identified in Figure 76 we compute

$$\begin{array}{llll} \text{Case 1:} & C_1 = Q_{111}/G_{111} & \alpha_1 = G_{122}/G_{111} & \alpha_2 = -G_{221}/G_{111} \\ \text{Case 2:} & C_2 = Q_{121}/G_{121} & \alpha_3 = -G_{211}/G_{121} & \alpha_4 = -G_{222}/G_{121} \\ \text{Case 3:} & C_3 = Q_{122}/G_{122} & \alpha_5 = G_{111}/G_{122} & \alpha_6 = -G_{221}/G_{122} \\ \text{Case 4:} & C_4 = Q_{211}/G_{211} & \alpha_7 = -G_{121}/G_{211} & \alpha_8 = G_{222}/G_{211} \\ \text{Case 5:} & C_5 = Q_{221}/G_{221} & \alpha_9 = -G_{111}/G_{221} & \alpha_{10} = -G_{122}/G_{221} \\ \text{Case 6:} & C_6 = Q_{222}/G_{222} & \alpha_{11} = -G_{121}/G_{222} & \alpha_{12} = G_{211}/G_{222} \end{array} \tag{6.7}$$

The negative signs on terms in (6.7) are introduced so that values of α remain positive; although, it will be shown subsequently that for large values of porosity some of these terms are negative. The general nature of (6.6) allows for orthotropic material symmetry, while the idealized microstructure possesses cubic symmetry in-plane. Preliminary simulations confirmed the

expected cubic symmetry of the unit cell response. Accordingly, the 18 parameters of (6.6) are reduced to the following nine parameters by,

$$\begin{array}{lll} C_1 = C_6 & \alpha_1 = \alpha_{12} & \alpha_2 = \alpha_{11} \\ C_2 = C_5 & \alpha_3 = \alpha_{10} & \alpha_4 = \alpha_9 \\ C_3 = C_4 & \alpha_5 = \alpha_8 & \alpha_6 = \alpha_7 \end{array} \tag{6.8}$$

Additionally, the minor symmetries indicated by (.), of the sixth-order stiffness tensor, $C_{i(jk)l(mn)}$, imply that a relationship exists between these nine parameters, further reducing the total number of independent elastic constants to six. However, the compliance matrix as expressed in the form of (6.6) is not symmetric. Because $G_{ijk} = G_{ikj} = \frac{1}{2}\left(G_{ijk} + G_{ikj}\right)$ and $Q_{ijk} = Q_{ikj} = \frac{1}{2}\left(Q_{ijk} + Q_{ikj}\right)$, the reduced 6x6 compliance matrix of (6.6) modified in accordance with (6.7) and expanded to a full 8x8 compliance relationship results in

$$\begin{Bmatrix} G_{111} \\ G_{112} \\ G_{121} \\ G_{122} \\ G_{211} \\ G_{212} \\ G_{221} \\ G_{222} \end{Bmatrix} = \begin{bmatrix} \frac{1}{C_1} & 0 & 0 & \frac{\alpha_5}{C_3} & 0 & -\frac{\alpha_4}{2C_2} & -\frac{\alpha_4}{2C_2} & 0 \\ 0 & \frac{1}{C_2} & 0 & 0 & -\frac{\alpha_6}{C_3} & 0 & 0 & -\frac{\alpha_2}{C_1} \\ 0 & 0 & \frac{1}{C_2} & 0 & -\frac{\alpha_6}{C_3} & 0 & 0 & -\frac{\alpha_2}{C_1} \\ \frac{\alpha_1}{C_1} & 0 & 0 & \frac{1}{C_3} & 0 & -\frac{\alpha_3}{2C_2} & -\frac{\alpha_3}{2C_2} & 0 \\ 0 & -\frac{\alpha_3}{2C_2} & -\frac{\alpha_3}{2C_2} & 0 & \frac{1}{C_3} & 0 & 0 & \frac{\alpha_1}{C_1} \\ -\frac{\alpha_2}{C_1} & 0 & 0 & -\frac{\alpha_6}{C_3} & 0 & \frac{1}{C_2} & 0 & 0 \\ -\frac{\alpha_2}{C_1} & 0 & 0 & -\frac{\alpha_6}{C_3} & 0 & 0 & \frac{1}{C_2} & 0 \\ 0 & -\frac{\alpha_4}{2C_2} & -\frac{\alpha_4}{2C_2} & 0 & \frac{\alpha_5}{C_3} & 0 & 0 & \frac{1}{C_1} \end{bmatrix} \begin{Bmatrix} Q_{111} \\ Q_{112} \\ Q_{121} \\ Q_{122} \\ Q_{211} \\ Q_{212} \\ Q_{221} \\ Q_{222} \end{Bmatrix} \tag{6.9}$$

Major symmetry of the compliance tensor $S_{ijklmn} = S_{lmnijk}$ requires that the 8x8 compliance matrix of (6.9) be symmetric. Symmetry of the compliance matrix results in the relationships:

$$\frac{\alpha_2}{C_1} = \frac{\alpha_4}{2C_2}; \quad \frac{\alpha_6}{C_3} = \frac{\alpha_3}{2C_2}; \quad \frac{\alpha_1}{C_1} = \frac{\alpha_5}{C_3} \tag{6.10}$$

Thus, there are six independent elastic constants relating the second gradient to second order stresses for a material with cubic symmetry in 2D.

6.4.2 Effect of Fine Scale FE Discretization on Error in Elastic Constants

A mesh refinement study was conducted on the baseline unit cell in order to establish the accuracy of the elastic constants determined by the method presented in (6.7). Results from simulations of the baseline unit cell utilizing mesh discretizations of five different characteristic element sizes were used to evaluate the effect of mesh discretization on the elastic constitutive parameters. In addition, this effort highlights that the mesh density needed to accurately capture elastic response of detailed microstructure (even for this simple example problem) is much finer than that needed to resolve heterogeneous features. Because of this, it will be argued that the hierarchical multiscale approach is much more efficient in attaining *numerically* accurate coarse scale response simulations than discrete incorporation of heterogeneous features.

The error estimates for each constitutive parameter were computed by a least squares fit of the asymptotic relationship

$$\begin{aligned} M\left(h\right) &= M^* + Ah^p \\ {}^*\mathrm{Error}(h) &= \left| \frac{M\left(h\right) - M^*}{M^*} \right| \end{aligned} \tag{6.11}$$

where $M(h)$ is the constitutive parameter computed using a finite element mesh whose characteristic element size is h, M^* is the extrapolated value, A is a constant, p is the observed order of convergence, and ${}^*\mathrm{Error}(h)$ is the *estimated* error in parameter M associated with the particular finite element discretization. For example, Figure 77 presents a plot of Young's moduli, E_x and E_y, versus the characteristic element size, h. The dashed and dotted lines represent least-squares fits of (6.11) to this data. The extrapolated value, $E^* = E\left(0\right)$, is the y-intercept of the least-squares fit.

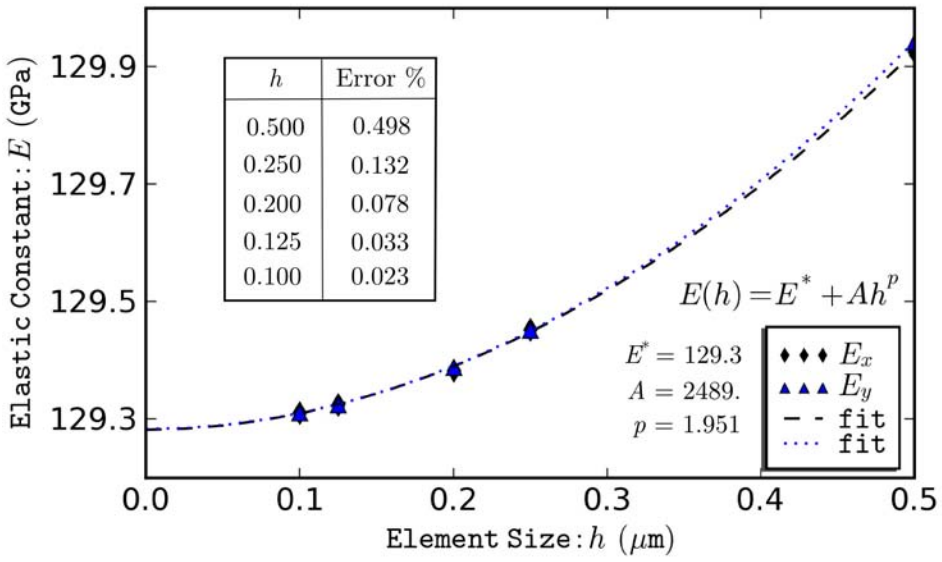

Figure 77. Sample results from mesh convergence study illustrating convergence in computed elastic constants.

Convergence of the computed elastic moduli towards their extrapolated value is monotonic with an observed order of convergence near the expected value of two. Furthermore, the asymmetry represented by the difference of E_x and E_y converges to zero, i.e. as the mesh discretization is refined the observed behavior approaches the expected cubic symmetry. Finally, the estimate of absolute error in the computed value of E_x associated with the characteristic element size, h is presented in the table in the upper left hand corner of Figure 77.

A posteriori error estimators such as (6.11) provide valuable insight regarding the mesh convergence of the simulation and provide a quantitative means to select an adequate mesh discretization for the intended purposes. Such an estimate is indicative of the total error, but cannot precisely characterize total error. Estimated percent error for each elastic constant associated with each of the finite element meshes is tabulated in Table 9. Richardson extrapolation is only valid for monotonically convergent solutions, which all of the elastic constants exhibit. Based on the results of this study, the discretization of $h = 0.02$ or, equivalently, $h / r_n = 0.02$ (whose row is printed in bold in Table 9), was selected for all

subsequent elastic computations. The estimated error is less than 0.2% for all elastic constants. The error estimates are tabulated against both the characteristic element size, h, and the ratio of element size to nearest-neighbor void spacing, h / r_n. It is actually this ratio, h / r_n, rather than the absolute element size, that is used to specify the mesh density for other rSVE simulations. Justification for this approach is based on the supposition that local error is proportional to the variation in strain across an element. Likewise, for a given value of second gradient, **G**, the variation in strain across any particular element is a function of h / r_n, rather than h. This specification is equivalent to imposing that all unit cells have 50 elements along each edge. This particular mesh density for the baseline unit cell is shown in Figure 78.

Table 9. Estimated percent error in elastic constants for various mesh densities.

Mesh Density		**Estimated Percent Error in Elastic Constants**								
h	h/r_n	E	G	ν	C_e	C_c	C_t	α_4	α_5	α_6
0.500	0.050	0.498	0.632	0.167	0.419	0.186	0.300	1.322	0.244	0.706
0.250	0.025	0.132	0.154	0.038	0.076	0.038	0.083	0.267	0.046	0.192
0.200	**0.020**	**0.078**	**0.096**	**0.023**	**0.043**	**0.022**	**0.053**	**0.149**	**0.027**	**0.123**
0.125	0.013	0.033	0.037	0.008	0.014	0.008	0.022	0.053	0.009	0.050
0.100	0.010	0.023	0.024	0.005	0.007	0.005	0.016	0.032	0.005	0.035

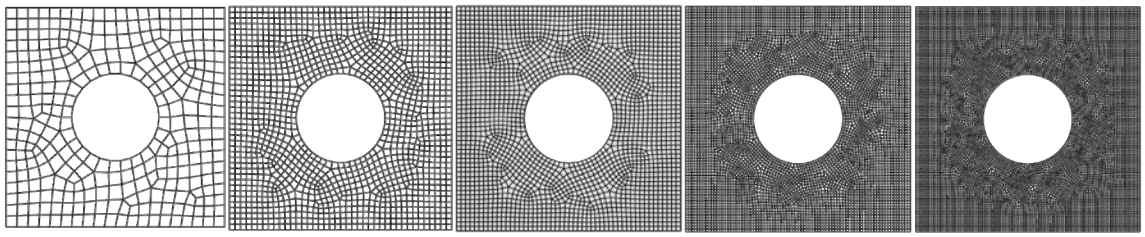

Figure 78. Finite element discretizations used in convergence study.

6.4.3 Identification of Porosity Dependent Elastic Stiffness Parameters

Additional unit cell simulations, i.e., $N = 1$, were conducted to assess the dependence of elastic constants on three morphological parameters, r_n, r_v, and the square of their ratio, i.e., $A_f = \pi\left(\frac{r_v}{r_n}\right)^2$. A separate unit cell was constructed for each combination of area fraction and r_n listed in Eq. (6.12) and discretized into a finite element mesh with 50 elements along each edge resulting in fifty distinct simulations. Elastic constants were computed from results of each of these simulations forming the basis of the following discussion. The first-order elastic constants, E, ν, and G are dependent on r_n and r_v only through the area fraction of porosity, A_f.

$$\begin{aligned} \left\{A_f\right\} &= \left\{0.02 \quad .04 \quad .06 \quad .10 \quad .15 \quad .20 \quad .25 \quad .30 \quad .40 \quad .50\right\} \\ \left\{r_n\right\} &= \left\{5 \quad 10 \quad 20 \quad 50 \quad 100\right\} \mu m \end{aligned} \tag{6.12}$$

Based on the single unit cell calculations, there is an apparent dependence of the second-order elastic constants, C_e, C_c, and C_t, on the void nearest-neighbor distance, r_n. However, sue to the aliasing between L_{rSVE} and r_n for single unit cell simulations, this dependence is actually on L_{rSVE} as confirmed by multi unit cell simulations, i.e. $N \neq 1$. In Figure 79 each of the computed second order elastic constants are plotted against area fraction showing the relationship between C_e, C_c, C_t, and A_f and L_{rSVE}.

Within an rSVE, the local strain energy is proportional to the square of local strain. Additionally, the mean local strain magnitude is proportional to L_{rSVE} for a given second gradient, i.e. $\left\langle\left|\varepsilon\right|\right\rangle \sim \mathbf{G} \cdot L_{rSVE}$. Therefore, the average strain energy increases with the square of rSVE size. and a superficial dependence of the second order elastic stiffness on the size of the rSVE is expected. This violates the notion that the response of an rSVE should converge to an rRVE for arbitrarily large L_{rSVE}. In order to recover such behavior, the second-order elastic constants are normalized by the rSVE size according to

$$\hat{C}_e = \frac{C_e}{L_{SVE}^2} \quad \hat{C}_c = \frac{C_c}{L_{SVE}^2} \quad \hat{C}_t = \frac{C_t}{L_{SVE}^2} \tag{6.13}$$

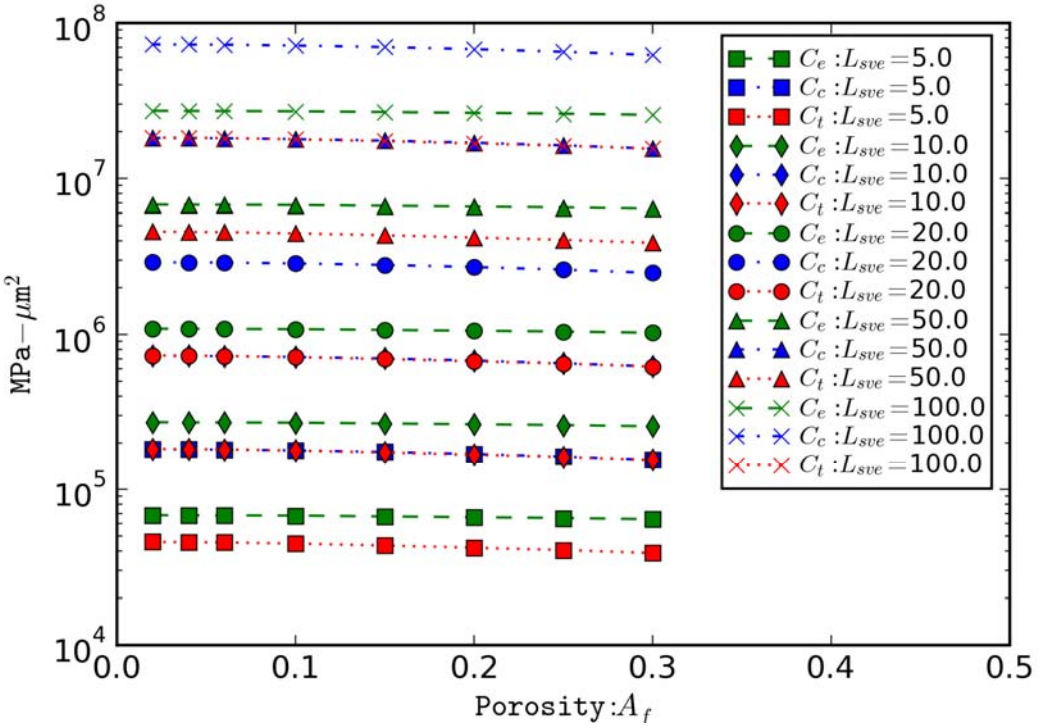

Figure 79. Dependence of second order elastic constants on porosity and size of rSVE.

This ensures convergent intrinsic properties computed from rSVE volume averages and eliminates the artificial dependence on rSVE size. The total second order elastic response is determined from the intrinsic material stiffness coupled with an extrinsic length scale which is ideally determined from the dominant microstructural response wavelength, $l^e = l^*$, i.e.,

$$\mathbf{C} = \left(l^e\right)^2 \hat{\mathbf{C}} \tag{6.14}$$

Figure 80 shows a plot of the second order elastic constants normalized by L_{rSVE} as in (6.13) versus porosity. Data markers from all values of L_{rSVE} lie directly on top of each other for a

given value of porosity. As suggested, this normalization effectively transforms $\hat{C}_i$ into an intrinsic material property.

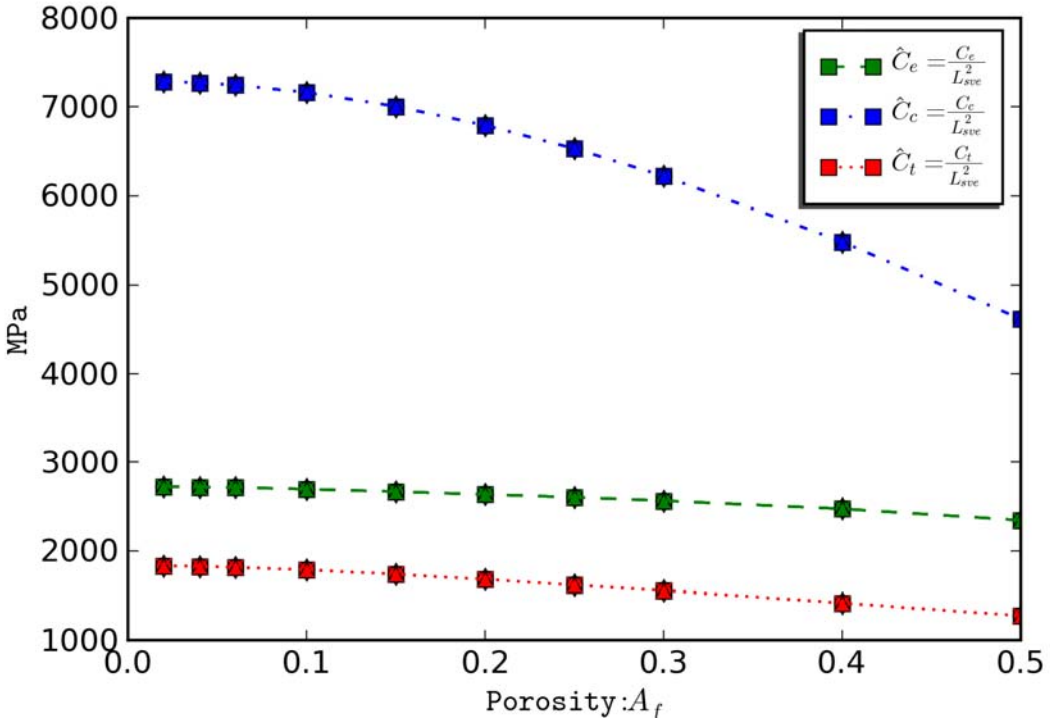

Figure 80. Effect of porosity on normalized second gradient stiffness components.

Figure 81 presents plots of each elastic constant versus porosity for the single unit cell calculations. As expected, stiffness moduli, as well as in-plane Poisson ratio, decrease with increasing porosity. The out-of-plane Poisson ratio is independent of porosity. With the exception of α_1 which couples G_{121} to G_{111}, the second-order coupling parameters, α also decrease with increasing porosity. The Poisson-like parameters α_2 and α_4 are negative for large values of porosity, indicating a change in the sign of kinematic coupling between second-gradient modes of response. For these simulations all values of α are less than one, which may be a

physical constraint on these parameters, although an analytical micromechanical analysis has not been conducted to establish strict physical limits such as this.

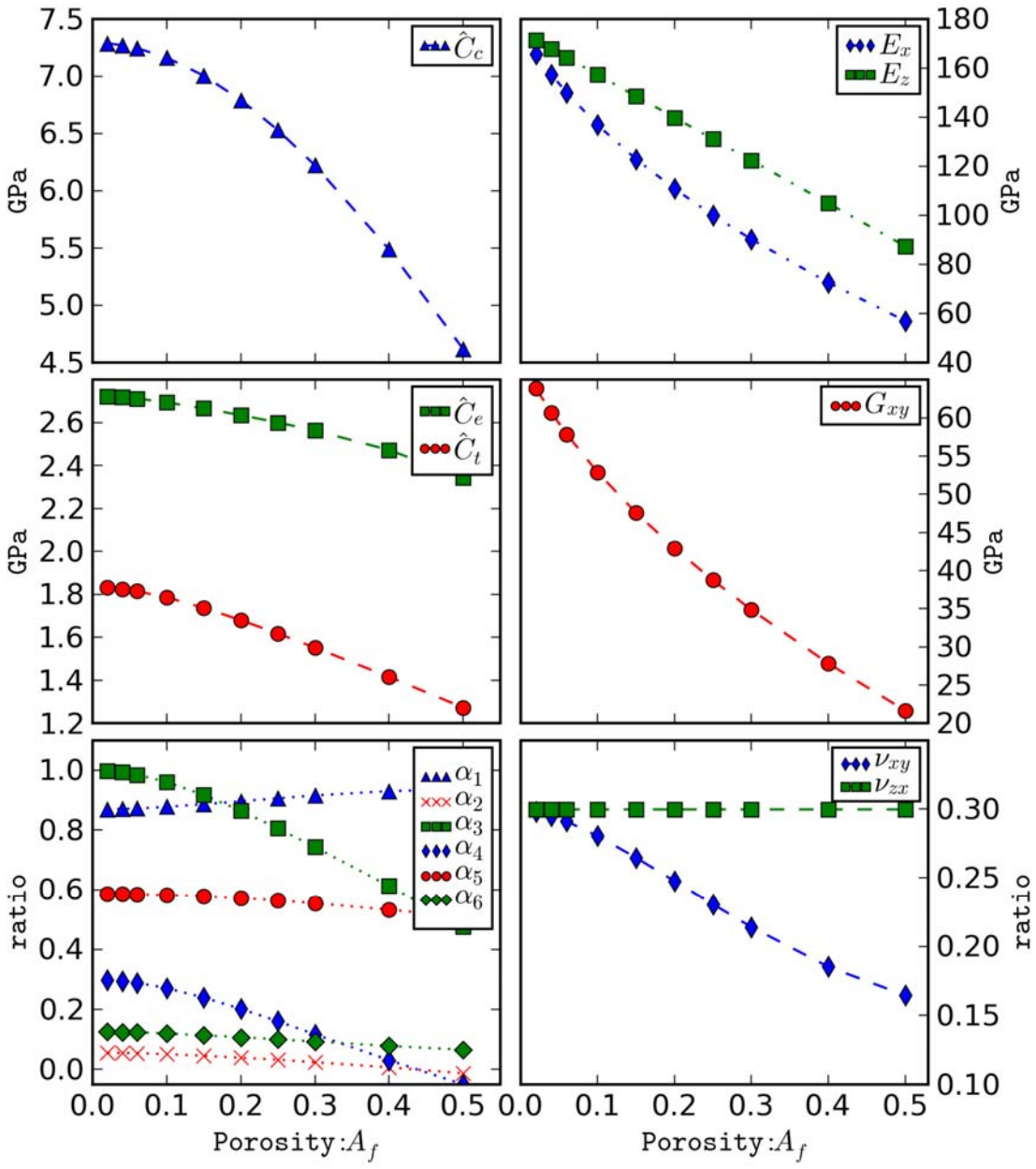

Figure 81. Variation of elastic constants versus porosity for single unit cell calculations.

The trends exhibited in Figure 81 motivate the following general equation to relate the elastic constants to porosity, i.e.,

$$P\left(A_f\right) = P_o \, \mathrm{e}^{-\left(\frac{A_f}{A_P}\right)^n} \tag{6.15}$$

which becomes an exponential decay for *n = 1* and a Gaussian function of porosity for *n = 2*. Equation (6.15) is a generalization of a common empirical relationship used to relate elastic moduli with porosity, (cf. Zhao et al., 1989; Luo and Stevens, 1996, 1999). Equation (6.15) was fit to computed elastic constants from the single unit cell calculations using nonlinear least-squares optimization. The resulting fitting parameters, P_{o}, A_P, and n, and the associated plots are not presented here, rather they are included in a discussion regarding the convergence of parameters observed for successively increasing L_{SVE}.

For the single unit cell calculations L_{rSVE} must equal r_n. In order to assess the effect of L_{rSVE} on the elastic constants and address whether or not the response can be considered truly representative, an additional set of simulations was conducted in which N was varied from one to seven. For each value of N, an rSVE consisting of an N by N tiling of unit cells was constructed and discretized using the same element size, h, as for the corresponding single unit cell. A total of 350 rSVE's representing the entire 50 unique combinations of A_f and r_n listed in Eq. (6.12) at each value of *N* from one to seven were analyzed. From each simulation the elastic constants were calculated as described above and the empirical relation of (6.15) was fit to their porosity dependent behavior. As an example, contour plots of the local Mises stress under second-gradient deformation modes for *N = 7* is shown in Figure 82. The variation of elastic constants with porosity and their associated empirical fits for the case of *N = 7* are shown in Figure 83 and Figure 84. Notice in particular, the distinct difference between the dependence of $\hat{C}$ on porosity for the case of a single unit cell, *N = 1*, in Figure 81 and the case of *N = 7* shown in Figure 83. This is due to the non-representative nature of a single void perfectly centered in the rSVE under gradient boundary conditions. The central voided region sees relatively less deformation than the outer void-free regions. For the single unit cell case, as porosity increases from zero, little of the additional voided area is in the region of large deformation response. However, as the value of

porosity grows significantly, each marginal increase in void size places a proportionally higher amount of voided area in the region of large deformation. This phenomena explains the shape of the $\hat{C}$ versus A_f plot in Figure 81 for the single unit cell case. As the number of unit cells, and consequently voids, in an rSVE increases, more of the voids become exposed to the higher deformation regions within the rSVE. Thus, the dependence of the second gradient moduli on porosity is more aligned with that of the first order elastic moduli.

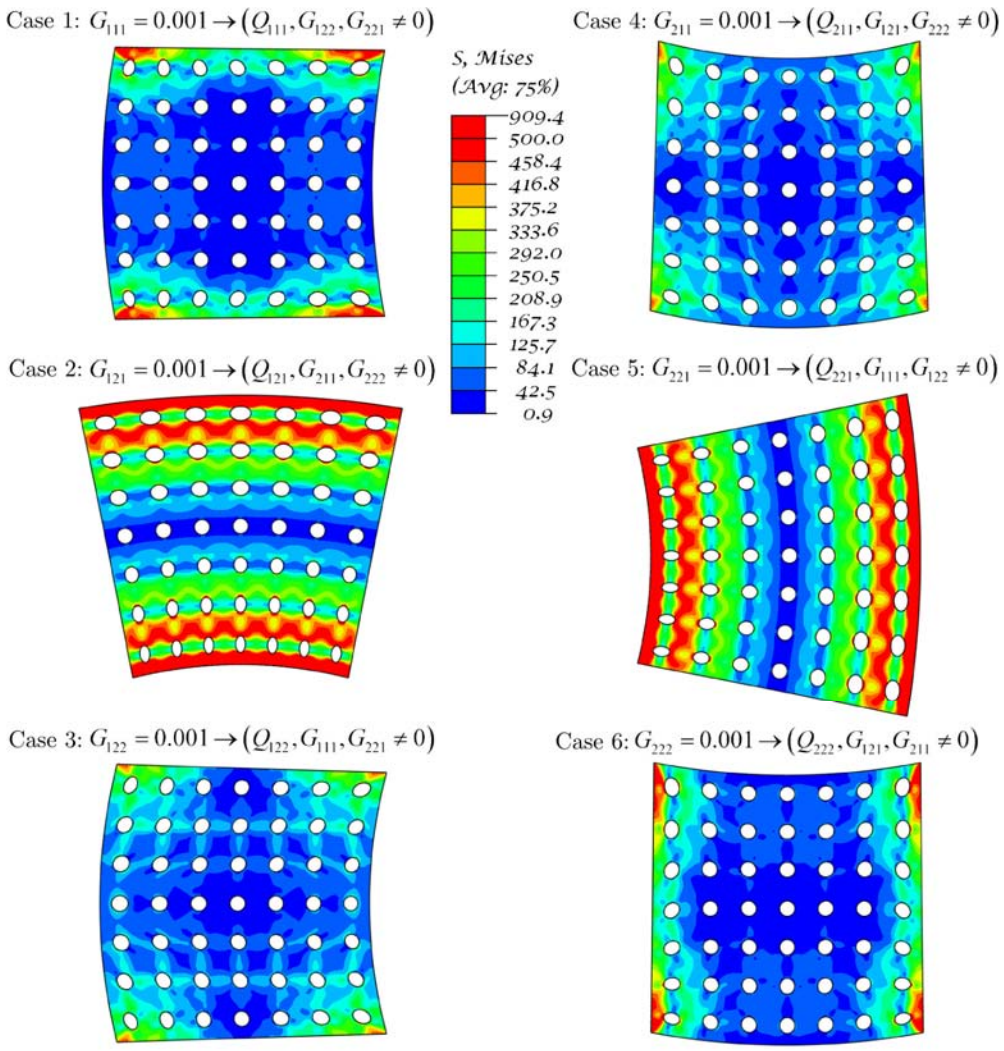

Figure 82. Contour plots of fine scale Mises stress for baseline simulations with N = 7.

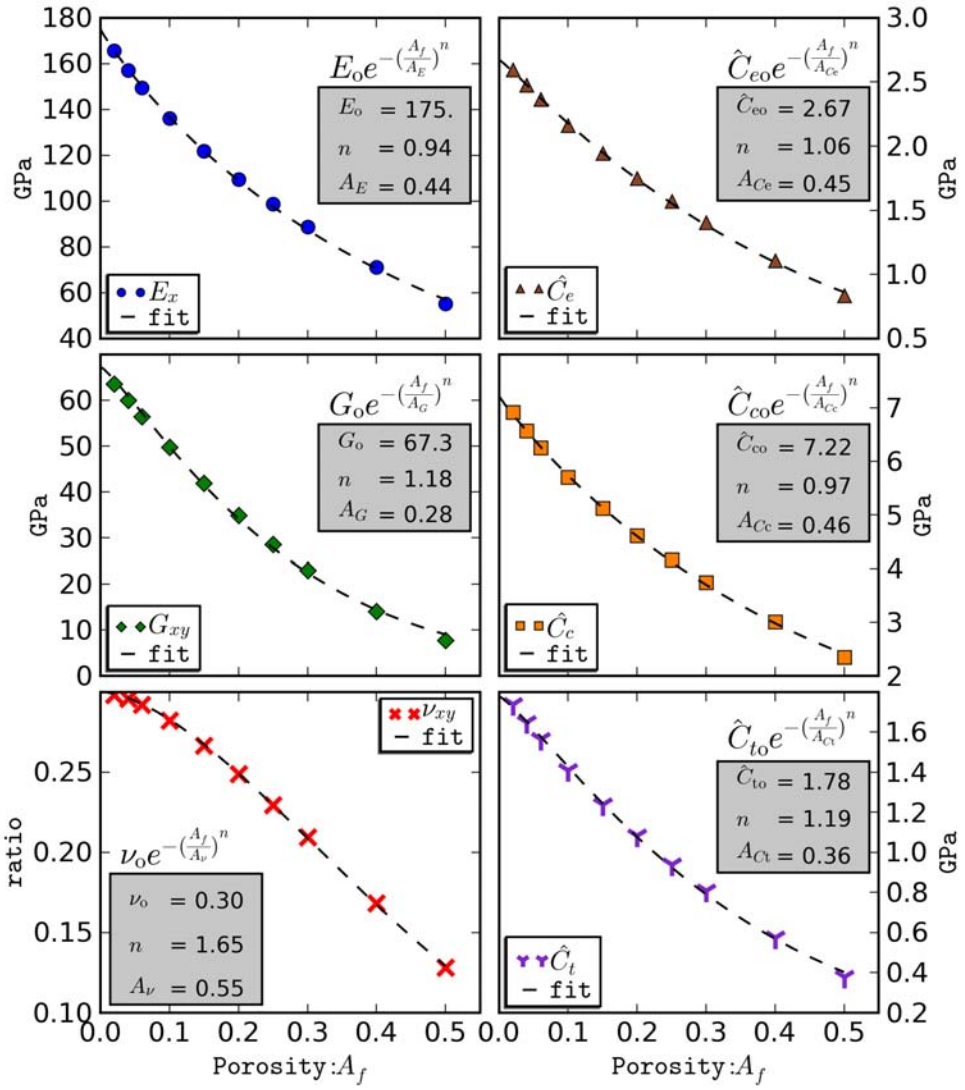

Figure 83. Computed elastic constants and their associated fits for N = 7.

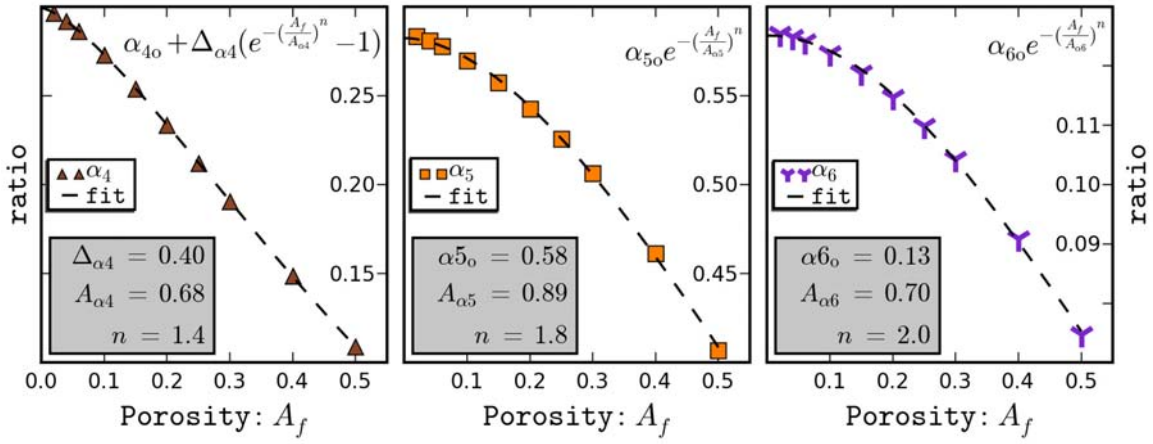

Figure 84. Computed second order coupling ratios and their associated fits for N = 7.

For all values of *N*, the obtained empirical fits are quite good with a coefficient of determination (r^2) generally near 0.9995 and always above 0.9950. Micromechanical analyses of voided microstructure have been performed by several authors including Luo and Stevens (1996, 1999) using Eshelby's self-consistent model, Zhao et al. (1989) using the Mori-Tanaka method, and Hasselman (1962) following work of Hashin (1961). These works resulted in an expression for the elastic moduli of porous materials of the form

$$E(A_f) = E_o \frac{1 - A_f}{1 + \frac{A_f}{A_E}} \tag{6.16}$$

The assumption central to this relationship is that porosity is described by a randomly distributed population of spheroidal voids. Such an assumption is not applicable for the idealized ordered microstructure considered in this chapter. For small *N*, the agreement of (6.16) with the computed first and second order elastic moduli is generally poor. As *N* grows larger the agreement between computed moduli with (6.16) increases substantially. However, (6.15) is preferred over (6.16) for the example provided here because it provides a better fit over the entire range of simulations considered. Consideration (a) enables a meaningful analysis of the convergence in elastic parameters as rSVE size grows. In any case, the equation used to fit the

physical constitutive constants to morphological parameters is empirical in nature, and, at best, phenomenological due to the idealized assumptions presented in equations such as (6.16).

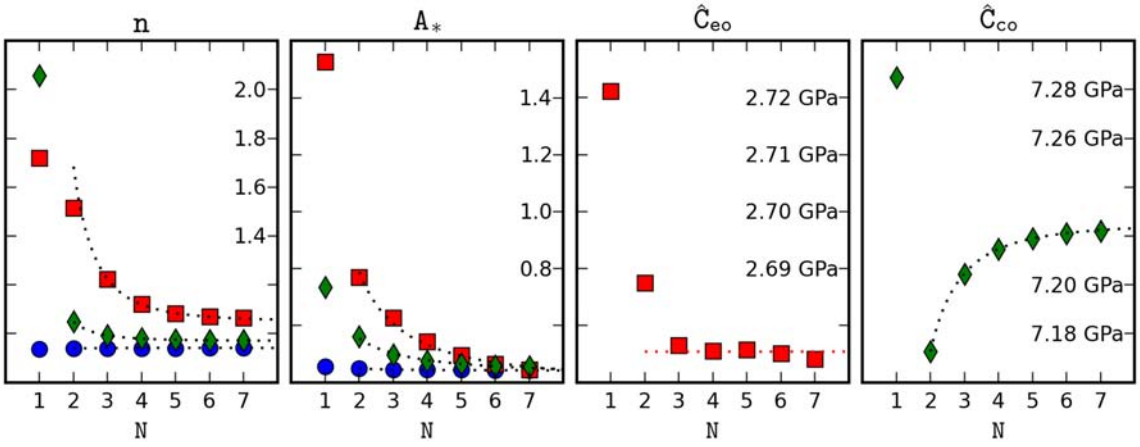

Figure 85. Effect of increasing rSVE size on empirical fitting parameters for elastic moduli.

Figure 85 contains four plots showing the convergence of empirical fitting parameters for E, $\hat{C}_e$, and $\hat{C}_c$ for increasing size of the rSVE (demarcated by *N*). The blue circles, red squares, and green diamonds represent the fit parameters for E, $\hat{C}_e$, and $\hat{C}_c$, respectively. The black dotted lines represent curves that were fit to the demonstrated asymptotically convergent behavior,

$$c = c_\infty + A \cdot L_{SVE}^{-p} \tag{6.17}$$

where *c* is the particular empirical parameter. The left-most plot shows the convergent trend in the exponent, *n*, of (6.15). For all of these elastic moduli, the exponent is converging to values near one. The normalizing area fraction, A_*, approaches a constant value near 0.44 for all three elastic moduli. The extrapolated values are 0.44, 0.42, and 0.40, for A_E, A_{Ce}, and A_{Cc}, and 0.94, 0.97, 1.05, for n_E, n_{Ce}, and n_{Cc}, respectively. While not identical, the similarity between

these asymptotes for E, $\hat{C}_e$, and $\hat{C}_c$ is striking, and therefore, they are grouped into a family. $\hat{C}_{\infty}$ shown in the right-most plot asymptotes to a value of 7.23 GPa. However, $\hat{C}_{e\infty}$ is not converging monotonically. It seems to be oscillating around a mean value of 2.7 GPa, which is depicted with a red dotted line. The remaining empirical parameters show similar trends and are summarized in Table 10.

Table 10. Values of empirical elastic constant asymptotes as size of rSVE grows large.

	E	G	ν	C_e	C_c	C_t
P_o	175.	67.3	0.30	2.7	7.23	1.76
A_p	0.44	0.27	0.55	0.40	0.42	0.33
n	0.94	1.20	1.71	1.05	0.97	1.20

Using the elastic free-energy function from Eq. (6.4), the elastic constitutive tensors from Eqs. (6.5) and (6.6), and the parameters fit to elastic unit cell simulations in this section, the elastic response for the second gradient porosity dependent coarse scale constitutive model is fully defined.

6.5 Development of constitutive description for inelastic response

Perhaps the most obvious approach to developing inelastic constitutive relations for the coarse scale response is based on second gradient adaptations of classical ISV models. One method to approach the extension is through the use of general representation theorems to construct an effective stress $\tau = \hat{\tau}\left(\tilde{\mathbf{S}}, \tilde{\mathbf{Q}}\right)$, i.e., a scalar valued function of tensoral arguments. Then, this effective stress can be substituted into conventional phenomenological constitutive models. . For example, a rate-independent associated flow model can be based on a yield threshold in generalized stress space, i.e.,

$$f = f(\tau) \leq 0 \tag{6.18}$$

Assuming associated flow for simplicity, the evolution equations take the form

$$\begin{gathered} \tilde{\mathbf{D}}^{in} = \dot{\lambda}\frac{\partial f}{\partial \tilde{\mathbf{S}}}, \quad L_v\left(\tilde{\mathbf{\Gamma}}^{in}\right) = \dot{\lambda}\frac{\partial f}{\partial \tilde{\mathbf{Q}}}, \\ L_v\left(\overline{\boldsymbol{\xi}}_1\right) = -\dot{\lambda}\frac{\partial f}{\partial \overline{\boldsymbol{\beta}}_1},\ L_v\left(\overline{\boldsymbol{\xi}}_2\right) = -\dot{\lambda}\frac{\partial f}{\partial \overline{\boldsymbol{\beta}}_2},\ \dot{\overline{\xi}}_3 = -\dot{\lambda}\frac{\partial f}{\partial \overline{\beta}_3} \end{gathered} \tag{6.19}$$

where the inelastic multiplier, $\dot{\lambda}$, has been introduced due to the non-unique definition of the convex threshold surface, and is solved in accordance with the Kuhn-Tucker and consistency conditions, i.e., $f\dot{\lambda} = 0$ and $\dot{\lambda} \leq 0$.

6.5.1 Inelastic Threshold Surface

For this example we use an anisotropic modification of the GLPD model, itself a second gradient extension of the Gurson model for a porous material (Enakoutsa and Leblond, 2009). This model is selected because it is based on the well known Gurson model of the inelastic yield surface in the presence of porosity with an elastic perfectly plastic matrix. A brief account of the Gurson model and its history is given here.

In its original form, the Gurson model is simply a yield function derived from an approximate analysis of the growth of a spherical void embedded in a perfectly plastic matrix (Gurson, 1977). The concept of effective stress (cf. Lemaitre, 1998) was applied to the matrix material that obeyed a Mises flow rule. The model was modified by Chu and Needleman (1980) to include nucleation effects and by Tvergaard and Needleman (1984) who added additional fitting parameters to Gurson's form and added a coalescence effect to simulate the rapid increase in damage evolution at the onset of failure. Thomason (1990) developed a plastic limit load coalescence criterion that Zhang et al. (2000) adopted to develop the so-called "complete Gurson model". As described by Zhang et al. (2000) the "complete" model consists of the yield function given in Eq. (6.2), where evolution of the scalar damage variable (porosity) is defined as $\dot{\overline{\xi}}_1 = \dot{\overline{\xi}}_{1,nuc} + \dot{\overline{\xi}}_{1,grow}$ and the porosity rate provided by contributions of nucleation and growth are, respectively, $\dot{\overline{\xi}}_{1,nuc} = a\dot{\overline{pp}}$ and $\dot{\overline{\xi}}_{1,grow} = \left(1 - \overline{\xi}_1\right) tr(\dot{\boldsymbol{\varepsilon}}^{in})$, where a is the nucleation rate constant and

$\overline{p} = \sqrt{\frac{2}{3}\boldsymbol{\varepsilon}^{in} : \boldsymbol{\varepsilon}^{in}}$. The porosity evolution during coalescence is enhanced by an intensification of the porosity growth rate after the onset of coalescence as determined by Thomason's plastic load limit criterion.

Without the plastic load limit criterion, the model historically gave reasonable fits to experimental behavior for stress states characterized by low triaxiality, but poor for high triaxiality. From the expression for the intensification of porosity growth given above, it is clear that non-unique results should be expected for an infinite combination of the constants. This was demonstrated in simulations conducted by Zhang et al. (2000). With the addition of the load limit criterion for the onset of coalescence Zhang et al. found the model is still insufficient to reflect stress triaxiality dependence, which is consistent with findings of Pardoen and Hutchinson (2000). Good fits were obtained for a limited set of tensile test data on a steel material with low initial porosity. The parameters were shown to be non-unique in describing the material behavior. Subsequent simulations where strong field gradients required the use of a refined mesh showed expected mesh dependency.

Several weaknesses of this model are now discussed. From the outset, it should be noted that this model was not originally developed within the thermodynamic framework described in Chapter 3. Over time, kinetic relations have been added, in an apparently *ad hoc* fashion, to match macroscopic behavior exhibited in experiments. As phenomenological modifications are added, the underlying physical mechanisms become increasingly obscured. The repeated conclusion that the model is providing non-unique matches to experimentally observed behavior would suggest a comprehensive suite of experiments would be necessary to pin down appropriate parameters. In any case, it is likely that while the introduced parameters are redundant, thus providing the non-unique behavior, they are at the same time insufficient to fully capture process dependencies on the state of the material.

More fundamental problems with this model arise in consideration of conservation of momentum and mass. While the application discussed immediately prior was for quasi-static loading, it should be noted that the evolution equations have been developed without consideration of a void's inertial resistance to growth. Dynamic finite-element codes apply conservation of

momentum at the macroscopic scale to obtain inertial forces resisting changes in the velocity field. Compliance with the conservation of momentum within the rSVE must be additionally ensured. Chen and Yu (1998) conducted simulations of dynamic ductile damage and fragmentation with a Gurson-based model assuming viscoplastic behavior of the matrix. They incorporated additional inertial terms for the growth behavior and demonstrated that the accumulation of damage was reasonably insensitive to inertia. The conclusion made was that Gurson-type models may be sufficiently extended to dynamic loading via rate dependent description of the plastic behavior of the matrix material. Molinari and Mericer (2001) arrived at a different conclusion. They also assume incompressible viscoplastic behavior for the matrix material of a Gurson-type model and apply the principle of virtual work locally within the rSVE. They demonstrate that for applications at high loading rates with low strain-rate sensitivity of the plastic hardening behavior, the effects of micro-inertia are significant. The behavior becomes more pronounced at increasing levels of porosity.

Santoaoja (2002) has applied the conservation of mass to Gurson's RVE and demonstrated that any porosity evolution other than that provided by growth violates the assumption of incompressible flow in the matrix. Thus modifications made to Gurson's original model to include nucleation and coalescence locally violate the conservation of mass without provisions for additional kinematics. It is also widely recognized that rate-independent models based on an assumption of local action exhibit strong mesh dependence at the onset of percolation.

The GLPD extension to the Gurson model adds a dependence of the yield surface on the second order stresses, $\tilde{\mathbf{Q}}$. Furthermore, in order to model the irreversible response, extensions to the GLPD model were made to account for (1) orthotropy due to the symmetry of the regular array of voids and (2) a new ISV to represent the heterogeneous distribution of fine scale inelastic response. We define an anisotropic quadratic relationship for the effective stress, namely

$$\tau^2 = \tilde{\mathbf{S}} : \mathbf{A}^{\tilde{\mathbf{S}}} : \tilde{\mathbf{S}} + \frac{1}{l_{in}^2} \tilde{\mathbf{Q}} \vdots \mathbf{A}^{\tilde{\mathbf{Q}}} \vdots \tilde{\mathbf{Q}} \tag{6.20}$$

where $\mathbf{A}^{\tilde{\mathbf{S}}}$ and $\mathbf{A}^{\tilde{\mathbf{Q}}}$ are fourth and sixth order, respectively, projection tensors that accommodate anisotropy in developing a scalar product for the stress terms, $\tilde{\mathbf{S}}$ and $\tilde{\mathbf{Q}}$ and l_{in} is a length scale

associated with the characteristic size of dominant inelastic microstructural response. Then the elastic threshold is defined by

$$f\left(\tau,\overline{\xi}_1,\overline{\xi}_2\right)=\frac{\tau^2}{\left(\overline{\xi}_2\tau_0\right)^2}+2\overline{\xi}_1 q_1\cosh\left(q_2\frac{3}{2}\frac{\tau_m}{\tau_0}\right)-1-q_3\overline{\xi}_1^{\,2} \tag{6.21}$$

where we have introduced the coarse scale kinematic internal variables $\overline{\xi}_1$ (which corresponds to the effective coarse scale porosity in the classical Gurson model) and $\overline{\xi}_2$ which reflects the fine scale heterogeneity of stress when accounting for the local fine scale yield stress, τ_0. The mean effective stress is defined as $\tau_m = tr\left(\tilde{\mathbf{S}}\right)$. Evolution equations for $\tilde{\mathbf{D}}^{in}$ and $\tilde{\mathbf{\Gamma}}^{in}$ take the associated form of Eq. (6.19), while evolution for $\overline{\xi}_1$ is dictated by conservation of mass, i.e., $\dot{\overline{\xi}}_1=\det\left(\tilde{\mathbf{D}}^{in}\right)$ and evolution of $\overline{\xi}_2$ is of the non-associated form, $\dot{\overline{\xi}}_2=H_{\overline{\xi}_2}\left\{1-\overline{\xi}_2\right\}\exp\left(\frac{-\overline{\xi}_2}{\hat{\overline{\xi}}_2}\right)\sqrt{\tilde{\mathbf{D}}^{in}:\tilde{\mathbf{D}}^{in}+L_v\left(\tilde{\mathbf{\Gamma}}^{in}\right)\vdots L_v\left(\tilde{\mathbf{\Gamma}}^{in}\right)}$, where Macauley brackets $\{\bullet\}$ are used to prohibit negative values of the argument.

6.5.2 Stored Free Energy Potential

The stored free energy depends directly only on $\overline{\xi}_2$ since that particular ISV was introduced as a kinematic measure of the development of heterogeneous fine scale stress field. Heterogeneity in the fine scale stress field is caused by fine scale residual elastic strain fields in the intermediate configuration and for the elastic perfectly plastic case are the only mechanism of energy storage. However, note that the dependence of the constitutive tensors on the porosity ISV ($\overline{\xi}_1 = A_f$) developed in 6.4.3 suggests that the recoverable (elastic) free energy is dependent on that ISV. Accordingly, an increase in porosity will result in a decrease in recoverable elastic energy in a manner consistent with concept the energy release rate associated with damage growth, i.e.,

$$\psi^s = \frac{1}{2}c\,\overline{\xi}_2^{\,2} \tag{6.22}$$

6.5.3 Fitting to Unit Cell Calculations

Because of the computationally intensive nature of the internal constraints needed for satisfaction of kinematic orthogonality in the presence of a second gradient, a minimal set of fine scale simulations was used to identify appropriate values for the parameters of the constitutive model. A finite element discretization of a single void unit cell with an element size to void spacing ratio of $h / r_n = 0.20$ was employed (cf. Figure 78) for the inelastic simulations. Generalized periodic boundary conditions with appropriate internal constraints were applied to the fluctuation field (cf. Chapter 4).

Six independent cases each of deformation gradient and second gradient time histories were simulated to develop a set of response data for fitting the constitutive parameters. In each case, a particular subset of components of either the deformation gradient or second gradient was specified and all other components were unrestrained such that the corresponding conjugate forces remained zero throughout that simulation case. The specified subset of components for each case are indicated in Table 11. The full deformation and stress history was computed and stored in accordance with procedures specified in Chapter 4 for further post-processing.

Contour plots of effective inelastic (or plastic) strain, i.e., PEEQ, are shown for representative first- and second-order cases in Figure 86 and Figure 87, respectively. The first order cases exhibit fine scale patterning with correlation lengths related to the unit cell size. Significant amounts of the overall coarse scale inelastic deformation are accommodated by intense bands of local fine scale inelastic deformation. As expected, the second gradient cases do not exhibit periodicity, but do show the local fine scale effects of porosity interacting with coarse scale gradients. Generalized stress-strain curves are plotted in Figure 88 for the corresponding representative first-order (L) and second-order (R) cases.

Table 11. Deformation components specified for inelastic unit cell simulations.

Inelastic Case	Specified Components of Deformation
FO-1	F_{11}
FO-2	F_{33}
FO-3	F_{11}, F_{22}, F_{33}
FO-4	F_{11}, F_{22}
FO-5	F_{11}, F_{33}
FO-6	F_{12}, F_{21}
SO-1	G_{111}
SO-2	G_{121}
SO-3	G_{122}
SO-4	G_{111}, G_{122}
SO-5	G_{111}, G_{221}
SO-6	G_{121}, G_{122}

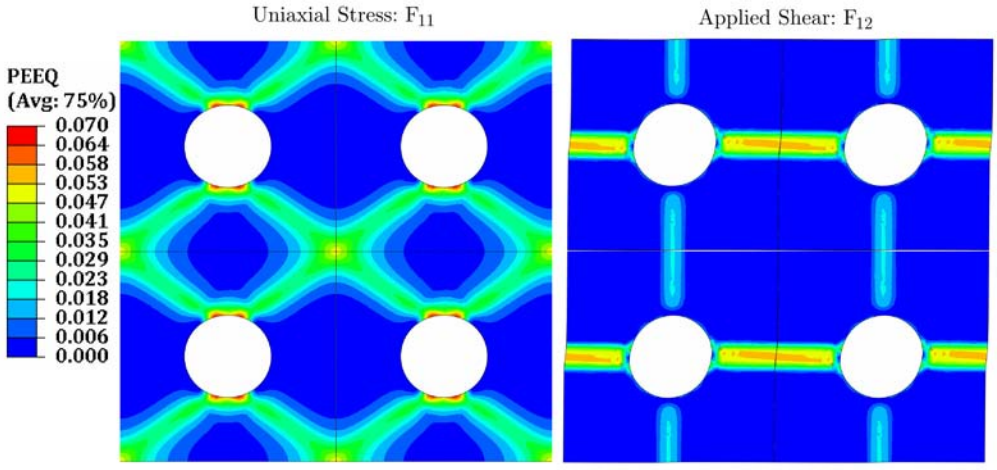

Figure 86. Contour plots of inelastic strain (PEEQ) for inelastic cases FO-1 and FO-6.

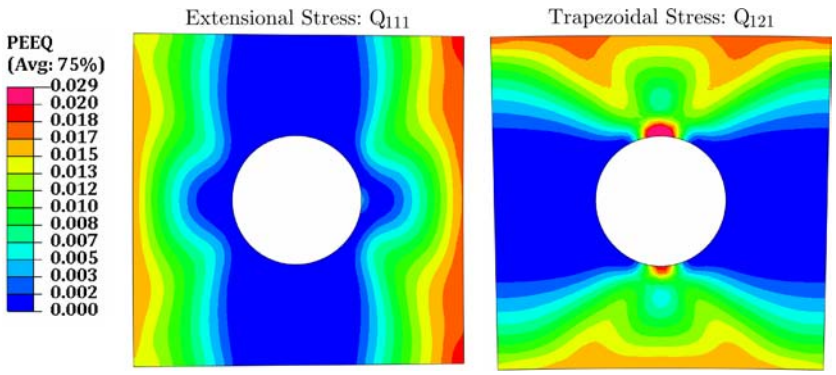

Figure 87. Contour plots of inelastic strain for inelastic cases SO-1 and SO-2.

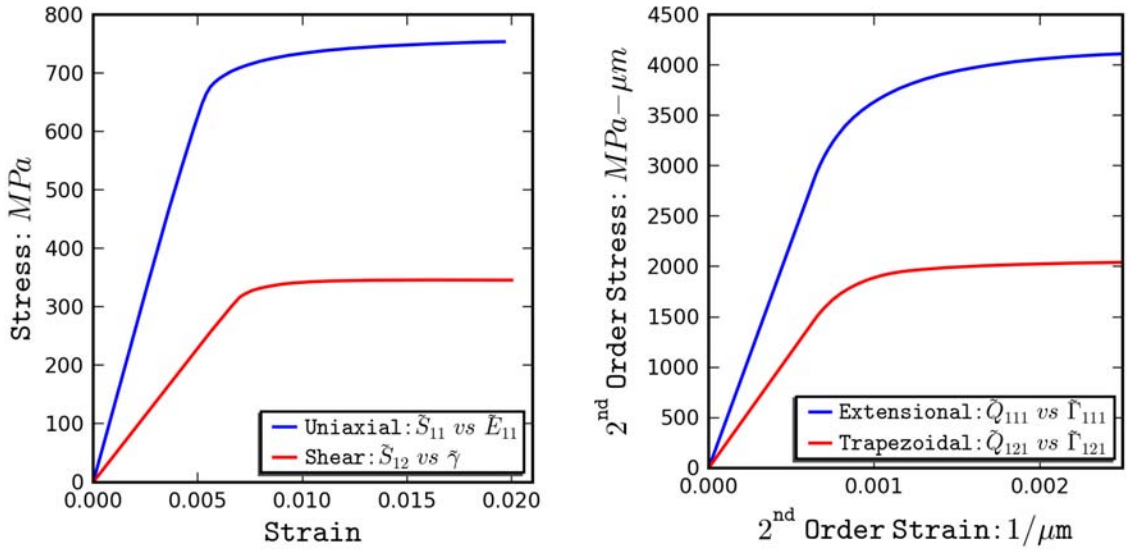

Figure 88. Representative generalized coarse scale stress-strain curves for (left) first order and (right) second order inelastic unit cell simulations.

The Gurson parameters and anisotropy matrix for first order stresses were fit to saturation stress results from the inelastic FO cases. The anisotropy matrix for SO cases were obtained from the saturation yield stress of the SO cases. Parameters for the heterogeneous evolution kinetics were

fit to the pre-saturation stress results from all cases. The parameters obtained by this approach for the idealized porous microstructure are reported in Table 12.

Because of the influence of length scales associated with long range response gradients and internal length scale parameters are not identifiable from the unit cell simulations and must be determined by some other means. Ideally this would be an intrinsic material property; however, the ensuing section will demonstrate that there is a definite contribution of the coarse scale geometry and response to these length scale parameters.

Table 12. Inelastic constitutive parameters fit to unit cell simulations.

$A_1^{\tilde{S}} = 0.34$	$A_1^{\tilde{Q}} = 9.70$	$A_4^{\tilde{Q}} = 2.20$	$\tau_0 = 1000$ MPa	$H_{\bar{\xi}_2} = 5.45\text{E}8$
$A_2^{\tilde{S}} = 0.52$	$A_2^{\tilde{Q}} = 19.8$	$A_5^{\tilde{Q}} = -7.40$	$q_1 = 4.10$	$\hat{\bar{\xi}}_2 = 0.075$
$A_3^{\tilde{S}} = 2.12$	$A_3^{\tilde{Q}} = 62.1$	$A_6^{\tilde{Q}} = -21.6$	$q_2 = 0.50$	$\bar{\xi}_{2,0} = 0.90$

6.6 Coarse Scale Simulations

A set of discretizations of the coarse scale geometry into the nine-node mixed-field finite elements described in Chapter 5 was developed using the mesh generation software, Cubit (2008). The typical mesh consisted of a refined region in the vicinity of the localization region, a low element density region (larger elements) away from the localization region and a region of mesh transition between the two. In order to address the issue of superficial mesh dependence, four separate discretizations consisting of characteristic elements sizes of *110μm*, *80μm*, *50μm*, and *20μm* in the localization region were employed. Entirely mapped (shared nodal connectivity) meshes were used in all cases.

The user-element developed in Chapter 5 and material constitutive behavior and properties developed in Sections 6.4 and 6.5 of this chapter are assigned to the entire domain of the problem

for modeling the coarse scale response. Boundary conditions consistent with those employed for the direct baseline simulations were applied to the model. These consisted of restrained vertical nodal displacements, $\overline{u}_2 = 0$, and relaxed deformation gradient, $\hat{F}_{21} = 0$, along the bottom edge, restrained horizontal displacements, $\overline{u}_1 = 0$, and relaxed deformation gradient, $\hat{F}_{12} = 0$, along the line of symmetry. The nodes along the top boundary are constrained to have $\hat{F}_{21} = 0$, while the vertical displacements are constrained equal to the specified top displacement, $\overline{u}_2 = \delta$.

The net resultant force per unit thickness versus specified top displacement are plotted in Figure 89 for each of the four mesh discretizations as well as the baseline direct solution. The coarse scale simulation results match the baseline direct solution well and do not exhibit noticeable mesh dependence. Contour plots of the coarse scale effective plastic strain (PEEQ) are plotted for the localization region for each of the four mesh discretizations and for the entire problem domain for the finest mesh discretization. The finite size of the localization band is maintained as the characteristic element size is successively reduced.

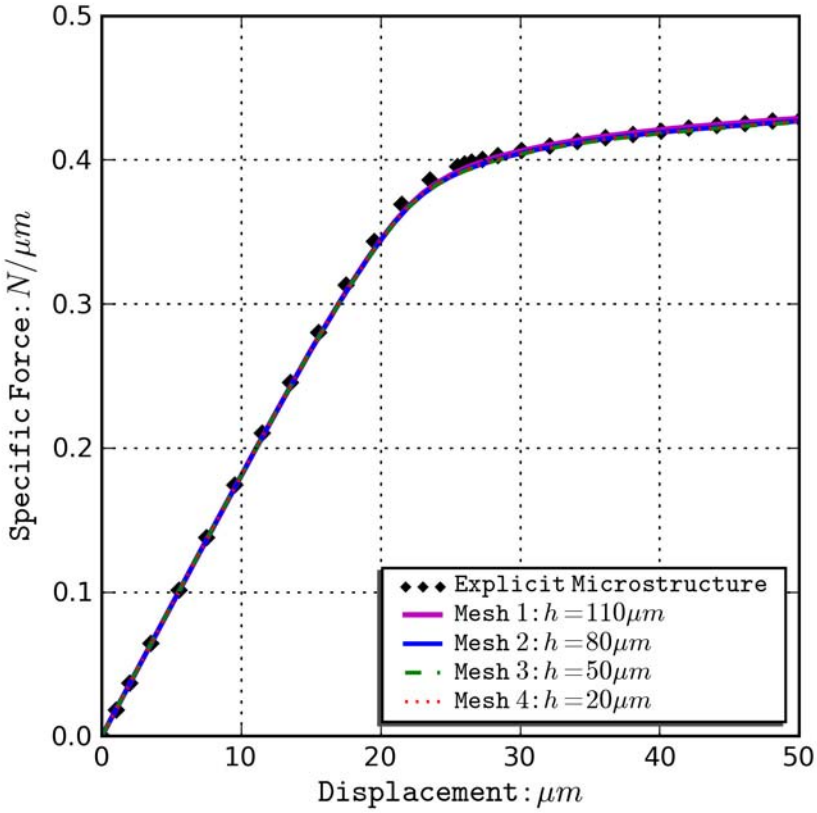

Figure 89. Force versus displacement for coarse scale simulations obtained separately using meshes with different characteristic element sizes compared to results for simulation with explicit treatment of microstructure.

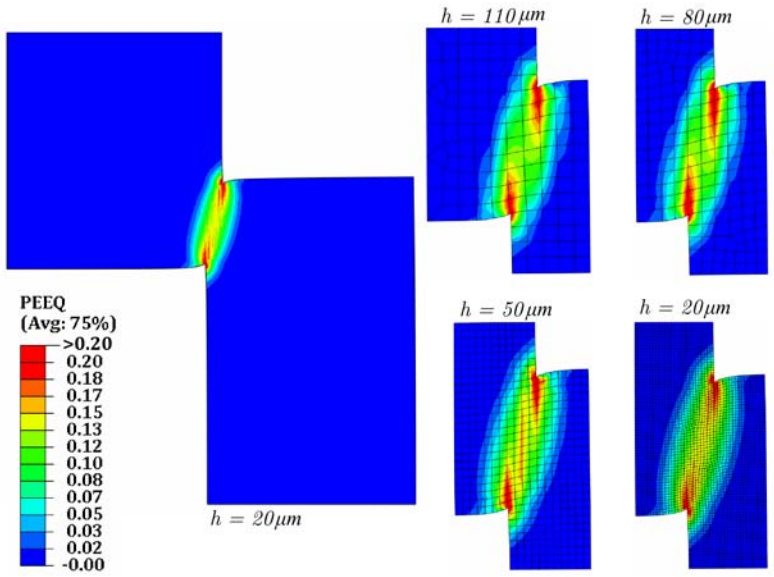

Figure 90. Contour plots of effective plastic strain (PEEQ) for coarse scale simulations obtained separately using different meshes with different characteristic element sizes.

These results correspond to elastic and inelastic microstructural length scales of $l^e = l^{in} = 140\mu m$. This particular value was selected based on the geometry of the problem, size of the localization band in the baseline simulation, and was adjusted to improve agreement of force versus displacement results between the coarse scale and direct baseline simulation. It would be beneficial if the necessary length scale parameters were intrinsically related to and determinable from fine scale simulations; however, as shown subsequently, they exhibit dependence on the geometry of the problem under consideration. This length scale issue warrants further investigation. Figure 91 shows plots of the net force versus platen displacement for four distinct length scale parameter values, $l^e = l^{in}$, and the direct baseline simulation. The case with $l^{in} = 140\mu m$ is highlighted in red. Note that an increase in the length scale parameter increases the second order stress associated with a particular value of second gradient *and* reduces the contribution of the second-order stress to the total effective stress in establishing the inelastic threshold. In this case the combined effect is to increase the region of elastic response and delay yield. Contour plots of effective plastic strain for each of the considered length scale values are

shown in Figure 92. As expected a decrease in the length scale parameter decreases the width and increases the local intensity of the shear band.

Note that, even for length scale parameters which provide a poor match to force versus displacement results, in all of these cases the rate of hardening in the second gradient coarse scale simulations matches the hardening exhibited by the explicit microstructure simulation. Presumably the dramatic improvement in this aspect of response over that of the Gurson based model illustrated in Figure 74 is attributed to the evolution of $\bar{\xi}_2$, reflecting kinematic hardening due to heterogeneous fine scale residual elastic strain fields.

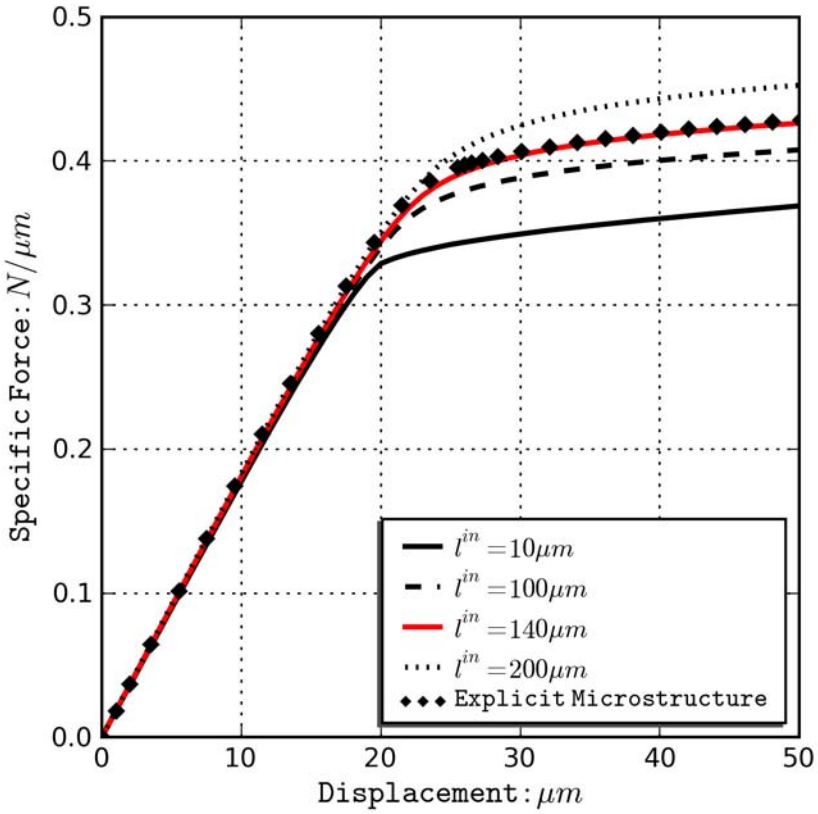

Figure 91. Force versus displacement for coarse scale simulations employing multiscale second gradient homogenization under different length scale parameters.

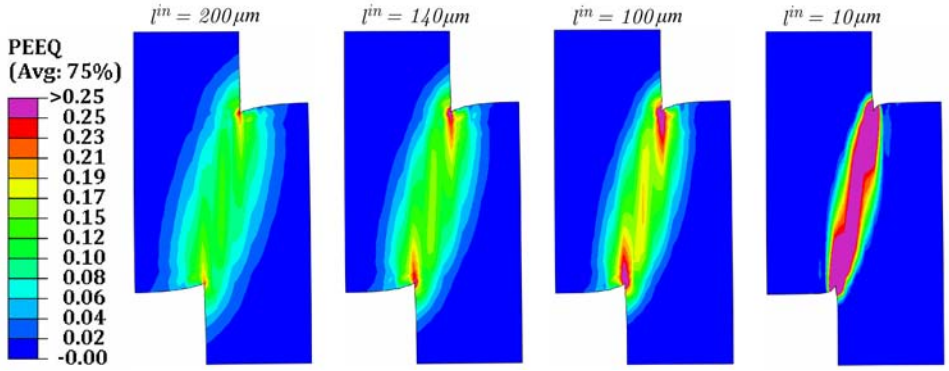

Figure 92. Contour plot of effective plastic strain (PEEQ) for coarse scale simulations employing multiscale second gradient homogenization under different length scale parameters.

The effect of independently varying the length scale parameters l^e and l^{in} was also assessed. Figure 93 compares the resultant force versus applied displacement results for various values of l^e while keeping l^{in} fixed at 140μm. The differences are subtle; there is a slight variation in the elastic portion of the curve and the initial yield point, but the hardening is mostly unaffected. Figure 94 compares the resultant force versus applied displacement results for various values of l^{in} while keeping l^e fixed at 140μm. In this case, the elastic portion of the curve and initial yield are mostly unaffected, while the hardening is appreciably different. The inelastic length scale parameter has a larger influence on the structural hardening aspects of the solution, while the elastic length scale parameter is manifest in the elastic response, namely initial stiffness and forces associated with yielding.

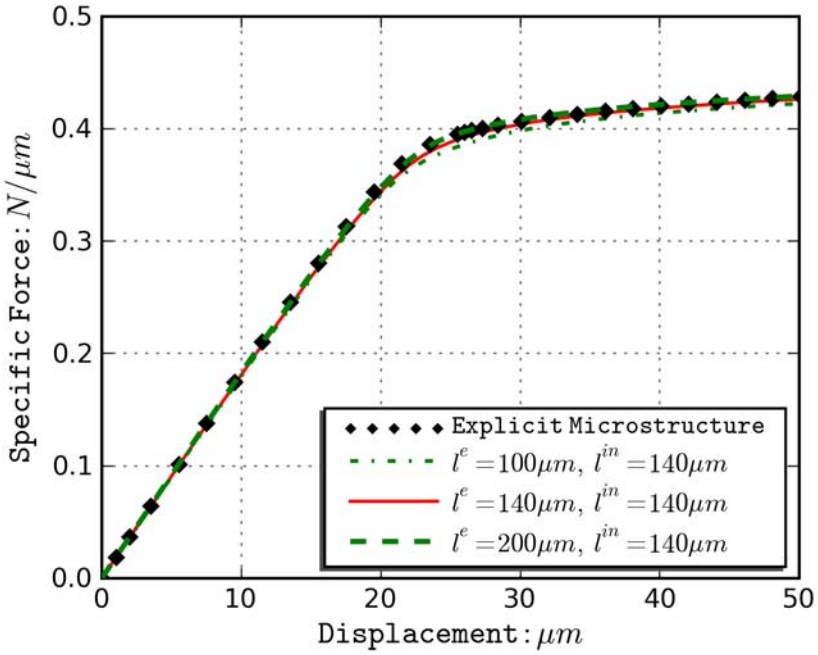

Figure 93. Comparison of resultant force versus applied displacement for variations of l^e while l^{in} remains fixed.

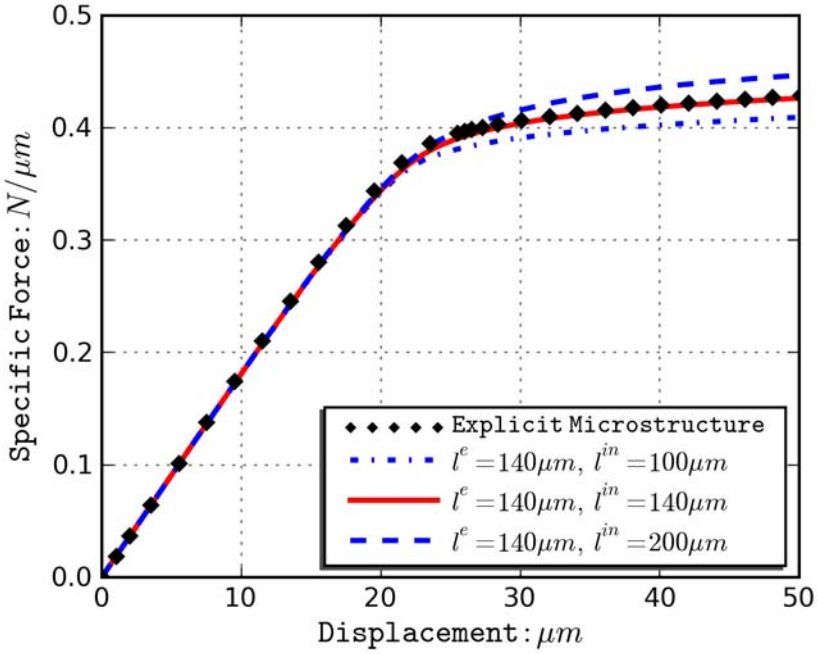

Figure 94. Comparison of resultant force versus applied displacement for variations of l^{in} while l^e remains fixed.

6.7 Dependence of Length Scale Parameters on Coarse Scale Boundary Value Problem

In this section, a coarse scale boundary value problem distinct from that in the previous section is studied in order to test the hypothesis that the length scale parameters l^e and l^{in} are not intrinsic microstructure specific parameters. The fine scale description of the material, i.e., microstructure is identical to that from the previous section and illustrated in Figure 95. The idea is that if the length scale parameters are solely dependent upon length scales of microstructure and its response, they should apply universally to any coarse scale boundary value problem (CSBVP). If, on the other hand, the length scale parameters appropriate for one CSBVP are not suitable for another CSBVP, then such length scale parameters are clearly not intrinsic parameters pertaining to the microstructure. This investigation has significance beyond the scope of the dissertation, as all nonlocal constitutive relations employ (either implicitly or explicitly) at lease one length scale parameter.

6.7.1 Problem Description

The multiscale problem, illustrated in Figure 95, consists of a thin (in x_1) layer of material undergoing shear deformation on account of displacement boundary conditions at $x_1 = 0$ and $x_1 = L_t$. Embedded along the center of this thin layer are elliptical holes of major radius r_a and minor radius r_b, shown in black at right of Figure 95, with a periodic spacing of L_p in the x_2 direction. The white region of the coarse scale problem reflects the porous microstructure shown at left of Figure 95 and identical to that introduced in Section 6.1. Two cases are considered and the parameter values for these cases are reported in Table 13.

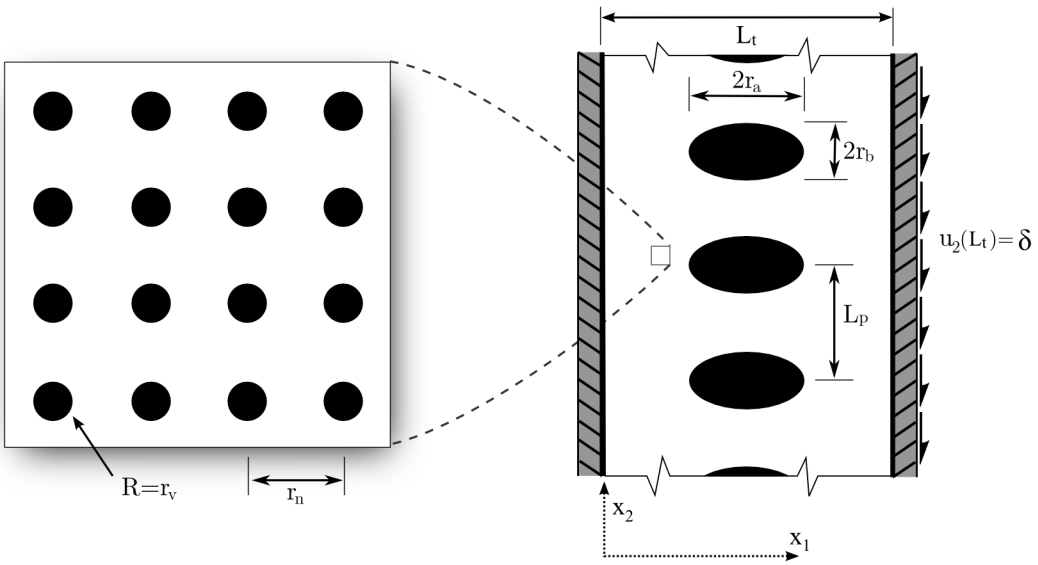

Figure 95. Illustration of multiscale problem used for length scale parameter investigation. At left is the microstructure, identical to that introduced in Section 6.1. At right is a thin layer shear problem with periodically spaced elliptical holes.

Table 13. Multiscale problem dimensions used for Cases B and C.

Parameter	Case B	Case C
r_a (μm)	108	108
r_b (μm)	36	72
L_t (μm)	684	576
L_p (μm)	288	576

6.7.2 Explicit Microstructure Baseline Simulations

As in the previous section a direct simulation with explicit treatment of the porous microstructure is constructed by including the fine scale voids in the coarse scale model geometry. For these simulations periodic symmetry in the x_2 direction is exploited by modeling only a region of one period with the elliptical hole located at the center of this region. Periodic displacement conditions are applied to the top and bottom edges of the modeled region such that, $u_2\left(x_1,\, x_2 = L_p\right) = u_2\left(x_1,\, x_2 = 0\right)$. A finite element mesh consisting of linear quadrilateral plane

strain (CPE4) elements approximately 1.5 μm in characteristic length was developed for each case using the preprocessing code Cubit. The finite element mesh for Cases B and C comprised approximately 88,000 and 113,000 elements and 92,000 and 120,000 nodes, respectively. The displacements are fixed, i.e., zero at the left edge ($x_1 = 0$) of the model. On the right edge ($x_1 = L_t$) of the model the horizontal displacements are restrained to zero, while the vertical displacements are prescribed as $u_2 = \delta$. As in the previous example, the constitutive model for the matrix material is elastic perfectly-plastic with Young modulus, Poisson ratio, and Mises yield stress of 175 GPa, 0.3, and 1000MPa, respectively. However, note that in this example explicit treatment of the microstructure is made everywhere within the problem domain, rather than in a focused area. This feature of the current model problem is made computationally feasible by virtue of the smaller structural domain.

6.7.3 Coarse Scale Simulations

The CSBVP consists of the same periodic rectangular region L_t by L_p as that considered for the baseline simulations. The coarse scale finite element meshes contain roughly 800 and 1350 of the mixed-field second gradient UELs, and 3400 and 5600 nodes for cases B and C, respectively. The characteristic element size was 15μm for both of these cases. As in the explicit microstructure simulations, the coarse scale UEL simulations employ periodic boundary conditions which consist of, in addition to the aforementioned periodicity of displacements, periodic constraints on the relaxed deformation gradient degrees-of-freedom. Coarse scale simulations were conducted with three sets of length scale parameters listed in Table 14; one being the set from the channel example problem of Sections 6.1-6.6, i.e., $l^e = l^{in} = 140\mu m$, and the other two being pertinent (as will be shown) to Cases B and C, respectively, of this section.

Table 14. Elastic and inelastic length scale parameters considered in this section.

Set	l^e (μm)	l^{in} (μm)
Set 1 (Channel)	140	140
Set 2 (Case B)	36	18
Set 3 (Case C)	72	36

6.7.4 Comparison of Results

A contour plot of the fine scale Mises effective stress field superposed on the deformed configuration for a boundary displacement of $\delta = 10\mu m$ for Case B is shown in Figure 96. Likewise, Mises stress for the coarse scale simulations of Case B employing length scale parameters of $l^e = 36\mu m$ and $l^{in} = 18\mu m$ is shown in Figure 97. Different scales are used for the contour plots in order to make the Figures visually comparable given the local (fine scale) enhancement of stress in the baseline simulations compared to the homogenized coarse scale description of the same. In other words, a particular coarse scale stress implies a larger fine scale stress due to heterogeneity. Accordingly, stresses occurring at different scales are not directly comparable to each other without taking into account this enhancement.

A contour plot of Q_{211}, the second order stress conjugated with the x_1 gradient of F_{21}, superposed on a periodic tiling of the deformed model is shown in Figure 98. The second order stresses form distinct bands in the x_2 direction due to gradients caused by the sharp corners of the elliptical hole. Finally, a comparison of the resultant force versus applied boundary displacement, δ, is shown in Figure 99, for each of the three length scale parameter sets and the baseline explicit microstructure simulation for Case B. The length scale parameters from the Channel example problem do not provide good agreement in the force displacement results. Instead, the set of parameters $l^e = 36\mu m$ and $l^{in} = 18\mu m$ provide the best agreement for Case B.

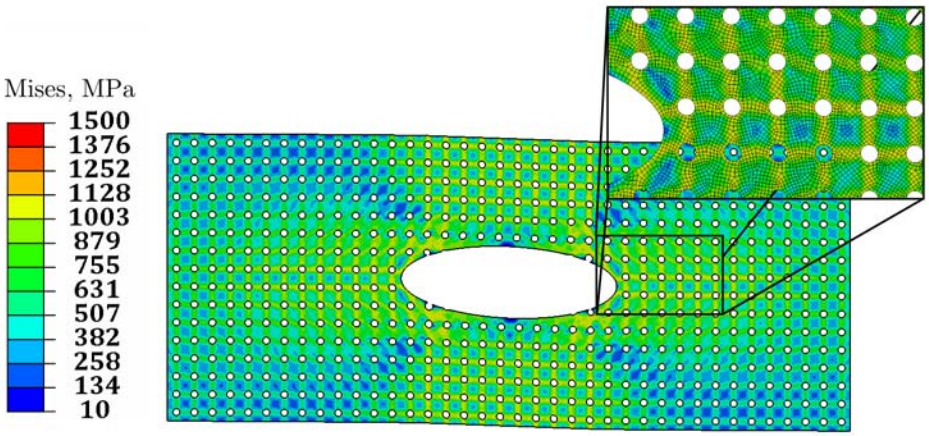

Figure 96. Contour plot of Mises stress for baseline simulation of Case B with explicit treatment of microstructure.

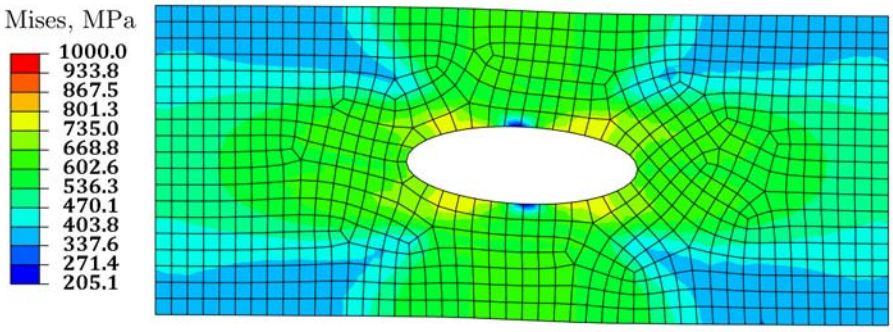

Figure 97. Contour plot of Mises stress for coarse scale (UEL) simulation of Case B with length scale parameters l^e = 36μm and l^{in} = 18μm.

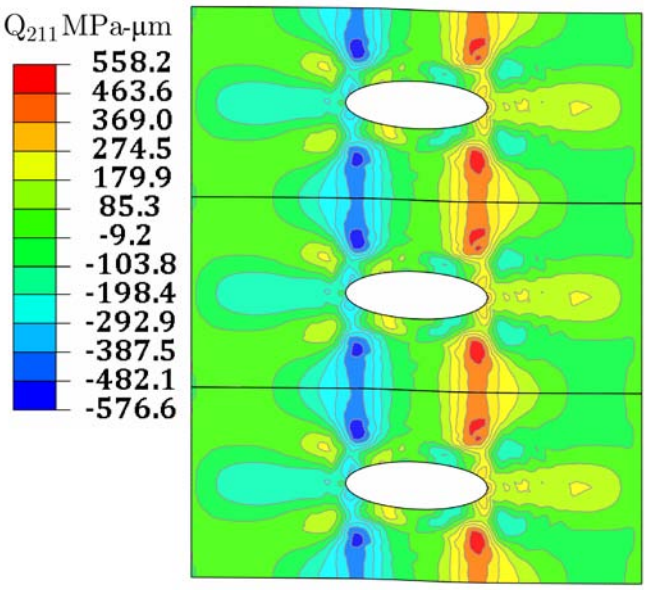

Figure 98. Contour plot of Q_{211} stress for coarse scale (UEL) simulation of Case B with length scale parameters l^e = 36μm and l^{in} = 18μm.

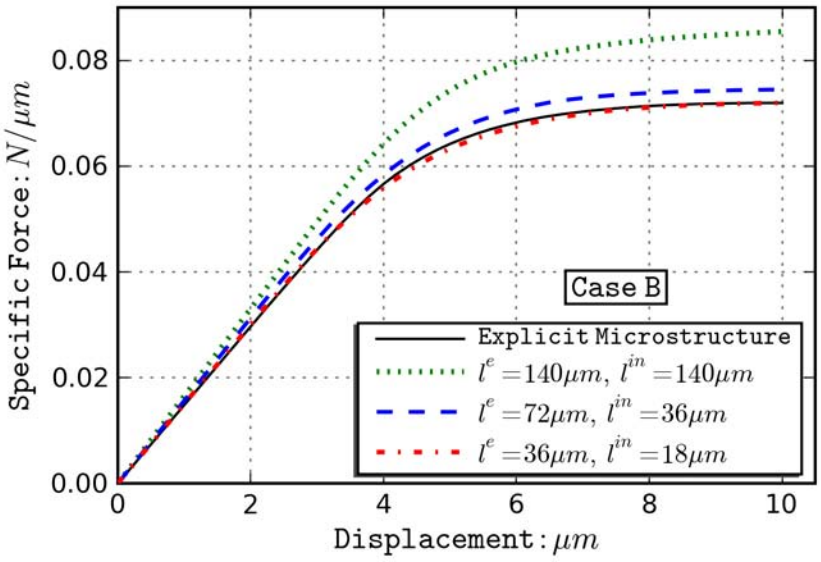

Figure 99. Comparison of resultant force versus applied boundary displacement for Case B.

The contour plot of Q_{211} for Case C in Figure 100 exhibits similar banding although with smoother bands of larger magnitude than for Case B. The resultant force versus applied displacement results for Case C are shown in Figure 101. Neither the length scale parameters used in the Channel example nor those used in Case B provide good agreement. Instead, the set with $l^e = 72\mu m$ and $l^{in} = 36\mu m$ provide the best agreement for Case C. Not only does the significant change in CSBVP affect the appropriate length scale parameters, but even a small variation in the dimensions from Case B to Case C are manifest in the length scale parameters. Thus, the length scale parameters employed in a nonlocal second gradient coarse scale continuum are not intrinsic microstructure parameters and are influenced by the boundary value problem itself. Finally, displacement profiles obtained from the coarse scale UEL simulations employing the length scale parameters relevant to the particular case are shown plotted against those obtained from the simulations of each case with explicit treatment of microstructure in Figure 102. In this figure, the displacement profile is the vertical displacement (u_2) along the periodic boundary at the top (and bottom) edges of the model versus position through the thickness (x_1) of the thin layer.

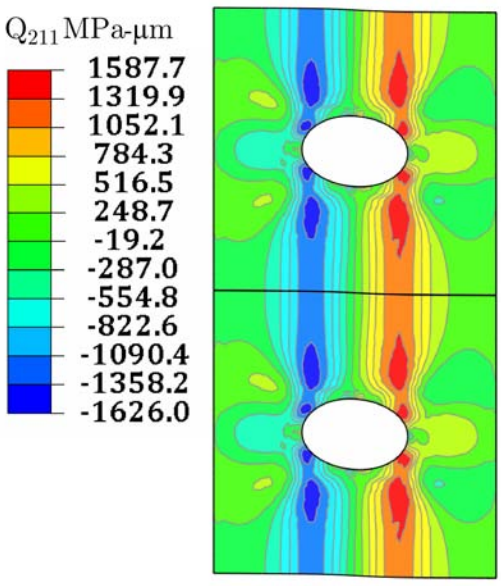

Figure 100. Contour plot of Q_{211} stress for coarse scale (UEL) simulation of Case C with length scale parameters l^e = 72μm and l^{in} = 36μm.

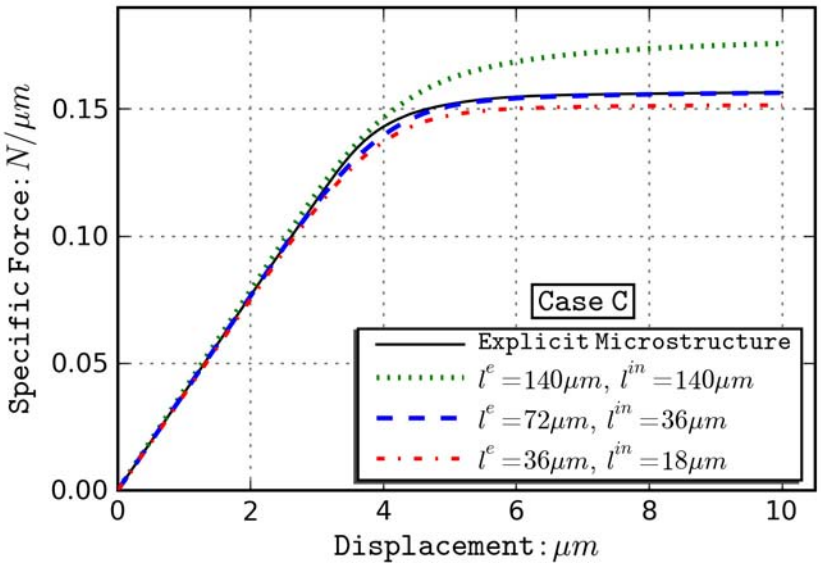

Figure 101. Comparison of resultant force versus applied boundary displacement for Case C.

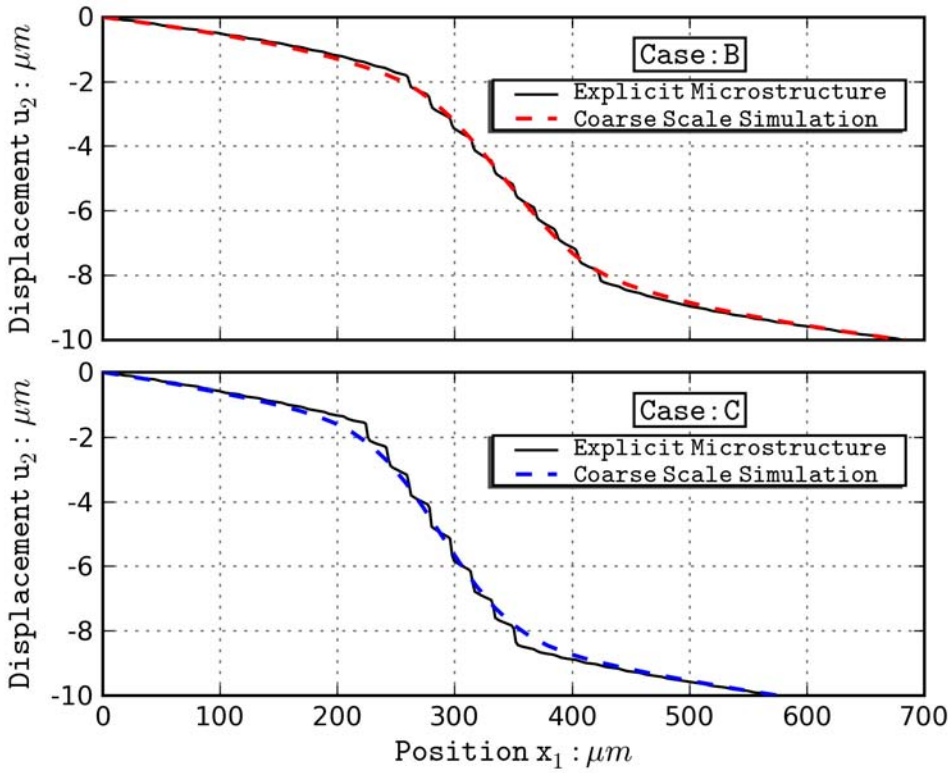

Figure 102. Comparison of vertical displacement profile (u_2 vs x_1) along the top boundary of the periodic region from explicit treatment of microstructure and coarse scale simulations for Case B (top) and Case C (bottom).

6.8 Summary

This chapter presents an example problem where the coarse scale response exhibits dependence on the heterogeneous distribution of features at a finer scale. The multiscale framework developed in Chapter 3 was employed to homogenize the response observed in fine scale rSVE (unit cell) simulations. These simulations were conducted according to the procedures detailed in Chapter 4 to generate data used to identify constitutive parameters. The constitutive approach used in this case reflects a detailed analysis of the porosity dependent orthotropic elastic stiffness parameters. This level of analysis has not been achieved in identifying elastic parameters for second-gradient stiffness response using numerical simulations of the fine scale response. The inelastic part of the response was modeled using an orthotropic extension to the GLPD model, which is based on Gurson's yield surface with a dependence on second order stresses. Performing a second-gradient homogenization to fit the concerned parameters from fine scale unit cell simulations is new to our knowledge. While this constitutive approach is rather crude by the intents and standards of the full framework, it demonstrates a new level of multiscale computational homogenization. Furthermore, advanced strategies for approaching the task of developing inelastic constitutive models are presented in Chapter 7.

One interesting feature of the coarse scale response elucidated by this exercise is the length scale parameters associated with elastic and inelastic features of the second gradient constitutive response. The results from these simulations lead to the conclusion that such parameters are not intrinsic material properties; rather, they are a combination and interaction of the coarse scale geometry and forces with the fine scale heterogeneity and response. Unfortunately, this implies that such length scale parameters are boundary value problem dependent and not amenable to identification solely from rSVE simulations of fine scale response. This conclusion has implication to all nonlocal multiscale models. This issue presents a tremendous opportunity for future research.

CHAPTER VII

ADVANCED CONSTITUTIVE STRATEGIES: PATH FORWARD FOR MULTISCALE MODEL DEVELOPMENT

The example presented in Chapter 6 utilizes a straightforward extension of a classical ISV model to the second gradient case. The parameters of this model were fit to a suite of rSVE simulations that explore the *domain* of state space as defined by the state variables, internal and observable. The disadvantage of this approach is the internal state variables are postulated phenomenologically, but do not relate to the actual kinematics of energy storage exhibited by the fine scale simulation. That is, they may be inferred from numerical observations of fine scale rSVEs, but they cannot be directly measured.

Motivated by a desire to directly represent the kinematics associated with energy storage, attention is now turned to an alternative constitutive strategy. In this approach we seek to construct internal state variables most closely associated with the observed kinematics of fine scale deformation.

7.1 Identification of ISVs from rSVE Simulations

Recall the fine scale multiplicative decomposition within the coarse scale intermediate configuration, i.e., $\tilde{\mathbf{f}} = \tilde{\mathbf{f}}^{e} \cdot \tilde{\mathbf{f}}^{in}$ from Chapter 3. Application of a polar decomposition $\tilde{\mathbf{f}} = \tilde{\mathbf{f}}^{e} \cdot \tilde{\mathbf{f}}^{in} = \tilde{\mathbf{r}} \cdot \left(\tilde{\mathbf{c}}^{e}\right)^{\frac{1}{2}} \cdot \tilde{\mathbf{f}}^{in}$ yields the right elastic Cauchy deformation tensor, $\tilde{\mathbf{c}}^{e}$, for the fine scale material point within the coarse scale intermediate configuration. It is this kinematic quantity that accommodates energy storage due to inelastic incompatibility at the fine scale. The precise details of the field

$$\tilde{\mathbf{c}}^{e}\left(\mathbf{y}_{\mathrm{o}}\right) \forall\, \mathbf{y}_{\mathrm{o}} \in \Omega_{\mathrm{o}}^{\mathrm{x}} \tag{7.1}$$

are directly obtainable from rSVE simulations. Accordingly, that part of coarse scale stored energy strictly due to elastic strains in the coarse scale intermediate configuration is given by

$$\overline{\rho}_{\mathrm{o}}\overline{\psi}^{s}\left(\mathbf{x}_{\mathrm{o}}\right)=\frac{1}{\Omega_{\mathrm{o}}^{x}}\int_{\Omega_{\mathrm{o}}^{x}}\rho_{\mathrm{o}}\tilde{\psi}^{e}\left(\tilde{\mathbf{c}}^{e}(\mathbf{y}_{\mathrm{o}})\right)d\Omega_{\mathrm{o}}^{x} \tag{7.2}$$

As discussed in Chapter 2, a hierarchical modeling approach seeks to reduce the degrees of freedom associated with a particular (fine) scale during transition to the next (coarse) scale. Building a coarse scale constitutive model dependent upon *all* details of the fine scale field description is contrary to the goal of the hierarchical approach and would be more conducive to concurrent methods (cf. Kouznetsova et al., 2002; Kouznetsova et al., 2004; Liu et al., 2006; Ghosh et al., 2007). The goal is to reduce this number of ISVs in the most efficient manner in order to approximate Eq. (7.2). Attention is now turned to maintaining the essence of the fine scale fluctuation gradient field through a finite number of ISVs during the requisite homogenization associated with a scale transition.

7.1.1 Statistical Moments of Fluctuation Field

Perhaps the most immediate quantity associated with $\tilde{\mathbf{c}}^{e}(\mathbf{y}_{\mathrm{o}})$ is its mean field value which, under conditions developed in Chapter 3 vanishes trivially. In this spirit, the following will introduce a non-vanishing norm of $\tilde{\mathbf{c}}^{e}(\mathbf{y}_{\mathrm{o}})$ and show its interpretation as the root mean square eigenstrain. This will motivate incorporation of additional higher-order statistical moments of the fluctuation gradient field as kinematic internal variables. One approach is to compute various statistical moments of the field in order to reduce these details to a few ISVs directly computed from fine scale rSVE simulations, i.e.,

$$\overline{\boldsymbol{\xi}}_{j}=\frac{1}{\Omega_{\mathrm{o}}^{x}}\int_{\Omega_{\mathrm{o}}^{x}}\left(\tilde{\mathbf{c}}^{e}\right)^{j}d\Omega_{\mathrm{o}}^{x} \tag{7.3}$$

where the operation performed within the integrand is the component wise exponentiation to the j^{th} power. As $j\rightarrow\infty$ the probability distribution of residual elastic field within the rSVE can be recreated entirely.

For example, the volume averaged mean of $\tilde{\mathbf{c}}^e(\mathbf{y}_o)$ is computed by integration over the rSVE, i.e.,

$$\bar{\xi}_1 = \frac{1}{\Omega_o^x}\int_{\Omega_o^x} \tilde{\mathbf{c}}^e d\Omega_o^x \tag{7.4}$$

An alternative approach would be to compute the rSVE mean value of the tensor invariants of $\tilde{\mathbf{c}}^e(\mathbf{y}_o)$. This alternative may be useful if the fine scale constitutive response is isotropic, for example.

The root-mean-square (RMS) value of the right elastic deformation tensor, $\tilde{\mathbf{c}}^e(\mathbf{y}_o)$, referred to the intermediate configuration is directly related to the second moment computed according to Eq. (7.3), i.e.,

$$RMS(\tilde{\mathbf{c}}^e) = \sqrt{\frac{1}{\Omega_o^x}\int_{\Omega_o^x}\left(\tilde{c}_{ij}^e\right)^2 d\Omega} = \sqrt{\bar{\xi}_2} \tag{7.5}$$

Therefore, $\bar{\xi}_2$ is related to the standard deviation of the residual elastic deformation tensor in the intermediate configuration, i.e., that part of the fine scale deformation in which energy is stored at the fine scale. This relationship motivates consideration of the statistical significance of $\bar{\xi}_2$. If the residual elastic deformation tensor at the fine scale intermediate configuration was normally distributed, it would be expected that 99.9% of the material in the vicinity of the coarse scale material point has a local fine scale residual elastic deformation tensor three standard deviations from the mean.

Of course, it is likely that $\tilde{\mathbf{c}}^e(\mathbf{y}_o)$ does *not* follow a normal distribution. Consequently, the relationship between the RMS value of $\tilde{\mathbf{c}}^e(\mathbf{y}_o)$ and the 2nd statistical moment of the associated probability density motivates capturing higher order statistical moments of the distribution, e.g.,

$$\bar{\xi}_2 = \frac{1}{\Omega_o^x}\int_{\Omega_o^x}\left(\tilde{\mathbf{c}}^e\right)^2 d\Omega_o^x = \left(RMS(\tilde{\mathbf{c}}^e)\right)^2 \tag{7.6}$$

$$\bar{\xi}_3 = \frac{1}{\Omega_o^x}\int_{\Omega_o^x}\left(\tilde{\mathbf{c}}^e\right)^3 d\Omega_o^x \tag{7.7}$$

$$\bar{\boldsymbol{\xi}}_4 = \frac{1}{\Omega_{\mathrm{o}}^x}\int_{\Omega_{\mathrm{o}}^x}\left(\tilde{\mathbf{c}}^e\right)^4 d\Omega_{\mathrm{o}}^x \tag{7.8}$$

These statistical-moments enable the following descriptors of the probability distribution of $\tilde{\mathbf{c}}^e(\mathbf{y}_{\mathrm{o}})$ within the rSVE. The variance of $\tilde{\mathbf{c}}^e(\mathbf{y}_{\mathrm{o}})$, given by (7.6), is indicative of the overall heterogeneity of the fine-scale response. The component-wise square root of the variance is the aforementioned RMS value of $\tilde{\mathbf{c}}^e(\mathbf{y}_{\mathrm{o}})$. The third statistical moment is used to compute skewness according to Eq. (7.9) which is one indicator of a lack of normality in the underlying probability distribution. Kurtosis, defined in Eq. (7.10), is another indicator that a probability distribution is not normal and is computed from the 4th statistical moment.

$$SKEW\left(P(\tilde{\mathbf{c}}^e)\right) = \frac{\bar{\boldsymbol{\xi}}_3}{(\bar{\boldsymbol{\xi}}_2)^{\frac{3}{2}}} \tag{7.9}$$

$$KURT\left(P(\tilde{\mathbf{c}}^e)\right) = \frac{\bar{\boldsymbol{\xi}}_4}{(\bar{\boldsymbol{\xi}}_2)^2} - 3 \tag{7.10}$$

Skewness indicates an expectation that a component value offset a certain distance from the mean will not occur with the same likelihood as a value offset the same distance in opposite direction from the mean. Or, in this case (with zero mean fluctuation), a positive value of skewness indicates a higher likelihood of an extreme positive fluctuation compared to the same extreme negative fluctuation; however, smaller negative fluctuations occur more often than small positive fluctuations for the same positive value of skewness. Positive skewness indicates an elongated tail on the positive side of the variable mean when compared to a normal probability distribution. Kurtosis is a measure of the 'peakedness' of a probability distribution. Compared to a normal distribution, there are more occurrences of values near the mean and extreme values for positive kurtosis. Values of kurtosis less than zero indicate a wider flattened peak and thinner tails of the probability density, such that values near the mean and extreme values are relatively unlikely compared to a normally distributed variable.

One can envision a variety of heterogeneous fields which have the same coarse scale kinematic description (**F**, **G**) and the same fine scale variance, but with dramatically different values of kurtosis and skewness. A few examples are illustrated in Figure 103 with the computed statistical

descriptors listed in Table 15. A histogram (blue) along with a normal probability distribution function (red) with zero mean and variance of 0.0625 is included in the inset of each example.

From a modeling perspective, these statistical moments give an indication of the level of approximation involved with the transition from the fine to coarse scale. Finally, and perhaps most importantly, from a purely kinematic standpoint, $\bar{\boldsymbol{\xi}}_j$ computed according to Eq. (7.3) are simply a measure of the sub-scale heterogeneity of deformation in the neighborhood of the coarse scale material point. Logically, the same treatment of any heterogeneous field variable can be performed to obtain additional ISVs and associated statistical field descriptions.

Table 15. Statistical descriptors of fluctuation patterns illustrated in Figure 103.

Fluctuation Pattern	**Mean**	**Variance**	**Skewness**	**Kurtosis**
(A) Checker Board	0.000	0.0625	0.0014	-1.848
(B) Stripe	0.000	0.0625	0.0156	1.857
(C) Grooves	0.000	0.0625	-1.413	0.2304
(D) Bessel	0.000	0.0625	0.2602	1.0308

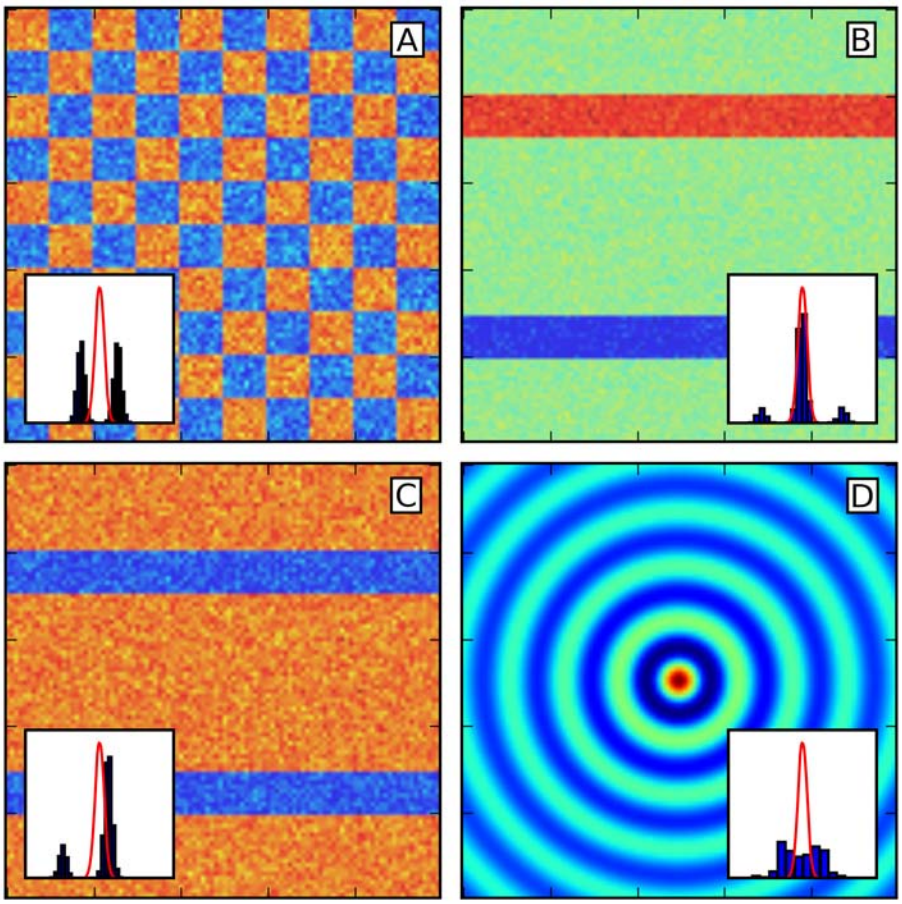

Figure 103. Example component fluctuation fields and their associated histograms.

7.1.2 Principal Component Analysis

Another approach is through the use of principal component analysis. Assuming one can construct a suite of rSVE simulations which thoroughly spans the domain of state space, then we can collect the data from each realization of the field given by Eq. (7.1). Suppose the total number of rSVE states available to analyze is *n*. They are samples from different points in time and can be associated with different coarse scale deformation histories. Furthermore, the spatial field in Eq. (7.1) is sampled at *d* fixed locations in space.

Without loss of generality, we assume that the fine scale free energy depends only upon the first two invariants of fine scale elastic strain, $\tilde{I}_1^e = \mathrm{tr}\left(\tilde{\boldsymbol{\varepsilon}}^e\right)$ and $\tilde{I}_2^e = \mathrm{tr}\left(\tilde{\boldsymbol{\varepsilon}}^e \cdot \tilde{\boldsymbol{\varepsilon}}^e\right)$, for example, through the potential function $\rho_{\mathrm{o}}\tilde{\psi}^e = \frac{1}{2}\lambda(\tilde{I}_1^e)^2 + \mu\tilde{I}_2^e$. This case reflects a microstructure whose fine scale is purely dissipative since there is no intrinsic fine scale mechanism for energy storage, e.g., elastic perfectly-plastic behavior. In such a case, heterogeneous response may still develop due to a spatially varying fine scale yield stress, for example.

From the rSVE simulations the fine scale invariants are computed and assembled in a data matrix, i.e.,

$$\left[X\right] = \begin{pmatrix} \tilde{I}_1^e(\mathbf{y}_1^{\mathrm{o}})_{n=1} & \tilde{I}_2^e(\mathbf{y}_1^{\mathrm{o}})_{n=1} & \tilde{I}_1^e(\mathbf{y}_2^{\mathrm{o}})_{n=1} & \tilde{I}_2^e(\mathbf{y}_2^{\mathrm{o}})_{n=1} & \cdots & \tilde{I}_2^e(\mathbf{y}_d^{\mathrm{o}})_{n=1} \\ \tilde{I}_1^e(\mathbf{y}_1^{\mathrm{o}})_{n=2} & \tilde{I}_2^e(\mathbf{y}_1^{\mathrm{o}})_{n=2} & \tilde{I}_1^e(\mathbf{y}_2^{\mathrm{o}})_{n=2} & \tilde{I}_2^e(\mathbf{y}_2^{\mathrm{o}})_{n=2} & \cdots & \tilde{I}_2^e(\mathbf{y}_d^{\mathrm{o}})_{n=2} \\ \vdots & \vdots & \vdots & \vdots & \ddots & \\ \tilde{I}_1^e(\mathbf{y}_1^{\mathrm{o}})_{n=N} & \tilde{I}_2^e(\mathbf{y}_1^{\mathrm{o}})_{n=N} & \tilde{I}_1^e(\mathbf{y}_2^{\mathrm{o}})_{n=N} & \tilde{I}_2^e(\mathbf{y}_2^{\mathrm{o}})_{n=N} & & \tilde{I}_2^e(\mathbf{y}_d^{\mathrm{o}})_{n=N} \end{pmatrix} \tag{7.11}$$

The column mean values of the data array are removed from each column and the covariance matrix is formed by

$$\left[Cov\right] = \left[X\right]^T\left[X\right] \tag{7.12}$$

An eigenvalue decomposition is performed on the covariance matrix, i.e.,

$$\left[Cov\right] = \left[\Phi\right]\left[\Lambda\right]\left[\Phi\right]^T \tag{7.13}$$

Together, the eigenvectors that compose columns of $\left[\Phi\right]$ form a complete orthogonal basis for the field data in (7.11). The eigenvectors associated with the largest eigenvalues represent the spatial distribution of the largest contributions to variance in the original field over all N increments. In order to reduce the number of variables defining the fine scale field of elastic invariants, only $q < 2d$ significant eigenvectors are retained to form $\left[\hat{\Phi}\right]$. Then we compute time histories of the ISVs that approximate the temporal field variations by

$$\overline{\xi}_i\left(t_n\right) = X_{nj}\hat{\Phi}_{ji} \tag{7.14}$$

Reconstruction of the approximated field is achieved by

$$\hat{X}_i\left(t_n\right) = \overline{\xi}_j\left(t_n\right)\hat{\Phi}_{ij} \tag{7.15}$$

such that, for this example, $\tilde{I}_1^e\left(t_n, \mathbf{y}_i^o\right) = \hat{X}_{n,2i-1} = \overline{\xi}_j\left(t_n\right)\hat{\Phi}_{2i-1,j}$ and $\tilde{I}_2^e\left(t_n, \mathbf{y}_i^o\right) = \overline{\xi}_j\left(t_n\right)\hat{\Phi}_{2i,j}$, which can be substituted back into the fine scale elastic free energy potential in order to evaluate the coarse scale stored energy potential in Eq. (7.2). Integration over the rSVE is performed numerically, for example, by Gauss quadrature using the original rSVE finite element mesh. This novel approach to developing hierarchical state functions provides a framework to directly compute meaningful kinematic ISVs from fine scale rSVE simulations and provides a scale transition for the stored free energy.

7.2 Evolution Kinetics

After identification of the set of internal state variables and development of the state function, all that remains to completely specify the constitutive behavior is the prescription of a set of kinetic relations that govern ISV evolution, i.e.,

$$\begin{aligned} \tilde{\mathbf{D}}^{in} &= \mathrm{K}_{\tilde{\mathbf{D}}^{in}}(\tilde{\mathbf{E}}^e, \tilde{\mathbf{\Gamma}}^e, \overline{T}, L_v(\tilde{\mathbf{\Gamma}}^{in}), L_v(\overline{\xi}^{(j)})) \\ L_v(\tilde{\mathbf{\Gamma}}^{in}) &= \mathrm{K}_{\dot{\tilde{\mathbf{\Gamma}}}^{in}}(\tilde{\mathbf{E}}^e, \tilde{\mathbf{\Gamma}}^e, \overline{T}, \tilde{\mathbf{D}}^{in}, L_v(\overline{\xi}^{(j)})) \\ L_v(\overline{\xi}^{(k)}) &= \mathrm{K}_{\dot{\overline{\xi}}^{(k)}}(\tilde{\mathbf{E}}^e, \tilde{\mathbf{\Gamma}}^e, \overline{T}, \tilde{\mathbf{D}}^{in}, L_v(\tilde{\mathbf{\Gamma}}^{in}), L_v(\overline{\xi}^{(j)})) \end{aligned} \tag{7.16}$$

These relations can be postulated in any of a number of ways so long as they obey the governing equations outlined previously and are consistent with observed behavior. A yield or threshold surface (generally distinct from the flow potential), $f = f\left(\tilde{\mathbf{S}}, \tilde{\mathbf{Q}}, T, \overline{\boldsymbol{\beta}}_{(k)}\right)$, can be used to define a domain inside which inelastic evolution does not occur. The framework of a flow potential (or combination of pseudo-potentials for various mechanisms) is a suitable, although inessential, format for the constitutive behavior. Alternatively, the kinetic equations for evolution of the internal state variables can be formed explicitly with (or without) coupling to the extent desired.

It would be convenient if there were an algorithmic approach to this step. For example, a dissipation function that is numerically fit to the results of a large suite of rSVE simulation results and then converted into a force potential suitable for Legendre-Fenchel transformation to a flow potential. From this flow potential all evolution equations could be derived, and one would have a rather automated process for transitioning between continuum level scales. However, the

dissipation function will all too often be of a form that cannot be transformed in such a manner. In order to preserve the generality of this hierarchical multiscale framework, we do not specify *a priori* the details of the evolution Eq. (7.16). The only requirement is that they satisfy the coarse scale CD inequality and the principle of scale invariance of dissipation.

Within the strategy being presented here, a modeling approach that treats the kinetics of evolution as a black-box to some extent is envisioned. There are many dynamical system modeling approaches which can be used to model the trajectory of microstructure, i.e., its evolution history, through state space. One example is through the use of artificial neural networks (ANN) which is presented in the context of the following example problem.

7.3 One DOF Example Problem: Heterogeneous Array of Bars

The multiscale constitutive strategy presented here is best illustrated by means of a relatively simple example. The pedagogical nature of the examples in this chapter motivates a simplistic and relatively limited adaptation of the general framework; however the overarching principles are all adhered to and, more importantly, the example provides a means to bridge to more useful constitutive approaches. A diagram of this example problem is presented in Figure 104. On the left side is an array of five bars of varying length, L_i, drawn in the reference configuration, Ω_o. The bars are connected to a rigid linkage which constrains the displacement of each of the bars to be equal to the linkage displacement, i.e., $\delta_i = \delta$, and this is referred to as the total displacement. At any given time under some applied traction, T, the current configuration, Ω, does not coincide (in general) with the reference configuration and is drawn in Figure 104 by dashed lines. Simultaneously, the system possesses an intermediate configuration (in the sense described in Chapter 3) associated with the removal of external tractions, T. This configuration represents an elastic unloading from Ω to $\tilde{\Omega}$. Recognize that each discrete bar in this system takes on the role of a fine scale material point located at a particular spatial position in the vicinity of a coarse scale rSVE.

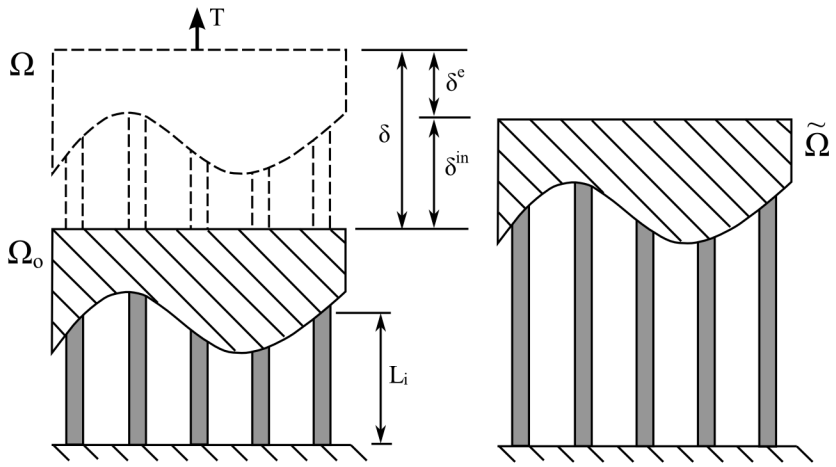

Figure 104. Diagram of five bar heterogeneous system.

7.3.1 Analytical Mechanics of Problem

Out of convenience each bar in the system has cross sectional area, $A_i = \frac{A}{N}$. Axial strain at the coarse scale is defined as $\bar{\varepsilon} = \frac{\delta}{L}$ and at the fine scale $\varepsilon_i = \frac{\delta}{L_i}$, where the system length is defined out of convenience as $L = \frac{1}{N}\sum_{i=1}^{N} L_i$. To kinematically link the fine and coarse scale, a multiscale decomposition of the strain field is used, i.e.,

$$\varepsilon_i = \bar{\varepsilon} + \hat{\varepsilon}_i \tag{7.17}$$

where $\hat{\varepsilon}_i$ is the local fluctuation strain associated with the fine scale location, *i*. Note that (7.17) is a simplistic analog to Eq. (3.2) for the more general framework presented in Chapter 3. The principle of kinematic consistency requires that there is zero projection of the fluctuation field onto coarse scale kinematic variables, thus,

$$\frac{1}{N}\sum_{i=1}^{N} \hat{\varepsilon}_i = 0 \tag{7.18}$$

The combination of (7.17), (7.18), and the kinematic definitions above result in

$$\varepsilon_i = c_i \overline{\varepsilon} \tag{7.19}$$

where the local geometric constant $c_i = \frac{L}{L_i}$ has been introduced and is subjected to the constraint

$$\frac{1}{N}\sum_{i=1}^{N} c_i = 1 \tag{7.20}$$

The coarse scale (nominal) stress is defined as the net traction force divided by the net system cross-sectional area,

$$\overline{\sigma} = \frac{T}{A} \tag{7.21}$$

At this point, scale invariance of momentum is imposed via the principle of virtual velocities,

$$\sum_{i=1}^{N} A_i \sigma_i \dot{\delta}^* = A\overline{\sigma}\dot{\delta}^* \tag{7.22}$$

where $\dot{\delta}^*$ is the virtual velocity. Equation (7.22) and the equality of each bars cross sectional area result in the following relationship between coarse and fine scale stresses, i.e.,

$$\overline{\sigma} = \frac{1}{N}\sum_{i=1}^{N} \sigma_i \tag{7.23}$$

Elastic recovery to the coarse scale intermediate configuration enables the decomposition of coarse scale strain into elastic and inelastic parts, i.e.,

$$\overline{\varepsilon} = \overline{\varepsilon}^e + \overline{\varepsilon}^{in} \tag{7.24}$$

where the elastic and inelastic strains are defined by $\overline{\varepsilon}^e = \delta^e \big/ L$ and $\overline{\varepsilon}^{in} = \delta^{in} \big/ L$, respectively. Note that this example is adopting additive decomposition and presumes small deformation. At the fine scale, the total strain of a bar within the coarse scale intermediate configuration is

$$\tilde{\varepsilon}_i = c_i \overline{\varepsilon}^{in} \tag{7.25}$$

and can be decomposed into $\tilde{\varepsilon}_i = \tilde{\varepsilon}_i^e + \tilde{\varepsilon}_i^{in}$. A set of kinematic ISVs associated with the storage of energy is now introduced, namely $\tilde{\varepsilon}_i^e$. Associated with each of these ISVs is a local internal force or "material force" associated with the evolution of microstructure, i.e.,

$$\tilde{\sigma}_i = E_i \tilde{\varepsilon}_i^e \tag{7.26}$$

An internal microforce balance is introduced in light of the result of PVV expressed in (7.23) and the traction-free definition of the intermediate configuration, i.e.,

$$\sum_{i=1}^{N} \tilde{\sigma}_i = 0 \tag{7.27}$$

In the current configuration, the fine scale elastic strain can now be decomposed according to

$$\varepsilon_i^e = \tilde{\varepsilon}_i^e + c_i \overline{\varepsilon}^e \tag{7.28}$$

and the fine scale stress distribution can be decomposed into the microforce and a projection of the coarse scale traction onto the fine scale, i.e.,

$$\sigma_i = \tilde{\sigma}_i + c_i \overline{\sigma} \tag{7.29}$$

Scale invariance of energy asserts that the total coarse scale free energy reflect all contributions from the fine scale. For this system, the fine scale free energy in each bar is $\psi_i = \frac{1}{2} E(\varepsilon_i^e)^2 = \frac{1}{2} E(\tilde{\varepsilon}_i^e + c_i \overline{\varepsilon}^e)^2$. For this discrete system of bars the analog to integration is summation, accordingly the coarse scale free energy is obtained from the contributions of each fine scale bar, i.e.,

$$\begin{aligned} \overline{\psi} &= \frac{1}{NLA} \sum_{i=1}^{N} A_i L_i \psi_i \\ &= \frac{1}{2} E(\overline{\varepsilon}^e)^2 + \frac{1}{N} \sum_{i=1}^{N} \frac{1}{2} \frac{E}{c_i} (\tilde{\varepsilon}_i^e)^2 \end{aligned} \tag{7.30}$$

permitting the decomposition of coarse scale free energy into elastically recoverable and stored components, i.e.,

$$\overline{\psi} = \overline{\psi}^e + \overline{\psi}^s \tag{7.31}$$

where the elastically recoverable free energy is $\overline{\psi}^e = \frac{1}{2} E(\overline{\varepsilon}^e)^2$ and the energy stored due to rearrangement of the microstructure is $\overline{\psi}^s = \frac{1}{N} \sum_{i=1}^{N} \frac{1}{2} \frac{E}{c_i} (\tilde{\varepsilon}_i^e)^2$. From thermodynamics of

irreversible processes and ISV theory presented in Chapter 3, the thermodynamic driving stresses are determined as,

$$\bar{\sigma} = \frac{\partial \bar{\psi}}{\partial \bar{\varepsilon}^e} = E\bar{\varepsilon}^e \tag{7.32}$$

$$q_i = \frac{\partial \bar{\psi}}{\partial \tilde{\varepsilon}_i^e} = \frac{E\tilde{\varepsilon}_i^e}{Nc_i} = \frac{\tilde{\sigma}_i}{Nc_i} \tag{7.33}$$

Note in particular, that the thermodynamic driving force associated with the i^{th} ISV, q_i, is related but not equal to the microforce associated with that same mechanism, i.e., $\tilde{\sigma}_i$. Scale invariance of dissipation is addressed by requiring the rate of dissipation at the coarse scale be equal to summation of each of the fine scale contributions. The rate energy is dissipated at the fine scale is $\Pi_{mec,i} = \sigma_i \dot{\tilde{\varepsilon}}_i^{in}$ and the mean contribution to the coarse scale is computed by $\bar{\Pi}_{mec} = \frac{1}{NLA}\sum_{i=1}^{N} A_i L_i \Pi_i$. After substitution of the fine scale stress and strain decompositions into the fine scale dissipation rate and summation into the mean coarse scale dissipation rate, one finds

$$\begin{aligned} \bar{\Pi}_{mec} &= \frac{1}{N}\sum_{i=1}^{N} \frac{1}{c_i}\left(\tilde{\sigma}_i + c_i\bar{\sigma}\right)\left(c_i\dot{\bar{\varepsilon}}^{in} - \dot{\tilde{\varepsilon}}_i^e\right) \\ &= \bar{\sigma}\dot{\bar{\varepsilon}}^{in} - \frac{1}{N}\sum_{i=1}^{N}\frac{\tilde{\sigma}_i\dot{\tilde{\varepsilon}}_i^e}{c_i} \end{aligned} \tag{7.34}$$

so that the expected form of dissipation function for a rate-independent dissipative system (Cf. Chapter 3) is recovered, i.e.,

$$\bar{\Pi}_{mec} = \bar{\sigma}\dot{\bar{\varepsilon}}^{in} - \sum_{i=1}^{N} q_i \dot{\tilde{\varepsilon}}_i^e \tag{7.35}$$

Note that the first term on the RHS of Eq. (7.35) reflects contribution from the coarse scale inelastic power, while the last term on the RHS accounts for the rate that energy is stored in each of the bars, i.e., rate of energy storage at fine scale. Evolution equations for the ISVs that reflect the kinetics of this irreversible system are developed through micromechanical analysis. First, one recognizes that there exists a threshold in generalized stress or, equivalently, generalized strain space that defines a region of purely reversible (elastic) response. Within this region none

of the bars will yield and there is no microstructural evolution. For each mechanism the fine scale elastic threshold is identified as $f_i = \left|\sigma_i\right| - k \leq 0$, which reflects that the particular bar will not yield if the absolute value of the total stress in that bar, σ_i, is less than the bar's fine scale yield stress, *k*. From previous results, a substitution is made enabling

$$f_i = \left|c_i\overline{\sigma} + \tilde{\sigma}_i\right| - k \leq 0 \tag{7.36}$$

At the coarse scale, the entire system will remain elastic if and only if all mechanisms in the system remain elastic permitting the coarse scale threshold function to be written as

$$\overline{f}^{\sigma} = \max\left(\left|c_i\overline{\sigma} + \tilde{\sigma}_i\right|\right) - k \leq 0 \tag{7.37}$$

in generalized stress space or, equivalently,

$$\overline{f}^{\varepsilon} = \max\left(\left|c_i\overline{\boldsymbol{\varepsilon}}^{e} + \tilde{\boldsymbol{\varepsilon}}_i^{e}\right|\right) - \tfrac{k}{E} \leq 0 \tag{7.38}$$

in generalized strain space. The stress space expression for the threshold function (7.37) can be rewritten in the form of classical multisurface plasticity, i.e.,

$$\overline{f} = \max\left(\left|\overline{\sigma} - b_i\right|\right) - R_i \leq 0, \tag{7.39}$$

where the *i*th backstress is $b_i = -\dfrac{\tilde{\sigma}_i}{c_i}$ and the radius of the *i*th yield surface is $R_i = \dfrac{k}{c_i}$. This connection with multisurface plasticity affirms the concept that heterogeneous inelastic response at the fine scale will manifest with some extent of kinematic hardening at higher scales and shows that commonly accepted phenomenology for backstress, such as dislocation pile-up, for example, need not be the only physical mechanism for such behavior.

While this multi-mechanism threshold is consistent with classical multisurface plasticity, the evolution equations do not follow Iwan or Mroz type rules. From previously established kinematic relations,

$$d\tilde{\varepsilon}_i = d\tilde{\varepsilon}_i^{e} + d\tilde{\varepsilon}_i^{in} = c_i d\overline{\varepsilon}^{in} \tag{7.40}$$

At the coarse scale, irreversible evolution occurs for $\overline{f}^{\sigma} = 0$. For each mechanism there are two distinct cases of evolution, namely, active for which $f_i = 0$ and passive $f_i < 0$. Note that even though a particular mechanism may not be active it will still evolve, in general, for coarse scale irreversible deformation. In such passive cases the fine scale inelastic strain is unchanging and from (7.40) the ISV evolution is

$$d\tilde{\varepsilon}_i^e = c_i d\overline{\varepsilon}^{in} \tag{7.41}$$

On the other hand, for an active mechanism the elastic-perfectly plastic nature of each mechanism in this example dictates that $d\varepsilon_i = \cancel{d\varepsilon_i^e} + d\varepsilon_i^{in} = c_i d\overline{\varepsilon}$, and when substituted into (7.40) one finds that $d\tilde{\varepsilon}_i^e = c_i d\overline{\varepsilon}^{in} - c_i d\overline{\varepsilon} = -c_i d\overline{\varepsilon}^e$. Combining this result for the active case with (7.41) from the passive case, the evolution equations are obtained, i.e.,

$$d\tilde{\varepsilon}_i^e = \begin{cases} c_i d\overline{\varepsilon}^{in} & if\ \overline{f}^{\sigma} = 0, f_i < 0 \quad (\text{passive}) \\ -c_i d\overline{\varepsilon}^e & if\ \overline{f}^{\sigma} = 0, f_i = 0 \quad (\text{active}) \end{cases} \tag{7.42}$$

In the context of multisurface plasticity, the **active** case resulting in a *decrease* in the ISV associated with the *i*th mechanism corresponds to an **increase in the equivalent corresponding backstress.** This behavior is consistent with classical multisurface plasticity. However, in the passive case the equivalent backstress *decreases* for this system, while according to classical multisurface plasticity theories (e.g. Mroz) a non-active mechanism sees no change in backstress (stationary yield surface.) Passive evolution of ISVs is due to the microforce balance imposed within the intermediate configuration, thus resulting in a non-associative microstructure evolution.

7.3.2 Direct Fine Scale Simulations

For this example problem, a numerical simulation of the direct fine scale system was developed in python.

1.) Initialize system: Define parameters for each bar in system

$$E = 10000\,MPa, k = 200\,MPa,$$
$$c = \begin{bmatrix} 0.75 & 0.80 & 0.95 & 1.20 & 1.30 \end{bmatrix}$$

For each increment in the strain history perform steps 2-8, beginning by performing the following for each bar in the system:

2.) Update the fine scale total kinematic strain based on (7.19).

3.) Satisfy the local inelastic threshold function, $f_i = \left|\sigma_i\right| - k \leq 0$, by solving for local plastic strain.

4.) Compute local stress and add contribution to global stress according to (7.23).

Then return the coarse scale stress for this increment and

5.) Create a copy of each bar in the system

6.) Unload duplicated system to a coarse scale stress free configuration (follow steps 2-5 until stress is zero) in order to determine state variables, i.e., $\bar{\varepsilon}^e$ and $\tilde{\varepsilon}_i^e$.

7.) Store the total strain $\bar{\varepsilon}$, elastic strain $\bar{\varepsilon}^e$, inelastic strain, $\bar{\varepsilon}^{in}$, and state variables, $\tilde{\varepsilon}_i^e$, and proceed to next increment (GOTO 2).

These steps were carried out in a python simulation script for a baseline case to inspect the results of the simulation tool and then for a large simulation suite as discussed subsequently. For the baseline case, the system response to a sawtooth strain history as shown in Figure 105 was simulated. The computed coarse scale stress versus strain is plotted in Figure 106.

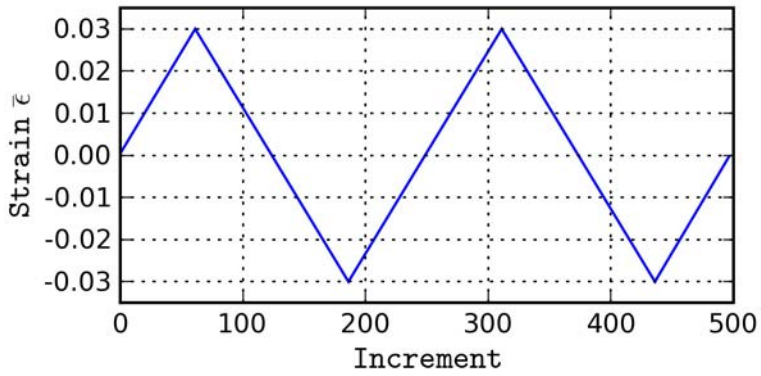

Figure 105. Strain time history for baseline case.

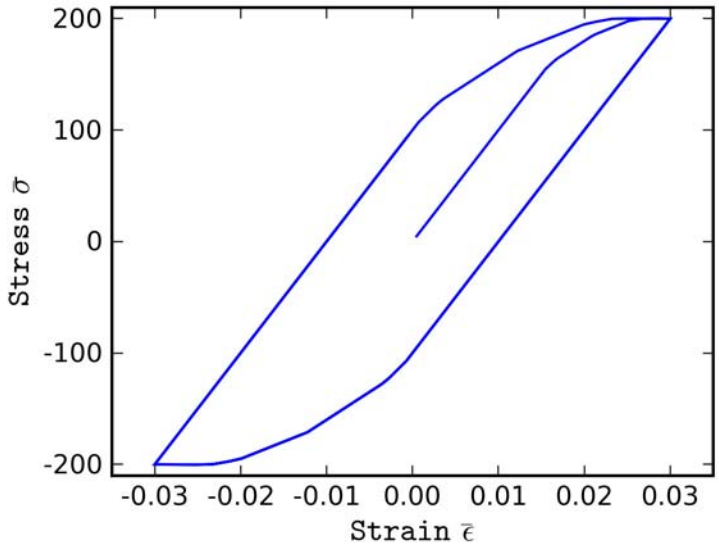

Figure 106. Coarse scale stress versus strain for baseline case.

The sawtooth strain history was used to demonstrate the kinematic hardening associated with the heterogeneous evolution of the system state variables, i.e., the residual elastic strains in the coarse scale stress free configuration. The corresponding kinematic hardening is evident in Figure 106 where after intial yielding the system saturates at a coarse scale yield stress of 200 MPa and upon reverse loading initiates yielding around 108 MPa. The presence of a saturation yield stress is due to the omission of a bar that cannot attain perfectly plastic behavior. The results of this case can be made more general by including varying local yield coefficients (or even isotropic or kinematic local hardening mechanisms). The piecewise linear stress-strain response is indicative of the underlying multiple mechanism threshold surfaces.

The history of ISV evolution is shown in Figure 107 and the associated stored energy history is shown in Figure 108. The ISVs evolve according to the analytical expression in Eq. (7.42). In particular, the transition from passive to active state of evolution for each of the five mechanisms is apparent in the ISV history, i.e., the slope of the ISV evolution changes within a region of constant strain rate (loading direction). As expected, evolution of all state

variables ceases under either purely elastic response or purely plastic (i.e., saturated hardening) behavior.

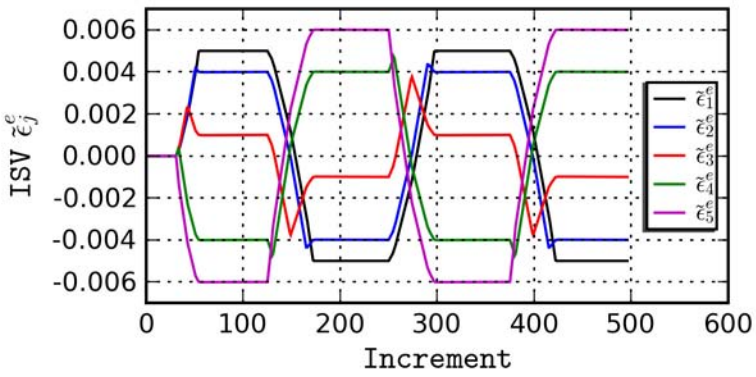

Figure 107. Evolution of ISVs for baseline case.

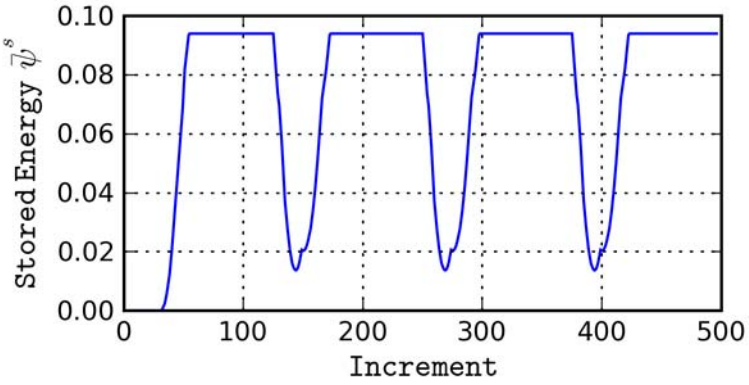

Figure 108. Stored free energy time history for baseline case.

The stored energy is zero initially, reflecting the virgin state of the system. In reality, initial residual elastic strain fields ought to be considered for realistic behavior of real material systems. Stored energy increases or decreases whenever coarse scale kinematic hardening is

occurring. Note, however, that whether the stored energy increases or decreases is not correlated with the sign of loading or unloading. After inelastic deformation causes structural rearrangement of the system, the heterogeneous nature of subsequent evolution of the ISVs causes the stored energy to not be able to return to zero. There is insufficient simultaneity of ISVs returning to a local virgin state of zero which implies that the system cannot be restored to its virgin state without external, independent means of rearrangement.

A suite of simulations was conducted in order to develop a dataset of state variable response that sufficiently spanned the entire valid domain of state space. For each of these simulations a unique coarse scale strain history was specified based on the template shown in Figure 109. The strain history is composed of a periodic sawtooth parameterized by its amplitude, $\bar{\varepsilon}_a$, and mean, $\bar{\varepsilon}_m$.

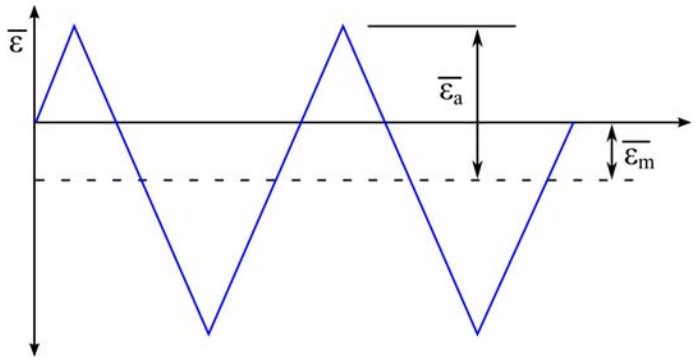

Figure 109. Periodic sawtooth time history used for simulation suite.

A total of 35 unique combinations of parameters sampled from,

$$\bar{\varepsilon}_a \in \left\{2.00 \quad 2.25 \quad 2.50 \quad 2.75 \quad 3.00\right\} \times 10^{-2}$$
$$\bar{\varepsilon}_m \in \left\{-2.0 \quad -1.0 \quad -0.5 \quad 0.0 \quad 0.5 \quad 1.0 \quad 2.0\right\} \times 10^{-2}$$

were used to develop the simulation database. The stress versus strain results from all of these simulations are included in Figure 110.

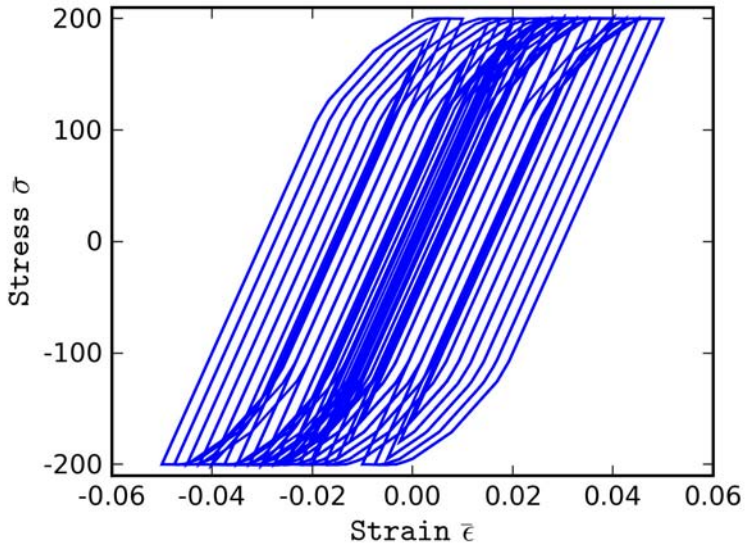

Figure 110. Stress versus strain for all simulations.

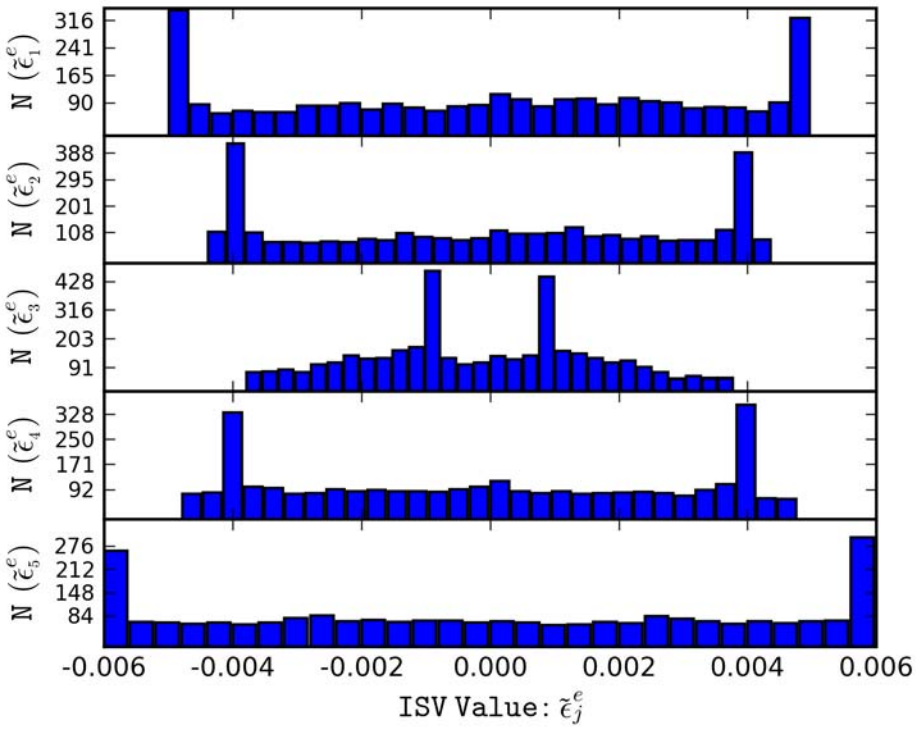

Figure 111. Histograms of ISV values for inelastic increments of all simulations.

Histograms of the values of all state variables in Figure 111 shows symmetry about zero, presumably implying symmetry in tension and compression response. Symmetric bimodal peaks in the histograms indicate the values of state variables attained at saturation, the regions where hardening is exhausted, and there is no further rearrangement of microstructure. The relatively even distribution of values away from these peaks is an indicator (although not a guarantee) that the domain of state space has been spanned uniformly, with the exception of the saturation regions. Saturation presents a beneficial nicety in developing the elastic threshold function. That is, based on our understanding of the underlying mechanics of this problem, the histogram peaks in Figure 111 could be used in conjunction with a histogram of elastic strain and correlation map to directly identify parameters for the threshold function.

Partial derivatives of the ISVs with respect to inelastic strain were computed as a descriptor of the inelastic response of the system. These partial derivative histories, each comprising all inelastic increments from one simulation, were concatenated together to create a single "quasi-sequential" inelastic increment history. Figure 112 contains a contour plot reflecting the relative occurrence of specific values of each partial derivative. Specifically, each vertical slice along the x-axis represents a histogram of partial derivative (response) data within a window of 500 increments beyond that x-location. The distinct bands allude to the existence of discrete sets of inelastic response behavior that correspond to different sub-domains of state space. Based on the presence of these regions of constant partial derivatives, a data analysis step was performed to identify unique sets of partial derivatives and the number of occurrences of each unique set. The algorithm used to identify the unique responses was

$$
\begin{aligned}
&M = 0 \\
&\text{for } k = 1 \text{ to } K: \\
&\quad Y_k = \left[\frac{\partial \tilde{\varepsilon}_1^e}{\partial \overline{\varepsilon}^{in}} \quad \frac{\partial \tilde{\varepsilon}_2^e}{\partial \overline{\varepsilon}^{in}} \quad \frac{\partial \tilde{\varepsilon}_3^e}{\partial \overline{\varepsilon}^{in}} \quad \frac{\partial \tilde{\varepsilon}_4^e}{\partial \overline{\varepsilon}^{in}} \quad \frac{\partial \tilde{\varepsilon}_5^e}{\partial \overline{\varepsilon}^{in}} \right]_k \\
&\quad unique = \text{TRUE} \\
&\quad \text{for } m = 1 \text{ to } M: \\
&\qquad \text{if } \left(Y_k - Z_m\right) \cdot \left(Y_k - Z_m\right) < tol: \\
&\qquad\quad N_m = N_{m+1} \\
&\qquad\quad unique = \text{FALSE} \\
&\quad \text{if } unique: \\
&\qquad M = M + 1 \\
&\qquad Z_M = Y_k;\ N_M = 1
\end{aligned}
\tag{7.43}
$$

where, k is the current inelastic increment, K is the total number of inelastic increments, M is a counter of the total unique responses, Z is the set of unique response vectors, and N is an array whose j^{th} element contains the number of occurrences of the j^{th} unique response vector.

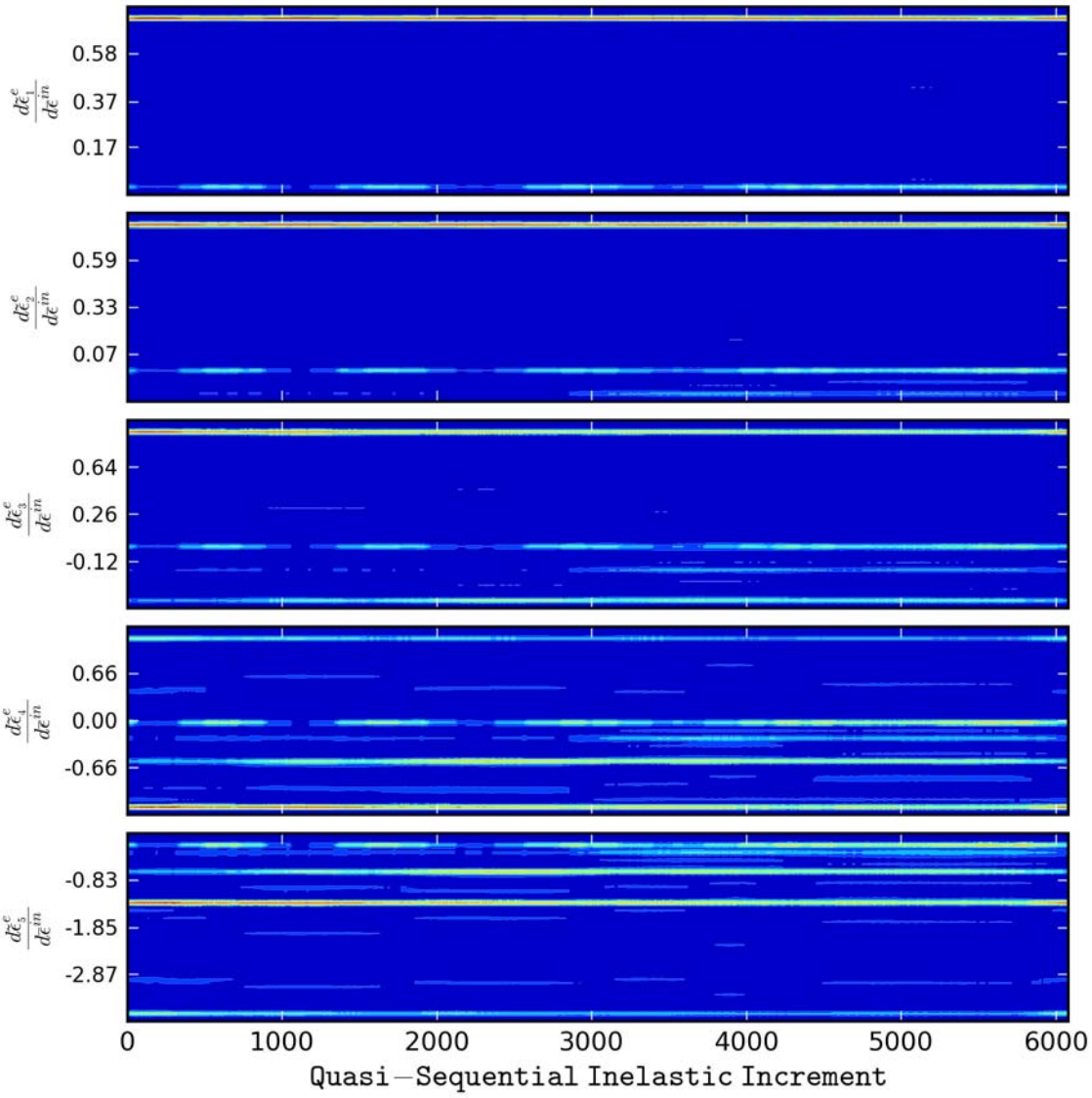

Figure 112. Plot indicating relative occurrence of distinct regimes of ISV response.

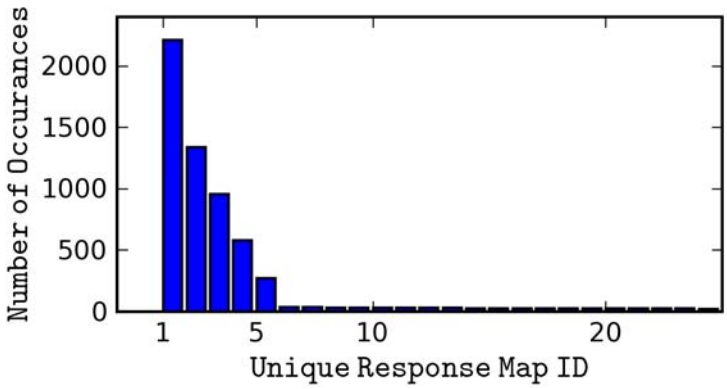

Figure 113. Number of occurrences of distinct response vectors.

The numbers of occurrences for each unique response vector computed by the process outlined in Equation (7.43) are shown in Figure 113. The unique response vector IDs have been rearranged in order of decreasing number of occurrences for this plot. Clearly, there are five prevalent response vectors. The negligibly low number of occurrences for other response vectors is presumably due to numerical error in the computation of derivatives or brief transitions in state space from one sub-domain to another. They could also be explained by regimes of response that were not adequately explored by the suite of simulations; however, this is not true for this case. In any event, one must make the assertion that the regime of response spanned by the fine scale simulation suite encompasses the targeted range of applicability for the coarse scale model. Based on the data presented in the above figures the following conclusions are drawn in order to develop the coarse scale constitutive model:

(1) The separation of response into elastic and inelastic categories implies the existence of a threshold function.

(2) The distinct response vectors imply sub-regions in state space that correspond to constant evolution rates with respect to inelastic strain.

(3) Histograms of state variables suggest symmetry in tension and compression.

(4) Stress-strain curves exhibit kinematic hardening.

7.3.3 Development of Coarse Scale Constitutive Relations

The first step is to identify the elastic threshold function and its parameters. In general, an appropriate form for the threshold function is unknown *a priori*. The general form of a threshold function must be convex, i.e., $f(wx+(1-w)y) \le w f(x)+(1-w) f(y)$; Examples of some convex functions are

$$\begin{aligned} f(x) &= x^{2n} \;\forall\, n \in Z^{+} \\ f(x) &= \left|x\right|^{p} \;\forall\, p \ge 1 \\ f(x) &= \exp(x) \end{aligned} \tag{7.44}$$

Affine functions, $f(Ax+b)$, are both convex and concave. The summation of convex functions, $g_i\left(x\right)$, is convex, i.e., $f(x) = g_1(x) + g_2(x) + \cdots + g_n(x)$ is convex. The maximal value over a set of convex functions is convex, i.e. $f(x) = \max_{i\in(1,n)}\{g_i(x)\}$ for arbitrary *n*. Compositions such as $c(x) = g(f(x))$ are convex if both functions are convex and ***g(x)*** increases monotonically. Finally, if ***f(x)*** is convex then $f(Ax+b)$ is convex. One can use elementary convex functions of single variables such as those in (7.44) to build threshold functions of several state variables using the rules for maintaining convexity. In this case, based on the data presented in Figure 107 and Figure 111, we expect a multimechanism threshold function of the form $f(\overline{\varepsilon}^{e}, \tilde{\varepsilon}_j^{e}) = \max_{i\in(1,5)}\{\hat{f}_i(\overline{\varepsilon}^{e}, \tilde{\varepsilon}_j^{e})\}$. It is reasonable to assume $\hat{f}_i(\overline{\varepsilon}^{e}, \tilde{\varepsilon}_j^{e}) = \left| a_i \overline{\varepsilon}^{e} + \sum_j B_{ij}\tilde{\varepsilon}_j^{e} \right| - R_i$. Of course, it is with the benefit of analytical insight, that the form

$$\overline{f} = \max\left(\left| A_i \overline{\varepsilon}^{e} + \tilde{\varepsilon}_i^{e} \right|\right) - R \le 0 \tag{7.45}$$

is assumed. Without this insight, one could approach this process by starting with simple convex expressions of the state variables and adding complexity until a satisfactory fit to the data is attained. Because the threshold function defines a hypersurface, i.e., a zero level set, in the space of state variables, it is non-unique and there may be more than one form that adequately represents the data. The threshold surface obtained by the equality in expression (7.45) was fit to data coinciding with inelastic response from the suite of simulations. Increments of response associated with inelastic behavior were identified by changes in the coarse scale inelastic strain

over the increment. An objective error function comprises the summation of the square of the yield function evaluated for each inelastic increment for a particular (fixed) set of parameters, A_i, R, i.e.,

$$\chi^2\left(A_i, R\right) = \sum_k \left[\bar{f}\left(A_i, R; \left\{\bar{\varepsilon}^e, \tilde{\varepsilon}_i^e\right\}_k\right)\right]^2 \tag{7.46}$$

The solution for ideal parameters A_i, R must also satisfy the constraint equation

$$\sum_i A_i = 1 \tag{7.47}$$

Minimization of (7.46) subject to the constraint (7.47) was performed using the open source optimization software *OpenOpt* (Kroshko, 2008), which is a python module that was imported into a script containing the data post-processing described above. According to the OpenOpt paradigm, this is a non-smooth minimization problem (NSP) which was solved using the r-algorithm with adaptive space dilation built into the OpenOpt module. Figure 114 shows a plot of convergence versus iteration for the r-algorithm. Satisfactory convergence was obtained for this non-smooth problem relatively quickly, e.g. less than five minutes using a single Intel T2300 1.6 GHz processor with 2GB RAM.

After identification and fitting of the threshold surface, attention is turned to developing evolution equations for the ISVs. Recognizing the nature of the response we break this into two steps: (1) identify linear evolution relationship maps, i.e. partial derivatives of ISVs with respect to inelastic strain, (2) use an artificial neural network to learn and subsequently model which discrete response maps apply to which sub-domains of the state space.

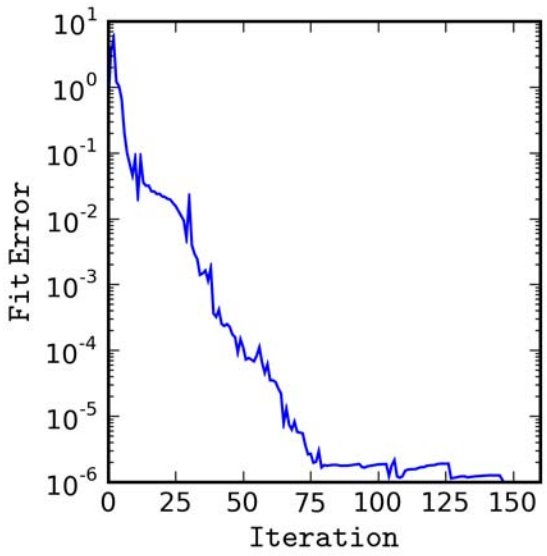

Figure 114. Convergence of the sum-of-squares error versus iteration during fitting of yield surface.

The unique partial derivatives were identified according to the algorithm of Equation (7.43), resulting in the histogram of unique responses shown in Figure 113 and discussed previously. Then, each realized point in state space, $\left\{\overline{\varepsilon}^{e}, \tilde{\varepsilon}_{1}^{e}, \tilde{\varepsilon}_{2}^{e}, \tilde{\varepsilon}_{3}^{e}, \tilde{\varepsilon}_{4}^{e}, \tilde{\varepsilon}_{5}^{e}\right\}_{k}$, from an inelastic increment is associated with one of the five distinct response regimes, i.e. classified, or if the observed response were ambiguous with respect to the five distinct regimes, that response point is discarded.

An artificial neural network (ANN) was used to learn the nonlinear (and non-smooth) relationship between sub-domains of state space and the associated classification of response. An artificial neural network, which is essentially nonlinear least squares, is generally a network comprising several neuron models (hereafter neuron) which receive input from and provide output to other neurons. The first (outer) layer of such networks is typically the input layer where each neuron receives one value from an input vector. The last (outer) layer is the output layer on which each neuron contains one element of the output vector. The ANN is developed and trained in order to reflect observed correlations between input and output vectors. A nonlinear model of a single

neuron is depicted in Figure 115. The rose colored box contains the inputs, x_j, to the neuron. The inputs are typically scaled such that their individual magnitudes span a similar range over the entire data set the ANN will be fit to; this is a numerical rather than conceptual issue. The neuron itself consists of the elements contained within the purple box. The j^{th} input is amplified by a corresponding weight, w_{ij}, associated with the i^{th} neuron. These weighted inputs are then summed with a neuron specific bias value to give an internal neural value of

$$\mathrm{v}_i = \mathrm{b}_i + \sum_{j=1}^{n} \mathrm{w}_{ij}\mathrm{x}_j \tag{7.48}$$

An activation function is applied to the internal neural value to determine the final neuron output, i.e.

$$\mathrm{y}_i = \varphi(\mathrm{v}_i) \tag{7.49}$$

A few examples of activation functions are identity, i.e., $\varphi(\mathrm{v}_i) = \mathrm{v}_i$, a simple heaviside threshold function, i.e.,

$$\varphi(\mathrm{v}_i) = \begin{cases} 1 & \text{if } \mathrm{v}_i > 0 \\ 0 & \text{otherwise} \end{cases} \tag{7.50}$$

and sigmoidal, for example,

$$\varphi(\mathrm{v}_i) = \frac{1}{1 + \exp\left(-\mathrm{v}_i\right)} \tag{7.51}$$

While there are other sigmoidal activiation functions, Equation (7.51) is the one used in this work.

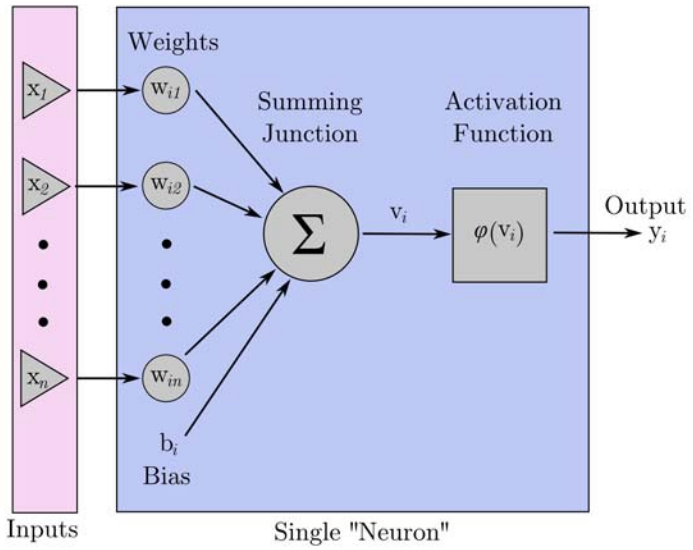

Figure 115. Model of a neuron for ANN.

Having established a nonlinear model for the behavior of a neuron, a feed-forward neural network is developed by building a network of such neurons in layers that take the outputs from previous layers as their input and direct their output to the input of subsequent layers. For example, consider the diagram of a feed-forward neural network with two hidden layers shown in Figure 116. More specifically, this feed-forward network is a multilayer perceptron, but this distinction is not elaborated here. The input layer is contained within the rose colored box on the left side of the diagram. Each of *n* inputs is fed into each of *q* neurons in the next (hidden) layer. In turn, each of the *q* outputs from the first hidden layer is fed into each of *p* neurons in the next hidden layer. Finally, each of the *p* outputs from the second hidden layer is fed into each of the *m* neurons in the output layer. In this manner the neural network provides a non-linear model of varying complexity between the inputs and outputs, i.e.,

$$\begin{Bmatrix} y_1 \\ y_2 \\ \vdots \\ y_m \end{Bmatrix} = ANN\left(\begin{Bmatrix} x_1 \\ x_2 \\ \vdots \\ x_n \end{Bmatrix} \right) \tag{7.52}$$

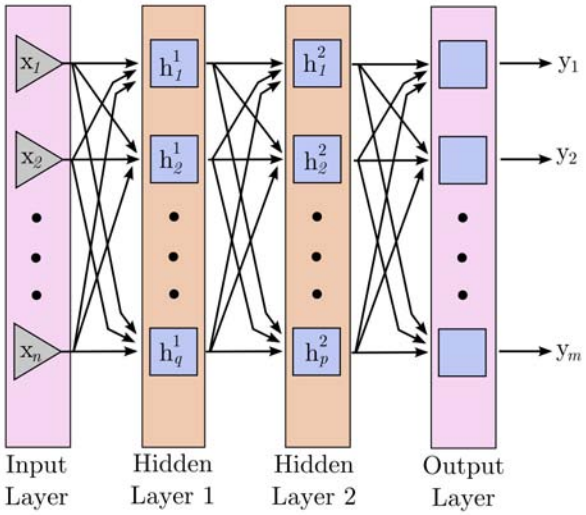

Figure 116. Schematic of a feed-forward neural network.

The parameters of an ANN are the neural weights and biases for neurons in each of the hidden and output layers. The parameters for a particular ANN design are fit to reproduce the observed relationship between inputs and outputs through a "learning" process. Details of specific learning algorithms are beyond the scope of this section; however, one example is backpropagation. Backpropagation exploits the mathematical form of a feed-forward neural network to assign weighted responsibility to each of the neurons for observed errors in the outputs. A forward pass through the network establishes errors at the output. The observed error is then back-propagated through the network to assign "credit" to each of the neurons for its contribution to the errors. The back propagation results in an approximate of the local gradient of output error with respect to neural weights. These gradients are then employed in a steepest descent method to optimize the neural weights. The nature of this problem lends directly to employing other numerical optimization methods such as conjugate gradient, truncated Newton-Cotes, and genetic algorithms, for example, in training ANNs.

The ANN constructed and used in this example were developed using the open source python module *ffnet* (Wojciechowski, 2007). This module provides python classes for feed-forward

neural networks which are instantiated by selecting a particular architecture. In this case a multilayer perceptron (*mlgraph*) with six input nodes, five output neurons, and two hidden layers each with ten neurons was selected. A sigmoid activation function of the type in Equation (7.51) was used on all neurons. Training data consisted of corresponding sets of input and output vectors obtained from inelastic increments. The input vectors consisted of the state variables for each inelastic increment. The output vectors are a coding of the five response classes in which the i^{th} element of the output vector, $\{y_i\}_k$, is one if the observed response for increment k is category i, and zero otherwise. A truncated Newton-Cotes (TNC) algorithm built into the *ffnet* module was used for training the ANN. Training was relatively rapid for the specified ANN architecture as indicated by the plot of chi-squared output error over all training data versus TNC iteration shown in Figure 117. In general, the design of ANN architecture and training process would be the most onerous aspect of the proposed constitutive strategy for the large dimensionality of response exhibited by continuum rSVE simulations. One means to mitigate the dimensionality of response is discussed in Section 7.5.

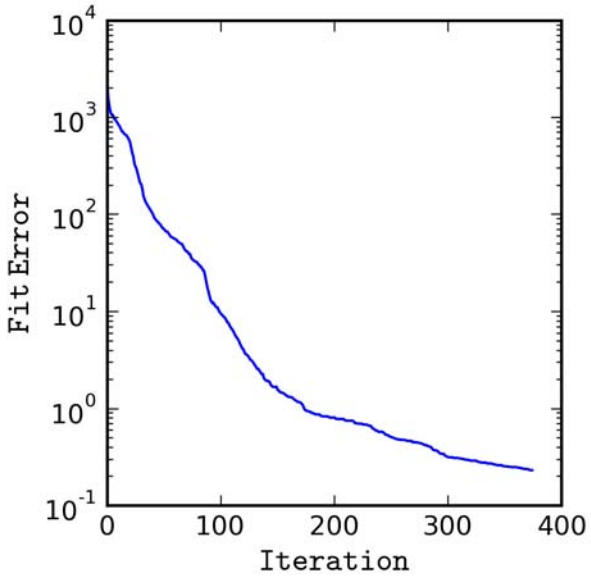

Figure 117. Chi-squared error over all ANN training data versus TNC iteration during training.

7.3.4 Comparison of Direct Simulation and Constitutive Description

Having identified a suitable representation of the elastic and inelastic constitutive response including evolution of ISVs in Section 7.3.3, this section discusses implementation of the coarse scale model for simulation of a test case and comparison to simulation results using the direct simulation method discussed in Section 7.3.2. The test problem consists of the system depicted in Figure 104 and discussed in detail in Section 7.3.1. Boundary conditions consist of the coarse scale strain history shown in Figure 118 applied to the system.

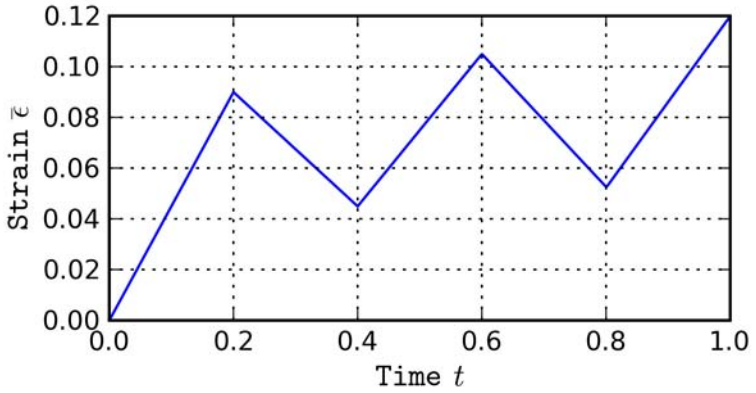

Figure 118. Nontrivial strain history to test numerically derived coarse scale constitutive description.

Constitutive models developed in the manner presented in this Chapter can be generally characterized as multi-mechanism inelastic models. Such models will often involve a multi-surface threshold that is piecewise continuous in state space (or equivalently, generalized stress space) with discontinuous gradients at the intersections. Integration algorithms for such models are prevalent in the literature of multisurface plasticity (cf. Simo et al., 1988; McDowell, 1989; Montans, 2000; Khoei and Jamali, 2005; Montans and Caminero, 2007; Choi and Pan, 2009; Tu

et al., 2009). Applicability of particular integration algorithms will depend significantly on the extent to which the evolution equations are associated with various threshold surfaces. For this example, a simple nonlinear solution algorithm detailed in Equations (7.53) and (7.54) was used.

$$
\begin{aligned}
&\text{Elastic Trial:}\\
&\quad \bar{\varepsilon}_0^e = \bar{\varepsilon}^{e,n} + \Delta\bar{\varepsilon};\ \bar{\varepsilon}^{in,n+1} = \bar{\varepsilon}^{in,n};\tilde{\varepsilon}_{i,0}^e = \tilde{\varepsilon}_i^{e,n}\\
&\\
&\text{if } \bar{f}\left(\bar{\varepsilon}_0^e, \tilde{\varepsilon}_{i,0}^e\right) < 0 : \text{Elastic Response}\\
&\quad \bar{\varepsilon}^{e,n+1} = \bar{\varepsilon}_0^e;\ \tilde{\varepsilon}_i^{e,n+1} = \tilde{\varepsilon}_{i,0}^e\\
&\\
&\text{else} : \text{Inelastic Response}\\
&\quad \frac{\partial\tilde{\varepsilon}_i^e}{\partial\bar{\varepsilon}^{in}} = \bar{K}_i\left(\bar{\varepsilon}^{e,n}, \tilde{\varepsilon}_i^{e,n}\right)\\
&\\
&\quad \text{solve} : \bar{g}\left(\gamma\right) = 0 \rightarrow \gamma\\
&\\
&\quad \Delta\bar{\varepsilon}^{in,n+1} = \gamma\,\text{sign}\left(\bar{\sigma}_0\right)\\
&\quad \bar{\varepsilon}^{e,n+1} = \bar{\varepsilon}_0^e - \Delta\bar{\varepsilon}^{in,n+1}\\
&\quad \tilde{\varepsilon}_i^{e,n+1} = \tilde{\varepsilon}_i^{e,n} + \frac{\partial\tilde{\varepsilon}_i^e}{\partial\bar{\varepsilon}^{in}}\Delta\bar{\varepsilon}^{in,n+1}\\
&\quad \bar{\varepsilon}^{in,n+1} = \bar{\varepsilon}^{in,n} + \Delta\bar{\varepsilon}^{in,n+1}
\end{aligned}
\tag{7.53}
$$

The definition of the nonlinear plasticity equation, i.e., $\bar{g}\left(\gamma\right)$ is

$$
\begin{aligned}
&\text{define } \bar{g}\left(\gamma_k\right):\\
&\quad \Delta\bar{\varepsilon}_k^{in} = \gamma_k\,\text{sign}\left(\bar{\sigma}_0\right)\\
&\quad \tilde{\varepsilon}_{i,k}^e = \tilde{\varepsilon}_i^{e,n} + \frac{\partial\tilde{\varepsilon}_i^e}{\partial\bar{\varepsilon}^{in}}\Delta\bar{\varepsilon}_k^{in}\\
&\quad \bar{\varepsilon}_k^e = \bar{\varepsilon}_0^e - \Delta\bar{\varepsilon}_k^{in}\\
&\quad \bar{g}\left(\gamma_k\right) = \bar{f}\left(\bar{\varepsilon}_k^e, \tilde{\varepsilon}_{i,k}^e\right)
\end{aligned}
\tag{7.54}
$$

and was solved using a bracket search algorithm for simplicity of implementation in this example. The evolution rate equation, i.e., $\bar{K}_i\left(\bar{\varepsilon}^{e,n}, \tilde{\varepsilon}_i^{e,n}\right)$ in Equation (7.53) is a wrapper around the ANN state classifier and the associated constant rates identified in Section 7.3.3. Note that the ISV update is based on explicit integration over an increment; However, if a transition in response regime (active mechanism) occurs during an increment that increment is split into two sub-increments allowing the appropriate rate equations to be used in an explicit fashion in each.

Coarse scale stress versus strain results from the direct numerical simulation are plotted by a black solid line in Figure 119, while the homogenized constitutive response is indicated by a red dashed line. It is evident from this figure that the coarse scale constitutive model has done an adequate job capturing the stress-strain response.

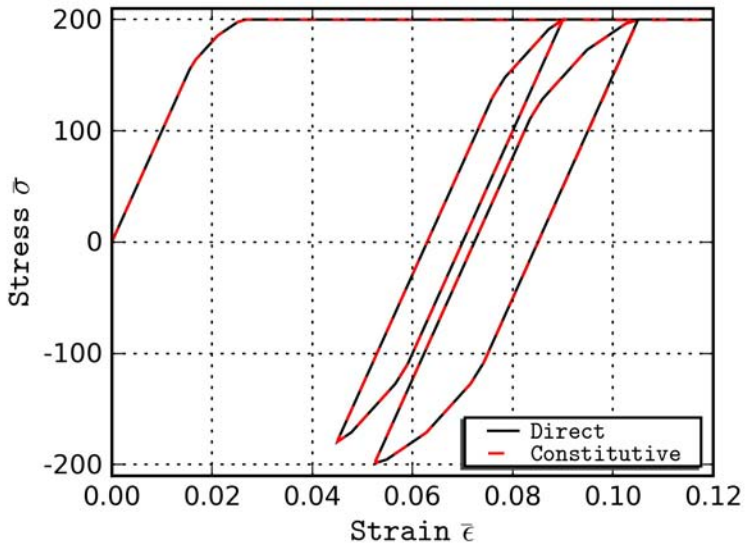

Figure 119. Comparison of stress versus strain resulting from constitutive test case and direct numerical simulation.

Stored free energy computed from these two methods are compared in a similar fashion in the top window of Figure 120. ISV time histories are compared in the bottom window of Figure 120. The constitutive strategy presented in this chapter clearly does an effective job capturing the essential details of the stored energy, ISV evolution, and coarse scale stress-strain behavior for this low dimensional response. The applicability of this strategy to (1) nonlocal second gradient kinematics and (2) high-dimensional response is addressed in Sections 7.4 and 7.5, respectively.

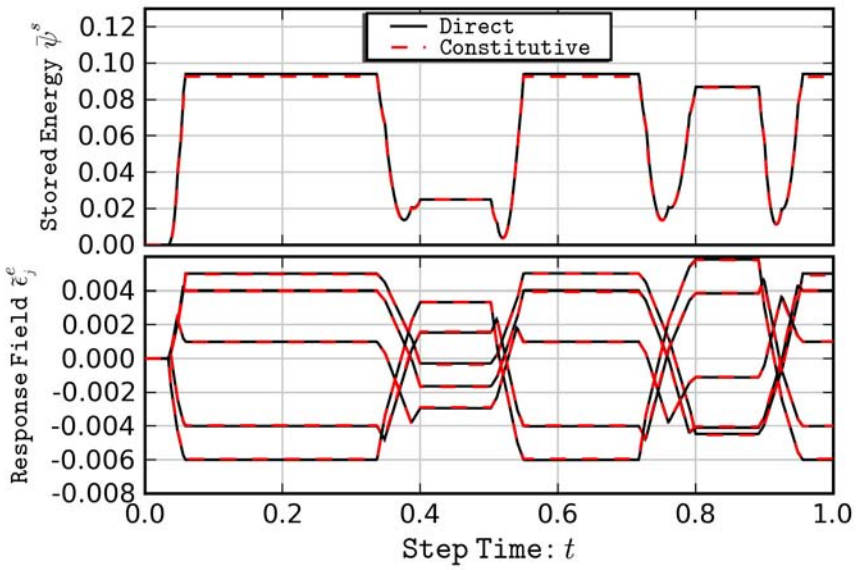

Figure 120. Comparison of Stored free energy (top) and ISV (bottom) time histories resulting from coarse scale constitutive test case and direct simulation of the heterogeneous system.

7.4 Two DOF Extension for Strain Gradient Case

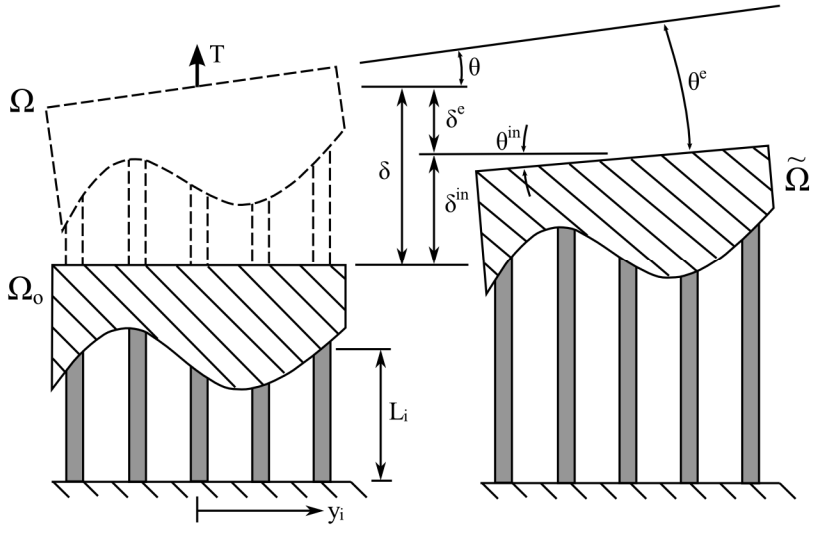

Figure 121. Diagram of discrete heterogeneous bar example extended to end rotations.

The extension to a two degree of freedom problem which introduces length scales and strain gradient is made by modifying the system of Figure 104 to that of Figure 121 through the addition of a net rotation, θ, which is decomposed additively into elastic and inelastic components, i.e., $\theta = \theta^e + \theta^{in}$. Also note, while not indicated by Figure 121, the following development assumes a symmetric spatial distribution of heterogeneity which decouples the extensional and rotational elastic stiffness behavior. This is done to simplify the analysis for purposes of this example problem.

The relevant second-order strain is defined as

$$\overline{\Gamma} = \frac{\partial \overline{\varepsilon}}{\partial y} = \frac{\theta}{L} \tag{7.55}$$

assuming small rotations such that $\sin\theta \approx \theta$. The fine scale strain within each bar becomes

$$\varepsilon_i = c_i \overline{\varepsilon} + c_i y_i \overline{\Gamma} \tag{7.56}$$

Applying PVV as done previously, the coarse scale stress and second order stress are

$$\overline{\sigma} = \tfrac{1}{N} \sum_{i=1}^{N} \sigma_i \tag{7.57}$$

and

$$\overline{Q} = \tfrac{1}{N} \sum_{i=1}^{N} y_i \sigma_i \tag{7.58}$$

respectively. Adopting an intermediate configuration as shown in Figure 121 introduces in additive decompositions of the strain and second-order strain into elastic and inelastic components, i.e.,

$$\begin{aligned} \overline{\varepsilon} &= \overline{\varepsilon}^e + \overline{\varepsilon}^{in} \\ \overline{\Gamma} &= \overline{\Gamma}^e + \overline{\Gamma}^{in} \end{aligned} \tag{7.59}$$

where $\overline{\Gamma}^e = \dfrac{\theta^e}{L}$ and $\overline{\Gamma}^{in} = \dfrac{\theta^{in}}{L}$ and the other terms are as defined previously. The fine scale strain in the intermediate configuration can be decomposed additively in two manners, i.e.

$$\tilde{\varepsilon}_i = \tilde{\varepsilon}_i^e + \tilde{\varepsilon}_i^{in} = c_i \overline{\varepsilon}^{in} + c_i y_i \overline{\Gamma}^{in} \tag{7.60}$$

where the $\tilde{\varepsilon}_i^e$ are again treated as internal state variables. The fine scale stresses within the intermediate configuration are still expressed as $\tilde{\sigma}_i = E_i \tilde{\varepsilon}_i^e$, but the internal microforce balance is extended to

$$\begin{aligned} \sum_{i=1}^{N} \tilde{\sigma}_i &= 0 \\ \sum_{i=1}^{N} y_i \tilde{\sigma}_i &= 0 \end{aligned} \tag{7.61}$$

The total elastic strain can now be expressed in terms of the residual elastic strain within the intermediate configuration (ISVs) and the projection of coarse scale elastic kinematic strains onto the fine scale, i.e.,

$$\varepsilon_i^e = \tilde{\varepsilon}_i^e + c_i \overline{\varepsilon}^e + c_i y_i \overline{\Gamma}^e \tag{7.62}$$

Enforcing scale invariance of energy results in essentially the same Helmholtz free energy decomposition as previously, i.e., $\overline{\psi} = \overline{\psi}^e + \overline{\psi}^s$, with the exception that the elastic strain energy now has a term due to the second order strain, i.e.,

$$\overline{\psi}^e = \tfrac{1}{2} E (\overline{\varepsilon}^e)^2 + \tfrac{1}{2} H (\overline{\Gamma}^e)^2 \tag{7.63}$$

Where the second-order stiffness parameter, H, is defined

$$H = \tfrac{1}{N} \sum_{i=1}^{N} c_i {y_i}^2 E \tag{7.64}$$

The coarse scale stress and thermodynamic driving forces acting on ISVs are as before, cf. Eqs. (7.32) and (7.33) The second order stress is computed from the Helmholtz free energy, i.e.,

$$\overline{Q} = \frac{\partial \overline{\psi}}{\partial \overline{\Gamma}^e} = H \overline{\Gamma}^e \tag{7.65}$$

and scale invariance of dissipation dictates a second-order term added to the dissipation rate, i.e.,

$$\overline{\Pi}_{mec} = \overline{\sigma} \dot{\overline{\varepsilon}}^{in} + \overline{Q} \dot{\overline{\Gamma}}^{in} - \sum_{i=1}^{N} q_i \dot{\tilde{\varepsilon}}_i^e \tag{7.66}$$

The elastic threshold function, expressed in strain space, becomes

$$\overline{f}^{\varepsilon} = \max\left(\left|c_i\overline{\varepsilon}^e + c_i y_i \overline{\Gamma}^e + \tilde{\varepsilon}_i^e\right|\right) - \tfrac{k}{E} \le 0 \tag{7.67}$$

In stress space this can be reformulate das,

$$\overline{f} = \max\left(\left|\overline{\sigma} + \hat{y}_i\overline{Q} - b_i\right|\right) - R_i \le 0 \tag{7.68}$$

where the length normalized length scale parameters, $\hat{y}_i = \dfrac{N y_i}{\sum_{i=1}^{N} c_i {y_i}^2}$, combine with the second order stress to act in opposition to the backstress, $b_i = -\dfrac{\tilde{\sigma}_i}{c_i}$, and the radius of the i^{th} nested yield surface is $R_i = \dfrac{k}{c_i}$. The evolution equations for each ISV are based on active and passive cases of evolution as before, with the addition of a dependence on increments in the second order inelastic (and consequently, elastic) strains, i.e.,

$$d\tilde{\varepsilon}_i^e = \begin{cases} c_i d\overline{\varepsilon}^{in} + c_i y_i d\overline{\Gamma}^{in} & if\ \overline{f}^{\sigma} = 0, f_i < 0 \quad (\text{passive}) \\ -c_i d\overline{\varepsilon}^{e} - c_i y_i d\overline{\Gamma}^{e} & if\ \overline{f}^{\sigma} = 0, f_i = 0 \quad (\text{active}) \end{cases} \tag{7.69}$$

To facilitate discussion on the response of this system over a range of conditions, cases of proportional and non-proportional deformation history were simulated. The simulations were generated following a similar procedure as that for the one DOF system. For the proportional cases, a deformation history was specified based on the profile shown in Figure 122.

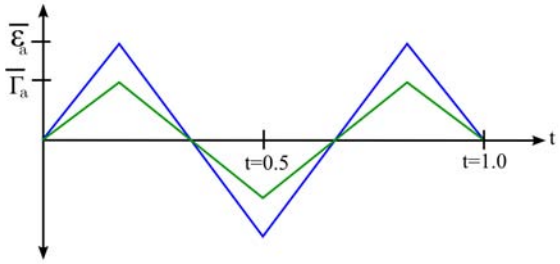

Figure 122. Proportional deformation time history profile.

First consider the case with $\bar{\varepsilon}_a = 0.01$ and $\bar{\Gamma}_a = 0.03$. The resulting stress versus strain and second order stress vs second order strain are shown on the left and right sides of Figure 123, respectively. The generalized stress strain behavior is largely consistent with the previously described one DOF case. Time histories for ISVs and stored energy are shown in the bottom and top of Figure 124, respectively. Opposite symmetrical pairs of ISV mechanisms are indicated by slid and dotted lines of the same color. Clearly, for combined deformation the ISV evolution is not symmetrical.

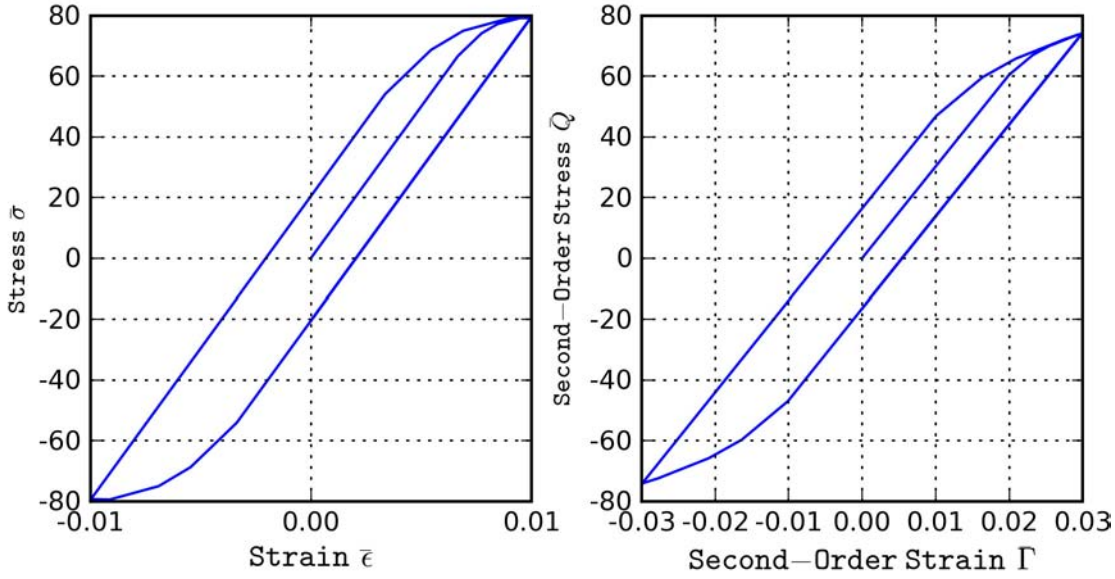

Figure 123. Generalized stress versus strain response for Case 1. First order stress-strain is shown at left and second order stress-strain response is shown at right.

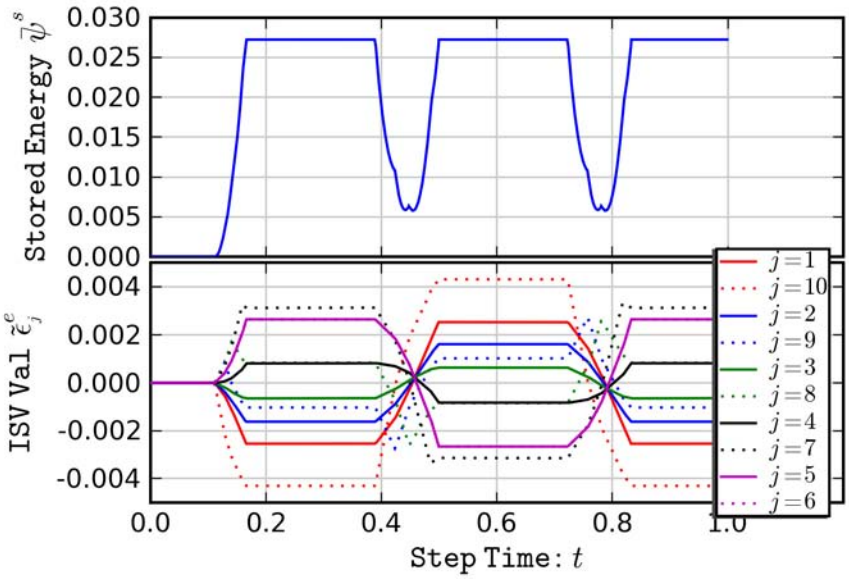

Figure 124. ISV and associated stored energy time histories for Case 1.

A generalized stress versus strain plot for Case 2 with $\bar{\varepsilon}_a = 0.01$ and $\bar{\Gamma}_a = 0.04$. This case represents a nominal increase in the amplitude of the second-order strain, which manifests as softening in the apparent stress versus strain curve associated with extensional behavior shown on the left of Figure 125. Conversely, Case 3 with $\bar{\varepsilon}_a = 0.03$ and $\bar{\Gamma}_a = 0.01$, shows uniform kinematic hardening in the stress-strain response which induces significant softening in the apparent second order stress versus second order strain behavior. This is shown in Figure 126. The ISV and stored energy histories for these cases are similar in nature to that of Case 1 and, accordingly, are not included here.

Non-proportional deformation, even with only two degrees of freedom, can produce complex behaviors in the apparent stress-strain behavior. As an example of a non-proportional deformation history the strain and second-order strain histories shown in Figure 127 were simulated. These histories consist of an oscillating sine wave with amplitude 0.02 for extensional strain, $\bar{\varepsilon}$, and a monotone ramp to a peak value of 0.02 for the second order strain, $\bar{\Gamma}$.

Stress versus strain plots for the non-proportional case are shown in Figure 128. Note that the gradually increasing second order strain has a progressive affect on the apparent stress versus strain response (Figure 128, left). Simultaneously, the oscillations in the first order strain cause oscillation in the second order stress (Figure 128, right). The evolution of ISVs and stored energy are also of greater complexity in the non-proportional case than for simple proportional deformation cycles as shown in Figure 129.

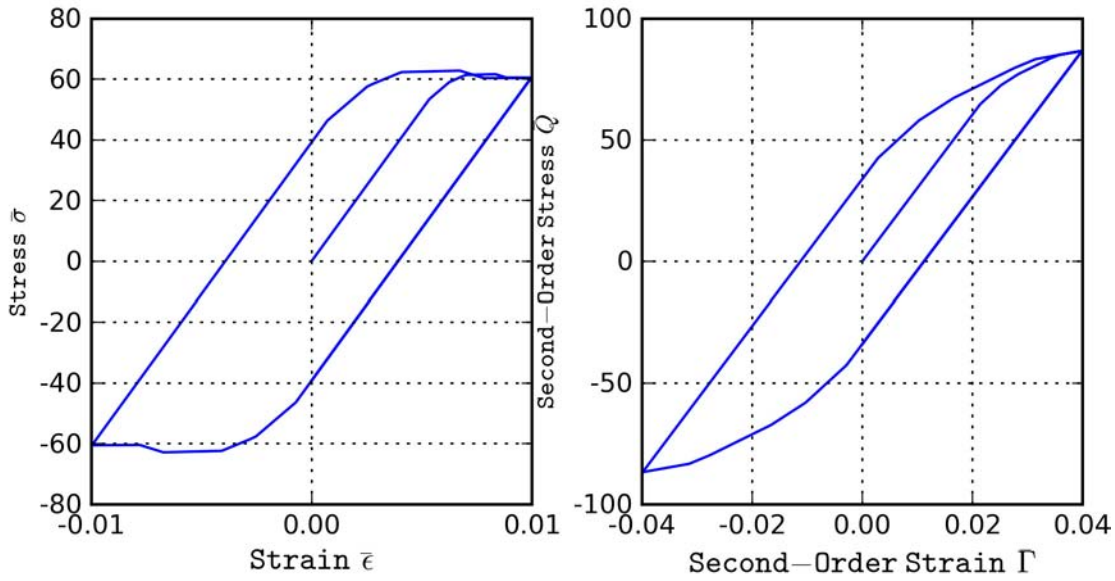

Figure 125. Generalized stress versus strain for Case 2. First order stress-strain is shown at left and second order stress-strain response is shown at right.

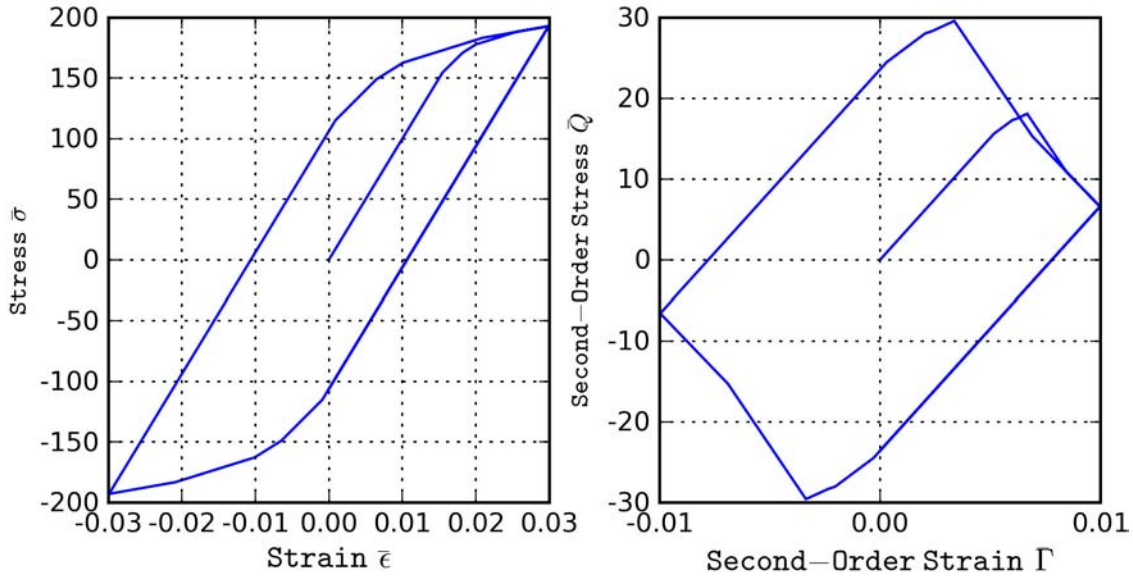

Figure 126. Generalized stress versus strain for Case 3. First order stress-strain is shown at left and second order stress-strain response is shown at right.

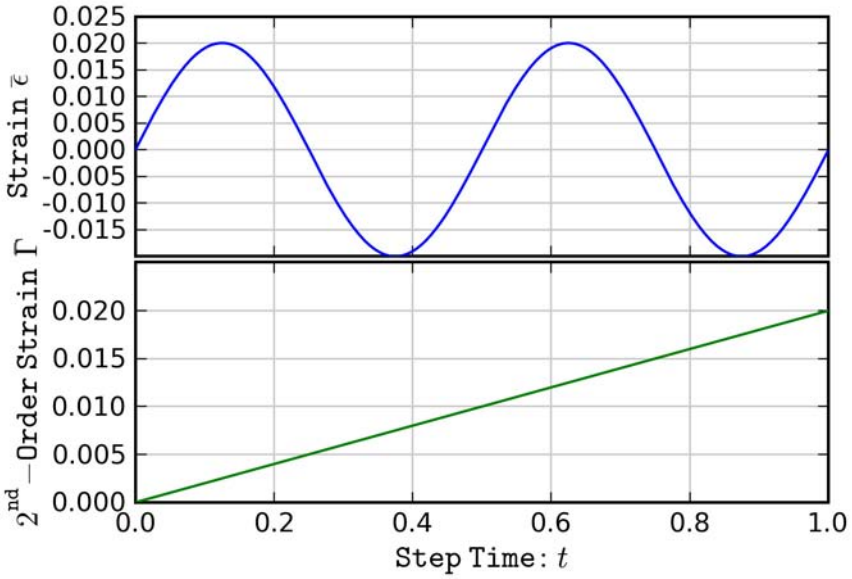

Figure 127. Non-proportional deformation time history. First order strain is shown on top in blue and second order strain is shown on bottom in green.

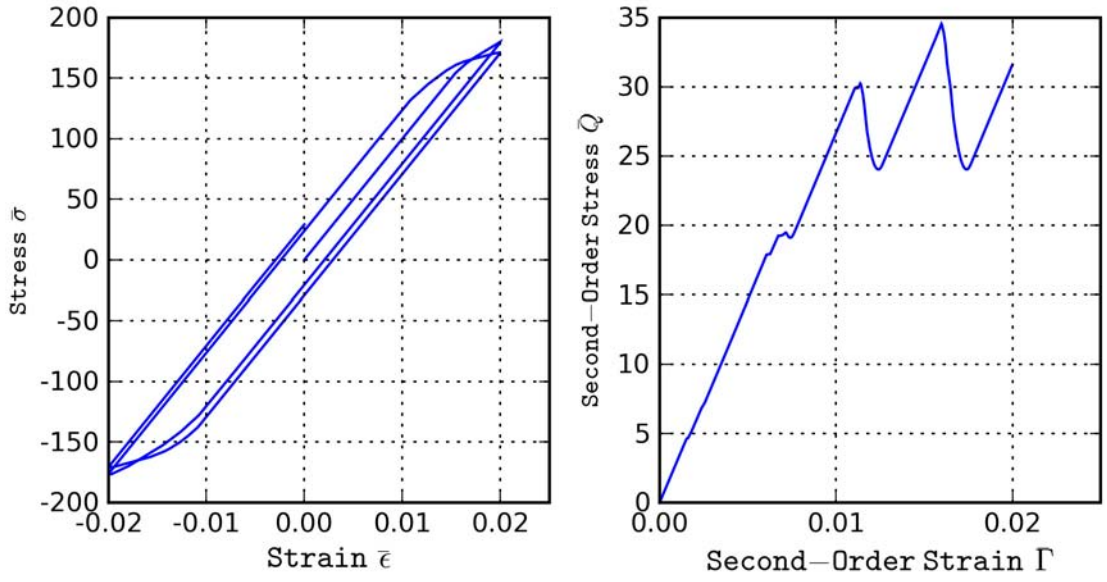

Figure 128. Generalized stress versus strain for non-proportional case. First order stress-strain is shown at left and second order stress-strain response is shown at right.

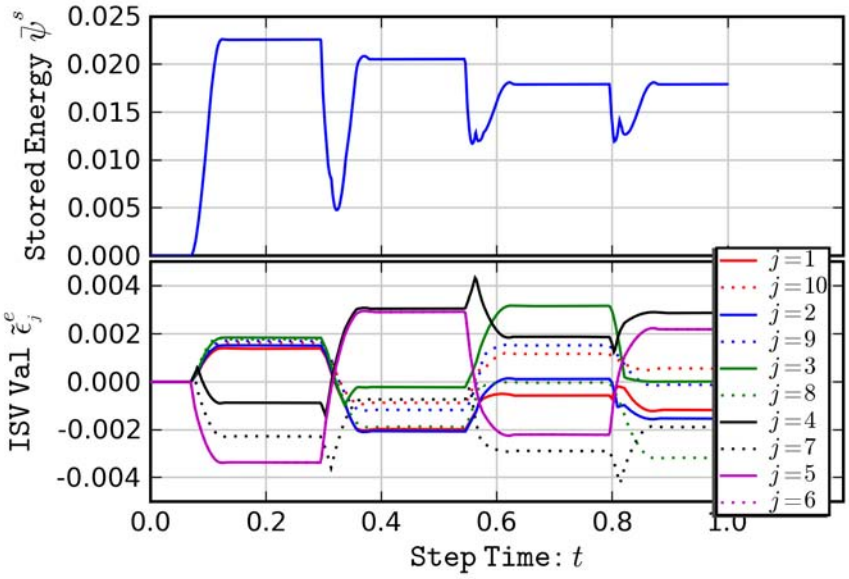

Figure 129. ISV and associated stored energy time histories for Case 1.

Clearly from the simulation results of this two DOF system, there is an interdependence of the first- and second-order response. It is through the coupling of the elastic threshold function in Eq. (7.68) as well as the evolution equations that the complexities of the two DOF system are born. For more general continuum rSVE problems, the complexities are expected to grow much larger such that developing an approach based on simple example problems such as that shown in this Chapter provide a testing ground for the more complex problem. The point of this section is that the modeling approach presented in this chapter can be extended to higher coarse scale system dimensionality (modes of deformation) and that significantly complex behaviors result from relatively few ISVs and straightforward evolution behavior.

7.5 Extension to High-Dimensional Descriptions of Fine Scale rSVE Field Response

Continuum fine scale rSVE simulations present significantly larger and more complex fields of data than the five and ten heterogeneous bars used in the preceding examples. To address large dimensionality of field response, attention is now turned to demonstrating the PCA based data reduction technique for a system similar to that of 7.3. Consider a system similar to that of Figure 104 comprising 50 distinct bars of differing lengths. The lengths of the 50 bars are divided into five groups in which each group's mean length is identical to the length of one of the bars in the five bar example.

The coarse scale stress versus strain behavior, shown in Figure 130, is similar to that for the five bar problem shown in Figure 106, except that the behavior is generally smoother, i.e., it is not piecewise linear.

The field response, i.e., residual elastic strain in the intermediate configuration for each of the 50 bars is shown in the bottom pane of Figure 131, while the associated stored energy is shown on the top pane of the same figure. The goal of this section is to identify a minimal set of ISVs from the time evolving response field and demonstrate that the important details of the field response and stored energy associated with inelastic evolution can be reconstructed from these relatively few ISVs.

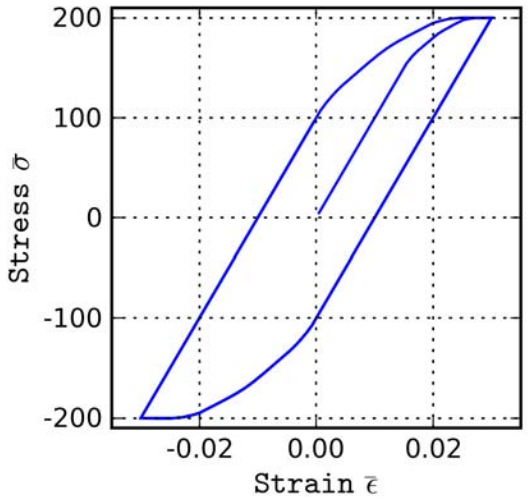

Figure 130. Stress versus strain for the 50 bar simulation.

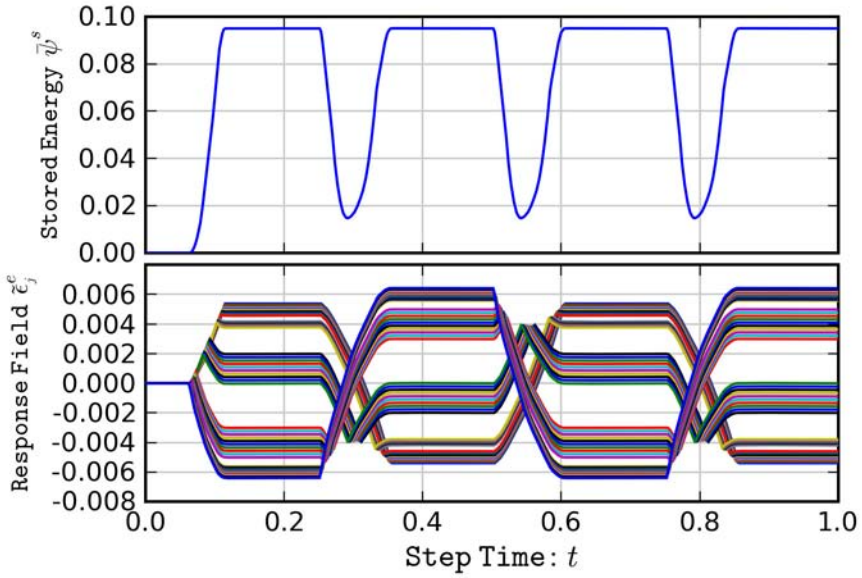

Figure 131. Evolution of response field (bottom) and associated stored free energy (top) for the 50 bar simulation.

The first step in this process is to compile data only for the inelastic increments of the system response. The response field data for the inelastic response is stored in an array, X_{nj}, where *n* is the inelastic increment number and *j* is the field variable location. The mean response is removed from each column, i.e.,

$$\bar{X}_{nj} = X_{nj} - \frac{1}{N}\sum_{n} X_{nj} \tag{7.70}$$

where N is the total number of inelastic increments and $\bar{X}_{nj}$ is the zero average data. A covariance matrix is formed,

$$C_{ij} = \sum_{n} \bar{X}_{ni}\bar{X}_{nj} \tag{7.71}$$

and then decomposed by its eigenvalues and eigenvectors, i.e.,

$$\left[C\right] = \left[\Phi\right]\cdot\left[\Lambda\right]\cdot\left[\Phi\right]^{T} \tag{7.72}$$

The eigenvalues resulting from this decomposition are shown in Figure 132, with the ten largest eigenvalues emphasized in the inset to the upper right. In the field of PCA there are various methods proposed for determining the number of the largest eigenvalues to retain from this decomposition; however, for this illustration five eigenvalues (and consequently ISVs) are retained to draw comparisons to the previous example.

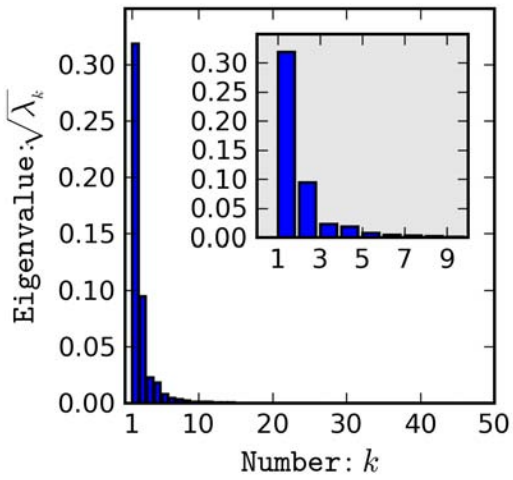

Figure 132. Eigenvalues from decomposition of covariance matrix.

The ISV temporal evolution is then computed as

$$\bar{\xi}_i = X_{nj}\hat{\Phi}_{ji} \tag{7.73}$$

where the columns of $\left[\hat{\Phi}\right]$ are the eigenvectors associated with the five largest eigenvalues of the covariance matrix and represent the basis function for distribution of ISVs onto the spatial field. The ISVs computed according to Equation (7.73) are shown in Figure 133. The entire field response can be reconstructed at any state described by ISVs $\bar{\xi}_j(t)$, using the retained basis functions $\left[\hat{\Phi}\right]$, i.e.,

$$\hat{\bar{X}}_i(t) = \hat{\Phi}_{ij}\,\bar{\xi}_j(t) \tag{7.74}$$

Performing this step on the original ISV history of Figure 133 results in a reduced reconstruction of the original field response time history as shown in Figure 134. Finally, the associated reconstructed stored free energy is shown in Figure 135 to have substantial agreement with the original data. In summary, a promising method of employing the proposed numerical approach to developing inelastic constitutive relations from fine scale rSVE simulations is to reduce field response data using PCA.

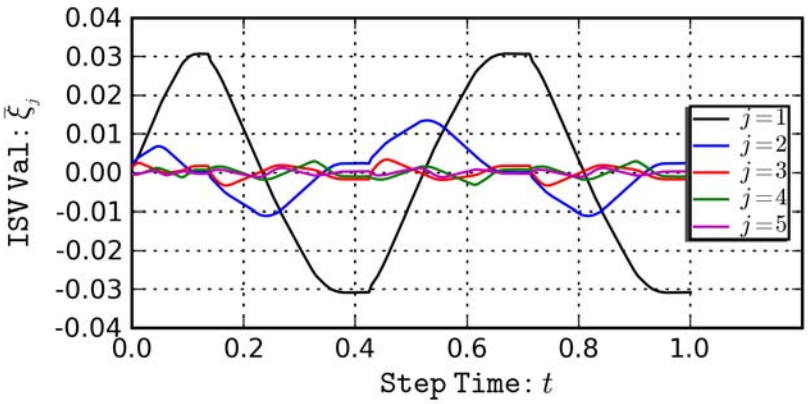

Figure 133. ISV evolution over inelastic increments.

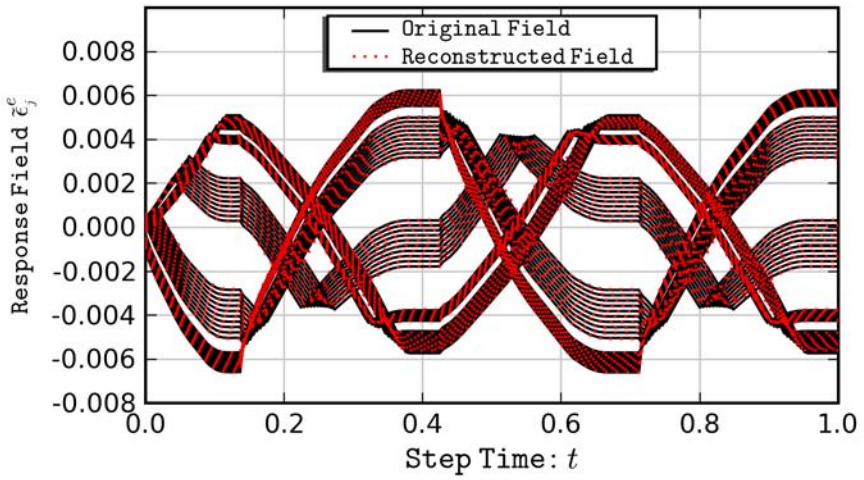

Figure 134. Comparison of response field evolution over inelastic increments for original simulation (black) and that reconstructed from retained ISVs.

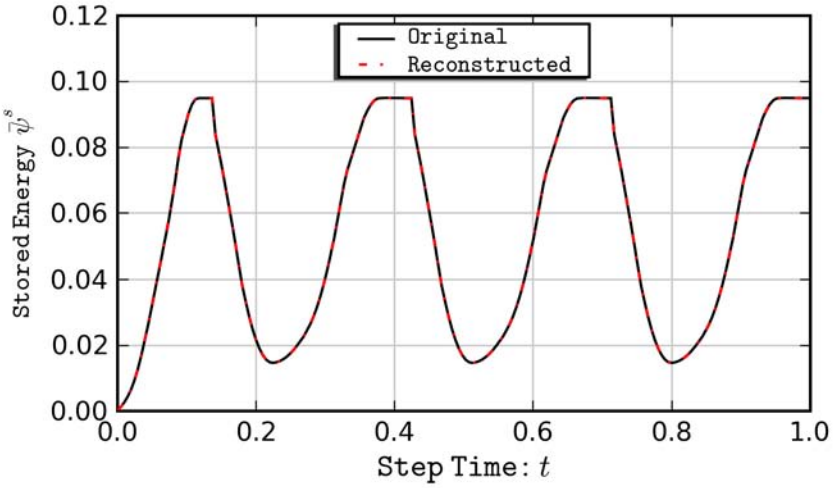

Figure 135. Comparison of stored free energy evolution over inelastic increments for original simulation (black) and that reconstructed from five retained ISVs.

7.6 Summary

This chapter introduces an advanced strategy for developing coarse scale constitutive models from the results of fine scale rSVE simulations. The key features of this approach are identifying and measuring ISVs that reflect the energy stored in finer scale inelastic processes and then developing a proper set of kinetic equations to describe the evolution of these ISVs. The general approach is to use principle components analysis to establish an efficient basis function that reduces the dimensionality of the heterogeneous field response. The eigenvectors obtained from this response are an integral part of the model that describe how ISVs project across the fine scale domain. The principal values take on the role of ISVs and their time histories are stored for developing evolution equations. The evolution equations are developed using dynamical state space models, in particular the idea of using feed-forward neural networks to accomplish this task is presented. For the example problem the task is separated into identifying distinct response regimes (behaviors) and a multiclass classification problem to identify distinct regimes of response in state space. More complex problems will likely not exhibit regions of constant response behavior; however, in many cases this will be an effective modeling assumption. For those cases where this assumption would be poor, the transition in response behavior is continuous and gradual rather than distinct. Accordingly, the neural network approach can still be used and would be better behaved than for the non-smooth classification problem. Clearly, the examples explored in this chapter are contrived and quite limited in complexity. The extension to realistic problems is not trivial and is an exciting area for future research.

CHAPTER VIII

SUMMARY AND CONCLUSIONS

8.1 Summary

A multiscale modeling approach has been developed which recognizes the non-uniform evolution of inelastic response of heterogeneous materials at each scale within a hierarchy of scales. The modeling approach employs hierarchical homogenization utilizing a framework that ensures physical consistency between distinct scales of observation. Physical principles are established that reflect this idea of inter-scale consistency. These physical principles are then implemented in a theoretical framework applicable to scale transitions for scales that permit modeling as a continuum. Note, however, the principles are generally applicable to other scales as well. Within this multiscale framework, the second gradient is used as a nonlocal kinematic link between the response of a material point at the coarse scale and the response of a neighborhood of material points at the fine scale. In addition to the satisfaction of classical continuum laws at each scale, the issues central to this framework are maintaining kinematic consistency and the invariance of mass, linear and angular momentum, and energy with respect to the scale at which a given set of mass particles are observed. Furthermore, we assert that in addition to scale invariance of the total energy, the partition of total energy into recoverable, stored, and dissipated energy shall also be invariant with respect to the scale at which a given set of mass particles are observed. Kinematic consistency between these scales results in specific requirements for constraints on the fluctuation field. The wryness tensor serves as a second-order measure of strain and decomposes into elastic and inelastic parts in a manner analogous to finite Green-Lagrange strain. The nature of the second-order strain induces anti-symmetry in the first order Cauchy stress at the coarse scale. Thermodynamics of irreversible processes and scale invariance of the involved thermodynamic quantities are used to develop a second-gradient internal state variable theory (ISV) at the coarse

scale. The multiscale ISV constitutive theory is couched in the coarse scale intermediate configuration.

Computational tools for the numerical implementation of the multiscale framework are developed and subjected to verification and numerical testing to demonstrate their accuracy. At the fine scale, boundary and internal fluctuation constraints are applied to the computational model via linear constraint equations. Various sets of these constraint equations are evaluated in the context of the fine scale deformation response of a porous material. The influence of fine-scale boundary conditions and geometric construction techniques on the distinction between statistical and representative volume elements is assessed. Numerical implementation of the framework at the coarse scale is achieved using a mixed field finite element method and a finite-deformation second-gradient anisotropic hyperelastic-inelastic constitutive update scheme. The coarse scale implementation is quantitatively compared to analytical solutions for certain elastic test cases and qualitatively evaluated for inelastic test problems that have no analytical solution.

These developed multiscale framework and computational tools are applied to example problems used to highlight certain aspects of the framework relevant to fine and coarse scales. In particular, the influence of ISVs introduced to reflect heterogeneity of the fine scale deformation field on kinematic hardening is established. Also, the nonlocal response and associated stability of localization bands under computational refinement are demonstrated. Effects and implications of varying length scale parameters related to nonlocal constitutive model are discussed.

Finally, a strategy for developing meaningful kinematic ISVs and the proper free energy functions and evolution kinetics is presented. This strategy focuses on the role of ISVs in storing free energy during irreversible processes and presents two techniques for directly computing ISVs from the heterogeneous fine scale response fields: (1) statistical moments of principle component analysis of response field data, (2) artificial neural networks (ANN) are proposed as a numerical method for developing the mapping between the material state (i.e., ISVs) and its evolution response. These concepts are applied to a few simple example problems to establish the feasibility of the approach and highlight connections with multisurface plasticity.

8.2 Unique Contributions

The major novel contributions of this dissertation are as follows. Specifically, this dissertation

- develops a formal framework for scale transitions between continuum scales that ensures physical consistency across scales including dissipation,
- employs this framework in the context of a complete second gradient kinematical description,
- develops new theoretical requirements for fine scale boundary conditions on microstructure simulations and approaches for numerical implementation,
- examines the relative effects of various sets of fine scale boundary conditions, including effects of nonzero second gradient,
- establishes the precise nature of antisymmetry of coarse scale Cauchy stress in second-gradient continua,
- establishes the importance of body forces in computation of coarse scale stresses especially regarding internal fluctuation constraints,
- develops a fully finite deformation hyperelastic inelastic constitutive integration algorithm for second gradient inelastic response,
- demonstrates application of the framework and implementation to a multiscale problem which highlights
    - ISVs that capture effects of heterogeneous microstructure evolution and the stored elastic energy arising from heterogeneity
    - The effect of nonlocality in coarse scale model on eliminating artificial mesh dependence of strain localization
    - The role of length scale parameters related to specific mechanisms of response, and

- proposes and demonstrates advanced strategies for computing coarse scale ISVs directly from fine scale simulations and constructing numerical models of their evolution kinetics.

8.3 Conclusions

The following conclusions are drawn from the work presented in this dissertation.

- The developed multiscale framework is theoretically sound and adheres to principles assuring physical consistency across scales.
- The coarse scale Cauchy stress resulting from second gradient homogenization is generally antisymmetric, reflecting contributions from microinertial effects and the polar interaction of second gradient and second order stress.
- Internal constraints on the fluctuation field are required when using fine scale referential statistical volume element (rSVE) models to simulate second gradient response.
- At the fine scale, generalized periodic boundary conditions are favorable to direct boundary conditions because they provide less overall constraint and therefore permit evolution of stronger heterogeneous fluctuations in field response. Periodic boundary conditions are also preferable to minimal boundary conditions because the latter extremely exaggerate response and result in stronger and earlier localization than would be expected *in-situ*.
- The implemented second-gradient continuum model for representing the coarse scale response was demonstrated to have convergent accuracy for elastic cases and demonstrates qualitatively credible and convergent response for inelastic cases.
- Inelastic length scale parameters in nonlocal models are a reflection of both the strength of long range gradients at the coarse scale and size and spatial distribution characteristics at the fine scale. Therefore, these parameters are not intrinsic material properties that can be determined directly from fine scale numerical simulations.
- Principal component analysis can be used to identify an efficient set of ISVs and basis functions that project these ISVs across the fine scale domain to represent the non-

uniform evolution of heterogeneous microstructure. The evolution of ISVs computed in this manner can be accurately modeled employing artificial neural networks.

8.4 Future Work

Throughout the dissertation, the scope of the work has been focused on developing the multiscale framework for modeling microstructure evolution in heterogeneous materials, implementing the framework in numerical models, and application of these models to example problems for obtaining results that highlight the intended approach. There are a few areas uncovered by this research that would provide fruitful research in the future. Directions for future research include further investigation of the nature of length scale parameters associated with nonlocal response. Ideally, this work would develop schemes which modify the inelastic length scale parameter based on the evolution of global response characteristics and provide a conceptual understanding of the physical mechanisms influencing this evolution. Additionally, further development of approaches to compute ISVs directly from fine scale simulations using principal component analysis and subsequent coarse scale modeling of their evolution using artificial neural networks would enhance the framework developed here. Finally, application of this framework to actual materials and validation against experimental data presents an area that will surely reveal additional enhancements through time. For example, this work would likely require the extension of developed codes and techniques to three dimensions.

APPENDIX A

DETAILS OF SECOND GRADIENT FINITE ELEMENT IMPLEMENTATION

The basic computational structure of the second gradient UEL used at the coarse scale and details of the particular element formulation are provided in this appendix. A diagram of the element and its nodal connectivity, nodal degrees of freedom, and integration points is shown in Figure 136. The element is a nine-node, two-dimensional, plane-deformation quadrilateral with quadratic interpolation of displacements, $\mathbf{u}$, linear interpolation of the mixed-field relaxed deformation gradient, $\hat{\mathbf{F}}$, and constant interpolation of Lagrange multiplier, $\boldsymbol{\lambda}$. The finite element equations, as derived in Section 5.1, are based on a total Lagrangian formulation. This provides a conceptual consistency with the theoretical framework developed in Chapter 3 and numerical homogenization outlined in Chapter 4, especially regarding the scale invariance of various quantities with respect to an *undeformed* reference configuration.

Notable arguments passed into the subroutine are a set of properties, an array of nodal coordinates, X_{Ki}^{o}, an array of solution variables, U_{Ki}, and an array of solution dependent internal variables. The user subroutine returns the element's contribution to the residual force vector and system Jacobian, and updates the solution dependent variables as necessary. Integration required for computing an element's contribution to the residual forces and system Jacobian is performed by Gauss quadrature with a total of four integration points whose isoparametric coordinates and quadrature weights are listed in the table on the right side of Figure 136.

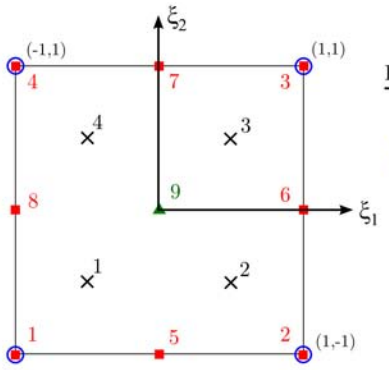

Gauss Points, Coord and Weight		
ξ_1	ξ_2	W
$-\frac{1}{\sqrt{3}}$	$-\frac{1}{\sqrt{3}}$	1.0
$\frac{1}{\sqrt{3}}$	$-\frac{1}{\sqrt{3}}$	1.0
$\frac{1}{\sqrt{3}}$	$\frac{1}{\sqrt{3}}$	1.0
$-\frac{1}{\sqrt{3}}$	$\frac{1}{\sqrt{3}}$	1.0

Figure 136. (L) Diagram of element's node connectivity and integration points in isoparametric coordinate system. (R) Table of integration point coordinates and weights.

Upon the initial call to the subroutine the residual force and Jacobian arrays are set to zero. The subroutine loops over each of the four integration points following the computational steps outlined below. Values for the element shape functions are computed using (A1.1), (A1.2), and (A1.3).

$$\begin{array}{l|l} {}^{u}N_1 = \frac{1}{4}(1-\xi_1)(1-\xi_2) - \frac{1}{2}({}^{u}N_8 + {}^{u}N_5) & {}^{u}N_5 = \frac{1}{2}(1-\xi_1^2)(1-\xi_2) \\ {}^{u}N_2 = \frac{1}{4}(1+\xi_1)(1-\xi_2) - \frac{1}{2}({}^{u}N_5 + {}^{u}N_6) & {}^{u}N_6 = \frac{1}{2}(1+\xi_1)(1-\xi_2^2) \\ {}^{u}N_3 = \frac{1}{4}(1+\xi_1)(1+\xi_2) - \frac{1}{2}({}^{u}N_6 + {}^{u}N_7) & {}^{u}N_7 = \frac{1}{2}(1-\xi_1^2)(1+\xi_2) \\ {}^{u}N_4 = \frac{1}{4}(1-\xi_1)(1+\xi_2) - \frac{1}{2}({}^{u}N_7 + {}^{u}N_8) & {}^{u}N_8 = \frac{1}{2}(1-\xi_1)(1-\xi_2^2) \end{array} \tag{A1.1}$$

$$\begin{aligned} {}^{\hat{F}}N_1 &= \tfrac{1}{4}(1-\xi_1)(1-\xi_2) \\ {}^{\hat{F}}N_2 &= \tfrac{1}{4}(1+\xi_1)(1-\xi_2) \\ {}^{\hat{F}}N_3 &= \tfrac{1}{4}(1+\xi_1)(1+\xi_2) \\ {}^{\hat{F}}N_4 &= \tfrac{1}{4}(1-\xi_1)(1+\xi_2) \end{aligned} \tag{A1.2}$$

$${}^{\lambda}N_9 = 1 \tag{A1.3}$$

The element shape function derivatives with respect to isoparametric coordinates, given by equations (A1.4) and (A1.5), are then computed.

$$ {}^{u}N'_{iJ} = \frac{\partial\, {}^{u}N_J}{\partial \xi_i} $$

${}^{u}N'_{11} = \frac{1}{4}(1-\xi_2)(2\xi_1+\xi_2)$	${}^{u}N'_{21} = \frac{1}{4}(1-\xi_1)(2\xi_2+\xi_1)$
${}^{u}N'_{12} = \frac{1}{4}(1-\xi_2)(2\xi_1-\xi_2)$	${}^{u}N'_{22} = \frac{1}{4}(1+\xi_1)(2\xi_2-\xi_1)$
${}^{u}N'_{13} = \frac{1}{4}(1+\xi_2)(2\xi_1+\xi_2)$	${}^{u}N'_{23} = \frac{1}{4}(1+\xi_1)(2\xi_2+\xi_1)$
${}^{u}N'_{14} = \frac{1}{4}(1+\xi_2)(2\xi_1-\xi_2)$	${}^{u}N'_{24} = \frac{1}{4}(1-\xi_1)(2\xi_2-\xi_1)$
${}^{u}N'_{15} = -\xi_1(1-\xi_2)$	${}^{u}N'_{25} = -\frac{1}{2}(1+\xi_1)(1-\xi_1)$
${}^{u}N'_{16} = \frac{1}{2}(1+\xi_2)(1-\xi_2)$	${}^{u}N'_{26} = -\xi_2(1+\xi_1)$
${}^{u}N'_{17} = -\xi_1(1+\xi_2)$	${}^{u}N'_{27} = \frac{1}{2}(1+\xi_1)(1-\xi_1)$
${}^{u}N'_{18} = -\frac{1}{2}(1+\xi_2)(1-\xi_2)$	${}^{u}N'_{28} = -\xi_2(1-\xi_1)$

(A1.4)

$$ {}^{\hat{F}}N'_{iJ} = \frac{\partial\, {}^{\hat{F}}N_J}{\partial \xi_i} $$

${}^{\hat{F}}N'_{11} = -(1-\xi_2)$	${}^{\hat{F}}N'_{21} = -(1-\xi_1)$
${}^{\hat{F}}N'_{12} = (1-\xi_2)$	${}^{\hat{F}}N'_{22} = -(1+\xi_1)$
${}^{\hat{F}}N'_{13} = (1+\xi_2)$	${}^{\hat{F}}N'_{23} = (1+\xi_1)$
${}^{\hat{F}}N'_{14} = -(1+\xi_2)$	${}^{\hat{F}}N'_{24} = (1-\xi_1)$

(A1.5)

The local element map from isoparametric coordinates to physical coordinates (i.e., integration point Jacobian) is computed as

$$ J_{ij} \equiv \frac{\partial X^{\circ}_i}{\partial \xi_j} = {}^{u}N'_{jK} X^{\circ}_{Ki} \tag{A1.6} $$

An integration quotient for the integration point is computed as,

$$ q\big(\xi_1, \xi_2\big) = W \det(\mathbf{J}) \tag{A1.7} $$

Then the shape function derivatives with respect to physical coordinates are computed, i.e.,

$$ \begin{aligned} {}^{u}\beta_{iJ} &= \frac{\partial\, {}^{u}N_J}{\partial \xi_i} = J^{-1}_{ki}\, {}^{u}N'_{kJ} \\ {}^{\hat{F}}\beta_{iJ} &= \frac{\partial\, {}^{\hat{F}}N_J}{\partial \xi_i} = J^{-1}_{ki}\, {}^{\hat{F}}N'_{kJ} \end{aligned} \tag{A1.8} $$

The displacement gradient, $\mathbf{H}$, deformation gradient, $\mathbf{F}$, and second gradient, $\mathbf{G}$, are computed by (A1.9)-(A1.11), respectively.

$$ H_{ij} = {}^{u}\beta_{jK} U_{Ki} \tag{A1.9} $$

$$F_{ij} = \delta_{ij} + H_{ij} \tag{A1.10}$$

$$\begin{aligned} \hat{G}_{ijk} &= {}^{\hat{F}}\beta_{kA}\hat{F}_{Aij} \\ G_{ijk} &= \tfrac{1}{2}\left(\hat{G}_{ijk} + \hat{G}_{ikj}\right) \end{aligned} \tag{A1.11}$$

Additionally, an error metric indicating the lack of symmetry in gradient of the relaxed deformation gradient field is defined and computed as

$${}^{G}\text{Error}_{ijk} = \tfrac{1}{2}\left(\hat{G}_{ijk} - \hat{G}_{ikj}\right) \tag{A1.12}$$

At which point the deformation gradient and second gradient are passed as arguments to the constitutive update subroutine which returns the nominal stress, $\mathbf{P}$, and second order stress, $\mathbf{Q}$, as well as the constitutive tangent stiffness tensors $C^{PF}_{ijkl}, C^{PG}_{ijklm}, C^{QF}_{ijklm}, C^{QG}_{ijklmn}$. Finally, coefficients in the residual force vector are updated according to

$$\begin{aligned} {}^{u}r_{iA} &= {}^{u}r_{iA} + q\left(P_{ki} - \lambda_{ki}\right){}^{u}\beta_{kA} \\ {}^{\hat{F}}r_{ijA} &= {}^{\hat{F}}r_{ijA} + q\left(Q_{ijk}\,{}^{u}\beta_{kA} + \lambda_{ji}\,{}^{\hat{F}}N_{A}\right) \end{aligned} \tag{A1.13}$$

and the element's contribution to the system Jacobian is updated

$$\begin{aligned} K^{uu}_{AiBk} &= K^{uu}_{AiBk} + q\,{}^{u}\beta_{jA}C^{PF}_{jikl}\,{}^{u}\beta_{lB} \\ K^{u\lambda}_{AiBnm} &= K^{u\lambda}_{AiBnm} - q\,{}^{u}\beta_{jA}\,{}^{\lambda}N_{B}\delta_{jm}\delta_{mi} \\ K^{\hat{F}\hat{F}}_{AijBnm} &= K^{\hat{F}\hat{F}}_{AijBnm} + q\,{}^{F}\beta_{iA}C^{QG}_{ijklmn}\,{}^{F}\beta_{lB} \\ K^{\hat{F}\lambda}_{AijBnm} &= K^{\hat{F}\lambda}_{AijBnm} + q\,{}^{\lambda}N_{B}\,{}^{F}N_{A}\delta_{jn}\delta_{im} \\ K^{\lambda\lambda}_{AijBnm} &= K^{\lambda\lambda}_{AijBnm} - \frac{q}{\alpha}\delta_{jn}\delta_{im}\,{}^{\lambda}N_{A}\,{}^{\lambda}N_{B} \end{aligned} \tag{A1.14}$$

$$\begin{aligned} K^{\hat{F}u}_{AijBn} &= K^{\hat{F}u}_{AijBn} + q\,{}^{F}\beta_{iA}C^{QF}_{ijknm}\,{}^{u}\beta_{mB} \\ K^{u\hat{F}}_{AiBkl} &= K^{u\hat{F}}_{AiBkl} + q\,{}^{u}\beta_{jA}C^{PG}_{jiklm}\,{}^{F}\beta_{mB} \end{aligned}$$

where the terms below the line have been shown through the course of this work to be negligible compared to those above the line. Accordingly terms below the line in Eq. (A1.14) were generally neglected for improved computational efficiency. This is repeated for each integration point and then the element's total contribution to the system residual force vector and jacobian matrix are returned from the user subroutine to Abaqus' internal solver.

REFERENCES

Abaqus (2007). Abaqus. Providence, RI, DS Simulia Corp.

Abu Al-Rub, R. K. and G. Z. Voyiadjis (2003). "On the coupling of anisotropic damage and plasticity models for ductile materials." International Journal of Solids and Structures **40**(11): 2611-43.

Amanatidou, E. and N. Aravas (2002). "Mixed finite element formulations of strain-gradient elasticity problems." Computer Methods in Applied Mechanics and Engineering **191**(15-16): 1723-51.

Amieur, M., S. Hazanov and C. Huet (1993). Numerical and experimental study of size and boundary-condition effects on the apparent properties of specimens not having the representative volume. Micromechanics of Concrete and Cementitious Composites, Lausanne, Switzerland.

Aravas, N. (1994). "Finite-strain anisotropic plasticity and the plastic spin." Modelling and Simulation in Materials Science and Engineering **2**(3A): 483-504.

Austin, R. A., D. L. McDowell and D. J. Benson (2006). "Numerical simulation of shock wave propagation in spatially-resolved particle systems." Modelling and Simulation in Materials Science and Engineering **14**(4): 537-61.

Babalievski, F. (1998). "Cluster counting: the Hoshen-Kopelman algorithm versus spanning tree approaches." International Journal of Modern Physics C **9**(1): 43-60.

Belytschko, T., W. Liu and B. Moran (2000). Nonlinear Finite Elements for Continua and Structures. Chichester, Wiley.

Berryman, J. G. (1985). "Measurement of spatial correlation functions using image processing techniques." Journal of Applied Physics **57**(7): 2374-84.

Blume, J. A. (1989). "Compatibility conditions for a left Cauchy-Green strain field." Journal of Elasticity **21**(3): 271-308.

Braides, A., A. J. Lew and M. Ortiz (2006). "Effective cohesive behavior of layers of interatomic planes." Archive for Rational Mechanics and Analysis **180**(2): 151-82.

Bridgman, P. W. (1941). Nature of thermodynamics, Harvard University Press, Cambridge, Mass, 1941.

Bronkhorst, C. A., E. K. Cerreta, Q. Xue, P. J. Maudlin, T. A. Mason and G. T. Gray Iii (2006). "An experimental and numerical study of the localization behavior of tantalum and stainless steel." International Journal of Plasticity **22**(7): 1304-1335.

Bronkhorst, C. A., B. L. Hansen, E. K. Cerreta and J. F. Bingert (2007). "Modeling the microstructural evolution of metallic polycrystalline materials under localization conditions." Journal of the Mechanics and Physics of Solids **55**(11): 2351-2383.

Carrere, N., R. Valle, T. Bretheau and J. L. Chaboche (2004). "Multiscale analysis of the transverse properties of Ti-based matrix composites reinforced by SiC fibres: from the grain scale to the macroscopic scale." International Journal of Plasticity **20**(4/5): 783-810.

Chambon, R., D. Caillerie and T. Matsuchima (2001). "Plastic continuum with microstructure, local second gradient theories for geomaterials: localization studies." International Journal of Solids and Structures **38**(46-47): 8503-27.

Chambon, R., D. Caillerie and C. Tamagnini (2004). "A strain space gradient plasticity theory for finite strain." Computer Methods in Applied Mechanics and Engineering **193**(27-29): 2797-2826.

Chawla, N., V. V. Ganesh and B. Wunsch (2004). "Three-dimensional (3D) microstructure visualization and finite element modeling of the mechanical behavior of SiC particle reinforced aluminum composites." Scripta Materialia **51**(2): 161-5.

Chen, Z. T. and S. W. Yu (1998). On the dynamic ductile damage and fragmentation in porous metallic materials. Key Engineering Materials, Switzerland, Trans Tech Publications.

Choi, K. S. and J. Pan (2009). "A generalized anisotropic hardening rule based on the Mroz multi-yield-surface model for pressure insensitive and sensitive materials." International Journal of Plasticity **25**(7): 1325-58.

Chu, C. C. and A. Needleman (1980). "Void nucleation effects in biaxially stretched sheets." Transactions of the ASME. Journal of Engineering Materials and Technology **102**(3): 249-56.

Clayton, J. D. (2005). "Dynamic plasticity and fracture in high density polycrystals: Constitutive modeling and numerical simulation." Journal of the Mechanics and Physics of Solids **53**(2): 261-301.

Clayton, J. D. (2006). "Continuum multiscale modeling of finite deformation plasticity and anisotropic damage in polycrystals." Theoretical and Applied Fracture Mechanics **45**(3): 163-185.

Clayton, J. D. and D. L. McDowell (2003). "A multiscale multiplicative decomposition for elastoplasticity of polycrystals." International Journal of Plasticity **19**(9): 1401-1444.

Clayton, J. D. and D. L. McDowell (2004). "Homogenized finite elastoplasticity and damage: Theory and computations." Mechanics of Materials **36**(9): 799-824.

Clements, B. E., E. M. Mas, J. N. Plohr, A. Ionita and F. L. Addessio (2006). "Dynamic response of PBX-9501 through the β-δ phase transition." AIP Conference Proceedings **845**(1): 204-7.

Coker, D. A. and S. Torquato (1995). "Extraction of morphological quantities from a digitized medium." Journal of Applied Physics **77**(12): 6087-99.

Copeland, A. C., G. Ravichandran and M. M. Trivedi (2001). "Texture synthesis using gray-level co-occurrence models: Algorithms, experimental analysis, and psychophysical support." Optical Engineering **40**(11): 2655-2673.

Corson, P. B. (1974a). "Correlation functions for predicting properties of heterogeneous materials. I. Experimental measurement of spatial correlation functions in multiphase solids." Journal of Applied Physics **45**(7): 3159-64.

Corson, P. B. (1974b). "Correlation functions for predicting properties of heterogeneous materials. II. Empirical construction of spatial correlation functions for two-phase solids." Journal of Applied Physics **45**(7): 3165-70.

Cosserat, E. and F. Cosserat (1909). Théorie des corps déformables. Paris.

Cubit (2008). Cubit 11.1. Albuquerque, Sandia National Laboratories.

Cule, D. and S. Torquato (1999). "Generating random media from limited microstructural information via stochastic optimization." Journal of Applied Physics **86**(6): 3428-37.

Dafalias, Y. F. (1998). "Plastic spin: Necessity or redundancy?" International Journal of Plasticity **14**(9): 909-931.

Eidel, B. and F. Gruttmann (2003). "Elastoplastic orthotropy at finite strains: Multiplicative formulation and numerical implementation." Computational Materials Science **28**(3-4 SPEC. ISS.): 732-742.

Enakoutsa, K. and J. B. Leblond (2009). "Numerical implementation and assessment of the GLPD micromorphic model of ductile rupture." European Journal of Mechanics, A/Solids **28**(3): 445-60.

Eringen, A. C. (1999). Microcontinuum field theories, Springer, c1999-.

Exner, H. (2004). "Stereology and 3D Microscopy: Useful alternatives or competitiors in the quantitative analysis of microstructures?" Image Analysis and Stereology **23**: 73-82.

Fleck, N. A. and J. W. Hutchinson (1993). "A phenomenological theory for strain gradient effects in plasticity." Journal of the Mechanics and Physics of Solids **41**(12): 1825-57.

Fleck, N. A. and J. W. Hutchinson (1997). "Strain gradient plasticity

" Advances in Applied Mechanics **33**: 295-361.

Gall, K., M. Horstemeyer, D. L. McDowell and J. H. Fan (2000a). "Finite element analysis of the stress distributions near damaged Si particle clusters in cast Al-Si alloys." Mechanics of Materials **32**(5): 277-301.

Gall, K., M. F. Horstemeyer, B. W. Degner, D. L. McDowell and J. H. Fan (2001). "On the driving force for fatigue crack formation from inclusions and voids in a cast A356 aluminum alloy." International Journal of Fracture **108**(3): 207-233.

Gall, K., M. F. Horstemeyer, M. Van Schilfgaarde and M. I. Baskes (2000b). "Atomistic simulations on the tensile debonding of an aluminum-silicon interface." Journal of the Mechanics and Physics of Solids **48**(10): 2183-212.

Garikipati, K. and T. J. R. Hughes (2000). "A variational multiscale approach to strain localization formulation for multidimensional problems." Computer Methods in Applied Mechanics and Engineering **188**(1-3): 39-60.

Garmestani, H., S. Lin, B. L. Adams and S. Ahzi (2001). "Statistical continuum theory for large plastic deformation of polycrystalline materials." Journal of the Mechanics and Physics of Solids **49**(3): 589-607.

Gegner, J. (2006). 2D-3D conversion of object size distributions in quantitative metallography. The Fourth International Conference on Mathematical Modeling and Computer Simulation of Materials Technologies. Ariel, Israel. **3:** 138-147.

Germain, P. (1973). "The method of virtual power in the mechanics of continuous media. I. The second gradient theory." Journal de Mecanique **12**(2): 235-74.

Germain, P., Q. S. Nguyen and P. Suquet (1983). "Continuum thermodynamics." Transactions of the ASME. Journal of Applied Mechanics **50**(4B): 1010-20.

Ghosh, S., J. Bai and P. Raghavan (2007). "Concurrent multi-level model for damage evolution in micro structurally debonding composites." Mechanics of Materials **39**(3): 241-266.

Ghosh, S., K. Lee and P. Raghavan (2001). "A multi-level computational model for multi-scale damage analysis in composite and porous materials." International Journal of Solids and Structures **38**(14): 2335-85.

Gokhale, A. M., A. Tewari and H. Garmestani (2005). "Constraints on microstructural two-point correlation functions." Scripta Materialia **53**(8): 989-93.

Graham-Brady, L. and X. F. Xu (2008). "Stochastic morphological modeling of random multiphase materials." Journal of Applied Mechanics, Transactions ASME **75**(6):

Gross, D. and L. Mo (2002). "Constructing microstructures of poly- and nanocrystalline materials for numerical modeling and simulation." Applied Physics Letters **80**(5): 746-8.

Gurson, A. L. (1977). "Continuum theory of ductile rupture by void nucleation and growth. I. Yield criteria and flow rules for porous ductile media." Transactions of the ASME. Series H, Journal of Engineering Materials and Technology **99**(1): 2-15.

Gurtin, M. E. and L. Anand (2005). "A theory of strain-gradient plasticity for isotropic, plastically irrotational materials. Part I: Small deformations." Journal of the Mechanics and Physics of Solids **53**(7): 1624-49.

Hao, S., W. K. Liu, B. Moran, F. Vernerey and G. B. Olson (2004). "Multi-scale constitutive model and computational framework for the design of ultra-high strength, high toughness steels." Computer Methods in Applied Mechanics and Engineering **193**(17-20): 1865-1908.

Hashin, Z. (1961). Elastic moduli of heterogeneous materials. American Society of Mechanical Engineers -- Papers, New York, NY, United States, American Society of Mechanical Engineers (ASME).

Hasselman, D. P. H. (1962). "On the porosity dependence of the elastic moduli of polycrystalline refractory materials." Journal of the American Ceramic Society **45**(9): 452-453.

Hazanov, S. and M. Amieur (1995). "On overall properties of elastic heterogeneous bodies smaller than the representative volume." International Journal of Engineering Science **33**(9): 1289-301.

Hill, R. (1972). "Constitutive macro-variables for heterogeneous solids at finite strain." Proceedings of the Royal Society of London Series A - Mathematical and Physical Sciences **326**(1565): 131-.

Hill, T. (1987). Statistical Mechanics: Principles and Selected Applications. New York, Dover.

Hodowany, J., G. Ravichandran, A. J. Rosakis and P. Rosakis (2000). "Partition of plastic work into heat and stored energy in metals." Experimental Mechanics **40**(2): 113-23.

Hoshen, J. (1999). "The application of the enhanced Hoshen-Kopelman algorithm for processing unbounded images." IEEE Transactions on Image Processing **8**(3): 421-5.

Hoshen, J. and R. Kopelman (1976). "Percolation and cluster distribution. I. Cluster multiple labelling technique and critical concentration algorithm." Physical Review B (Solid State) **14**(8): 3438-45.

Houlsby, G. T. and A. M. Puzrin (2006). Principles of Hyperplasticity: An Approach to Plasticity Theory Based on Thermodynamic Principles. London, Springer-Verlag.

Hughes, T. J. R. and G. Sangalli (2007). "Variational multiscale analysis: The fine-scale green's function, projection, optimization, localization, and stabilized methods." SIAM Journal on Numerical Analysis **45**(2): 539-557.

Ionita, A., E. M. Mas and B. E. Clements (2006). Two-scale FEM in the dynamic response of a heterogeneous material. AIP Conference Proceedings, Melville, NY, American Institute Physics.

Ionita, A. and Y. J. Weitsman (2006). "Randomly reinforced composites: Properties, failure and aspects of material design." Probabilistic Engineering Mechanics **21**(1): 64-72.

Jefferson, G., H. Garmestani, R. Tannenbaum, A. Gokhale and E. Tadd (2005). "Two-point probability distribution function analysis of Co-polymer nano-composites." International Journal of Plasticity **21**(1): 185-98.

Jou, D., J. Casasvazquez and G. Lebon (1988). "Extended irreversible thermodynamics." Reports on Progress in Physics **51**(8): 1105-79.

Kaczmarczyk, L., C. J. Pearce and N. Bicanic (2008). "Scale transition and enforcement of RVE boundary conditions in second-order computational homogenization." International Journal for Numerical Methods in Engineering **74**(3): 506-522.

Kadowaki, H. and W. K. Liu (2004). "Bridging multi-scale method for localization problems." Computer Methods in Applied Mechanics and Engineering **193**(30-32): 3267-3302.

Kestin, J. (1992). "Local-equilibrium formalism applied to mechanics of solids." International Journal of Solids and Structures **29**(14-15): 1827-1836.

Kestin, J. (1993). "Internal variables in the local-equilibrium approximation." Journal of Non-Equilibrium Thermodynamics **18**(4): 360-79.

Khoei, A. R. and N. Jamali (2005). "On the implementation of a multi-surface kinematic hardening plasticity and its applications." International Journal of Plasticity **21**(9): 1741-1770.

Kouznetsova, V. (2002). Computational homogenization for the multi-scale analysis of multi-phase materials. Eindhoven, The Netherlands, Eindhoven : Technische Universiteit.

Kouznetsova, V., M. G. D. Geers and W. A. M. Brekelmans (2002). "Multi-scale constitutive modelling of heterogeneous materials with a gradient-enhanced computational homogenization scheme." International Journal for Numerical Methods in Engineering **54**(8): 1235-60.

Kouznetsova, V. G., M. G. D. Geers and W. A. M. Brekelmans (2004). "Multi-scale second-order computational homogenization of multi-phase materials: a nested finite element solution strategy." Computer Methods in Applied Mechanics and Engineering **193**(48/51): 5525-50.

Kroshko, D. L. (2008). OpenOpt. Ukraine, National Academy of Sciences of Ukraine.

Kumar, R. S., A. J. Wang and D. L. McDowell (2006). "Effects of microstructure variability on intrinsic fatigue resistance of nickel-base superalloys - A computational micromechanics approach." Internaitonal Journal of Fracture **137**(1-4): 173-210.

Kwon, Y. W. (2004). "Multi-scale modeling of mechanical behavior of polycrystalline materials." Journal of Computer-Aided Materials Design **11**(1): 43-57.

Lacy, T. E., D. L. McDowell and R. Talreja (1999). "Gradient concepts for evolution of damage." Mechanics of Materials **31**(12): 831-60.

Larsson, R. and S. Diebels (2007). "A second-order homogenization procedure for multi-scale analysis based on micropolar kinematics." International Journal for Numerical Methods in Engineering **69**(12): 2485-2512.

Lebon, G., J. Casasvazquez, D. Jou and M. Criadosancho (1993). "Polymer solutions and chemical reactions under flow: a thermodynamic description." Journal of Chemical Physics **98**(9): 7434-9.

Lemaitre, J. (1998). A Course on Damage Mechanics. Berlin, Springer Verlag.

Lemaitre, J. and J.-L. Chaboche (1990). Mechanics of solid materials. Cambridge, Cambridge University Press, 1990.

Liu, W. K., E. G. Karpov, S. Zhang and H. S. Park (2004). "An introduction to computational nanomechanics and materials." Computer Methods in Applied Mechanics and Engineering **193**(17/20): 1529-78.

Liu, W. K. and C. McVeigh (2008). "Predictive multiscale theory for design of heterogeneous materials." Computational Mechanics **42**: 147-170.

Liu, W. K., H. S. Park, D. Qian, E. G. Karpov, H. Kadowaki and G. J. Wagner (2006). "Bridging scale methods for nanomechanics and materials." Computer Methods in Applied Mechanics and Engineering **195**(13-16): 1407-1421.

Lundh, F. (2005). Python Imaging Library Documentation. LINKÖPING, Secret Labs AB, Sweden.

Luo, J. and R. Stevens (1996). "Micromechanics of randomly oriented ellipsoidal inclusion composites. II. Elastic moduli." Journal of Applied Physics **79**(12): 9057-63.

Luo, J. and R. Stevens (1999). "Porosity-dependence of elastic moduli and hardness of 3Y-TZP ceramics." Ceramics International **25**(3): 281-286.

Markovic, D., A. Ibrahimbegovica, R. Niekampc and H. Matthiesc (2004). "A multi-scale finite element model for inelastic behavior of heterogeneous structures and its parallel computing implementation."

Mas, E. M., B. E. Clements, A. Ionita and P. Peterson (2006). "Finite element method calculations on statistically consistent microstructures of PBX 9501." AIP Conference Proceedings **845**(1): 487-90.

Matsushima, T., R. Chambon and D. Caillerie (2002). "Large strain finite element analysis of a local second gradient model: application to localization." International Journal for Numerical Methods in Engineering **54**(4): 499-521.

McDowell, D. L. (1989). "Evaluation of intersection conditions for two-surface plasticity theory." International Journal of Plasticity **5**(1): 29-50.

McDowell, D. L. (1997). Multiple Scales and Averaging Concepts for ISV Theories. Proc. Plasticity '97: 6th Int. Symp. on Plasticity and its Current Applications, Physics and Mechanics of Finite Plastic and Viscoplastic Deformation, Juneau, Alaska.

McDowell, D. L. (2005). Internal State Variable Theory. Handook of Materials Modeling, Part A: Methods. S. Yip and M. F. Horstemeyer. The Netherlands, Springer**:** 1151-1170.

McVeigh, C., F. Vernerey, W. K. Liu and L. C. Brinson (2006). "Multiresolution analysis for material design." Computer Methods in Applied Mechanics and Engineering **195**(37-40): 5053-5076.

McVeigh, C., F. Vernerey, W. K. Liu, B. Moran and G. Olson (2007). "An interactive micro-void shear localization mechanism in high strength steels." Journal of the Mechanics and Physics of Solids **55**(2): 225-244.

Mesarovic, S. D. and J. Padbidri (2005). "Minimal kinematic boundary conditions for simulations of disordered microstructures." Philosophical Magazine **85**(1): 65-78.

Mindlin, R. D. (1964). "Micro-Structure in Linear Elasticity." Archive for Rational Mechanics and Analysis **16**(1): 51-78.

Molinari, A. and S. Mercier (2001). "Micromechanical modelling of porous materials under dynamic loading." Journal of the Mechanics and Physics of Solids **49**(7): 1497-1516.

Montans, F. J. (2000). "Implicit algorithms for multilayer J2-plasticity." Computer Methods in Applied Mechanics and Engineering **189**(2): 673-700.

Montans, F. J. and M. A. Caminero (2007). "On the consistency of nested surfaces models and their kinematic hardening rules." International Journal of Solids and Structures **44**(14-15): 5027-5042.

NIST (2008). OOF: Finite Element Analysis of Microstructures. Gaithersburg, MD, US National Institute of Standards and Technology.

Ostoja-Starzewski, M. (1998). "Random field models of heterogeneous materials." International Journal of Solids and Structures **35**(19): 2429-55.

Ostoja-Starzewski, M. (2006). "Material spatial randomness: From statistical to representative volume element." Probabilistic Engineering Mechanics **21**(2): 112-132.

Otsu, N. (1979). "A threshold selection method from gray-level histograms." IEEE Transactions on Systems, Man and Cybernetics **SMC-9**(1): 62-6.

Pardoen, T. and J. W. Hutchinson (2000). "An extended model for void growth and coalescence." Journal of the Mechanics and Physics of Solids **48**(12): 2467-512.

Park, H. S., E. G. Karpov and W. K. Liu (2004). "A temperature equation for coupled atomistic/continuum simulations." Computer Methods in Applied Mechanics and Engineering **193**(17/20): 1713-32.

Reusch, F., C. Hortig and B. Svendsen (2008). "Nonlocal modeling and simulation of ductile damage and failure in metal matrix composites." Journal of Engineering Materials and Technology **130**(2): 021009-1-7.

Rice, J. R. (1971). "Inelastic constitutive relations for solids: an internal-variable theory and its application to metal plasticity." Journal of the Mechanics and Physics of Solids **19**(6): 433-55.

Roache, P. (1998). Verification and Validation in Computational Science and Engineering. Albuquerque, Hermosa.

Rong, F., H. Y. Wang, M. F. Xia, F. J. Ke and Y. L. Bai (2006). "Catastrophic rupture induced damage coalescence in heterogeneous brittle media." Pure and Applied Geophysics **163**(9): 1847-1865.

Rosakis, P., A. J. Rosakis, G. Ravichandran and J. Hodowany (2000). "Thermodynamic internal variable model for the partition of plastic work into heat and stored energy in metals." Journal of the Mechanics and Physics of Solids **48**(3): 581-607.

Rozman, M. G. and M. Utz (2001). "Efficient reconstruction of multiphase morphologies from correlation functions." Physical Review E (Statistical, Nonlinear, and Soft Matter Physics) **63**(6): 066701-2.

Saheli, G., H. Garmestani and B. L. Adams (2004). "Microstructure design of a two phase composite using two-point correlation functions." Journal of Computer-Aided Materials Design **11**(2-3): 103-15.

Santaoja, K. (2002). "Evaluation of the Gurson-Tvergaard material model by using damage mechanics and thermomechanics." Proceedings of the Estonian Academy of Sciences **8**(4): 248-269.

Serdyukov, S. I. (2004). "Generalization of the evolution criterion in extended irreversible thermodynamics." Physics Letters A **324**(4): 262-71.

Shan, Z. and A. M. Gokhale (2004). "Digital image analysis and microstructure modeling tools for microstructure sensitive design of materials." International Journal of Plasticity **20**(7): 1347-1370.

Sheehan, N. and S. Torquato (2001). "Generating microstructures with specified correlation functions." Journal of Applied Physics **89**(1): 53-60.

Shu, J. Y. and C. Y. Barlow (2000). "Strain gradient effects on microscopic strain field in a metal matrix composite." International Journal of Plasticity **16**(5): 563-591.

Shu, J. Y. and N. A. Fleck (1998). "Prediction of a size effect in micro-indentation." International Journal of Solids and Structures **35**(13): 1363-1383.

Shu, J. Y., W. E. King and N. A. Fleck (1999). "Finite elements for materials with strain gradient effects." International Journal for Numerical Methods in Engineering **44**(3): 373-391.

Siad, L., M. Ould Ouali and A. Benabbes (2008). "Comparison of explicit and implicit finite element simulations of void growth and coalescence in porous ductile materials." Materials and Design **29**(2): 319-329.

Simo, J. C., J. G. Kennedy and S. Govindjee (1988). "Non-smooth multisurface plasticity and viscoplasticity. Loading/unloading conditions and numerical algorithms." International Journal for Numerical Methods in Engineering **26**(10): 2161-85.

Smyshlyaev, V. P. and N. A. Fleck (1996). "The role of strain gradients in the grain size effect for polycrystals." Journal of the Mechanics and Physics of Solids **44**(4): 465-95.

Spearot, D. E., K. I. Jacob and D. L. McDowell (2004). "Non-local separation constitutive laws for interfaces and their relation to nanoscale simulations." Mechanics of Materials **36**(9): 825-847.

Stroeven, M., H. Askes and L. J. Sluys (2004). "Numerical determination of representative volumes for granular materials." Computer Methods in Applied Mechanics and Engineering **193**(30-32): 3221-3238.

Stummel, F. (1980). "Limitations of the patch test." Int J Numer Methods Eng **15**(2): 177-188.

Terada, K., M. Hori, T. Kyoya and N. Kikuchi (2000). "Simulation of the multi-scale convergence in computational homogenization approaches." International Journal of Solids and Structures **37**(16): 2285-2311.

Thomason, P. (1990). Ductile fracture of metals, Pergamon Press, Oxford.

Torquato, S. (2001). Random Heterogeneous Materials: Microstructure and Macroscopic Properties. New York, Springer-Verlag.

Torquato, S. and G. Stell (1982). "Microstructure of two-phase random media. I. The n-point probability functions." Journal of Chemical Physics **77**(4): 2071-7.

Toupin, R. A. (1963). "Elastic materials with couple-stresses." Archive for Rational Mechanics and Analysis **11**(5): 385-414.

Tu, X., J. E. Andrade and Q. Chen (2009). "Return mapping for nonsmooth and multiscale elastoplasticity." Computer Methods in Applied Mechanics and Engineering **198**(30-32): 2286-2296.

Tvergaard, V. and A. Needleman (1984). "Analysis of the cup-cone fracture in a round tensile bar." Acta Metallurgica **32**(1): 157-69.

Une, K., K. Nogita, T. Shiratori and K. Hayashi (2001). "Rim structure formation of isothermally irradiated UO-2/ fuel discs." Journal of Nuclear Materials **288**(1): 20-28.

van der Sluis, O., P. J. G. Schreurs, W. A. M. Brekelmans and H. E. H. Meijer (2000). "Overall behaviour of heterogeneous elastoviscoplastic materials: Effect of microstructural modelling." Mechanics of Materials **32**(8): 449-462.

Vernerey, F. J., W. K. Liu, B. Moran and G. Olson (2008). "A micromorphic model for the multiple scale failure of heterogeneous materials." Journal of the Mechanics and Physics of Solids **56**(4): 1320-1347.

Voyiadjis, G. Z., B. Deliktas and E. C. Aifantis (2001). "Multiscale analysis of multiple damage mechanisms coupled with inelastic behavior of composite materials." Journal of Engineering Mechanics **127**(7): 636-645.

Wagner, G. J. and W. K. Liu (2003). "Coupling of atomistic and continuum simulations using a bridging scale decomposition." Journal of Computational Physics **190**(1): 249-74.

Wang, Z.-P. and C. T. Sun (2002). "Modeling micro-inertia in heterogeneous materials under dynamic loading." Wave Motion **36**(4): 473-485.

Wojciechowski, M. (2007). Feed-forward neural network for python, Technical University of Lodz (Poland).

Wojnar, L., K. J. Kurzydłowski and J. Szala (2004). ASM Handbook. Volume 9, Metallography and Microstructures: Quantitative Image Analysis, ASM International

Xia, L. and S. V. Hanagud (2007). "A nonequilibrium irreversible thermodynamics model for material damping." International Journal of Solids and Structures **44**(10): 3278-303.

Xia, Z. C. and J. W. Hutchinson (1996). "Crack tip fields in strain gradient plasticity." Journal of the Mechanics and Physics of Solids **44**(10): 1621-1648.

Xu, X. F. and L. Graham-Brady (2005). "A stochastic computational method for evaluation of global and local behavior of random elastic media." Computer Methods in Applied Mechanics and Engineering **194**(42-44): 4362-4385.

Yang, Q., X. Chen and W. Y. Zhou (2006). "On multiscale significance of Rice's normality structure." Mechanics Research Communications **33**(5): 667-73.

Yeong, C. L. Y. and S. Torquato (1998). "Reconstructing random media." Physical Review E (Statistical Physics, Plasmas, Fluids, and Related Interdisciplinary Topics) **57**(1): 495-506.

Yu, H. L., X. H. Liu and X. W. Li (2008). "FE analysis of inclusion deformation and crack generation during cold rolling with a transition layer." Materials Letters **62**(10-11): 1595-1598.

Zavattieri, P. D. and H. D. Espinosa (2001). "Grain level analysis of crack initiation and propagation in brittle materials." Acta Materialia **49**(20): 4291-311.

Zervos, A., P. Papanastasiou and I. Vardoulakis (2001). "A finite element displacement formulation for gradient elastoplasticity." International Journal for Numerical Methods in Engineering **50**(6): 1369-1388.

Zhai, J., V. Tomar and M. Zhou (2004). "Micromechanical simulation of dynamic fracture using the cohesive finite element method." Journal of Engineering Materials and Technology, Transactions of the ASME **126**(2): 179-191.

Zhang, Z. L., C. Thaulow and J. Odegard (2000). "A complete Gurson model approach for ductile fracture." Engineering Fracture Mechanics **67**(2): 155-68.

Zhao, Y. H., G. P. Tandon and G. J. Weng (1989). "Elastic-moduli for a class of porous materials." Acta Mechanica **76**(1-2): 105-130.

Zhou, M. (2003). "A new look at the atomic level virial stress: on continuum-molecular system equivalence." Proceedings of the Royal Society of London A **459**: 2347-2392.

Zhou, M. and D. L. McDowell (2002). "Equivalent continuum for dynamically deforming atomistic particle systems." Philosophical Magazine A: Physics of Condensed Matter, Structure, Defects and Mechanical Properties **82**(13): 2547-2574.

Ziegler, H. (1977). An introduction to thermomechanics, Amsterdam, Netherlands : North-Holland, 1977.

Zienkiewicz, O. C. and R. L. Taylor (1997). "Finite element patch test revisited. A computer test for convergence, validation and error estimates." Computer Methods in Applied Mechanics and Engineering **149**: 223-254.


Los Alamos
NATIONAL LABORATORY
EST. 1943